Thermal Characterization of a Pool Fire in Crosswind With and Without a Large Downwind Blocking Object

by

Cecilia S. Lam

A thesis
presented to the University of Waterloo
in fulfillment of the
thesis requirement for the degree of
Doctor of Philosophy
in
Mechanical Engineering

Waterloo, Ontario, Canada, 2009

I hereby declare that I am the sole author of this thesis. This is a true copy of the thesis, including any required final revisions, as accepted by my examiners.

I understand that my thesis may be made electronically available to the public.

Abstract

Experiments were conducted to investigate the macroscopic thermal behaviour of 2 m diameter Jet A fires in crosswinds of 3 m/s to 13 m/s. Two scenarios were considered: with and without a 2.7 m diameter, 10.8 m long, blocking object situated 3.4 m downwind of the fire. These scenarios simulated transportation accidents with the fire representing a burning pool of aviation fuel and the object simulating an aircraft fuselage. To date, the limited number of experiments that have been conducted to examine wind effects on fire behaviour have been performed at small scale, which does not fully simulate the physics of large fires, or in outdoor facilities, with poorly controlled wind conditions. This thesis presents the first systematic characterization of the thermal environment in a large, turbulent fire under controlled wind conditions, with and without a large downwind blocking object. In experiments without the object, flame geometry was measured using temperature contour plots and video images, and the results compared to values predicted using published correlations. Results were greatly affected by the method used to measure flame geometry and by differences in boundary conditions between experiments. Although the presence of the blocking object prevented direct measurement of flame geometry due to interaction between the fire plume and object, temperature and heat flux measurements were analyzed to describe overall effects of the object on fire plume development. The fire impinged on the blocking object at wind speeds below 7 m/s and interacted with the low-pressure wake region behind the object.

Laboratory-scale experiments were also conducted to examine the responses of different heat flux gauges to controlled heating conditions simulating those found in wind-blown fires. Schmidt-Boelter, Gardon and Hemispherical Heat Flux gauges and a Directional Flame Thermometer were exposed to a convective flow and to radiation from a cone calorimeter heater. Measurements were influenced by differences between the calibration and measurement environments, differences in sensor surface temperature, and unaccounted thermal losses from the sensor plate. Heat flux results from the fires were consistent with those from the cone calorimeter, but were additionally affected by differences in location relative to the hot central core of the fire.

Acknowledgements

I would first like to thank my supervisor, Dr. Elizabeth Weckman, for her generous advice, wisdom and patience. I would also like to express my gratitude to Gord Hitchman and Dr. Allan Strong for their technical expertise and guidance; Drs. Walt Gill and Alex Brown of Sandia National Laboratories for their support during the initial iterations of the experiments with the blocking object; Chris Best, Bill Falagitis, Eerik Randsalu, Jennifer Weisinger and the many undergraduate and high school co-op students who have been involved in these experiments; Rick Hummel and the staff at the Waterloo Region Emergency Services Training and Research Complex (WRESTRC) for their cooperation and help in scheduling the large-scale tests; and my family and friends for their enormous support.

In addition, I would like to acknowledge contributions and funding from the Natural Sciences and Engineering Research Council of Canada (NSERC), Sandia National Laboratories, Canada Foundation for Innovation, Ontario Innovation Trust, and the Region of Waterloo fire departments that were present during the large-scale tests.

Contents

List of Tables

List of Figures

Nomenclature

α	Thermal diffusivity
α_s	Surface absorptivity
β	Volumetric thermal expansion coefficient
ϵ	Flame emissivity
ϵ_s	Surface emissivity
μ_a	Viscosity of ambient air
ν	Kinematic viscosity
ϕ	Angular location on blocking object or calorimeter; see Figure 5.9
ρ_a	Density of ambient air
ρ_g	Density of fuel vapours
ρc_p	Volumetric heat capacity
σ	Stefan-Boltzmann constant
τ	Atmospheric transmissivity
θ	Flame tilt angle; see Figure 2.4
B_i	Elemental systematic uncertainty
B_t	Total systematic uncertainty; see Equation 4.2
D	Diameter of fuel pool or for rectangular pools, length of fuel pool in direction of wind

D'	Length of elongated flame base when flame drag is present; see Figure 2.4
d	Thickness of sensor plate of heat flux gauge; see Equation 3.1
F	Geometric view factor between fire and external target
Fr	Froude number, U^2/gD
g	Gravitational acceleration
h	Convection coefficient
ΔH_c	Heat of combustion
k	Thermal conductivity
L	Flame length; see Figure 2.4
l	Characteristic length of heat flux gauge (e.g. diameter for Schmidt-Boelter and Gardon gauges, length of one side for DFT)
$\dot{m}'$	Mass burning rate of fuel per unit length of fuel source
$\dot{m}''$	Mass burning rate of fuel per unit area of fuel
Pr	Prandtl number, ν/α
Q_{conv}	Convective heat flux; see Equation 3.4
Q_{natl}	Natural convective heat flux; see Equation 3.8
Q_{net}	Net absorbed heat flux
Q_{rad}	Incident radiative heat flux
Q_{tot}	Incident total heat flux; see Equation 3.7
R	Radial coordinate; see Equation 3.9
r	Number of future temperatures; see Equation 3.1
Ra_l	Rayleigh number, $g\beta\left(T_s - T_a\right)l^3/\left(\nu\alpha\right)$
Re_D	Reynolds number, $UD\rho_a/\mu_a$

Re_l	Reynolds number, $Ul\rho_a/\mu_a$
Re_X	Reynolds number, $UX\rho_a/\mu_a$
S_i	Elemental precision uncertainty
S_t	Total precision uncertainty; see Equation 4.3
T	Temperature
T_∞	Temperature of convective flow; see Figure 3.1
T_a	Temperature of ambient air
T_f	Flame temperature
T_{init}	Temperature measured immediately prior to test
T_{max}	Maximum temperature measured by thermocouple mounted on inside surface of blocking object
T_s	Surface temperature of heat flux gauge
T_{ss}	Average temperature measured during period of steady burning
ΔT_{diff}	Quantity to characterize test-to-test repeatability; see Equation 4.4
t	Time; for fire tests, time after surface of fuel pool is first completely covered by flame
Δt_{exp}	Experimental time step; see Equation 3.1
U	Speed of wind or convective flow
$U_{c,a}$	Minimum wind speed required for flame tilt to occur; see Equation 2.3
$U_{c,b}$	Minimum wind speed required for flame tilt to occur; see Equation 2.8
U_t	Total uncertainty; see Equation 4.1
X	Distance from outlet of heat gun to centre of heat flux gauge
x	Coordinate specifying distance from fuel pan centre in direction of wind; see Figure 4.6

y	Coordinate specifying distance from fuel pan centre perpendicular to direction of wind; see Figure 4.6
Z	Axial coordinate; see Equation 3.9
z	Coordinate specifying height above floor; see Figure 4.4

Chapter 1

Introduction

Large hydrocarbon pool fires can result from transportation accidents. A historical survey of over 6000 accidents involving hazardous materials revealed that 42% of the accidents included a fire [1]. Among these fires, 59% involved a liquid fuel and 27% occurred during transportation of the hazardous material [1]. These types of accidents have become more common in recent decades, with the majority occurring since the early 1960s, due to increasing frequency of transportation of hazardous materials [1,2]. A separate survey of over 1900 accidents involving transportation of hazardous substances by road and rail found that 74% of the accidents were caused by impact or collision of the vehicle and 28% of them led to fires [2]. As most transportation accidents occur outdoors, an ambient wind is likely to be present and will influence the fire scenario. A large blocking object, such as a rail car, transport truck or aircraft fuselage, may be located next to the fire. Smaller cargo packages containing unreleased hazardous materials may also be scattered in the vicinity of the fire.

The interaction between fire, wind and objects is complex, but understanding this interaction is vital to improved assessment of the hazards posed by the fire in these scenarios [3–6]. To this end, researchers at the University of Waterloo (UW) and at Sandia National Laboratories in Albuquerque, New Mexico, have collaborated to investigate the behaviour of fires in simulated transportation accidents. In 2001, Sandia researchers performed large-scale outdoor experiments involving a cylindrical blocking object representing an aircraft fuselage on the leeward side of a 20 m diameter aviation fuel fire [5, 7]. However, poorly controlled wind conditions limited the quantity and quality of data, as well as the level of detail in the information that could be obtained. In 2003, construction of a new Live Fire

Research Facility at UW was completed; one of the novel features of this building is a wind generation system large enough to permit study of fires up to 2 m diameter in controlled wind conditions. As part of the collaboration between UW and Sandia, a set of large-scale experiments was conducted in the UW facility to examine a potential transportation accident scenario involving a 2 m diameter fire in winds of up to 13 m/s, with a 2.7 m diameter blocking object downwind of the fire. The object would simulate an aircraft fuselage and the fire would represent a burning pool of aviation fuel of fixed size. (Growing fuel pools, such as those that might be generated by fuel leaks, were not considered in this study.) The design of these experiments was described in the author's M.A.Sc. thesis [8] and the first set of preliminary tests was conducted in August 2003. Since these were the very first fire tests conducted in the new facility, iterations of the experimental design were expected and additional tests were performed in 2003-2004. A subsequent iteration ensued and the final set of tests was conducted in 2006. The setup and results of these final tests are reported in the present thesis.

To help analyze and understand the results from the above experiments, a reference set of experiments was conducted to examine the behaviour of unobstructed wind-blown fires. These involved the same 2 m diameter fire, but without the blocking object, in the test area. The experiments were performed in late 2006, after the final set of fire/wind/object tests. The reference cases were deemed important for proper interpretation of the experimental results involving the obstructed fire scenarios. Due to a large number of measurement parameters in the fire/wind/object experiments, the distribution of the available data channels in these tests was such that only coarse characterization of the thermal field in the fire plume could be achieved [8]. However, in the tests without the blocking object, more detailed characterization of the fire environment could be completed because more data channels could be dedicated to measurement of temperature and heat flux in the fire plume. Therefore, these latter tests provide additional detail to help elucidate the effects of the blocking object on the wind-blown fire.

During preliminary analysis of the data from the fire experiments, difficulties were encountered in analysing and interpreting the heat flux measurements. Since radiation is usually considered to be the dominant mode of heat transfer in medium to large fires [9–14], most types of heat flux gauge used in fires have been characterized in radiative environments [15–18]. However, convection could also play a significant role in wind-blown fires, so as part of the present study, a separate set of experiments was conducted to investigate the thermal response of heat flux gauges

to controlled, mixed radiative-convective conditions [19]. The results of these experiments were then used to help interpret the heat flux data from the fire tests.

The present work discusses results from the three sets of experiments outlined above. The overall objectives of the study are as follows:

- To begin development of a comprehensive dataset for validation and future improvement of numerical fire models and hazard analysis tools
- To use the measured data to improve understanding of the physics of thermal interactions between fires, wind and large objects and to gain further insight into published correlations for predicting flame geometry
- To enhance understanding of heat flux measurement results in fires and other high-temperature applications involving mixed modes of heat transfer

Specific objectives of the research are as follows:

- To characterize global characteristics of a wind-blown fire plume, particularly flame geometry, with and without a large downwind blocking object present
- To characterize the temperature field in the fire plume, both in the combustion zone and in the downwind flow of hot product gases, with and without the blocking object
- To characterize the heat flux to the ground at various locations near the fire
- To characterize the heat flux to, and temperature distribution along, the surface of the blocking object
- To assess the response of different types of heat flux gauge in mixed radiative-convective environments, such as those that occur in large wind-blown fires

In Chapter 2, the literature on wind-blown pool fires is reviewed. This chapter describes important physical parameters for thermal characterization of fires in crosswind. Effects of large objects located in or beside fires are also discussed.[1] Additionally, since assessment of heat flux gauges is one of the objectives listed

[1]Additional literature on fire topics not directly related to this thesis (e.g. fuel regression rate measurements) have been reviewed in the author's M.A.Sc. thesis [8] and in the theses of Randsalu [20] and Best [21].

above, heat flux measurement techniques are reviewed to provide background for this portion of the research.

The remainder of the thesis describes the setup, data and results of the three experiments forming the present study. To facilitate readability and understanding of the results, the heat flux gauge experiments are presented first (Chapter 3), followed by the experiments involving the unobstructed wind-blown fires (Chapter 4) and the experiments involving the wind-blown fires with the downwind blocking object (Chapter 5). The analysis and discussion of data from each set of experiments make use of results from the preceding chapters. Final conclusions and recommendations from all three experiments are presented in Chapter 6.

Chapter 2

Literature Review

This chapter reviews the current understanding of the thermal behaviour of medium- and large-scale fires in the presence of wind and/or large objects. Only pool fires of fixed size will be considered; growing pool fires and spreading of flames across a fuel surface are outside the scope of the present work. The first section provides relevant background information on the behaviour of fires in quiescent conditions. It is followed by a discussion on how wind affects the overall characteristics of fires. Then, effects of large objects in and near fires are described. Finally, a review of heat flux measurement techniques applicable for fires is included.

2.1 Fires in Quiescent Wind Conditions

One of the motivations for research into fire behaviour is to improve the ability to predict hazards from a fire in a given accident scenario [22–25]. In order to analyze a given scenario, one must first determine (either by modelling or by direct observation) how large the fire is and how intensely it is burning, requiring knowledge of such characteristics as flame geometry, flame temperature and heat release rate. Once the size and intensity of the fire are established, heat transfer models can be used to predict hazard levels to the fire surroundings [9–11]. Collection of quality experimental data is critical to verifying the accuracy of such predictions and model validation is indeed an important part of fire model development [26]. Therefore, experimental simulation of realistic, yet controlled, accidental fire scenarios is necessary for improvement of existing fire models and development of new models.

To date, most of the experimental research into fire behaviour has been conducted on fires in quiescent atmospheres, with smaller fires typically studied in controlled laboratory environments [27–33] and larger fires studied outdoors under calm or very low (<2 m/s) wind conditions [32, 34–38]. General areas of research have included fire plume structure [27, 29, 31, 37, 38] and heat transfer from the fire [28, 30–37]. Some of the literature relevant to the present work is discussed below.

The general structure of a natural fire is shown in Figure 2.1. The turbulent plume of combustion gases in a fire can be divided into three regions: the persistent flame zone, the intermittent flame zone and the buoyant plume [22, 39]. As indicated by the terminology, luminous flame is continually present in the persistent flame zone at the base of the fire and intermittently present higher up in the intermittent flame zone. Above these two zones is the buoyant plume, which contains hot combustion products and unburnt fuel. The velocity along the centreline of the fire generally increases with increasing height in the persistent flame zone due to buoyant acceleration, reaches a near-constant maximum value in the intermittent flame zone and decreases with further increases in height due to mixing and entrainment of cooler surrounding air in the buoyant plume [27, 39]. Meanwhile, the centreline temperature increases to a maximum in the persistent flame zone before decreasing with increasing height through the intermittent flame zone and buoyant plume [27, 39]. Together, all three zones make up the fire plume. For hazard calculations, the mean height of the fire is often defined as the location along the plume centreline and in the intermittent region where flame is present 50% of the time (i.e. 50% intermittency) [40].

In a pool fire, fuel vapour is continuously supplied from the liquid pool to the combustion region. The production of vapour is maintained by heat transfer from the combustion region back to the fuel surface [22, 33, 41]. The rates of burning and total heat release thus depend on the rate at which fuel vapour is supplied, which in turn depends on the rate of heat feedback to the liquid pool. The amount of air available for combustion also affects the heat release from a fire. Over the continuous flame zone, most of the air entrained into a fire is thought to support combustion in the outer regions, and very little air is transported to the interior of the fire, particularly near the base [27, 38]. Consequently, a non-combusting vapour zone, which is rich in fuel vapours but starved of oxygen, forms inside the continuous flame zone above the fuel surface. The structure and composition of

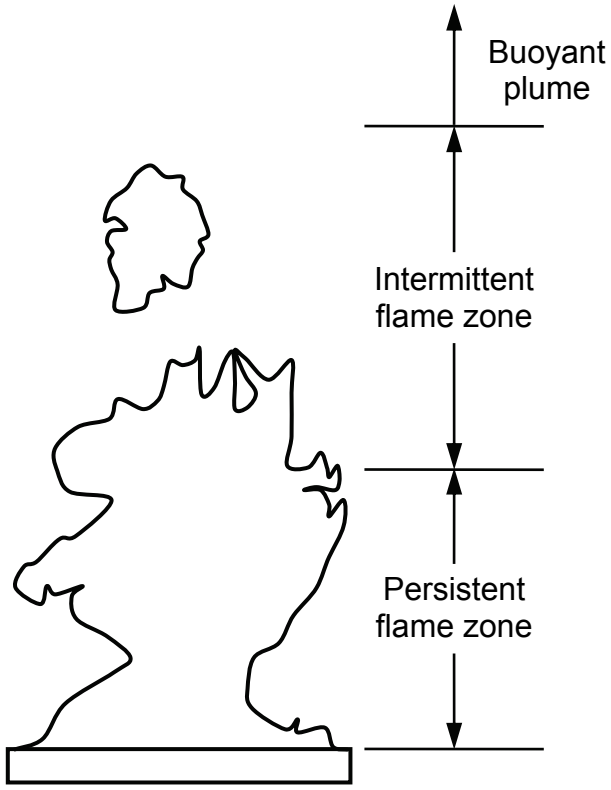

Figure 2.1: Sketch of the fire plume

this region strongly influences the transfer of heat back to the fuel pool [12, 42–45] and subsequent fire plume development.

Taking a different view, fires can be categorized into different burning regimes according to their size [46,47]. Laminar, transitional and turbulent burning regimes have been identified based on pool diameter and liquid fuel regression rate[1], as denoted in Figure 2.2 [46, 48, 49]. This graph shows that as the pan diameter increases, the regression rate first decreases rapidly, passes through a minimum, then increases to an almost constant value at large pool diameters. The laminar regime applies to fires less than 0.1 m in diameter, for which regression rate decreases as a function of pan diameter. This trend is consistent with the notion that most of the heat feedback to the fuel occurs by conduction through the pan walls and by convection from the heated walls to the liquid fuel [48, 50]. At the other extreme, the turbulent regime applies to fires greater than 1 m in diameter, for which the regression rate is relatively unaffected by increasing diameter. In such large fires, conduction and convection from the pan walls are expected to play a much smaller role in the heat feedback to the fuel and radiation is the dominant mechanism of heat transfer [46, 47].

In contrast to the trends indicated in Figure 2.2, several studies have reported an increase in regression rate with increasing diameter among intermediate and large fires [11, 32, 51, 52]. In Figure 2.3, the data shown in Figure 2.2 for pool diameters greater than 0.1 m are plotted together with regression rate values published in the literature for similar fuels and fire sizes [31, 32, 36, 52–58]. The regression rate appears to increase with increasing pool diameter above 1 m, in conflict with Figure 2.2. Significant scatter is also evident, even among data corresponding to a single fuel type (e.g. gasoline). These observations reflect potential differences in ambient conditions, test configurations and regression rate measurement methods among different studies and indicate that additional parameters beyond pool diameter and fuel type are important in determining fuel regression rate in fires [20, 30, 35, 41, 47, 51, 57].

To analyze hazards in a particular fire scenario, heat flux from the fire to the surroundings must be estimated. Along these lines, Babrauskas [47] divided the radiation-dominated turbulent regime into optically thin and optically thick categories (Table 2.1). Although his classification of burning regimes is slightly different

[1]The regression rate is a measure of the burning rate of the liquid fuel in a pool fire. The units are typically mm/min, representing the velocity at which the fuel surface recedes.

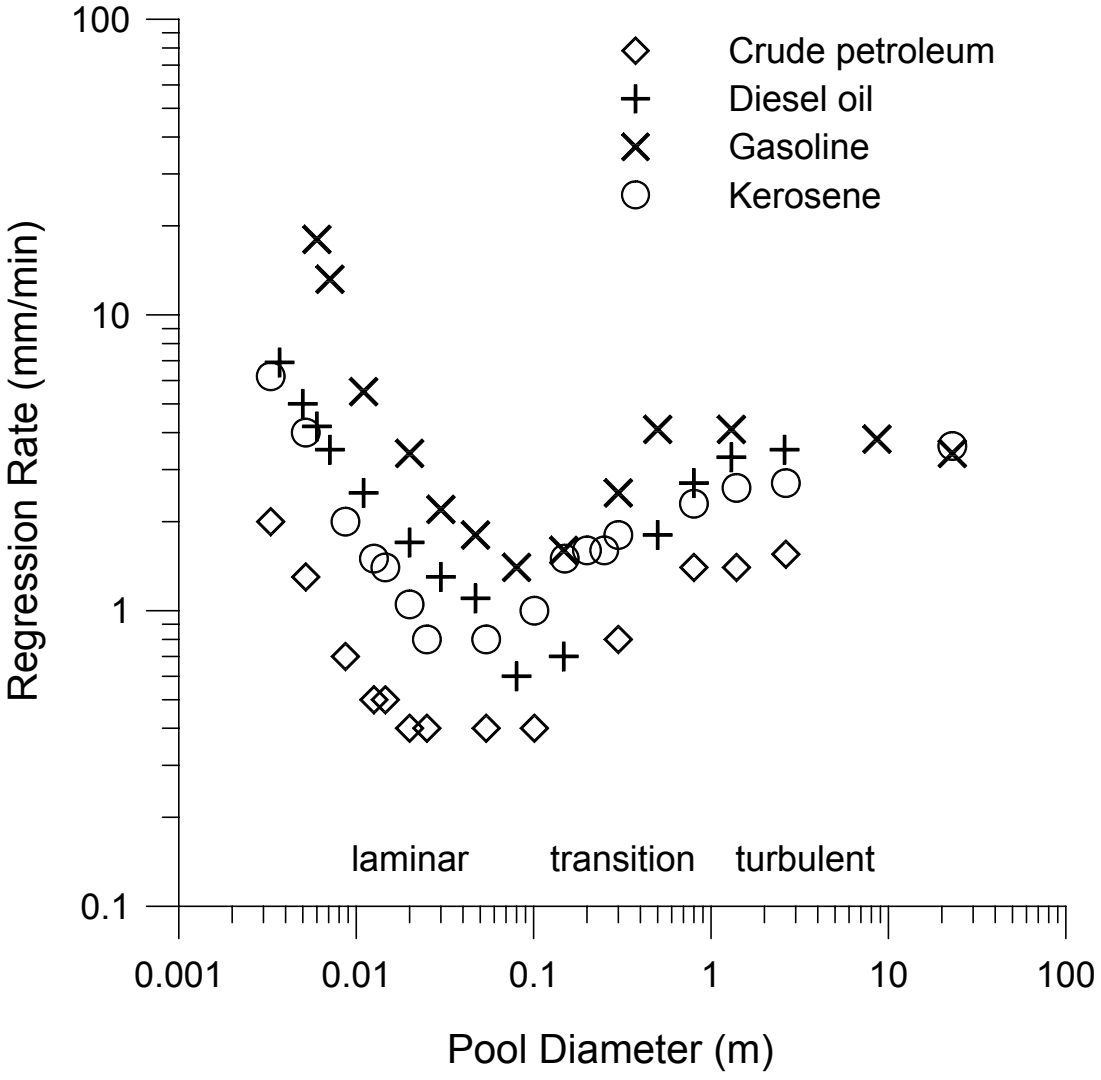

Figure 2.2: Modes of burning in pool fires in quiescent conditions [46, 48, 49]

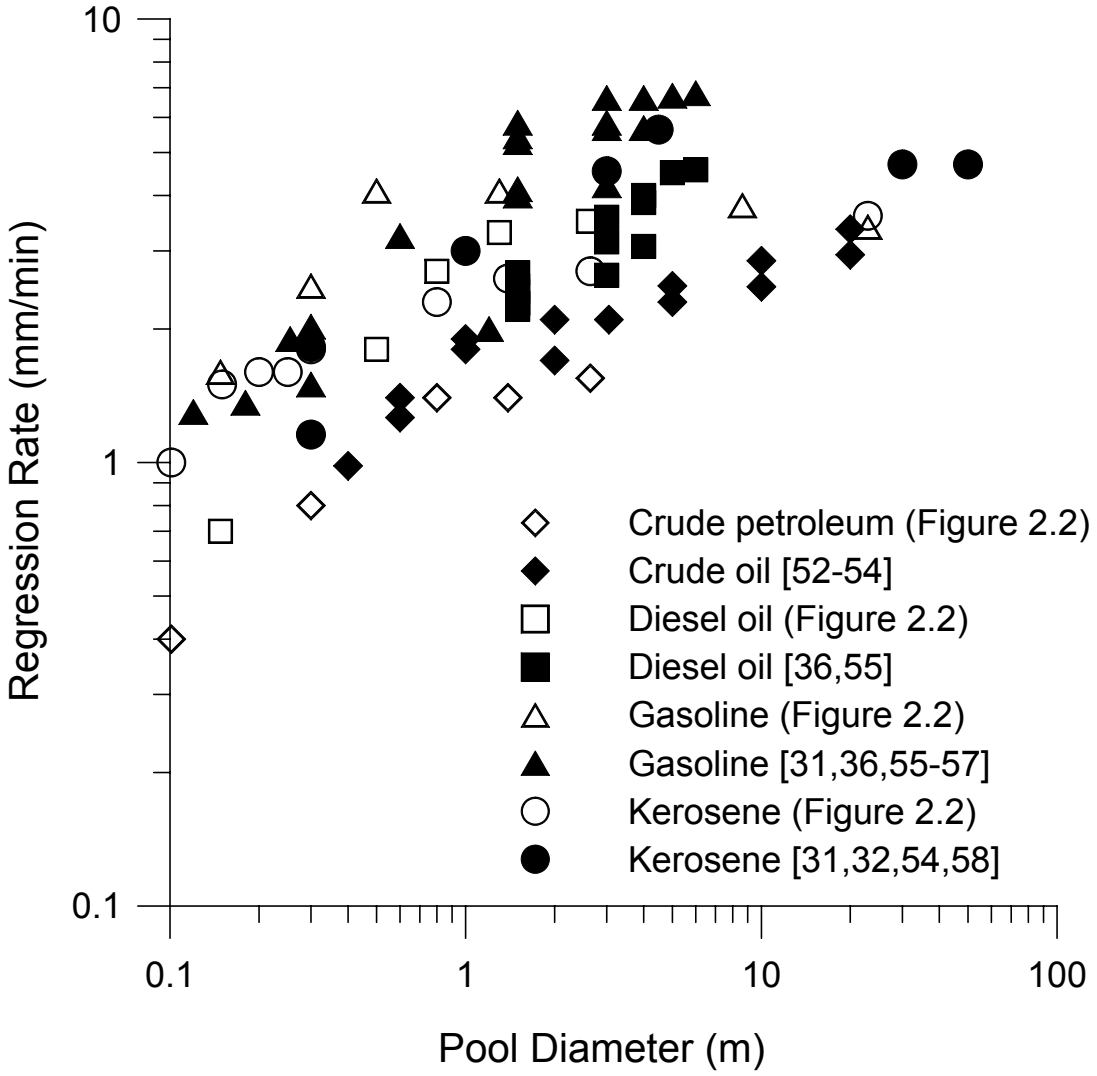

Figure 2.3: Effect of pool diameter on fuel regression rate in quiescent and low (<3 m/s) wind conditions

Table 2.1: Modes of Pool Fire Burning According to Babrauskas [47]

Pool Diameter	Burning Mode
< 0.05 m	convective, laminar
0.05 m to 0.2 m	convective, turbulent
0.2 m to 1.0 m	radiative, turbulent, optically thin
> 1.0 m	radiative, turbulent, optically thick

than that shown in Figure 2.2, it maintains the trend of smaller diameter fires being laminar and convection-dominated, and larger diameter fires being turbulent and radiation-dominated. The importance of radiation in large hydrocarbon fires has been discussed by many researchers [9, 12–14, 37, 42, 56, 59]. The solid flame radiation model is used in standard practice to predict heat flux from the fire to a target in the near-field surroundings outside the flame volume [9–11, 60–64]. This model approximates the luminous portion of the fire as a cylinder or cone that emits radiation uniformly from its entire surface. The heat flux incident on the target is calculated using Equation 2.1, where F accounts for the angle of view between the radiating fire and the target and τ accounts for effects of atmospheric transmissivity when the target is at very large distances from the fire.

$$Q_{rad} = \tau F \epsilon \sigma T_f^4 \tag{2.1}$$

The accuracy of the above heat flux approximation is affected by many parameters. First, use of a solid flame model is limited to large, optically thick fires. Due to the assumption that the luminous flame volume radiates uniformly from its surface, the fire must be large enough for the flame to be radiation-dominated and optically thick (Table 2.1). Second, calculations of view factors between upright cylinders and surfaces of differential areas are readily available [65–67], but knowledge of the fire geometry (e.g. flame height) is required and a cylindrical flame representation may not always be suitable. In cases where wind is significant, view factor estimations have been developed for tilted cylinders and tilted cones to represent wind-blown fires [67–71], but the suitability of those shapes to represent the fire geometry is again an important concern. Third, computation of the overall flame emissivity can be complex due to the different natures of the pockets of hot gases and soot comprising the luminous flame [9, 10, 61]. De Ris [13] discussed the applicability of treating luminous flames as a homogeneous gray mixture; this

assumption is considered appropriate for sooty fires of intermediate scale. Large fires ($D > 3$ m) are often treated as blackbodies and a value of unity is assigned to the flame emissivity [9, 61, 62]. At these diameters, substantial amounts of smoke typically surround much of the visible flame, and regions of highly luminous flame tend to break through the smoke layer intermittently and increase the overall radiation from the otherwise obscured fire [9, 72]. Ways to account for this smoke obscuration and its transient effects are discussed by Smith [72] and Considine [10]. Lastly, determination of a representative flame temperature can be difficult [73, 74] because of changes in temperature with location in the fire, but it is critical because the radiation heat flux is dependent on the fourth power of T_f and is therefore highly sensitive to this value of temperature. Since the product $\epsilon\sigma T_f^4$ represents the flame emissive power, some variations of the solid flame model estimate the emissive power using the heat of combustion and mass burning rate of the fuel (i.e. $\dot{m}''\Delta H_c$) instead of the flame emissivity and flame temperature [14, 75, 76]. However, determination of the heat of combustion and mass burning rate is no simpler than determination of flame emissivity and flame temperature. Like regression rate, the mass burning rate is affected by pool diameter, fuel type, ambient conditions and test configuration [20, 35, 48, 51], making it difficult to predict for a given fire. Also, not all of the heat released by the combustion process is radiated to the surroundings, so the heat of combustion must be multiplied by an estimated radiative fraction in order to obtain an effective emissive power at the flame surface [14, 76]. Estimation of the radiative fraction is difficult, with a wide range of values (between 0.03 and 0.50) reported depending on fuel type, fire size and measurement method [32, 34, 52, 76–79]. Furthermore, as in the case of flame emissivity, effects of smoke obscuration may need to be included in the determination of effective emissive power [14, 76].

Flame geometry, temperature and emissivity are important parameters when determining heat flux from a fire. In some cases, fuel regression rate or burning rate, which is affected by fire size, is also required. These parameters can change greatly when crosswinds are present, affecting hazard levels in the vicinity of the fire. Characteristics of wind-blown fires are discussed in the next section.

2.2 Fires in Crosswind

Research into wind-blown pool fires has largely focussed on flame geometry, which is necessary for calculating radiative heat transfer from the fire [55, 61, 80–82]. The main parameters characterizing the geometry of a wind-blown fire are the tilt, length and drag of the flame [9, 10, 82], but the definitions of these parameters are not consistent in the literature. Flame tilt is typically defined as the angle measured from the vertical to a line drawn from the centre of the burner surface to the tip of the visible flame envelope, as illustrated in Figure 2.4a [81, 83]. Flame length is defined as the length of the latter line.[2] However, in many instances, particularly when the top of the burner is flush with the ground plane, trailing of the flame beyond the downwind edge of the burner can be observed [80, 82]. This is most pronounced in the central downwind portion of the fire, with little change in either the width or upwind edge of the flame. This extension of the flame base is termed flame drag and is characterized by D' in Figure 2.4b. The area of the flame base becomes larger than the area of the burner and the centre of the flame base is shifted downwind of the burner centre. The angle determined using a line drawn from the burner centre to the flame tip is thus an overestimate of the true flame tilt. Consequently, in situations with significant flame drag, flame tilt and flame length are usually based on a line drawn from the centre of the elongated flame base (i.e. half the distance of the pool diameter and length of flame drag) to the tip of the visible flame envelope, as shown in Figure 2.4b [80, 82].

Although flame tilt is typically described using a single angle, it is rarely uniform throughout the fire. The tilt angle may decrease along the length of the flame due to buoyant effects caused by the changing density of flame gases as they rise from the pool surface [84–86]. It may also differ between the windward and leeward sides of the flame, due to increased horizontal momentum on the former side and the dominance of buoyancy on the latter side [87]. However, the ease of using a single tilt angle has permitted development of semi-empirical correlations between tilt angle and wind speed. These correlations are presented in this section, along with correlations for flame length and flame drag.

[2]Note that this definition of flame length is different from the 50% intermittency criterion commonly used to characterize the height of the flame in quiescent conditions [40].

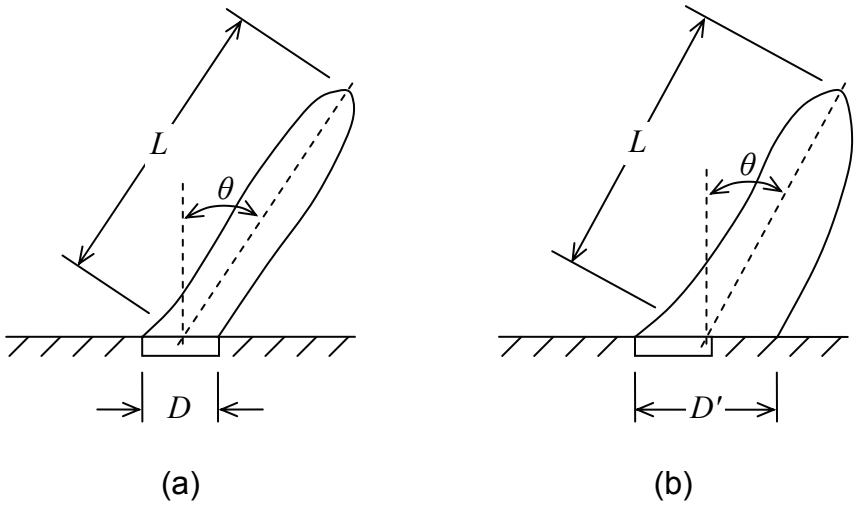

Figure 2.4: Geometrical parameters of a fire in crosswind, (a) without flame drag, (b) with flame drag

2.2.1 Tilt Angle Correlations

Various researchers have proposed different correlations to characterize the tilt angle of wind-blown fires. Welker and Sliepcevich [80] based their correlation on data from experiments involving 0.1 m to 0.6 m diameter pool fires and wind speeds of 0.2 m/s to 2.1 m/s. The fuel pan, which was filled with acetone, benzene, n-hexane, cyclohexane or methanol, was placed with its top rim flush with the floor of a wind tunnel and the fuel was maintained at a constant level near the top of the pan. The tilt angle of the fires was measured from photographs, based on a line drawn from the flame tip to the centre of the flame base. The experimental data were used to estimate a drag coefficient for the flame in each case (giving a total of 85 data points), which was then inserted into a momentum balance to obtain the semi-empirical correlation shown in Equation 2.2.

$$\frac{\tan\theta}{\cos\theta} = 3.3 Re_D^{0.07} Fr^{0.8} \left(\frac{\rho_g}{\rho_a}\right)^{-0.6} \tag{2.2}$$

The momentum balance included assumptions of a steady cylindrical flame with constant volume across all angles of tilt, a constant density ratio of flame gases to ambient air (which was incorporated into the constant coefficient), negligible momentum contribution from the fuel vapours (indicating that the fire was buoyancy driven), and no net momentum influx with air entrainment (which was assumed to

occur uniformly around the fire). Although the assumption of no net momentum contribution by the entrained air may have been appropriate at the low wind conditions considered by Welker and Sliepcevich [80], the same assumption may not be valid at higher wind speeds.

Thomas [81,88] proposed a different correlation based on a series of experiments involving wooden cribs. The cribs had a width much greater than the length and height in order to represent two-dimensional fires. Wooden sticks of different thickness (6 mm to 25 mm) were used to build cribs of dimensions varying from 0.13 m length by 0.91 m width by 0.10 m height to 0.61 m length by 0.91 m width by 0.15 m height. The moisture content of the wood was kept at $12\% \pm 3\%$ of the dry weight. Each crib was mounted in the test section of a wind-producing facility such that its base was level with a constructed ground plane, allowing the flame to burn along the top and leeward sides of the crib. The tilt of the flame under winds ranging from 1.5 m/s to 5.6 m/s was measured directly from photographs, using a line drawn from the flame tip to the centre of the top surface of the wooden crib. A total of 33 tilt angles were obtained, with each one averaged over approximately ten photographs.

To develop a correlation for flame tilt, a dimensional analysis was used to propose two non-dimensionalized parameters to describe the length of the flame and the height of the flame tip above the crib surface. Similar to Welker and Sliepcevich [80], Thomas [81] considered a momentum balance for the fire, in which the initial momentum of the fuel vapours was assumed to be negligible and the density ratio of flame gases to ambient air was assumed to be constant. However, Thomas [81] also assumed that the momentum flux of the entrained air was proportional to the momentum flux of the flame gases and that the mass rate of air entrainment was proportional to the fuel mass burning rate. Based on these assumptions, he obtained functional forms for the flame length and flame height, which were dependent on the the mass burning rate per unit area of fuel, air density and length of the fuel source in the direction of the wind. A regression analysis on the experimental data then led to semi-empirical correlations based on these functional forms. Further manipulation of these correlations allowed their dependence on the length of the fuel source to be removed, resulting in correlations for a "line source" of fuel. The ratio of the line source correlation for flame length to the corresponding correlation for flame height gave the cosine of the tilt angle, resulting in Equation 2.3. In this equation, $U_{c,a}$ is the characteristic minimum wind speed

required for flame tilt to occur; if $U < U_{c,a}$, then $\cos\theta$ is set to 1 and there is no flame tilt.[3]

$$\cos\theta = 0.7\left(\frac{U}{U_{c,a}}\right)^{-0.49} \text{ where } U \geq U_{c,a} \text{ and } U_{c,a} = \left(\frac{g\dot{m}'}{\rho_a}\right)^{1/3} \tag{2.3}$$

Moorhouse [82] adapted Equations 2.2 and 2.3 for large rectangular liquid natural gas (LNG) fires in winds ranging from 1.8 m/s to 14.4 m/s. Various sizes of fuel pool were tested, with dimensions ranging from 6.1 m by 6.1 m to 15.2 m by 12.2 m and the length-to-width ratio ranging from 1 to 2.5. The outdoor fuel pit was recessed into the ground so that the top of the pit was level with the ground plane. Since LNG fires are characterized by very little soot, the flame geometry could be determined directly from cine film images of the fire. For each image, both a cone and cylinder were used to represent the flame geometry, allowing comparison between the two idealizations. First, the location of a virtual flame tip was selected so that the total area of the cone or cylinder when viewed from the side was equal to the corresponding area of the flame as measured from the photographic image. The tilt angle was then measured from the vertical to a line drawn from the centre of the elongated flame base to the virtual flame tip. The use of a virtual flame tip was intended to correct for the tendency of a cylindrical representation to overestimate the area of flame near the top of the luminous flame zone. Twenty to thirty images were taken at each wind speed and the tilt angles averaged over these images, giving a total of 29 data points. Applying the forms of Equations 2.2 and 2.3 to the experimental data resulted in the two sets of correlations shown below, one for each of the conical and cylindrical representations of the flame geometry. With only one fuel (LNG) tested, the density ratio in Equation 2.2 was incorporated into the constant coefficients in Equations 2.4 and 2.6.

Conical flame representation:

$$\frac{\tan\theta}{\cos\theta} = 3.0 Re_D^{0.011} Fr^{0.422} \tag{2.4}$$

$$\cos\theta = 0.87\left(\frac{U}{U_{c,a}}\right)^{-0.272} \tag{2.5}$$

[3]Also, $\dot{m}'$ is often taken as $\dot{m}''D$ for pool fires [82, 89].

Cylindrical flame representation:

$$\frac{\tan\theta}{\cos\theta} = 1.9 Re_D^{0.050} Fr^{0.399} \tag{2.6}$$

$$\cos\theta = 0.86 \left(\frac{U}{U_{c,a}}\right)^{-0.250} \tag{2.7}$$

Similar to Moorhouse [82], the form of Equation 2.3 was applied to large outdoor LNG fires of 1.8 m to 24.4 m diameter by Atallah and Raj [61]. The fuel pool was contained within a dike of 0.46 m height sitting on top of a level ground. The wind speed in the tests ranged from 1.3 m/s to 7.9 m/s. Flame geometry measurements were made from images that were averaged over five movie frames capturing the fire. A total of 53 tilt angles were measured, based on a line drawn from the tip of the averaged flame image to the centre of the dike. Equations 2.2 and 2.3 were used to predict the tilt angle of the LNG fires, and although the predicted values from both equations compared reasonably well to the measurements [90, 91], Equation 2.3 was considered to be a better correlation by Atallah and Raj [61] because the experimental data showed less scatter when plotted using the parameters of that equation. Equation 2.3 was thus adapted to fit the LNG data, resulting in Equation 2.8 below. The main change implemented by Atallah and Raj [61] to improve the fit of the correlation to the data was the use of fuel vapour density instead of ambient air density to determine $U_{c,b}$.

$$\cos\theta = \left(\frac{U}{U_{c,b}}\right)^{-0.5} \text{ where } U > U_{c,b} \text{ and } U_{c,b} = \left(\frac{g\dot{m}''D}{\rho_g}\right)^{1/3} \tag{2.8}$$

Researchers from the Universitat Politècnica de Catalunya [55,92] examined the suitability of Equations 2.3, 2.6, 2.7 and 2.8 for predicting measured tilt angles in outdoor fires of 1.5 m to 6 m diameter. A fixed quantity of either gasoline or diesel oil was floated on top of a water layer in a fuel pan situated with its base along the ground plane [93]. Tilt angles were determined using video images of the fires. Neglecting smoke-obscured regions of the flame, the flame tip was assumed to be located at the highest point of the visible flame zone in each image. Tilt angles were measured based on a line drawn from the flame tip to the centre of the fuel pool. Time-averaged values were determined over periods of steady wind speed, which ranged from 0 m/s to 2.3 m/s over a total of 22 experiments. Equations 2.7 and 2.8 (using $U_{c,a}$ in both cases) were found to correlate well with the experimental

data, better than Equation 2.3. Equation 2.6 was found to correlate poorly with the data; according to the authors, this was because this equation was based on tilt angles measured at wind speeds higher than 2.3 m/s [55]. However, this does not seem consistent given that Equations 2.6 and 2.7 were developed using the same data. In any case, the form of Equation 2.7 was used to develop a new correlation for the reported data, resulting in Equation 2.9 [92]. In this new correlation, the coefficient of 0.92 and exponent of -0.26 were chosen specifically to fit the data from the diesel fires [92].

$$\cos\theta = 0.92\left(\frac{U}{U_{c,a}}\right)^{-0.26} \tag{2.9}$$

De Faveri *et al.* [83] developed a different form of correlation for flame tilt in 0.04 m to 0.11 m diameter fires in 0.19 m/s to 0.89 m/s winds. Two types of fuel, diesel and an oil-diesel mixture, were placed in a bowl, the top of which was flush with the floor of a wind tunnel. The tilt angle was measured visually, based on a line drawn from the tip of the visible flame to the centre of the fuel pool. A total of 12 data points were obtained and all fires were observed to be conical in shape, with no significant flame drag. A correlation for tilt angle was developed based on the momentum balance analysis of Pipkin and Sliepcevich [94], which was similar to the momentum balance analysis used to derive Equation 2.2 [80]. Unlike Equation 2.2, the density ratio of flame gases to ambient air was not assumed to be constant and was instead represented by a corresponding temperature ratio via the assumption of ideal gas behaviour [83]. Upon making additional simplifications involving estimation of a drag coefficient for the flame at large Reynolds number and large pool diameter, Equations 2.10 and 2.11 below were obtained for tilt angle in conical and cylindrical flames. Due to the extrapolation of the drag coefficient to large pool diameters, these equations were not developed directly from the experimental data described above. Further, the validity of the drag extrapolation was questionable because the simplification used to estimate the drag coefficient was based on very limited observations [94].

$$\frac{\tan\theta}{(\cos\theta)^{1.38}} = \frac{8.62Fr}{1 - T_a/T_f} \qquad \text{(conical flame)} \tag{2.10}$$

$$\frac{\tan\theta}{(\cos\theta)^{0.515}} = \frac{5.75Fr}{1 - T_a/T_f} \qquad \text{(cylindrical flame)} \tag{2.11}$$

As seen above, three different forms of correlation (represented by Equations 2.2, 2.3 and 2.10) have been proposed for predicting the tilt angle in wind-blown fires. All forms were developed using momentum balances for the fire, but different assumptions were incorporated in each one. For instance, the net momentum influx due to air entrainment was assumed to be negligible in Equations 2.2 and 2.10, but not in Equation 2.3. Further, the density ratio of the flame gases to ambient air was assumed to be constant in Equations 2.2 and 2.3, but was represented by the temperature ratio of the flame gases to ambient air in Equation 2.10. The summary shown in Table 2.2 shows that the forms of Equations 2.2 and 2.3 have been applied through several studies to rectangular and circular fires for a wide variety of burner sizes, fuels and wind speeds. However, the form of Equation 2.10 has so far been used in only one study.

Additional differences between the studies reviewed above are outlined in Table 2.3. First, although all tilt angles were measured from recorded images of the fire, variations existed among the methods used to define flame tilt. In cases where flame drag was observed (as for Equations 2.2 and 2.4−2.7), the tilt angle was measured using a line passing through the centre of the flame base and the flame tip. This typically corresponded to situations in which the rim of the fuel pan was level with the ground plane. In cases where no flame drag was observed, the base of the flame was contained to the area of the fuel surface, so the centre of the fuel surface was used in determining the tilt angle. Second, various methods were used to define the location of the flame tip. In most cases, the flame tip was selected based on visual observation as the point on the main luminous body furthest from the fuel surface (Figure 2.4). This could be easily done in fires with low levels of smoke production, such as the small fires associated with Equations 2.2 and 2.3, and the LNG fires associated with Equation 2.8. However, the large gasoline and diesel fires associated with Equation 2.9 produced significant amounts of smoke, which may have caused scatter in the estimates of the flame tip location [92]. Thus the effectiveness of this visual procedure becomes limited in large, sooty fires. In an attempt to improve the accuracy of the tilt angle estimates in the LNG experiments corresponding to Equations 2.4−2.7, a virtual flame tip based on idealized conical and cylindrical representations of the instantaneous flame shape was used. Finally, slight differences existed in the methods used to evaluate the average values of tilt angle. In all experiments except that corresponding to Equation 2.8, instantaneous values of tilt angle were determined from individual video images before averaging

Table 2.2: Summary of Tilt Angle Correlations

Eqn. No.	Correlation	Wind Speed	Burner Size	Fuel	Measured Tilt Angles
2.2	$\frac{\tan\theta}{\cos\theta} = 3.3 Re_D^{0.07} Fr^{0.8} \left(\frac{\rho_g}{\rho_a}\right)^{-0.6}$	0.2 to 2.1 m/s	0.1 to 0.6 m diameter	Acetone, benzene, methanol, n-hexane, cyclohexane	Not specified
2.3	$\cos\theta = 0.7 \left(\frac{U}{U_{c,a}}\right)^{-0.49}$	1.5 to 5.6 m/s	0.91 m × 0.13 m to 0.91 m × 0.61 m	Wooden cribs	49° to 80°
2.4	$\frac{\tan\theta}{\cos\theta} = 3.0 Re_D^{0.011} Fr^{0.422}$	1.8 to 14.4 m/s	6.1 m × 6.1 m to 15.2 m × 12.2 m	LNG	11° to 70°
2.5	$\cos\theta = 0.87 \left(\frac{U}{U_{c,a}}\right)^{-0.272}$				
2.6	$\frac{\tan\theta}{\cos\theta} = 1.9 Re_D^{0.050} Fr^{0.399}$				
2.7	$\cos\theta = 0.86 \left(\frac{U}{U_{c,a}}\right)^{-0.250}$				
2.8	$\cos\theta = \left(\frac{U}{U_{c,b}}\right)^{-0.5}$	1.3 to 7.9 m/s	1.8 to 24.4 m diameter	LNG	30° to 74°
2.9	$\cos\theta = 0.92 \left(\frac{U}{U_{c,a}}\right)^{-0.26}$	0 to 2.3 m/s	1.5 to 6 m diameter	Gasoline, diesel oil	22° to 53° (for $U/U_{c,a} \geq 1$)
2.10	$\frac{\tan\theta}{(\cos\theta)^{1.38}} = \frac{8.62 Fr}{1 - T_a/T_f}$	0.19 to 0.89 m/s	0.04 to 0.11 m, extrapolated to large diameters	Diesel, oil-diesel mixture	41° to 59°
2.11	$\frac{\tan\theta}{(\cos\theta)^{0.515}} = \frac{5.75 Fr}{1 - T_a/T_f}$				

Table 2.3: Experimental Details Related to Tilt Angle Correlations

Eqn. No.	Tilt Angle Measurement Method	Location of Ground Plane	Fuel Quantity	Test Facility
2.2	Flame tip to flame base centre	Level with rim of fuel pan	Constant level	Wind tunnel
2.3	Flame tip to centre of crib surface	Level with base of crib	Fixed quantity, adapted for line source	Unspecified wind facility
2.4 2.5 2.6 2.7	Virtual flame tip to flame base centre	Level with rim of fuel pit	Fixed quantity	Outdoor facility
2.8	Flame tip (averaged) to fuel pool centre	Level with base of fuel dike	Fixed quantity	Outdoor facility
2.9	Flame tip to fuel pool centre (smoke obscuration neglected)	Level with base of fuel pan	Fixed quantity	Outdoor facility
2.10 2.11	Flame tip to fuel pool centre	Level with rim of fuel pan	Fixed quantity	Wind tunnel

the results, while in the development of Equation 2.8, tilt angles were measured directly from time-averaged images of the fire.

The above discussion illustrates difficulties in comparing tilt angle data from different studies. Although all estimates of tilt angle were made using visual images of the fire, the various methods used to analyze and measure tilt angle may partly account for the lack of agreement on the most appropriate form of correlation to use for collapsing the data. Differences in the physical parameters affecting flame tilt, such as wind speed, burner size and fuel type, also need to be considered, along with the physical assumptions inherent in each correlation. Additional insight into how these parameters and assumptions affect predictions of flame geometry may be gained by looking at the correlations for flame length and flame drag. These are discussed in the next two sections.

2.2.2 Flame Length Correlations

Flame lengths were determined in the same manner as tilt angle, using a line drawn from the centre of either the fuel pool or flame base to the tip of the visible flame (Figure 2.4). The flame length correlations shown in Equations 2.12 and 2.13 were developed by Thomas [81] for the wooden crib fires associated with Equation 2.3. Equation 2.12 was developed directly from the crib fire data, while Equation 2.13 resulted from adaptation of Equation 2.12 to apply to a line source of fuel.

$$\frac{L}{D} = 70 \left(\frac{\dot{m}''}{\rho_a \sqrt{gD}} \right)^{0.86} Fr^{-0.11} \tag{2.12}$$

$$\frac{L}{D} = 55 \left(\frac{\dot{m}''}{\rho_a \sqrt{gD}} \right)^{2/3} \left(\frac{U}{U_{c,a}} \right)^{-0.21} \quad \text{where } U \geq U_{c,a} \tag{2.13}$$

Equation 2.12 was based on the momentum balance analysis used to develop Equation 2.3. Through this analysis, the flame length was determined to be a function of the mass burning rate per unit area of fuel, the air density and the length of the fuel source, expressed in the form $\dot{m}''/\rho_a\sqrt{gD}$. The wind speed was included through the use of a Froude number, with the assumption that the flames were fully turbulent so that the flame length could be considered independent of viscosity and hence Reynolds number. Thomas [81] reported that although the experimental data indicated a slight increase in flame length with increasing Reynolds number

($L/D \propto Re_D^{0.08}$ [81]), this dependence was not considered to be significant and thus the Reynolds number was not included in the correlations. A regression analysis on the experimental flame length data using the non-dimensionalized mass burning rate and the Froude number resulted in Equation 2.12. Equation 2.13 was subsequently obtained through manipulation of Equation 2.12 to apply to a line source of fuel. As suggested by the inclusion of the characteristic minimum wind speed $U_{c,a}$ in Equation 2.13, flame length was expected to remain approximately constant for wind speeds below $U_{c,a}$. For $U \geq U_{c,a}$, flame length decreased with increasing wind speed (as indicated by the negative exponent), likely due to improved entrainment of air into the fire, which would result in better fuel-air mixing in the core of the fire and thus a shorter flame length. By similar reasoning, the flame length predicted by Equation 2.12 for a rectangular source of fuel was expected to be less than that predicted by Equation 2.13 for a line source of fuel, due to higher levels of air entrainment expected in the former case [81]. It may be noted that the ratio $U/U_{c,a}$ used in Equation 2.13 represents similar physics to the Froude number used in Equation 2.12 because the Froude number relates the inertial forces of the wind to buoyancy forces in the fire [22, 27], while $U/U_{c,a}$ characterizes the wind speed required to counteract the upward, buoyancy-induced acceleration of the fire and thereby produce flame tilt.

Moorhouse [82] proposed the flame length correlations shown in Equations 2.14 and 2.15, which use the same form as Equation 2.13 above. These were developed specifically to fit data taken in the LNG experiments corresponding to Equations 2.4−2.7. The correlations indicate an increase in flame length with increasing mass burning rate and decreasing wind speed, in agreement with Equation 2.13.

$$\frac{L}{D} = 4.7 \left(\frac{\dot{m}''}{\rho_a \sqrt{gD}} \right)^{0.121} \left(\frac{U}{U_{c,a}} \right)^{-0.114} \qquad \text{(conical flame)} \tag{2.14}$$

$$\frac{L}{D} = 6.2 \left(\frac{\dot{m}''}{\rho_a \sqrt{gD}} \right)^{0.254} \left(\frac{U}{U_{c,a}} \right)^{-0.044} \qquad \text{(cylindrical flame)} \tag{2.15}$$

Researchers from the Universitat Politècnica de Catalunya [55, 92] examined flame length correlations in relation to the fires associated with Equation 2.9. Since the flame length data described in Muñoz *et al.* [55] appear to have been either remeasured or reanalyzed in Ferrero *et al.* [92], only the correlation presented in the latter publication will be included here. Equation 2.16 follows the same form as

Equation 2.13 and corresponds to the average flame length as determined from video images using a 50% intermittency criterion [40]. Values predicted using Equation 2.15 were also found to be reasonably close to the experimentally determined flame lengths [92].

$$\frac{L}{D} = 4.201 \left(\frac{\dot{m}''}{\rho_a \sqrt{gD}} \right)^{0.181} \left(\frac{U}{U_{c,a}} \right)^{-0.082} \tag{2.16}$$

The form of Equation 2.13 was also used by Atallah and Raj [61] to correlate flame length data from their LNG fires, described previously with Equation 2.8. Unlike the studies discussed above, flame length was found to increase with increasing wind speed and decrease with increasing fuel mass burning rate, as indicated by Equation 2.17. At the same time, changes in wind speed were not found to significantly affect mass burning rate for a given pool size in these tests. This discrepancy indicates that additional parameters may influence flame length.

$$\frac{L}{D} = \left(\frac{\dot{m}''}{\rho_a \sqrt{gD}} \right)^{-0.19} \left(\frac{U}{U_{c,b}} \right)^{0.06} \tag{2.17}$$

In the small diesel fire experiments associated with Equations 2.10−2.11, de Faveri *et al.* [83] investigated the influence on flame length of the Froude number, Reynolds number and mass burning rate, thereby adapting the form of Equation 2.12 accordingly. They found that the flame length data could be grouped according to whether the Froude number was greater or less than 0.1, so separate correlations were derived for each group, as shown below in Equations 2.18 and 2.19.

$$\frac{L}{D} = 43.4 \left(\frac{\dot{m}''}{\rho_a \sqrt{gD}} \right)^{1.22} Fr^{-0.4} Re_D^{0.0243} \qquad 0 < Fr < 0.1 \tag{2.18}$$

$$\frac{L}{D} = 11.6 \left(\frac{\dot{m}''}{\rho_a \sqrt{gD}} \right)^{2.65} Fr^{-0.125} Re_D^{0.890} \qquad Fr \geq 0.1 \tag{2.19}$$

In both groups, flame length decreased with increasing Froude number and increased with increasing Reynolds number, consistent with the results of Thomas [81] as discussed earlier. The Reynolds number had a greater effect on flame length than the Froude number when $Fr \geq 0.1$, whereas the opposite was true when $Fr < 0.1$. Thus, an increase in wind speed would cause an increase in flame length when $Fr \geq 0.1$ and a decrease in flame length when $Fr < 0.1$. However, the effect of the

mass burning rate dominated over those of the Froude and Reynolds numbers, as indicated by the fact that the exponent of the mass burning rate term was one order of magnitude greater than those of the other parameters. As a result, a change in mass burning rate could override the combined contribution of the Froude and Reynolds numbers.

The flame length correlations reviewed above are listed in Table 2.4, together with the corresponding experimental parameters from Table 2.2. Two forms of equations are evident – one based on the Froude and Reynolds numbers and the other based on the velocity ratio $U/U_{c,a}$ or $U/U_{c,b}$. Both types of correlations include the same parameter representing a non-dimensionalized mass burning rate. As mentioned earlier, the velocity ratio and Froude number represent similar physics, but it does not appear that either of these terms, in combination with the mass burning rate term, provides a universal correlation for the flame length data. As with tilt angle, the discrepancy between correlations from different studies may be partly due to differences in the methods used by various researchers to define and measure flame length, and partly due to differences in the assumptions made in developing the correlations. In addition, since mass burning rate is important in determining flame length, difficulties in estimating mass burning rate may be another source of discrepancy between the correlations. Much scatter has been found to exist among measured burning rate data in fires, due to differences in such parameters as pool diameter, wind speed, fuel type, test configuration, measurement method and ambient conditions [51].[4] This indicates a need for better understanding of the effect on flame geometry and mass burning rate of the different physical parameters governing fire plume behaviour.

2.2.3 Flame Drag Correlations

As part of the overall characterization of the wind-blown flame geometry, a few attempts have been made to correlate flame drag with wind speed. Flame drag

[4] As with the data for fires above 1 m diameter in quiescent conditions, conflicting trends have been reported for regression rate as a function of wind speed. Some studies have found regression rate to increase with increasing wind speed [35, 36, 43, 48, 87, 95], likely due to an increase in air entrainment and mixing in the fire, resulting in more complete combustion and greater heat feedback to the fuel surface [48,51,87]. On the other hand, other studies have reported a decrease in regression rate with increasing wind speed [96–98]. This was thought to be caused by a decrease in geometric view factor from the flame to the fuel surface as the fire tilted further over, resulting in lower radiative feedback to the fuel surface [51, 98]. The current lack of understanding of the physics governing trends in regression rate hinders our ability to fully establish the effect of regression rate on flame geometry.

Table 2.4: Summary of Flame Length Correlations

Eqn. No.	Correlation	Wind Speed	Burner Size	Fuel	Measurement Method
2.12	$\frac{L}{D} = 70 \left(\frac{\dot{m}''}{\rho_a \sqrt{gD}}\right)^{0.86} Fr^{-0.11}$	1.5 to 5.6 m/s	0.91 m × 0.13 m to 0.91 m × 0.61 m	Wooden cribs	Flame tip to centre of crib surface
2.13	$\frac{L}{D} = 55 \left(\frac{\dot{m}''}{\rho_a \sqrt{gD}}\right)^{2/3} \left(\frac{U}{U_{c,a}}\right)^{-0.21}$				
2.14	$\frac{L}{D} = 4.7 \left(\frac{\dot{m}''}{\rho_a \sqrt{gD}}\right)^{0.121} \left(\frac{U}{U_{c,a}}\right)^{-0.114}$	1.8 to 14.4 m/s	6.1 m × 6.1 m to 15.2 m × 12.2 m	LNG	Virtual flame tip to flame base centre
2.15	$\frac{L}{D} = 6.2 \left(\frac{\dot{m}''}{\rho_a \sqrt{gD}}\right)^{0.254} \left(\frac{U}{U_{c,a}}\right)^{-0.044}$				
2.16	$\frac{L}{D} = 4.201 \left(\frac{\dot{m}''}{\rho_a \sqrt{gD}}\right)^{0.181} \left(\frac{U}{U_{c,a}}\right)^{-0.082}$	0 to 2.3 m/s	1.5 to 6 m diameter	Gasoline, diesel oil	Flame tip to fuel pool centre (smoke obscuration neglected)
2.17	$\frac{L}{D} = \left(\frac{\dot{m}''}{\rho_a \sqrt{gD}}\right)^{-0.19} \left(\frac{U}{U_{c,b}}\right)^{0.06}$	1.3 to 7.9 m/s	1.8 to 24.4 m diameter	LNG	Flame tip (averaged) to fuel pool centre
2.18	$\frac{L}{D} = 43.4 \left(\frac{\dot{m}''}{\rho_a \sqrt{gD}}\right)^{1.22} Fr^{-0.4} Re_D^{0.0243}$ for $0 < Fr < 0.1$	0.19 to 0.89 m/s	0.04 to 0.11 m diameter	Diesel, oil-diesel mixture	Flame tip to fuel pool centre
2.19	$\frac{L}{D} = 11.6 \left(\frac{\dot{m}''}{\rho_a \sqrt{gD}}\right)^{2.65} Fr^{-0.125} Re_D^{0.890}$ for $Fr \geq 0.1$				

was usually determined directly from photographs or video images, as indicated in Figure 2.4b. The correlation in Equation 2.20[5] was proposed by Welker and Sliepcevich [80] for the fires associated with Equation 2.2, but no derivation of this correlation was provided.

$$\frac{D'}{D} = 2.1 Fr^{0.21} \left(\frac{\rho_g}{\rho_a} \right)^{0.48} \tag{2.20}$$

The authors expected flame drag to occur when the density of the fuel vapours was greater than that of the surrounding air, causing the vapours to remain near the ground until they were heated sufficiently to rise due to buoyancy. Since these vapours would be burning near the outer edges, where there was sufficient air, the flame would appear to be trailing along the ground downwind of the fuel pan until the vapours started to rise, resulting in flame drag [80]. Although this may be true at the relatively low wind speeds considered by Welker and Sliepcevich [80] (Table 2.2, first row), flame drag at much higher wind speeds would likely be caused by the horizontal momentum of the wind overcoming the buoyancy forces in the fire and pushing the flame close to the ground.

Correlations similar to the one shown above were proposed by Moorhouse [82] specifically for the LNG fires related to Equations 2.4−2.7. Since the fuel pool in these experiments was rectangular rather than circular and the wind direction was not always aligned with one side of the pool, the flame drag was nondimensionalized by the maximum dimension of the pool in the direction of the wind instead of the pool diameter. With only one fuel tested, the density ratio in Equation 2.20 was incorporated into the constant coefficients in Equations 2.21 and 2.22. Moorhouse [82] also suggested that flame drag would correlate with the term $1/cos\theta$, since the angle of flame tilt would be expected to be related to the amount of flame drag. However, although the LNG data indicated that such a correlation existed, the flame drag ratios were somewhat less than the values given directly by $1/cos\theta$. No further steps were taken to identify an appropriate correlation between flame tilt and flame drag.

$$\frac{D'}{D} = 1.6 Fr^{0.061} \qquad \text{(conical flame)} \tag{2.21}$$

$$\frac{D'}{D} = 1.5 Fr^{0.069} \qquad \text{(cylindrical flame)} \tag{2.22}$$

[5]The error in the sign of the exponent of the Froude number has been corrected.

Mudan [9] combined Equations 2.20 and 2.22 (without providing justification) to propose a generalized correlation for hydrocarbon fires, shown in Equation 2.23.[6] Lautkaski [99] subsequently argued that there should be an additional coefficient to account for the vapour density of LNG and allow Equation 2.23 to match Equation 2.22 for that particular fuel. The revised correlation is shown in Equation 2.24.

$$\frac{D'}{D} = Fr^{0.069} \left(\frac{\rho_g}{\rho_a} \right)^{0.48} \tag{2.23}$$

$$\frac{D'}{D} = 1.2 Fr^{0.069} \left(\frac{\rho_g}{\rho_a} \right)^{0.48} \tag{2.24}$$

Although this form of correlation suggests that flame drag would increase with increasing fuel vapour density, Lautkaski [99] did not find evidence of this trend when comparing flame drag measurements from fires with different fuel vapour densities ($1.6 \leq \rho_g/\rho_a \leq 2.7$). Unlike Welker and Sliepcevich [80], who thought that flame drag was caused by the fuel vapours being denser than the surrounding air, Lautkaski [99] thought that the extent of flame drag would be determined by a balance between the wind-driven plume flow and the flow of air being entrained into the leeward side of the fire, in a direction opposite to the wind. Since this air entrainment is induced by the upward momentum of the buoyant flame gases, the density of the fuel vapours would not be a controlling parameter in determining flame drag. Lautkaski [99] therefore suggested that the density ratio ρ_g/ρ_a be omitted from the correlations and recommended Equation 2.22 as the most appropriate correlation for predicting flame drag in large hydrocarbon pool fires.

The above studies clearly show the current lack of understanding of the physical processes affecting flame drag. The lack of agreement among correlations published not only for flame drag, but also for tilt angle and flame length, indicates that the correlations do not model all of the relevant physics in wind-blown fires. It may be noted that all of the studies reviewed above involve making measurements of flame geometry using visual images of the fire. Differences between measurement methods used by different researchers, along with difficulties in making such measurements, particularly in large, sooty fires, can cause significant scatter in the data. In light of this, the present study involves characterizing the flame shape using the temperature field in the fire plume, supported by measurements from video images of the

[6] The error in the density fraction, which was inadvertently inverted by Mudan [9] when he misquoted Equation 2.20, has been corrected.

fire. This will lead to more detailed measurements of flame geometry than have been previously presented. These, in turn, will lead to enhanced understanding of the physics affecting wind-blown fires.

As shown in the above sections, crosswinds greatly affect the overall characteristics of a fire. Large thermally massive objects located in or near fires can also influence the shape, flow and thermal field within a fire. This situation can occur in large industrial or transportation accidents, in which containers of hazardous materials become engulfed in fires. Due to their importance in hazard analysis, interactions between large objects and fires are considered in the next section.

2.3 Fires with Large Objects

Motivations for understanding the coupled response of large objects and fires include the improvement of methods for evaluating container design and performance and the development of better fire protection and mitigation systems [4, 6, 24, 100, 101]. Over the past two decades, several experiments involving thermally massive objects engulfed in fires have been conducted. One of these used a 1.4 m diameter by 6.4 m long steel pipe centred inside a 9.1 m by 18.3 m JP-4 fire [102, 103]. The bottom of the pipe was located 0.9 m above the initial fuel surface. Four smaller cylinders were also placed inside the fire near the large pipe. These objects were 0.1 m to 0.2 m in diameter and 0.2 m long. All cylinders were oriented with their longitudinal axis parallel to the fuel surface. During the tests, slight winds of up to 2 m/s were measured. Time variations in the local heat flux to the objects reflected changes in the wind speed and direction [102]. The bottom of the large pipe experienced a maximum local net heat flux, while the top of the pipe experienced a minimum local net heat flux [103]. In addition, the windward side of the pipe experienced a lower net heat flux than the leeward side. The variation in heat flux around the circumference of the pipe was thought to result from a lower flame thickness, and therefore lower radiative exposure, along the upper and windward sides of the object. For surface temperatures between 127°C and 177°C, the heat flux to the 1.4 m diameter pipe was 66% to 80% of that to the smaller objects, depending on height above the pool surface [103]. However, no difference was observed at higher surface temperatures (greater than approximately 527°C), suggesting that when the objects were at a temperature much lower than that of the fire, the larger object had greater influence on the surrounding flames.

A similar experiment was performed using a 1.5 m diameter by 6.4 m long cylinder placed inside a 9 m by 18 m JP-4 fire [104]. The cylinder was offset from the centre of the fuel pool by approximately 4.5 m (one-quarter the length of the pool) and situated at an unspecified elevation with its axis parallel to the fuel surface. Two 0.1 m diameter by 0.2 m long cylinders were installed in the same orientation at an elevation of 2 m above the bottom of the pool and a distance of approximately 2 m from the centre of the pool. An average wind speed of 2.8 m/s was measured during the test. As in the above study, higher levels of heat flux were measured along the bottom and leeward sides of the large cylinder than along the top and windward sides, due to differences in flame thickness and radiative exposure. In contrast, the smaller cylinders were uniformly engulfed in the fire and received higher, more spatially uniform levels of heat flux along their surface than the large cylinder.

More recently, an experiment was conducted with a 1.2 m diameter by 4.6 m long steel pipe centred in a 7.2 m diameter JP-8 fire [105, 106]. The cylinder was supported 1 m above the fuel surface, with its axis parallel to the fuel surface. A wind varying from 0 m/s to 2 m/s was observed during the test. As in the studies above, the change in wind speed was shown to greatly affect the measurements. At the beginning of the test, when the wind speed was greatest, the emissive power of the fire was measured to be highest on the leeward side of the object. This suggested that a recirculation zone, with enhanced mixing of fuel and air, formed behind the object [105]. Also, the bottom and leeward sides of the object received higher levels of heat flux and were thus hotter. Radiation to the object was thought to be affected by the presence of a cool, soot-laden boundary layer next to the object surface, particularly early in the test [106]. Near the end of the test, when the wind died down and the pipe was more uniformly engulfed in the fire, the heat flux to the leeward side decreased while that to the windward side increased slightly [105]. At this time, the optical thickness of the flame covering the leeward side of the object would have decreased, allowing this side of the object to radiate to the cooler surroundings outside the fire [106]. In addition, the flame emissive power decreased near the bottom of the cylinder, suggesting the presence of an oxygen-starved, fuel-rich, vapour zone below the pipe during this period [105]. The presence of such a region was previously observed in some large fires in quiescent and low wind conditions and it was surmised that surfaces located inside this zone received less heat flux from the fire [38, 43].

Heat flux to an engulfed object in the early developing stages (first 60 s after ignition) of a fire has also been investigated [101]. In this experiment, a 1.2 m diameter by 3 m long cylinder was located in a 1 m by 4 m hexane fire in quiescent conditions. Similar to the tests described previously, the bottom of the object received greatest exposure to the flames and underwent the most intense heating. The authors quantified the effect of the object on the fire by introducing a factor for "efficiency of hindered combustion." This factor describes the ratio of heat released by a fire when an object is engulfed in the flame to the maximum theoretical heat release calculated by assuming that combustion is complete and no obstacle is present in the fire. For the 4 m^2 pool of hexane, this efficiency was approximately 47% when the object was present, whereas the normal combustion efficiency was estimated to be 88% when the object was removed [101]. The above result indicated that the presence of the engulfed object significantly lowered the heat release rate of the fire.

Vertical plates have also been used to model objects in or adjacent to fires [87, 104, 107–109]. Little change in the overall thermal behaviour of a fire and an engulfed object has been reported to result from the change in object geometry. However, one case worth mentioning involves a 2.1 m by 4.6 m plate situated at the edge of a 20 m diameter JP-4 fire in quiescent conditions [87]. Since the plate was located outside the fire, the main flame volume did not appear to be affected by the presence of the object. However, a small secondary flame zone developed and became attached to the fire-facing side of the plate, as a result of restriction of air entrainment by the plate. This secondary zone contained two vertical counter-rotating vortices that impinged on the plate surface and had a diameter equal to half the width of the plate. The formation of this zone demonstrated that the presence of a large object close to a fire can induce turbulent effects and alter the thermal hazard posed by the fire to its surroundings.

Pool fires with engulfed objects are a subject of interest for those studying boiling liquid expanding vapour explosions (BLEVEs) of pressurized vessels [110–113]. In such cases, critical parameters include the time to failure and the mode of failure of the engulfed container, which are affected by container design. Experimental studies have been conducted to examine the thermal response of pressurized vessels in fire environments, but test conditions have typically involved propane burners rather than open pool fires [111, 112]. Pool fires are considered to be more susceptible to ambient wind conditions, affecting the repeatability of tests, while burners can be positioned to provide more controlled, uniform engulfment of the container

by the fire [112]. The thermal response of the engulfed container is influenced by the operation of pressure relief valves in the vessel as well as by differences in heating of the liquid and vapour inside the vessel [64, 111–114]. Although details of the pressurized vessel response are outside the scope of the present work, it should be mentioned that in one study involving a container engulfed in an open pool fire, slight winds were found to cause higher temperatures in the downwind region of the fire and on the downwind side of the container [113].

In all of the experiments mentioned above, minimal information on the effects of wind on fire plume development was actually obtained. When fires were too large to be held indoors, either fences were erected to block any ambient wind [105,109,113], or attempts were made to conditionally sample the data to distinguish time periods of very low wind (when the fire was not tilted significantly) from those of higher wind (when flames were absent from certain regions above the pool due to tilting of the fire) [102–104, 107]. To date, only two experiments have been conducted to investigate the interaction between fire, wind and a large cylindrical object [5,7,115]. Both experimental configurations were similar to the scenario being considered in the present study. The experiment of Suo-Anttila and Gritzo [5, 7] involved a 3.7 m diameter, 18.3 m long steel culvert sized to represent an aircraft fuselage. As depicted in Figure 2.5, it was placed at the leeward edge of a 18.9 m diameter outdoor pit that was filled with JP-8. The object was raised approximately 0.6 m above the initial level of the fuel surface and oriented with its longitudinal axis perpendicular to the direction of the prevailing wind. Average wind speeds of up to 10 m/s were measured during periods of quasi-steady fire behaviour.

The observed behaviour of the fire changed greatly with variations in wind speed [5, 7]. In low winds (less than 3 m/s), the fire remained mainly on the windward side of the object. A low-temperature, oxygen-starved vapour region was detected immediately above the fuel surface, consistent with previous large fire experiments [38, 43]. As the wind speed increased (3 to 8 m/s), the fire plume enveloped the central section of the cylinder and high temperatures were measured on both the windward and leeward sides of the object. A low-temperature, oxygen-starved zone was detected between the fuel surface and the central windward side of the culvert, indicating a reduction in air entrainment to this region of the fire due to thick flame cover and the presence of the object. In some instances, the oxygen-starved region extended underneath the culvert [7].

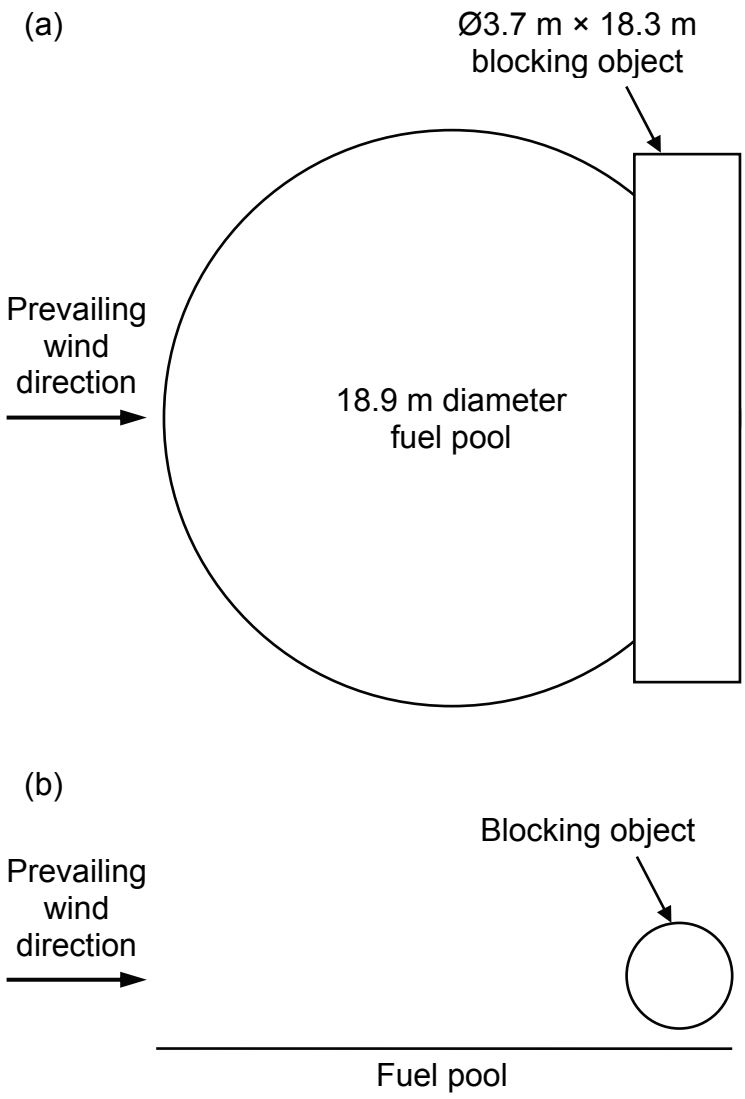

Figure 2.5: Experimental configuration for Suo-Anttila and Gritzo [7], (a) top view, (b) side view

At high wind speeds (8 to 10 m/s), the flame was observed to travel underneath the cylinder and attach to the downwind side of the object [7]. High temperatures and heat flux were recorded on the lower windward side of the object, indicating impingement of flame on this portion of the culvert. Heat flux to the fuel surface was greatest in the region underneath the cylinder, indicating high levels of mixing and combustion in the flow passing through this region and reradiation from the object to the fuel surface [7]. However, small oxygen-starved areas above the fuel surface were detected upwind of this region, at a slight distance away from the windward surface of the object. These results suggest that although the wind may have enhanced air entrainment and mixing in the fire, regions of the fire near the object and close to the fuel surface remained starved of oxygen. A slightly lower average fuel burning rate was measured due to redirection of the flame zone away from the pool surface [7]. Downwind of the object, large columnar vortices were observed in the fire plume behind the culvert [7]. These vortices were thought to enhance the entrainment of air and mixing in the wake of the object, resulting in increased combustion efficiency in this region. Consequently, the highest temperatures (over 1327°C) and heat flux (over 300 kW/m^2) were recorded on the leeward side of the object [7]. The heat flux magnitudes were approximately double those measured at the fuel surface and were larger than those previously measured along the surface of objects engulfed in fires in low wind conditions (up to 160 kW/m^2 [87,102,103,105,109]). These results suggest that although the presence of an object may reduce the combustion efficiency in a fire (as indicated by the "efficiency of hindered combustion" [101]), the additional presence of a crosswind may counter this reduction due to enhanced mixing and induced turbulent effects.

A similar experiment was conducted by Blanchat *et al.* [115] to characterize the thermal environment in an outdoor fire established over a 7.9 m diameter pit filled with JP-8. Steel cylinders representing weapons of various sizes were placed on the leeward side of the fuel pool, as illustrated in Figure 2.6. The largest cylinder was 1.2 m diameter by 4.6 m long and was located at the leeward edge of the fuel pool, 0.9 m above the ground plane. A medium-sized cylinder of 0.3 m diameter and 2 m length was placed further downwind, 8.5 m from the centre of the fuel pool and 0.3 m above the ground plane. The smallest cylinders were 0.3 m in diameter and 0.4 m long and were placed 1.4 m and 2.4 m downwind of the fuel pool centre, approximately 0.15 m above the ground plane. Two tests were conducted with the large blocking object in place and two additional tests were conducted without it. The two small cylinders and the medium-sized cylinder were present during all four

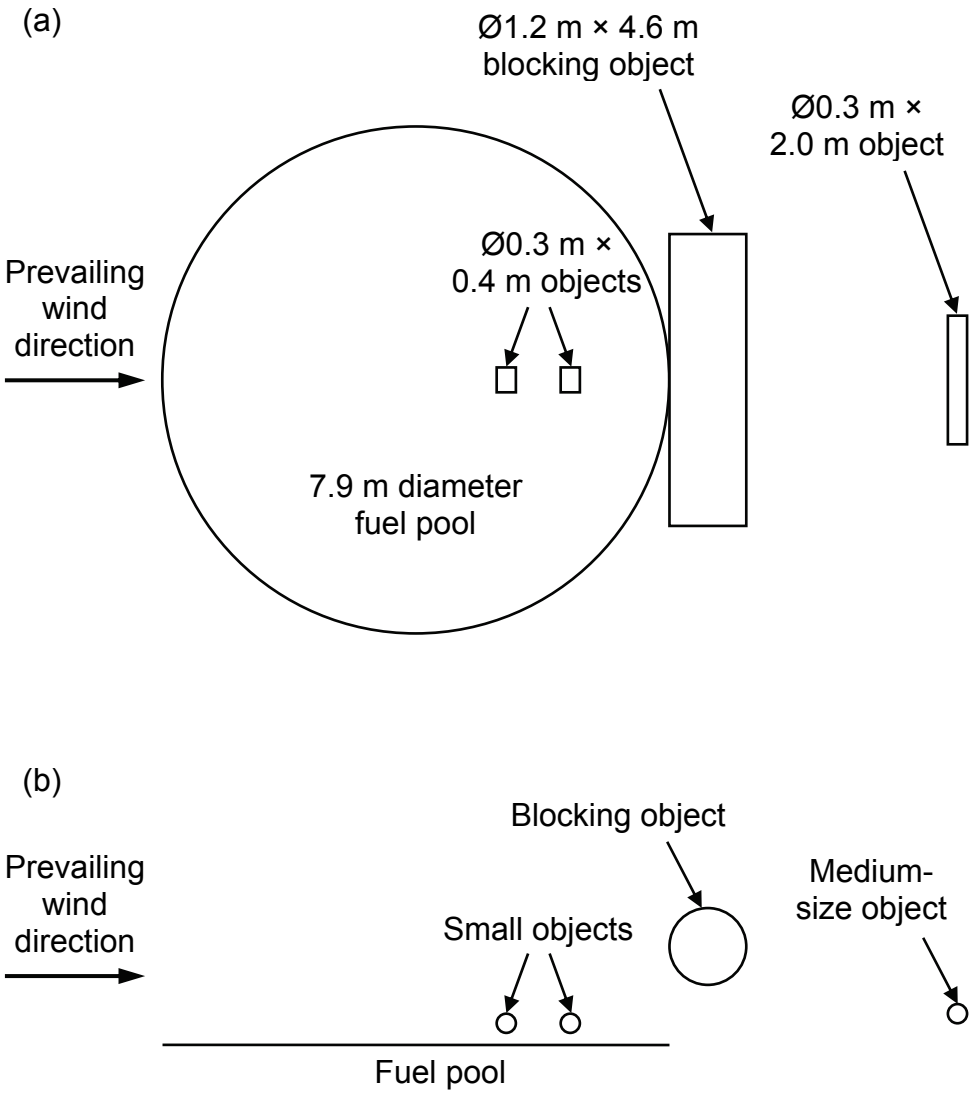

Figure 2.6: Experimental configuration for Blanchat *et al.* [115], (a) top view, (b) side view

tests. Average wind speeds ranging from 0.7 m/s to 6.1 m/s were measured during periods of quasi-steady fire behaviour.

Wind speed was observed to have a significant impact on the fire behaviour [115]. The effect of the blocking object was difficult to distinguish from the effect of wind because wind conditions were not exactly the same between tests with and without the large object. At the lowest wind speed (0.7 m/s), the fire plume was approximately vertical, indicating minimal influence of wind in this case. The interior of the fire contained an oxygen-starved region (similar to Suo-Anttila and Gritzo [7]), as evidenced by reduced levels of heat feedback to the fuel surface near the centre of the fuel pool [115]. The two small cylinders located downwind of the pool centre consequently received higher levels of heat flux along their top surface than along their bottom surface. Measurements of incident heat flux along the large blocking object reached up to 80 kW/m^2, with the highest levels occurring along the side facing the fire [115]. Heat flux to the medium-sized cylinder was dominated by radiation from the fire and remained low due to the large distance between the fire plume and the object.

At higher wind speeds, the plume tilted away from the vertical towards the large and medium-sized cylinders. Columnar vortices directed along the length of the plume were observed, and reduced levels of heat flux to the fuel surface were measured in the region between these vortices as a result of cooler ambient air being entrained into the plume [115]. No distinct oxygen-starved region was detected in the fire, so the heat flux incident on the two small cylinders was more uniform than during the tests in which the oxygen-starved region was present. The heat flux to the large blocking object was highest along the leeward surface, reaching up to 210 kW/m^2, due to increased fuel-air mixing in the wake region behind the blocking object [115]. Further downwind, the fire plume impinged intermittently on the medium-sized cylinder, resulting in measured heat flux levels of up to 250 kW/m^2 along the object surface [115].

Data from the above two experiments have been used for validation of computational fire physics models [115] and of simpler computational fire risk assessment models [116, 117]. In these validation simulations, the specific layout of the experiment was modelled accurately and output data were generated to allow direct comparison with the experimental results. Although the simulation results typically compared well with the experimental measurements, no further simulations using these models and different fire/object configurations have been reported, thus

limiting the ability to understand the overall physics of the interaction between wind-blown fires and large blocking objects. To this end, only one publication has been found describing a numerical analysis of fires in crosswinds of different speeds, with a large blocking object placed at various positions downwind of the fire [118].[7] This thesis outlined the development of a two-dimensional model for simulating turbulent buoyant flow around a circular cylinder located near the ground. The model was based on a semi-implicit, upwind finite-difference scheme and used a hybrid mesh that combined cylindrical coordinates near the cylinder with Cartesian coordinates far away from the cylinder. The overall computational domain spanned a length of 73.2 m by a height of 48.8 m. The fire was situated on the ground and was 6.1 m long. It was modelled using a constant heat source of 76 MW and a constant smoke source with a production rate of 0.13 kg/s. Uniform crosswinds with speeds of 3.0 m/s, 6.1 m/s and 9.1 m/s were imposed on the fire. A 4.9 m diameter cylinder was positioned with its windward edge aligned with the leeward edge of the fire (similar to the blocking object shown in Figure 2.6), at elevations of 2.4 m, 4.9 m and 7.3 m above the ground. These elevations were selected so that the ratio of the cylinder height to cylinder diameter would be 0.5, 1.0 and 1.5, respectively.

Time-varying velocity fields and smoke concentration fields were determined in each of the nine simulation runs [118]. For a cylinder height-to-diameter ratio of 0.5 and a wind speed of 3.0 m/s, the fire plume was vertical and did not impinge on the cylinder, indicating that buoyancy of the hot plume gases dominated the flow. When the wind speed was increased to 6.1 m/s, the plume tilted over and came into contact with the cylinder, oscillating between flowing along the windward and top surfaces of the blocking object and wrapping completely around it [118]. In this case, both momentum of the crosswind flow and buoyancy of the hot plume gases were important. At the highest wind speed of 9.1 m/s, the plume flowed horizontally along the ground underneath the cylinder, indicating that the flow in this region was dominated by inertial effects, before lifting off the ground approximately 30 m downwind of the cylinder [118].

Similar flow patterns were observed when the cylinder was situated at a height-to-diameter ratio of 1.0 [118]. In the 3.0 m/s wind condition, the plume impinged

[7] Although several radiation models of wind-tilted fires with objects have been developed, these models are typically analytical and are restricted to either the case of full engulfment of an object inside the fire [119, 120] or the case of an object sufficiently far from the fire that the plume does not impinge on it [64, 75]. The case in which the object obstructs the fire plume flow without necessarily being fully engulfed has not yet been addressed in detail.

slightly on the windward side of the cylinder, but remained mostly vertical. At a higher wind speed of 6.1 m/s, the plume fully engulfed the cylinder, oscillating between flowing mainly over the top of the blocking object and flowing mainly underneath it. At the highest wind speed of 9.1 m/s, the plume flowed along the ground underneath the cylinder and remained horizontal for almost the entire length of the computational domain. Simulation results for the case involving a cylinder height-to-diameter ratio of 1.5 were very similar to those discussed for the ratio of 1.0 [118]. Unfortunately, none of the simulation results were compared to experimental data. Such a comparison would be limited by the fact that the model was two-dimensional and did not include any combustion chemistry or radiation effects [118].

The studies described in this section all indicate that the behaviour of a fire can be greatly affected by the presence of an object, whether it is fully engulfed in the flame or located adjacent to the fuel pool. This is particularly apparent when the size of the object is comparable to that of the fire. The presence of the object restricts air entrainment into the fire and can reduce the level of combustion and heat release from the fire, as well as alter the geometry of the fire. Meanwhile, the presence of even very slight winds can affect the interaction between the fire and object by changing the global direction and geometry of the fire, changing the flame thickness around the object, producing recirculation zones behind the object, increasing air entrainment into the fire and enhancing fuel-air mixing in the fire. All of these effects influence the heat transfer from the fire to the object, making hazard analysis much more complex than would be suggested by the radiation theories highlighted in Section 2.1. Clearly, the fire environment in both the quiescent and windy conditions is dependent on the position, geometry and orientation of the object. Although the main aspects of the interaction between fires and large objects have been identified, much more detailed experimentation is needed to fully characterize the behaviour of a fire with an engulfed, thermally massive object.

When assessing the thermal hazards from a fire to a nearby object, heat flux is a critical parameter that must be evaluated. Difficulties in predicting heat flux levels from fires were previously discussed in Section 2.1; thus, heat flux is often measured in experimental fire scenarios. A number of different heat flux measurement techniques have been developed for high-temperature, transient applications such as fires. These are discussed in the next section.

2.4 Heat Flux Measurement

Heat flux is a measure expressing the rate of heat transfer to or from a surface per unit area [121]. It can be expressed as an incident flux or a net absorbed flux, the latter containing only the non-reflected component of the incident flux and thus dependent on the absorptivity of the surface. Total heat flux includes contributions by radiation, convection and conduction. The ability to measure total heat flux from a fire is important when convective and/or conductive effects are significant in addition to radiation (Table 2.1).

Unlike temperature, heat flux cannot be measured directly [122, 123]. Heat flux measurements are usually based on temperature measurements. Heat flux gauges can be divided into various categories based on operating principle, but because different authors make different distinctions between sensors [122–126], it appears that no one set of categories can be used to satisfactorily separate the many types of gauges. Consequently, in this section, heat flux sensors are discussed chronologically: a description of circular foil gauges and thermopiles, which have been used traditionally in fire studies, are given first, followed by a description of the more recently adopted thin-skin sensors and methods based on one-dimensional transient conduction analyses.

Circular foil gauges, commonly called Gardon gauges, consist of a thin circular disk connected at its circumference to a heat sink [17, 127]. The disk is often made from constantan and the heat sink is a copper cylinder that is typically water-cooled. Heat flux measurements are based on determining the temperature difference between the centre and edge of the disk using a differential thermocouple comprised of the copper cylinder, the constantan foil, and a copper wire attached to the centre of the foil. Under appropriate conditions, the voltage output of the thermocouple is linearly related to the incident heat flux. However, caution must be taken when interpreting data from these gauges, as they respond differently to different modes of heat flux [124, 128–132]. The calibration curve for voltage output versus incident heat flux is, to a good approximation, linear for radiative heat transfer, but it is non-linear for convective heat transfer due to variations in temperature across the circular foil of the gauge [128, 130, 131]. Although most Gardon gauges are presently calibrated using radiation sources, they are often applied in environments with both radiative and convective heat transfer. Corrections may be applied to data from these gauges when they are used in mixed environments [128, 129]. The error resulting from the discrepancy between the calibration and application environments

can be reduced by using smaller diameter gauges, but this comes at the expense of decreased gauge sensitivity[8] [129,132]. Other errors associated with Gardon gauges include heat loss through the wire at the centre of the foil, asymmetric heating caused by shear flows across the face of the gauge, and changes in absorptivity of the sensor surface coating across the radiation spectrum in fires [122,124,133–135]. In previous fire experiments, Gardon gauges were used to measure heat flux to the fuel surface and to locations outside the fire [7,37,42,115]. Measurements of both total and radiative heat flux were made, depending on whether or not the sensor surface was covered by a window to minimize convective effects.

In contrast to Gardon gauges, thermopile gauges contain a thermal resistance layer with one side exposed to the incident heat flux [123,125]. Thermocouples connected in series are used to measure the decrease in temperature across the depth of the resistance layer. Based on Fourier's Law and an assumption of steady, one-dimensional conduction through the resistance layer, the incident heat flux is proportional to the measured temperature difference over a specific range of temperatures. The use of a thermopile instead of a single differential thermocouple permits increased sensitivity because the signal from an individual thermocouple pair becomes multiplied by the number of thermocouple pairs present in the thermopile. One popular implementation of the thermopile gauge, called the Schmidt-Boelter gauge, consists of a thermal resistance layer around which a wire formed from one of the thermocouple materials is wound [136]. One half of this wire is electroplated with the other thermocouple material so that a set of thermocouple junctions is formed at the top and bottom of the resistance layer where the electroplated coating ends. The entire assembly is typically placed on top of a heat sink. Although this method of fabrication produces a sensor that is not a true thermopile [136], Schmidt-Boelter gauges generate voltages that are directly proportional to the incident heat flux over a broad range of temperatures. Errors associated with this type of gauge arise from the fact that one-dimensional heat transfer is not entirely maintained [125]. Like Gardon gauges, thermopiles are thought to have different sensitivities for radiative versus convective heat transfer [137]. Furthermore, for the high temperatures typical of fires, the linearity of the calibration curve may not hold, depending on the type of thermocouples used [124]. Thermopiles have been conventionally employed in fire studies to measure radiative heat flux to locations outside the fire [34,37,59,77,100].

[8]Gauge sensitivity is the voltage output per unit of heat flux (often in $\mathrm{mV/(W/cm^2)}$). The sensitivity decreases when the temperature differential measured by the sensor is reduced [128,132].

Other heat flux measurement techniques involve determining the change in energy of a thermally isolated sensor that is exposed to the heat flux being measured [122,123,125]. This calculation requires knowledge of the thermal capacitance of the sensor and the rate of change of the mean temperature of the sensor. The sensor can be made from a thin metal plate that has a thermocouple attached to the back surface (termed a "thin-skin sensor") [122, 123, 125]. The back surface of the plate is usually insulated to minimize convective losses. The measured temperature is assumed to be the same as the temperature of the exposed front surface and any lateral conduction along the surfaces is ignored.[9] Due to the small thickness of the plate, conduction along the thermocouple wires creates uncertainty in the measurement [134]. Other errors include disturbance of the surface thermal field due to the presence of the thermocouple, contact resistance between the thermocouple and the sensor plate, and displacement of the effective thermocouple junction location from the sensor plate surface [141]. Furthermore, since the sensor is not cooled, the measured net absorbed heat flux decreases as the gauge temperature approaches that of the surrounding medium and must be adjusted to represent an incident heat flux before being compared to data from water-cooled gauges [142].

In cases where significant thermal losses from thin-skin sensors may occur (e.g. as an inherent part of the sensor installation), heat flux can be estimated by means of a one-dimensional transient conduction analysis of the measured temperature-time histories [143]. This method may be applied to temperatures measured inside or on the surface of objects of any thermal mass [122]. When sensors with greater thermal mass are used, slower transient responses are associated with this measurement method than with Gardon or thermopile gauges. For temperatures measured inside the object, one-dimensional inverse heat conduction codes are often employed to calculate the heat flux absorbed at the surface [144, 145]. The measured temperatures are used in conjunction with a finite-element based conduction solution to determine the surface heat flux. One-dimensional transient conduction analyses have been used in previous studies to determine hazards to objects engulfed in

[9]This type of sensor is often used to measure flame temperature and is known as a Directional Flame Thermometer (DFT) or Plate Thermometer (PT) [4, 73, 138–140]. When placed inside a fire, the thin metal plate rapidly achieves thermal equilibrium with the surrounding flames. Assuming that convection effects are negligible, the thermocouple measures the temperature of a blackbody that emits a radiative flux equivalent to the flux incident on the front surface of the plate [138, 140]. Thus, these temperature measurements can be compared to those from freestanding thermocouples in the flame gases. If required, correction for convection effects along the sensor plate can be made using an assumed value for the convection coefficient of the surrounding flame gases.

fires [87, 100, 103–105, 107, 115] and to assess the response of skin simulants in flash fires [146, 147].

For all of the heat flux gauges described above, perturbation of the thermal and flow fields in the vicinity of the sensor is a source of error that must be considered, particularly if the sensor is embedded in a surface [148–150]. Changes in surface temperature and surface absorptivity/emissivity, as well as generation of turbulence and increased mixing, can all affect the accuracy of the heat flux measurements [122, 123, 125, 129, 148–150]. Gauges that are water-cooled tend to become affected by condensation and soot deposition on the sensor surface [142]. As mentioned previously, large errors in measured heat flux values can arise from differences between the calibration and measurement environments [148, 149]. These differences include not only the mode of heat flux applied to the sensor but also the conditions of installation, such as the type of substrate surrounding the sensor and the temperature of the cooling water [149, 151]. If large changes in temperature are expected during an experiment, the dependence on temperature of the material properties (e.g. conductivity and specific heat) of the sensor can also affect the gauge sensitivity [122].

For the wind-blown fire scenarios considered in the present study, discrepancy between the calibration environment and the measurement fire environment is a potential major source of error that can greatly affect the heat flux data. Large fires are typically considered to be radiation-dominated (Table 2.1) and most types of heat flux gauge have been calibrated in radiative environments [15]. However, convection can play a significant role in wind-blown fires, yet heat flux gauges have not been characterized extensively in mixed radiative-convective conditions. As a result, improved understanding of the thermal response of heat flux gauges in mixed radiative-convective environments is required.

2.5 Summary

As indicated in this chapter, the ability to accurately predict the behaviour of a fire in real-life accident scenarios remains limited. Experimentally, it has been difficult to simulate such scenarios, since tests with small-scale fires do not fully simulate the physics of large-scale fires, and few research facilities can accommodate large-scale fire tests. Of the large-scale fire testing facilities that are currently available, most are located outdoors, where wind conditions are poorly controlled. This has

severely restricted the quantity and quality of data, as well as the level of detail in the information that has been acquired. Some research has been conducted to characterize the geometry of wind-blown fires, but the results have not been consistent due not only to differences in physical parameters such as wind speed, fire size and fuel type, but also to differences in methods of defining and measuring the geometrical parameters. The visual methods that have been used to characterize flame geometry have had limited effectiveness in large, sooty fires. More detailed measurements and analysis are therefore needed in order to develop a set of general correlations that can accurately predict the geometry of any wind-blown fire. The addition of fully or partially engulfed objects in the wind-blown fire scenario has been shown to complicate characterization of the fire environment by further altering the global geometry of the fire, patterns of air entrainment and fuel-air mixing in the fire, and levels of heat release from the fire. Most of the research to date has been focussed on either the interaction of wind and fires or the interaction of fires and large objects. Only two experimental studies have so far been performed to examine the behaviour of fires in medium to high winds with large objects located in or near the fire. Both were conducted in outdoor facilities, with little control of ambient conditions. The present study builds upon the above research through a series of controlled, large-scale experiments to investigate the thermal environment encountered in a transportation accident scenario with a pool fire in crosswind, with and without a large blocking object situated downwind of the fuel pool. Through characterization of the temperature field in the fire plume, the overall geometry of the fire can be described in greater detail than by looking at video images alone, as was done in previous studies of unobstructed, wind-blown fires. Measurements of temperature and heat flux along the surface of the blocking object, as well as of heat flux to the ground near the fire, contribute further information towards understanding the interaction between fires, wind and large objects.

As mentioned above, heat flux is a parameter of particular interest to fire researchers, as it is needed in the assessment of hazards in fire-related accident scenarios. However, proper interpretation of heat flux measurement results in wind-blown fires can be hindered by a lack of congruity between the calibration and measurement environments. Convective effects can be significant in wind-blown fires, yet most heat flux gauges have been tested mainly in radiative applications and are not normally intended for use in mixed radiative-convective conditions. To improve interpretation of the heat flux data to be obtained in the wind-blown fires of the present study, a systematic comparison of the responses of four different heat flux

gauges in various controlled radiative and mixed radiative-convective environments was first conducted. This set of experiments forms the subject of the next chapter.

Chapter 3

Heat Flux Measurement in Mixed Radiative-Convective Environments

This chapter describes experiments to examine the thermal response of four heat flux gauges in radiative and mixed radiative-convective environments. The purpose of these experiments was to enhance understanding of the gauge behaviour in different thermal conditions and consequently to improve interpretation of heat flux measurement results from the fire tests. A modified version of this chapter was recently published as Lam and Weckman [19]. The following sections present the setup and boundary conditions of the heat flux experiments, as well as results from each of the four heat flux gauges.

3.1 Experimental Setup and Methods

A controlled radiative environment was produced using a cone calorimeter manufactured by Fire Testing Technology Limited of East Grinstead, UK [152]. The unit contained a heating coil wound in the shape of a truncated cone. This conical heater, which had a base diameter of 160 mm, imposed a constant radiative heat flux on the surface of the heat flux gauge, which was placed at a distance of 75 $\pm$ 3 mm below the base of the heater (Figure 3.1). Two heat flux levels were considered: a lower level (nominally 15 kW/m^2) corresponding to a temperature setting of 600°C on the cone calorimeter, and a higher level (nominally 30 kW/m^2) corresponding

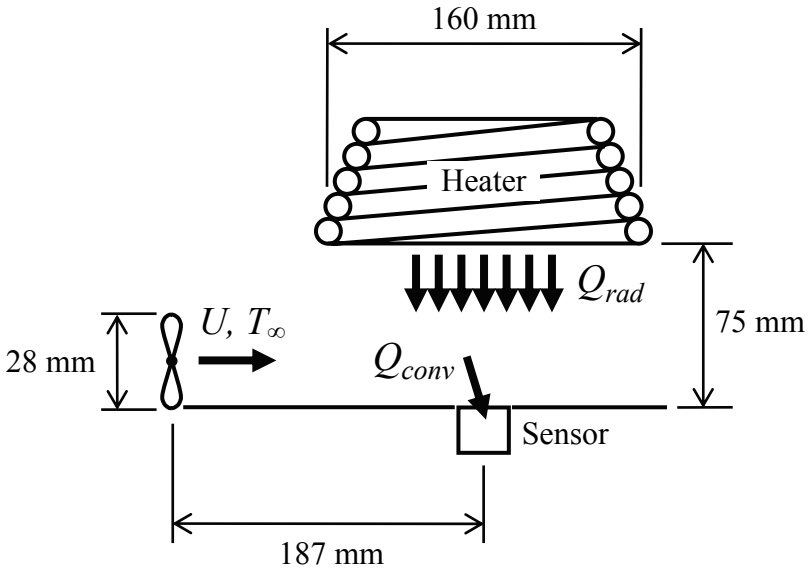

Figure 3.1: Sketch of experimental setup

to a temperature setting of 760°C. Convective and mixed radiative-convective environments were achieved by using a heat gun to propel a continuous stream of air across the face of the heat flux gauge while the gauge was centred underneath the conical heater (Figure 3.1). For convective conditions, the heater was turned off, while for mixed radiative-convective conditions, the heater was maintained at one of the two temperature settings listed above. The outlet of the heat gun was 28 mm in diameter and was positioned at a distance of 187 ± 3 mm from the centre of the gauge. To maintain similar flow conditions over all gauges, each one was mounted so that the sensor surface was flush with a surrounding, 13 mm thick, cement board that extended to the outlet of the heat gun. Different heat gun settings permitted control of the temperature and speed of the "convective" airstream. Additional description of the radiative and convective sources is provided later in Section 3.2.

Four total heat flux gauges were considered in this study: the Schmidt-Boelter gauge, the Gardon gauge, the Directional Flame Thermometer (DFT) and the Hemispherical Heat Flux Gauge (HFG). The former two gauges were water-cooled, with the sensing element producing a voltage output that was linearly related to the incident heat flux through a manufacturer-provided calibration constant. In contrast, the latter two gauges were not water-cooled and required use of an inverse conduction analysis to obtain estimates of the total incident flux.

The Schmidt-Boelter gauge (Figure 3.2) was a windowless, water-cooled sensor (Model GTW-10-32-485A) manufactured by Medtherm Corporation of Huntsville,

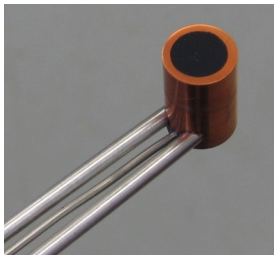

Figure 3.2: Photograph of Schmidt-Boelter gauge

Figure 3.3: Photograph of Gardon gauge

AL. It was provided by the manufacturer of the cone calorimeter to calibrate the conical heater.[1] The gauge was 13 mm in diameter and 19 mm tall, with a sensing area of 9.5 mm diameter. A sensing surface absorptivity of 0.94 and a full-scale output of 100 kW/m^2 were specified by the gauge manufacturer. As mentioned in Section 2.4, the gauge produced a voltage corresponding to the difference in temperature across a thin thermal resistance layer situated at the sensing surface [136]. A calibration constant (based on irradiation over a hemisphere, 2π steradians [153]) was supplied to permit reduction of gauge voltage measurements to incident heat flux values. The calibration accuracy was stated as $\pm 3\%$, at a 95% confidence level. The temperature of the cooling water was maintained within ± 7°C of the calibration water temperature of 27.4°C. Under ambient conditions, an increase of 15°C in cooling water temperature was determined to decrease the heat flux readings by 0.17 kW/m^2, one to two orders of magnitude smaller than the expected measured heat flux values.

The Gardon gauge (Figure 3.3) was a windowless, water-cooled sensor (Model Thermogage^{TM} 1000-1) manufactured by Vatell Corporation of Christiansburg, VA. It was 25 mm in diameter and 25 mm tall. The sensing foil of the gauge was 4.7 mm

[1]Since this gauge was used to calibrate the cone calorimeter, it served as a reference gauge to which other types of heat flux sensors could be compared. Accordingly, it was not used in any fire experiments; however, other Schmidt-Boelter and thermopile gauges were available for testing in the fire experiments of Chapter 5 and will be described later in Section 5.1.3.

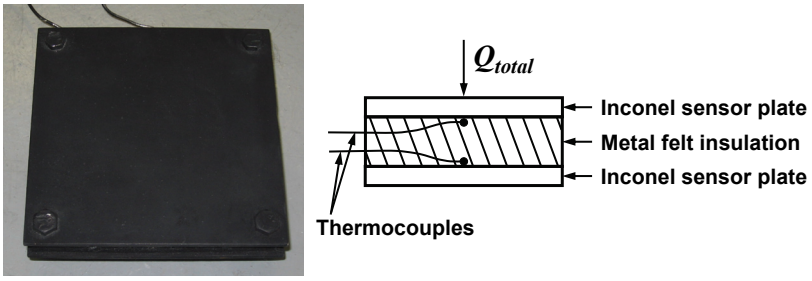

Figure 3.4: Photograph and cross-sectional sketch of DFT

in diameter and 0.013 mm thick [154]. The manufacturer-specified sensing surface emissivity was 0.94 and the full-scale output was 150 kW/m^2. Since no calibration water temperature was provided, the cooling water temperature was maintained above the dew point to prevent condensation on the sensor surface [124, 131]. The gauge produced a voltage corresponding to the difference in temperature between the centre and edge of the sensing foil [127] (Section 2.4). Like the Schmidt-Boelter gauge, a calibration constant, based on irradiation over 2π steradians and with a stated accuracy of $\pm 3\%$, was supplied with the gauge to permit reduction of the voltage measurements to incident heat flux values.

The last two gauges were thin-skin sensors (Section 2.4). The DFT (Figure 3.4) [139], which was manufactured by Ktech Corporation of Albuquerque, NM, consisted of two 120 mm by 120 mm by 3.2 mm thick Inconel sensor plates separated by a 12 mm thick layer of 7% dense, FeCrAlM metal felt insulation. Single, Inconel-sheathed, chromel-alumel (Type K) thermocouples with outer diameters of 1.6 mm were attached to the centre of the unexposed face of each sensor plate. The exposed faces of the plates were coated with Pyromark Series 2500 flat black paint (with an emissivity of 0.85 [155]) to achieve diffuse, gray surfaces.[2] With only one plate facing the heater of the cone calorimeter, the other sensor plate was insulated with two layers of 25 mm thick ceramic fibre insulation (which were compressed to a combined thickness of approximately 41 mm due to the weight of the gauge) in order to minimize any convective and conductive effects along the back surface of the DFT. As will be discussed later (Section 3.2), the DFT sensor plate was larger than the width of the airflow passing over it during the convective tests.

The HFG (Figure 3.5) [155] was manufactured by Sandia National Laboratories of Albuquerque, NM. It contained a 102 mm by 102 mm by 0.25 mm thick stainless

[2] A construction similar to the DFT was used to measure heat flux to larger cylindrical calorimeters in the fire experiments of Chapter 5. These calorimeters are described in Section 5.1.3.

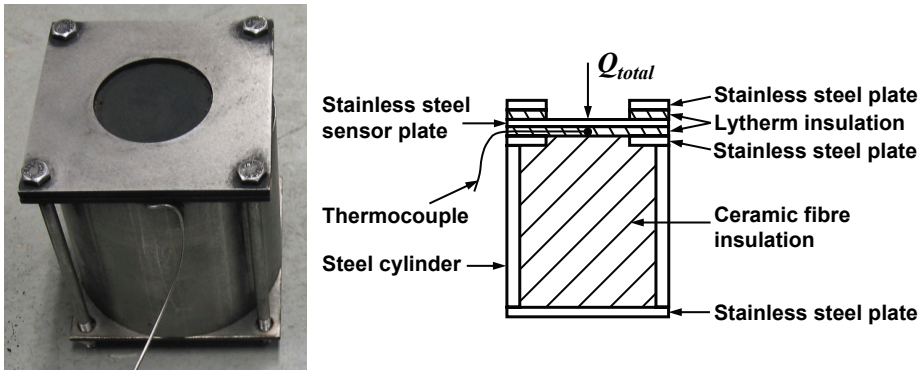

Figure 3.5: Photograph and cross-sectional sketch of HFG

steel sensor plate with a 50 mm diameter exposed sensing area in the centre. The area of the plate around the exposed sensing area was sandwiched between two layers of 3.2 mm thick Lytherm® insulation; that combination was then sandwiched between two 3.2 mm thick stainless steel plates, each with a 50 mm diameter hole in the centre. The sensing surface was therefore recessed below the top surface of the gauge housing by 6.4 mm. Like the DFT, the exposed area of the sensor plate was coated with Pyromark black paint to achieve a diffuse, gray surface. A 1.6 mm diameter, Inconel-sheathed, chromel-alumel (Type K) thermocouple was attached to the centre of the unexposed side of the sensor plate. The entire insulation and steel plate assembly was placed against one end of a 102 mm diameter by 102 mm long by 5.7 mm thick steel cylinder that formed the body of the gauge. The volume inside the cylinder was filled with ceramic fibre insulation to minimize heat losses from the rear face of the sensor plate. Previous preliminary tests indicated that HFG heat flux measurements were significantly affected by convective losses from the steel housing [156]; thus in the present tests, the HFG was wrapped with a layer of 25 mm thick ceramic fibre insulation to minimize such convective effects.

All gauges were connected to a Keithley Model 2700 data acquisition system with a Model 7708 switching module. Data were recorded to a computer using Keithley's ExceLINX software at a rate of approximately 2 Hz.

Temperature data from the DFT were reduced to heat flux using the one-dimensional inverse heat conduction program IHCP1D of Beck Engineering Consultants Company in Okemos, MI [144]. This program could capture time variations in heat flux as it does not require quasi-steady conditions to be attained by the gauge. A two-layer, planar wall was used to model the sensor plate and the metal felt insulation. Table 3.1 shows the temperature-dependent thermal properties used

Table 3.1: Temperature-Dependent Thermal Properties Used in IHCP1D for DFT

Inconel sensor plate:				
Temperature (°C)	-17	200	427	870
Thermal conductivity (W/m/°C)	14.0	17.5	20.8	28.8
Temperature (°C)	25	204	650	
Volumetric heat capacity ($J/m^3/°C$)	3740000	4080000	4880000	

Metal felt insulation:				
Temperature (°C)	20	300	650	910
Thermal conductivity (W/m/°C)	0.07	0.20	0.31	1.2
Temperature (°C)	25	330	730	
Volumetric heat capacity ($J/m^3/°C$)	305560	383570	585110	

for each layer [157]. The measured data from the thermocouple that was attached to the modelled sensor plate were input to the program, while the data from the remaining thermocouple were used to prescribe a temperature time history at the other side of the insulation as a "known" boundary condition. Calculation nodes were distributed across each layer of the wall, in the direction normal to the wall. The total number of nodes used was 101, the maximum allowed by the program. Trial runs using half this number produced heat flux values that were less than 1% different from those calculated using the maximum possible number of nodes. Since computational time was not significantly affected by the number of nodes, the maximum number was used, with 23 nodes in the sensor plate and 78 nodes in the insulation. This distribution was chosen so that the spacing of nodes throughout the wall would be relatively uniform.

Also included in the IHCP1D program input was the number of future temperatures (r) to be used. Future temperatures (or temperatures measured at times greater than the calculation time) were required by the algorithm for estimation of heat flux [144, 158]. Equation 3.1 was provided in the IHCP1D manual [144] to assist in the choice of an appropriate value for r.

$$r = 1 + 0.18\left(d^2/\alpha\Delta t_{exp}\right) \tag{3.1}$$

The minimum recommended value of r was 2 and higher values (typically 3 or 4) were advised for situations involving large random variations or noise in the temperature input data [144]. Increasing the number of future temperatures would

improve stability in the inverse calculations, but decrease the accuracy of the solution by damping the results [103, 144, 159, 160]. Although Equation 3.1 suggested that two future temperatures be used for the DFT, a value of three was selected for r in order to reduce effects of random variations in the thermocouple data.[3] It should be noted that when similar one-dimensional inverse conduction models were previously applied to evaluate heat flux to objects in large fires, between three and five future temperatures were typically used [87, 103, 105, 160].

Temperature data from the HFG were analyzed using the data reduction routine described in Blanchat *et al.* [155]. This program, which was developed by Sandia National Laboratories specifically for their HFG and implemented using Microsoft Visual Basic, was based on heat conduction equations derived from first principles. It modelled the gauge response to an applied heat flux as the one-dimensional response of a heated composite wall composed of the sensor plate and the insulation. The model accounted for reradiation from the sensor surface, storage of sensible heat in the sensor plate, and conduction of heat through the layer of insulation. If required, convection losses could be included by defining an appropriate convection term in the code.[4] The program input consisted of the data from the thermocouple attached to the sensor plate. Temperature-dependent thermal properties for the sensor plate were based on standard values available for AISI 304 [121, 155], while thermal properties for the insulation were estimated using Equations 3.2 and 3.3 [155, 162]. Further details of the thermal model are contained in Blanchat *et al.* [155].

$$k(T) = -6.05 \cdot 10^{-3} + 6.98 \cdot 10^{-5} \cdot T + 1.04 \cdot 10^{-7} \cdot T^2 \tag{3.2}$$

$$\rho c_p(T) = 128\left(6.73 \cdot 10^{2} + 4.52 \cdot 10^{-1} \cdot T - 1.09 \cdot 10^{-4} \cdot T^2\right) \tag{3.3}$$

[3] Large temporal variations were expected to be encountered when measuring temperature in fires [73, 103, 107, 161], so three future temperatures were considered appropriate for data taken in the fire experiments of the next two chapters. Since the cone calorimeter tests were intended to compare the behaviour of the heat flux gauges used in the fires, the same IHCP1D program input values were used to analyze the data in both the cone calorimeter experiments and the fire experiments.

[4] In this case, no convection term was needed to produce an output of incident total heat flux (Section 3.3.3).

Table 3.2: Convective Flow Conditions

Convective Condition	Representative Speed (m/s)	Representative Temperature (°C)
1	4.6 ± 0.1	80 ± 4
2	6.2 ± 0.1	102 ± 4
3	8.3 ± 0.2	139 ± 6

3.2 Boundary Conditions

The uniformity of the radiative heat flux field across the horizontal measurement plane was examined using the Schmidt-Boelter gauge. The measured heat flux varied in an approximately parabolic manner as a function of radial distance from the vertical central axis of the cone heater, with a peak value measured underneath the centre of the heater and decreasing values measured as the gauge was moved outwards from the central axis. The measured heat flux remained within 15% and 18% of the peak (centreline) value over a distance of 45 mm from the central axis for the lower and higher heat flux settings, respectively. This decreasing trend in measured local heat flux with increasing distance from the axis was compared to the corresponding change in view factor from a disk representing the heat source to a differential element representing the heat flux gauge (configuration B22 in Howell [65]). As the differential element was offset from the central axis of the disk, the view factor decreased parabolically, in agreement with the observed trend in the measurements.

Three convective conditions, summarized in Table 3.2, were considered. To define these conditions, several measurements of velocity and temperature were made at different positions in the flow field using a 4 mm diameter pitot tube and 1.6 mm diameter, Inconel-sheathed thermocouple, both aligned with the mean flow direction and pointing upwind. The representative values reported in Table 3.2 were measured at heights between 5 mm and 15 mm above the centre of the gauge surface. Measurements along a line perpendicular to the mean flow axis and the central axis of the cone heater showed that the velocity remained within 12% of the listed values across a ±8 mm distance and within 64% across a ±23 mm distance from the central axis. The temperature remained within 16% of the listed values across a ±8 mm distance and within 56% across a ±23 mm distance. The total width of the jet flow (based on the velocity measurements) was approximately 65 mm at the leading edge of the HFG and DFT and approximately 100 mm at

the trailing edge. These widths were larger than the sensing areas of the Schmidt-Boelter gauge, Gardon gauge and HFG, but smaller than the 120 mm wide sensor plate of the DFT.

Based on the Schmidt-Boelter measurements presented in the next section, the convective portion of the total heat flux in the mixed radiative-convective conditions was 26%, 35% and 47% (for the first, second and third convective flows, respectively) when the cone calorimeter was set to 600°C (nominally 15 kW/m^2), and 17%, 22% and 32% when the cone was set to 760°C (nominally 30 kW/m^2). The decrease in convective fraction for the higher setting on the cone calorimeter was expected due to the increased radiative load with increased cone temperature.

3.3 Results

As explained above, measurements of incident total heat flux from each of the four heat flux gauges were taken under two radiative conditions, three convective conditions and six mixed radiative-convective conditions. This section presents results first from the Schmidt-Boelter and Gardon gauges, then from the DFT and finally from the HFG.

3.3.1 Schmidt-Boelter and Gardon Gauges

Figure 3.6 contains a typical time trace of incident total heat flux from the Schmidt-Boelter and Gardon gauges for the radiation-dominated reference test with the cone calorimeter at 600°C and no airflow. (For reference, additional plots showing typical time traces of heat flux measured in the convective and mixed radiative-convective conditions are provided in Appendix A.) The plot indicates that both gauges were at steady state during the measurement period, as expected since the data were collected after the cone heater had reached steady state. Time-averaged values of the heat flux measured by each gauge in the convective, radiative and mixed radiative-convective conditions are shown in Tables 3.3 and 3.4. Due to their small size, both sensors recorded local values of radiation underneath the centre of the heater. Measurements in the top row, made with only the radiative source, serve as a basis through which to compare the responses of all the gauges to a radiation-dominated environment. Measurements in the leftmost column, made with only the convective heat source, were taken in an attempt to isolate the response of

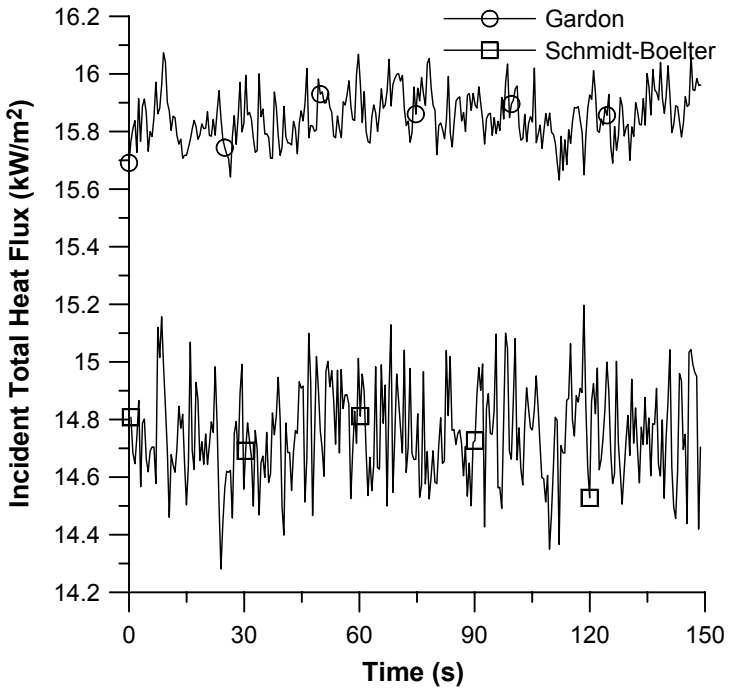

Figure 3.6: Time trace of incident total heat flux from Schmidt-Boelter and Gardon gauges in test condition with cone calorimeter at 600°C and no airflow

Table 3.3: Schmidt-Boelter Gauge Incident Total Heat Flux Measurements (kW/m^2)

	No imposed radiation	Cone at 600°C	Cone at 760°C
No forced convection	0.0 ± 0.0	14.7 ± 0.2	29.7 ± 0.3
Convective flow #1	3.4 ± 0.1	19.7 ± 0.2	35.7 ± 0.2
Convective flow #2	6.4 ± 0.2	22.4 ± 0.2	38.2 ± 0.3
Convective flow #3	11.7 ± 0.3	27.7 ± 0.3	43.4 ± 0.3

Table 3.4: Gardon Gauge Incident Total Heat Flux Measurements (kW/m^2)

	No imposed radiation	Cone at 600°C	Cone at 760°C
No forced convection	0.0 ± 0.0	15.9 ± 0.1	31.9 ± 0.2
Convective flow #1	3.0 ± 0.1	18.0 ± 0.1	32.9 ± 0.1
Convective flow #2	5.4 ± 0.1	19.6 ± 0.1	33.9 ± 0.1
Convective flow #3	9.6 ± 0.2	23.0 ± 0.2	36.5 ± 0.2

each gauge to the various convective flow conditions.[5] The value of 0.0 kW/m^2 with no imposed radiation or convection indicates that bias errors in the gauges were minimal and that negligible heat transfer occurred between the water-cooled gauges and the ambient surroundings.

The Schmidt-Boelter data measured under the convective conditions (Table 3.3, leftmost column) were compared to predicted values of centreline heat flux determined theoretically via Equation 3.4, in which h was estimated using an empirical correlation for the Nusselt number [121]. Considering that the gauge was mounted flush to a flat plate and exposed to a turbulent flow, h was initially calculated using Equation 3.5 (with thermal properties pertaining to air) to estimate a local convection coefficient for turbulent flow over a flat surface.

$$Q_{conv} = h\left(T_\infty - T_s\right) \tag{3.4}$$

$$h = (k/X)\left(0.0296 Re_X^{0.8} Pr^{1/3}\right) \tag{3.5}$$

[5]For the purposes of this discussion, these two situations will be referred to as "no forced convection" and "no imposed radiation", respectively. It is recognized that there may still be effects of natural convection and ambient radiation from the surroundings.

Using a gauge surface temperature of 32°C, which was the average temperature of the cooling water during the tests, and dividing by the gauge absorptivity to permit comparison with the measurements, the resulting predictions for heat flux under the three convective flow conditions were 1.1 kW/m^2, 2.0 kW/m^2 and 3.7 kW/m^2, all of which were approximately 68% lower than the measured values. Considering that the gauge surface temperature was likely higher than the temperature of the cooling water, the discrepancy between the measured and these theoretical values would be even larger.

Reasons for the discrepancy include the applicability of a flat plate boundary layer Nusselt number correlation to the rough surface of the board surrounding the gauge, as well as the assumption of turbulent boundary layer flow. With regard to the latter assumption, use of the corresponding laminar flat plate correlation did not result in higher values of predicted heat flux, since the dependence on the Reynolds number was weaker (exponent of 0.5 instead of 0.8 [121]). Perhaps more importantly, the temperature difference between the cooler water-cooled gauge and the hotter surrounding cement board introduced a surface temperature discontinuity, which would disturb the boundary layer and affect convection heat transfer [130, 148, 150]. When h was calculated as an average coefficient over the surface of the gauge, using the correlation in Equation 3.6 for laminar flow over a flat surface, predicted heat flux values of 3.8 kW/m^2, 6.4 kW/m^2 and 11.2 kW/m^2 were much closer (within 12%) to the measured values in Table 3.3.

$$h = (k/l)\left(0.664 Re_l^{0.5} Pr^{1/3}\right) \tag{3.6}$$

The convection coefficients estimated using Equation 3.6 were over three times those calculated using Equation 3.5. This indicates the importance of the choice of correlation used to calculate the convection coefficient above a gauge surface, when convective heat transfer effects are significant. The influence of this parameter on heat flux measurements has been previously discussed by others [16]. It should also be noted that, due to the increased convection caused by "tripping" of the boundary layer at the leading edge of the gauge, the heat flux measured by a water-cooled gauge would not likely be representative of the heat flux to an undisturbed surrounding material, which is allowed to heat up (i.e. if no sensor were present) [148, 150].

Comparison of the Schmidt-Boelter data in Table 3.3 with the Gardon data in Table 3.4 shows that in the radiative environments, the Gardon measurements were higher by 7-8%. This discrepancy may have been partly due to differences in the calibration method used by the individual manufacturers (note that the manufacturer-specified calibration uncertainty for each gauge was ±3%) and partly due to the different sensitivities of the two gauges. This latter factor is particularly important because the measured values were at the low end of the measurement range for both gauges. (Heat flux levels closer to the full range could not be considered in this study because the temperature setting of 760°C was the highest setting at which the cone heater was able to operate safely for continuous periods.)

In the convective and the mixed radiative-convective environments, the Gardon measurements were lower than the Schmidt-Boelter measurements by 8-18%. This difference increased as the radiative portion of the total heat flux decreased and the convective portion increased. Under a uniform radiative heat flux, the surface temperature of the Gardon gauge varied radially, with the peak temperature located at the centre of the gauge and the magnitude of the variation dependent on the level of heat flux incident on the gauge [128, 131, 132]. Asymmetric heating of the Gardon sensing surface by a convective flow would have resulted in non-uniformities in the sensing surface temperature along the flow direction (shifting the peak temperature away from the centre of the gauge) and thus different sensitivities to the convective and radiative portions of the total heat transfer [124, 128–132]. In this case, application of a radiation-based calibration constant to data taken in mixed environments, as was done for the values in Table 3.4, would introduce error into the results. This error could be reduced by use of a correction factor [128, 129], but the correction factor depends on an estimation of the convection coefficient, for which there is also significant uncertainty, particularly in mixed heat transfer environments (as discussed previously). The ratio of the Schmidt-Boelter data to Gardon data in the mixed conditions was between 1.1 and 1.2, in good agreement with the range of typical correction factors shown in Kuo and Kulkarni [129]. This ratio was larger than the manufacturer-specified, radiation-based calibration uncertainty of ±3% for the gauge. Therefore, manufacturer-listed uncertainty limits must be modified for measurements made using a Gardon gauge in environments where convection effects are significant.

To investigate whether the response of the gauges to mixed radiative-convective conditions could be better understood through superposition of their individual responses to radiative and convective conditions, the mixed radiative-convective

measurements were compared to the sum of the radiative and convective measurements. For instance, in Table 3.3, the value of 19.7 kW/m^2 measured under the first convective flow condition and with the cone calorimeter at 600°C was compared to the sum of the value measured with no forced convection and the cone at 600°C, and the value measured under the first convective flow condition with no imposed radiation (14.7 + 3.4 = 18.1 kW/m^2). For the Schmidt-Boelter gauge, the summed results were all lower than the measurements by up to 8%, with the difference increasing as the convective flow velocity decreased. This indicates that in the mixed radiative-convective measurement situation, the air in the "convective" flow heated up as it passed underneath the radiative cone heater, particularly at the lower flow velocities, resulting in higher overall heat transfer to the water-cooled gauge. In contrast, for the Gardon gauge, the summed results were all higher than the measurements by up to 13%, with the difference increasing as the flow velocity increased. This is consistent with the above discussion of the Gardon gauge results and would suggest that the error caused by the nonlinear response of the Gardon gauge became more prominent as convection heat transfer became more dominant. In general, measurements made separately under characteristic radiative and convective conditions should not be summed because in real situations, the two modes of heat transfer are interrelated through their effects on the surface temperature of the gauge. In this case, the comparison serves to further explain some of the differences in the observed gauge responses.

3.3.2 Directional Flame Thermometer (DFT)

Temperature data collected from the DFT were used in the IHCP1D inverse heat conduction program to produce estimates of the gauge surface temperature and of the net heat flux passing through the heated surface of the gauge. Measurements from the DFT were taken over a duration of 20 minutes at each test condition. Figure 3.7 contains a typical time trace of temperatures from the two thermocouples in the DFT, as well as the corresponding time trace of calculated net heat flux and total incident heat flux, for the radiation-dominated reference test with the cone calorimeter at 600°C and no airflow. (Additional plots showing typical time traces of heat flux and temperature measured in the convective and mixed radiative-convective conditions are included in Appendix A.) Due to the thermal inertia of the gauge, longer times were required for the DFT to reach quasi-steady equilibrium with an environment than typically expected with smaller, water-cooled gauges.

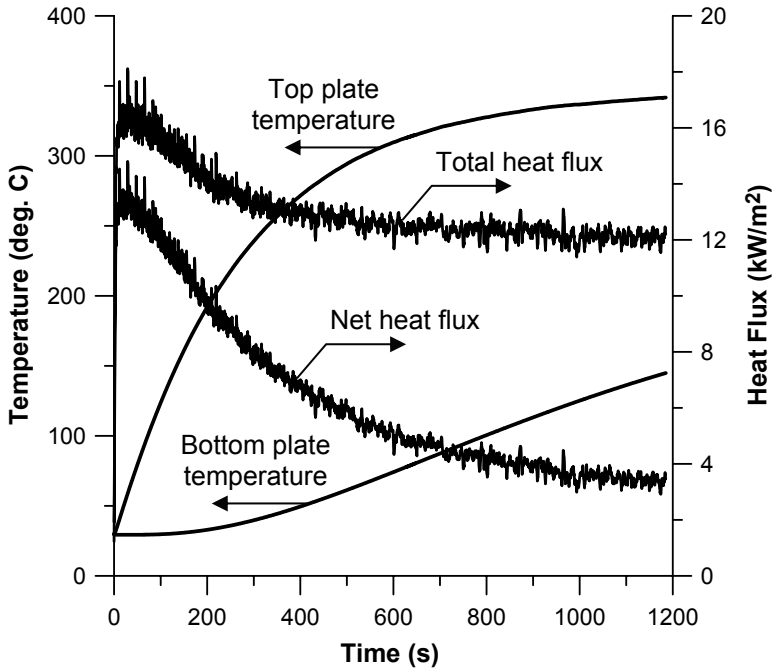

Figure 3.7: Time trace of DFT temperatures and incident total heat flux for test condition with cone calorimeter at 600°C and no airflow

The values of incident total heat flux shown in Figure 3.7 were calculated by adding reradiation from the DFT surface to the net heat flux output by the IHCP1D program, as in Equation 3.7, and dividing the sum by the surface absorptivity (which was assumed to be equivalent to the surface emissivity).

$$Q_{tot} = Q_{rad} + \frac{h\left(T_\infty - T_s\right)}{\alpha_s} = \frac{Q_{net} + \epsilon_s \sigma T_s^4}{\alpha_s} \tag{3.7}$$

The initial sharp increase in heat flux seen in Figure 3.7 corresponded to the step change increase in radiation incident on the gauge when the shutter doors at the base of the heater were opened and several pieces of insulating fibreboard covering the gauge were simultaneously removed. A decrease in total heat flux of approximately 3.5 kW/m^2 was then observed during the first 400 seconds of the test. This corresponded to the inside of the heater becoming cooler via exposure to the ambient surroundings after the shutter doors were opened [163]. The calculated total heat flux then gradually decreased by an additional 1 kW/m^2 over the remainder of the test. Greater decreases in net heat flux (approximately 8 kW/m^2 in total) were observed during the test, reflecting the fact that as the temperature of the DFT increased, less heat could be absorbed by the gauge. For the present

Table 3.5: DFT Incident Total Heat Flux Measurements (kW/m^2)

	No imposed radiation	Cone at 600°C	Cone at 760°C
No forced convection	–	12.0 ± 0.2	25.5 ± 0.4
Convective flow #1	1.0 ± 0.1	6.9 ± 0.1	16.2 ± 0.2
Convective flow #2	1.2 ± 0.1	6.4 ± 0.1	14.4 ± 0.1
Convective flow #3	2.0 ± 0.1	6.6 ± 0.1	13.8 ± 0.1

Table 3.6: DFT Temperatures Measured at Top Sensor Plate (°C)

	No imposed radiation	Cone at 600°C	Cone at 760°C
No forced convection	–	336 ± 3	499 ± 4
Convective flow #1	61 ± 2	277 ± 2	421 ± 3
Convective flow #2	87 ± 3	268 ± 2	399 ± 3
Convective flow #3	119 ± 2	271 ± 2	390 ± 3

study, a test duration of 20 minutes was selected in an attempt to make measurements when quasi-steady conditions had been established. The values of incident total heat flux shown in Table 3.5 and the temperature measurements from the top sensor plate shown in Table 3.6 were averaged over data taken during the last several minutes of each test.

The DFT had a much larger surface area than either the Schmidt-Boelter or the Gardon gauge. Therefore, the data in Table 3.5 should be compared to spatial averages of local heat flux values measured over the surface area of the DFT. As mentioned in Section 3.2, the local incident flux decreased parabolically by 15-18% over a distance of 45 mm from the central axis of the cone heater unit. The average heat flux over the surface of the DFT could thus be estimated by fitting a second-order polynomial to the local heat flux measurements taken with the Schmidt-Boelter gauge and integrating over the area of the DFT. The spatially averaged heat flux over an area of 120 mm diameter was determined to be approximately 87% of the peak measurement. Applying this factor to the values shown in the first row of Table 3.3, the estimated spatial averages of heat flux based on the Schmidt-Boelter measurements made in the radiation-dominated conditions were 12.8 kW/m^2 and 25.8 kW/m^2 for the lower and higher radiative levels, respectively. Comparison of these values to the corresponding DFT data in Table 3.5 showed that the DFT values were 1-6% lower. Since the Gardon data in the radiative environments were 7-8% higher than the Schmidt-Boelter measurements, an even greater difference existed between the DFT and Gardon gauge values. Correction of the Gardon

values in the first row of Table 3.4 yielded spatial averages of 13.8 kW/m^2 and 27.8 kW/m^2 for the lower and higher radiative levels, respectively, 9-15% higher than the measurements from the DFT.

In the above comparison, natural convection, which would have occurred from the heated surface of the DFT when no forced convection was applied, was not included in the analysis as a potential heat loss term. To account for this, the DFT data from the tests in the radiative environments were re-evaluated to include the additional loss term shown in Equation 3.8. This equation (with thermal properties pertaining to air) is based on an empirical Nusselt number correlation applicable to an upward-facing, heated horizontal plate [164].

$$Q_{natl} = (k/l)\left(0.54Ra_l^{1/4}\right)(T_s - T_a) \tag{3.8}$$

Adding the estimated natural convective heat flux to the measured data (initially using an assumed ambient room temperature of 22°C and the sensor surface temperature calculated by IHCP1D) led to corrected heat flux values of 15.2 ± 0.3 kW/m^2 and 30.7 ± 0.4 kW/m^2 for the lower and higher radiative levels, respectively. These results were 19% higher than the Schmidt-Boelter average measurements of 12.8 kW/m^2 and 25.8 kW/m^2, and 10% higher than the Gardon average measurements of 13.8 kW/m^2 and 27.8 kW/m^2. The overestimation was likely due to the assumed ambient temperature of 22°C, which was lower than the actual temperature of the air underneath the cone heater. Positioning a thermocouple underneath the cone heater but shielded from direct radiation from the heater yielded estimates for the "ambient" air temperature of 110°C and 155°C at the lower and higher radiative flux levels, respectively. The values of heat flux from the DFT, corrected for effects of natural convection, then became 14.0 ± 0.3 kW/m^2 and 28.8 ± 0.4 kW/m^2, which were greater than the Schmidt-Boelter averages by 9-12% and greater than the Gardon averages by 1-4%. Given estimations in the correction terms, the approximate method of measuring the ambient air temperature and the 7-8% difference between heat flux measured using the Schmidt-Boelter and Gardon gauges in radiation-dominated environments, heat flux values measured using the DFT were, after appropriate correction, comparable to measurements from the other two gauges.

In the mixed radiative-convective environments, it was much more difficult to determine heat flux levels from the DFT and to compare results between different

Table 3.7: DFT Incident Radiative Heat Flux Measurements (kW/m^2)

	Cone at 600°C	Cone at 760°C
Convective flow #1	12.4 ± 0.1	25.6 ± 0.2
Convective flow #2	11.8 ± 0.1	23.9 ± 0.1
Convective flow #3	11.5 ± 0.1	23.1 ± 0.1

gauge types. The DFT data were initially significantly lower (by 55-76%) than the Schmidt-Boelter data. However, it can be seen that for the case of the DFT, the convective term in Equation 3.7 should actually be treated as a heat loss in the mixed conditions, since the temperature of the heated surface of the DFT (Table 3.6) was greater than the temperature of the air flowing above it (Table 3.2). By moving the convective term to the right-hand side of Equation 3.7 as a heat loss term, values of incident *radiative* flux in the mixed environment could be calculated. These are shown in Table 3.7 using values of h based on Equation 3.6. Since the choice of correlation for calculating the convective coefficient, h, was previously shown to be important, several different correlations were tried and although the values for h varied significantly, the overall trends in the calculated incident radiative flux for the DFT were not affected.

The incident radiative heat flux values in a given column in Table 3.7 should be constant regardless of the convective flow because the radiative heat source did not change from test to test. However, Table 3.7 shows that as the convective flow increased, the estimated incident radiative values decreased by up to 10%. While there is no simple theoretical model to justify this, the decrease in value was most likely due to the effects of lateral conduction along the Inconel sensor plate [18]. As mentioned in Section 3.2, the jet flow was approximately 65 mm wide at the leading edge of the DFT and approximately 100 mm wide at the trailing edge. Since the DFT was 120 mm wide, a significant temperature gradient would exist across the surface of the gauge in a direction perpendicular to the flow. With the flow temperature lower than that of the DFT surface (Tables 3.2 and 3.6), the temperature difference between the surface and the flow passing over it would be greatest near the edges and least in the centre of the gauge (assuming that the DFT surface temperature was relatively uniform and that the temperature of the jet decreased from the centre to the edge as a result of air entrainment). As a result of this, coupled to the fact that an additional portion at the edge of the DFT was exposed to the ambient room environment, more convective cooling of the surface

would have occurred near the edges of the DFT than in the centre, resulting in conduction of heat from the centre toward the edges. Any lateral conduction loss would cause the estimated incident radiative flux to be lower, since conduction losses were not accounted for in Equation 3.7. With the flow temperature gradient being steepest in the hottest (third) convective flow condition, the difference in cooling rate between the edge and centre of the DFT, and thus the lateral conduction loss, would be greatest. This is supported by the results in Table 3.7, which show the estimated incident radiative flux decreasing as the convective portion of the total heat transfer increased.

For the convection-dominated conditions (Table 3.5, leftmost column), the DFT data suggest heat flux levels that were 70-83% lower than those indicated by the Schmidt-Boelter data. This may be explained, however, since the DFT heated up during operation, so the relative temperature difference between the gauge surface and the heated "convective" flow decreased over time, resulting in lower effective heat transfer levels. Lateral conduction losses may also have influenced the readings, as in the tests under mixed conditions. Because the convective flow was hotter than the DFT surface, the temperature difference between the surface and the flow at a given downstream distance was greatest toward the centre and lower near the edge. Furthermore, longitudinal conduction along the sensor plate in the direction of the flow would have occurred due to the development of the jet, and thus change in local flow temperature, from the leading to trailing edge of the gauge. The increase in measured heat flux with increasing flow temperature suggests that in convection-dominated conditions, the temperature difference between the DFT surface and the flow (and thus convective heating of the sensor plate) remained greater than the temperature difference between the centre and edges of the DFT surface, thus limiting the effect of lateral conduction along the plate.

3.3.3 Hemispherical Heat Flux Gauge (HFG)

The data reduction routine [155] used to process the HFG temperature data outputs the incident total heat flux as described in Equation 3.7. Following the same procedure as that used for the DFT, each test with the HFG was continued for 20 minutes in order to allow quasi-steady conditions to become established. Figure 3.8 contains a typical time trace of the sensor plate temperature and incident total heat flux from the HFG for the radiation-dominated reference test with the cone calorimeter at 600°C and no airflow. (Additional plots showing typical time

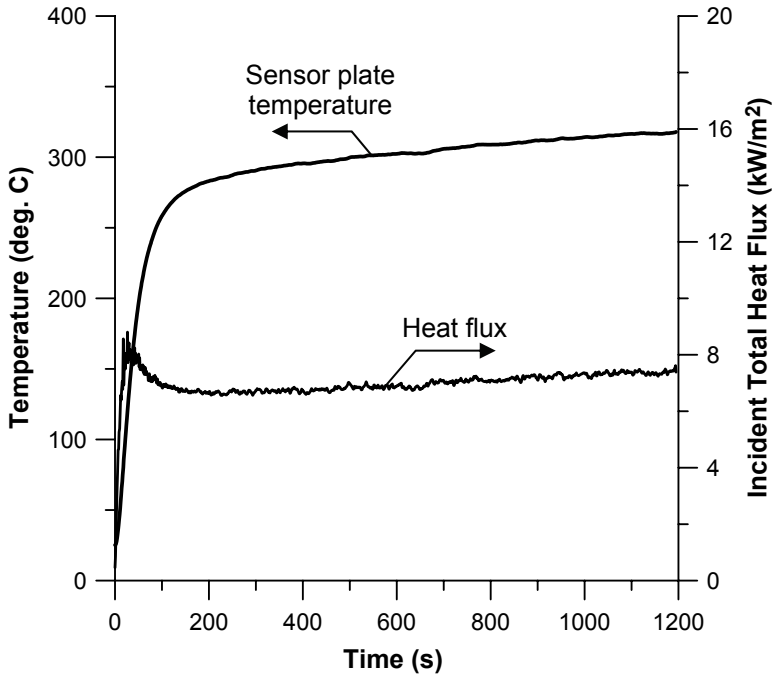

Figure 3.8: Time trace of HFG temperature and incident total heat flux for test condition with cone calorimeter at 600°C and no airflow

traces of heat flux and temperature measured in the convective and mixed radiative-convective conditions are included in Appendix A.) The initial increase in heat flux corresponded to the step change increase in radiation to the gauge when the shutter doors at the base of the heater were opened and several pieces of insulating fibre-board covering the gauge were simultaneously removed. A decrease in heat flux of approximately 1.5 kW/m^2 was then observed during the first 100 s of the test, corresponding to the inside of the heater becoming cooler via exposure to the ambient surroundings through the open shutter doors [163]. A gradual increase in heat flux of approximately 0.6 kW/m^2 was subsequently observed during the remainder of the test. The time-averaged incident total heat flux values summarized in Table 3.8 are average values obtained over a quasi-steady period of several minutes near the end of each test. The corresponding temperatures measured at the sensor plate are reported in Table 3.9.

Heat flux estimates from the HFG under radiative conditions were 35-48% lower than the corresponding Schmidt-Boelter measurements. This difference was too large to be reasonably attributed to natural convection effects or to the size of the sensing area (which was smaller than that of the DFT). Looking instead to possible causes due to the design of the sensor (Figure 3.5), it should be noted that the

Table 3.8: HFG Incident Total Heat Flux Measurements (kW/m^2)

	No imposed radiation	Cone at 600°C	Cone at 760°C
No forced convection	–	7.6 ± 0.1	19.3 ± 0.1
Convective flow #1	0.8 ± 0.1	4.2 ± 0.1	10.9 ± 0.1
Convective flow #2	1.1 ± 0.1	4.1 ± 0.1	9.7 ± 0.1
Convective flow #3	1.6 ± 0.1	4.6 ± 0.1	9.4 ± 0.1

Table 3.9: HFG Sensor Plate Temperatures (°C)

	No imposed radiation	Cone at 600°C	Cone at 760°C
No forced convection	–	322 ± 2	484 ± 4
Convective flow #1	69 ± 2	252 ± 2	392 ± 3
Convective flow #2	94 ± 2	246 ± 2	370 ± 3
Convective flow #3	134 ± 2	259 ± 2	366 ± 3

0.25 mm thick sensor plate was sandwiched between two layers of 3.2 mm thick insulation and the entire combination was sandwiched between two 3.2 mm thick stainless steel plates [155]. One of these plates was placed against the end of a 102 mm diameter by 102 mm long by 5.7 mm thick steel cylinder. Although the sensor plate and the inside of the cylinder were insulated, the cylinder and steel plates represented a significant thermal mass relative to the thin sensor plate. If the insulation between the sensor plate and the gauge housing did not provide an effective thermal barrier, losses via conduction to the gauge housing could be significant and the one-dimensional assumption inherent in the data reduction routine would be inappropriate.

To test the validity of the one-dimensional assumption used in determining the heat flux values, a simple, two-dimensional model was programmed in Matlab to simulate the heat transfer along a longitudinal cross-section of the gauge. The model was based on the two-dimensional, cylindrical coordinate form of the heat diffusion equation with temperature-dependent properties and no internal heat generation [121]:

$$\frac{1}{R}\frac{\partial}{\partial R}\left(kR\frac{\partial T}{\partial R}\right)+\frac{\partial}{\partial Z}\left(k\frac{\partial T}{\partial Z}\right)=\rho c_p\frac{\partial T}{\partial t} \tag{3.9}$$

This equation was cast in an implicit, finite difference form using central difference approximations in space and backward difference approximations in time. As

illustrated in Figure 3.9, eight nodes were specified in the radial direction, while ten nodes were specified in the axial direction (eight for the insulation inside the cylinder and two for the sensor plate). The temperature time trace measured at the centre of the sensor plate and that measured by an intrinsic thermocouple attached to the top edge of the gauge were used to specify a Dirichlet boundary condition along the face adjoining the sensor plate and the insulation. The temperatures along this boundary were assumed to decrease linearly from the centre to the edge. The heat transfer from the sensor plate into the insulation was assumed to be ideal (i.e. no air gap or contact resistance). The boundary conditions for the edge, bottom and central axis of the cylinder were all assumed to be adiabatic. All thermal properties were evaluated at the nodal temperature calculated at the preceding time step. The system of equations for each time step was solved using the Gaussian elimination matrix inversion function available in Matlab. The solution contained all nodal temperatures, plus the temperatures along the heated surface of the sensor plate. The amount of heat passing through the surface of the sensor plate could be subsequently estimated using Fourier's law together with the surface and neighbouring nodal temperatures. Reradiation based on the surface temperatures was added and the sum divided by the surface emissivity to obtain an estimate of the incident radiation.

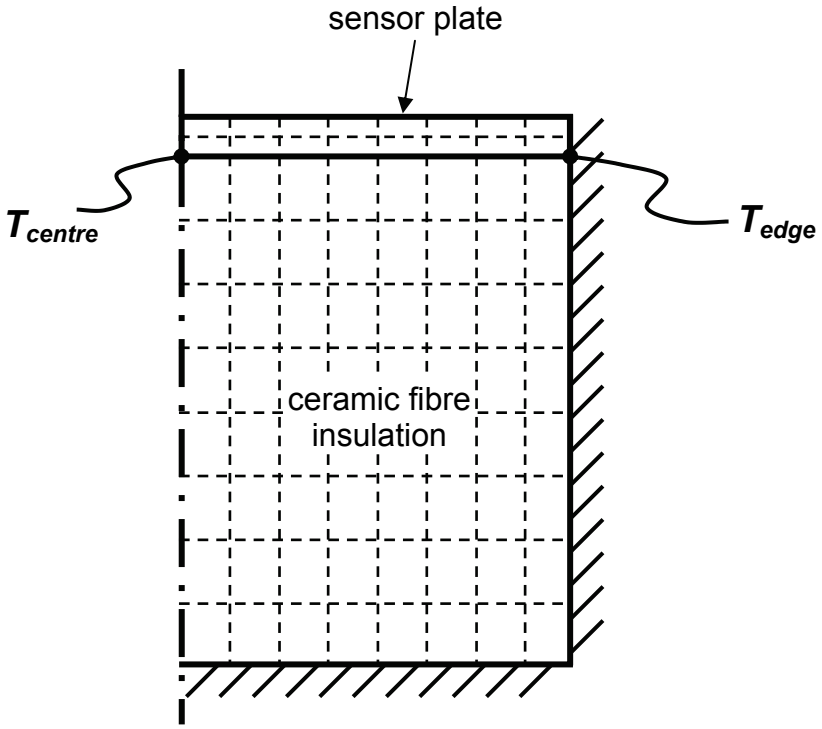

Figure 3.9: Sketch of two-dimensional model of HFG

Two test cases were run using the temperature data measured with the cone calorimeter set at 600°C and no convective flow applied. In the first test case, the temperature measured at the centre of the sensor plate (Table 3.9) was used to prescribe a uniform temperature boundary condition along the entire face adjoining the sensor plate and the insulation. This yielded a one-dimensional situation that assumed no conduction loss from the sensor plate other than to the insulation and served as a reference case to verify that the results from the model were reasonable. The results of this test case were expected to be similar to the measured value given in Table 3.8 for the 600°C temperature setting and no convective flow. The total radiation incident on the exposed, or active, area of the sensor plate ($0 < r \leq 25$ mm) was estimated by the model to be 16 W, while that incident on the rest of the sensor plate ($25 \text{ mm} < r \leq 50$ mm), which would be covered by the 3.2 mm thick insulation layer, was estimated to be 47 W. These values would correspond to an incident radiative flux of approximately 8 kW/m^2, which, given the simplifications and assumptions, is reasonably close to the measured value of 7.6 kW/m^2 listed in Table 3.8. The agreement is consistent with the fact that the values in Table 3.8 were obtained using a one-dimensional assumption.

A second test case was then run to estimate the amount of heat lost due to conduction from the sensor plate to the housing of the gauge. The heat loss was modelled by specifying a boundary condition in which the temperature decreased from the centre of the sensor plate to the edge along the face adjoining the sensor plate and the insulation. The amount of radiation incident on the exposed (active) area of the sensor plate was predicted to be 15 W, while that incident on the remaining (inactive) area of the sensor plate was predicted to be 22 W.

Comparison of values from the first and second test cases indicates a loss of approximately 26 W of incident radiation, almost entirely from the non-sensing area of the sensor plate. If this 26 W were added to the 15 W incident on the active sensor region, giving an upper bound for the incident heat flux if no heat loss occurred, the resulting estimated incident flux would be 20 kW/m^2. This number is somewhat larger than the 15 kW/m^2 measured by the Schmidt-Boelter gauge, due to the many approximations made in the model, including the assumption that the temperature measured at the edge of the top steel plate of the gauge was equivalent to the temperature at the edge of the sensor plate itself. Given the larger thermal mass of the top plate, the measured temperatures were likely lower than the actual temperatures at the edge of the sensor plate, resulting in an overestimate of the heat losses from the sensor plate. Nevertheless, the increase in incident heat

flux between the two test cases suggests that the loss of heat from the sensor plate to the housing of the gauge could account for the extremely low values of heat flux measured by the HFG in the radiation-dominated conditions. Conversely, it should be noted that the HFG is intended for use in fire environments where it should be immersed entirely in hot plume gases and allowed to achieve equilibrium with its local environment [7, 87, 105]. This will minimize heat losses from, and thermal gradients within, the gauge.

The HFG data in Table 3.8 for the mixed radiative-convective conditions were 70-84% lower than the corresponding Schmidt-Boelter measurements, while the data for the convection-dominated conditions were 76-86% lower. Similar to the case for the DFT, some of this difference was caused by the HFG surface being hotter than that of the Schmidt-Boelter gauge. In addition, the HFG readings were affected by a combination of the following: lateral conduction along the gauge surface due to the diameter of the flow outlet being smaller than that of the sensing area; loss of heat from the sensor plate to the steel housing of the gauge; perturbation of the flow field by the sensor surface being recessed below the top surface of the gauge housing; and, for the mixed conditions only, cooling of the HFG surface by the convective flow, which would result in further loss of energy from the sensor plate. In the mixed conditions at the higher radiative level, the trend of decreasing measured heat flux with increasing convective flow temperature indicates that the conductive losses were dominant over the decrease in convective cooling. On the other hand, for the convection-dominated environments, the trend of increasing heat flux with increasing flow temperature indicates that the convective heating of the gauge was dominant over the conductive losses. The lack of a consistent trend in the measured heat flux data for the mixed conditions at the lower radiative level suggests that the decrease in convective cooling was of similar order to any change in conductive losses from the sensor plate as the convective conditions were varied.

3.4 Summary

In this chapter, the steady-state responses of four heat flux gauges (Schmidt-Boelter gauge, Gardon gauge, DFT and HFG) were examined under various radiative and convective conditions. In radiative environments, Gardon measurements were up to 8% higher than Schmidt-Boelter measurements, likely due to differences in gauge sensitivity and calibration method by the different manufacturers. In mixed

radiative-convective environments, Gardon measurements were 8-18% below those of the Schmidt-Boelter gauge, with the difference increasing as the convective portion of the total heat transfer increased. This could be attributed to discrepancies between the radiation-based calibration environment and measurement environments in which a convective flow caused asymmetric heating of the Gardon sensing surface, altering the gauge sensitivity to the total heat transfer. Uncertainty in measured heat flux values will therefore be higher than the manufacturer-listed uncertainties for either gauge when applied in mixed radiative-convective environments, with the most significant change expected for the Gardon gauge. In general, use of the Schmidt-Boelter and Gardon gauges in mixed radiative-convective environments should be avoided, unless the sensors have been calibrated specifically for those environments.

For the DFT, data measured in radiative environments were comparable to the Schmidt-Boelter and Gardon values (within 15%), with the difference largely attributed to natural convection losses from the DFT surface. The HFG heat flux estimates were 35-48% lower than the Schmidt-Boelter measurements under radiative conditions, influenced by large conduction losses from the sensor plate to the gauge housing. All losses from the sensor plate should thus be either minimized or modelled and accounted for in order to obtain valid results from the DFT and HFG. In mixed radiative-convective environments, measured total heat flux values from the DFT and HFG were significantly lower than those from the Schmidt-Boelter and Gardon gauges, due to differences in the surface temperatures of the gauges. This resulted in the convective flow cooling, rather than heating, the DFT and HFG. The DFT and HFG are therefore more suitable than the water-cooled Schmidt-Boelter and Gardon gauges for estimating heat flux to a surrounding surface in mixed radiative-convective conditions, particularly if that surface is not similarly cooled in the application of interest.

The results of this chapter help quantify uncertainty in using the four different heat flux gauges under mixed modes of heat transfer. It may be noted that for large, optically thick, hydrocarbon fires under low wind conditions, uncertainties in steady-state measurements of incident radiative heat flux have been found to be approximately 39% for a Schmidt-Boelter gauge, 27-40% for a DFT-type gauge based on inverse conduction methods, and 24-42% for a thin-skin sensor like the HFG [137]. For similar measurements under high wind conditions, the corresponding uncertainties were estimated to be 23% for the Schmidt-Boelter gauge, 25-27% for the inverse conduction-based gauge and 21-31% for the thin-skin sensor [137].

The results of the present chapter indicate that Gardon gauges would have additional uncertainty on top of those mentioned above for the Schmidt-Boelter gauge when used in wind-blown fires. Also, as mentioned earlier, measurements from the DFT and HFG would likely have lower uncertainty than those seen in the present chapter when the gauges are fully immersed in large fires and thus heated more uniformly. In the next two chapters, measurements of heat flux and temperature in wind-blown fires will be examined.

Chapter 4

Fire in Wind With No Blocking Object

The present chapter describes experiments to characterize the thermal environment in a 2 m diameter, wind-blown fire with no downwind blocking object. As mentioned in Chapter 1, the setup of these experiments was based on the experimental design described in the author's M.A.Sc. thesis [8], which included a blocking object, so that results from the two test cases could be compared. This chapter details the setup, methodology and results of a series of experiments conducted without the blocking object.

4.1 Experimental Setup

All experiments were performed in the University of Waterloo Live Fire Research Facility. The test enclosure and wind generation system in the facility are outlined here. Also described are the burner and instrumentation layout. Since there was no blocking object in these tests, the layout of the instrumentation differed from that specified in the author's M.A.Sc. thesis [8]. This section concludes with a description of the test protocol and summary of the conducted tests.

4.1.1 Test Enclosure

The test enclosure of the University of Waterloo Live Fire Research Facility (Figures 4.1 and 4.2) was designed to allow repeatable experiments involving large fires in

Figure 4.1: University of Waterloo Live Fire Research Facility

controlled and fully characterized crosswinds. The enclosure had a floor area of 19.5 m by 15.4 m and was surrounded by corrugated steel walls and a corrugated steel, gable roof. The height of the enclosure was 7.6 m at the walls and 12.8 m along the longitudinal midplane. A wind generation system, composed of six large fans and a connecting plenum, was located at the west end of the test enclosure. This system is described in the next section. The east end of the building contained a 7.9 m by 7.9 m door, consisting of seven overlapping steel panels. A chain drive system was used to lift the panels up and down, thereby opening and closing the door. For the present tests, the door was kept fully open whenever the fans were in operation.

A control room housing computer, audio-visual, and other data acquisition equipment was located adjacent to the test enclosure, as illustrated in Figure 4.2. A 1.2 m by 1.2 m by 1.4 m underground pit was also available at the centre of the enclosure to allow placement of data acquisition hardware. This pit was connected to the control room via an underground trench so that data acquisition cables in the test area could be safely run underground to computer equipment located in the control room.

At the southeast corner of the test enclosure was a 5.4 m by 6.3 m by 3.6 m room containing a furniture calorimeter (Figure 4.2). This room was enclosed on three sides and the side adjoining the main test area was open. For the present

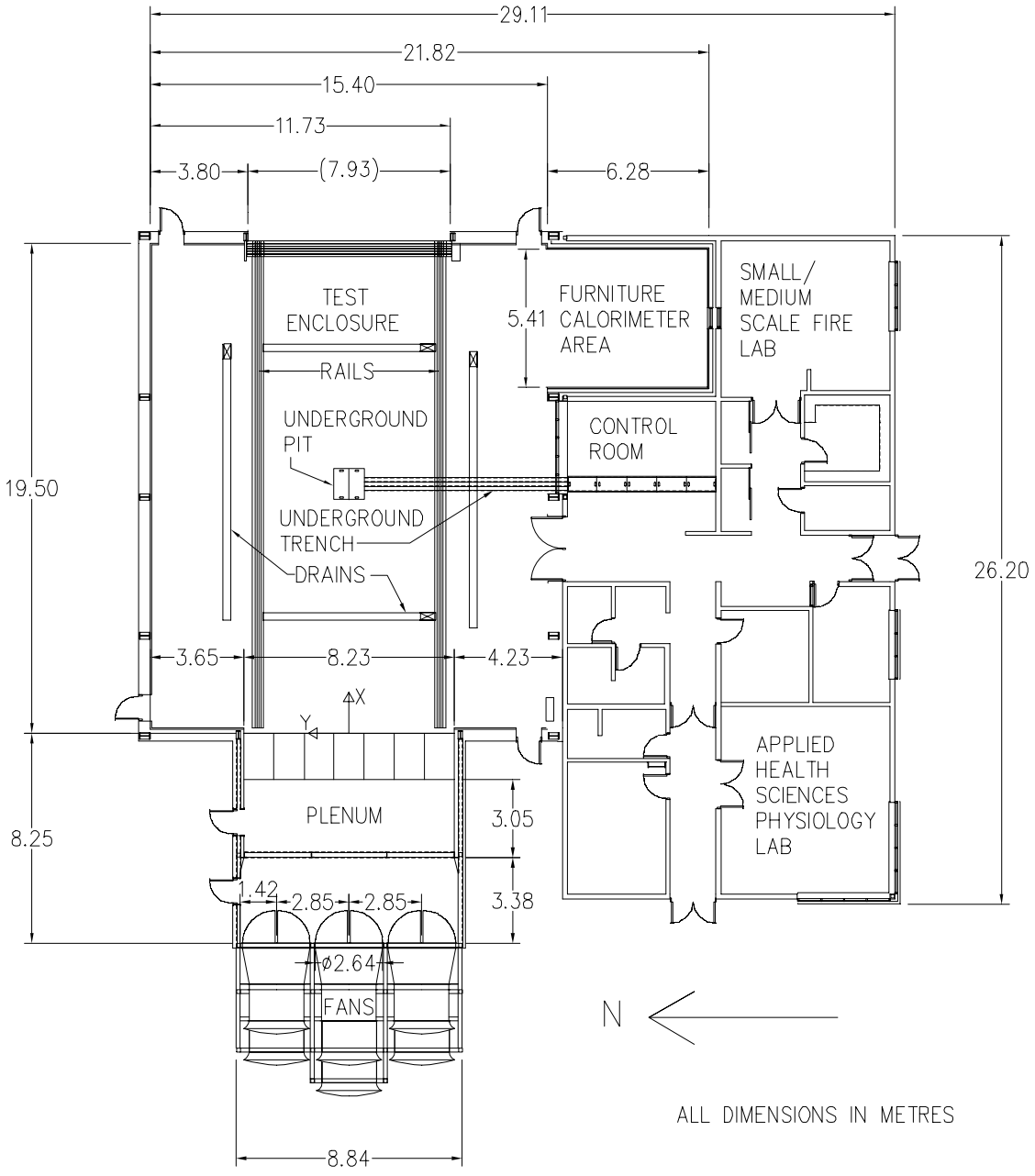

Figure 4.2: University of Waterloo Live Fire Research Facility, floor plan

tests, the open side was blocked with a large piece of tarp in order to minimize the effect of the presence of this room on the flow field inside the test enclosure.

Additionally, the facility contained a 8.8 m by 7.6 m by 7.4 m, two-storey, steel structure (not shown in Figure 4.2) for experimental simulation of house fires in controlled wind environments. This structure could be moved along a set of rails into and out of the test enclosure through the large exit door. For the present study, the structure was kept outside the test enclosure, at the maximum distance of 3.7 m from the exit door. This distance was restricted by overall site dimensions as well as the total length of the rails. Experimental characterization of the flow inside the empty test enclosure indicated that the presence of this structure outside the building formed a blockage to the free flow of the wind exiting through the large door, causing static pressure inside the test enclosure to increase over a distance of approximately 4.5 m upwind of the door [165]. As a result, the structure was kept at the same position relative to the exit door for all experimental testing and measurements inside the test enclosure were restricted to locations upwind of this region of increased static pressure.

4.1.2 Wind Generation System

The wind generation system was composed of six vane axial fans (Model 78-26 Series 1000) manufactured by Howden Buffalo Inc. of Camden, SC. A detailed description of this system is contained in Weisinger [165], with a brief summary of the main features provided here. Each fan was 2.0 m in diameter and had a specified maximum flow rate and rotational speed of 78.7 m^3/s and 1185 rpm, respectively. Variable frequency drives on the fan motors permitted operation at lower flow rates. The fans were arranged in a bank of two rows with three fans each, one stacked on top of the other (Figure 4.1). The flow from the fans passed through a plenum of 8.2 m by 5.9 m cross-sectional area and 8.3 m length. The plenum contained two vertical screens located approximately 3.4 m and 3.6 m in front of the exit plane of the fans. The screens were composed of 29 mm squares and were supported by a steel grid and steel cross-bracing. An array of square ducts (seven across by five tall, with the same total cross-sectional area as the plenum) was located at the exit of the plenum. Each duct had a cross-sectional area of 1.2 m by 1.2 m and a length of 1.8 m. The screens and ducts provided a basic level of conditioning to the crosswind flow before it entered the test enclosure.

Characterization studies of the flow field inside the test enclosure were performed by Weisinger [165] and Best [21]. Details of the flow field are provided in these two theses and are not reported here, except as needed to explain results from the fire tests.

4.1.3 Burner

The burner used in the experiments, shown in Figure 4.3, was a fixed quantity, stainless steel pan with a mean inside diameter of 1.97 m and depth of 0.18 m.[1] This size of pan was expected to produce fires in the fully turbulent burning regime (Figure 2.2), thus allowing realistic simulation of an accidental fire scenario. It could also be reasonably accommodated within the working section of the test enclosure. The pan was centred 5.94 m downwind of the exit plane of the fan plenum, on the longitudinal midplane of the test enclosure. Fires were established using Jet A, a kerosene-based aviation turbine fuel (Table 4.1). This fuel is very similar to military-grade JP-8, which has been used in previous large-scale fire experiments [7, 43, 105]. Before each test, a known quantity of fuel (approximately 100 L, equivalent to a depth of approximately 33 mm) was poured into the pan on top of a water substrate of 320 L (105 mm depth). The presence of the substrate provided a quantifiable boundary condition and helped to reduce the thermal stress on the fuel pan during testing [7, 36, 37, 52, 109, 115].

A raised floor surround was situated around the fuel pan to represent a ground plane level with the top of the pan. As shown in Figures 4.3 to 4.5, the floor surround spanned an area of 2.69 m by 2.69 m, with the fuel pan located in the centre. It was composed of a single layer of insulating fire bricks that were raised on concrete blocks such that the top surface of the bricks was flush with the rim of the pan. In order to prevent buildup of fuel vapours within the floor surround [168], the concrete blocks were oriented such that the flow from the fans could pass through them and enter/exit the space underneath the fire bricks (Figure 4.3).[2] Based on preliminary testing, the upwind extent of the floor surround was lengthened via four fibre-reinforced cement boards joined to form a 2.44 m by 4.88 m area. This

[1] For the purposes of this thesis, the pan diameter will hereafter be referred to by its nominal value, 2 m.

[2] A preliminary test was performed in which the crosswind flow was prevented from entering the space underneath the floor surround. This configuration resulted in burning of instrumentation cables that ran through that space, so the blockage was removed in subsequent tests to minimize the potential for further damage.

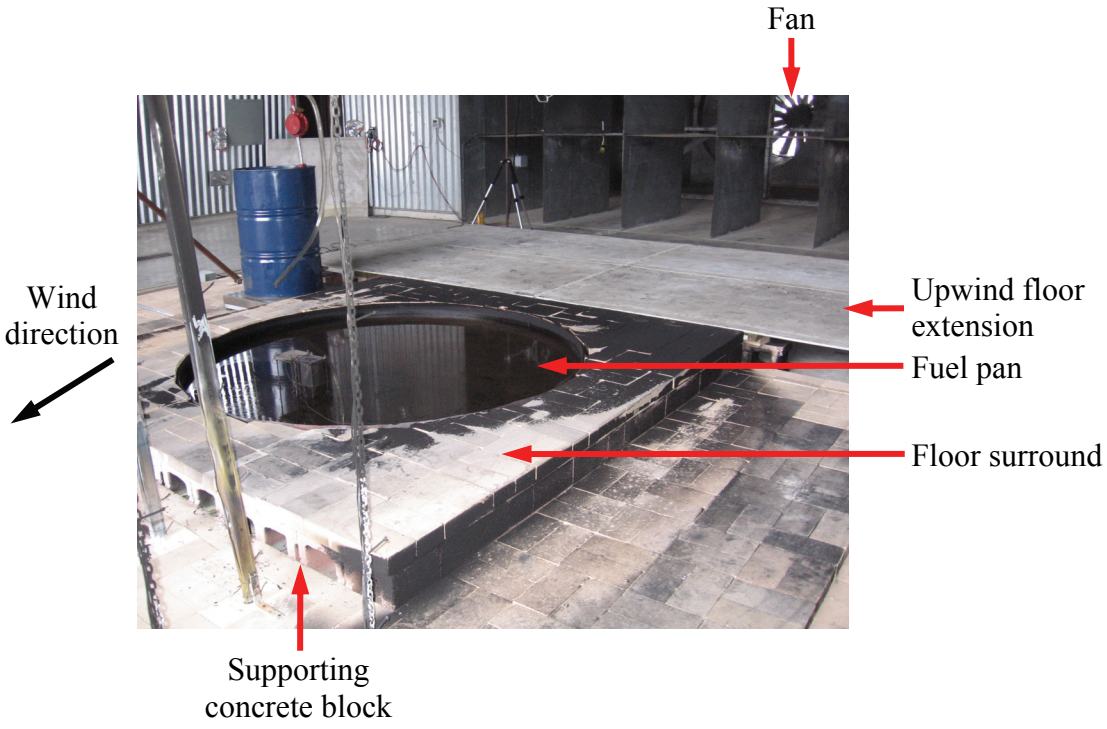

Figure 4.3: Setup of fuel pan and raised floor surround

Table 4.1: Thermophysical Properties of Jet A Fuel [166, 167]

Composition:	Kerosene
Aromatics (max. % volume)	25
Sulphur, total (max. % weight)	0.30
Sulphur, mercaptan (max. % weight)	0.003
Boiling point	160°C - 300°C
Density (15°C)	775 - 840 kg/m^3
Vapour density (air=1)	5.7 (approx.)
Vapour pressure (37.8°C)	1 kPa
Viscosity (-20°C)	8 mm^2/s (max.)
Specific gravity (15.6°C)	0.81
Net heat of combustion	42.8 MJ/kg (min.)
Flammability limits in air (% volume)	lower: 0.7, upper: 5
Flashpoint (Tagliabue Closed Cup)	38°C (min.)
Autoignition	210°C

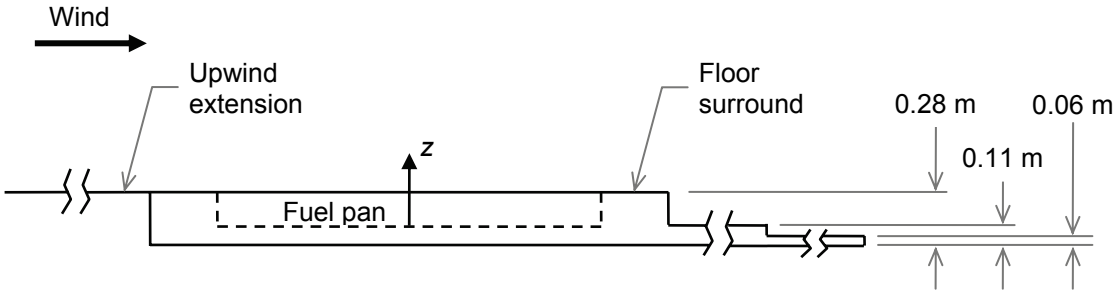

Figure 4.4: Geometry of raised floor surround and surrounding brick layout, side view

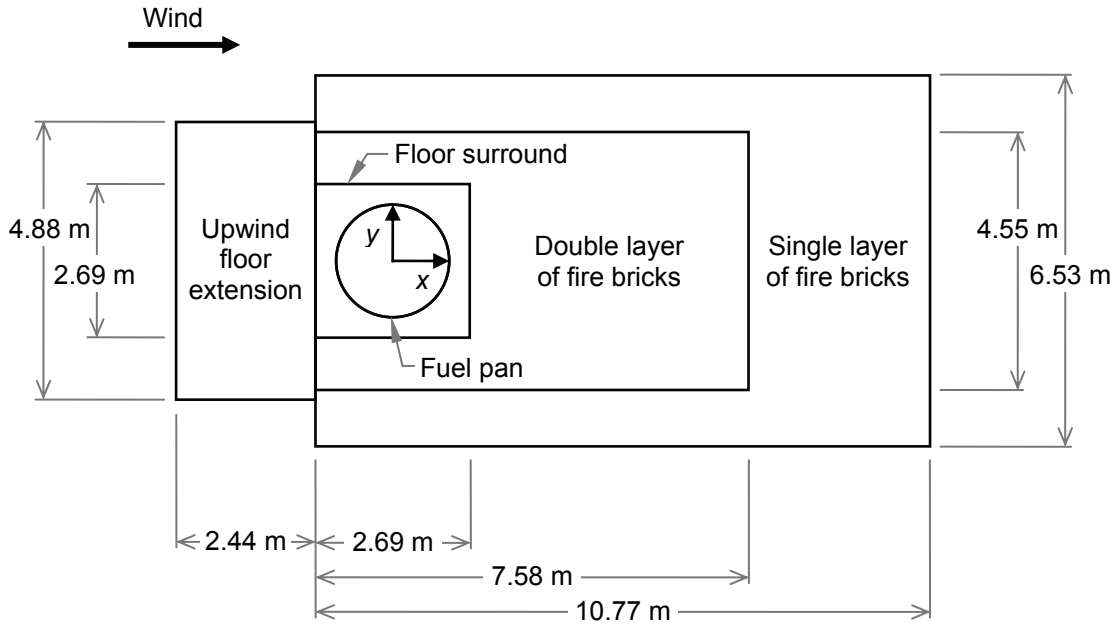

Figure 4.5: Geometry of raised floor surround and surrounding brick layout, plan view

extension was required to prevent the fire from becoming attached to the upwind edge of the floor surround (as observed during preliminary tests performed without the boards). The boards were supported on concrete blocks so that they were flush with the top surface of the fire bricks. The concrete blocks were oriented in the same manner as those of the floor surround in order to minimize disruption to the flow along the floor underneath the fuel pan.

The edges of the floor surround were formed by a sharp, step-down transition to a double layer of fire bricks protecting the test enclosure floor (Figure 4.4). This double layer of bricks, with a total thickness of 0.11 m, covered an area of the floor that was expected to receive significant exposure to the hot fire plume. As

illustrated in Figure 4.5, the double layer spanned a total length of 7.58 m, starting at the upwind edge of the floor surround, and extended past each side of the floor surround by a width of 0.93 m (giving a total width of 4.55 m). Beyond the double layer of bricks was a thinner, single layer, which spanned a total length of 10.77 m and extended past the double layer on each side by a width of 0.99 m (giving a total width of 6.53 m).

4.1.4 Instrumentation

The coordinate system used for describing the location of the instrumentation was defined with its origin located at the centre of the fuel pan. As depicted in Figures 4.4 and 4.5, the positive x direction was in the mean direction of the wind, the positive y direction was in the cross-stream direction and the positive z direction was vertically upward.

Temperatures in the downwind region of the fire were measured using 24-gauge (0.51 mm diameter), chromel-alumel (Type K) thermocouples. The thermocouple wires were insulated with Nextel ceramic fibre and covered with protective Inconel braiding. The thermocouples were formed with exposed junctions and mounted pointing upwind on vertical chains. As illustrated in Figure 4.6, these chains were aligned along seven measurement planes situated downwind of the fuel pan and normal to the x direction. The measurement planes were located at distances of 0.75, 1, 1.5, 2, 3, 4 and 4.6 pan diameters from the fuel pan centre. Since the actual diameter of the pan was 1.97 m, these distances corresponded to 1.48 m, 1.97 m, 2.96 m, 3.94 m, 5.92 m, 7.89 m and 9.15 m, respectively; however, for simplicity, the nominal distances of 1.5 m, 2 m, 3 m, 4 m, 6 m, 8 m and 9.2 m will be used when discussing the results. The thermocouples were distributed along each measurement plane to capture the cross-sectional extent of the fire plume. The spacing of the thermocouples varied from 0.50 m to 1.00 m in the y direction and from 0.11 m to 1.00 m in the z direction, with the coarser spacing applied to thermocouples located further from the fuel pan. The thermocouple locations are sketched in Figures 4.6 and 4.7, and their coordinates are listed in Appendix B. The total number of thermocouples was 396, distributed over 53 rakes.

Heat flux to the ground was measured along a plane located at a distance of x=2.64 m downwind of the fuel pan centre (Figure 4.6). Groups of heat flux sensors, each consisting of a Gardon gauge, HFG and DFT (described in Chapter 3), were

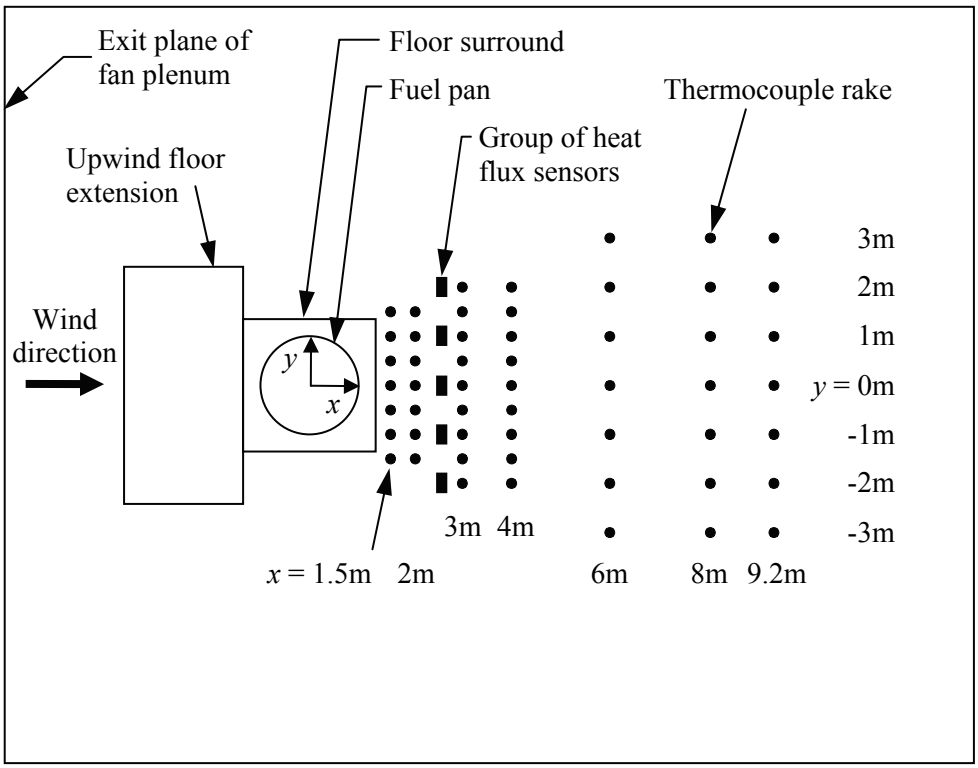

Figure 4.6: Sketch of experimental setup, plan view (nominal distances shown)

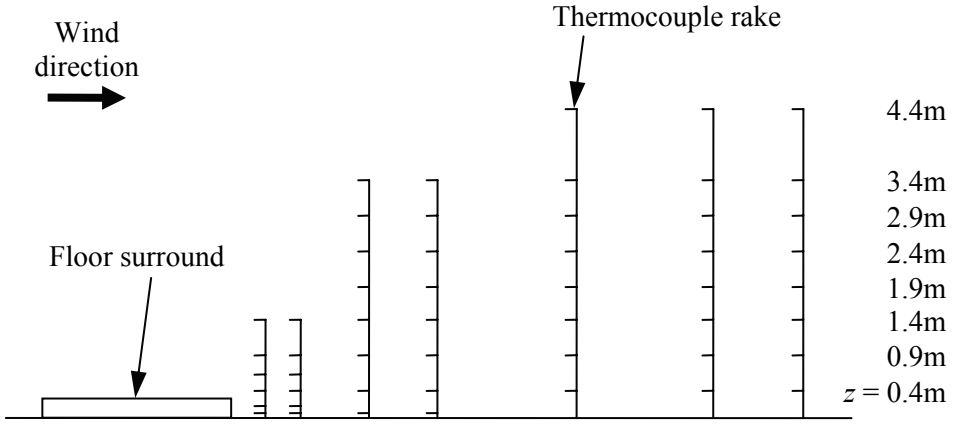

Figure 4.7: Sketch of experimental setup, side view (nominal distances shown)

Table 4.2: Y Locations of Heat Flux Gauges and Associated Thermocouples (x=2.64 m; z=0 m for heat flux gauges, z=0.03 m for thermocouples)

Nominal location (m)	-2	-1	0	1	2
Measured location of Gardon gauge (m)	-2.11	-1.12	-0.11	0.90	1.91
Measured location of DFT (m)	-2.01	-1.03	-0.03	0.99	2.00
Measured location of HFG (m)	-1.88	-0.90	0.10	1.10	2.12
Measured location of thermocouple (m)	-1.94	-0.96	0.04	1.05	2.06

positioned at the following nominal y locations: on the longitudinal midplane, ±1 m from the midplane, and ±2 m from the midplane. Within each group, the gauges were placed adjacent to each other so that the same x location was maintained while the y location of the gauges varied by no more than ±0.12 m from the nominal positions listed above. The y coordinate of each heat flux gauge (measured to the centre of the gauge surface) is listed in Table 4.2. In addition, a thermocouple was included with each group of gauges to measure the local gas temperature and was positioned (pointing upwind) between the HFG and DFT at approximately 25 mm above the surface of the sensors (z=0.03 m).

The DFTs and HFGs were installed in a manner similar to that employed in Chapter 3. The DFT was placed on top of two layers of 25 mm thick ceramic fibre insulation, while the cylindrical housing of the HFG was surrounded by one layer of the same insulation. The gauges and insulation were recessed into the brick floor by custom fitting the fire bricks around them so that the gauge surfaces were approximately flush (within 1 cm) with the top surface of the bricks (Figure 4.8).

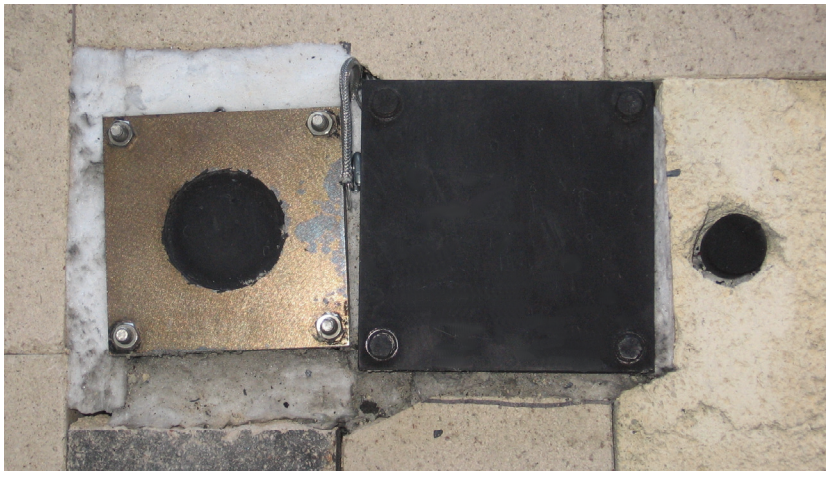

Figure 4.8: Setup of heat flux gauges in brick floor

All wires leading to the thermocouples and heat flux gauges were run underneath the layer of fire bricks protecting the test enclosure floor in order to minimize heat exposure to the instrumentation cables. In addition, for thermocouples located along the three measurement planes closest to the fuel pan (x=1.5 m, 2 m and 3 m), the lengths of thermocouple wire running down the chains were insulated to prevent failure due to extreme heat exposure, which had occurred during preliminary testing with non-insulated thermocouple wire installation.

Additional instrumentation was included for measuring fuel regression rate and plume velocities. Since these measurements are the focus of the thesis by Best [21], they will not be discussed in the present work. Photographs of the overall experimental layout are provided in Figures 4.9 and 4.10. The heat flux gauges and thermocouple chains located downwind of the fuel pan, up to x=4 m, are shown in Figure 4.9, while the overall setup of the thermocouple chains and their supporting frames is shown in Figure 4.10. The longitudinal midplane y=0 m is approximately aligned with the centre of the photograph in Figure 4.10.

Data acquisition was conducted using a Compact FieldPoint, PC-based, distributed system manufactured by National Instruments of Austin, TX. This system consisted of a modular set of backplanes linked through Ethernet cables to a computer running LabVIEW acquisition software. Due to the extensive number of data channels, data were sampled at a rate of approximately 0.4 Hz, the maximum attainable by the system. Five video cameras were also distributed around the test enclosure to record macroscopic features of the fire. Footage included an overhead view as well as several upwind, downwind and profile views of the fire plume.

Outdoor ambient temperature, relative humidity and wind velocity were monitored using a Wireless Vantage Pro2 Precision Weather Station (Model 6152) manufactured by Davis Instruments of Hayward, CA. The weather station was located in an open area upwind (west) of the wind generation system, at a distance of approximately 65 m from the inlet of the fans. This location was selected to minimize disruption to the measurements by the intake flow of the fans and by nearby buildings. The temperature and relative humidity sensor was situated 2.0 m above the ground, while the wind anemometer was situated 2.4 m above the ground. Weather data were logged at a rate of once per minute and subsequently downloaded to a computer. These data were verified against hourly measurements taken by a separate weather station (from Campbell Scientific of Logan, UT) located on the same complex as the test facility, approximately 185 m north of the Vantage Pro2 sys-

Figure 4.9: Photograph of experimental layout, side view

Figure 4.10: Photograph of experimental layout, view looking upwind

tem. In this station, which was run by the Region of Waterloo, the temperature and relative humidity probe (Model HMP45C) was situated nominally 2 m above the ground, while the wind monitor (R.M. Young, Model 05103-10) was situated nominally 10 m above the ground, providing additional data to serve as a consistency check.

4.1.5 Test Protocol

Up to three tests (including preliminary runs) were conducted on a test day. Due to facility operational procedures that required firefighters to be present during testing, tests had to be run consecutively in order to maximize efficiency in scheduling. Prior to each test, the level of water substrate in the fuel pan was verified and topped up as necessary. Next, fuel was pumped into the pan and the fuel level recorded. Since the time required for each fan to ramp up to its operating speed was on the order of half a minute, four fans were turned on and allowed to reach their operating speed before the fuel was ignited so that the duration of steady burning could be maximized. These four fans were the top three fans and the bottom fan on the side of the test enclosure furthest from where ignition would occur. Ignition of the fuel was achieved by means of a propane torch. As soon as the fuel was ignited, the remaining two fans were turned on and allowed to run.

After each test, the fans were run at full speed for at least 45 minutes to cool down the test enclosure and instrumentation. Differences in initial air temperature between consecutive tests were within 7°C. The water substrate in the fuel pan was topped up as necessary, but not fully replaced, between tests due to the lack of an efficient drainage system from the pan as well as the limited time available between consecutive tests.

4.1.6 Summary of Conducted Tests

Table 4.3 summarizes the tests conducted without the blocking object. The listed wind speeds are representative average values based on measurements made by Best [21] to characterize the flow field within the test enclosure at the specified fan drive frequencies. Further details of the flow field are provided in his work.

Table 4.3: Tests Conducted with Fire in Crosswind

Test Date	Test Number	Fan Drive Frequency	Nominal Wind Speed	Fuel Quantity	Outdoor Ambient Temperature
19 Oct 2006	38	22 Hz	5 m/s	103 L	9°C
24 Oct 2006	42	47 Hz	10 m/s	92 L	5°C
25 Oct 2006	43	34 Hz	7 m/s	80 L	4°C
26 Oct 2006	44	15 Hz	3 m/s	105 L	1°C

4.2 Determination of the Steady Burning Period of the Fire

For each test, the steady burning period of the fire was determined based on temperatures measured in the downwind fire plume. A typical time trace of temperatures measured along a thermocouple chain placed in the longitudinal midplane, one pan diameter downwind of the fuel pan centre, is shown in Figure 4.11. The time t=0 s was defined as the instant when the surface of the fuel pool was first observed to be fully covered by flame.

High temperatures (above 700°C) were measured near the floor, between z= 0.03 m and 0.39 m, indicating the location of the hot combustion zone of the fire. Since the temperatures measured at z=0.03 m were typically lower than the cor-

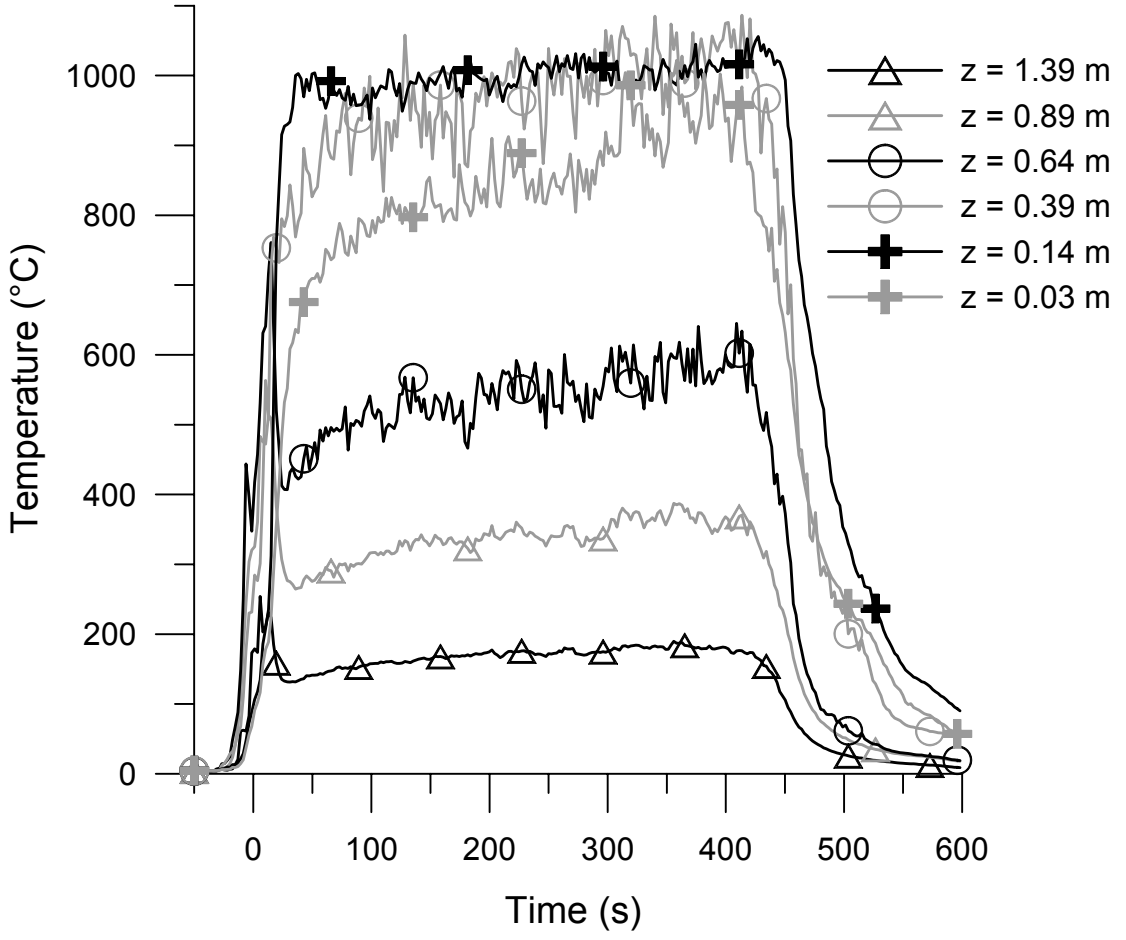

Figure 4.11: Typical time histories of plume temperatures, 7 m/s wind (x=2 m, y=0 m)

responding temperatures measured at z=0.14 m and 0.39 m, the thermocouples at the two higher elevations were likely closer to the plume centre than the thermocouple at the lowest elevation. For elevations of 0.39 m and above, a temperature stratification could be readily observed, with decreasing temperatures at increasing elevations above the brick floor. This stratification indicated that the upper thermocouples were situated in increasingly cooler outer regions of the fire plume. The individual time traces were characterized by an initial sharp increase in temperature as the fuel was ignited, followed in many cases by a more gradual increase in temperature (lasting until t=150-200 s in Figure 4.11) before finally levelling off to a steadier value. These trends indicate that the fire reached a steady state of burning within a relatively short period of time after ignition, thus permitting temporal averaging of measurements during the steady burning period.

A method for establishing the time extent of the steady burning period was developed in order to maintain consistency among analysis of the data for all tests. For each temperature time trace, a 95-point moving average was calculated in order to damp out high-frequency fluctuations in the data. A period of quasi-steady temperatures was then determined, based on the slope of the moving average over time. The start and end of this period were taken to be the times when the slope first dropped below 0.2°C/s and -0.2°C/s, respectively. These limits, as well as the number of points used in the moving average, were varied initially, but finally were selected so that the results would match visual estimates of the quasi-steady period in the temperature time traces as well.

In order to avoid having separate start and end times for the individual time traces in each test, a single start time and a single end time were selected for all thermocouples. These were taken conservatively to be the latest value among the individual start times and the earliest value among the individual end times. Some filtering of the start and end times was required because not all temperature time traces exhibited the ideal shape of a sharp increase, gradual levelling off and subsequent decrease in temperature. For instance, in Figure 4.11, the thermocouples located between elevations of 0.64 m and 1.39 m experienced a sudden spike in temperature at the beginning of the test (-20 s $<$ t $<$ 30 s) due to flames passing over the thermocouples as the fire tilted with the startup of the two bottom fans (Section 4.1.5). This spike caused the slope of moving average over time to drop below the lower limit of -0.2°C/s at two different instances: once during the latter half of the temperature spike and once near the end of the test as the fire burned out. The former time was not related to the steady burning period, while the latter

Table 4.4: Duration of Steady Burning Period for Fire-in-Crosswind Tests

Test Number	Wind Speed	Total Test Length	Start of Steady Burning	Duration of Steady Burning
38	5 m/s	750 s	320 s	231 s
42	10 m/s	597 s	235 s	178 s
43	7 m/s	552 s	223 s	179 s
44	3 m/s	825 s	378 s	225 s

time did designate the end time for the steady burning period. As a final consistency check, the chosen start and end times for each test were visually checked against each individual temperature time trace to ensure that the selected times encompassed a period of quasi-steady temperatures. For the test shown in Figure 4.11, the steady burning period was established as ranging from 223 s to 402 s. The periods of steady burning for all tests are summarized in Table 4.4.

The sensitivity of the time-averaged temperature data to the selected steady burning period was examined by varying the start and end times by ±30 s for each test. The temperature averages were found to vary by up to 9%, with greater percent variations occurring further from the fuel pan due to lower temperatures being measured further downwind in the plume. For the region of the plume that was within 6 m (or 3 pan diameters) downwind from the fuel pan centre, the variation in time-averaged temperature was within 5% for a 30 s variation in the start and end times of the chosen steady burning period. Thus, the selected steady burning periods in Table 4.4 were considered reasonable.

In addition to the above sensitivity to the selected steady burning period, the experimental results were affected by sources of uncertainty related to the instrumentation and data acquisition system. These sources of uncertainty are discussed in the next section, after which the time-averaged measurement results are presented.

4.3 Experimental Uncertainties and Sources of Error

Experimental uncertainty provides an estimate of the error in a measurement, i.e. the difference between a measured value and the true value [169–171]. Since the

true value is rarely known, the measurement error is usually not known; therefore, it is specified in terms of an uncertainty interval with a specific confidence level. This uncertainty is composed of systematic and precision components. Systematic, or bias, uncertainties are often (but not always) the same for all determinations of a given quantity in an experiment, while precision, or random, uncertainties result from variations in values between repeated measurements and may be characterized using the standard deviation of these variations. The two types of uncertainty may then be combined to give a value for total uncertainty. Different methods have been proposed for combining systematic and precision uncertainties; most involve a root-sum-square calculation and multiplication by a confidence level or coverage factor [171].[3] One such method is shown in Equation 4.1, which assumes a Student's t value of 2 for a coverage factor of 95% and at least 30 degrees of freedom [170,171].

$$U_t = \pm 2 \left[(B_t/2)^2 + (S_t)^2 \right]^{1/2} \text{ where} \tag{4.1}$$

$$B_t = \left[\sum_i (B_i)^2 \right]^{1/2} \text{ and} \tag{4.2}$$

$$S_t = \left[\sum_i (S_i)^2 \right]^{1/2} \tag{4.3}$$

In Equations 4.2 and 4.3, the elemental systematic and elemental precision uncertainties, B_i and S_i, are used to calculate the total systematic and total precision uncertainties, B_t and S_t. The elemental uncertainties are assumed to be uncorrelated and are either expressed in absolute terms using consistent units or normalized in order to avoid adding terms with different units. Further information on evaluating uncertainties is provided in Coleman and Steele [172, 173].

As discussed in Section 4.1.4, the setup of the present experiments contained mostly thermocouples and heat flux gauges. As a result, this section focusses on uncertainties related to these types of instrumentation.

[3] In accordance with Nakos [170] and Dieck [171], the term "coverage" instead of "confidence" is used when applied to uncertainties that are not statistically derived, e.g. most bias uncertainties.

4.3.1 Thermocouple Measurements

Systematic uncertainties in thermocouple measurements include calibration uncertainties related to the thermocouple wire, thermocouple extension wire and data acquisition system [170]. The standard calibration uncertainty for a Type K thermocouple is the larger of ±2.2°C or ±0.75% of the measured temperature above 0°C [174]. For a maximum temperature of 1174°C measured during the tests, the corresponding calibration uncertainty is ±8.8°C. The thermocouples on the thermocouple rakes and in the heat flux gauges were connected to extension-grade thermocouple wire outside the high temperature region of the fire. This extension wire had its own calibration uncertainty of ±2.2°C [174] and was connected to the data acquisition system. The input modules of the data acquisition system had a manufacturer-specified uncertainty that included errors related to gain, offset, nonlinearity, quantization, noise, linearization and measurement of cold-junction temperature [175]. For a maximum measured temperature of 1174°C, this uncertainty was stated to be no more than ±2.2°C. Although this value contained contributions from both systematic and precision errors, it could be considered a systematic uncertainty, since the only obvious source of precision error was noise. All of the above uncertainties were assumed to provide a 99% (3σ) level of coverage [170]. The equivalent values for a 95% (2σ) level of coverage were ±1.5°C or ±0.5% of the measured temperature above 0°C (whichever is larger) for the thermocouple wire, and ±1.5°C for both the extension wire and the data acquisition system.

Decalibration of thermocouples can occur with exposure of the thermocouple wire to high temperatures or steep temperature gradients [174, 176]. To minimize this error, thermocouples in the three measurement planes nearest the fuel pan (x=1.5 m, 2 m and 3 m) were protected from the extreme heat of the fire by insulating the length of wire running down the support chains. Furthermore, all temperature time traces were checked for irregularities at the end of each test and ambient temperature measurements from all thermocouples were analyzed for consistency prior to beginning the next test. By comparing measurements between thermocouples (particularly when all should be reading similar ambient temperatures), errant values could be identified and the corresponding thermocouples replaced. Although in-situ calibration of the thermocouples at the end of each test would have been ideal, this was not considered feasible due to the large number of thermocouples involved (396 channels) and the range of heights (up to 4.4 m) at which they were

located. Instead, exposure to extremely high temperatures and steep temperature gradients was minimized, and suspect thermocouples were identified and replaced after each test. As a result, decalibration was expected to contribute a minimal amount of uncertainty (assumed to be within 3%) to the measured results.

The temperature results were also affected by uncertainties in the locations of the thermocouples and in the selection of the time-averaging period. As mentioned in Section 4.2, an uncertainty in the averaged temperatures of approximately 5% was associated with selection of the start and end times of the steady burning period. With respect to sensor location, the thermocouples were carefully positioned and aligned prior to testing, but some of them shifted in location during the tests due to lengthening of the thermocouple support chains in the extreme heat of the fire. Furthermore, oscillation of the chains under high wind speeds contributed additional uncertainty to the thermocouple location on any given instantaneous temperature. In general, these combined factors affected the thermocouple positions by 0.01 m to 0.05 m (depending on the location of the chain and whether or not it was insulated). In a few regions, the thermocouples shifted by up to 0.14 m. Based on the temperature contour plots shown in the next section, the uncertainty in thermocouple location was estimated to affect the measured temperatures by approximately 10%, mostly due to changes in the vertical direction, along which the steepest temperature gradients occurred.

Additional systematic errors for thermocouple measurements include time lag, radiation effects and conduction losses, which are harder to quantify than the calibration and position uncertainties discussed above [124, 170]. Of these, radiation is probably the most important [161, 177–181]. Since the temperature measured by a thermocouple is determined by the sum of all energy contributions to, and energy losses from, the thermocouple junction, a thermocouple will not measure the true local gas temperature when the net radiation balance between the thermocouple and its surroundings is not negligible. For example, a thermocouple located outside a fire would experience significant radiation from the hot flame zone but be surrounded by cooler gases; thus the thermocouple (if not shielded or aspirated[4]) would measure a temperature higher than the true local gas temperature. Pitts *et al.* [180] found that a 0.25 mm exposed (bare-bead) thermocouple placed in

[4]To reduce radiation errors, thermocouples can be installed with radiation shields, but these are not always used due to non-uniform heating of the shield and constantly changing flow direction in fires [142]. Aspirated thermocouples may also reduce radiative effects, but increased perturbation of the surrounding environment results from the larger probe sizes and the forced flow of gases around the thermocouple junctions [180, 182].

the cool, lower layer of a compartment fire measured temperatures that were up to 75% higher than the local gas temperature obtained using an aspirated thermocouple, due to radiation contributions from the luminous flame, the hot upper layer of gases and the heated walls of the compartment. Conversely, when the bare-bead thermocouple was placed in the hot upper layer of the compartment fire, the temperature readings were approximately 7% lower than those from the aspirated thermocouple due to radiation losses from the bare-bead thermocouple to the cooler lower gas layer. A number of researchers have modelled the energy balance in bare-bead thermocouples and most have estimated the radiation error to be at least 10% [161, 177–179, 183, 184].

Several additional comments on radiation errors can be made. First, as the optical thickness of the local gases surrounding a thermocouple increases, the thermocouple measurement becomes less affected by radiation to/from the far (ambient) surroundings [124, 161]. Thus, a thermocouple immersed in optically thick flames would likely achieve approximate thermal equilibrium with the local surrounding environment. In the present experiments, such a situation would occur for thermocouples situated well inside the fire (e.g. along the flame axis in the persistent flame zone), but not for thermocouples situated near the edge of or outside the fire. Since the estimates of radiation error discussed above refer to optically thin environments, the error associated with thermocouples placed well inside optically thick flames would be expected to be lower [161]. Second, radiation error increases with increasing thermocouple emissivity (e.g. when covered with soot), increasing junction size, and decreasing velocity of gases flowing past the thermocouple [124, 178, 180, 184]. This indicates that during the tests at the highest wind speed, radiation error would be lowest and convective effects would be dominant in determining the temperature of the thermocouple junction. Considering all the above effects, the uncertainty due to radiation error in the present experiments was assumed to be 10% in the core of the fire and 20% near the edge of the fire.

Time lag errors in thermocouple meaurements occur because the thermal mass of a thermocouple affects its time response to changes in the turbulent temperature field in large fires. This error decreases with decreasing wire diameter and with use of exposed, rather than sheathed, thermocouple junctions. Compensation of the thermocouple signal via a mathematical model of the thermocouple junction (e.g. as a lumped capacitance) can reduce the effects of time lag on temperature measurements. For instance, Young [184] found that for thermocouples made from 75 μm diameter wire, compensation of temperature data taken in a 0.3 m diameter

fire reduced the error in the measured mean temperature by up to 1% along the central axis of the fire and up to 9% near the edge of the flame. At the same time, compensation affected the standard deviation of the temperature measurements by between 100% and 237%, indicating the level of difficulty involved in capturing the rapid changes in temperature caused by turbulent fluctuations in the fire. Given that larger thermocouples (0.51 mm diameter) were used in the present experiments, the uncertainty due to time lag would be expected to be greater than that reported by Young [184]. Walker and Stocks [185] reported that average flame temperatures measured by thermocouples of 0.51 mm diameter were up to 20% lower than those measured by thermocouples of 0.13 mm diameter. However, as mentioned earlier, the thermocouple wire diameter influences not only the time response of the thermocouple but also radiation to the thermocouple, so the 20% error reported by Walker and Stocks [185] cannot be solely attributed to differences in thermocouple time response. It should be noted that in the thermocouple compensation study of Young [184], radiation effects were neglected, although it was recognized that radiation could contribute approximately 10% error to the measurements. Correspondingly, Brohez *et al.* [177] estimated that an increase in thermocouple size from 0.25 mm to 1 mm doubled the radiation error, but they did not consider the superimposed effects of the time lag of the thermocouple. For the present experiments, the time lag error was assumed to be 5% of the measured value in the core of the fire and 10% near the edge of the fire.

Conduction losses can occur through the leads of a thermocouple, particularly when the length of the sensing element is short and when the thermocouple wire passes through a steep temperature gradient [186]. Bradley and Matthews [187] found that for fine-wire thermocouples attached to thicker lead wires, conduction errors were typically within 3%. In the present experiments, a single wire diameter was employed, so conduction errors would not be expected to be greater than 3%.

The above discussion illustrates some of the sources involved in establishing uncertainties in thermocouple measurements based on the physics of thermocouple response to the surrounding environment. For the temperature results presented in this chapter, which were averaged over the steady burning period of the fire (Section 4.2), the radiation error would generally be expected to dominate the errors caused by time lag and conduction loss. However, the radiation error at a given thermocouple location is difficult to estimate because it depends on the position of the thermocouple relative to the constantly fluctuating fire, the local velocity of gases flowing past the thermocouple, and the quantity of soot accumulating on the

Table 4.5: Estimated Systematic Thermocouple Uncertainties (95% Coverage), Based on Temperature Measurements of 800°C and 300°C

Uncertainty	Core of Fire (800°C)	Edge of Fire (300°C)
Thermocouple calibration	0.5%	0.5%
Extension wire calibration	0.2%	0.5%
Data acquisition system calibration	0.2%	0.5%
Decalibration	3%	3%
Time-averaging period	5%	5%
Thermocouple location	10%	10%
Radiation	10%	20%
Time lag	5%	10%
Conduction	3%	3%

thermocouple bead (which changes the emissivity and thermal mass of the thermocouple) during the test. As a result, the temperature results in this chapter are reported without correction for radiation, conduction or time lag effects. Nevertheless, based on the preceding discussion, it should be kept in mind that the uncertainty associated with temperatures measured near the edge of the fire would generally be greater than that associated with temperatures measured well inside the fire. Table 4.5 summarizes the sources of systematic uncertainty discussed above, with estimated values listed for a region in the core of the fire and a region near the edge of the fire.

In addition to systematic uncertainties, precision uncertainties, which are related to random variations between repeated measurements, must be considered. Sources of these variations include noise in the measurement system and turbulent fluctuations in the fire. Variations caused by turbulent fluctuations are part of the physics that one tries to measure and therefore are not a measurement uncertainty. Yet they do contribute to the variability in the data measured at a particular location and thus will be briefly discussed here. The variations are typically characterized using the standard deviation of data taken over the steady burning period of the fire, but this parameter includes effects of noise and other sources of random variations in the measurement system. Also, as demonstrated by Young [184], standard deviations calculated using uncompensated thermocouple data are significantly smaller than those determined using the compensated signal. Nevertheless, comparison of the relative magnitudes of standard deviation provides insight into

the variability occurring at different locations in the fire.[5] In the present experiments, the standard deviation was less than 10% in the core region of the fire, while it increased to 30% toward the edges of the fire. This was not unexpected, since the turbulent motions of the fire would have produced larger temperature fluctuations near the edges of the plume, and it augmented the trend observed in the systematic uncertainties, which were highest near the edges of the fire.

According to Coleman and Steele [172], the above values of standard deviation should not be used as estimates of precision uncertainty. The data measured over the steady burning period of a single test would constitute only a single measurement because it would be unlikely for all factors causing variation in the measurements to experience several fluctuation cycles during the 3-4 minute steady burning period of a test. As a result, the repeatability of measurements taken across multiple tests must be evaluated. Although the test series described in this chapter contained only one test at each wind speed, preliminary testing included two tests conducted at the 7 m/s wind speed. Thus, the repeatability of the measurements could be analyzed using data collected during these two preliminary tests. The tests were conducted on separate days, one (test "P1") as the second test of the day and the other (test "P2") as the first test of the day. The outdoor ambient temperature was approximately 7°C higher during the former test than during the latter test. Accordingly, pre-test measurements from the thermocouple chains were higher during the former test by 8°C to 15°C, with larger differences occurring near the brick floor. Since the floor was unable to cool completely between tests that were conducted on the same day, higher pre-test temperatures were expected to occur near the floor during the latter part of a test day.

To permit comparison between tests, initial temperatures (T_{init}), which were evaluated by averaging the thermocouple data over three minutes immediately prior to startup of the first fan[6], were subtracted from the temperatures averaged over the steady burning period (T_{ss}). This resulted in values for the increase in temperature from the beginning of the test to the period of steady burning. The test-to-test repeatability of the measurements was analyzed in terms of the difference in temperature increase between the two preliminary tests expressed as a percentage of the average of the two temperature increases, i.e.

[5]For reference, the values of standard deviation based on the uncompensated thermocouple data are listed in Appendix B.

[6]The standard deviation of the temperatures measured over these three minutes was typically within 1°C, indicating that temperatures were steady during this period.

$$\Delta T_{diff} = \frac{|(T_{ss} - T_{init})_{P2} - (T_{ss} - T_{init})_{P1}|}{\text{average of } (T_{ss} - T_{init})_{P1} \text{ and } (T_{ss} - T_{init})_{P2}} \times 100\% \qquad (4.4)$$

Contour plots of the values of ΔT_{diff} are shown in Figure 4.12 for the measurement planes x=2 m, 4 m and 6 m. (Note that the area plotted in each measurement plane is not the same.) Along the plane x=2 m (Figure 4.12a), ΔT_{diff} values of less than 10% were observed over approximately 80% of the 3 m wide by 1.4 m high measurement area. For the same area (-1.5 m $\leq$ y $\leq$ 1.5 m, z $\leq$ 1.4 m) along the plane x=4 m (Figure 4.12b), ΔT_{diff} remained below 10% over approximately 85% of this area. Along the plane x=6 m (Figure 4.12c), the area within which ΔT_{diff} remained below 10% lay mostly below z=3.3 m and between y=-1 m and 1 m. Since the fuel pan was centred at y=0 m and had a diameter of 2 m, the above results indicate that the test-to-test repeatability was within 10% in the core region of the fire plume.

Large values of ΔT_{diff}, near 80%, were observed at the edges of the contour plots, along y=-2 m in Figure 4.12b and along y=-3 m in Figure 4.12c. These locations were in the cooler regions outside the plume and experienced small changes in temperature during each test. Figure 4.13 contains corresponding plots of the absolute difference in temperature increase between the two tests, expressed by the numerator of ΔT_{diff}, $|(T_{ss} - T_{init})_{P2} - (T_{ss} - T_{init})_{P1}|$. As evident in Figures 4.13b and 4.13c, temperature differences of up to 15°C were measured along y=-2 m in the plane x=4 m, while temperature differences of up to 10°C were measured along y=-3 m in the plane x=6 m. Thus in these regions, a small difference in temperature between the two tests translated into a large percentage difference when calculating ΔT_{diff}. Conversely, larger temperature differences of up to 50°C occurred in the core of the plume along the measurement plane x=2 m (Figure 4.13a), but these represented ΔT_{diff} values of less than 20% due to the high plume temperatures in that region (Figure 4.12a). The above results indicate that large values of ΔT_{diff} were primarily induced by small magnitudes of temperature and did not likely reflect the actual test-to-test repeatability of measurements taken outside the plume. As a result, for this analysis, the test-to-test repeatability of measurements made near the edges of the fire was assumed to be the same as that in the core of the fire, 10%.

Based on the preceding discussion, rough estimates could be made for the total uncertainty in temperature measured in the core and edge regions of the fire. It may

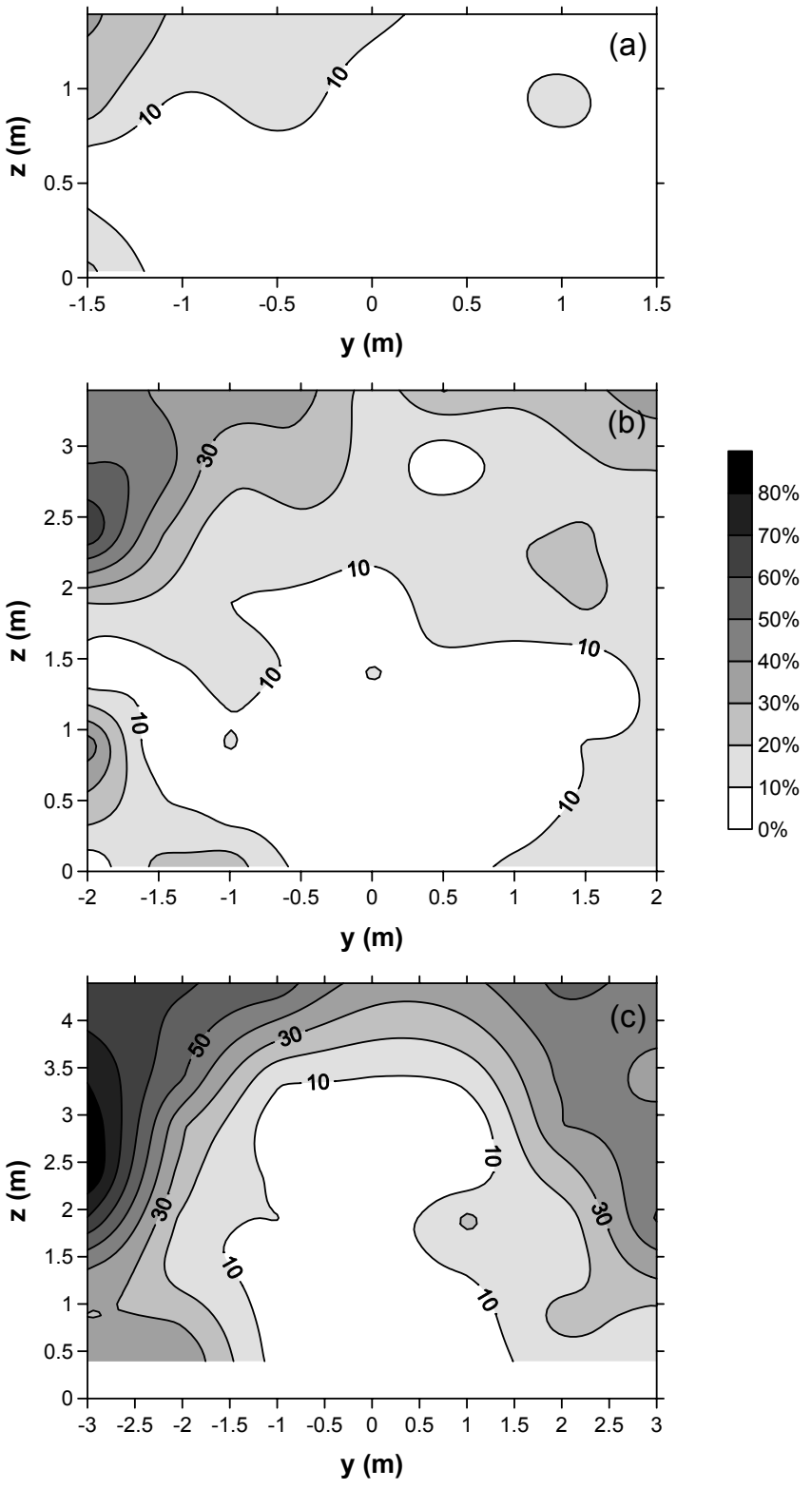

Figure 4.12: Percentage difference of $T_{ss} - T_{init}$ between Preliminary Tests P1 and P2, 7 m/s wind (Equation 4.4), (a) x=2 m, (b) x=4 m, (c) x=6 m (note that scale of each plot is not the same)

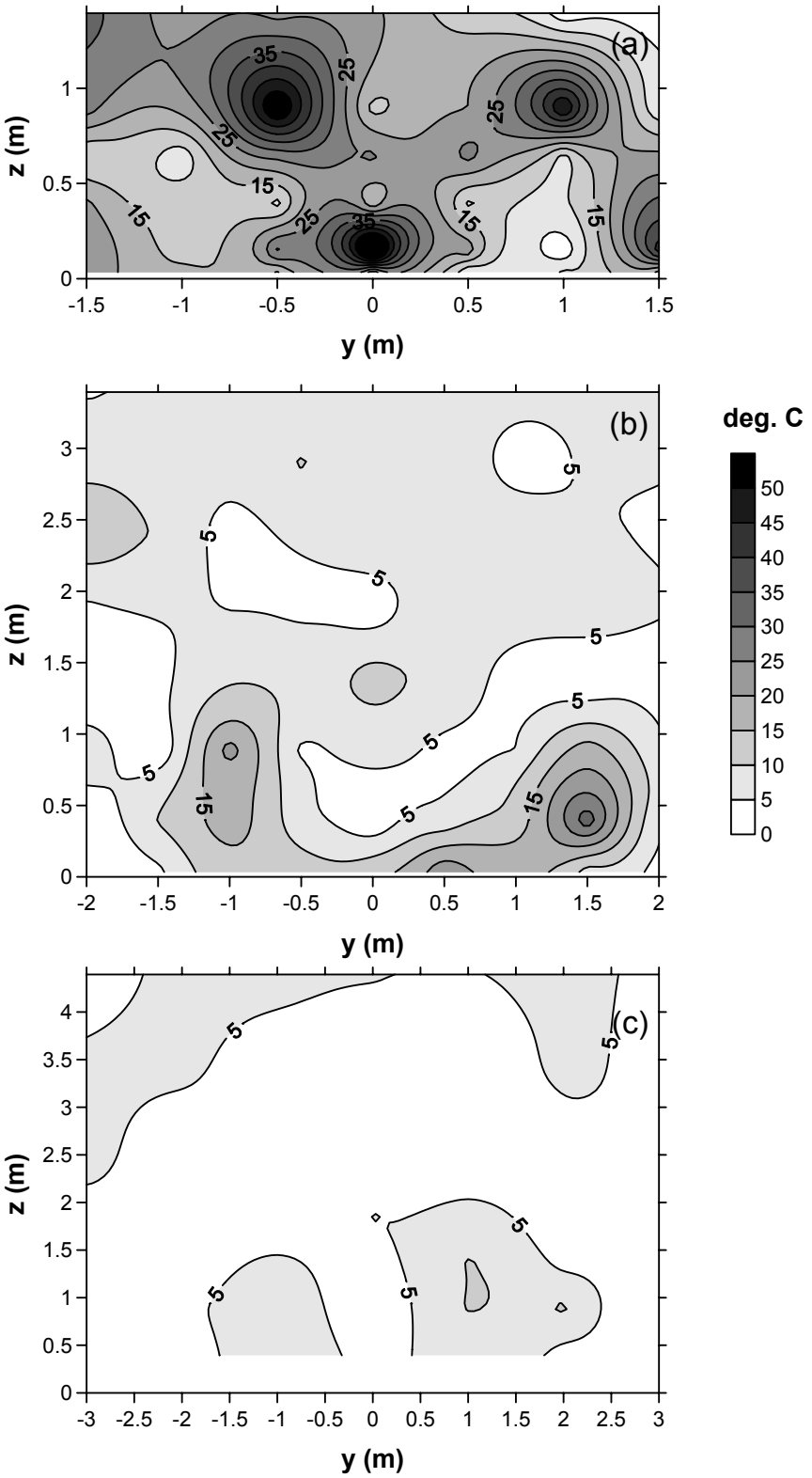

Figure 4.13: Absolute difference in $T_{ss} - T_{init}$ between Tests P1 and P2, 7 m/s wind (numerator of Equation 4.4), (a) x=2 m, (b) x=4 m, (c) x=6 m (note that scale of each plot is not the same)

Table 4.6: Estimated Total Thermocouple Uncertainties (95% Coverage)

Uncertainty	Core of Fire	Edge of Fire
B_t	16%	25%
S_t	10%	10%
U_t	26%	32%

be recalled that the total uncertainty is calculated using Equations 4.1 to 4.3, where the values of the elemental systematic uncertainties are listed in Table 4.5 and the values of the elemental precision uncertainty are as determined above, 10% both in the core of the fire and near the edges of the fire. The resulting estimates for the total systematic uncertainty (B_t), total precision uncertainty (S_t), and total overall uncertainty (U_t) are listed in Table 4.6. As expected, the total overall uncertainty near the edges of the fire was estimated to be greater than that in the core region of the fire, mainly due to greater uncertainty related to radiation effects.

4.3.2 Heat Flux Measurements

Uncertainty in heat flux measurements was examined in Chapter 3 via comparison of measurements made under controlled radiative and mixed radiative-convective conditions. For the Gardon gauge, the measurement uncertainty consisted of not only the manufacturer-specified calibration uncertainty but also the uncertainty in gauge sensitivity caused by differences between the calibration and measurement heating environments (e.g. added convective effects). For the DFT and HFG, the measurement uncertainty was shown to be dominated by effects of natural convection, lateral conduction and conduction from the sensor plate to the housing of the gauge. It should be noted that since the 2 m diameter fire was much larger than the cone calorimeter heater and the heat gun providing the convective flow in Chapter 3, more uniform heating of the gauges could be expected (depending on their location in the fire), thus reducing the effects of the conduction losses. Heat flux measurements made by the different gauges were also affected by differences in temperature of the sensor surfaces; thus the sensor surface temperature must be considered when comparing heat flux levels measured by the water-cooled Gardon gauge with those measured by the DFT and HFG.

As mentioned at the end of Chapter 3, estimates of measurement uncertainty have been made by Nakos [137] for DFT, HFG and Schmidt-Boelter type gauges

Table 4.7: Estimated Uncertainties for Heat Flux Gauges (95% Coverage)

Gauge	Uncertainty in Low Wind Conditions	Uncertainty in High Wind Conditions
Gardon	40%	40%
DFT	40%	30%
HFG	40%	30%

in large hydrocarbon fires under low and high wind conditions. These values were used, along with the results of Chapter 3, to estimate the uncertainty in measurements made by the DFT, HFG and Gardon gauge in the present experiments. For the DFT and HFG, the uncertainty (at 95% coverage) was assumed to be approximately 40% in low wind conditions and 30% in high wind conditions, based on the values reported by Nakos [137] for those types of sensors. For the Gardon gauge, the experiments in Chapter 3 indicated that the measurement uncertainty was similar to that of the Schmidt-Boelter gauge in radiative environments, but not in mixed radiative-convective environments. Thus, in low wind conditions, the Gardon gauge uncertainty was assumed to be 40%, based on the value reported by Nakos [137] for the Schmidt-Boelter gauge. In high wind conditions, the Gardon uncertainty was estimated by adding the 23% uncertainty estimated by Nakos [137] for the Schmidt-Boelter gauge to the 18% difference observed between the Gardon and Schmidt-Boelter results in Chapter 3, resulting in a total uncertainty of approximately 40%. The above uncertainty estimates for the DFT, HFG and Gardon gauge are summarized in Table 4.7.

With the preceding uncertainty discussion in mind, the results from the fire-in-crosswind experiments are now presented. The temperature data are discussed first, followed by the heat flux results.

4.4 Results and Discussion: Temperature

This section describes macroscopic features of the 2 m diameter Jet A fire under wind speeds of 3 m/s, 5 m/s, 7 m/s and 10 m/s. For each wind condition, video images are first presented to show the overall features of the fire. Then, the temperature data are discussed to provide more detailed characterization of the fire. Extents of flame drag, flame tilt and flame length, determined using both the temperature and video data, are subsequently compared to values predicted using

published correlations in order to gain further insight into the interaction between the wind and the fire.

The measured thermocouple data in each test were used to generate contour plots of the time-averaged increase in temperature, $T_{ss} - T_{init}$. The plots were based on the steady burning periods identified in Section 4.2 and produced using the Kriging gridding method [188–190]. The Kriging method is robust and suitable for almost any type of data set, providing a visually plausible and accurate representation of the data. It involves an inherent interpolation of the input data, as opposed to a direct fit of the data points.

Of the 396 thermocouples used in the experiments, between 3 and 11 thermocouples (1% to 3%) failed during a test due to intense heating by the fire. Since most of the failures occurred well after the initial increase in temperature at the beginning of each test, values measured by these thermocouples prior to failure could still be included in the contour plots. The measured values were averaged over a quasi-steady period lasting between 65 s and 226 s immediately prior to failure, with the appropriate duration determined through visual examination of the corresponding temperature time curves. The maximum duration of the averaging period was limited to that of the steady burning period listed in Table 4.4 for the corresponding test. All data used to generate the contour plots, including those from the thermocouples that eventually failed, are listed in Appendix B.

4.4.1 Fire in 3 m/s Wind

Figure 4.14 contains a typical frame taken from the video showing a profile view of the fire in the 3 m/s wind condition. In the region immediately above the fuel pan, the flame exhibited a significant degree of tilt, with the leading edge of the luminous flame envelope inclined at an angle of approximately 75° from the vertical posts of the thermocouple support frame. Analysis of additional video frames indicated that the angle of tilt did not vary significantly during the steady burning period of the fire and had an uncertainty of ±2°. This consistency was supported by the time-averaged image of the fire shown in Figure 4.15. In this image, which was averaged over 60 frames, each taken half a second apart, the leading edge of the fire remained well-defined, whereas the downwind portion of the fire was smeared out, indicating significant variations in the shape of the flame envelope in that region.

Figure 4.14: Typical video frame showing profile view of fire in 3 m/s wind

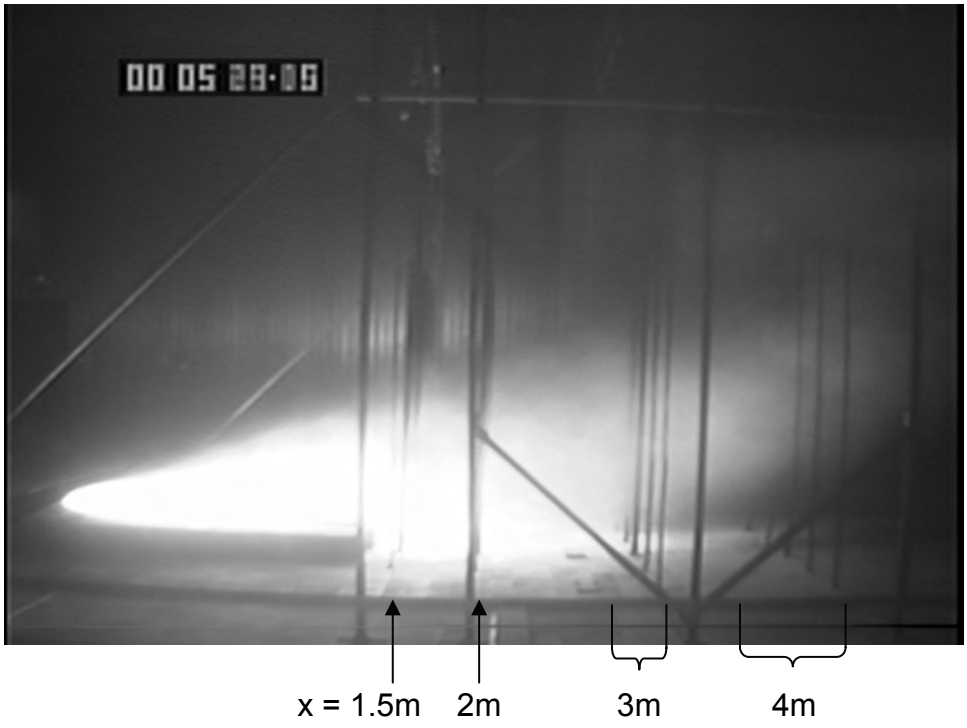

Figure 4.15: Typical 60-frame time-averaged image showing profile view of fire in 3 m/s wind

Several characteristics of the fire in the region downwind of the fuel pan could be observed in the two Figures. Near the pan, the flame was attached to the raised floor surround and to the brick floor immediately downwind of the raised surround. The extent of flame drag could be estimated based on the locations of the thermocouple chains visible in each image. Four groups of vertical chains could be discerned – two of these corresponded to thermocouples situated along x=1.5 m and 2 m and could be seen close together in the middle of the image (as denoted in Figure 4.15), while the other two corresponded to thermocouples situated along x=3 m and 4 m and could be seen further apart in the right half of the image. With nine chains spaced equally along x=3 m, the bases of at least five chains should be visible if there was no flame drag in this plane. Careful examination of Figure 4.15, along with additional video images, revealed that the bases of the five chains closest to the camera were not obscured by flame; therefore, flame drag did not extend to this downwind distance. As evident in the images, downwind of x=3 m, the flame started to lift off the ground due to buoyancy. This region of the fire exhibited large amounts of smoke, significant turbulence and rapid variations in shape, as indicated by the presence of discrete flaming packets in Figure 4.14 and the blurriness in the right half of Figure 4.15. As a result, attempts to estimate from the video images plume shape and tilt in this region of the fire were extremely difficult.

The temperature contour plot along the centreline plane y=0 m (Figure 4.16) provided a much clearer picture of the shape and extent of the downwind fire plume. In this plot, the coordinates (x,y)=(0,0) are located at the centre of the fuel pan, while z=0 m is very close to the top surface of the 0.11 m thick brick layer downwind of the fuel pan (Figure 4.4). The temperature contours were not extrapolated beyond any measurement points; therefore, the contours do not extend below x=1.5 m or z=0.03 m.

The temperature contours clearly show the change in direction of the fire plume as it travelled away from the fuel pan and lifted off the ground. For $x < 3$ m, the plume appeared to be tilted at an angle of $75° \pm 2°$, based on the direction of the 300°C to 700°C contours. This angle was consistent with the one determined from the video images for the region of visible flame immediately above the fuel pan. At x=3 m, a change in direction of the upper contours was observed, indicating that buoyancy effects started to play a dominant role in plume development and that the plume started to lift off the ground. This was consistent with the earlier observation that flame drag did not extend beyond x=3 m.

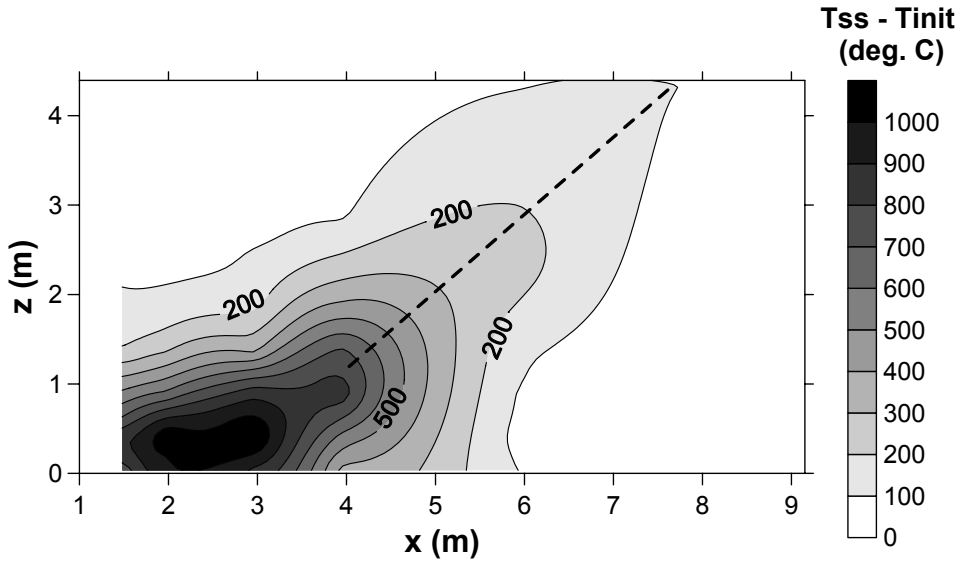

Figure 4.16: Contour plot of increase in temperature under 3 m/s wind, y=0 m

To estimate the extent of flame drag directly from Figure 4.16, an appropriate temperature would have to be selected to represent the edge of the luminous flame drag region. Comparison of Figures 4.15 and 4.16 suggested that a temperature of 900°C would be appropriate. This temperature was compared to centreline temperatures in the persistent flame zone of axisymmetric buoyant diffusion flames, as published by McCaffrey [39]. The selected temperature of 900°C was found to be greater than the 800°C value characterizing the persistent flame zone [39], but the 800°C values were measured using a thermocouple placed in a 0.3 m square methane fire in quiescent conditions and would have been lower than the actual gas temperature by approximately 20% due to radiation to the ambient surroundings (Section 4.3.1). For the current 2 m wind-blown fire, temperature measurements made in the region of flame drag along the centreline plane were expected to have lower radiation error because the flame thickness was greater and the floor was covered with insulating fire bricks, minimizing radiation loss from the thermocouples to the surroundings. As a result, a temperature of 900°C $\pm$ 50°C for estimating the extent of flame drag was considered reasonable. Based on Figure 4.16, this would suggest that flame drag occurred until x=2.9$\pm$0.2 m, similar to that observed from the video images.

Additionally, if the 100°C contour were used to represent the edge of the thermal plume in the fire, Figure 4.16 would suggest that the plume lifted completely off the ground at x=6 m. This indicates that the downwind side of the plume interacted

with the floor until x=6 m. Along this downwind side, the temperature contours showed relatively little tilt, particularly at low elevations (e.g. 100°C to 400°C, x > 4.5 m, z < 1.4 m). The direction of these contours was likely influenced by effects of buoyancy in this region. Also, the temperature gradients in the x direction on the downwind side of the plume were lower than those in the z direction on the upwind side (x < 3 m), indicating that as the plume started to lift off the ground downwind of x=3 m, cooler ambient air became entrained underneath the rising plume core and mixed with gases in the edge regions of the plume.

As discussed in Section 2.2, flame tilt is conventionally defined as the angle from the vertical to a line drawn from the tip of the visible flame envelope to either the centre of the fuel pan or the centre of the elongated flame base if flame drag is present. The length of the line also provides an estimate of the flame length. The location of the flame tip can be estimated as the location along the plume centreline where the temperature increase above ambient is 550°C (corresponding to 50% flame intermittency [22, 39]). This is usually considered to provide a more reliable estimate of the flame tip location than direct measurement from the video images, since significant amounts of smoke can obscure the luminous flame. Thus, this method should be an improvement upon the visual method used by Ferrero [92] (in which smoke-obscured areas were neglected) to estimate tilt angles in the development of Equation 2.9.

Applying the 550°C temperature criterion to Figure 4.16, the flame tip was estimated to lie at (x,z)=(4.4 m, 1.5 m). Next, the centre of the flame base was estimated to be located at (x,z)=(0.95 m, 0.1 m). This assumed that the flame base extended from x=-1 m (the leading edge of the pan) to x=2.9 m (the estimated extent of flame drag) and that the average height of the fuel surface was situated at z=0.1 m. The corresponding tilt angle and flame length were subsequently determined to be 68° and 3.7 m, respectively. The ±0.2 m uncertainty in the estimated flame drag extent affected the tilt angle by less than 1°, while the flame length changed by approximately 0.1 m. Meanwhile, a ±0.1 m uncertainty in the flame tip location affected the tilt angle and flame length by 2° and 0.1 m, respectively. The combined uncertainties (based on a root-sum-square method similar to Equation 4.2) were therefore approximately ±2° for the tilt angle and ±0.1 m for the flame length. When the centre of the fuel pan, rather than the centre of the flame base, was considered, the flame length increased to 4.6 m and the tilt angle increased to 72°. This tilt angle was 4% lower than the 75° angle estimated

from the temperature contours in the upwind portion of the plume ($1.5 < x < 3$ m), while the 68° angle was 9% lower.

In the downwind portion of the plume ($x \geq 4$ m), the direction of overall plume travel could be estimated from the dotted line shown in Figure 4.16, which approximates the location of the plume centreline in this region. The tilt angle of the dotted line was 49°, with an uncertainty of ±1°. This angle could be compared with one that was determined from temperature contour plots of different cross-sections of the plume, which are shown in Figures 4.17 and 4.18. (Note that in Figure 4.18, a lower temperature scale was used.) Again, the contours in the cross-sectional plots were not extrapolated beyond the lowest measurement point on the thermocouple chains, z=0.03 m in Figure 4.17 and z=0.4 m in Figure 4.18.

Closest to the fuel pan, along x=1.5 m and 2 m (Figures 4.17a and 4.17b), the hot core of the fire plume was centred at heights of approximately z=0.30 m and 0.35 m, respectively. Further downwind, along x=3 m and 4 m (Figures 4.17c and 4.17d), the plume core was centred at heights of approximately 0.5 m and 1.0 m. These changes in height were in agreement with the observation from Figure 4.16 that the plume started to lift off the ground around 3 m downwind of the fuel pan centre. At x=6 m (Figure 4.18a), the height of the plume centre was estimated to be 2.4 m, based on the temperatures along y=0 m. At x=8 m (Figure 4.18b), the plume centre was estimated to be 4.3 m high. Using the above heights from x=2 m to 8 m, the angle of tilt of the plume was calculated to be 56°. An uncertainty of ±0.25 m[7] in the height of the plume centre in each cross-sectional plane corresponded to an uncertainty of ±4° in the tilt angle. The 56° value was 14% higher than the 49° angle determined from the centreline contour plot in Figure 4.16. However, it should be noted that the estimate of 49° was based on the portion of the plume downwind of x=4 m. Accordingly, if the plume centre heights from only x=4 m, 6 m and 8 m were considered (thus neglecting the region of the plume affected by flame drag), the angle of tilt would be 50°, in much closer agreement with the 49° angle from Figure 4.16. This result highlights a major difficulty in describing the tilt of a fire when there is significant flame drag and subsequent downwind curvature in the plume.

Several features may be noted in the cross-sectional structure of the plume as it travels downwind. From x=1.5 m to 4 m (Figure 4.17), the core region of the plume was observed to transition from an elliptical shape to a circular shape. Although the

[7]This is half the spacing between the thermocouples on each thermocouple chain.

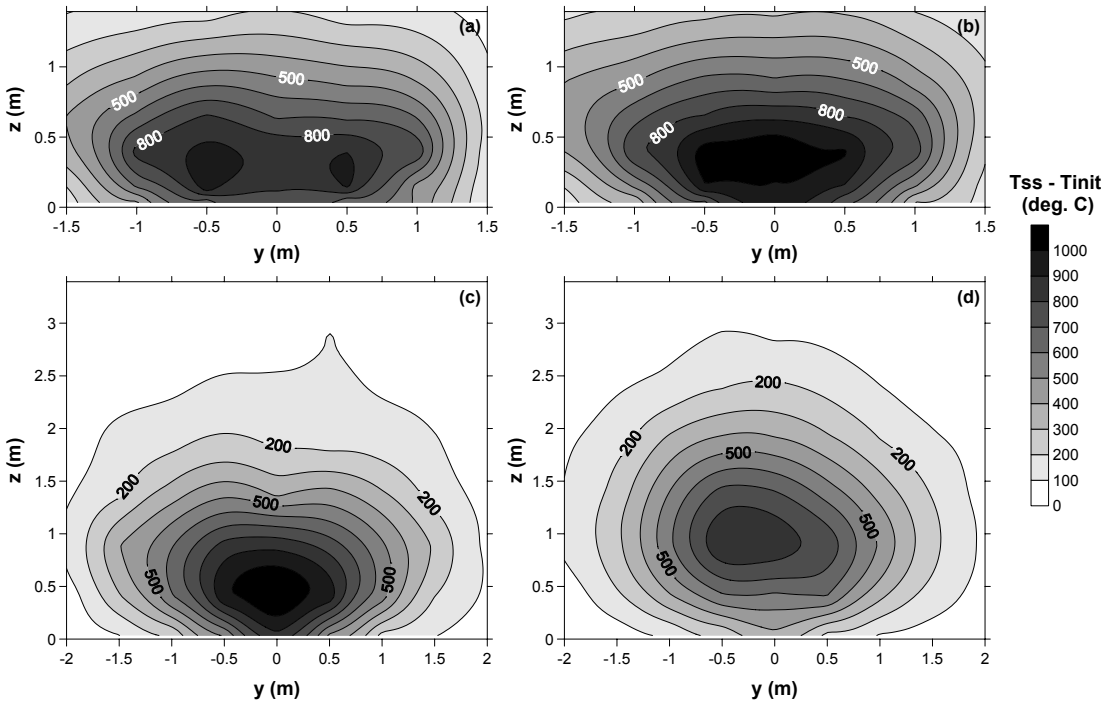

Figure 4.17: Contour plots of increase in temperature under 3 m/s wind, (a) x=1.5 m, (b) x=2 m, (c) x=3 m, (d) x=4 m

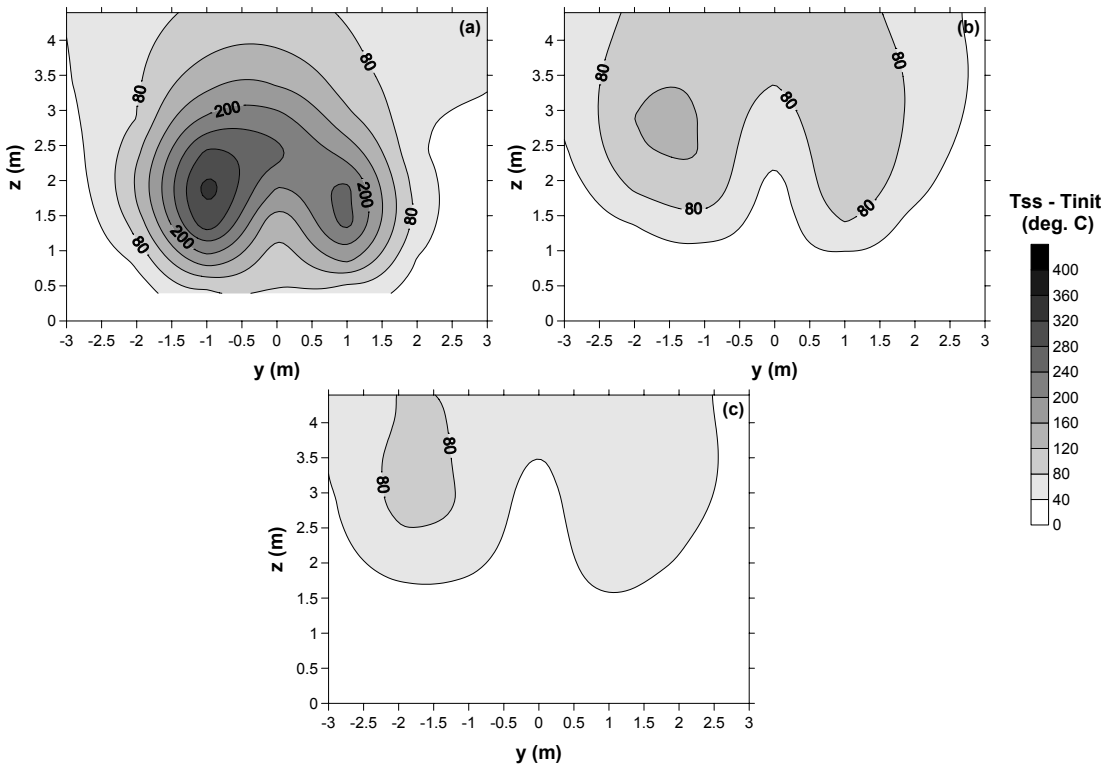

Figure 4.18: Contour plots of increase in temperature under 3 m/s wind, (a) x=6 m, (b) x=8 m, (c) x=9.2 m

plots in Figure 4.17 show temperature, a scalar parameter, they suggest an evolution in the fire plume similar to that reported in previous work with rectangular jets [191, 192]. This type of evolution is thought to be related to entrainment and lateral velocity in the jet plume [191]. From x=6 m to 9.2 m (Figure 4.18), the development of counter-rotating vortices, with their axes of rotation oriented along the direction of plume travel, was observed. Similar vortices have been previously seen in large, wind-blown fires [52,193] and circular jets in crossflow [194]. At x=6 m (Figure 4.18a), the vortices were centred at a height of approximately z=1.9 m, 0.5 m below the overall plume centre determined using the temperature profile along y=0 m. The presence of counter-rotating vortices in the plots of Figure 4.18 is consistent with the observation from Figure 4.16 that the trailing edge of the plume (represented by the 100°C contour) did not lift off the ground until x=6 m, because the leeward side of the plume could not have been interacting with the floor in order for such vortices to be clearly visible.

4.4.2 Fire in 5 m/s Wind

A typical single-frame image and 60-frame, time-averaged image of the fire in the 5 m/s wind are shown in Figures 4.19 and 4.20, respectively. Similar to the fire in the 3 m/s wind, the region of flame immediately above the fuel pan was tilted significantly, with the leading edge of the luminous envelope at a tilt angle of $78° \pm 2°$. The flame was also attached to the raised floor surround and the brick floor downwind of the raised surround. Flame drag appeared to extend beyond x=3 m because the bases of four, rather than five, thermocouple chains at this downwind distance were visible in the time-averaged image, indicating that the centremost chain was surrounded by flame down to the floor. As in the 3 m/s wind condition, the downwind region of the fire was characterized by significant smoke obscuration, turbulence and rapid variations in shape, as indicated by the presence of discrete flaming packets in Figure 4.19 and the blurriness in the right half of Figure 4.20.

Figure 4.21 contains a plot of temperature contours along the centreline plane y=0 m. At $x < 3.7$ m, the contours from 300°C to 700°C were tilted at an angle of $76° \pm 2°$. This angle is in good agreement with the $78° \pm 2°$ angle determined from the video images for the region of the fire immediately above the fuel pan. Based on the 900°C contour (with an uncertainty of ±50°C), flame drag appeared to extend until x=3.4±0.2 m, consistent with the observations made from the video images.

Figure 4.19: Typical video frame showing profile view of fire in 5 m/s wind

Figure 4.20: Typical 60-frame time-averaged image showing profile view of fire in 5 m/s wind

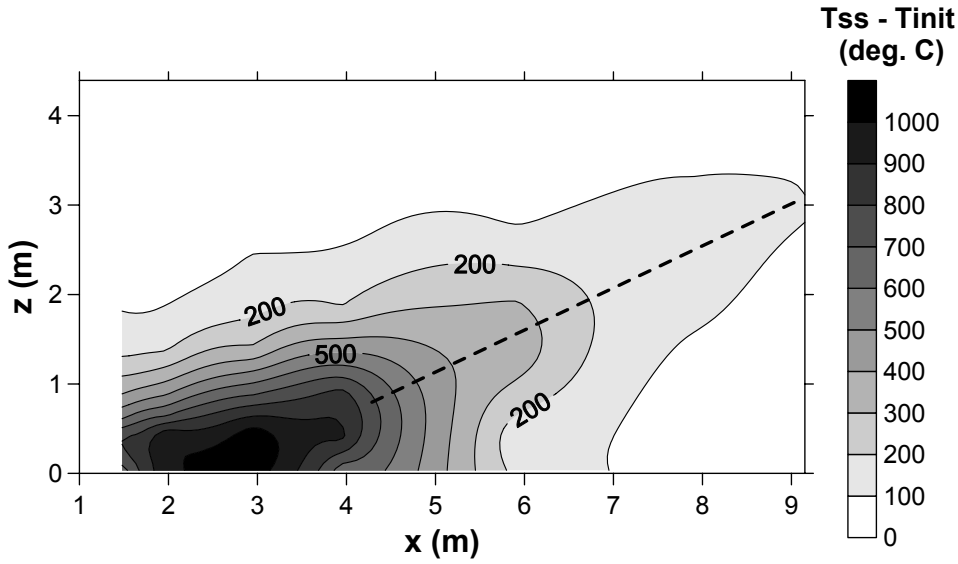

Figure 4.21: Contour plot of increase in temperature under 5 m/s wind, y=0 m

Furthermore, based on the 100°C contour, the plume appeared to lift completely off the ground at a downwind distance of 7 m. These distances were greater than those corresponding to the 3 m/s wind condition, as expected due to the decrease in magnitude of buoyancy relative to wind momentum and therefore increase in plume tilt. The importance of buoyancy was still evident on the leeward side of the plume, based on the approximately vertical temperature contours downwind of x=4.4 m, near the ground ($z < 0.5$ m). Similar to those shown in Figure 4.16, the temperature gradients in the x direction across this region were much lower than those in the z direction along the upwind side of the plume ($x < 3.7$ m), indicating entrainment and mixing of cooler ambient air underneath the rising plume core.

Values for tilt angle and flame length were also determined using the conventional definitions of flame tilt and Figure 4.21. In this Figure, the flame tip was situated at approximately (x,z)=(4.6 m, 1.0 m), where the temperature increase along the plume centreline was 550°C. The centre of the flame base was assumed to be at (x,z)=(1.2 m, 0.1 m), with the flame base extending from x=-1 m to 3.4 m and the fuel surface situated at an average height of z=0.1 m. Thus, based on a line drawn from the flame tip to the centre of the flame base, the tilt angle and flame length were determined to be 75° and 3.5 m, respectively. The ±0.2 m uncertainty in the flame base extent and ±0.1 m uncertainty in the flame tip location combined to give uncertainties of ±2° for the tilt angle and ±0.1 m for the flame length. For a line drawn from the flame tip to the fuel pan centre, the tilt angle and flame length

were 79° and 4.7 m, respectively. This tilt angle and the one based on the flame base centre were in close agreement with the 76° tilt of the temperature contours in the region upwind of x=3.7 m in Figure 4.21. On the other hand, they were somewhat larger than the direction of overall plume travel in the region downwind of x=4 m, which was estimated to have a tilt angle of $65° \pm 2°$, based on the dotted line approximating the location of the plume centreline in Figure 4.21.

Figure 4.22 shows temperature contour plots along cross-sectional planes situated from 1.5 m to 4 m downwind of the fuel pan centre. At x=1.5 m and 2 m, the hot core of the plume was centred at a height of approximately z=0.25 m. Given that the rim of the pan and the top surface of the raised floor surround were situated at a height of z=0.17 m (Figure 4.4), these data indicate that the fire plume was attached to the top of the floor surround and the brick floor downwind of the raised surround, in agreement with the video images of the fire (Figures 4.19 and 4.20). Along the planes x=3 m and 4 m, the core of the plume appeared to be approximately 0.4 m and 0.6 m high, respectively, based on the location and extent of the 900°C contour. The shape of the contours in Figure 4.22c indicates that the plume was still attached to the floor 3 m downwind of the fuel pan centre, consistent with the observation of flame drag occurring until x=3.4 m in Figure 4.21.

Temperature contour plots along cross-sectional planes situated at downwind distances of 6 m to 9.2 m are shown in Figure 4.23. At x=6 m, the core of the plume was centred at a height of approximately 1.4 m, indicating that it had lifted off the ground due to buoyancy. At x=8 m, the centre of the plume was 2.4 m high (based on the temperatures along y=0 m), while at x=9.2 m, the centre of the plume was approximately 3.0 m high. Using these heights and the ones mentioned above for x=2 m, 3 m and 4 m, the angle of plume tilt was estimated to be 69°, with an uncertainty of ±4° due to an uncertainty of ±0.25 m in the height of the plume centre in each cross-sectional plane. This angle was 6% larger than the 65° value estimated from Figure 4.21. Although this comparison was reasonably close, calculation of a tilt angle using only plume heights at $x \geq 4$ m (the range of downwind distances used to estimate the 65° angle in Figure 4.21) resulted in an even better match, with a modified estimate of 65°.

The development of counter-rotating vortices in the plume was apparent at x=8 m and 9.2 m, with the vortices centred lower than the overall plume centre by approximately 0.6 m and 0.8 m, respectively. Since the plume had to lift completely off the ground before such vortices would be clearly visible, the presence of counter-

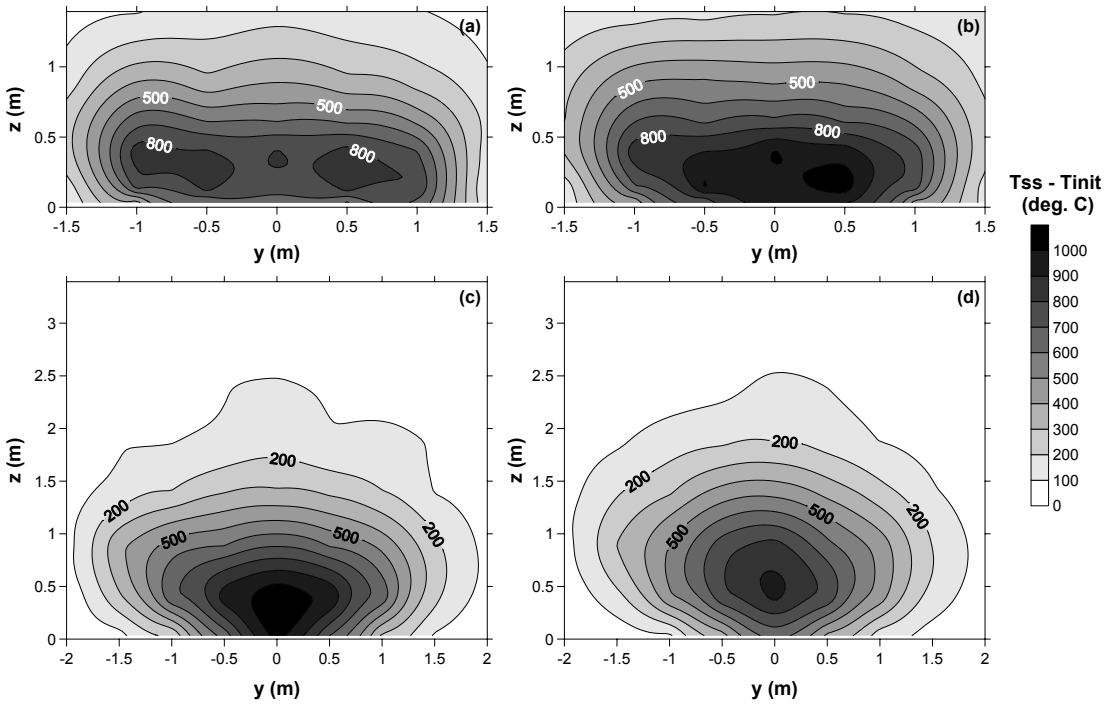

Figure 4.22: Contour plots of increase in temperature under 5 m/s wind, (a) x=1.5 m, (b) x=2 m, (c) x=3 m, (d) x=4 m

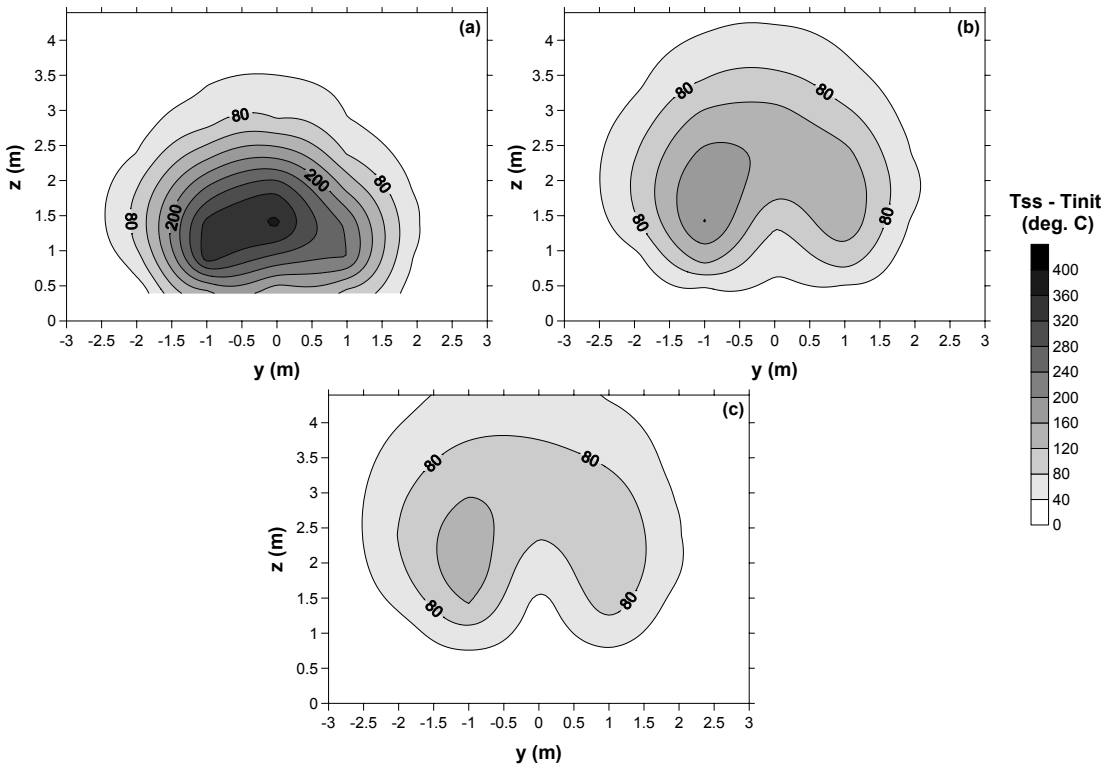

Figure 4.23: Contour plots of increase in temperature under 5 m/s wind, (a) x=6 m, (b) x=8 m, (c) x=9.2 m

rotating vortices in these two measurement planes is consistent with the plot in Figure 4.21, which shows the leeward edge of the plume (represented by the 100°C contour) lifting off the ground at approximately x=7 m.

4.4.3 Fire in 7 m/s Wind

Figures 4.24 and 4.25 show a typical single-frame image and 60-frame, time-averaged image of the fire in the 7 m/s wind condition. The leading edge of the luminous flame envelope above the fuel pan was tilted by an angle of $81° \pm 2°$. Similar to the previous wind conditions, the luminous flame was attached to the raised floor surround and the brick floor downwind of the raised surround. The fire lay flatter at the 7 m/s wind speed than at the lower wind speeds, so the vertical height spanned by the plume downwind of the fuel pan was narrower, as evident when comparing the various time-averaged images of the fire (Figures 4.15, 4.20 and 4.25). Also evident in these images was the trend that the visible flame became less obscured by smoke at the higher wind speeds, particularly in the area upwind of x=3 m, likely due to greater removal of smoke from the edge regions of the fire by the stronger winds. At the same time, the upper boundary of the luminous flame envelope in this upwind region became better defined, indicating less fluctuation in the overall shape of the flame envelope near the fuel pan.

In Figure 4.25, flame drag appeared to occur beyond x=3 m because the bases of only three thermocouple chains were visible at this downwind distance, indicating that the centremost chains were surrounded by flame. Figure 4.25 also appeared to show flame drag occurring at x=4 m, but the combination of smoke obscuration and poor image contrast made the plume and thermocouple chains very difficult to distinguish from the image background. In an initial attempt to verify the presence of flame drag at this location, Figure 4.26, which contains a time-averaged image of the fire from a downwind viewing position, was examined. The bases of four thermocouple chains along the x=4 m plane could be readily seen, while the centre chain appeared to be obscured by not only smoke but also flame (because the plume here was brighter in colour than it was further downwind where only smoke was present). This suggested that flame drag extended to a distance of 4 m downwind of the fuel pan centre.

Additional evidence for the presence of flame drag at x=4 m was provided by the temperature contours along the centreline plane y=0 m (Figure 4.27). Based on

Figure 4.24: Typical video frame showing profile view of fire in 7 m/s wind

Figure 4.25: Typical 60-frame time-averaged image showing profile view of fire in 7 m/s wind

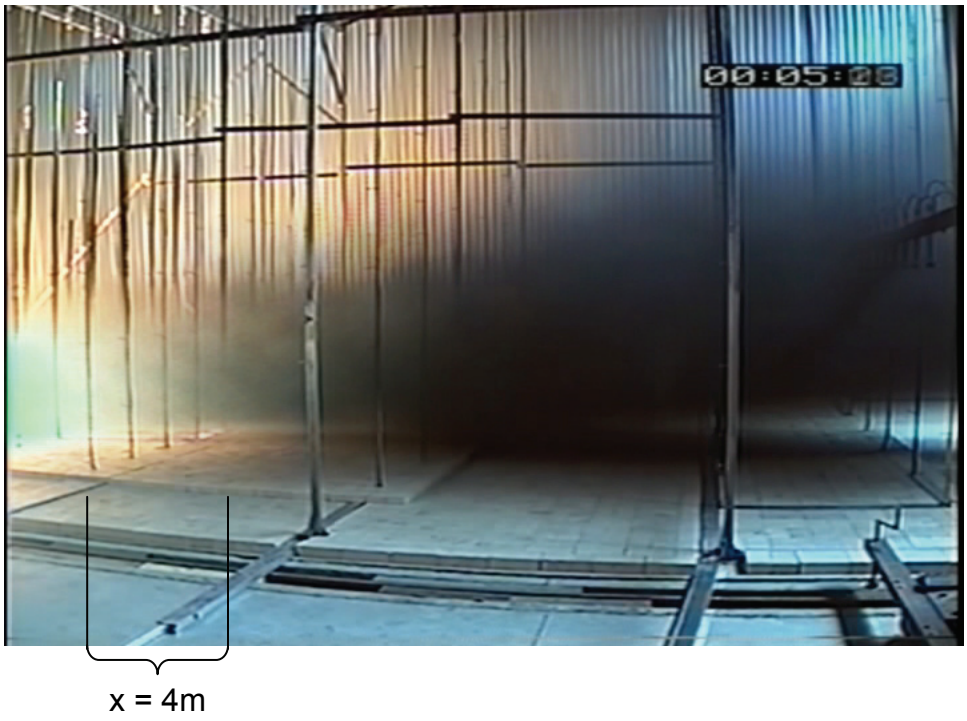

Figure 4.26: Typical 60-frame time-averaged image showing downwind view of fire in 7 m/s wind

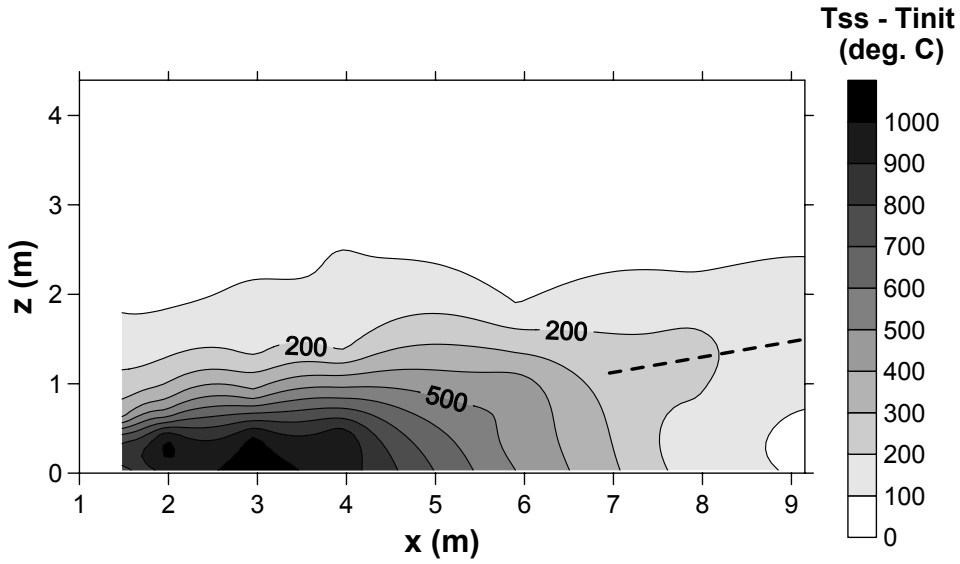

Figure 4.27: Contour plot of increase in temperature under 7 m/s wind, y=0 m

the 900°C contour, flame drag appeared to occur up to x=4.2 m. An uncertainty of ±50°C in the selection of this contour corresponded to an uncertainty of ±0.3 m in the extent of flame drag. This result was consistent with the observation of flame drag at a downwind distance of x=4 m in the video images. In addition, the "nose" shape formed by the 200°C contour downwind of x=7.5 m in Figure 4.27 suggests that in this region, the plume was starting to lift off the ground due to buoyancy effects. Based on the 100°C contour, the plume did not appear to lift completely off the ground until x=9 m, indicating that the leeward side of the plume lay against the floor along most of the test section.

Estimates of tilt angle could be made based on the temperature contours shown in Figure 4.27. Between x=2.4 m and 4 m, the 300°C to 700°C contours were tilted by an angle of approximately 85° ± 2°. This angle was comparable to the angle of 81°±2° estimated from the video images for the region of the fire immediately above the fuel pan. Further downwind, for x > 7 m, the tilt angle of the plume could be estimated based on the dotted line shown in Figure 4.27, which approximates the location of the plume centreline. This angle was found to be 80° ± 3°, very close to the 81° angle estimated from the video images.

Application of the conventional definitions of flame tilt to the fire in the 7 m/s wind condition was more difficult due to the shape of the temperature contours between 500°C and 600°C in Figure 4.27. The location of the flame tip, based on the intersection of the 550°C contour with the plume centreline, could only be estimated by extending the dotted line in Figure 4.27 upwind of x=7 m. Although such an extension was not clearly supported by the shape of the contours, the resulting flame tip location, (x,z)=(4.9 m, 0.7 m), indicated tilt angles comparable to those estimated previously from the contour plot and video images. The tilt angle based on a line drawn from the flame tip to the flame base centre, located at (x,z)=(1.6 m, 0.1 m), was 80°, while the tilt angle based on a line drawn from the flame tip to the fuel pan centre was 83°. Correspondingly, the flame length relative to the flame base centre was 3.4 m, while the flame length relative to the fuel pan centre was 4.9 m. The ±0.3 m uncertainty in the flame base extent and ±0.2 m uncertainty in the flame tip location combined to give uncertainties of ±4° for the tilt angle and ±0.3 m for the flame length.

For comparison to the above values, a separate estimate of plume tilt angle was made based on plume centre heights determined from the cross-sectional tempera-

ture contour plots shown in Figures 4.28 and 4.29.[8] At x=1.5 m, the centre of the plume core was approximately 0.2 m high, while at both x=2 m and 3 m, it was approximately 0.25 m high. The plume core then rose to a height of approximately 0.4 m at x=4 m, before reaching heights of approximately 0.8 m, 1.2 m and 1.5 m at x=6 m, 8 m and 9.2 m, respectively. Based on the estimated heights at $x \geq 4$ m, the tilt angle of the plume was calculated to be 78°, in reasonable agreement with the 81° angle estimated from the video images and the 80° angle estimated from Figure 4.27 for $x > 7$ m. An uncertainty of ±6° in the 78° tilt angle resulted from a ±0.25 m uncertainty in the height of the plume centre in each cross-sectional plane.

Comparison of the plots in Figures 4.28 and 4.29 with the corresponding plots for the 3 m/s and 5 m/s wind conditions revealed several effects of increasing wind speed on fire behaviour. As the wind speed increased, the plume was pushed closer to the ground, with the hot core near the fuel pan spreading laterally while spanning a smaller vertical extent. This trend was consistent with the increasing plume tilt and increasing flame drag at higher wind speeds. The edges of the plume were also characterized by steeper temperature gradients, particularly along measurement planes from x=1.5 m to 3 m. This observation was consistent with the time-averaged images of the fire, which showed the edges of the luminous flame envelope becoming better defined at higher wind speeds. Close examination of the videos indicated that fewer and smaller "fingers" of flame formed along the top edge of the luminous flame envelope at the 7 m/s wind speed than at the 3 m/s wind speed. At such high wind speeds, the strong momentum of the crosswind flow thus dominated over effects of buoyancy in governing plume development. In addition, no distinct counter-rotating vortices were seen in any of the cross-sectional temperature contour plots for the 7 m/s wind condition, although the kidney-shaped region enclosed by the 120° contour in Figure 4.29c suggested that such vortices were starting to form. These vortices likely would have become more clearly visible further downwstream, after the plume lifted completely off the ground.

4.4.4 Fire in 10 m/s Wind

A typical single-frame image and 60-frame, time-averaged image of the fire in the 10 m/s wind condition are shown in Figures 4.30 and 4.31, respectively. These

[8] In Figure 4.28a, the 900°C contours are not shown because the spatial resolution of the measurements taken in the central region of the plume core was insufficient to provide a reasonable representation of the 900°C isotherm. The same applied to the 1000°C contours in Figure 4.28b.

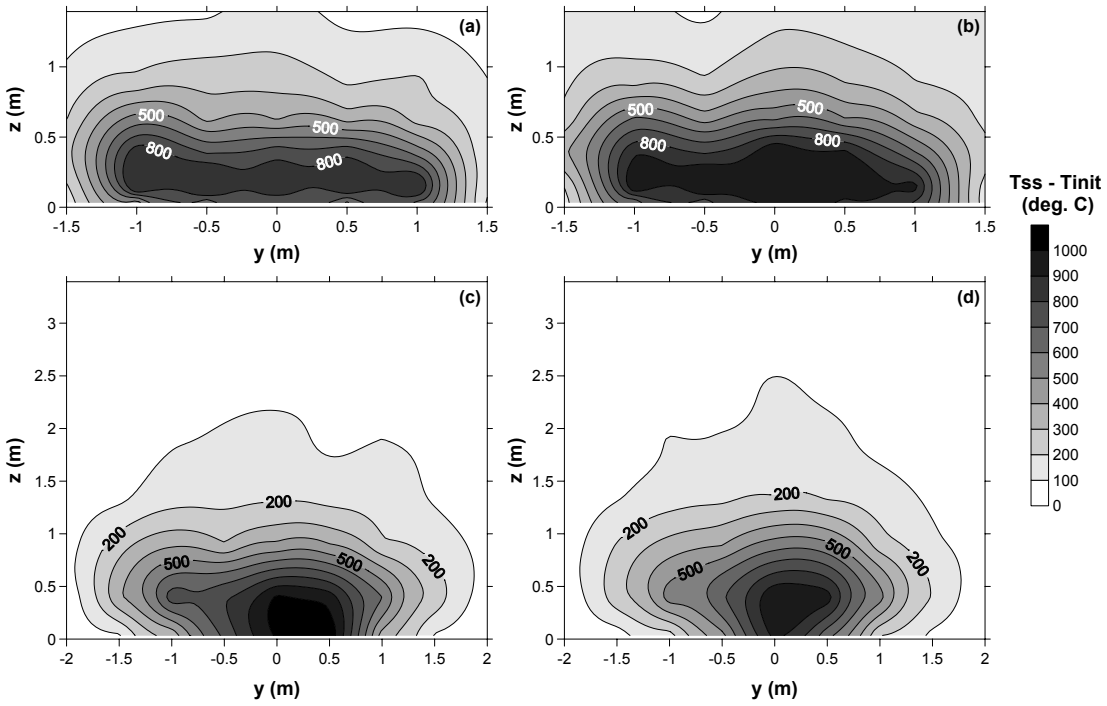

Figure 4.28: Contour plots of increase in temperature under 7 m/s wind, (a) x=1.5 m, (b) x=2 m, (c) x=3 m, (d) x=4 m

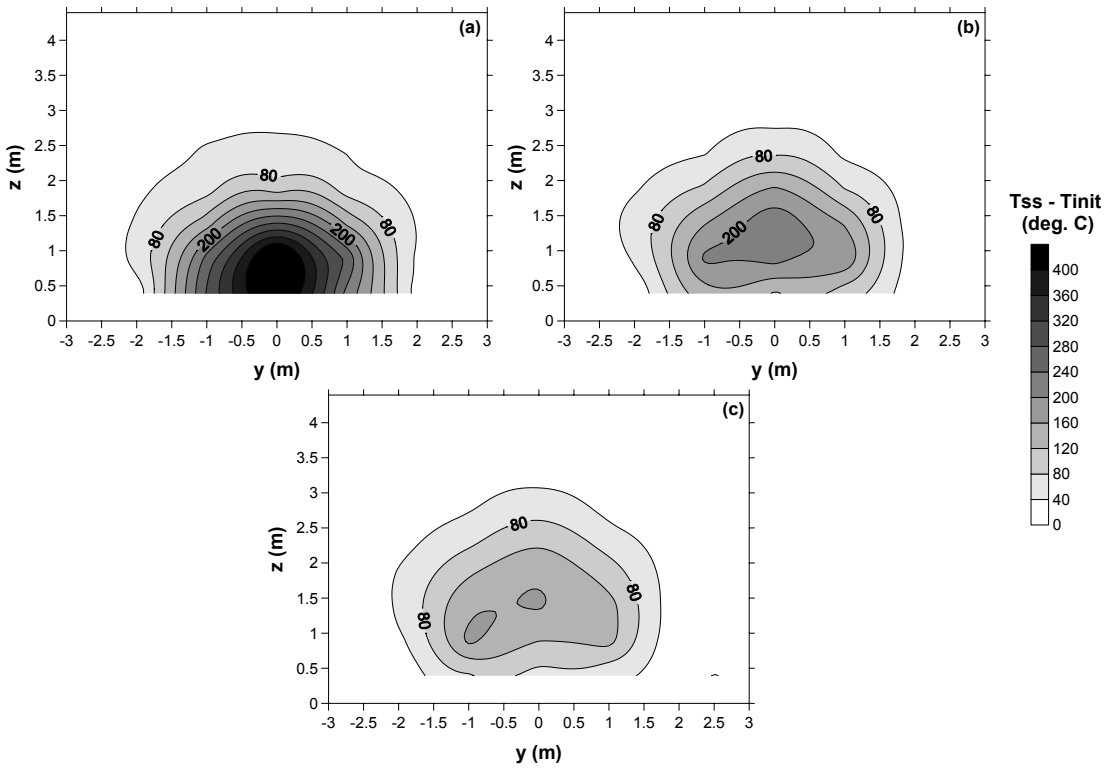

Figure 4.29: Contour plots of increase in temperature under 7 m/s wind, (a) x=6 m, (b) x=8 m, (c) x=9.2 m

Figure 4.30: Typical video frame showing profile view of fire in 10 m/s wind

Figure 4.31: Typical 60-frame time-averaged image showing profile view of fire in 10 m/s wind

images look similar to those for the 7 m/s wind speed (Figures 4.24 and 4.25), with the fire tilted significantly and lying flat along the ground. The leading edge of the luminous flame envelope above the fuel pan was tilted by an angle of 82° ± 2°, while downwind of the pan, the flame was approximately horizontal. Flame drag appeared to extend beyond 4 m downwind of the fuel pan centre because the bases of the centremost thermocouple chains at x=3 m and 4 m could not be seen through the fire. In the time-averaged image (Figure 4.31), the upper boundary of the luminous flame envelope was very well-defined up to x=3 m, indicating little fluctuation in the overall shape of the flame envelope in the upwind portion of the fire. Although smoke was visible downwind of x=3 m, comparison of Figures 4.25 and 4.31 indicated that there was less smoke obscuration of the luminous flame in the 10 m/s wind than in the 7 m/s wind. This likely resulted from greater removal of smoke from the edge regions of the fire under the higher wind speed.

Observations from the plot of temperature contours along the centreline plane y=0 m (Figure 4.32) were consistent with the above images. In this plot, the plume was seen to lie flat along the ground over the entire length of the test section. Based on the 900°C contour with an uncertainty of ±50°C, flame drag appeared to extend until x=4.7±0.4 m. Between x=2.5 m and 6 m, the contours from 300°C to 600°C were approximately horizontal. Downwind of x=6 m, the contours started to slope down towards the floor, indicating that heat inside the plume was being dissipated. Based on this observation, the flame tip was estimated to be located at x=6 m and

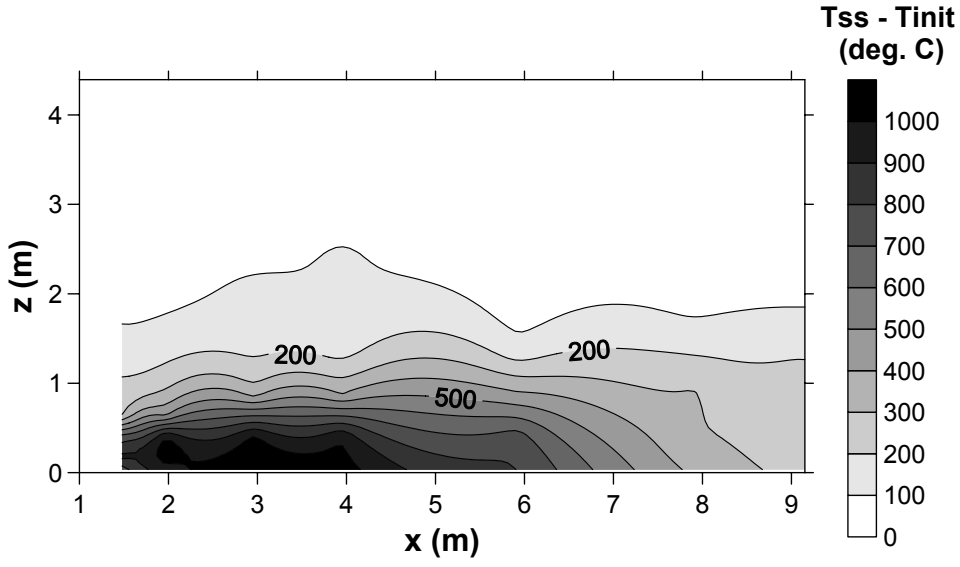

Figure 4.32: Contour plot of increase in temperature under 10 m/s wind, y=0 m

z=0.7 m, the height of the 550°C contour. Although the shape of the temperature contours downwind of x=4 m did not lend well to discernment of a plume centreline, thus preventing the flame tip location from being determined via the intersection of the plume centreline and the 550°C contour as at the lower wind speeds, the tilt angles estimated using the conventional definitions of flame tilt and a flame tip location of (x,z)=(6 m, 0.7 m) were comparable to those estimated from the video images. The tilt angle based on a line drawn from the flame tip to the flame base centre, located at (x,z)=(1.85 m, 0.1 m), was 82°, while the tilt angle based on a line drawn from the flame tip to the fuel pan centre was 84°. The corresponding flame lengths were 4.2 m and 6.0 m, respectively. The ±0.4 m uncertainty in the flame base extent and ±0.2 m uncertainty in the flame tip location combined to give uncertainties of ±3° for the tilt angle and ±0.3 m for the flame length.

Although the tilt angle of the downwind plume could not be determined directly from Figure 4.32 due to difficulties in identifying a plume centreline, it could be estimated from the cross-sectional temperature contour plots shown in Figures 4.33 and 4.34.[9] The centre of the plume core appeared to be located at a height of 0.2 m in all measurement planes from x=1.5 m to 4 m (Figure 4.33). At x=6 m and 8 m (Figure 4.34), the plume centre was approximately 0.5 m high, while at x=9.2 m, it was approximately 0.9 m high. Based on the heights from x=4 m to 9.2 m, the tilt angle of the plume was estimated to be 84°, with an uncertainty of ±6° due to a ±0.25 m uncertainty in the height of the plume centre in each cross-sectional plane. The 84° angle agrees well with the 82° angle determined from the video images of the fire.

The plots in Figures 4.33 and 4.34 were similar to the corresponding plots for the 7 m/s wind condition. There was no clear evidence of counter-rotating vortices at the 10 m/s wind speed, although such vortices would have likely started to develop downstream of the final measurement position (x=9.2 m). Also, the 10 m/s results followed the previously identified trends of increasing plume tilt, increasing flame drag and steeper temperature gradients with increasing wind speed.

[9] As in Figure 4.28, the 900°C and 1000°C contours are not shown in Figures 4.33a and 4.33b, respectively, because of insufficient spatial resolution in the measurements taken in the central region of the plume core, preventing a reasonable representation of the corresponding isotherms from being obtained.

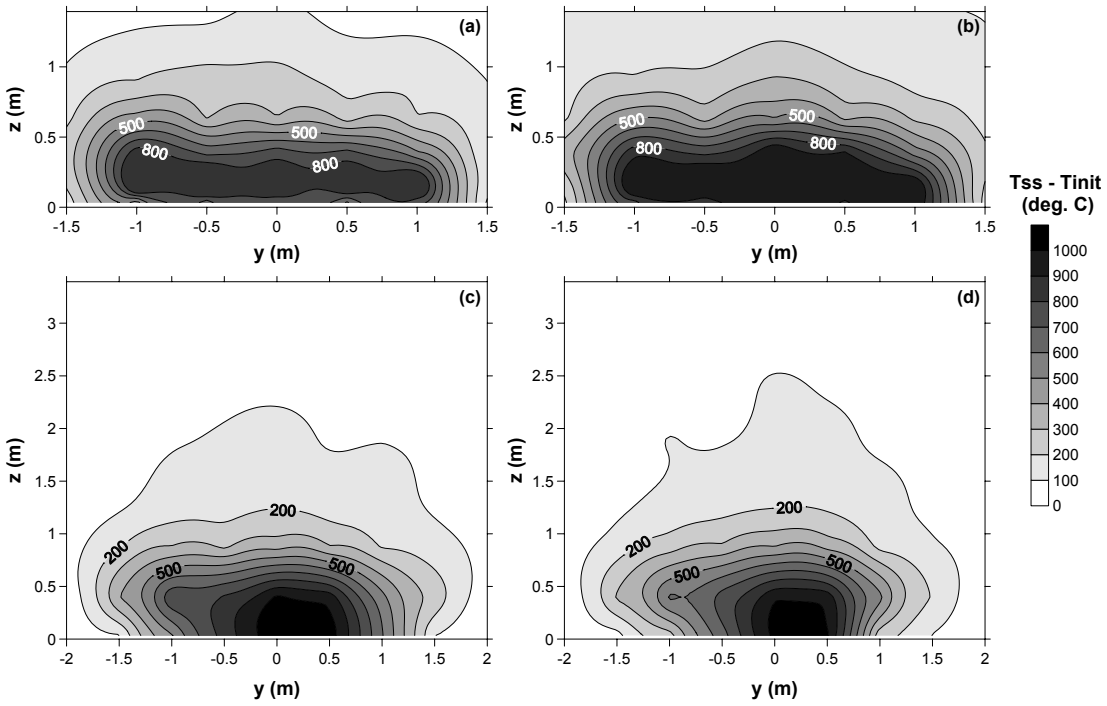

Figure 4.33: Contour plots of increase in temperature under 10 m/s wind, (a) x=1.5 m, (b) x=2 m, (c) x=3 m, (d) x=4 m

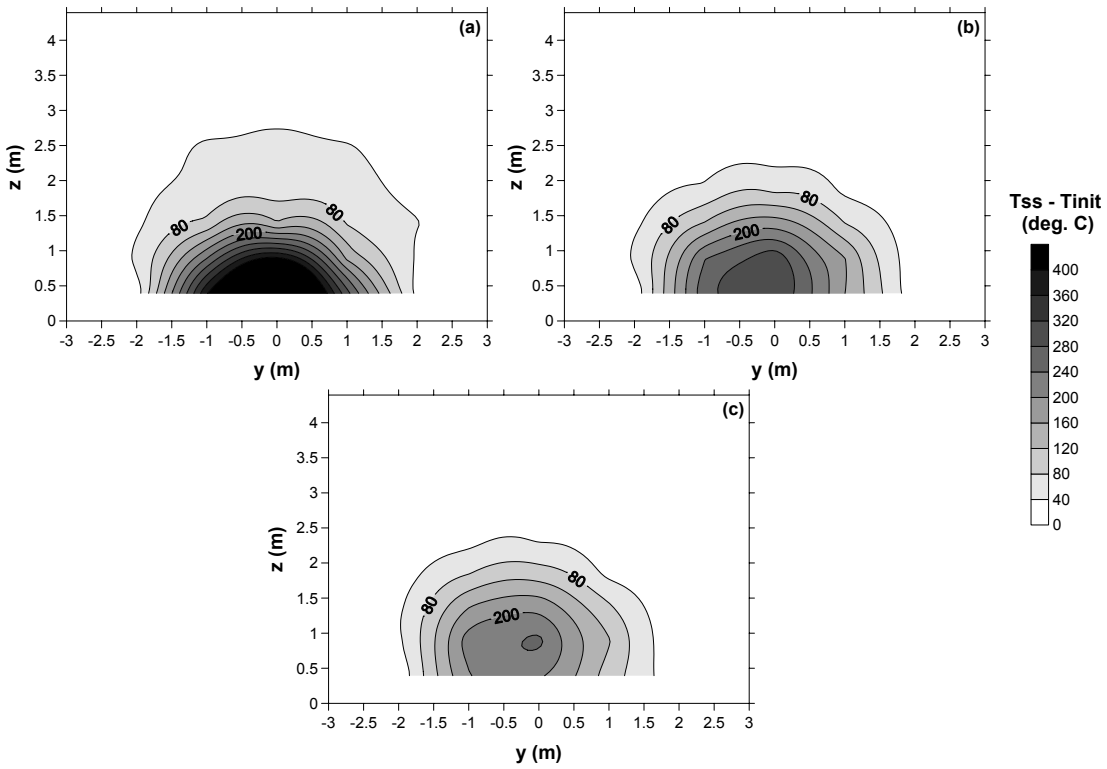

Figure 4.34: Contour plots of increase in temperature under 10 m/s wind, (a) x=6 m, (b) x=8 m, (c) x=9.2 m

Table 4.8: Comparison of Measured Values of D' and Values Predicted from Semi-Empirical Correlations for 2 m Diameter Jet A Fire

Wind Speed	3 m/s	5 m/s	7 m/s	10 m/s
Measured	3.9 m	4.4 m	5.2 m	5.7 m
Equation 2.21	3.1 m	3.2 m	3.4 m	3.5 m
Equation 2.22	2.8 m	3.1 m	3.2 m	3.4 m
Equation 2.23	4.4 m	4.7 m	4.9 m	5.2 m
Equation 2.24	5.2 m	5.6 m	5.9 m	6.2 m

4.4.5 Effect of Wind Speed on Flame Drag

In order to compare the shape of the fire at all four wind speeds, it is useful to focus on the three key descriptors of flame geometry (Section 2.2): flame drag (as indicated by D'), flame tilt angle (θ) and flame length (L). The effects of wind speed on these three parameters are now discussed in detail.

Estimated values of D' (referenced to the leading edge of the fuel pan, as shown in Figure 2.4b) are summarized in Table 4.8 for the four wind speeds considered in this study. The values were determined based on the 900°C temperature contour in the y=0 m plots and had uncertainties between ±0.2 m and ±0.4 m. As expected, the amount of flame drag increased as the fire tilted further over with increasing wind speed.

The measured values of D' were compared to values predicted for a 2 m diameter Jet A fire using the semi-empirical correlations described in Section 2.2.3. In these equations, the density of Jet A fuel vapours, a required input, was taken from Table 4.1.

Equation 2.20 was found to greatly overpredict measured values of flame drag by 111% to 139%. Although no derivation was actually provided, this particular equation was proposed based on the notion that flame drag was caused by fuel vapours being denser than the surrounding air and remaining near the ground until they were heated sufficiently to rise due to buoyancy [80]. Based on the temperature contour plots of the 2 m diameter fire presented in the previous sections, flame drag appeared to have been affected significantly by the horizontal momentum of the wind overcoming the buoyancy forces in the fire and pushing the fire close to the ground, particularly at the higher wind speeds. Although the physical basis used to explain Equation 2.20 may apply at the lower wind speeds considered in the development of that correlation (up to 2.1 m/s), it would be unlikely to

be a dominant factor under the higher wind conditions considered in the present experiments. Additionally, Equation 2.20 was based on measurements of flame drag in fires of 0.1 m to 0.6 m diameter, which belong to the transitional burning regime (Figure 2.2), whereas the 2 m diameter fire of the present study belongs to the turbulent burning regime. Due to the discrepancies in the ranges of fire size and wind speed between the experiments associated with Equation 2.20 and the present study, use of this correlation led to significant overprediction of flame drag in the present fires and was thus not considered further.

Table 4.8 and Figure 4.35 compare the measured values of D' to the values predicted by the remaining correlations discussed in Section 2.2.3. As seen in the Figure, values of flame drag predicted by Equations 2.21 and 2.22 were 22% to 41% lower than those measured in the present experiments. This could potentially be attributed to the much greater vapour density of Jet A compared to LNG, the fuel on which these equations were based (ρ_g/ρ_a is approximately 1.6 for LNG [99] and approximately 5.7 for Jet A (Table 4.1)). Since the fuel vapour-to-air density ratio was included in the constant coefficients of both equations, this change in fuel vapour density could not be directly accounted for in the predictions. The poor

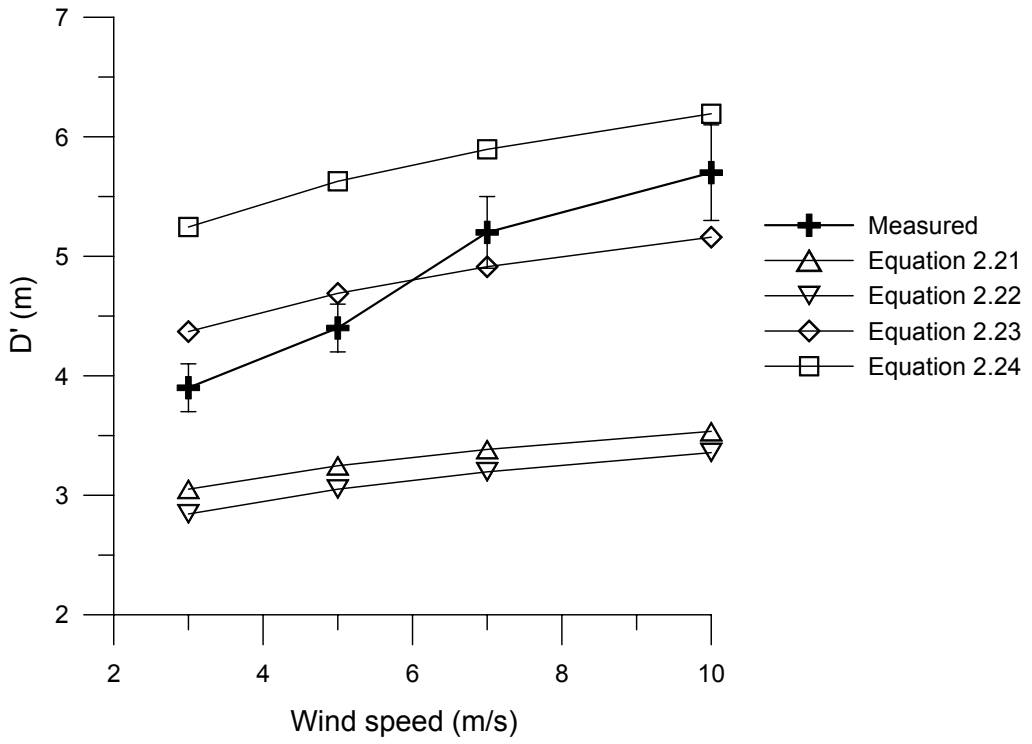

Figure 4.35: Comparison of predicted and measured values of D' for 2 m diameter Jet A fire

agreement between the measured values and those predicted by Equations 2.21 and 2.22 contradicted results reported by Lautkaski [99], who did not find fuel vapour density in the relatively small range of $1.6 \leq \rho_g/\rho_a \leq 2.7$ to noticeably affect flame drag and recommended Equation 2.22 as the most appropriate correlation to use for large hydrocarbon pool fires (Section 2.2.3). It should be noted, however, that Lautkaski [99] based his conclusions on measurements from three large fires (20 m to 52 m diameter), two of which were very sooty.

Figure 4.35 shows that the measured values of D' were in better agreement with the values predicted by Equation 2.23 (within 12% at all wind speeds) and Equation 2.24 (within 13% at the two higher wind speeds, but up to 34% at the two lower wind speeds). Given that these two equations were proposed as generalized correlations for hydrocarbon fires, the agreement suggests that the form of the correlations is appropriate; however, no physical explanation was provided to justify the generality of Equation 2.23 [9]. In addition, Equation 2.24 overpredicted the flame drag at all wind speeds, particularly at 3 m/s and 5 m/s. As mentioned in Section 2.2.3, this equation is the same as Equation 2.23, but multiplied by a factor of 1.2 so that it would match Equation 2.22 for the fuel of LNG [99]. The poor agreement of the values predicted by Equation 2.24 with those measured in the present study suggests that this factor, 1.2, is too high. A potential reason for this is that the value used to estimate the vapour density of LNG in the development of Equation 2.24 was taken from a study different from the one used to develop Equation 2.22 [99], so differences in LNG composition and thus vapour density may have affected the accuracy of the factor.

For each consecutive increase in wind speed considered in the present experiments, the measured values of flame drag increased by an amount greater than that predicted by any of the correlations (i.e. the measured values followed a steeper slope). This suggests that the dependence of flame drag on wind speed may have been greater than that indicated by the correlations or that the correlations could not fully account for the physics in the present situation. Part of the discrepancy may have been caused by differences in the method of estimating flame drag, since the measured values listed in Table 4.8 were determined using the 900°C temperature contour in the y=0 m plots (and supported by the video images), while in all previous studies, flame drag was determined solely from visual images of the fire. Smoke blockage effects can make it difficult to estimate flame drag accurately using visual methods, particularly in large, sooty fires [99]. Also, the fires in the present study were surrounded by a floor that contained a 0.17 m step decrease in elevation

at a distance of 0.35 m downwind of the leeward edge of the fuel pan (Figure 4.4), but the same configuration was not used in any of the other studies considered. This difference in layout of the surrounding floor may have influenced the extent of flame drag, although further experimentation would be needed to verify such an effect.

The above results, along with the temperature contour plots shown in the previous sections, appear to be consistent with the notion suggested by Lautkaski [99] that the extent of flame drag would be determined by a balance between the wind-driven plume flow and the flow of air being entrained opposite to the wind into the leeward side of the fire. The horizontal momentum of the wind is clearly dominant on the upwind side of the fire near the fuel pan, while buoyancy effects (which induce air entrainment) are dominant further downwind, particularly in low to moderate wind conditions. The region in which both of these effects become significant would be expected to be related to the extent of flame drag. Although the relationship between the momentum of the wind and the buoyancy forces in the fire is primarily captured by use of the Froude number in the correlations, the difference in density between the flame gases and the surrounding air has not been typically included because it is assumed constant (Section 2.2.1). The importance of this assumption should therefore be further investigated. In addition, as already mentioned, the ratio of fuel vapour density to air density appears to affect flame drag, in contrast to the findings by Lautkaski [99], and should be further examined. Clearly, the details of the physics affecting flame drag are not yet well understood and additional research in this area is recommended to improve the flame drag correlations.

In general, differences in fuel vapour density, fire size, wind speed, floor configuration and measurement method contribute to discrepancies between predicted and measured values of flame drag in the present experiments. The lack of concrete physical justification for two of the correlations also suggests that the existing correlations may not capture all of the pertinent physics affecting flame drag. Yet, flame drag can greatly affect measurements of flame tilt and flame length, as shown in the following sections.

4.4.6 Effect of Wind Speed on Flame Tilt

The tilt angles identified in Sections 4.4.1 to 4.4.4 are summarized in Table 4.9. The first two rows describe the tilt of the fire near the fuel pan, based on the video

Table 4.9: Summary of Measured Tilt Angles

Wind Speed	3 m/s	5 m/s	7 m/s	10 m/s
Near Fuel Pan:				
Video images (immediately above pan)	75°	78°	81°	82°
y = 0 plot (immediately downwind of pan)	75°	76°	85°	90°
Downwind of x = 4 m:				
Cross-sectional plots	50°	65°	78°	84°
y = 0 plot	49°	65°	80°	–
Conventional Definitions:				
To flame base centre	68°	75°	80°	82°
To fuel pan centre	72°	79°	83°	84°

images (which show the luminous flame above the fuel pan) and the temperature contour plot along the centreline plane y=0 m (which shows the plume immediately downwind of the fuel pan). The next two rows apply to the region of the plume downwind of x=4 m and describe the tilt of the plume centreline estimated from either the cross-sectional temperature contour plots or the temperature contour plot along y=0 m. The final two rows are based on the conventional definitions of flame tilt and correspond to the tilt of a line drawn from the flame tip to either the centre of the flame base or the centre of the fuel pan. The uncertainties in the tilt angles were estimated to be between ±1° and ±4° for the 3 m/s and 5 m/s wind speeds, and between ±2° and ±6° for the 7 m/s and 10 m/s wind speeds.

A trend of increasing plume tilt with increasing wind speed was observed among all methods of estimating tilt angle. The tilt angle in the region downwind of x=4 m showed a much greater increase with wind speed than that in the region near the fuel pan, due to differences in where the plume started to lift off the ground. At the 3 m/s and 5 m/s wind speeds, buoyancy effects greatly influenced the downwind development of the plume, as shown by an observable decrease in tilt angle as the plume curved upwards and lifted off the ground well inside the test section (e.g. Figure 4.16). In contrast, at the 7 m/s and 10 m/s wind speeds, the momentum of the wind remained dominant relative to the buoyancy forces over a much greater length, causing the plume to remain attached to the ground along most of the test section. This resulted in an approximately constant, large angle of tilt along the plume throughout the test section. (In this case, a decrease in tilt angle would be expected to occur further downwind, as the plume eventually lifted off the ground.) As a result, the effect of wind speed on tilt angle was much more pronounced for measurements taken in the region of the plume downwind of x=4 m than in the

Table 4.10: Tilt Angles Predicted from Semi-Empirical Correlations for 2 m Diameter Jet A Fire

Wind Speed	3 m/s	5 m/s	7 m/s	10 m/s
Equation 2.2	47°	61°	68°	73°
Equation 2.3	67°	72°	75°	77°
Equation 2.4	55°	61°	65°	69°
Equation 2.5	51°	56°	60°	62°
Equation 2.6	56°	62°	66°	69°
Equation 2.7	50°	55°	58°	61°
Equation 2.8	65°	71°	74°	76°
Equation 2.9	47°	53°	57°	59°
Equation 2.10	62°	72°	76°	80°
Equation 2.11	66°	78°	82°	85°

region near the fuel pan, where the plume was attached to the ground in all four tests.

The values estimated using the conventional definitions of flame tilt (the last two rows in Table 4.9) were up to 9% lower than the tilt angles measured near the fuel pan (the first two rows in Table 4.9). This was most pronounced at the lowest wind speed, when plume curvature was the most significant. These results were consistent with the notion that under significant plume curvature, the tip of the flame was located at a higher elevation than if no curvature existed, causing a line drawn from the flame tip to the centre of either the flame base or the fuel pan to lie at a smaller angle of tilt. Conversely, the conventionally-defined estimates of flame tilt overpredicted (by up to 47%) the tilt angles measured downwind of x=4 m (the middle two rows in Table 4.9), which describe, at the two lowest wind speeds, the tilt of the plume after it lifted off the ground. Thus, changes in tilt angle along the length of the plume due to the increasing effect of buoyancy hindered description of the plume tilt by a single angle.

The tilt angles summarized in Table 4.9 could be compared to those predicted for a 2 m diameter Jet A fire using the semi-empirical correlations described in Section 2.2.1. The predicted angles are shown in Table 4.10, with most of them plotted in Figure 4.36 for visual comparison to the results in Table 4.9. In the correlations, the Reynolds number at each wind speed was calculated using air properties corresponding to the ambient temperatures listed in Table 4.3. Fuel properties were obtained from Table 4.1, with the liquid fuel density assumed to be 800 kg/m^3. The fuel mass burning rates used to calculate $U_{c,a}$ and $U_{c,b}$ were taken

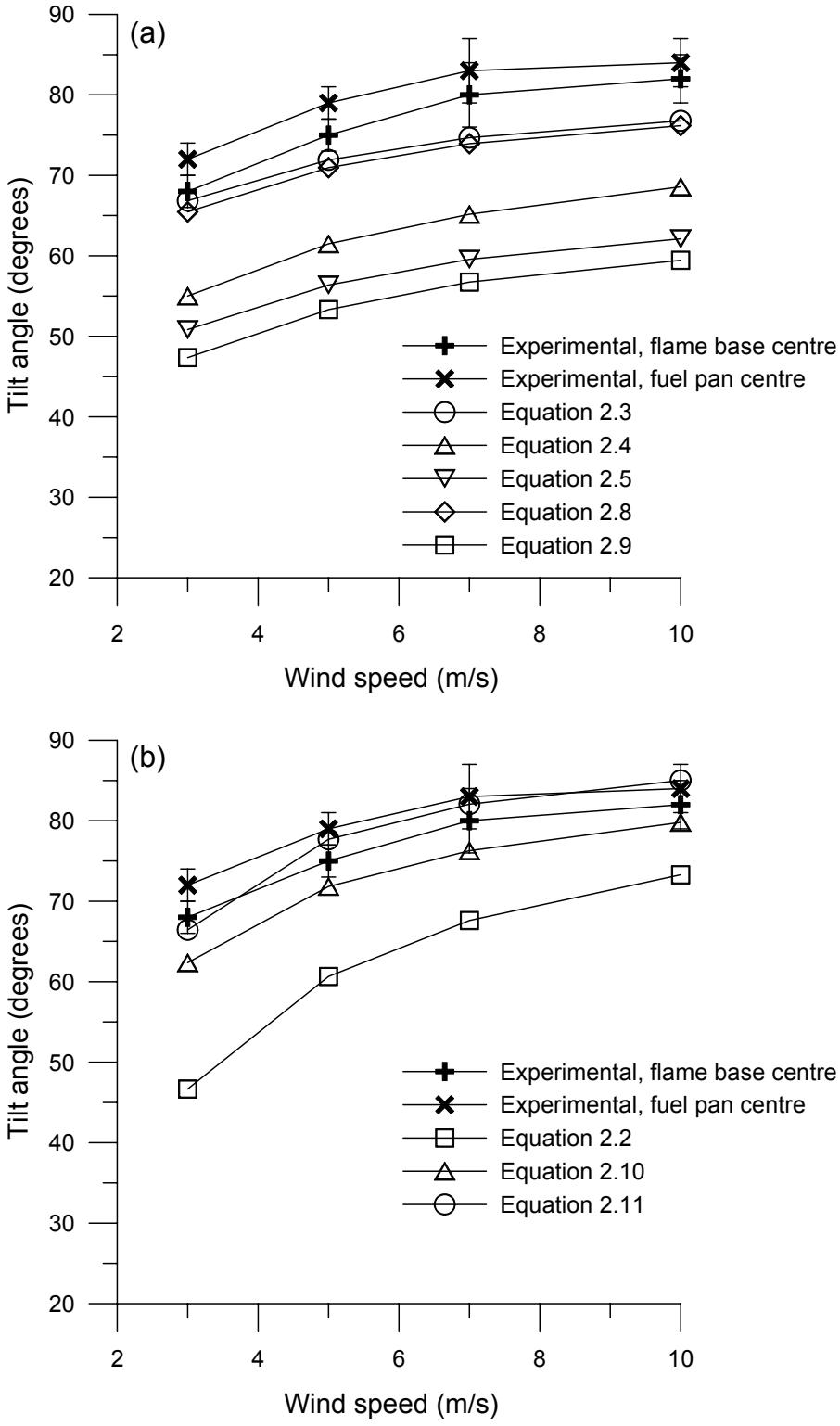

Figure 4.36: Comparison of predicted tilt angles to angles measured using conventional definitions; plots split into parts (a) and (b) for clarity

Table 4.11: Fuel Mass Burning Rates, Based on Load Cell Measurements of Best [21]

Wind Speed	3 m/s	5 m/s	7 m/s	10 m/s
Fuel regression rate (mm/min)	3.8	4.2	4.3	5.2
Mass burning rate (kg/m^{2}s)	0.050	0.055	0.057	0.070

from Best [21] and are listed in Table 4.11. For Equations 2.10 and 2.11, the flame temperature was assumed to be a representative value of 1000 K; variation of this value by ±200 K resulted in a difference of no more than ±2° in the predicted tilt angles.

The equations in Table 4.10 were all based on the conventional definitions of flame tilt (Table 2.3), so the predicted values were initially compared to the angles in Table 4.9 determined using the same methods. Figure 4.36a shows the predicted angles from Equations 2.3, 2.4, 2.5, 2.8 and 2.9 alongside the values in Table 4.9 estimated using the conventional definitions. (Since the angles predicted by Equations 2.6 and 2.7 were very close to those from Equations 2.4 and 2.5, respectively, they were not included in the plot to improve visual clarity. Also, error bars are shown to provide a sense of the uncertainty in the measured values taken from Table 4.9.) As evident in the plot, the measured angles were consistently higher than the predicted angles while following a trend similar in shape to those shown by the predicted values. A possible cause of the higher observed tilt angles was the 0.17 m step decrease in the elevation of the brick floor at the edges of the raised floor surround (Figure 4.4). Since flame attachment was observed to occur not only along the raised surround but also along the floor immediately downwind of the surround (e.g. Figures 4.14 and 4.30), the fire could have been tilted by a larger angle than if the step decrease in floor height had not existed and the entire floor been at the same level as the raised surround. This notion was supported by the fact that Equations 2.3 and 2.8 predicted higher values of tilt angle than Equations 2.4 and 2.5 in Figure 4.36a. In the wooden crib and LNG experiments for which Equations 2.3 and 2.8 were respectively developed, the ground was located along the same plane as the base of the crib or fuel dike (Table 2.3), so flame could descend below the top of the crib or fuel dike once it had blown past the fuel source. However, in the LNG experiments corresponding to Equations 2.4 and 2.5, the fuel pit was recessed into the ground, so flame could exist only above the ground plane on the leeward side of the fuel pool. Consequently, the tilt angle may have been smaller

in the latter experiments because of the ground plane constraining the leeward side of the flame. In addition, the flame tilt data used to develop Equations 2.3 and 2.8 were measured based on the centre of the fuel surface, while those corresponding to Equations 2.4 and 2.5 were measured based on the centre of the flame base (Table 2.3). As indicated in Section 2.2, this would have further contributed to Equations 2.3 and 2.8 producing higher values of tilt angle than Equations 2.4 and 2.5.

For Equation 2.9, which was also included in Figure 4.36a, the predicted angles were lower than those of Equations 2.4 and 2.5, even though the ground plane was level with the base of the fuel pan (Table 2.3). The inconsistency of these predicted values with the trends noted in the above discussion was likely due to the fact that Equation 2.9 was developed for very low wind speeds (Table 2.2), using flame tilt data that were measured with the smoke-obscured regions of the fire neglected and the flame tip assumed to be located at the highest point in the remaining visible flame zone. Both of these factors were biased towards lower values of tilt angle and thus may have caused the tilt angle to be underestimated at higher wind speeds. This shows how discrepancies in the experimental boundary conditions and the method of measuring tilt angle can affect the level of agreement between predicted and measured values of tilt angle.

Of the equations plotted in Figure 4.36a, all except Equation 2.4 were based on the form of correlation proposed by Thomas [81]. This could account for the similarity in trend among the predicted values. Equation 2.4 was a correlation of the type proposed by Welker and Sliepcevich [80] and developed at the same time as Equation 2.5 [82]. These two equations were fit to the same data and would be expected to provide reasonably similar predictions. Any offset between the values indicates that there were differences in the physics modelled by the different types of correlation. Nevertheless, the similarity in shape of the curves plotted in Figure 4.36a suggests that the Thomas-type correlation is suitable for predicting the increase in conventionally-defined angles of flame tilt with increasing wind speed.

Figure 4.36b compares values of flame tilt predicted by Equations 2.2, 2.10 and 2.11 to the angles in Table 4.9 estimated using the conventional definitions of flame tilt. The values predicted by Equation 2.11 were within 8% of the measured angles, while those predicted by Equation 2.10 were up to 13% lower. Overall, the trends followed by these two equations were relatively close to those followed by the measured angles and by the equations plotted in Figure 4.36a. However, the increase in tilt angle predicted by Equations 2.10 and 2.11 between each pair of

consecutive wind speeds (e.g. 3 m/s and 5 m/s) was typically higher. Even greater increases in tilt angle were predicted by Equation 2.2, which also yielded values up to 35% lower than the measured angles, particularly at the 3 m/s wind speed.

Although reasons for the above observations are not immediately clear, insight into the differences may be gained by comparing the values predicted by Equation 2.2 to the tilt angles measured in the plume downwind of x=4 m (Table 4.9). As shown in Figure 4.37, the predicted values were within 7% of the measured values at the 3 m/s and 5 m/s wind speeds, and up to 15% lower at the 7 m/s and 10 m/s wind speeds. Table 2.2 shows that Equation 2.2 was based on flame tilt data taken in 0.1 m to 0.6 m diameter fires in wind speeds of up to 2.1 m/s; the reported range of Froude numbers was 0.02 to 0.9 [80]. Given that the range of Froude numbers considered in the present experiments was 0.5 to 5.1, the predicted values corresponding to the 7 m/s and 10 m/s wind speeds were unlikely to be valid, hence only the values at the two lowest wind speeds are considered. The close agreement between the predicted angles and those measured in the plume downwind of x=4 m suggests a lack of significant flame drag and plume curvature in the smaller fires used

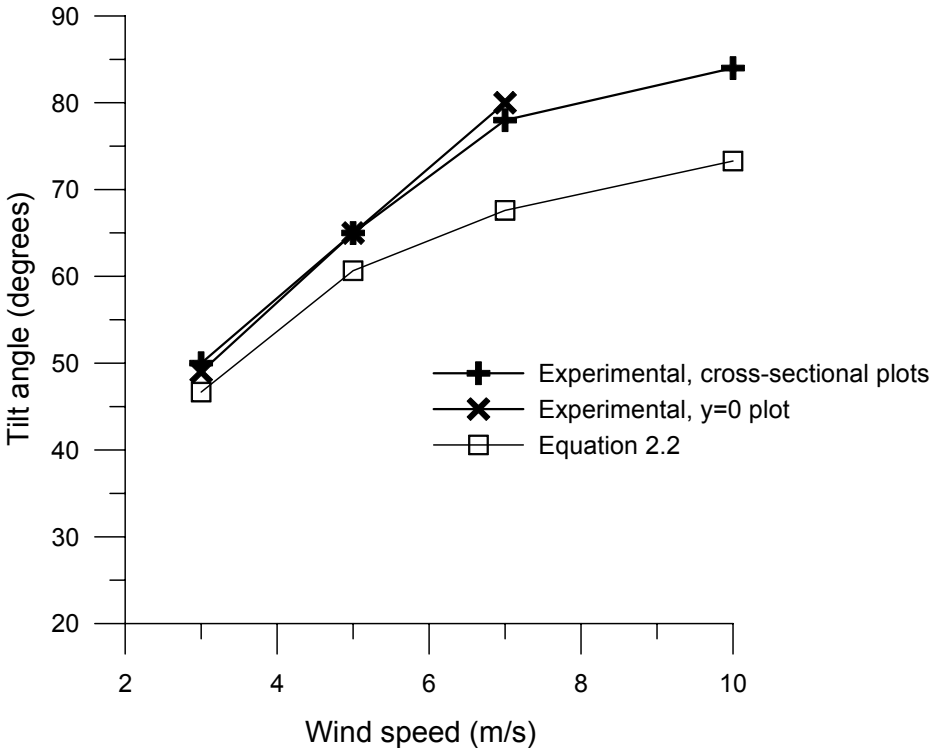

Figure 4.37: Comparison of tilt angles predicted using Equation 2.2 to angles measured in plume downwind of x=4 m

to develop the correlation. Although flame drag was mentioned in the experiment related to Equation 2.2, it did not appear to be large enough to affect the overall tilt of the fire, as indicated by photographs of the fires [80]. As a result, angles of tilt estimated using the conventional definitions would have been reasonably similar to the actual tilt of the downwind plume.

The above notion is supported by Figure 4.38, which contains a photograph of a 0.3 m diameter acetone fire previously investigated by the author [8] ($Fr = 0.2$). In Figure 4.38, the flame drag ratio D'/D is approximately 1.4, indicating that flame drag extended less than half a pan diameter downwind of the leeward edge of the fuel pan. This is smaller than the values of 2.0 and 2.2 measured at wind speeds of 3 m/s and 5 m/s, respectively, in the 2 m diameter fire of the present study (Table 4.8). Curvature in the flame is clearly evident in the photograph, with the tilt angle in the region immediately above the pan greater than the tilt angle further downwind, where buoyancy effects became more pronounced and the fire plume lifted off the ground. While temperature profiles taken downwind of the fuel pan indicated a tilt angle in the downwind plume of approximately 44° [8], the angle estimated by drawing a line from the tip of the visible flame to the centre

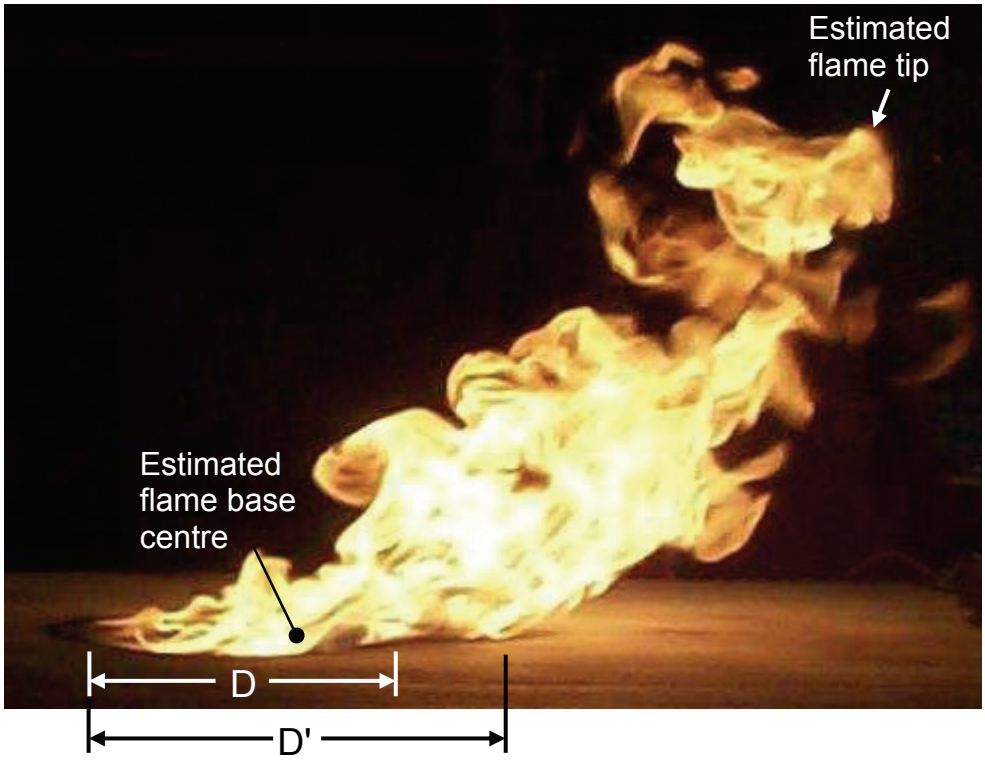

Figure 4.38: 0.3 m diameter acetone fire in a 0.8 m/s crosswind

of the flame base (shown in Figure 4.38) was 49°. Thus, although the presence of flame drag caused the conventionally-defined tilt angle to be larger, the two angles estimated for the 0.3 m diameter fire were still reasonably similar. In comparison, flame drag in the 2 m diameter fire was greater, with $D'/D = 2.0$ in the 3 m/s wind condition (Figure 4.14). Due to this longer region of flame drag, caused by increased inertial effects of the wind ($Fr = 0.5$), the tilt angles estimated for the larger fire using the conventional definitions were higher than the actual tilt angles of the downwind plume. This highlights a major drawback in using a single angle to characterize plume tilt.

Based on the above discussion, differences between measured and predicted values of tilt angle could be attributed to differences in the method of measuring tilt angle, the layout of the ground plane and the amount of flame drag and plume curvature among different experiments. (As mentioned earlier, flame drag depends partly on fire size, wind speed and fuel vapour density.) The general trends in tilt angle predicted using the Thomas-type correlations (Equations 2.3, 2.5, 2.7, 2.8 and 2.9) agreed reasonably well with those shown by the angles measured using the conventional definitions of flame tilt, although values predicted by the different correlations were offset from each other. In contrast, the equation developed by Welker and Sliepcevich [80] (Equation 2.2) predicted more closely the angles measured in the plume downwind of x=4 m, after the fire lifted off the ground, because it was based on data obtained from fires exhibiting little flame drag and plume curvature. The presence of significant plume curvature was shown to greatly hinder description of plume tilt by a single angle. Flame length was also seen to be greatly affected by high levels of flame drag, as discussed in the next section.

4.4.7 Effect of Wind Speed on Flame Length

Table 4.12 summarizes the values of flame length determined in Sections 4.4.1 to 4.4.4. The flame lengths were measured using the conventional definitions shown in Figure 2.4 and had uncertainties between ±0.1 m and ±0.3 m.

As the wind speed increased from 3 m/s to 7 m/s, the flame length measured to the centre of the flame base decreased while the flame length measured to the centre of the fuel pan increased. This apparent conflict could be explained by examining the change in location of the flame base centre relative to the fuel pan centre. Since the location of the fuel pan was fixed, the increasing trend in flame length measured

Table 4.12: Summary of Measured Flame Lengths

Wind Speed	3 m/s	5 m/s	7 m/s	10 m/s
To flame base centre	3.7 m	3.5 m	3.4 m	4.2 m
To fuel pan centre	4.6 m	4.7 m	4.9 m	6.0 m

using the fuel pan centre indicated that the flame tip moved further downwind from the pan with higher wind speed. At the same time, Table 4.8 (in Section 4.4.5) shows that the total length of the flame base, D', increased, so the centre of the flame base also moved downwind from the fuel pan. For a given increase in wind speed, the flame drag increased by a greater amount than the pan-based flame length, so the flame base centre moved downwind at a quicker rate than the flame tip. As a result, the flame length estimates based on the flame base centre initially decreased with increasing wind speed, a trend opposite to the estimates based on the fuel pan centre.

Considering only the results relative to the fuel pan centre (a fixed point), the trend of increasing flame length with increasing wind speed from 3 m/s to 7 m/s indicated a decrease in overall air entrainment into the flame and consequently less efficient combustion. This was consistent with the observed increase in flame drag, which would be expected to inhibit entrainment into the leeward side of the plume. As the wind speed increased further, from 7 m/s to 10 m/s, the flame length was seen to increase significantly, by approximately 22%. This increase in flame length was evident even in the measurements made using the flame base centre (Table 4.12) and signified a large decrease in air entrainment, likely due to the extreme tilt of the fire. Given that the fire at this highest wind speed lay flat against the ground (Figure 4.32), the wind direction would have been almost parallel to the upwind side of the plume. Mixing of the air and plume gases would have been more difficult because the wind was no longer blowing into a rising flame. With the large amount of flame drag observed at the 10 m/s wind speed, air entrainment into the plume would have been greatly impeded (because air could only be entrained along the top and sides of the plume) and an increase in flame length with increasing wind speed could thus be expected.

To gain further insight into the measured trends, the semi-empirical correlations described in Section 2.2.2 were used to predict values of flame length for a 2 m diameter Jet A fire, as shown in Table 4.13. Here, Equations 2.18 and 2.19 were not considered because they were developed using data taken in very small fires

Table 4.13: Flame Lengths Predicted from Semi-Empirical Correlations for 2 m Diameter Jet A Fire

Wind Speed	3 m/s	5 m/s	7 m/s	10 m/s
Based on flame base centre:				
Equation 2.14	4.7 m	4.4 m	4.3 m	4.3 m
Equation 2.15	3.6 m	3.6 m	3.5 m	3.7 m
Based on fuel pool centre:				
Equation 2.12	2.7 m	2.6 m	2.4 m	2.7 m
Equation 2.13	3.7 m	3.6 m	3.4 m	3.6 m
Equation 2.16	3.3 m	3.2 m	3.1 m	3.1 m
Equation 2.17	5.4 m	5.5 m	5.6 m	5.5 m

(0.04 m to 0.11 m diameter, as listed in Table 2.4) lying in the laminar burning regime (Figure 2.2) and were not deemed appropriate for predicting the flame length of a 2 m diameter fire, which lies in the turbulent burning regime.

Among the remaining equations, the predicted flame lengths in Table 4.13 were compared to the measured flame lengths in either the first or second row of Table 4.12, depending on whether the corresponding correlation was associated with the flame base centre or the fuel pool centre (Table 2.4). Figure 4.39a shows the predicted and measured values of flame length determined using the flame base centre. For wind speeds between 3 m/s and 7 m/s, the values predicted by Equation 2.15 were within 5% of the measured data, while the values predicted by Equation 2.14 were 25%-28% higher than the measurements. Both equations indicated a decreasing trend in flame length, in agreement with the measured results. The values obtained from Equation 2.14 were expected to be higher than those from Equation 2.15 because the two equations were based on conical and cylindrical representations of the flame shape, respectively, and the length of each shape was adjusted so that its longitudinal cross-section would have the same area as the profile image of the fire (Section 2.2.1). Since a cylinder with a given area is shorter than a cone with the same area, Equation 2.15 would be expected to produce values smaller than those of Equation 2.14. The closer agreement of the measured flame lengths with the values predicted by Equation 2.15 at the 3 m/s to 7 m/s wind speeds suggests that a cylindrical representation of the flame geometry would be more appropriate for these fires.

For a further increase in wind speed to 10 m/s, Equation 2.14 predicted that the flame length would remain approximately the same, while Equation 2.15 predicted that the flame length would increase by 0.2 m. Although the latter equation

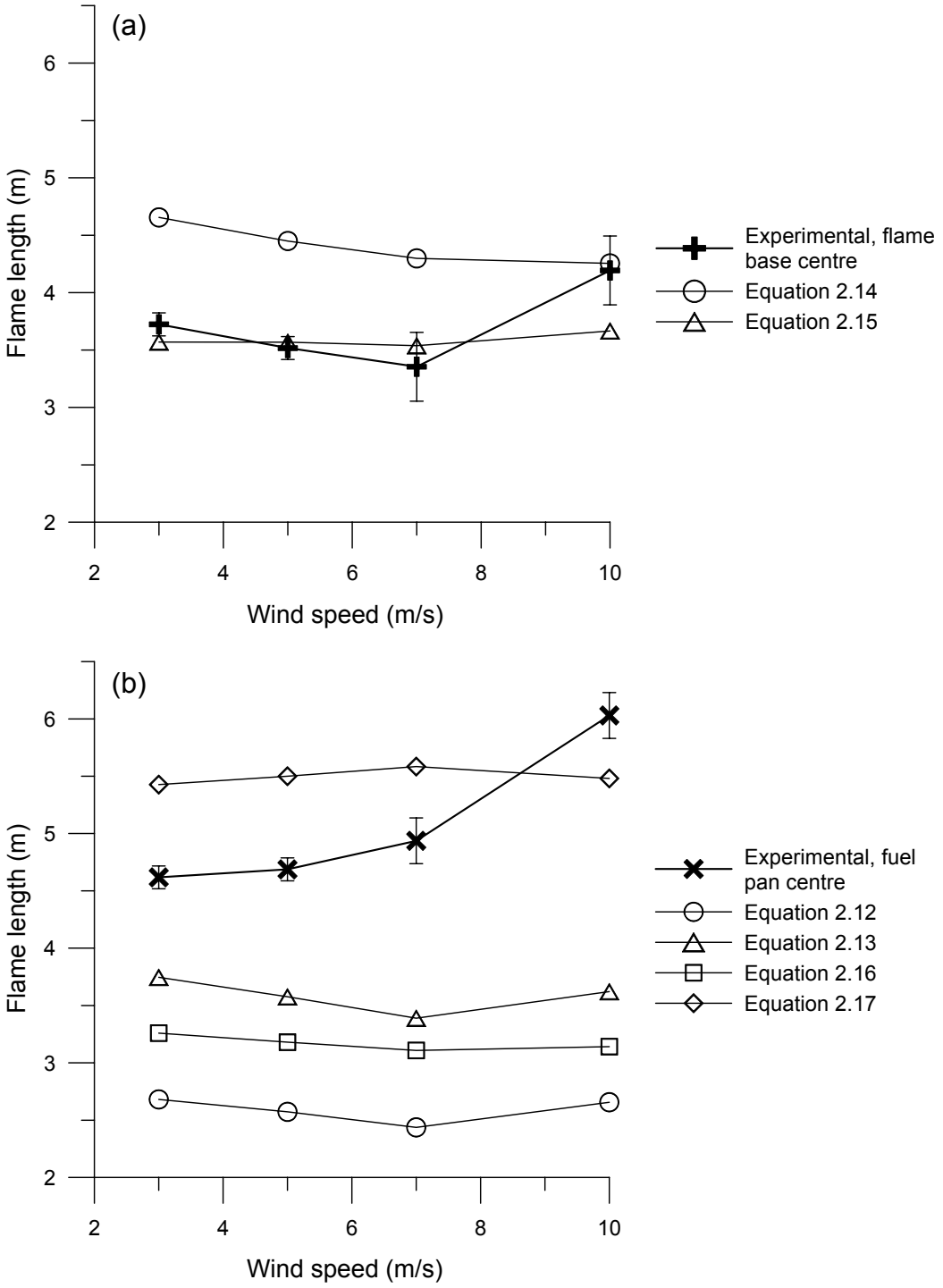

Figure 4.39: Comparison of predicted and measured flame lengths for 2 m diameter Jet A fire, (a) flame lengths based on flame base centre, (b) flame lengths based on fuel pool centre

appeared to capture the reversing trend seen in the measured values, the predicted increase was much smaller than that indicated by the measured data. The large increase observed in the measured flame lengths has not been previously reported in the literature, possibly due to the fact that very few studies have examined the geometry of fires in wind speeds of sufficient velocity to achieve extremely high values of tilt angle and flame drag. For instance, Table 2.2 shows that the study corresponding to Equation 2.3 (and also Equations 2.12 and 2.13) was the only one in which a tilt angle of 80° was measured. In light of this, the results reported in the present study show how the flame geometry changes as the wind speed is increased beyond that required to attain a tilt angle of 80°.

For flame lengths determined using the fuel pan centre, predicted values from Table 4.13 were compared to measured values from Table 4.12 in Figure 4.39b. At wind speeds between 3 m/s and 7 m/s, the measured flame lengths were within the range of predicted values; however, this range was relatively large, spanning differences of up to 3.2 m. Some of the variation among the predicted flame lengths could be explained by examining the assumptions and methods underlying the correlations. For instance, the values predicted by Equation 2.16 were expected to be low because the data on which the equation was based were measured with the smoke-obscured regions of the fire neglected and the flame tip located at the highest point in the visible flame zone (Table 2.4), resulting in underestimates of the true flame length. Also, as mentioned in Section 2.2.2, the values predicted by Equation 2.12 were expected to be less than those predicted by Equation 2.13. Since Equation 2.12 was developed for a rectangular source of fuel while Equation 2.13 was developed for a line source of fuel, higher levels of air entrainment expected in the rectangular fire would lead to lower flame lengths. Finally, all equations required input of a fuel mass burning rate which, as indicated in Section 2.1, is affected by much physics, the details of which are not yet fully understood, particularly in large fires in the crosswind situation [51]. Despite the wide range in the predicted values, the fact that the measured flame lengths were within this range indicated that the method used to determine flame length from the temperature contours in Sections 4.4.1 to 4.4.4, rather than from video images as was done previously in the literature, produced reasonable results.

Figure 4.39b shows that from 3 m/s to 7 m/s, the values predicted by Equation 2.17 supported the measured trend of increasing flame length with increasing wind speed. However, Equations 2.12, 2.13 and 2.16 predicted the opposite trend because their exponents had signs opposite to those in Equation 2.17 (Table 2.4). Given that

the mass burning rate was observed to increase with higher wind speed (Table 4.11), the predicted decreasing trend in flame length could not have been caused by the increase in burning rate. Rather, this predicted trend must have been determined by the increase in wind speed influencing the Froude number and the wind speed ratios $U/U_{c,a}$ and $U/U_{c,b}$. This suggests that for a particular fire under varying wind conditions, flame length is dictated mostly by changes in air entrainment into the plume. Although flame drag was not mentioned in any of the reports describing Equations 2.12, 2.13, 2.16 or 2.17, it may have occurred in the large LNG fires used to develop Equation 2.17, since flame drag was observed in similar large LNG fires studied by Moorhouse [82] (corresponding to Equations 2.14-2.15). An increase in wind speed would then correlate with an increase in flame length due to the reduction in air entrainment caused by increasing flame drag. Higher overall values of flame length at each wind speed would also be expected, compared to the case with no flame drag. Conversely, if flame drag did not occur in the fires used to develop Equations 2.12, 2.13 and 2.16, then increases in wind speed would improve mixing of air and flame gases along the windward side of the fire and, without the opposing effect of increasing flame drag, cause the flame length to decrease. It should be noted that for the wooden crib fires associated with Equations 2.12 and 2.13, the ground plane was level with the base of the crib and little flame drag was evident in published photographs of the fires [81]. Also, for Equation 2.16, flame drag may not have been significant at the very low wind speeds (0 to 2.3 m/s) considered in this experiment (Table 2.4). Although the presence/absence of flame drag may explain the conflicting trends predicted by the various equations, more detailed data would be needed to verify the surmised differences in entrainment levels and the inconsistent trends in flame length, as well as to develop an improved correlation for predicting flame length.

Similar to Figure 4.39a, Figure 4.39b shows that the large increase in flame length that was observed as the wind speed increased from 7 m/s to 10 m/s was not predicted by any of the equations. Like Equation 2.15, Equations 2.12, 2.13 and 2.16 predicted a small increase in flame length, much less than that shown by the measured values. In contrast, Equation 2.17 predicted a decrease in flame length, but this may have been due to the fact that the correlation was based on the same form as Equation 2.13, except with opposite signs in the exponents. As indicated earlier, the lack of agreement between the predicted and measured values would suggest that the 10 m/s wind speed was beyond the range of validity for using the equations in this particular fire, due to the extremely high tilt angle and

large amount of flame drag incurred. A first guess at a non-dimensional parameter suitable for expressing this range of validity would be $U/U_{c,a}$, which represents the wind speed required to obtain a certain angle of tilt (e.g. Equation 2.3).[10] However, this parameter does not take into account differences in the experimental layout, which can also affect the extent of tilt, drag and length of the flame. For instance, although the maximum value of $U/U_{c,a}$ in the wooden crib experiments related to Equations 2.12 and 2.13 was 11 [81], the value at the 10 m/s wind speed for the fire in the present study was 10, yet the tilt angle and flame drag in the latter fire were much greater partly due to differences in the arrangement of the surrounding floor. As a result, the range of validity of the flame length equations would depend not only on wind speed but also the experimental layout, both of which affect entrainment and mixing in the fire.

This section shows that differences in the observed trends in flame length with increasing wind speed depended on whether the flame length was measured relative to the flame base centre or the fuel pool centre. At the highest wind speed of 10 m/s, the measured flame length increased significantly above that measured at 7 m/s due to high levels of flame tilt and flame drag, which greatly reduced air entrainment into the fire. This sharp increase in flame length has not been previously reported in the literature. At the lower wind speeds of 3 m/s to 7 m/s, the measured flame lengths agreed reasonably well with the predicted values, with differences attributed to variations in the method of measuring flame length and in the amount of flame drag incurred in the experiments on which the equations were based.

4.5 Results and Discussion: Heat Flux

As mentioned in Section 4.1.4, measurements of heat flux to the ground were made along x=2.64 m, at nominal y locations of 0 m, ±1 m and ±2 m. Typical time traces of incident total heat flux to the Gardon gauge, DFT and HFG located at y=0 m (Figure 4.6) are shown in Figure 4.40. A time trace of net heat flux absorbed by the DFT (as calculated by the IHCP1D program) is also included. The corresponding temperatures measured by the thermocouples attached to the sensor plates of the DFT and HFG, as well as by an exposed thermocouple located 25 mm above the ground plane between the two gauges (Section 4.1.4), are shown in Figure 4.41.

[10] A Froude number was also considered, but as mentioned in Section 2.2.2, it represents similar physics to $U/U_{c,a}$, so it would be affected by the same issues as those discussed for $U/U_{c,a}$.

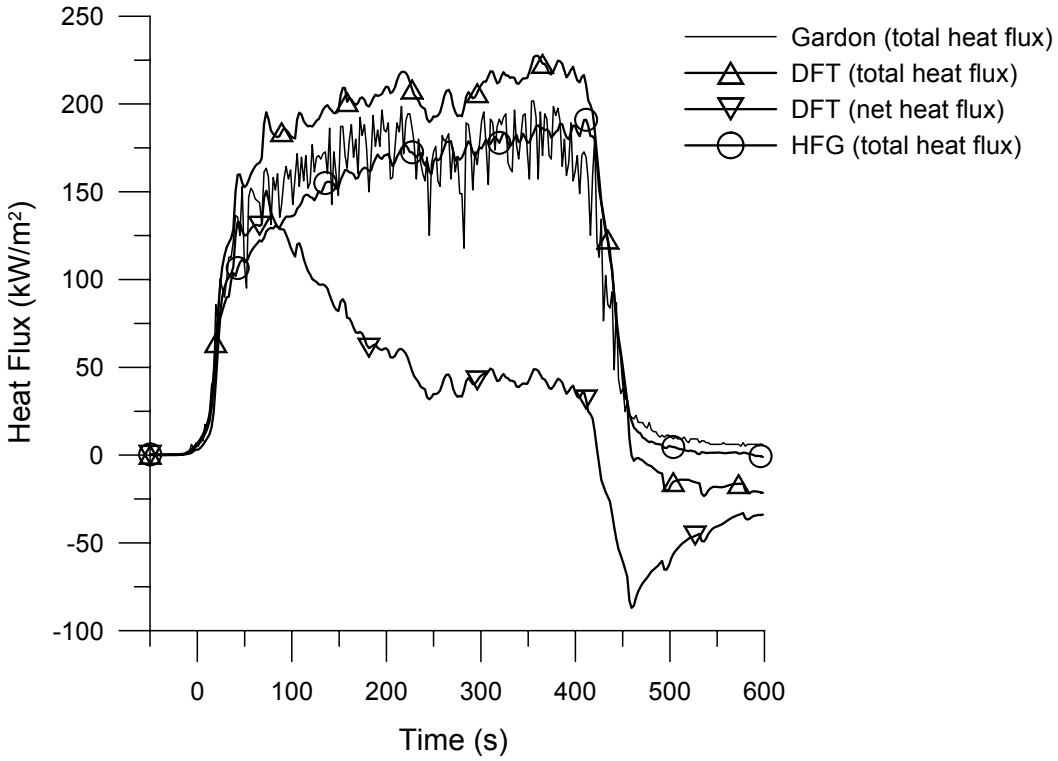

Figure 4.40: Typical plot of heat flux to the ground, 7 m/s wind (x=2.64 m, y≈0 m)

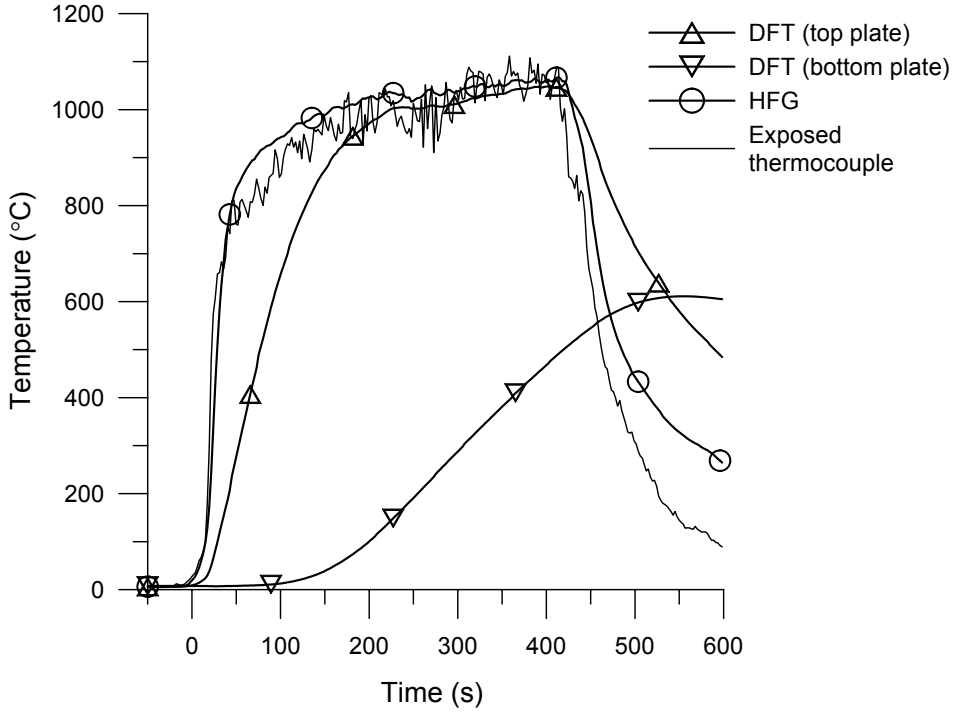

Figure 4.41: Temperatures corresponding to heat flux data shown in Figure 4.40

(For reference, plots showing time traces of heat flux and temperature measured at y=0 m under all wind speeds are provided in Appendix C.)

At the beginning of the test, the sensor plate of the HFG heated up more quickly than the thicker top plate of the DFT (Figure 4.41), but by the start of the steady burning period (223 s, Table 4.4), the temperatures of the exposed sensor plates in the two gauges were within 40°C of each other.[11] These temperatures were similar to those measured by the exposed thermocouple, although the HFG and DFT time traces did not exhibit the same level of temporal fluctuation as the thermocouple time trace due to the larger thermal mass (slower time response) of the sensor plates. In the time traces of incident total heat flux (Figure 4.40), there was no initial decrease like the ones previously observed in Figures 3.7 and 3.8. (On the other hand, a decrease in net absorbed heat flux was evident, as expected, as the DFT approached thermal equilibrium with the local fire environment.) The total heat flux levels from all three gauges increased until they reached quasi-steady levels during the steady burning period of the fire (223 s to 402 s, Table 4.4), permitting time-averaged values across the steady burning period to be evaluated and compared.

Table 4.14 lists time-averaged values of the measured total heat flux incident on the gauges in the ground, along with their corresponding standard deviations to provide a sense of the variation experienced within a test. The corresponding temperatures measured by the DFT, HFG and neighbouring exposed thermocouple are contained in Table 4.15. The average values were calculated using the same procedure as that employed for the thermocouple data in Section 4.4, by subtracting the initial value of heat flux (averaged over three minutes immediately prior to startup of the first fan) from the value averaged over the steady burning period. The initial value accounted for background heat transfer between the gauge and the surroundings as well as any offset errors in the gauge readings. Although measurements were obtained from the Gardon gauge located at y=0 m, they were beyond the range of calibration of the gauge (150 kW/m^2 maximum) and thus removed from the following analysis. Furthermore, no results were available from the HFG located at y=1 m, due to failure of the thermocouple on the sensor plate early in the test series.

Table 4.14 indicates that gauges placed at the same nominal distance to either side of the centreline (e.g. y=±1 m or ±2 m) measured relatively similar levels of

[11] This is similar to the results in Chapter 3 (Figures 3.7 and 3.8).

Table 4.14: Increase in Incident Total Heat Flux to the Ground (kW/m^2)

Nominal y Location	-2 m	-1 m	0 m	1 m	2 m
3 m/s Wind:					
Gardon	14 ± 3	40 ± 8	–	51 ± 9	16 ± 3
DFT	7.9 ± 0.6	42 ± 3	212 ± 7	38 ± 3	5.1 ± 0.6
HFG	4.1 ± 0.6	41 ± 3	157 ± 10	–	1.2 ± 0.2
5 m/s Wind:					
Gardon	13 ± 2	45 ± 9	–	64 ± 10	13 ± 2
DFT	7.5 ± 0.9	48 ± 3	220 ± 4	54 ± 5	4.8 ± 0.7
HFG	3.8 ± 0.5	46 ± 4	176 ± 4	–	1.0 ± 0.1
7 m/s Wind:					
Gardon	8.9 ± 1.5	64 ± 11	–	79 ± 10	8.1 ± 0.8
DFT	7.0 ± 0.8	64 ± 4	210 ± 10	69 ± 5	3.4 ± 0.5
HFG	2.7 ± 0.6	59 ± 4	177 ± 7	–	0.5 ± 0.1
10 m/s Wind:					
Gardon	9.7 ± 1.6	83 ± 11	–	101 ± 10	7.9 ± 0.9
DFT	5.6 ± 1.0	93 ± 4	241 ± 8	99 ± 11	2.8 ± 0.5
HFG	2.4 ± 0.6	94 ± 4	199 ± 7	–	0.4 ± 0.1

Table 4.15: Temperature Increases Measured by Heat Flux Gauges and Exposed Thermocouples (°C)

Nominal y Location	-2 m	-1 m	0 m	1 m	2 m
3 m/s Wind:					
DFT	187 ± 15	578 ± 7	1032 ± 12	537 ± 17	140 ± 10
HFG	225 ± 9	630 ± 8	1001 ± 17	–	105 ± 4
Thermocouple	54 ± 2	235 ± 9	977 ± 50	184 ± 10	40 ± 2
5 m/s Wind:					
DFT	157 ± 16	576 ± 18	1029 ± 9	604 ± 25	114 ± 12
HFG	208 ± 8	646 ± 13	1022 ± 6	–	89 ± 6
Thermocouple	44 ± 2	274 ± 14	1057 ± 29	251 ± 12	35 ± 2
7 m/s Wind:					
DFT	120 ± 15	645 ± 24	1015 ± 17	627 ± 45	62 ± 8
HFG	173 ± 9	720 ± 9	1037 ± 12	–	48 ± 3
Thermocouple	39 ± 2	375 ± 17	1024 ± 46	303 ± 13	27 ± 1
10 m/s Wind:					
DFT	97 ± 13	750 ± 22	1061 ± 13	750 ± 42	58 ± 7
HFG	154 ± 8	840 ± 8	1073 ± 13	–	41 ± 3
Thermocouple	36 ± 2	565 ± 19	1088 ± 32	477 ± 38	25 ± 1

heat flux, attesting to reasonable symmetry within the fire plume. The values from the Gardon gauges located at y=±1 m differed by up to 19 kW/m^2 (or 35% of the average value measured by both gauges), while the values from the corresponding DFTs differed by up to 6 kW/m^2 (or 11% of the average value measured by both gauges). At the measurement location y=±2 m, the data from the Gardon gauges, DFTs and HFGs differed by up to 2 kW/m^2, 4 kW/m^2 and 3 kW/m^2, respectively. Due to the low levels of heat flux measured at this distance (e.g. 0.4 to 4.1 kW/m^2 for the HFG), these differences corresponded to larger percentage differences relative to the average measurement (up to 113% for the HFG) than at y=±1 m. In general, the Gardon data taken at y=1 m and 2 m were higher than those taken at y=-1 m and -2 m, consistent with the fact that the Gardon gauges on the +y side of the test enclosure were approximately 0.2 m closer to the fire than those on the -y side (Table 4.2). The reverse applied to the HFGs at y=-2 m and 2 m. No consistent trend was exhibited in the DFT data (the values measured 2 m away from the centreline were higher on the -y side of the test enclosure, while the values measured 1 m away from the centreline were generally higher on the +y side) because the DFTs were closely centred on the nominal y locations and thus equidistant from the centreline of the test enclosure and the fire plume (Table 4.2). The above results indicate that the plume was largely symmetrical across the y=0 m plane, in agreement with the temperature contour plots of Section 4.4. Indeed, as shown in Table 4.15, the thermocouples located immediately above the gauges at y=±1 m measured temperatures within 88°C of each other (17% of the average measurement), while the thermocouples located at y=±2 m measured temperatures within 14°C of each other (29% of the average measurement).

Comparison of the measured temperatures from the exposed thermocouples, DFTs and HFGs (Table 4.15) provided an indication of the relative importance of radiation and convection in the total heat flux measurements. At y=0 m, the sensor plate temperatures of the DFT and HFG were within 55°C, or 6%, of the temperature measured by the exposed thermocouple, which ranged from 977°C to 1088°C in the four wind conditions. This close agreement indicated that the sensors were fully immersed in the radiative, optically thick flames of the fire. Although some convective heating of the gauges may have occurred, the thermal conditions at this location were likely radiation-dominated (Section 2.1). In contrast, the sensor plate temperatures were higher than the thermocouple measurements by up to 395°C (168%) at y=±1 m and up to 171°C (318%) at y=±2 m. This was likely due to increased convective effects at these locations, which would have affected the sen-

sor plates and exposed thermocouples differently due to their different geometries. As mentioned in Section 4.3, the temperatures measured by the thermocouples were driven mainly by convection (with some error due to radiation), but the temperatures measured by the DFT and HFG would have been affected more significantly by radiation from the fire due to the larger size of the sensor plates. Although similar temperatures would be expected to be measured by both types of sensors when placed in heating conditions in which either radiation or convection dominated, differences between the thermal responses of the sensors to the two heating modes would become important when the sensors were placed in mixed conditions in which both radiation and convection were significant. Thus, the differences between the temperatures of the sensor plates and those measured by the exposed thermocouples at y=±1 m and ±2 m were largest at the lowest wind speed (Table 4.16), when convection and radiation were both expected to be significant. As the wind speed increased, these differences would have decreased if convection became dominant relative to the expected radiation from the fire. Additionally, it should be mentioned that differences in conduction losses (e.g. through the thermocouple leads versus through the unexposed face of the sensor plate) and in radiation viewing angle (e.g. radiation from the floor was incident on the exposed thermocouple, but not the DFT or HFG) would have contributed to differences between the measured temperatures, but these effects were likely smaller than those discussed above.

The heat flux results in Table 4.14 generally supported the trend observed in Chapter 3, in which the Gardon data were higher than the DFT data, which were in turn higher than the HFG data. This was particularly evident among the data taken at y=±2 m, as well as among the available data at y=0 m and 1 m. As shown in Table 4.15, the DFT and HFG sensor surfaces were hotter than the gases immediately above those surfaces at all locations except y=0 m, so convective cooling of these gauges, and thus biases in the results similar to those seen in Chapter 3, would be expected. At y=-1 m, however, the values from the Gardon gauge were slightly below those from the corresponding DFT and HFG at three of the four wind speeds. This may have been because the gauges at this location were situated near the edge of the plume, with the Gardon gauge furthest from the longitudinal midplane of the test enclosure (Table 4.2). The Gardon gauge then would have received less heat from the fire than the other two gauges, reducing the effect of the bias inherent in using the different types of heat flux gauge. Table 4.17 shows the difference between the Gardon and DFT data at each location and wind

Table 4.16: Differences between Temperatures of Heat Flux Gauge Sensor Plates and Exposed Thermocouples (°C)

Nominal y location	-2 m	-1 m	0 m	1 m	2 m
Difference between DFT and Thermocouple:					
3 m/s wind	133	342	55	353	100
5 m/s wind	113	302	-27	352	79
7 m/s wind	81	269	-9	324	35
10 m/s wind	61	185	-28	274	33
Difference between HFG and Thermocouple:					
3 m/s wind	171	395	24	–	65
5 m/s wind	164	372	-35	–	54
7 m/s wind	135	345	13	–	21
10 m/s wind	118	275	-15	–	16

Table 4.17: Differences between Gardon and DFT Heat Flux Data from Table 4.14 (in kW/m^2 and as Percentage of Gardon Value)

Nominal y location	-2 m	-1 m	0 m	1 m	2 m
3 m/s wind	5.9 kW/m^2 (43%)	-2.6 kW/m^2 (-7%)	–	12 kW/m^2 (24%)	11 kW/m^2 (69%)
5 m/s wind	5.3 kW/m^2 (41%)	-3.2 kW/m^2 (-7%)	–	11 kW/m^2 (17%)	8.7 kW/m^2 (64%)
7 m/s wind	1.9 kW/m^2 (22%)	0.2 kW/m^2 (0.2%)	–	9.4 kW/m^2 (12%)	4.7 kW/m^2 (58%)
10 m/s wind	4.1 kW/m^2 (42%)	-9.7 kW/m^2 (-12%)	–	1.5 kW/m^2 (2%)	5.0 kW/m^2 (64%)

speed, both in kW/m^2 and as a percentage of the Gardon value. The differences at y=1 m and 2 m were greater than the corresponding values at y=-1 m and -2 m by 12% to 36%, supporting the notion that the bias in the Gardon measurement was less pronounced on the -y side of the test enclosure due to the greater distance of this gauge from the plume axis.

The temperatures of the sensor plates in the DFTs and HFGs (Table 4.15) also showed differences consistent with the y coordinates of the individual gauges. On the -y side of the test enclosure, the HFG was closer to the plume than the DFT, while on the +y side, it was further away (Table 4.2). Thus, the temperature of the HFG sensor plate was higher than that of the DFT sensor plate in the former case, but lower in the latter case. This did not appear to affect the heat flux results from the opposite sides of the test enclosure, however, since heat flux depends more greatly on rates of temperature change over a given time period (cf. Equation 3.9 on page 65) than on the absolute magnitude of temperature at a given time.

Trends in heat flux with increasing wind speed (Table 4.14) were consistent with the temperature results of Section 4.4. As the wind speed increased from 3 m/s to 10 m/s, the heat flux at y=0 m increased from 212 kW/m^2 to 241 kW/m^2 for the DFT and from 157 kW/m^2 to 199 kW/m^2 for the HFG, corresponding to gains of 14% and 26%, respectively. This was consistent with the fire tilting over and lying flatter along the ground at the higher wind speeds. The heat flux values measured at y=$\pm$1 m also increased with higher wind speed, but by larger amounts than the values at y=0 m. For instance, increases from 38 kW/m^2 to 99 kW/m^2 (159%) and from 41 kW/m^2 to 94 kW/m^2 (130%) were measured by the DFT at y=1 m and the HFG at y=-1 m, respectively. The larger increases in heat flux level at y=$\pm$1 m suggested that these gauges, which were closer to the edges of the plume, became more fully immersed in the hot plume gases as plume tilt increased with increasing wind speed. Comparison of Figures 4.17c, 4.22c, 4.28c and 4.33c supports this notion. In contrast, the gauges at y=0 m were fully immersed in the fire at all four wind speeds, so the increasing tilt of the plume would have had less impact on the measured heat flux at this location. At y=$\pm$2 m, the heat flux levels measured by all three types of heat flux gauge *decreased* with increasing wind speed, opposite to the trend observed at the other measurement locations (Table 4.14). The low values of heat flux (3 to 8 kW/m^2 for the DFT, 0.4 to 4 kW/m^2 for the HFG, and 8 to 16 kW/m^2 for the Gardon gauge) indicated that the gauges were situated mainly outside the plume, so heat transfer from the fire to the sensor surfaces would have occurred mostly through radiation (rather than convection

from the hot plume gases). As the fire tilted with increasing wind speed, it would have occupied less of the viewing angle of each gauge, resulting in smaller view factors and lower measured heat flux values. Higher wind speeds would have also increased convective cooling of the DFT and HFG sensor surfaces, further lowering the values of heat flux measured by these gauges.

In general, the levels of heat flux shown in Table 4.14 fall within the range of values found in the literature for medium to large hydrocarbon pool fires [11, 14, 34, 76, 84, 115, 137, 195]. Not surprisingly, the variation among published values is large (up to 400 kW/m^2 difference) because the measured values depend on many factors, including measurement method, measurement location, fire size and fuel type. In the present study, the heat flux data measured at y=0 m were comparable to published values of local emissive power from luminous portions of the flame (120-200 kW/m^2), which were typically measured using narrow angle radiometers placed in the centre of the fire [14]. As mentioned previously, the heat flux gauges at y=0 m were fully immersed in the fire due to significant flame drag occurring downwind of the fuel pan, so the measured heat flux levels should be consistent with values of local emissive power. In contrast, the heat flux data measured at y=$\pm$1 m were up to 174 kW/m^2 lower than those measured at y=0 m and were comparable to published values of average emissive power from the entire surface area of the flame to a remote target. The average emissive power is usually lower (by 30% to 50%) than the local emissive power because it encompasses the entire surface area of the flame, part of which may be blocked by smoke [76]. This smoke blockage, combined with the fact that the gauges at y=$\pm$1 m were further from the flame, would readily account for the lower measured heat flux levels.

4.6 Summary

In this chapter, video, temperature and heat flux data were presented for a 2 m diameter Jet A fire in crosswinds of 3 m/s to 10 m/s. Changes in wind speed were observed to greatly affect the fire geometry. At the 3 m/s wind speed, the fire plume was attached to the floor immediately downwind of the fuel pan, then lifted off the ground and curved upwards due to the increasing effect of buoyancy with increasing distance downwind of the fuel pan. Counter-rotating vortices, with their axes of rotation directed along the length of the plume, developed downstream of where the leeward side of the plume lifted off the ground. As the wind speed

increased, the plume was pushed closer to the ground and steeper temperature gradients were measured along the plume edges in the cross-sectional temperature contour plots. Flame drag, flame tilt and flame length (measured relative to the fuel pan centre) also increased, with very high extents of all three parameters observed at the 10 m/s wind speed. There was little evidence of counter-rotating vortices in the plume under the highest wind speed, although such vortices were expected to develop further downstream of the measurement region, after the plume lifted off the ground.

Experimental measurements of flame drag, flame tilt and flame length were obtained using the temperature contour plots and video images and were compared to values predicted using published semi-empirical correlations. Various methods were used to estimate the angle of tilt at each wind speed, with the resulting values varying greatly in cases where plume curvature was significant (e.g. at the two lowest wind speeds). Estimates of flame length depended on how the parameter was defined, with different definitions of flame length (based on the fuel pan centre versus the flame base centre) producing opposing trends with increasing wind speed up to 7 m/s. Discrepancies between the measured and predicted values of flame drag, flame tilt and flame length could be attributed to differences in the method of measuring the geometrical parameters among experiments and in the range of applicable experimental conditions, such as wind speed, fire size and fuel type, for the correlations. Also, the configuration of the floor surrounding the fuel pan appeared to contribute to discrepancies in the measured and predicted values of flame drag and plume tilt. This in turn affected the flame length by changing the levels of air entrainment into the plume.

Heat flux data were shown to be consistent with the results from Chapter 3. Differences between measured values were affected by gauge type, sensor location relative to the fire and the importance of convection versus radiation in the total heat transfer to the gauge. As the wind speed increased, the heat flux measured at y=0 m and $\pm$1 m increased as a result of the fire tilting further over and the gauges becoming more fully immersed in the hot plume gases. On the other hand, the heat flux measured at y=$\pm$2 m decreased with increasing wind speed because of decreasing view factors for radiation from the fire to the gauges, which lay outside the fire plume.

In the next chapter, the effects of a large downwind blocking object on the wind-blown fire will be examined.

Chapter 5

Fire in Wind With Blocking Object

This chapter describes experiments involving the 2 m diameter fire from the previous chapter, with a 2.7 m diameter blocking object situated on the downwind side of the fire. The design of these experiments was previously presented as part of the author's M.A.Sc. thesis [8]. Based on visual observations of the fire made during preliminary tests that were conducted as closure to the author's M.A.Sc. project [8], several key changes to the experimental layout were recommended and implemented for the present study. The final setup of these experiments is described in this chapter, followed by presentation and discussion of temperature and heat flux results.

5.1 Experimental Setup

The experiments with the blocking object were based on the same setup as the experiments without the blocking object. Since all tests were performed in the University of Waterloo Live Fire Research Facility, the test enclosure and wind generation system were the same as those described in Sections 4.1.1 and 4.1.2. The same pan burner was also used, in the location specified in Section 4.1.3, but slight modifications were made to the brick floor surrounding the fuel pan. The present section describes these changes, along with the layout of the blocking object and the corresponding instrumentation. A summary of the conducted tests is included to end the section.

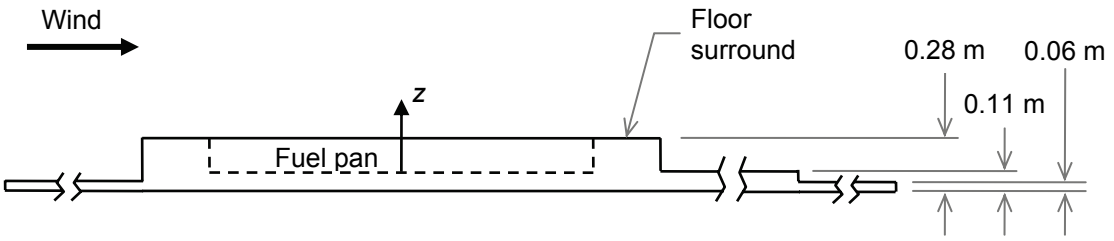

Figure 5.1: Geometry of raised floor surround and surrounding brick layout for experiments involving blocking object, side view

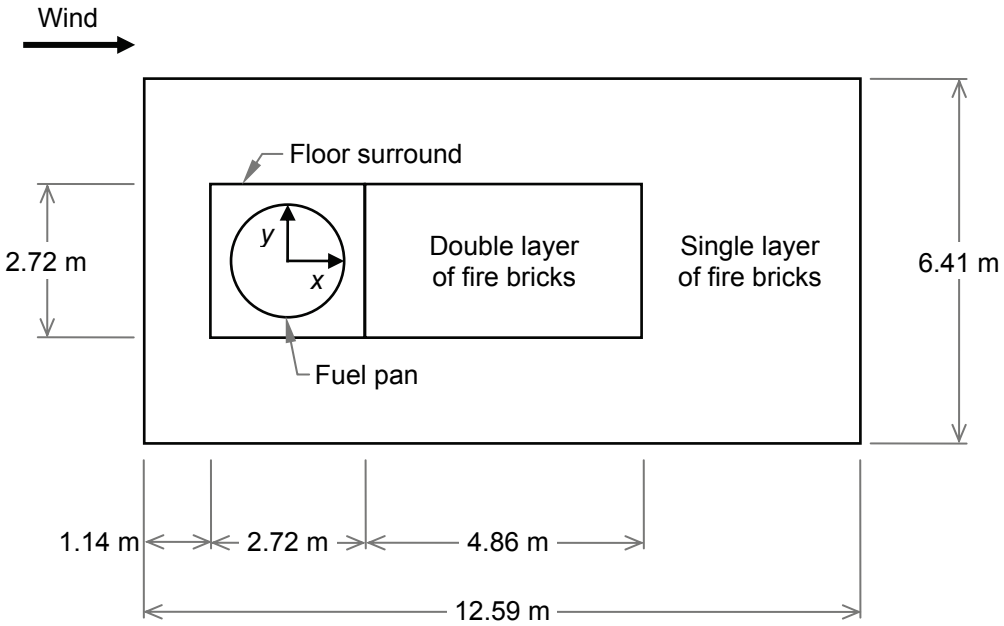

Figure 5.2: Geometry of raised floor surround and surrounding brick layout for experiments involving blocking object, plan view

5.1.1 Changes to Layout of Brick Floor

Similar to the configuration for the tests without the blocking object, a raised floor surround of 2.72 m by 2.72 m area was situated around the fuel pan, but with no upwind extension formed by cement boards.[1] A double layer of fire bricks protected the test enclosure floor immediately downwind of the floor surround, spanning approximately the same width as the floor surround and a length of 4.86 m (Figures 5.1 and 5.2). Surrounding this double layer and the floor surround was a single layer of fire bricks, which spanned a total width of 6.41 m and total

[1] As mentioned in Section 4.1.3, an upwind extension was required in tests without the blocking object to prevent the fire from becoming attached to the upwind edge of the floor surround, but this behaviour was not observed in tests with the blocking object in place.

length of 12.59 m, starting at a distance of 1.14 m upwind of the leading edge of the floor surround.

5.1.2 Blocking Object

The blocking object was a nominally 2.74 m diameter, 10.78 m long cylinder assembled from two culvert sections made of 14-gauge, corrugated alumized steel. The sections, which were 4.63 m and 6.15 m in length, were joined using a 0.68 m wide steel band that was wrapped around the outside of the culvert ends and tightened with bolts to hold the two pieces together (Figure 5.3).

The entire blocking object was nominally centred on the longitudinal midplane of the test enclosure, at a distance of 3.44 m downwind from the fuel pan centre. The cylinder was oriented with its longitudinal axis parallel to the floor and perpendicular to the direction of the wind flow. It was elevated on four steel support stands such that the bottom of the cylinder was raised 1.07 m above the top surface of the double brick layer. Each stand had a base area of 0.9 m by 1.4 m and contained a supporting V-shaped frame to act as a cradle for the culvert. The stands supporting the middle of the blocking object were wrapped in a protective layer of ceramic fibre blanket insulation and were located at least 1.17 m from the longitudinal midplane of the test enclosure so that they would not be directly in the path of the downwind fire plume.

During post-test measurements, the blocking object was found to be shifted by approximately 0.20 m in the +y direction. This was due to the inherent difficulty

Figure 5.3: Photograph of blocking object

in accurately positioning such a large cylinder inside the test enclosure and likely influenced the symmetry of the wind-blown fire plume across the longitudinal mid-plane of the test enclosure (seen later in Section 5.3). Uncertainties in the position of the blocking object along the other axes were ± 0.07 m in the x direction and ± 0.02 m in the z direction.

5.1.3 Instrumentation

The coordinate system used in the present experiments was the same as that used in the experiments without the blocking object. As depicted in Figures 5.1 and 5.2, the coordinate system origin was located at the centre of the fuel pan, with the positive x direction following the mean direction of the wind, the positive y direction following the cross-stream direction and the positive z direction pointing vertically upward.

Temperatures in the downwind region of the fire were measured using 24-gauge (0.51 mm diameter), chromel-alumel (Type K) thermocouples. The thermocouple wires were insulated with Nextel ceramic fibre and covered with protective Inconel braiding. To measure plume temperatures, thermocouples with exposed junctions were mounted (pointing upwind) on either vertical chains or a horizontal steel bar. A total of 163 thermocouples were distributed both upwind and downwind of the blocking object to characterize the temperature field in the fire plume. Measurement planes oriented normal to the direction of the crosswind flow were situated at approximately the same distances downwind of the fuel pan as in the experiments without the blocking object (Section 4.1.4). As illustrated in Figures 5.4 and 5.5, 15 vertical thermocouple rakes were positioned along three measurement planes upwind of the blocking object and two measurement planes underneath the blocking object. Another 12 vertical rakes were installed along three measurement planes downwind of the blocking object (the open circles in Figure 5.4 denote three vertical rakes that were included in the latter half of the experiment only). A horizontal thermocouple rake with adjustable height was also installed to capture the width of the plume in the y direction. The total number of thermocouples available to measure fire plume temperatures in these experiments was less than that for the experiments without the blocking object due to a larger number of measurement parameters in these tests [8]. For instance, temperature and heat flux along the surface of the blocking object had to be measured, so fewer data channels were available for measuring plume temperatures. As a result, most of

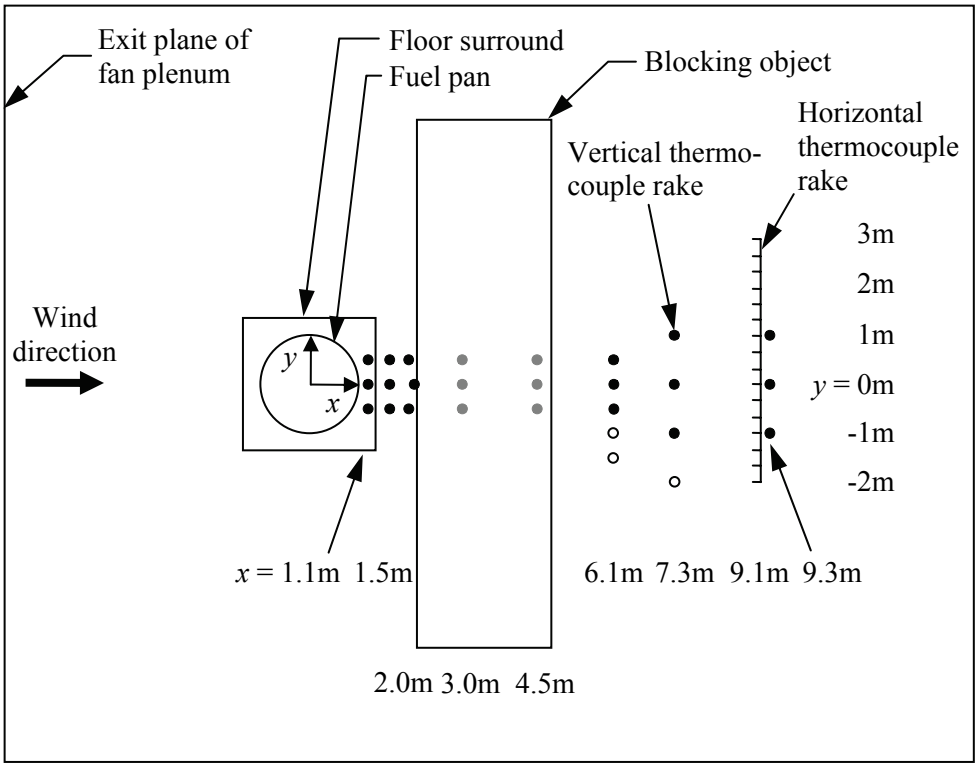

Figure 5.4: Sketch of thermocouple rake locations, plan view (nominal distances shown, black dots indicate thermocouple rakes located upwind and downwind of blocking object, gray dots indicate thermocouple rakes located underneath blocking object, open dots indicate rakes that were present in tests 29 to 32 only)

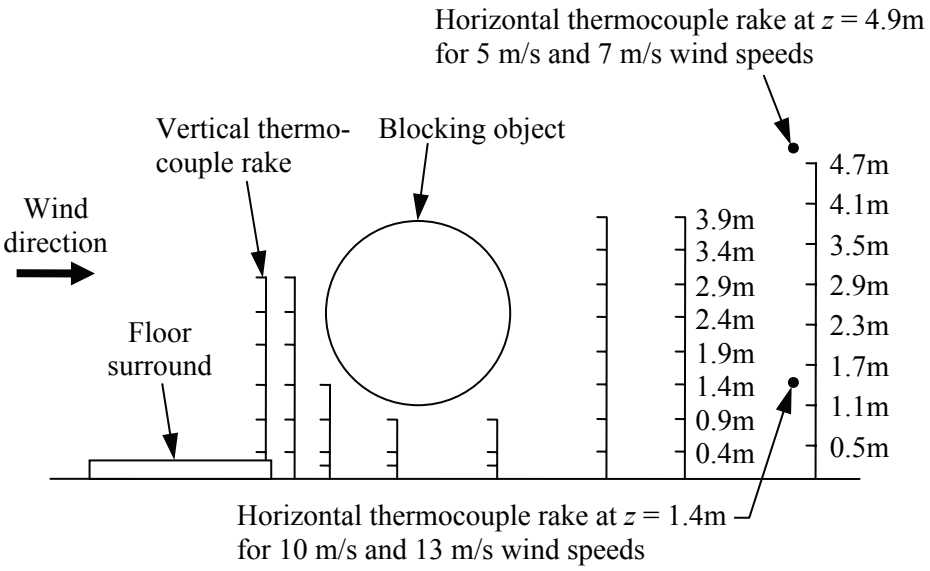

Figure 5.5: Sketch of thermocouple heights, side view (nominal distances shown)

the vertical thermocouple rakes were concentrated near the longitudinal midplane of the test enclosure to measure temperatures in the core region of the fire plume. A few (e.g. the three rakes added in the latter half of the experiment) were placed further away from the midplane to capture the cross-sectional extent of the plume. The spacing of the thermocouples varied from 0.33 m to 1.00 m in the y direction, and from 0.20 m to 1.00 m in the z direction, with the coarser spacing applying to thermocouples located further from the fuel pan. The thermocouple locations are sketched in Figures 5.4 and 5.5 and the corresponding coordinates are listed in Appendix D. For simplicity, the nominal distances used to indicate the thermocouple locations in Figures 5.4 and 5.5 will be employed when discussing the results.

Thermocouples were also used to measure temperatures along the inside surface of the blocking object. These thermocouples were of the same gauge and type as those used to measure plume temperature, but intrinsic thermocouple junctions were formed by individually spot-welding the two lead wires of each thermocouple directly to the object surface. Thermocouples with intrinsic junctions generally have lower error in measuring surface temperature than thermocouples in which a beaded junction is attached directly to the surface, due to lower heat transfer through the thermocouple wires to the surroundings [196]. A total of 52 thermocouples were mounted along the inside surface of the culvert. The internal mounting minimized disturbance by the thermocouple wires to the plume flow around the object. The junctions were spaced 30° to 90° apart along seven cross-sectional planes along the cylinder. These planes were located at y=-2.00 m, -1.15 m, -0.20 m, 0.00 m, 0.50 m, 1.00 m and 2.00 m. The planes y=-1.15 m and -0.20 m were selected such that the measurement locations would not be covered by the steel band used to join the culvert sections together (Section 5.1.2), as measurement under this band would result in significantly lower temperatures.

Heat flux was measured using DFTs, HFGs and Gardon gauges, which were described in Chapter 3. Two thermopiles were also included to provide comparative data. One was an RdF Microfoil® gauge (model 27650) from RdF Corporation of Hudson, NH [197] (Figure 5.6). Like the Gardon gauge, this was a windowless, water-cooled gauge, with cooling water maintained above the dew point. It was 25 mm in diameter and 19 mm tall, with a sensing area of 6 mm by 6 mm. The manufacturer-specified absorptivity was 0.90 and the full-scale output was 113 kW/m^2 (10 Btu/ft^{2}s). A calibration constant with an accuracy of ±5% was supplied to permit reduction of voltage output data to values of absorbed heat flux. Values of incident heat flux were subsequently obtained by dividing the absorbed

Figure 5.6: RdF Microfoil® gauge

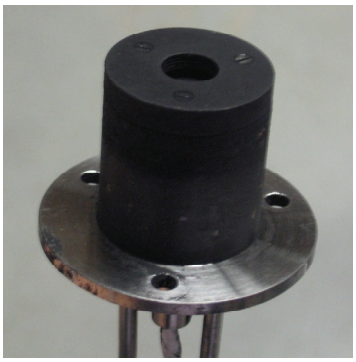

Figure 5.7: Medtherm Schmidt-Boelter gauge

flux by the surface absorptivity.[2] The other thermopile was a water-cooled Schmidt-Boelter gauge (model 64-20SB-20) from Medtherm Corporation of Huntsville, AL (Figure 5.7). It was 25 mm in diameter and 25 mm tall, and the sensing surface was covered by a 4 mm thick view restrictor containing a windowless opening of 8 mm diameter to restrict the viewing angle to 90°.[3] An absorptivity of 0.96 and a full-scale output of 200 kW/m^2 were specified by the manufacturer. A calibration constant with an accuracy of ±3% was supplied to allow determination of incident heat flux values from measured voltage data.

The various heat flux gauges were distributed around the test enclosure, as illustrated in Figure 5.8. The coordinates of each gauge, measured to the centre of the sensing surface, are listed in Table 5.1. Three Gardon gauges were positioned

[2]Reradiation was not added to the absorbed heat flux because the surface temperature was not known. If the surface temperature was assumed to be 100°C, then approximately 1 kW/m^2 of reradiation would have to be added to the values of incident heat flux. In most cases, this was not expected to be a significant contribution to the incident flux.

[3]It should be noted that when a view restrictor is present, convective heat transfer to the gauge is reduced because of lower flow velocities over the sensor surface [198]. As a result, gauges with view restrictors may be considered to be radiometers, measuring only the radiative portion of the total heat flux.

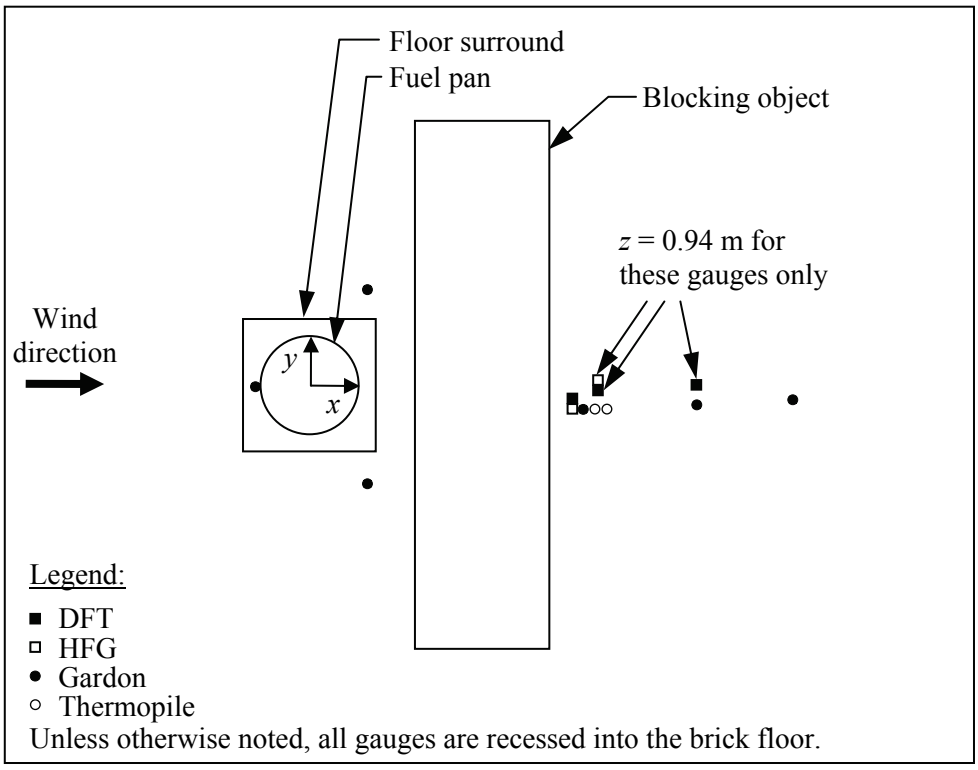

Figure 5.8: Sketch of heat flux gauge locations, plan view

Table 5.1: Locations of Heat Flux Gauges, Measured to the Centre of the Sensing Surface

Gauge	x (m)	y (m)	z (m)
Gardon	-1.09	-0.08	0.17
Gardon	1.17	-2.00	-0.05
Gardon	1.15	1.97	-0.05
DFT	5.35	-0.30	0.02
HFG	5.34	-0.41	0.02
Gardon	5.58	-0.48	0.00
RdF thermopile	5.81	-0.48	0.01
Medtherm thermopile	6.04	-0.48	0.03
DFT	5.86	-0.06	0.94
HFG	5.86	0.10	0.94
Gardon	7.90	-0.39	-0.05
DFT	7.87	0.03	0.94
Gardon	9.85	-0.29	-0.05

near the fuel pan: one at the upwind edge of the pan along the longitudinal midplane of the test enclosure and the other two near the downwind edge of the pan, at a distance of approximately 2 m to either side of the longitudinal midplane. These gauges were mounted in the brick floor with the sensing surface flush with the top of the fire brick. They would measure heat flux levels from the fire to the ground in regions where direct flame contact was not expected.

Downwind of the blocking object, several types of heat flux gauge were placed in approximately the same location in order to permit comparison of their measurements. A DFT, HFG and Gardon gauge, as well as the two thermopiles, were mounted beside each other in the brick floor, at distances of 5.34 m to 6.04 m downwind of the fuel pan centre and 0.30 m to 0.48 m to one side of the longitudinal midplane of the test enclosure. Due to the difference in height of the gauges, as well as the presence of cooling tubes protruding from the back of the water-cooled gauges, not all of the sensors could be positioned flush with the top surface of the fire bricks. The sensing surfaces were instead kept within 0.03 m above the top of the bricks. The gauges were mounted in a manner similar to that described in the previous chapter (Figure 4.8), except in the present setup, the HFG housing was not surrounded by any ceramic fibre insulation. For additional comparison, a DFT and HFG were placed beside each other at a distance of 5.86 m downwind of the fuel pan, with their sensing surfaces elevated by a height of 0.94 m above the brick floor. These two gauges were raised on a steel post and mounted in the same orientation as the gauges in the floor, with the sensing surface facing upward.

Further downwind of the blocking object, three gauges were installed to measure heat flux from the fire plume after it passed the culvert (Figure 5.8). Two Gardon gauges were mounted in the brick floor at distances of 7.90 m and 9.85 m downwind of the fuel pan centre. A DFT was placed near the first Gardon gauge, at a downwind distance of 7.87 m and elevated by a height of 0.94 m above the floor.

Six heat flux gauges were distributed around the circumference of the blocking object to estimate heat flux levels from the fire to the culvert. These gauges were positioned near the cross-sectional midplane of the object, offset from this plane by a distance of up to 0.14 m due to the presence of thermocouples on the inside surface of the culvert. The locations of the gauges are given in Figure 5.9. The first was a DFT bolted to the underside of the blocking object, separated from the outside surface of the culvert by a distance of 12 mm. Five additional HFGs were distributed around the circumference of the object, with two located at an angle of

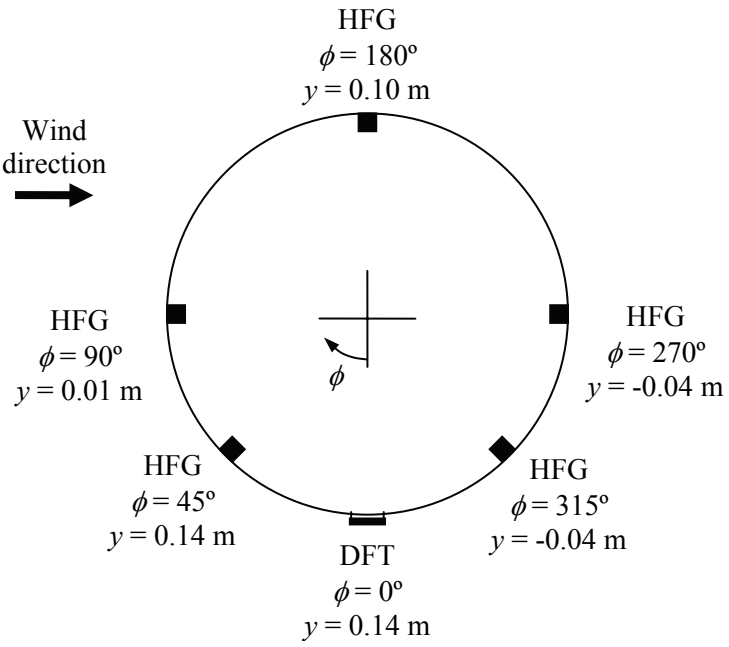

Figure 5.9: Locations of heat flux gauges on blocking object

45° to either side of the DFT, two located at an angle of 90° to either side of the DFT, and one located at the top of the culvert. Each HFG was positioned inside a square opening in the culvert wall (cut just large enough to fit the gauge) and clamped so that its sensing surface was flush with the outer surface of the culvert. Like the HFG in the floor, the housing of these gauges was not surrounded by any insulation.

In addition to the above sensors, several small cylinders were distributed in the vicinity of the fire to represent cargo packages scattered from the aircraft in the transportation accident scenario. These cylinders, termed "calorimeters"[4], were designed to measure heat flux in a manner similar to the DFT, based on an inverse conduction analysis (Section 2.4) [8]. With an outer diameter of 0.30 m and a length of 0.61 m, the calorimeters were considerably larger than the DFT and HFG, but significantly smaller than the blocking object (Section 5.1.2). They were constructed from 0.010 m thick stainless steel pipe, the inside of which was filled with 8-pound density (128 kg/m^3) ceramic fibre insulation. The outer surface was painted with Pyromark Series 2500 flat black paint, similar to the DFT and HFG, in order to achieve a diffuse, gray surface. Construction drawings of the calorimeter

[4]A calorimeter is an instrument for measuring quantities of thermal energy.

were presented in the author's M.A.Sc. thesis [8]. For reference, the exploded assembly drawing is reproduced in Figure 5.10.

Each calorimeter contained eight measurement stations, spaced uniformly around the circumference of the pipe along the cross-sectional midplane. Each measurement station consisted of two 24-gauge (0.51 mm diameter), chromel-alumel (Type K), intrinsic thermocouples, one mounted to the inner surface of the pipe and the other offset radially from the first thermocouple by a 0.025 m thick layer of ceramic fibre insulation. The latter thermocouple was held in place by mounting it to the outer surface of a 0.61 m long, 0.23 m diameter cylinder that was rolled from shim steel of 0.40 mm thickness (28-gauge). This smaller cylinder was held in position inside the pipe by means of 0.025 m long, 0.013 m diameter, stainless steel pegs welded to the inside wall of the pipe, along with split rings of adjustable diameter that were placed inside the shim cylinder to press the shim against the pegs. As already mentioned, the space between the pipe and shim cylinder, as well as the remaining space inside the shim cylinder, were filled with ceramic fibre insulation in order to minimize any convective effects inside the calorimeter. The insulation inside the shim cylinder was inserted as two pieces – a shell to fit over the split rings and a core to fill the remaining inner space. A 0.025 m wide by 0.002 m thick crosspiece spanned across each end of the pipe to prevent the insulation from sliding out the ends of the calorimeter. Additionally, each end was capped by a piece of ceramic fibre blanket insulation to protect the crosspieces and thermocouple wires exiting the cylinder. Figure 5.11 shows two calorimeters as installed on the ground underneath the blocking object.

Similar to the DFT, the thermocouple data from each measurement station in the calorimeter were used in the one-dimensional inverse heat conduction program IHCP1D of Beck Engineering Consultants Company [144] to evaluate the heat flux to the outer surface of the calorimeter. A two-layer, cylindrical wall was used to model the outer pipe wall and the 0.025 m thick layer of ceramic fibre insulation. The data measured by the thermocouple that was attached to the pipe wall were input to the program, while the data from the thermocouple attached to the shim were used to prescribe a temperature time history at the other side of the insulation as a "known" boundary condition. In the IHCP1D program input, a total of 101 calculation nodes (73 in the pipe wall and 28 in the insulation) were specified. Temperature-dependent thermal properties for each layer of the wall were based on those reported for the HFG (Section 3.1). Three future temperatures were selected, as recommended by Equation 3.1 (page 50).

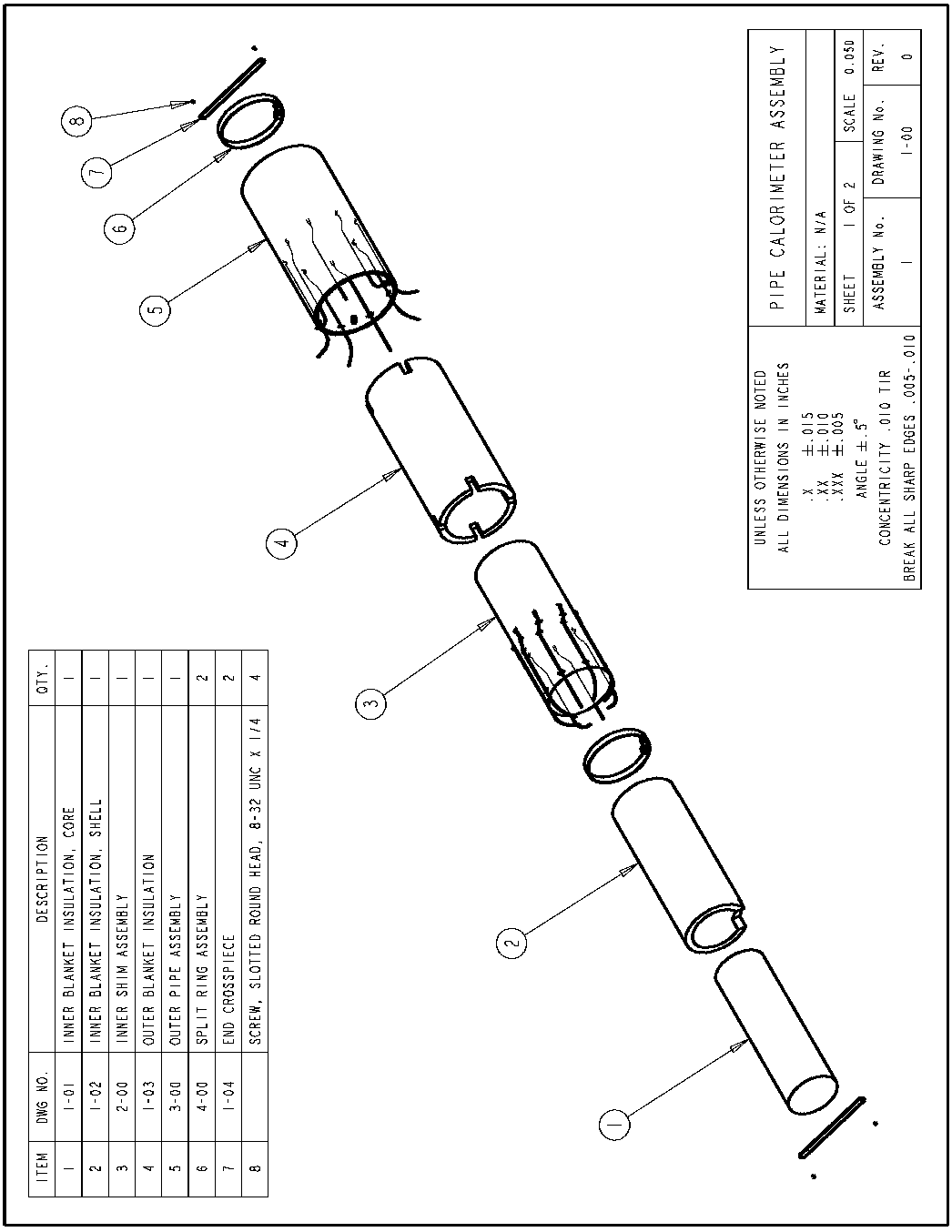

Figure 5.10: Exploded assembly drawing of calorimeter

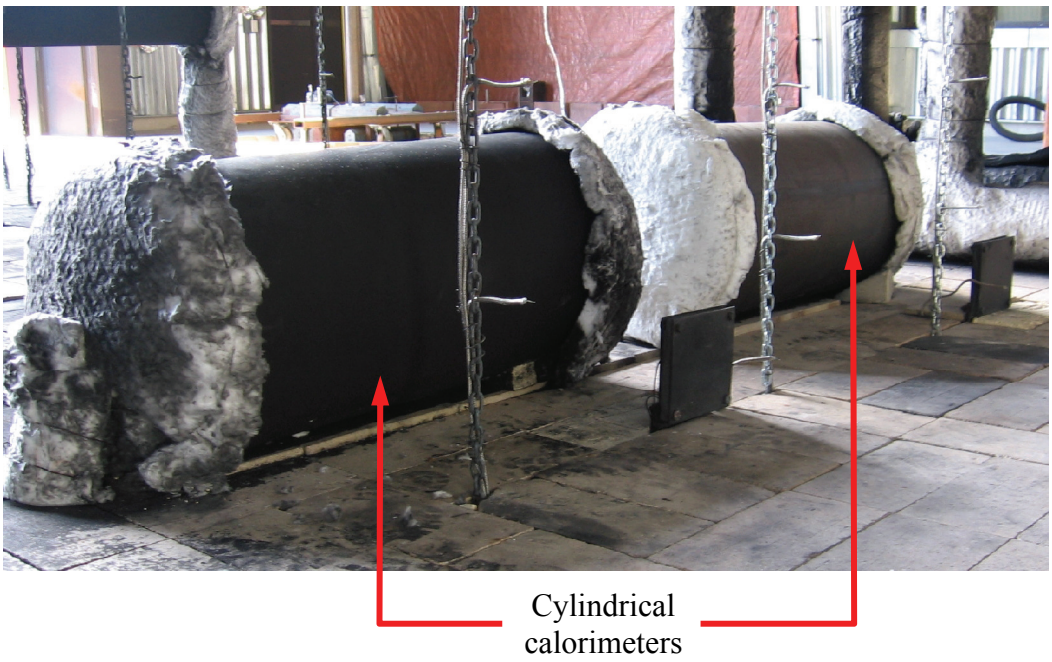

Figure 5.11: Photograph of calorimeters located underneath blocking object (locations 'D' and 'E' in Figure 5.12)

Six calorimeters were located downwind of the fuel pan in regions where high temperatures or high thermal gradients were expected. Two of these (labelled 'A' and 'B' in Figure 5.12) were placed underneath the windward edge of the blocking object, centred on and 1.00 m away from the longitudinal midplane of the test enclosure. Each cylinder was aligned so that its longitudinal axis was horizontal and perpendicular to the wind direction. A third calorimeter ('C') was similarly oriented underneath the leeward edge of the blocking object, near the test enclosure midplane. All three calorimeters were suspended by chains from the culvert so that they were centred between 0.59 m and 0.64 m above the brick floor. This configuration was expected to result in full envelopment of the cylinders by the fire plume. Two additional calorimeters ('D' and 'E') were placed on the ground, underneath and aligned with the longitudinal axis of the blocking object. The centres of these calorimeters were offset by 0.40 m to 0.44 m to either side of the longitudinal midplane of the test enclosure. Finally, a calorimeter ('F') was centred 6.55 m downwind of the fuel pan, offset by 0.50 m to one side of the test enclosure midplane and oriented in the same manner as the other cylinders. This calorimeter was supported on a brick stand so that it was centred at an elevation of 0.67 m, similar to the suspended calorimeters. Table 5.2 contains the coordinates of each calorimeter, measured to the centre of the cylinder.

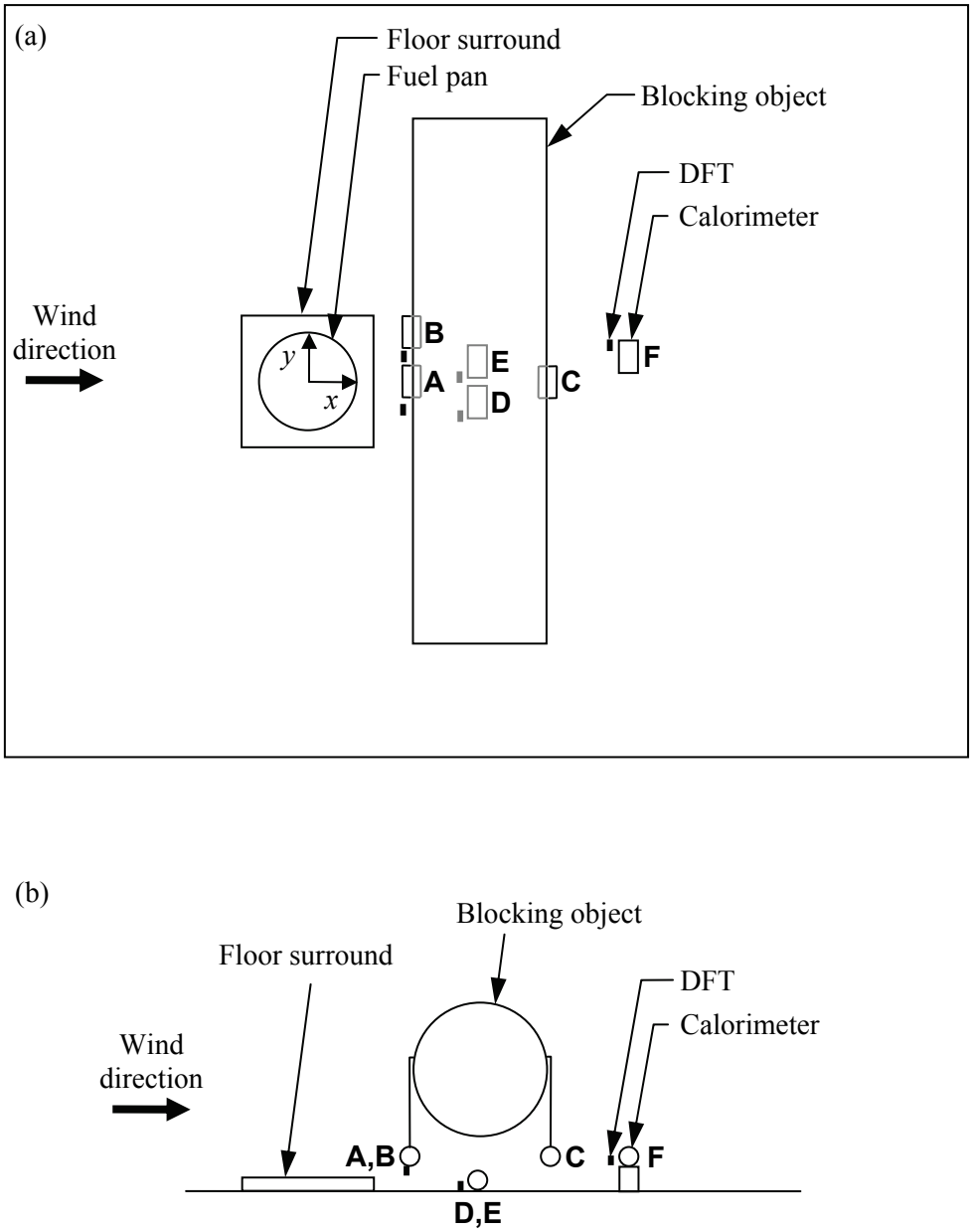

Figure 5.12: Sketch of calorimeter locations, labelled 'A' to 'F', (a) plan view, (b) side view

Table 5.2: Locations of Calorimeters, Measured to the Centre of the Cylinder

Calorimeter	x (m)	y (m)	z (m)
A	1.99	0.00	0.59
B	1.99	1.00	0.61
C	4.89	-0.06	0.64
D	3.40	-0.44	0.16
E	3.40	0.40	0.16
F	6.55	0.50	0.67

Table 5.3: Locations of DFTs Positioned Near Calorimeters

Nearest Calorimeter	x (m)	y (m)	z (m)
A	1.98	-0.54	0.44
B	1.91	0.54	0.44
D	3.07	-0.67	0.07
E	3.08	0.16	0.07
F	6.15	0.72	0.63

As shown in Figure 5.12, DFTs were located beside five of the six calorimeters (all except 'C'). This would allow comparison of heat flux results from sensors of different thermal mass. The DFTs were oriented such that the sensing surfaces were normal to the x direction (i.e. the opposing sensing surfaces faced upwind and downwind). They were mounted as necessary on steel posts to elevate them above the brick floor. The measured coordinates of the centre of each DFT are listed in Table 5.3.

As in the experiments without the blocking object (Chapter 4), instrumentation was included for measuring fuel regression rate and plume velocities. Since these measurements are the focus of the theses by Randsalu [20] and Best [21], they will not be discussed in the present work. Figures 5.13 to 5.15 show photos of the overall experimental layout upwind and downwind of the blocking object.

Data acquisition was based on the same Compact FieldPoint system as that used in the experiments without the blocking object (Section 4.1.4). The sampling rate of each data channel was 0.5 Hz. Five video cameras distributed around the test enclosure recorded upwind, downwind, overhead and profile views of the fire plume. Weather data for each test were taken from the Region of Waterloo weather station described in Section 4.1.4; the Vantage Pro2 station mentioned in that section was not available for use during the experiments discussed in this chapter.

Figure 5.13: Photograph of experimental layout upwind of blocking object, side view

Figure 5.14: Photograph of experimental layout downwind of blocking object, side view

Figure 5.15: Photograph of experimental layout downwind of blocking object, looking upwind

5.1.4 Summary of Conducted Tests

Table 5.4 summarizes the tests conducted with the blocking object. The test protocol was similar to that described in Section 4.1.5 for the experiments without the blocking object. Approximately 100 L of fuel were used in each test. Actual fuel quantities were not measured, so they are not listed in Table 5.4. Also, no tests were conducted at the 3 m/s wind speed examined in Chapter 4 because preliminary observation of the fire in the presence of the blocking object indicated that the object and its instrumentation were unlikely to withstand the sustained, high thermal load on the object posed by the fire in this wind condition. Tests were instead performed at a higher wind speed of 13 m/s in addition to the 5, 7 and 10 m/s winds examined in Chapter 4.

Table 5.4: Tests Conducted with Fire in Crosswind and Blocking Object

Test Date	Test Number	Fan Drive Frequency	Nominal Wind Speed	Outdoor Ambient Temperature
26 Apr 2006	25	60 Hz	13 m/s	8°C
26 Apr 2006	26	47 Hz	10 m/s	12°C
26 Apr 2006	27	22 Hz	5 m/s	14°C
27 Apr 2006	28	34 Hz	7 m/s	4°C
5 May 2006	29	47 Hz	10 m/s	7°C
5 May 2006	30	60 Hz	13 m/s	12°C
5 May 2006	31	34 Hz	7 m/s	14°C
17 May 2006	32	22 Hz	5 m/s	12°C

5.2 Experimental Uncertainties and Sources of Error

Uncertainties in the thermocouple measurements of the present experiments were expected to be similar to those discussed previously in Section 4.3. Since the same temperature measurement system was used, the systematic uncertainties related to calibration of the data acquisition system components remained the same. Further, the setup and installation of the thermocouples were similar to the methods described in the previous chapter, so uncertainties related to thermocouple location, decalibration, time lag and conduction losses would be comparable to those listed in Table 4.5. Post-test processing of the thermocouple data also remained the same, so the uncertainty related to determination of the time-averaging period would not change. However, with the presence of the blocking object, the uncertainty due to radiation effects would likely be larger than in the experiments without the blocking object because the thermally massive culvert presented a large cold surface to the thermocouples at the beginning of each test and a large hot surface to the thermocouples at the end of the test. Assuming that the uncertainty related to radiation was 20% in the core of the fire and 30% near the edge of the fire, the total systematic uncertainty for measured temperatures in those regions would be 24% and 34%, respectively.

Measured temperatures along the surface of the blocking object were affected by sources of error similar to those discussed above and in Section 4.3, but not necessarily to the same extent as the percentages listed in Table 4.5. In particular, uncertainty in the thermocouple location was much smaller because the thermocou-

ple leads were welded to the object surface and could not shift in location during a test. However, greater uncertainty due to conduction losses could be expected because conduction could occur not only along the lead wires of the thermocouple, but also laterally along the surface of the blocking object between the two attachment points of the thermocouple leads [141]. This lateral conduction may have been important in regions of steep thermal gradients along the culvert. Also, since the inside surface of the blocking object was not insulated, radiative and convective heat losses could occur from the region of the object surface between the two attachment points of the thermocouple leads [141]. Assuming that the uncertainties corresponding to the thermocouple location, conductive heat losses, and radiative/convective losses were 1%, 10% and 20%, respectively, then, with values for all other systematic uncertainties taken from the last column of Table 4.5, the total systematic uncertainty for the blocking object temperatures would be 25%.

As discussed in Section 4.3, estimates of precision uncertainty in the measured temperatures could be made by examining the repeatability of measurements taken across multiple tests conducted at the same wind speed. As shown in Table 5.4, two tests were conducted at each of four wind speeds: 5 m/s, 7 m/s, 10 m/s and 13 m/s. The test-to-test repeatability of plume temperatures measured at each wind speed was evaluated using both the quantity ΔT_{diff} (Equation 4.4 on page 95), which is expressed as a percentage, and the numerator of ΔT_{diff}, $|(T_{ss} - T_{init})_{\text{2nd test}} - (T_{ss} - T_{init})_{\text{1st test}}|$, which gives the absolute difference between corresponding measurements from repeated tests. Typical values of these two quantities are plotted in Figures 5.16 and 5.17 for locations underneath and downwind of the blocking object. For clarity, only locations along the longitudinal measurement plane y=0 m are shown.

The plots in both Figures suggest that the test-to-test repeatability was poorer in the experiments with the blocking object than in the experiments without the blocking object (Section 4.3.1). At a wind speed of 5 m/s, values of ΔT_{diff} were within 18% (Figure 5.16a), with absolute differences ranging up to 102°C (Figure 5.17a).[5] At a wind speed of 7 m/s, values of ΔT_{diff} increased up to 45% (Figure 5.16b), with absolute differences ranging up to 185°C (Figure 5.17b). Even higher differences were recorded at the 10 m/s and 13 m/s wind speeds – up to 70% and 371°C at 10 m/s (Figures 5.16c and 5.17c) and up to 112% and 222°C at

[5]In general, the location corresponding to the highest percentage difference in temperature increase was not the same as the location corresponding to the highest absolute difference in temperature increase.

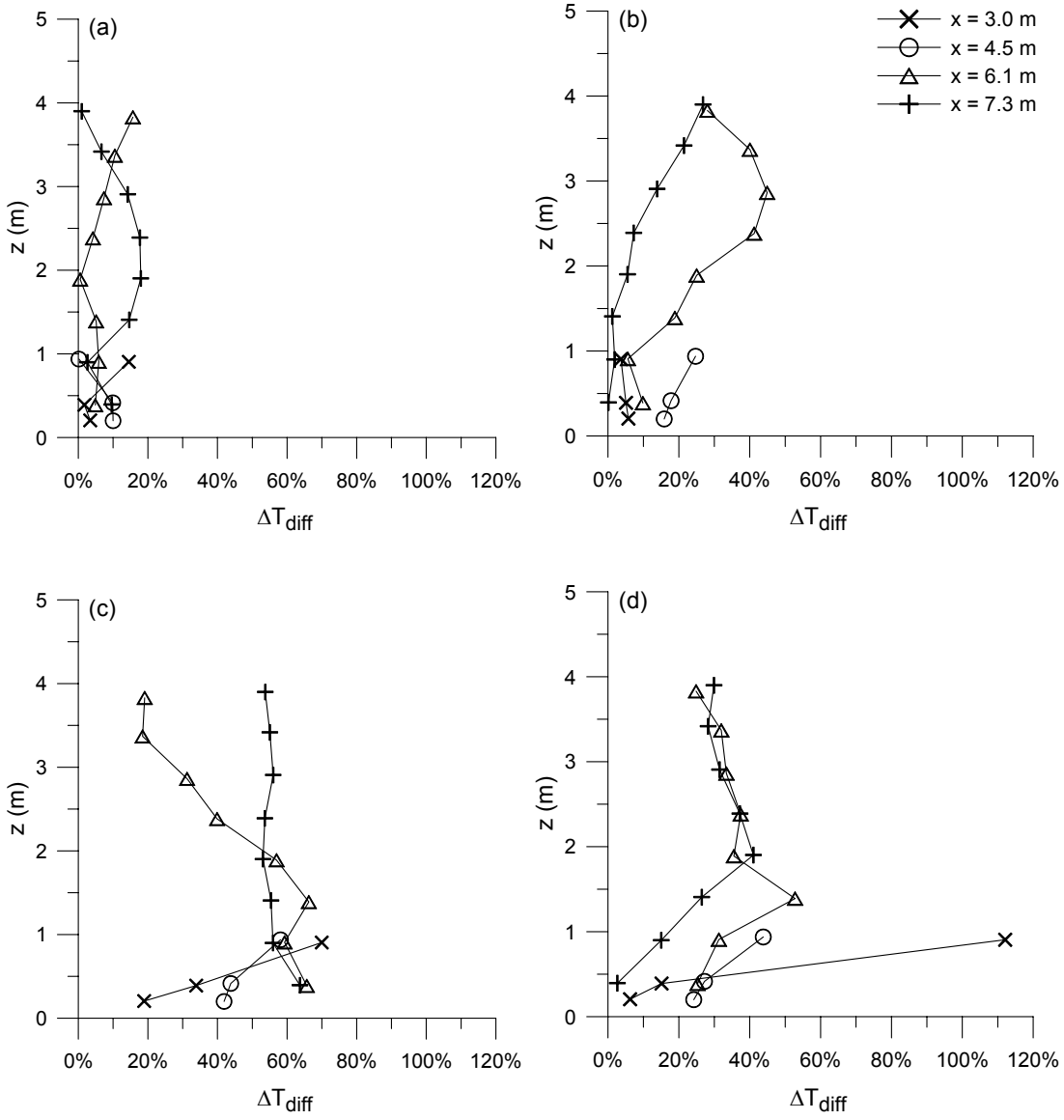

Figure 5.16: Percentage difference of $T_{ss} - T_{init}$ between tests conducted at the same wind speed (Equation 4.4), at y=0 m, (a) 5 m/s wind, (b) 7 m/s wind, (c) 10 m/s wind, (d) 13 m/s wind

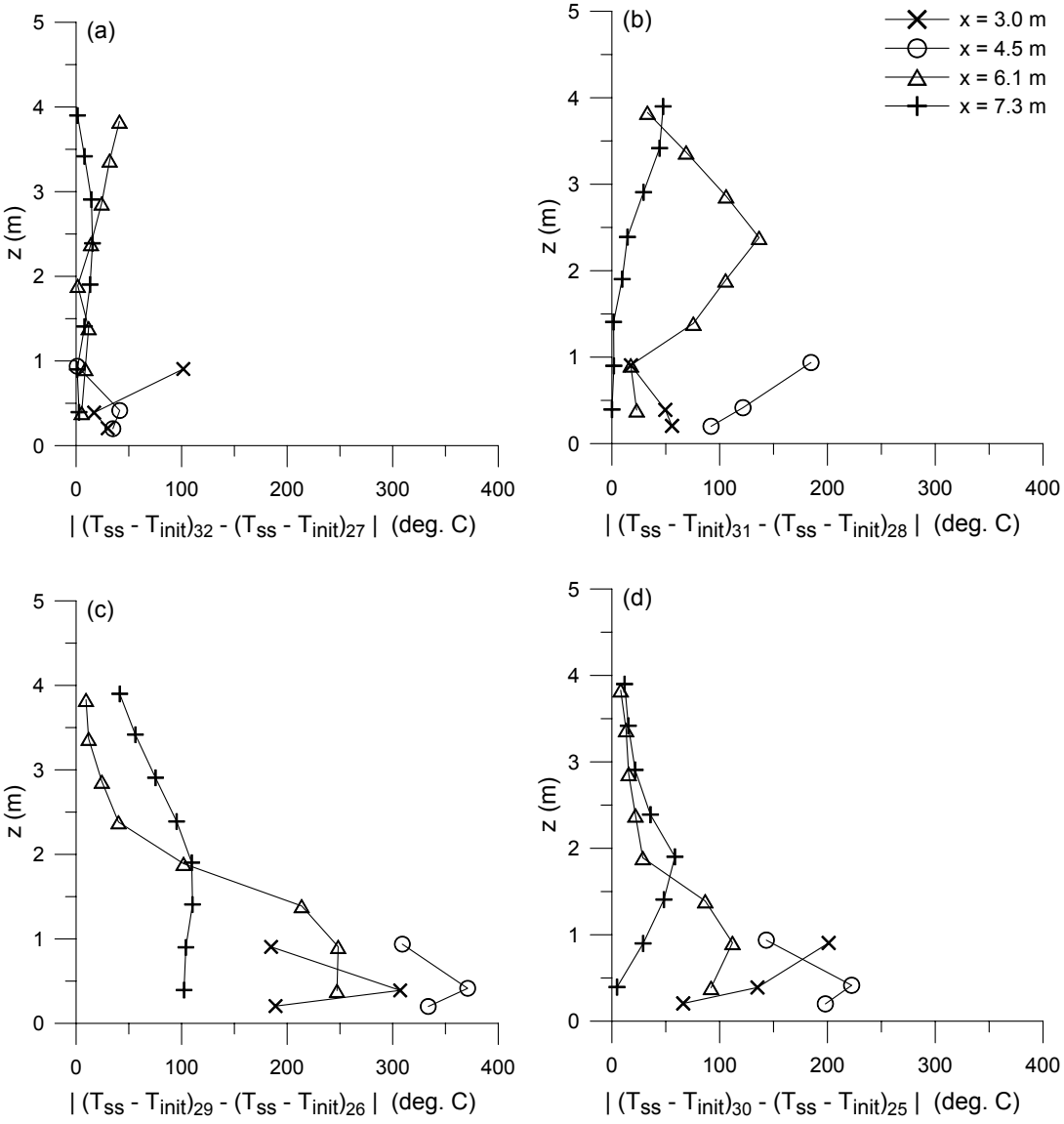

Figure 5.17: Absolute difference in $T_{ss} - T_{init}$ between tests conducted at the same wind speed (numerator of Equation 4.4), at y=0 m, (a) 5 m/s wind, (b) 7 m/s wind, (c) 10 m/s wind, (d) 13 m/s wind

Table 5.5: Fuel Mass Burning Rates, Based on Load Cell Measurements of Best [21]

Wind Speed	Test Number	Fuel Regression Rate (mm/min)	Mass Burning Rate (kg/m^{2}s)
5 m/s	27	4.5	0.060
	32	4.5	0.060
7 m/s	28	4.4	0.058
	31	4.7	0.063
10 m/s	26	4.6	0.061
	29	5.4	0.072
13 m/s	25	5.1	0.068
	30	6.0	0.080

13 m/s (Figures 5.16d and 5.17d). The large absolute differences of several hundred degrees at the lower elevations under these two highest wind speeds suggest major differences in temperature within the core region of the plume, which was not observed in the tests without the blocking object.[6] As shown previously in Figure 4.13, absolute differences between measured temperatures from repeated tests were typically less than 50°C when the blocking object was not in place, but this was based on only one set of repeated measurements and would need to be verified by additional tests without the object.

The poor test-to-test repeatability in the experiments conducted with the blocking object was supported by measurements of fuel regression rate made during the tests. Table 5.5 lists the burning rates measured by Best [21] using load cells placed underneath the fuel pan.[7] The difference in regression rate between tests conducted at the same wind speed was largest at the 10 m/s and 13 m/s wind speeds, consistent with the differences in plume temperature mentioned above. This was to be expected because fuel regression rate and plume temperature are interrelated, with higher plume temperatures increasing the fuel regression rate through greater heat feedback to the fuel surface. It should be mentioned, however, that other factors, such as ambient temperature, can also affect the fuel regression rate [20, 21, 51].

A potential cause of the large differences between measurements taken under the same wind speed is indicated by the temperatures measured along the blocking object at the beginning of each test. Figure 5.18 shows the initial blocking object

[6]However, as will be shown in later sections, part of this difference was caused by differences in symmetry of the plume across the longitudinal midplane y=0 m.

[7]An uncertainty of ±0.4 mm/min (or ±0.005 kg/m^{2}s) was previously estimated by Randsalu [20] for the load cell method of measuring fuel regression rate.

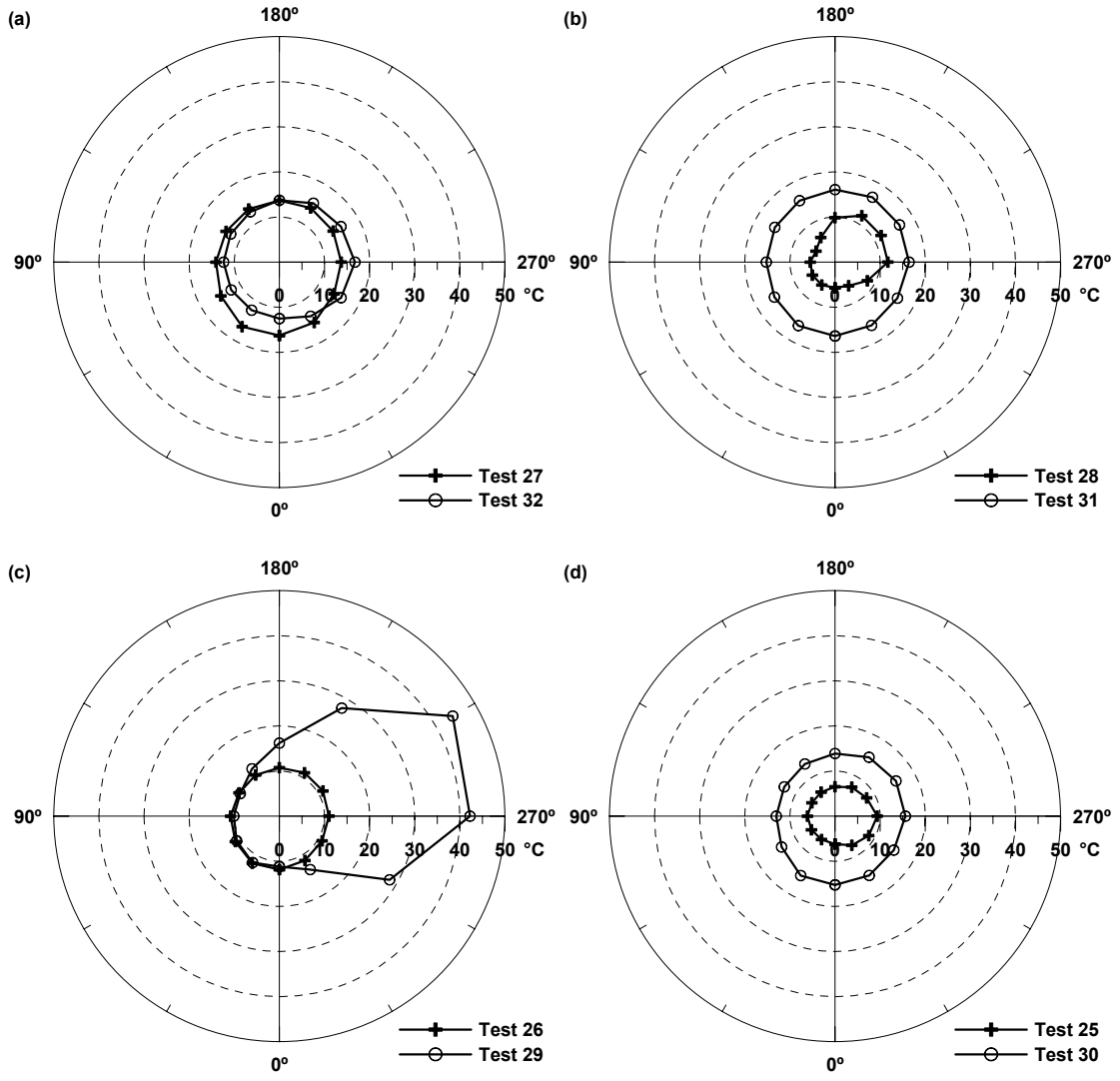

Figure 5.18: Initial temperatures along blocking object, y=0 m, (a) 5 m/s wind, (b) 7 m/s wind, (c) 10 m/s wind, (d) 13 m/s wind

temperatures measured along y=0 m immediately prior to startup of the first fan in each test. For the two tests involving the 5 m/s wind (Figure 5.18a), the initial temperatures differed by less than 5°C, while for the tests involving the 7 m/s and 13 m/s winds (Figure 5.18b and 5.18d), the initial temperatures differed by up to 11°C and 10°C, respectively. For the tests involving the 10 m/s wind (Figure 5.18c), the initial temperatures on the windward side of the object ($0° \leq \phi \leq 150°$) differed by less than 2°C, while those on the leeward side of the object ($180° \leq \phi \leq 330°$) differed by up to 33°C. This large difference on the leeward side of the object was due to radiation from the sun passing through the open exit door of the test enclosure and impinging on the blocking object in test 29. The initial temperature field along the blocking object likely would have influenced the overall thermal development of the fire, since less net radiation would occur from the fire to a warmer object. The higher initial object temperatures measured in tests 31, 29 and 30 for the 7 m/s, 10 m/s and 13 m/s wind conditions, respectively, could thus be a primary reason for the poor repeatability of the tests at these wind speeds.

Another possible contribution to differences between measurements taken in repeated tests was potential differences in the composition of the fuel. Although the fuel used in all eight tests arrived as a single shipment, it was divided among four drums, each with a capacity of 205 L. Since the fuel in each drum was used for two consecutive tests, the fuel burned in tests 29 and 30 may have been of slightly different composition than that burned in tests 25 and 26, further contributing to the differences in fuel regression rate shown in Table 5.5 and the larger values of ΔT_{diff} shown in Figures 5.16c and 5.16d.

Based on the above discussion, the test-to-test repeatability of the measured temperatures, a precision uncertainty, would form the dominant part of the total measurement uncertainty in the present experiments. However, this repeatability depends on experimental boundary conditions such as the initial temperature of the blocking object. Thus, the temperature differences seen in Figures 5.16 and 5.17 occurred not only due to random variations but also due to changes in the initial boundary conditions. When the initial boundary conditions were similar, as in tests 27 and 32 for the 5 m/s wind condition, the test-to-test repeatability of the plume temperatures was within 18% (Figure 5.16a). This value could therefore be used to estimate the precision uncertainty for the plume temperatures and, since the plume and object temperatures are interrelated through heat transfer effects, also the object temperatures. Combination of the precision and systematic uncertainties using Equation 4.1 (page 88) then results in estimated values of 43%, 49% and 44%

for the total measurement uncertainty in temperatures measured in the core of the fire, near the edge of the fire and along the blocking object, respectively.

A final note on uncertainty should be made with regard to the calorimeters described in Section 5.1.3. Since the calorimeter was based on the same principle of measuring heat flux as the DFT, it would be expected to be influenced by the same sources of error as those discussed for the DFT in Chapters 3 and 4. In particular, effects of lateral conduction would be expected to be significant, especially if the calorimeter was not fully engulfed in the fire. Previous investigations into the error in using a one-dimensional conduction assumption for this type of calorimeter in fires indicated uncertainties of 10-20%, depending on how uniformly the calorimeter was heated [159,199]. This could be combined with the 20% uncertainty estimated by Figueroa *et al.* [160] (which did not include effects of two- or three-dimensional conduction) associated with using IHCP1D to determine the net heat flux to calorimeters similar to those used in the present study. For incident heat flux results, the uncertainty associated with the emissivity of the calorimeter surface would also need to be considered and has been estimated by others to be approximately 10% [137]. If the above uncertainties were combined using a root-sum-square method, the total uncertainty for the measured heat flux values from the calorimeter would be 24-30%. These estimates do not include the uncertainty associated with repeatability of the measurements, which would depend on the initial temperature conditions of the test section, the blocking object and each calorimeter.

Since the tests repeated at each wind speed appeared to be affected by the initial temperature field along the blocking object, the results of individual tests (rather than values averaged over the two tests conducted at each wind speed) will be reported in this chapter. As in the previous chapter, experimental data will be presented in terms of *increases* in temperature or heat flux in order to minimize differences in initial temperatures between tests. Temperatures measured in the fire plume and along the blocking object will be discussed in the next section, followed by selected heat flux results.

5.3 Results and Discussion: Temperature

A typical time trace of temperatures measured along a thermocouple chain situated 1.52 m downwind of the fuel pan centre (1.92 m upwind of the longitudinal axis of

the blocking object) is shown in Figure 5.19. The plot clearly shows the temperature decreasing with increasing height above the floor, as well as the general pattern of an initial increase in temperature after ignition, followed by a marked period of steady burning. Given the similarity in shape of the temperature curves between this plot and the one in Figure 4.11 for the experiments without the blocking object, the technique used to reduce the temperature data in Chapter 4 (i.e. calculation of $T_{ss} - T_{init}$) was considered appropriate for the present tests as well. Table 5.6 lists the duration of the steady burning period for each test, determined using the procedure described in Section 4.2.

Of the 163 thermocouples used to measure plume temperature, up to 21 thermocouples (13%) failed during a test due to intense heating by the fire. Most of the failures occurred in tests 25 to 28. The number of failures in tests 29 to 32 was minimized by insulating the lengths of thermocouple running down the six chains

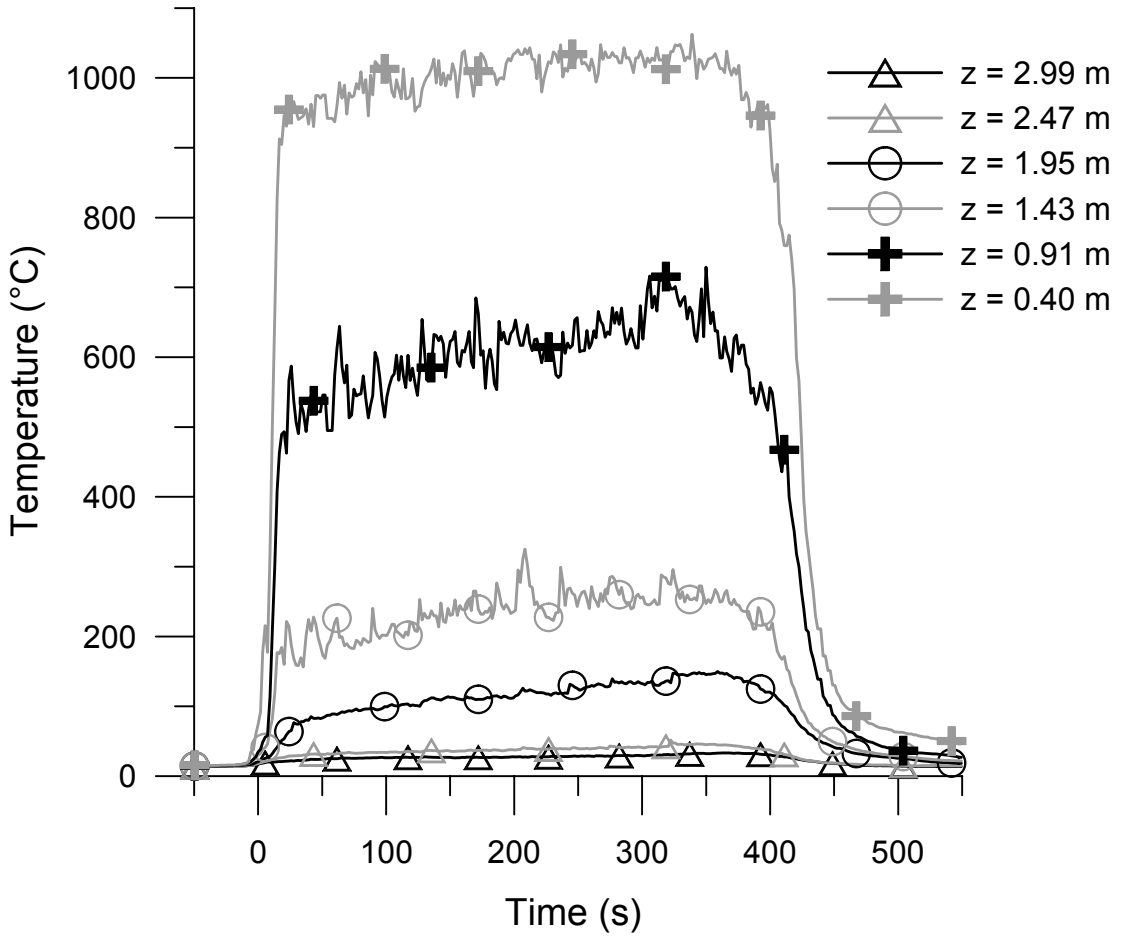

Figure 5.19: Typical plot of plume temperatures, 7 m/s wind (test 31), x=1.52 m, y=0.00 m

Table 5.6: Duration of Steady Burning Period for Tests with Blocking Object

Test Number	Wind Speed	Total Test Length	Start of Steady Burning	Duration of Steady Burning
25	13 m/s	475 s	213 s	138 s
26	10 m/s	485 s	218 s	147 s
27	5 m/s	600 s	208 s	221 s
28	7 m/s	523 s	196 s	176 s
29	10 m/s	534 s	225 s	150 s
30	13 m/s	399 s	159 s	137 s
31	7 m/s	490 s	227 s	132 s
32	5 m/s	597 s	239 s	172 s

located nearest the fuel pan (Figure 5.4, x=1.1 m and 1.5 m). Despite the relatively large number of failed thermocouples in tests 25 to 28, the data recorded prior to failure could still be used to obtain estimates of plume temperature. A quasi-steady burning period occurring after the initial increase in temperature and prior to failure of the thermocouple could be identified in most of the temperature time traces. Averaged temperatures were calculated over these quasi-steady periods, which lasted between 25 s and 150 s. These were included in the results presented in this section. For up to six failed thermocouples per test, no quasi-steady period could be identified in the temperature time curves, so no averaged data were available at the corresponding thermocouple locations. All averaged temperatures reported in this section are listed in Appendix D.

Figure 5.20 shows a typical time trace of temperatures measured along the centreline of the blocking object in the plane y=0.00 m. (For clarity, not all temperatures measured in this plane are shown. Time traces of object temperatures measured at other wind speeds are contained in Appendix E.) It is clear from the plot that temperatures measured near the bottom of the object ($\phi = 0°$, $30°$ and $330°$) were much hotter than those at the top of the object ($\phi = 180°$). Due to the large thermal mass of the blocking object, no steady-state temperatures were reached over the duration of the test. Instead, the temperature curves continuously increased until approximately 360 s, which corresponded to the end of the steady burning period (Table 5.6), and then decreased as the fuel burned out. In order to characterize the effect of the fire on the object at each wind speed, the maximum temperature measured by each thermocouple in the object was deemed to be the most appropriate comparison parameter. However, the maximum temperature at each measurement location did not occur at exactly the same time during a test.

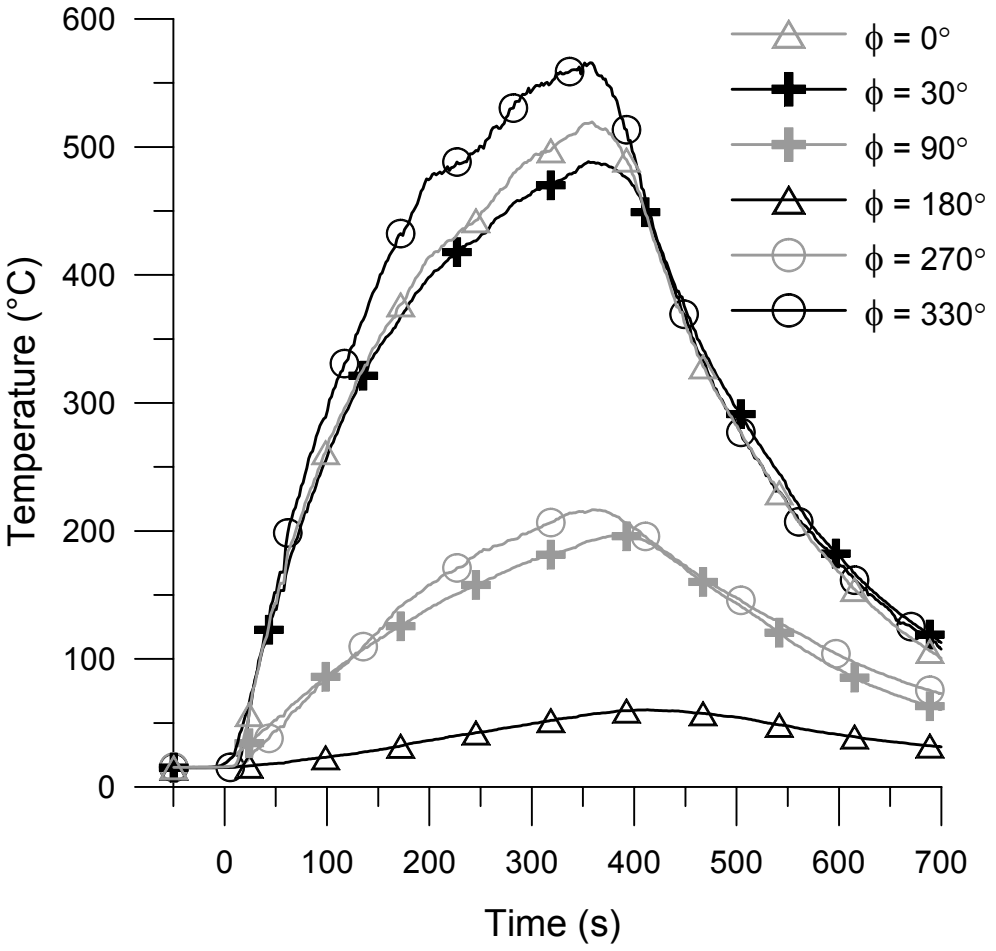

Figure 5.20: Typical plot of temperatures along inside surface of blocking object, 7 m/s wind (test 31), y=0.00 m

Due to the thermal inertia of the blocking object, measurements from thermocouples exposed least directly to the fire (e.g. at $\phi = 180°$ and along y=2 m) reached a maximum value up to 1.5 minutes later than measurements from thermocouples exposed most directly to the fire (e.g. at $\phi = 0°$ and along y=0 m). To avoid having to report a different time for each maximum temperature, a single time, at which most of the measured object temperatures were at or very close to their maximum, was selected for each test. The temperatures measured at this selected time, minus initial values measured immediately prior to startup of the first fan, are presented in this section and listed in Appendix F. Differences between the listed temperatures and the true maximum temperatures attained by the thermocouples were within 10°C, which typically represented 5% of the maximum temperature.

In the following sections, the macroscopic characteristics of the fire will be discussed for each of the 5 m/s, 7 m/s, 10 m/s and 13 m/s wind speeds. For each wind condition, video images are first presented to show the overall features of the fire. This is followed by discussion of temperature data measured in the fire plume and along the blocking object.

5.3.1 Fire in 5 m/s Wind with Blocking Object

Typical single-frame images of the fire from video cameras placed upwind and downwind of the blocking object are shown in Figure 5.21 for the 5 m/s wind condition. Corresponding time-averaged images, based on 60 frames sampled half a second apart, are shown in Figure 5.22. As in the test without the blocking object (Section 4.4.2), the fire was tilted significantly and was attached to the raised floor surround and brick floor downwind of the fuel pan. However, comparing Figure 5.22a with Figure 4.20, the leading edge of the luminous envelope immediately above the fuel pan appeared to be less well-defined when the blocking object was in place, indicating higher levels of turbulence and greater variations in shape of the luminous flame zone. Further, as evident in Figure 5.21, the fire impinged on the lower windward side and bottom of the blocking object before spreading up the leeward side. Significant smoke obscuration was apparent in the region downwind of the object (Figure 5.22b). No angles of plume tilt were measured due to interference on the plume by the blocking object and the consequent lack of a meaningful definition of plume tilt for this situation.

Figures 5.23 and 5.24, which contain plots of the time-averaged increase in plume temperature along the longitudinal midplane y=0 m for the two tests at

Figure 5.21: Typical video frames showing fire in 5 m/s wind, (a) upwind of blocking object, (b) downwind of blocking object

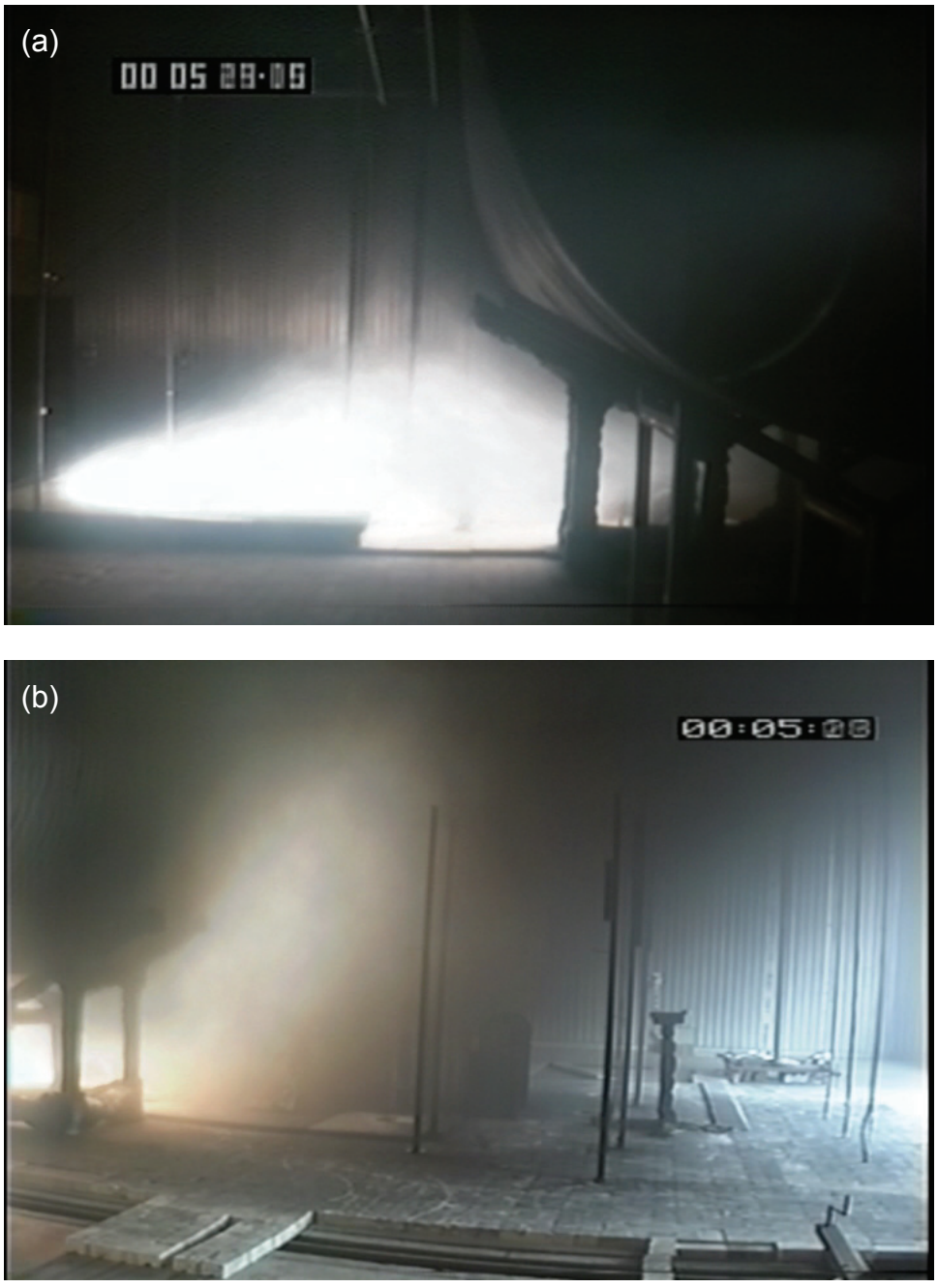

Figure 5.22: Typical 60-frame time-averaged images showing fire in 5 m/s wind, (a) upwind of blocking object, (b) downwind of blocking object

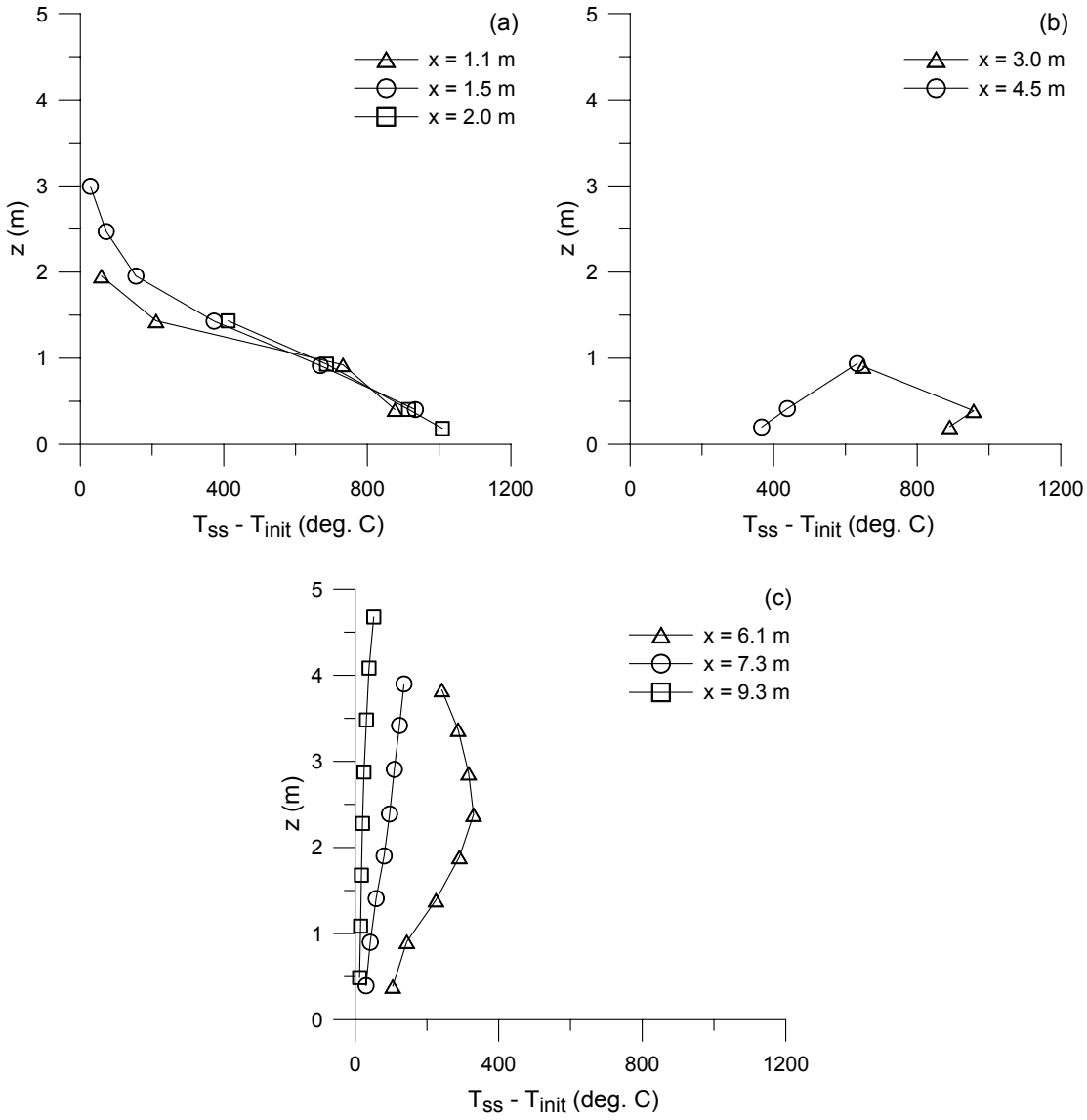

Figure 5.23: Line plot of increase in plume temperature under 5 m/s wind (test 27), y=0 m, (a) upwind of blocking object, (b) underneath blocking object, (c) downwind of blocking object

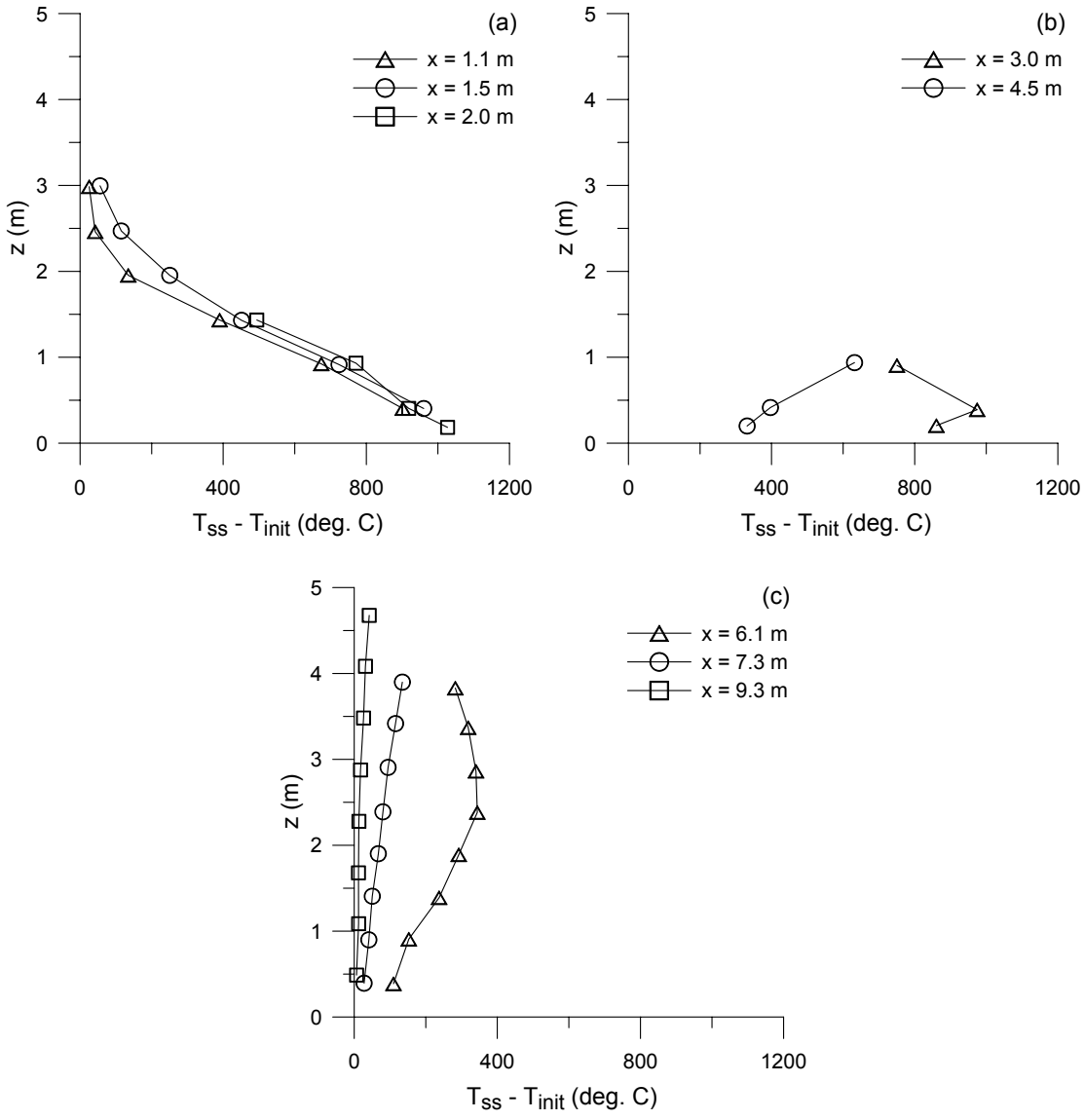

Figure 5.24: Line plot of increase in plume temperature under 5 m/s wind (test 32), y=0 m, (a) upwind of blocking object, (b) underneath blocking object, (c) downwind of blocking object

the 5 m/s wind speed, show trends in plume behaviour consistent with the video images. The plume was attached to the ground up to 2 m downwind of the fuel pan centre, as indicated by the trend of increasing temperature with decreasing elevation in each of the temperature profiles shown in Figures 5.23a and 5.24a. The plume appeared to lift off the ground as it passed underneath the blocking object (Figures 5.23b and 5.24b) and quickly gained height as it rose up the leeward side of the culvert (Figures 5.23c and 5.24c). The centre of the plume was located at a height of approximately z=2.4 m along the measurement plane x=6.1 m, while further downwind, along the planes x=7.3 m and 9.3 m, the plume centre was above the highest thermocouples.

To augment the temperature line plots shown in Figures 5.23 and 5.24, contour plots of the same temperature data were generated and are included in Figures 5.25 and 5.26. Due to the presence of the blocking object, each contour plot was created in three sections corresponding to regions between the downwind edge of the fuel pan and the upwind edge of the object (1.1 m $\leq$ x $\leq$ 2.0 m), underneath the object (2.0 m $\leq$ x $\leq$ 6.1 m) and downwind of the object (6.1 m $\leq$ x $\leq$ 9.3 m). Data from these sections were then superimposed to produce the contour plots seen in Figures 5.25 and 5.26. Although insufficient temperature measurements prevented generation of valid contours in the region immediately downwind of the blocking object (4.5 m $\leq$ x $\leq$ 6.1 m, z $\geq$ 1 m), an overall picture of the plume could still be obtained from the superimposed plot. The shape of the contours indicated that the plume was attached to the ground immediately downwind of the fuel pan and that hot gases impinged on the lower windward side of the culvert, consistent with the video images. The plume also appeared to be wrapped around the bottom of the culvert, rising on the leeward side. Comparing both contour plots to Figure 4.21, which shows the corresponding plot without the blocking object, the direction of plume travel was clearly affected by the presence of the object. For instance, Figure 4.21 indicates that the centre of the plume at a downwind distance of x=6.1 m was located at a height of 1.6 m, whereas Figures 5.25 and 5.26 indicate that the centre of the plume at the same downwind distance was located at a height of approximately 2.7 m. In addition, temperatures measured underneath the blocking object were lower than those measured in the same locations without the object in place. For example, Figure 4.21 indicates that temperatures greater than 1000°C occurred at a downwind distance of x=3 m, at z $\leq$ 0.5 m, and that temperatures up to 900°C occurred 1 m further downwind, at x=4 m and between z=0.2 m and 0.9 m. However, when the blocking object was present (Figures 5.25 and 5.26),

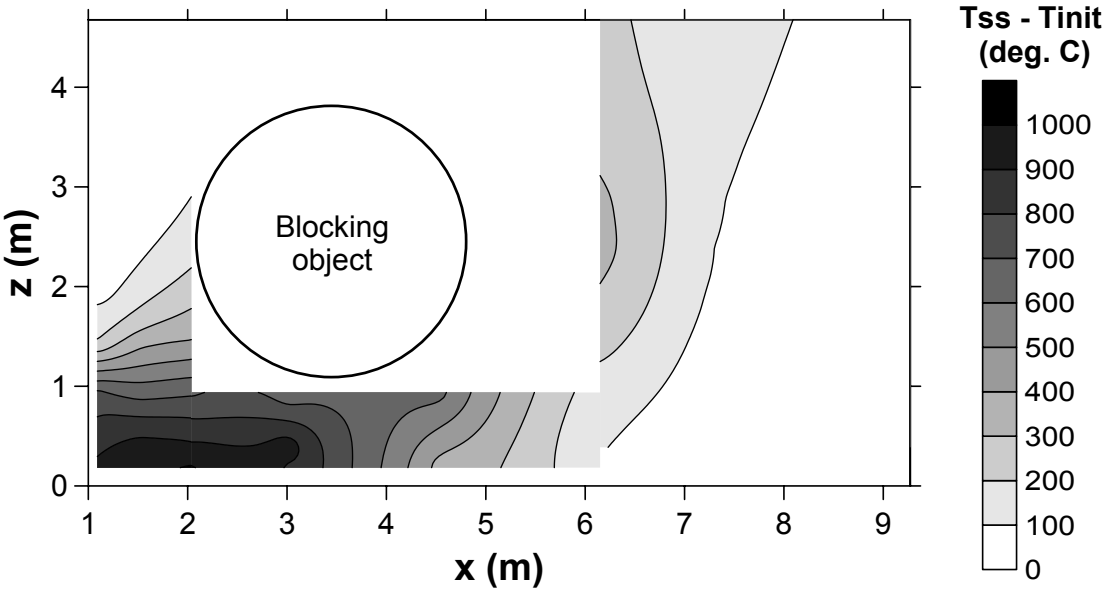

Figure 5.25: Contour plot of increase in plume temperature under 5 m/s wind (test 27), y=0 m

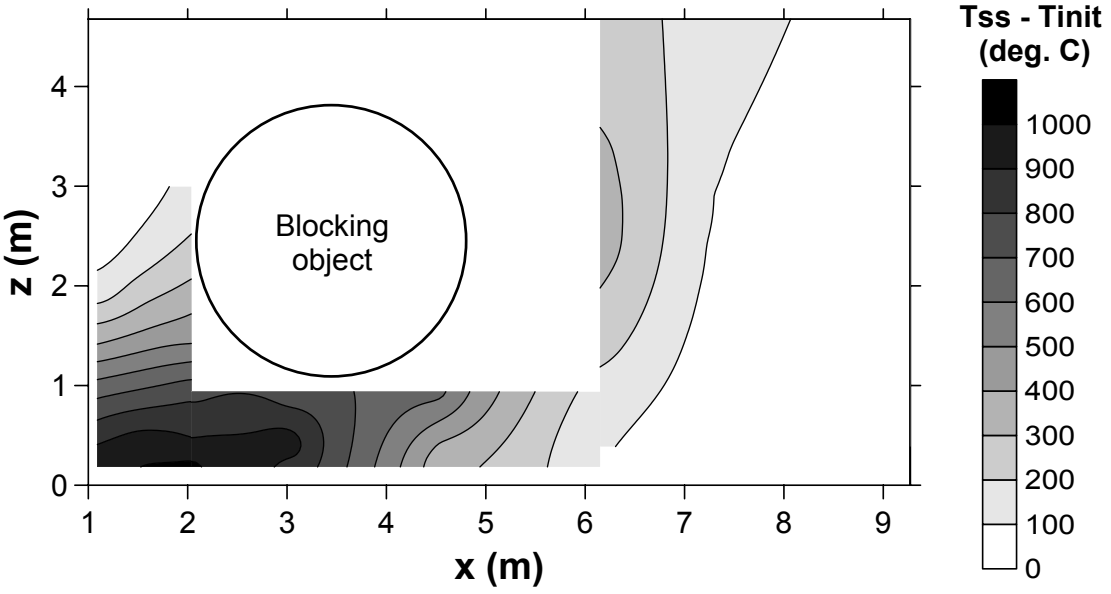

Figure 5.26: Contour plot of increase in plume temperature under 5 m/s wind (test 32), y=0 m

temperatures remained less than 1000°C along x=3 m and less than 700°C along x=4 m, suggesting that impingement of the fire plume on the thermally massive blocking object lowered plume temperatures in that region by up to 200°C.

The maximum increases in temperature measured along the inside surface of the blocking object in the plane y=0 m were consistent with the shape of the plume described above. As shown in Figure 5.27, the largest temperature increases, ranging between 560°C and 664°C, occurred along the bottom and leeward side of the object (ϕ=0°, 30°, 300° and 330°), indicating the region of greatest exposure to the fire plume.[8] Temperature increases ranging from 420°C to 546°C occurred further up the object on both sides, at ϕ=60° and 270°. The top portion of the object, from ϕ=120° to 210°, experienced the lowest temperature increases, less than 155°C.

Changes in temperature across the width of the plume upwind and downwind of the blocking object are shown in Figures 5.28 and 5.29, respectively. The plotted data depict horizontal temperature profiles along different heights and at various downwind distances. Figure 5.28 shows temperature profiles along two or more heights in each of the measurement planes x=1.1 m, 1.5 m and 2.0 m, while Figure 5.29 shows two temperature profiles along the plane x=3.0 m and one temperature profile along each of the planes x=4.5 m, 6.1 m, 7.3 m and 9.1 m. The temperature profiles plotted for the downwind distances between x=4.5 m and 9.1 m were selected to correspond to a height located near the plume centre. Upwind of the object (Figure 5.28), the temperature profiles did not consistently exhibit a maximum value at the same y location. In general, the profiles corresponding to higher elevations indicated higher temperatures on the -y side of the test enclosure, while those near the floor (at z=0.2 m or 0.4 m) were reasonably symmetrical and indicated a maximum temperature in the longitudinal midplane y=0 m. A similar trend could be observed in the temperature profiles along x=3.0 m (Figure 5.29). Given that the fire was attached to the ground at these downwind distances (Figures 5.25 and 5.26), this suggested that the fire was initially centred on the longitudinal midplane, but tended to move in the -y direction with increasing height. The skew in plume direction was clearly supported by the temperature profiles measured downwind of the object in Figure 5.29. Post-test examination of the experimental layout revealed that the blocking object was shifted off centre by approximately 0.20 m in the +y direction, due to inherent difficulties in accurately positioning such a large cylinder

[8]No data point was available at the measurement location ϕ=30° in test 32 due to failure of the thermocouple midway through the test.

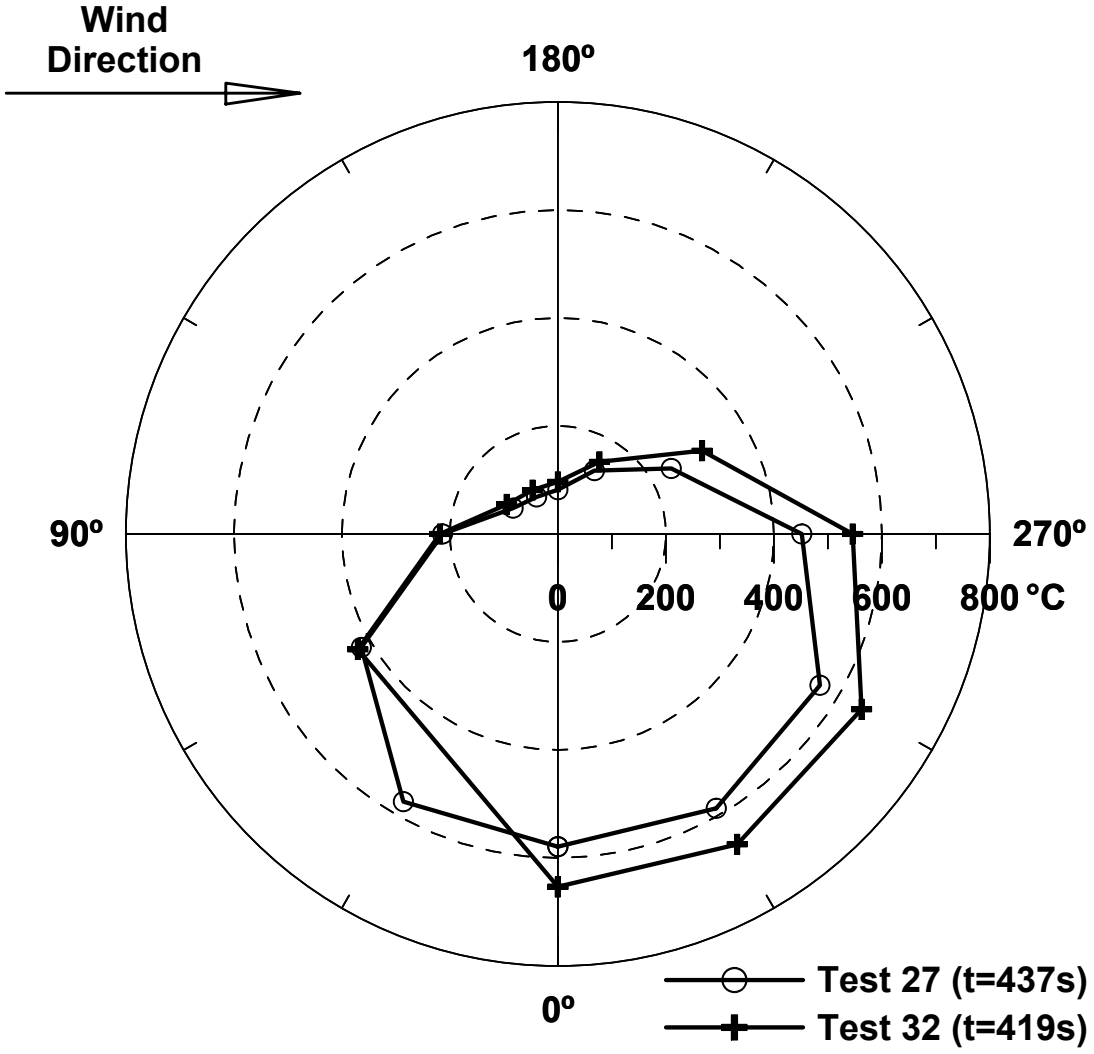

Figure 5.27: Temperature profile along inside surface of blocking object, y=0 m, 5 m/s wind

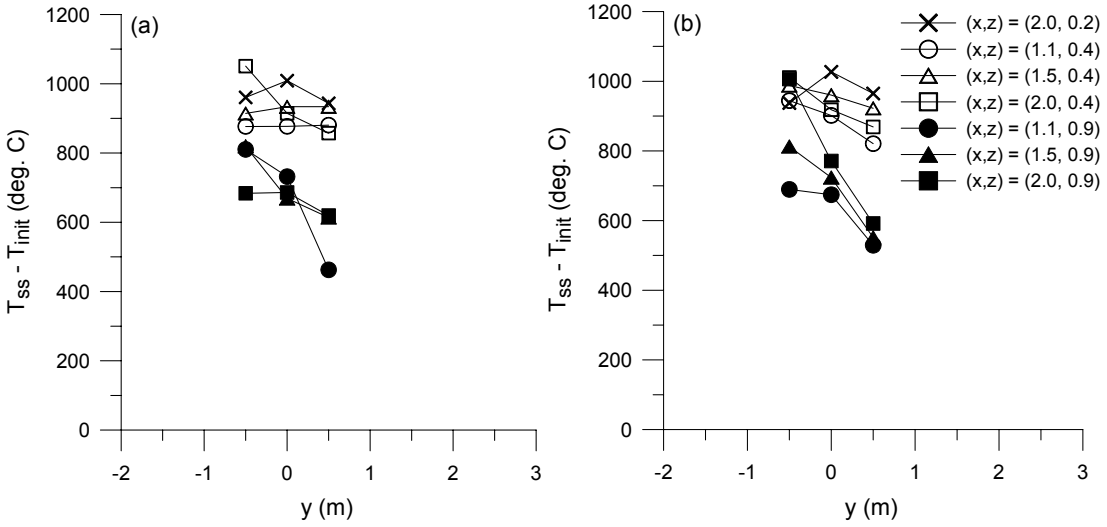

Figure 5.28: Temperature profile across width of plume upwind of blocking object, 5 m/s wind (x and z coordinates in metres), (a) test 27, (b) test 32

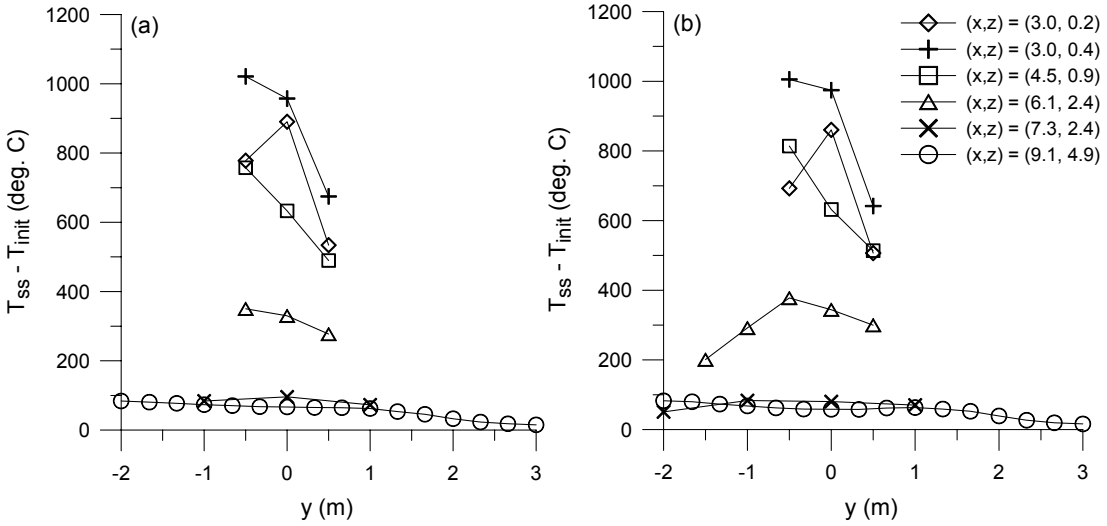

Figure 5.29: Temperature profile across width of plume underneath and downwind of blocking object, 5 m/s wind (x and z coordinates in metres), (a) test 27, (b) test 32

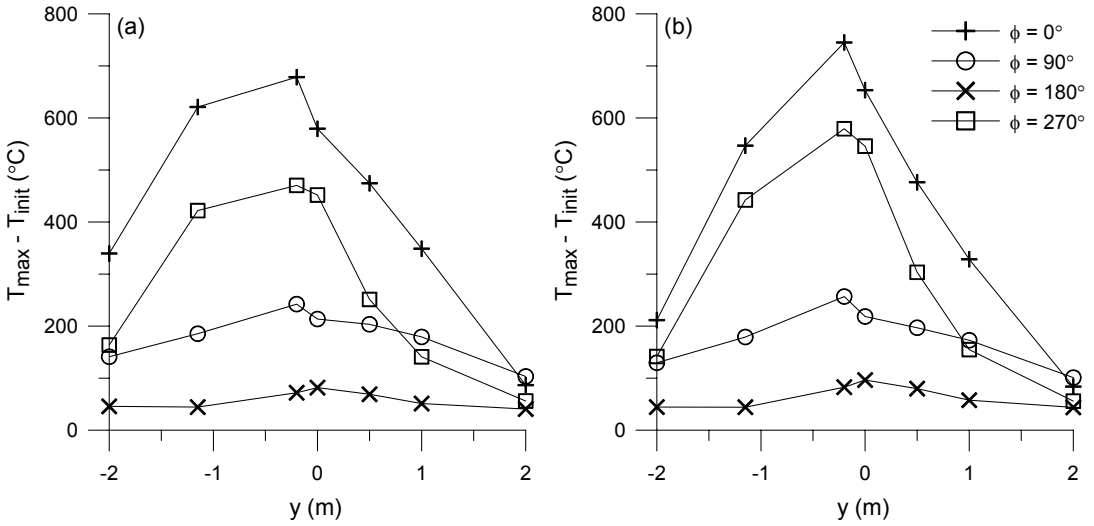

Figure 5.30: Temperature profile along inside surface of blocking object in longitudinal direction, 5 m/s wind, (a) test 27, (b) test 32

inside the test enclosure. As the flow from the fans passed through the enclosure, this offset may have been sufficient to cause the pressure on the -y side of the test section to be lower than that on the +y side, resulting in a tendency for the fire plume to become skewed in the -y direction. At a downwind distance of x=6.1 m, the plume was centred at approximately y=-0.5 m (Figure 5.29b), indicating an overall skew angle of approximately 5°.

Temperature profiles measured along the blocking object in the longitudinal (y) direction were consistent with the observation of a skewed plume. As shown in Figure 5.30, the highest temperature increase in each test was measured along the bottom of the object (ϕ=0°) at y=-0.20 m. No object temperatures were measured at locations between y=-0.20 m and -1.15 m because they would have been taken behind the steel band used to join the culvert sections together (Section 5.1.2) and thus would have been lower than expected. In each of the tests shown, the temperature profile measured along ϕ=270° (denoted by square symbols) was of similar shape to that measured along ϕ=0° (denoted by '+' symbols), consistent with the observation that the bottom and leeward side of the blocking object were most directly exposed to the plume. In contrast, regions along ϕ=90° and 180° received much less exposure to the plume, so the corresponding temperature profiles were of lower magnitude and less asymmetrical than those at ϕ=0° and 270°.

5.3.2 Fire in 7 m/s Wind with Blocking Object

Typical single-frame and time-averaged images of the fire in the 7 m/s wind condition are shown in Figures 5.31 and 5.32. Compared to the 5 m/s wind condition (Figures 5.21 and 5.22), the fire was tilted further over and appeared to impinge on the bottom of the blocking object, but not on the lower windward side of the culvert. The flaming region also did not appear to spread significantly up the leeward side of the culvert at this higher wind speed. High levels of smoke production were evident in the region downwind of the blocking object (Figure 5.32b).

Figures 5.33 to 5.36 contain line and contour plots of the time-averaged increase in plume temperature along the longitudinal midplane y=0 m. Comparison of Figures 5.33 and 5.35 to Figures 5.34 and 5.36, respectively, shows that higher temperature increases were measured in test 31 than in test 28 at locations in the core region of the plume underneath and downwind of the blocking object. (A similar general trend could be seen in the region upwind of the object, although the differences were much more obvious in the regions underneath and downwind of the object.) As discussed in Section 5.2, this was likely due to higher initial temperatures in the blocking object in test 31, causing the object to receive less net radiation from the fire and resulting in higher temperatures in the plume at a given downwind distance. Although differences in the measured temperatures ranged up to 185°C, as indicated in Figure 5.17b, the overall shape of the plume in both tests was similar, permitting characterization of the macroscopic features of the plume from the temperature data.

Noticeable differences in plume shape and travel were observed when the fire was in the 7 m/s wind, compared to the 5 m/s wind. The plume remained attached to the ground up to at least x=3.0 m (based on Figures 5.33 and 5.34) and the temperature contours in this region were oriented approximately parallel to the ground, as seen most evidently in Figure 5.36. Temperature gradients measured along the vertical thermocouple rakes were steeper in the 7 m/s wind condition than in the 5 m/s wind condition (e.g. compare Figures 5.33a and 5.24a), consistent with the notion of the plume lying closer to the ground under a higher wind speed. The plume continued to hug the ground until it was underneath the leeward half of the blocking object, when the hot gases rose due to buoyancy (Figures 5.35 and 5.36). The plume centre then reached a height of approximately 1.9 m by a downwind distance of x=6.1 m, based on the temperature profiles shown in Figures 5.33c and 5.34c. At x=7.3 m, the plume centre was located between z=2.9 m and 3.4 m, with

Figure 5.31: Typical video frames showing fire in 7 m/s wind, (a) upwind of blocking object, (b) downwind of blocking object

Figure 5.32: Typical 60-frame time-averaged images showing fire in 7 m/s wind, (a) upwind of blocking object, (b) downwind of blocking object

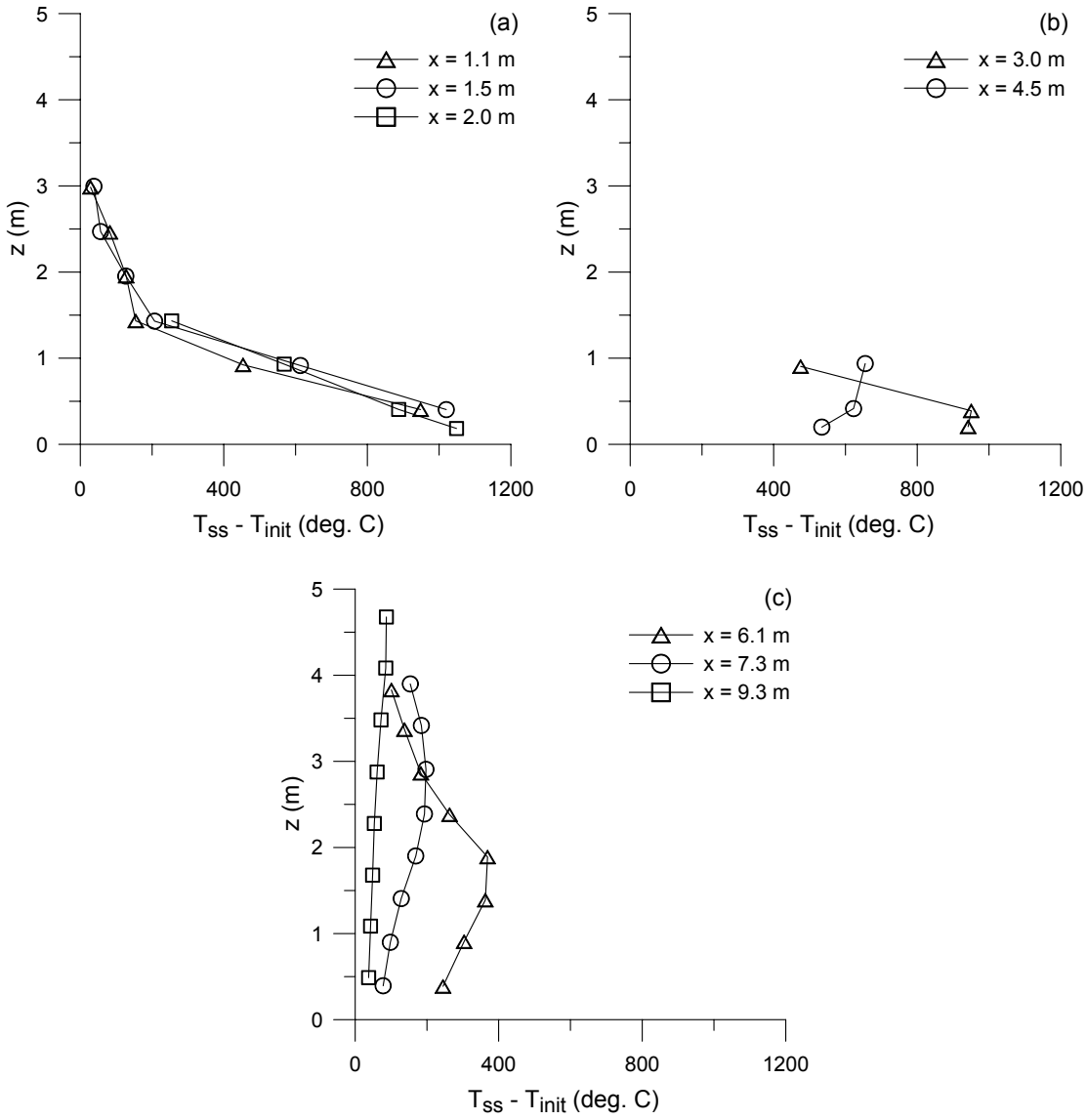

Figure 5.33: Line plot of increase in plume temperature under 7 m/s wind (test 28), y=0 m, (a) upwind of blocking object, (b) underneath blocking object, (c) downwind of blocking object

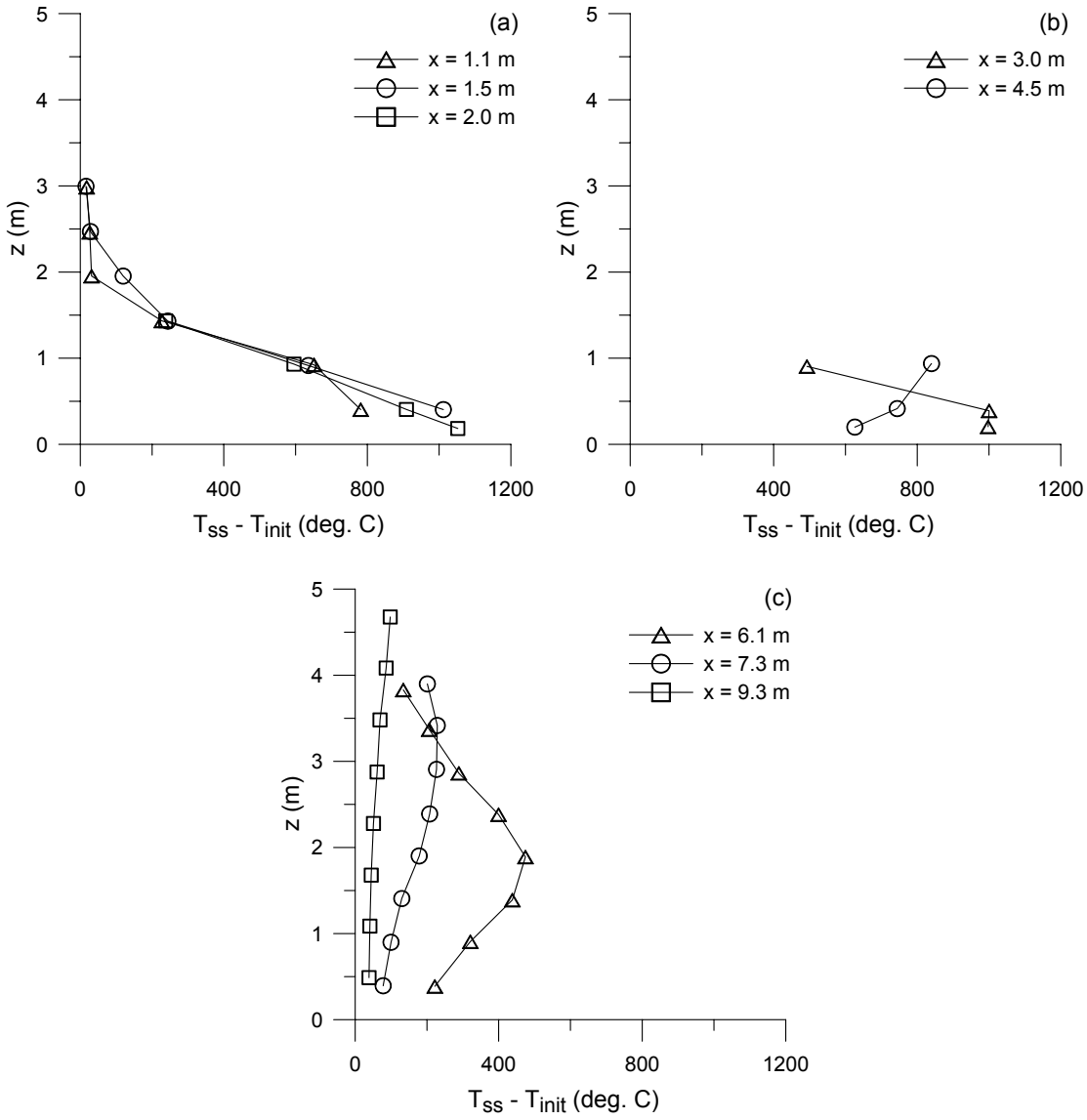

Figure 5.34: Line plot of increase in plume temperature under 7 m/s wind (test 31), y=0 m, (a) upwind of blocking object, (b) underneath blocking object, (c) downwind of blocking object

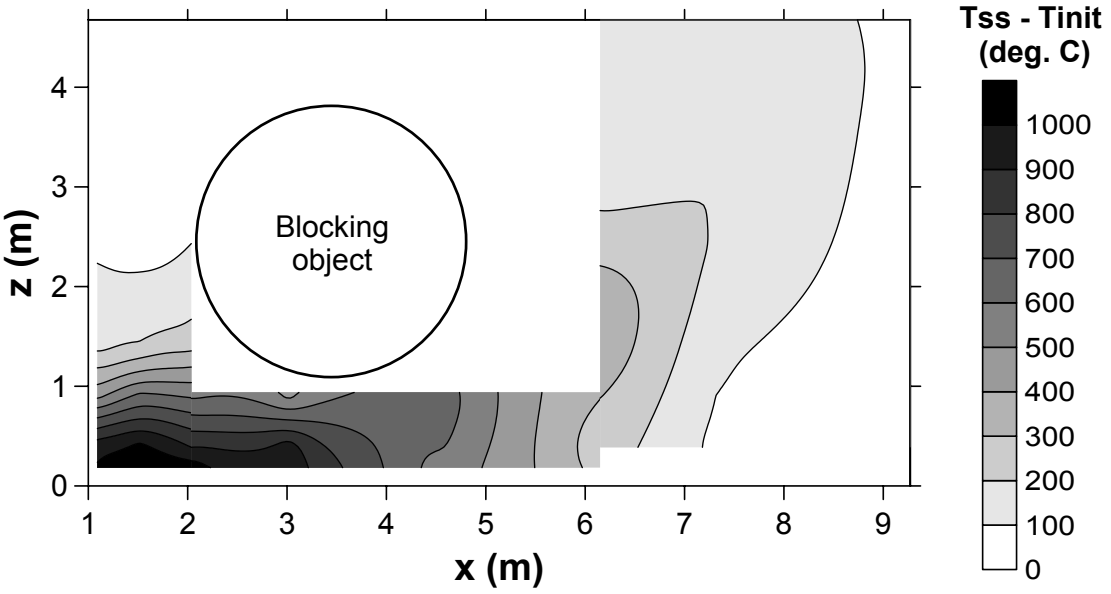

Figure 5.35: Contour plot of increase in plume temperature under 7 m/s wind (test 28), y=0 m

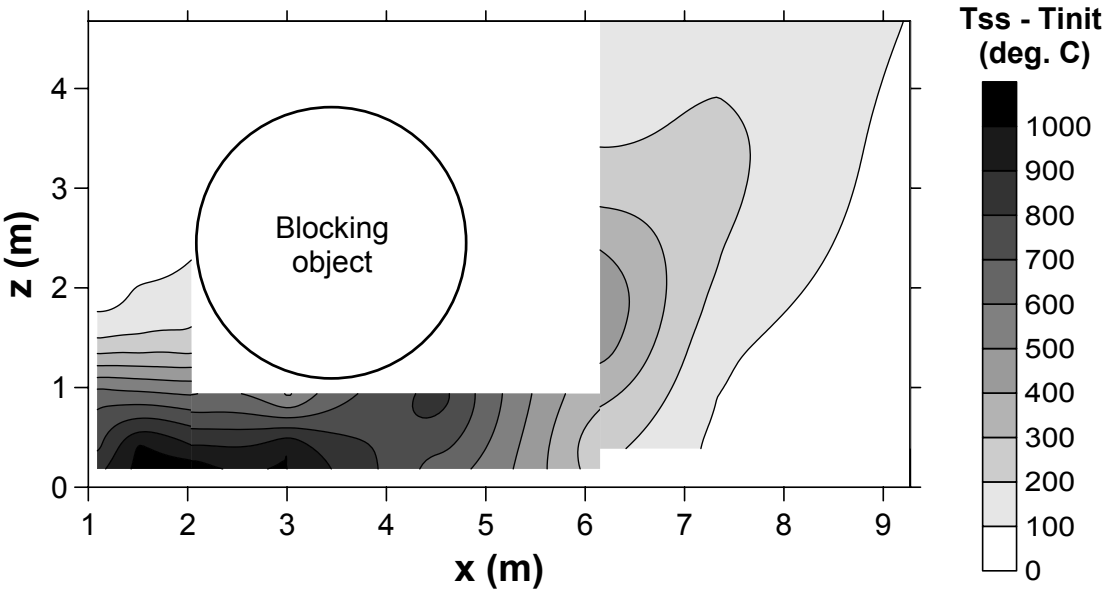

Figure 5.36: Contour plot of increase in plume temperature under 7 m/s wind (test 31), y=0 m

the lower elevation corresponding to test 28 (Figure 5.33c) and the higher elevation corresponding to test 31 (Figure 5.34c).

Comparison of Figures 5.35 and 5.36 to Figure 4.27, which contains the corresponding contour plot without the blocking object, shows the effect of the object on the direction of plume travel. In Figure 4.27, the shape of the contours indicates that the plume remained close to the ground until approximately x=7 m, whereas in Figures 5.35 and 5.36, the plume remained close to the ground only until approximately x=4 m. This difference suggests that both buoyancy and the low-pressure wake region immediately downwind of the object contributed to the rising of the plume gases underneath the leeward half of the blocking object.

Temperature increases measured along the inside surface of the blocking object were consistent with the above description of the plume. The greatest increases occurred near the bottom of the culvert, at ϕ=0°, 30° and 330° (Figure 5.37). At these locations, the measured temperature increases were between 456°C and 549°C, lower than the corresponding temperature increases recorded for the 5 m/s wind condition (Figure 5.27). This was consistent with the observation that the plume lay closer to the ground under the higher wind speed because it would have been located effectively further from the outside surface of the object, resulting in lower temperatures along the object. The temperature profiles in Figure 5.37 also indicated that at the 7 m/s wind speed, the windward and leeward sides of the blocking object received similar levels of thermal exposure, supporting the observation from the video images that the flaming region did not spread significantly up the leeward side of the object.

Temperature profiles measured along the width of the plume (Figures 5.38 and 5.39) indicated that the fire was generally skewed toward the -y side of the test enclosure, similar to the 5 m/s wind condition. Based on the profiles from x=1.1 m to 3.0 m, the fire appeared to develop somewhat symmetrically across the longitudinal midplane of the test enclosure at the lowest elevations, but shift in the -y direction with increasing height. This shift in plume direction was supported by temperature profiles measured both downwind of and along the bottom of the blocking object (Figures 5.39 and 5.40). The plots in Figure 5.39 indicate a similar angle of skew in the plume as for the 5 m/s wind condition, with the plume centre located at approximately y=-0.5 m at downwind distances of x=6.1 m and 7.3 m. The temperature profile corresponding to ϕ=0° on the blocking object also peaked at y=-0.2 m (Figure 5.40), similar to the 5 m/s wind tests.

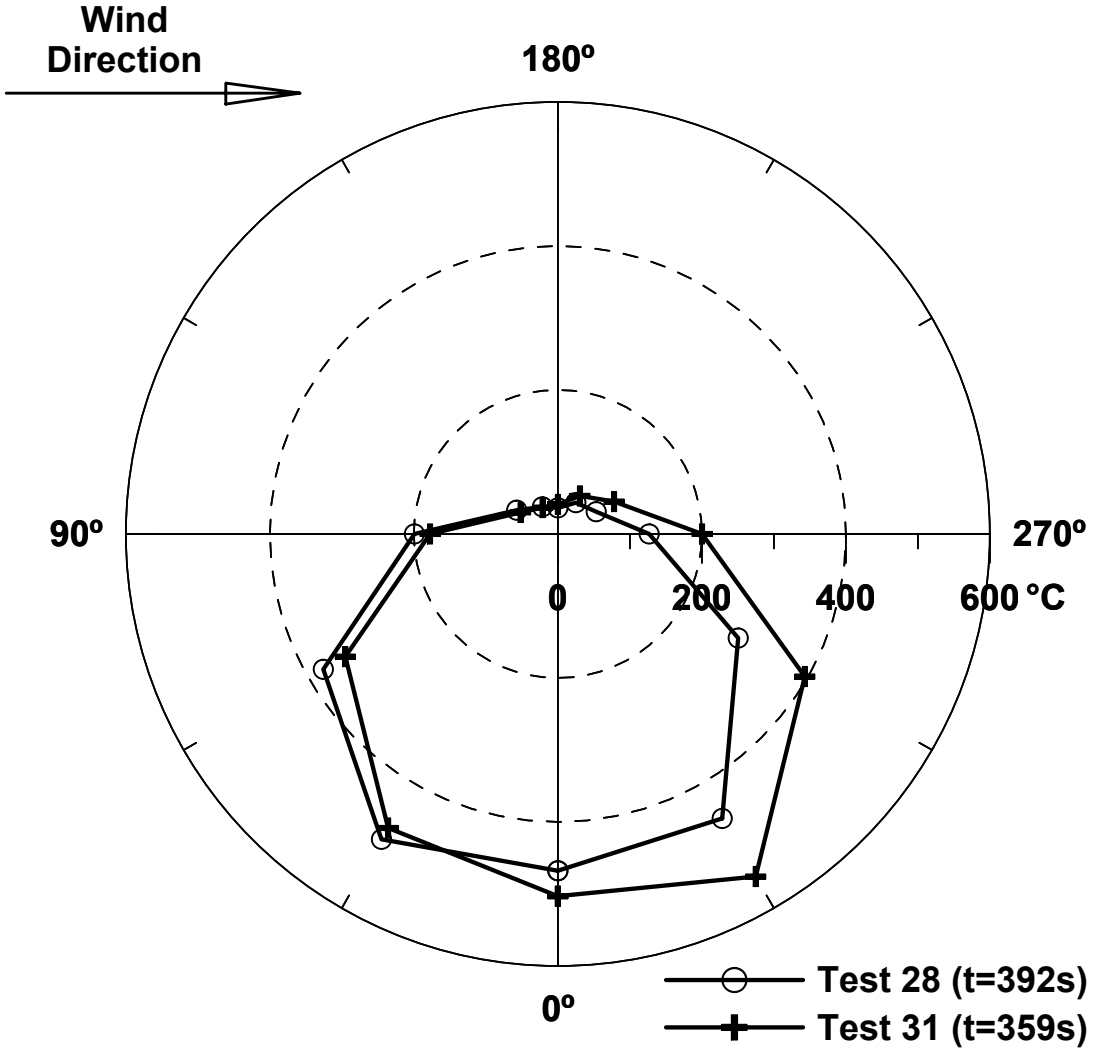

Figure 5.37: Temperature profile along inside surface of blocking object, y=0 m, 7 m/s wind

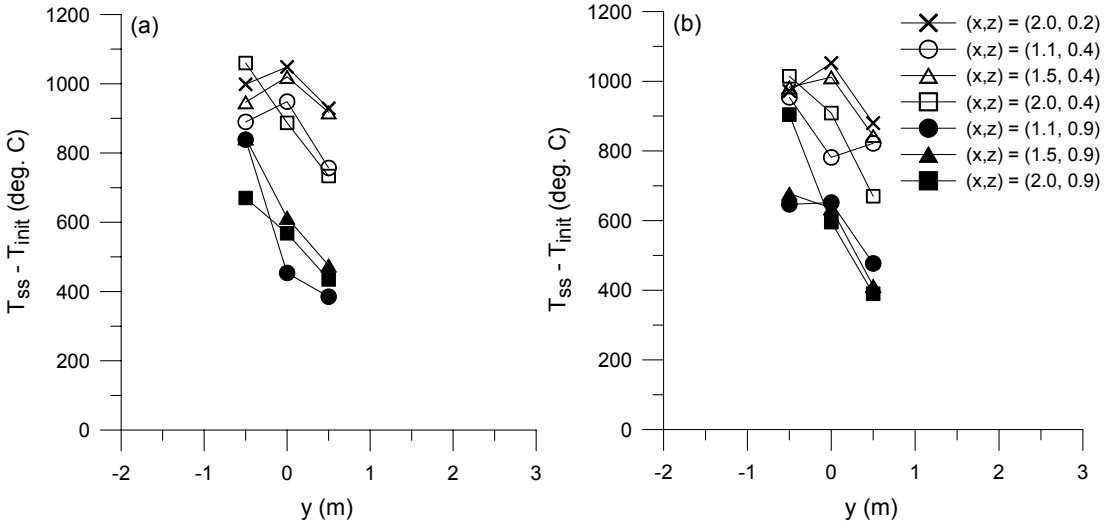

Figure 5.38: Temperature profile across width of plume upwind of blocking object, 7 m/s wind (x and z coordinates in metres), (a) test 28, (b) test 31

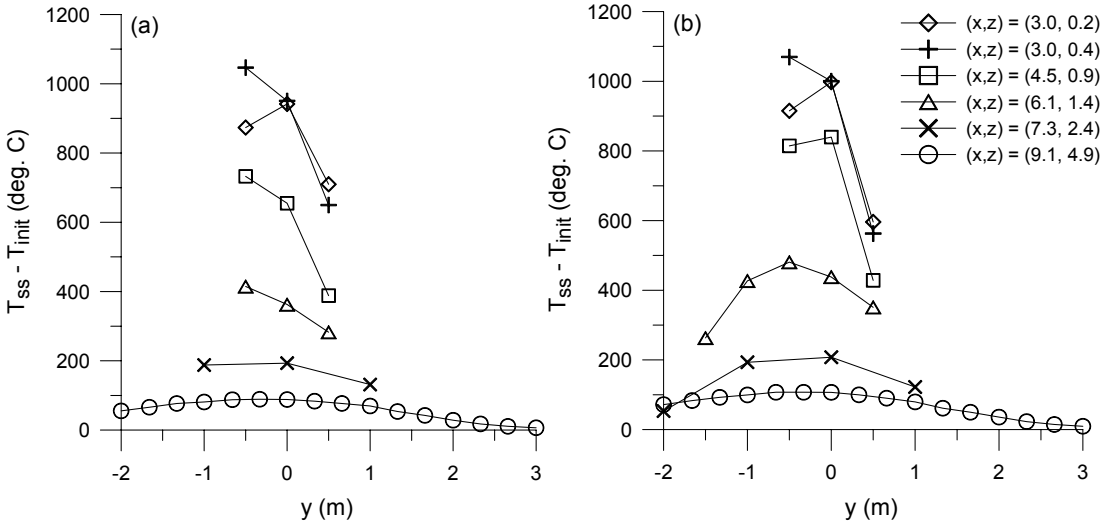

Figure 5.39: Temperature profile across width of plume underneath and downwind of blocking object, 7 m/s wind (x and z coordinates in metres), (a) test 28, (b) test 31

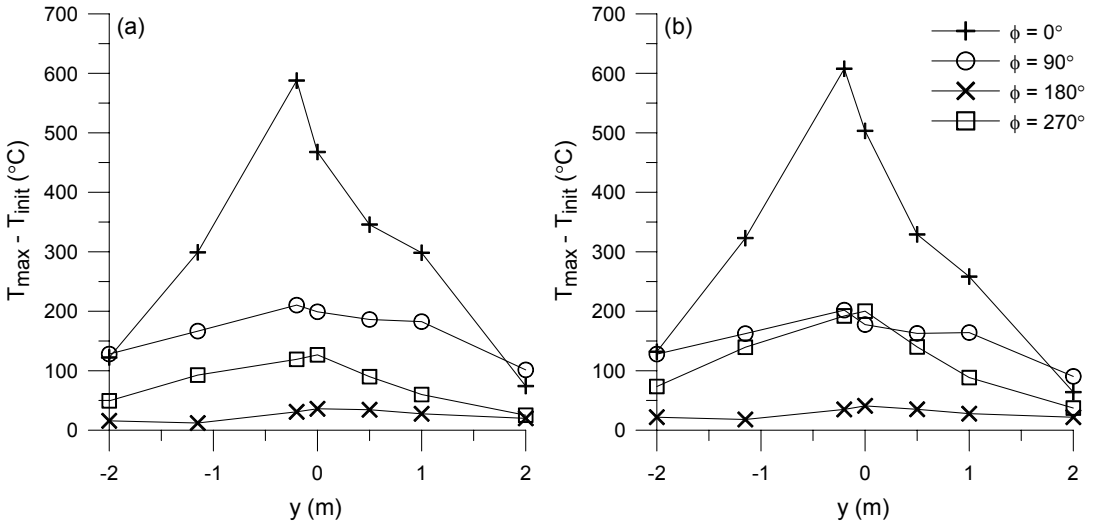

Figure 5.40: Temperature profile along inside surface of blocking object in longitudinal direction, 7 m/s wind, (a) test 28, (b) test 31

Difficulties in measuring temperature in the hot flaming core of the fire were demonstrated by the apparent conflicting trend observed in the temperature profiles measured along x=1.1 m and z=0.4 m during the two tests conducted at the 7 m/s wind speed (Figure 5.38, denoted by open circles). In test 28 (Figure 5.38a), a profile maximum was measured at y=0 m, but in test 31 (Figure 5.38b), a profile minimum was measured at the same y location. Since profile maxima were measured at y=0 m at other nearby locations (e.g. (x, z)=(1.5 m, 0.4 m) and (x, z)=(2.0 m, 0.2 m)), the profile minimum observed in test 31 at (x, z)=(1.1 m, 0.4 m) appeared at first to be an anomaly. However, as shown later in Figures 5.48 and 5.58, this minimum was also observed in tests 29 and 30 at the 10 m/s and 13 m/s wind speeds, respectively. Possible causes of this minimum include conduction losses through the thermocouple wire, decalibration of the thermocouple wire and the presence of an oxygen-starved region near the fuel pan at the base of the fire. Although conduction losses may have occurred during these experiments, they were unlikely to have caused the measured temperature to decrease by over 170°C, or 22% (the difference between the profile maximum of 954°C at y=-0.5 m and the profile minimum of 781°C at y=0 m in test 31 (Figure 5.38b)). Also, decalibration of the thermocouple wires was considered to have been a minor contributor because the thermocouple chains at x=1.1 m and 1.5 m were insulated during tests 29 to 32. Examination of the temperature time traces corresponding to the temperature profile at (x, z)=(1.1 m, 0.4 m) did not reveal any obvious failure of the thermocouples during tests 29 to 32; however, the thermocouples lo-

cated along the chains in the measurement plane x=1.1 m tended to fail partway through the test when the chains were uninsulated in tests 25 to 28 (see Appendix D). Because the temperature data measured immediately prior to thermocouple failure were used to generate some of the temperature profiles in test 28 (Figure 5.38a), there was greater uncertainty in the temperature data corresponding to the profile at (x, z)=(1.1 m, 0.4 m) in this test than in the same data corresponding to test 31. The above issues indicate the tremendous difficulty in obtaining accurate temperature measurements at the base of the fire in large-scale experiments. Since the temperatures measured in test 31 with the insulated thermocouple chains were considered more reliable, the existence of a profile minimum at y=0 m would suggest the presence of an oxygen-starved region at the base of the fire, in agreement with the study of Suo-Anttila and Gritzo [7] involving large wind-blown fires with a large downwind blocking object. However, this clearly remains an area requiring significantly more research.

5.3.3 Fire in 10 m/s Wind with Blocking Object

Figures 5.41 and 5.42 contain typical single-frame and time-averaged images of the fire in the 10 m/s wind condition. In Figure 5.42a, the region of luminous flame immediately above the fuel pan was of similar shape to that observed in the 7 m/s wind condition (Figure 5.32a), but immediately downwind of the fuel pan, the flame lay closer to the ground under the higher wind speed. Downwind of the blocking object (Figure 5.42b), most of the plume remained near the ground, with significant smoke obscuration near the bottom of the thermocouple chains positioned downwind of the culvert. This contrasted with the image taken in the 7 m/s wind condition (Figure 5.32b), in which most of the smoke obscuration occurred near the top of the thermocouple chains.

Further details about the plume could be obtained from Figures 5.43 to 5.46, which show line and contour plots of the time-averaged increase in plume temperature along the longitudinal midplane y=0 m. The temperature increases measured at locations in the core region of the plume underneath and downwind of the blocking object were higher in test 29 than in test 26. Similar to the tests in the 7 m/s wind, these differences corresponded to differences in the initial temperature of the blocking object. The overall shape of the plume was similar in both tests and thus could be characterized. As indicated by Figures 5.45 and 5.46, the plume hugged the ground as it moved downwind of the fuel pan and underneath the blocking ob-

Figure 5.41: Typical video frames showing fire in 10 m/s wind, (a) upwind of blocking object, (b) downwind of blocking object

Figure 5.42: Typical 60-frame time-averaged images showing fire in 10 m/s wind, (a) upwind of blocking object, (b) downwind of blocking object

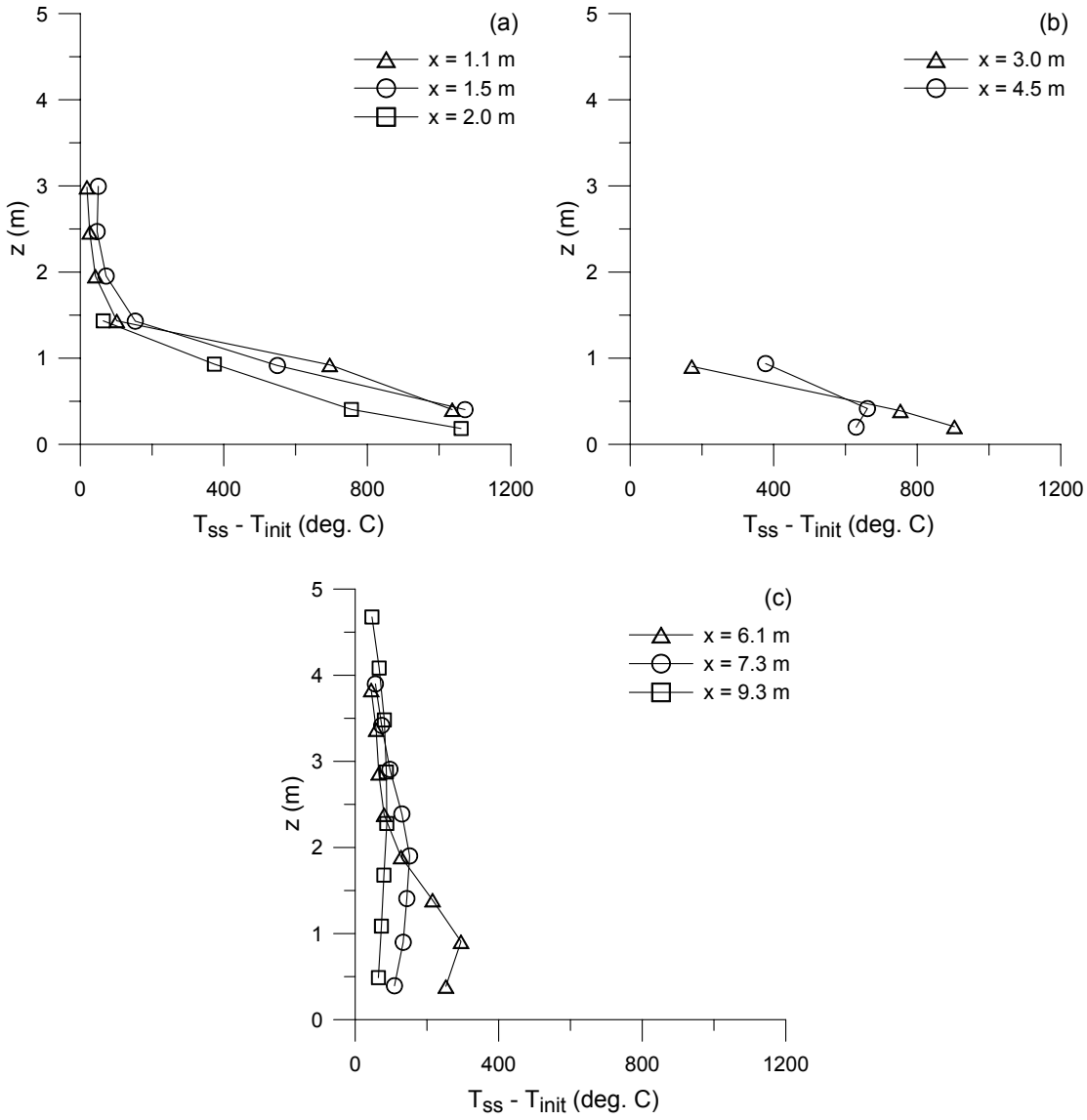

Figure 5.43: Line plot of increase in plume temperature under 10 m/s wind (test 26), y=0 m, (a) upwind of blocking object, (b) underneath blocking object, (c) downwind of blocking object

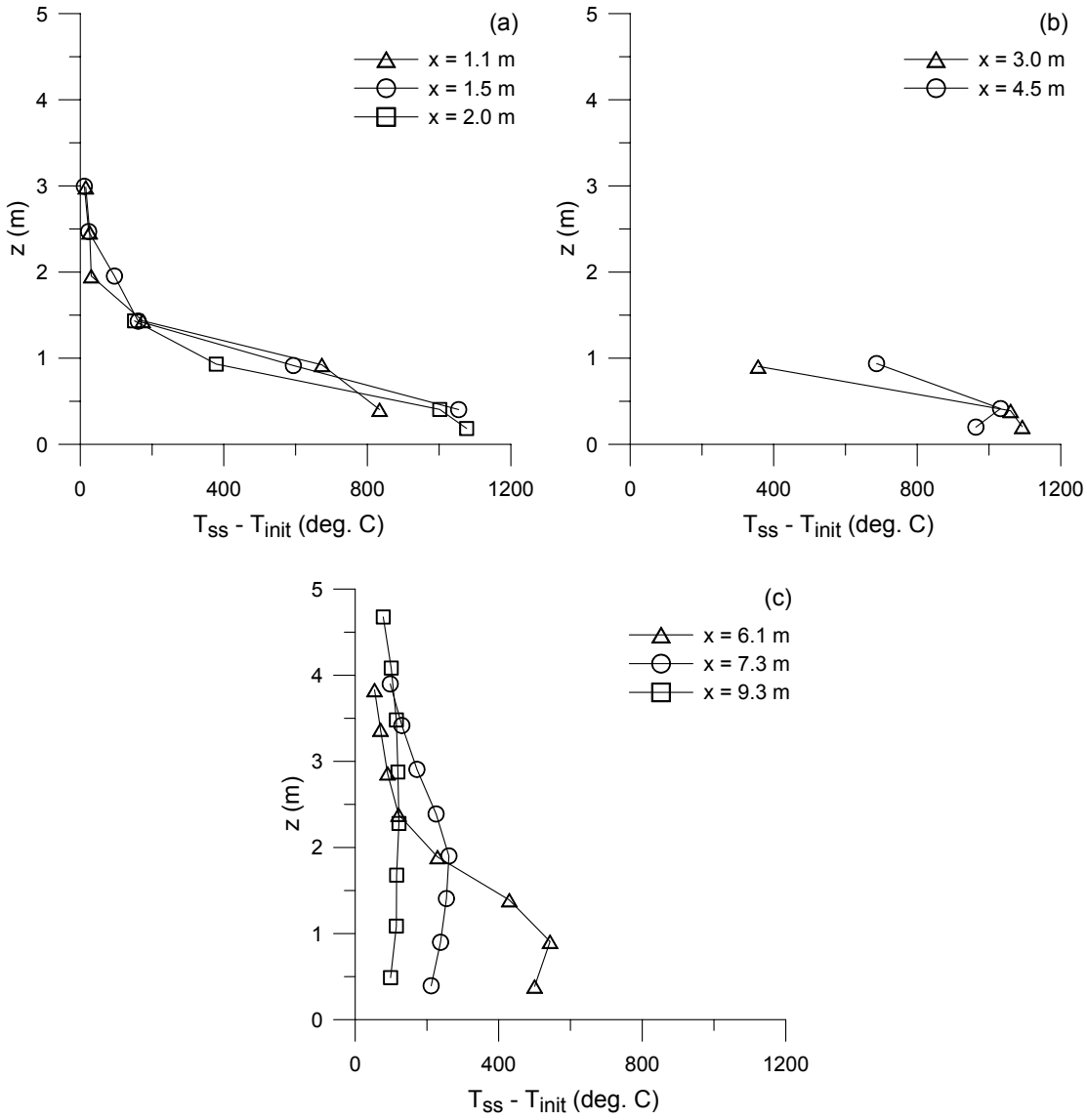

Figure 5.44: Line plot of increase in plume temperature under 10 m/s wind (test 29), y=0 m, (a) upwind of blocking object, (b) underneath blocking object, (c) downwind of blocking object

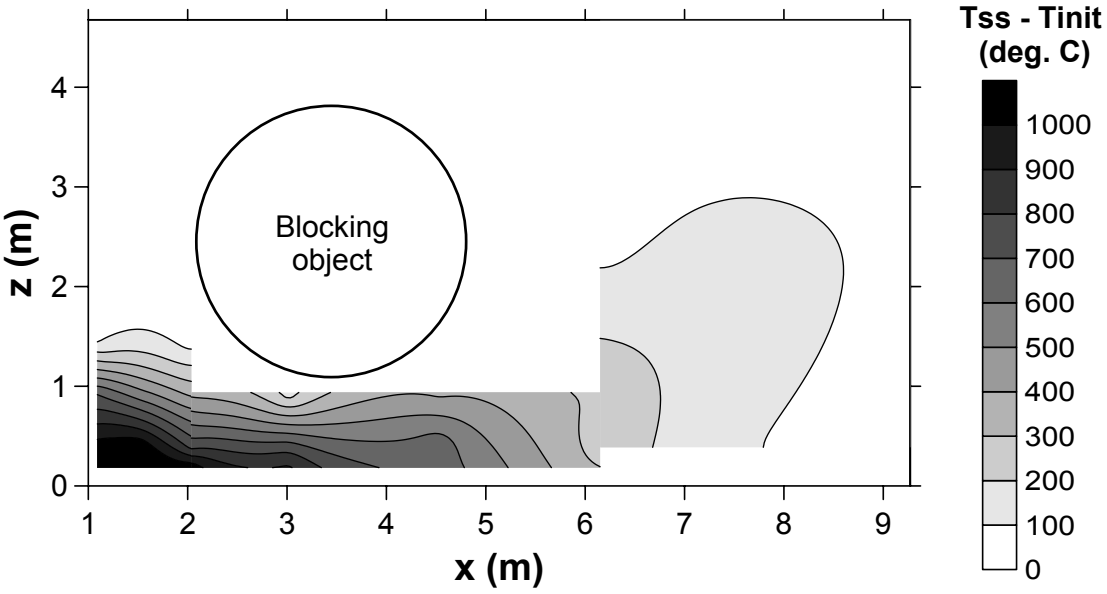

Figure 5.45: Contour plot of increase in plume temperature under 10 m/s wind (test 26), y=0 m

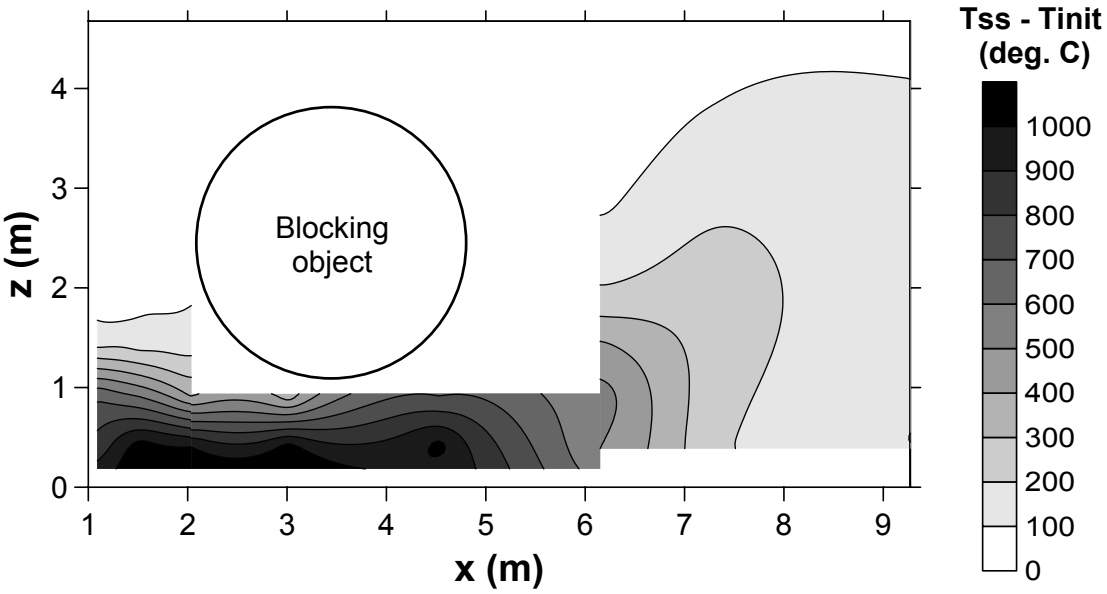

Figure 5.46: Contour plot of increase in plume temperature under 10 m/s wind (test 29), y=0 m

ject. Temperature contours upwind of the object (particularly in Figure 5.45) were suggestive of velocity contours that might be observed in studies of two-dimensional flow around a cylinder, and indicated that the height of the plume decreased as it approached the blocking object. (This may also have been partly caused by the presence of a backwards-facing step formed by the leeward edge of the raised floor surround.) This observation was not evident at the lower wind speeds (e.g. Figures 5.35 and 5.25) because in those cases, the inertial forces of the wind were not sufficient to overcome the buoyancy forces in the fire. Vertical temperature gradients upwind of and underneath the blocking object were steeper in the 10 m/s wind condition than in the 7 m/s wind condition (Figures 5.35 and 5.36), consistent with the notion of the plume being pushed closer to the ground by the higher ambient wind. The plume then lifted off the ground downwind of the blocking object, with its centre reaching heights of approximately z=0.9 m, 1.9 m and 2.3 m at downwind distances of x=6.1 m, 7.3 m and 9.3 m, respectively (Figures 5.43c and 5.44c). This was clearly different from the test in the 10 m/s wind without the object (Figure 4.32), in which the plume was pushed close to the ground over the entire length of the test section.

Figure 5.47 shows profiles of the increase in temperature along the inside surface of the blocking object at y=0 m. The temperature increases measured along the lower half of the object were higher in test 29 than in test 26, particularly at ϕ=0° and 330°, where differences of up to 153°C were observed. This was likely due to increased heating of the culvert by the plume, which was up to 371°C hotter in test 29 in the region underneath the leeward side of the blocking object (Figures 5.43b and 5.44b, x=4.5 m profiles). Despite the relatively large test-to-test differences at the 10 m/s wind speed, the temperature profiles in Figure 5.47 showed consistent trends when compared to those in Figure 5.37 for the 7 m/s wind speed. Temperatures measured along the top and windward sides of the culvert (ϕ=30° to 180°) were relatively similar, within 56°C (or 18%), under the two wind speeds. In contrast, temperatures measured along the lower leeward side of the culvert (ϕ=0° and 270° to 330°) were up to 230°C (96%) cooler in the 10 m/s wind tests. This was consistent with the observation that the plume lay closer to the ground (and therefore further away from the object) and lifted off the ground further downwind of the object at the higher wind speed (cf. Figures 5.45-5.46 and 5.35-5.36), thus reducing thermal exposure of the lower leeward side of the culvert to the fire plume.

Temperature profiles along the width of the plume (Figures 5.48 and 5.49) and blocking object (Figure 5.50) indicated that the fire was generally skewed in the

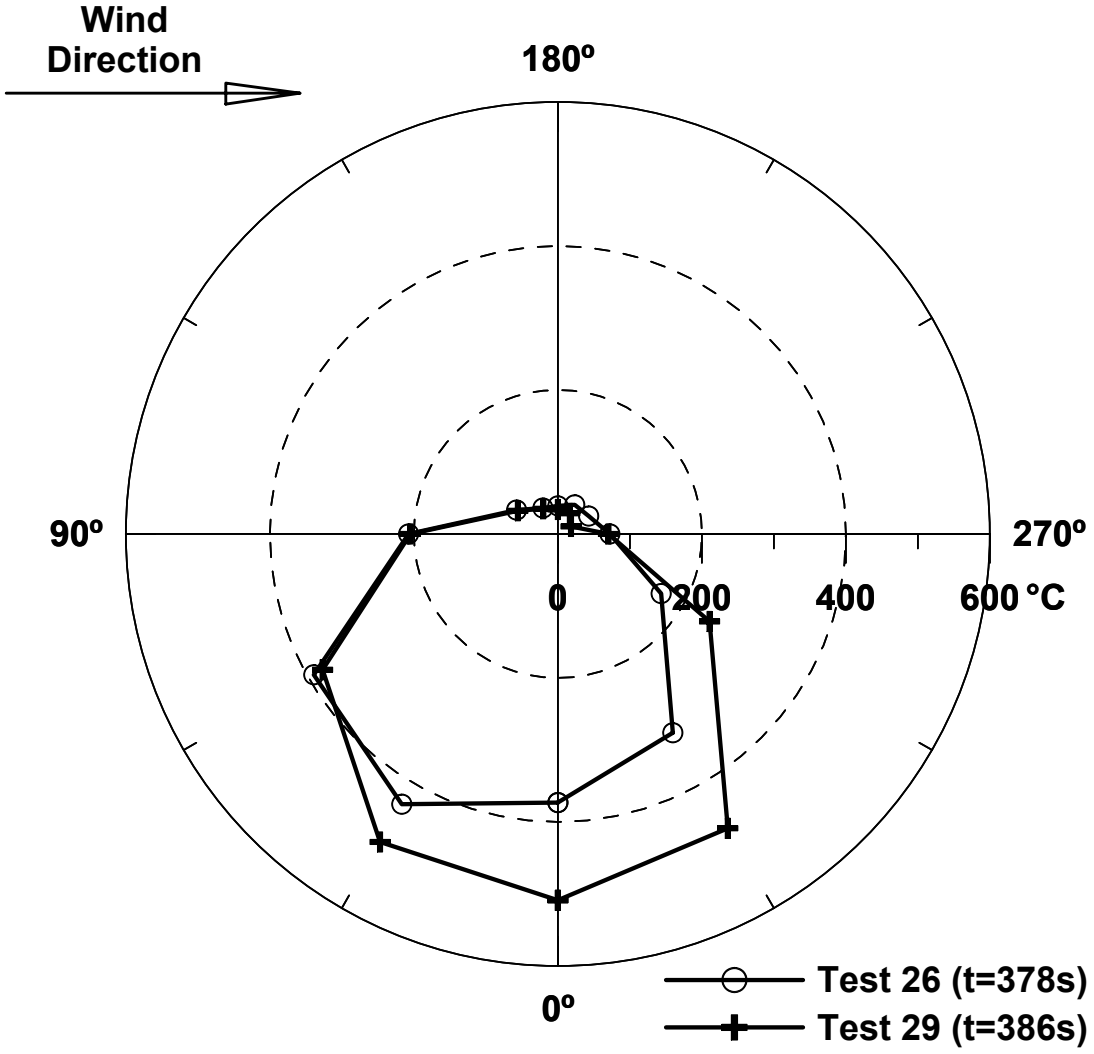

Figure 5.47: Temperature profile along inside surface of blocking object, y=0 m, 10 m/s wind

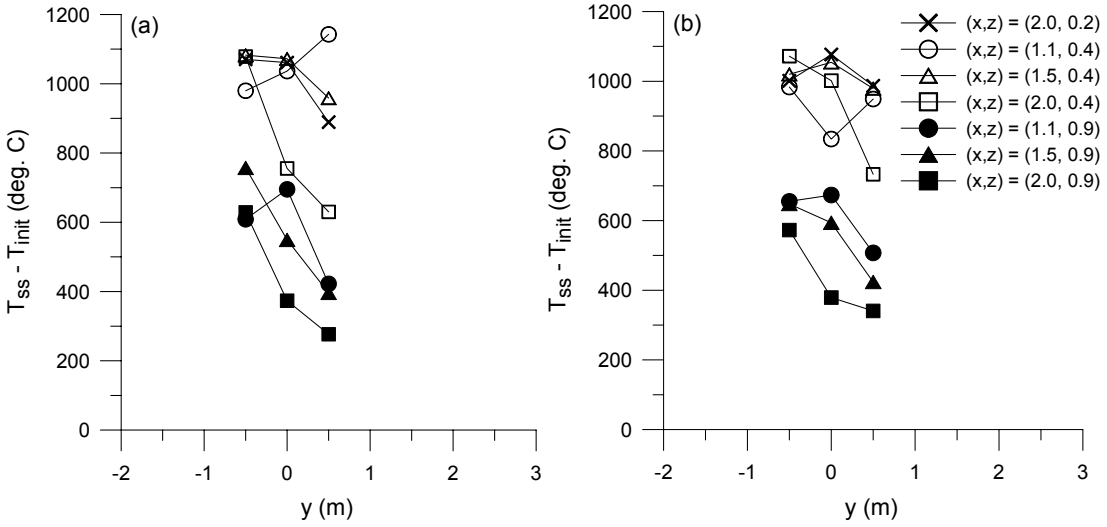

Figure 5.48: Temperature profile across width of plume upwind of blocking object, 10 m/s wind (x and z coordinates in metres), (a) test 26, (b) test 29

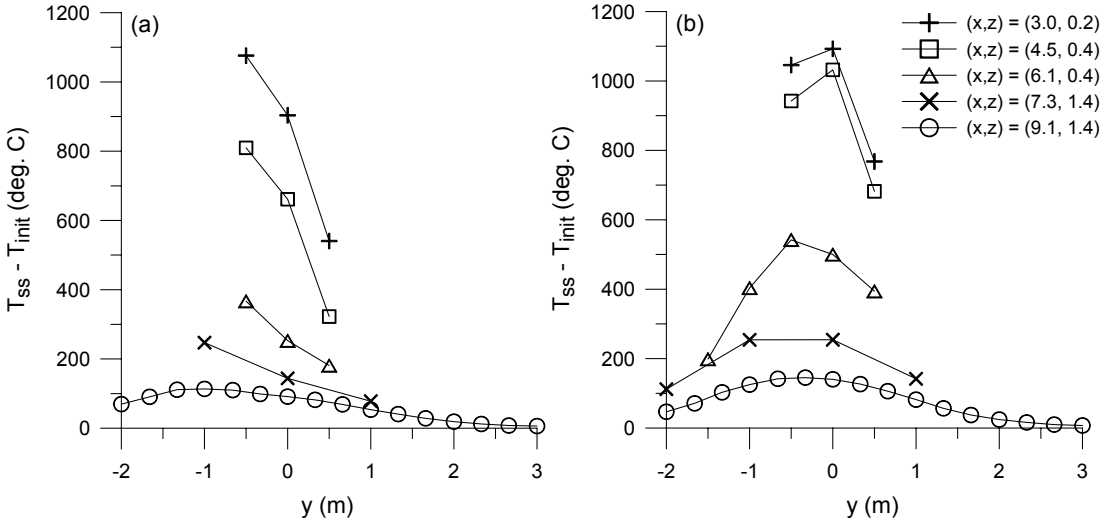

Figure 5.49: Temperature profile across width of plume underneath and downwind of blocking object, 10 m/s wind (x and z coordinates in metres), (a) test 26, (b) test 29

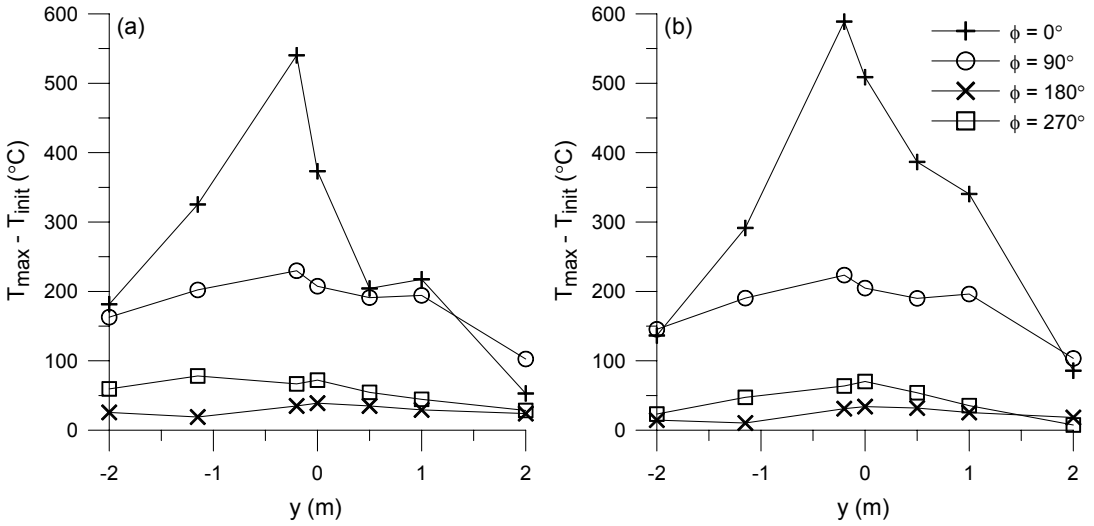

Figure 5.50: Temperature profile along inside surface of blocking object in longitudinal direction, 10 m/s wind, (a) test 26, (b) test 29

-y direction, as observed at the lower wind speeds. In test 26, the plume centre appeared to have shifted by 1 m in the -y direction by the time it reached downwind distances of x=7.3 m and 9.1 m (Figure 5.49a), while in test 29, it appeared to have shifted by 0.5 m (Figure 5.49b). Along the bottom of the blocking object (Figure 5.50, ϕ=0°), the maximum temperature increase was located at y=-0.2 m in both tests, but temperatures on the +y side of the object were much lower in test 26 than in test 29, consistent with the observation that the plume was skewed more significantly to the -y side of the test enclosure during the earlier test. Overall, the skew angle of the plume was consistent with previous observations, ranging from 4° to 8°, based on the temperature profiles for x=7.3 m shown in Figure 5.49.

As observed in the 7 m/s wind condition, the profile measured along x=1.1 m and z=0.4 m was inconsistent with those measured along similar elevations at x=1.5 m and 2.0 m (Figure 5.48). For instance, in test 26, the profile measured along (x, z)=(1.1 m, 0.4 m) suggested that the fire was skewed in the +y direction, as opposed to the -y direction indicated further downwind. Likewise, in test 29, the profile measured at (x, z)=(1.1 m, 0.4 m) exhibited a minimum value at y=0 m, rather than a maximum value as evident in the corresponding profile at x=1.5 m. As mentioned in Section 5.3.2, these inconsistencies may have been due to the use of temperatures measured immediately prior to thermocouple failure (which have a greater uncertainty) to generate the temperature profiles in Figure 5.48, or the

presence of an oxygen-starved region near the fuel pan at the base of the fire. More detailed measurements are required in order to resolve these inconsistencies.

5.3.4 Fire in 13 m/s Wind with Blocking Object

Figures 5.51 and 5.52 show typical single-frame and time-averaged images of the fire in the 13 m/s wind condition. The shape of the flame upwind of the blocking object (Figures 5.51a and 5.52a) was similar to that observed in the 10 m/s wind condition (Figures 5.41a and 5.42a). As the fire passed underneath the object, however, it lay closer to the ground under the higher wind speed. This was evidenced by a large visible gap between the bottom of the culvert and top of the flame in Figures 5.51b and 5.52b. Downwind of the object, the plume remained near the ground until it exited the test section, as indicated by significant smoke obscuration of the lower portion of the thermocouple chains in Figure 5.52b.

To provide additional detail, line and contour plots of the time-averaged increase in plume temperature along the longitudinal midplane y=0 m are shown in Figures 5.53 to 5.56.[9] Similar to the 7 m/s and 10 m/s wind tests, differences in the initial temperature of the blocking object contributed to higher temperature increases in the core region of the plume underneath and downwind of the blocking object in test 30 (Section 5.2). Despite this, the overall shape of the plume was reasonably similar in both tests and could be characterized. The plume lay close to the ground as it passed underneath the blocking object, with temperature profiles and contours in the region upwind of x=3 m similar to those reported for the 10 m/s wind tests. Downwind of the blocking object, the plume continued to hug the ground and appeared to do so more closely in test 25 than in test 30. The temperature profiles in Figure 5.53 all peaked at their lowest measurement locations, while those in Figure 5.54 indicated that the plume started to lift off the ground downwind of x=6.1 m, reaching heights of 0.9 m and 1.7 m at downwind distances of x=7.3 m and 9.3 m, respectively (Figure 5.54). In both these tests, the plume lay closer to the ground than in the 10 m/s wind condition, consistent with the video images of the downwind portion of the fire (Figures 5.51b and 5.52b).

Temperature increases measured along the inside surface of the blocking object at y=0 m are shown in Figure 5.57. In both tests, the highest temperature increases

[9] In Figure 5.56, poor alignment of the contours upwind and downwind of x=2.0 m was due to a missing data point at x=2.0 m and z=0.9 m, caused by failure of the corresponding thermocouple at the beginning of the test.

Figure 5.51: Typical video frames showing fire in 13 m/s wind, (a) upwind of blocking object, (b) downwind of blocking object

Figure 5.52: Typical 60-frame time-averaged images showing fire in 13 m/s wind, (a) upwind of blocking object, (b) downwind of blocking object

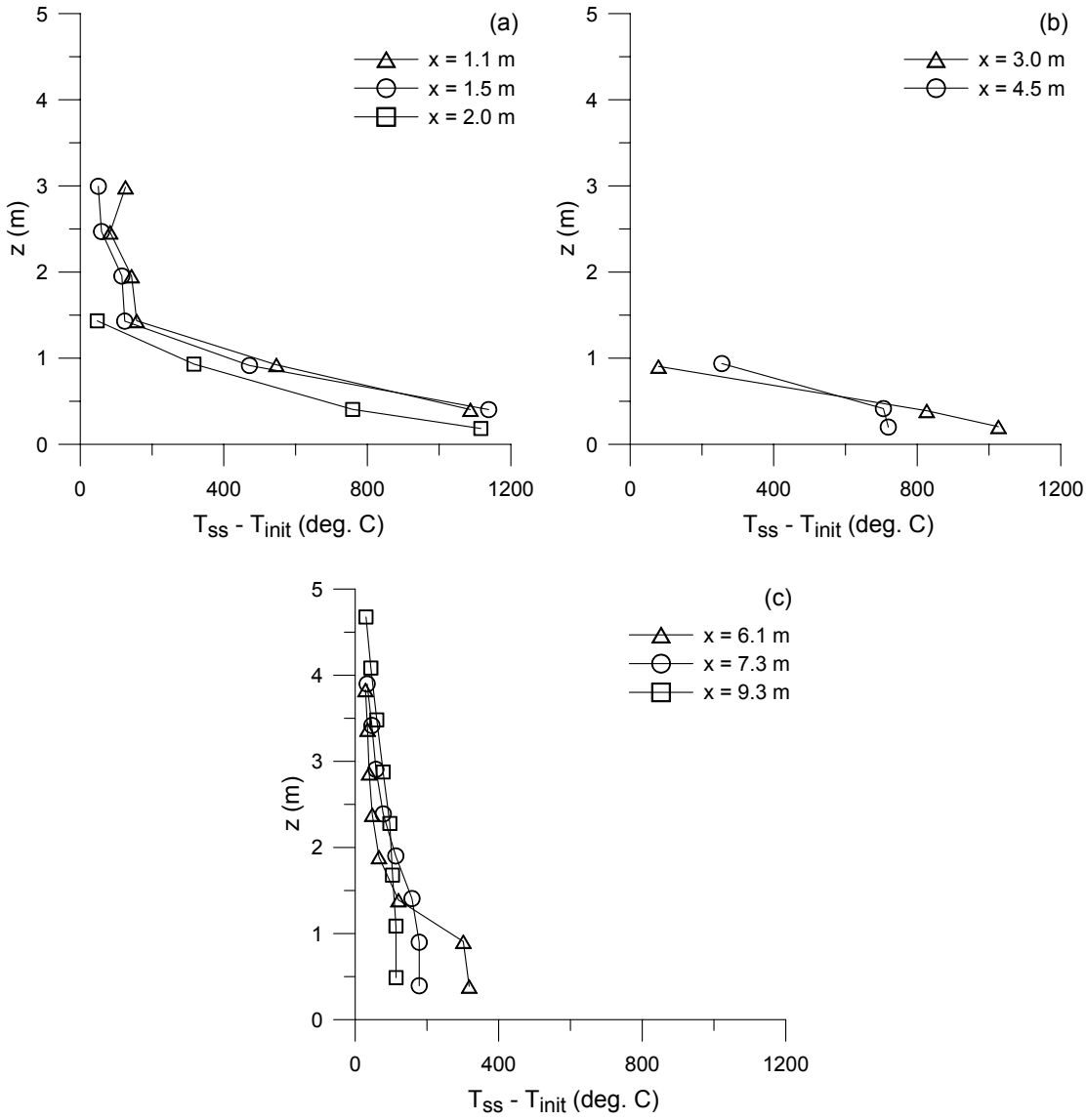

Figure 5.53: Line plot of increase in plume temperature under 13 m/s wind (test 25), y=0 m, (a) upwind of blocking object, (b) underneath blocking object, (c) downwind of blocking object

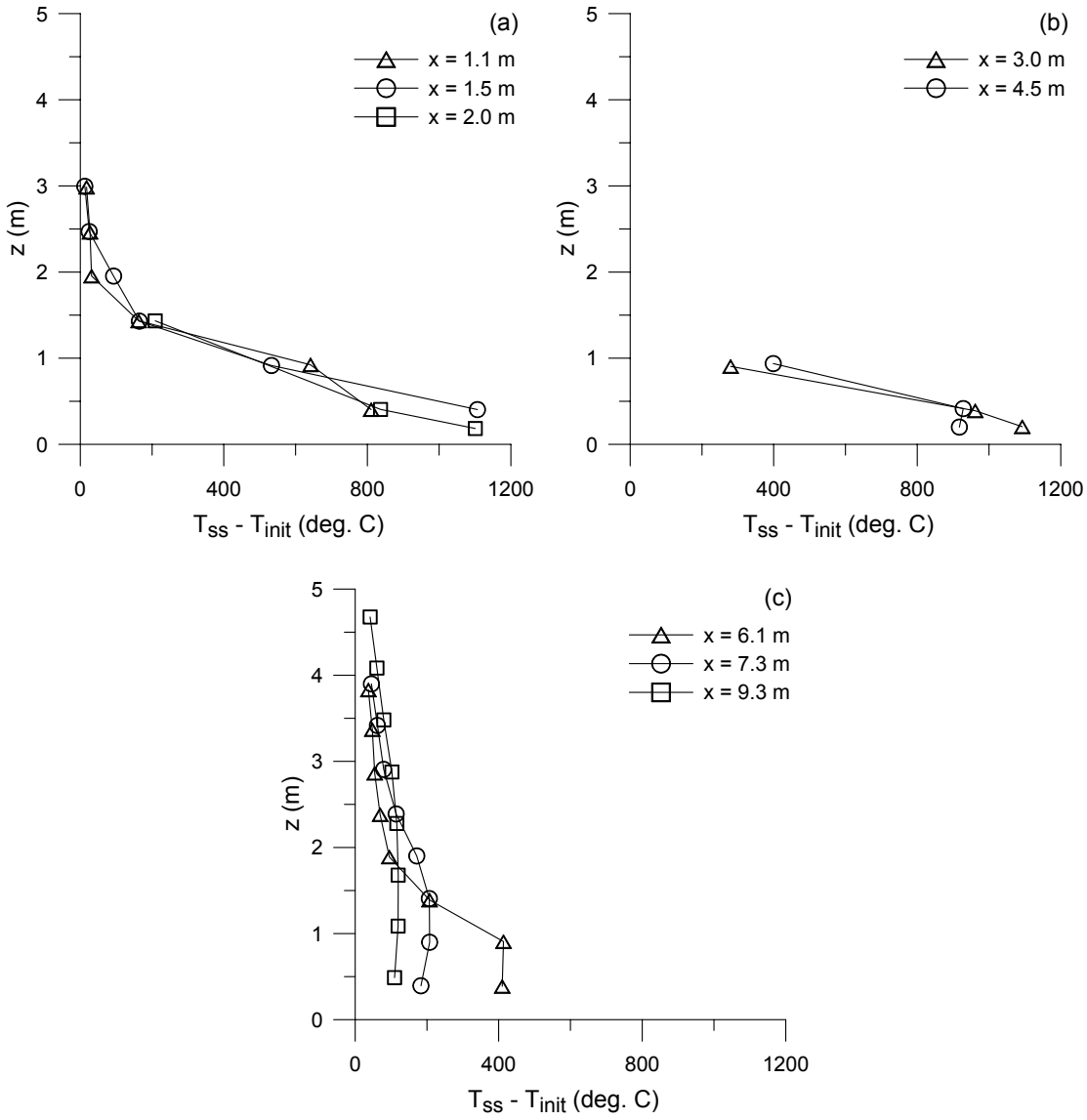

Figure 5.54: Line plot of increase in plume temperature under 13 m/s wind (test 30), y=0 m, (a) upwind of blocking object, (b) underneath blocking object, (c) downwind of blocking object

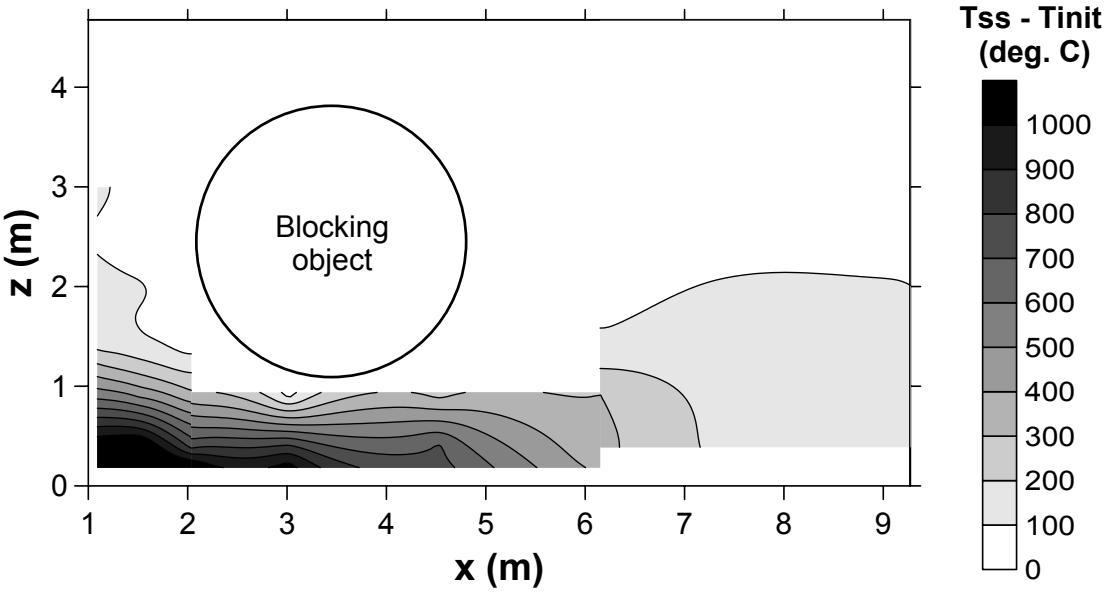

Figure 5.55: Contour plot of increase in plume temperature under 13 m/s wind (test 25), y=0 m

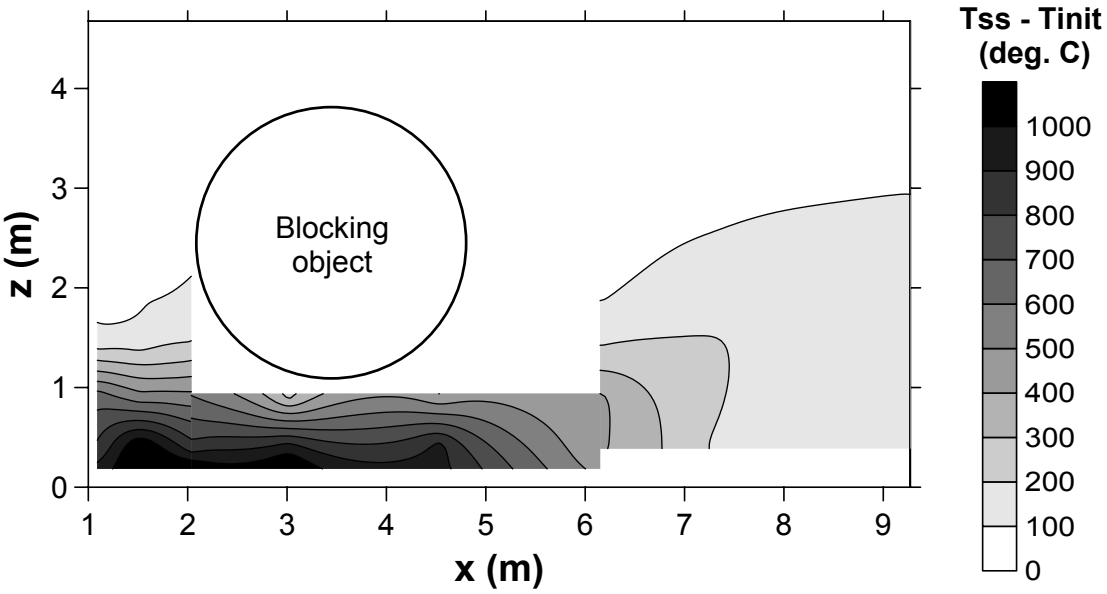

Figure 5.56: Contour plot of increase in plume temperature under 13 m/s wind (test 30), y=0 m

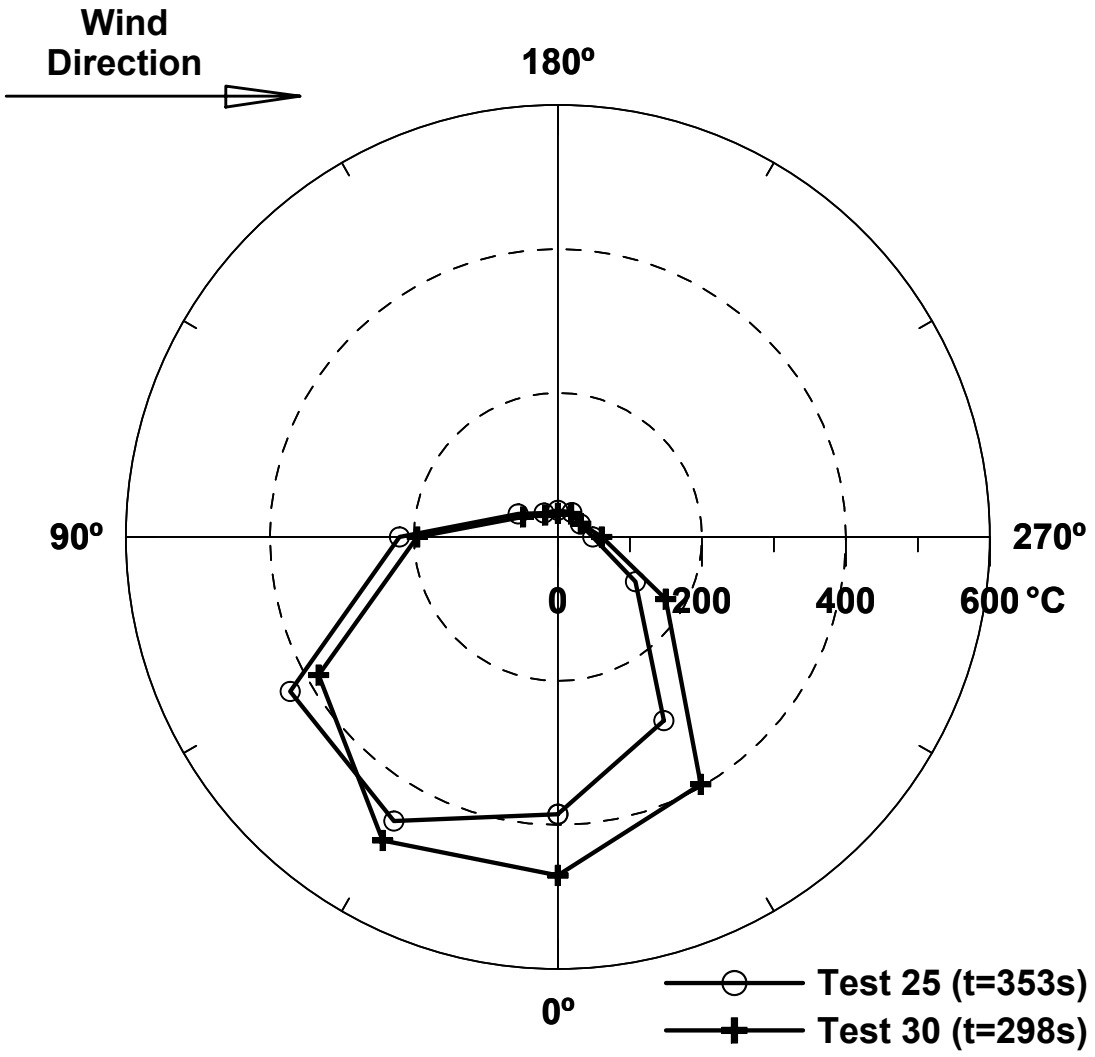

Figure 5.57: Temperature profile along inside surface of blocking object, y=0 m, 13 m/s wind

(384°C to 487°C) were measured along the lower windward side of the culvert (ϕ=0° to 60°), although in test 30, a temperature increase of 397°C was also measured at ϕ=330° due to higher plume temperatures underneath the object (Figure 5.54b). The temperature profiles were similar in shape to those measured at the 10 m/s wind speed (Figure 5.47), particularly when tests conducted on the same day (i.e. tests 25 and 26, tests 29 and 30) were compared. The temperature increases along the windward side of the object (ϕ=30° to 180°) were similar in magnitude to the corresponding values in the 10 m/s wind tests, but those along the lower leeward side of the culvert (ϕ=300° to 330°) were smaller than the corresponding values in the 10 m/s wind tests. This was consistent with the observation that the plume remained closer to the ground, and thus further from the outside surface of the culvert, in the region downwind of the object during the 13 m/s wind tests.

Temperature profiles measured along the width of the plume and blocking object (Figures 5.58 to 5.60) showed trends similar to those measured at the 10 m/s wind speed. The plume was clearly skewed in the -y direction, with its centre located at approximately y=-1 m in the region downwind of the object (Figure 5.59, x $\geq$ 6.1 m). The inconsistencies in the temperature profiles corresponding to (x, z)=(1.1 m, 0.4 m), described in Section 5.3.3, were observed at the 13 m/s wind speed. In the blocking object, temperatures measured along ϕ=0° peaked at y=-0.2 m and were generally hotter on the -y side, consistent with the plume temperature profiles.

As indicated in the above sections, the shape of the plume was greatly influenced by the wind speed and presence of the blocking object. In the 5 m/s wind condition, the blocking object interfered significantly with the plume, which impinged on the lower windward portion and bottom of the culvert before spreading upward along the leeward side. In the 7 m/s wind condition, the plume tilted further over and although it continued to impinge on the bottom of the blocking object, it did not spread significantly up the leeward side of the culvert. As the wind speed increased to 10 m/s, there was no discernible impingement of the fire on the object and the plume lay close to the ground, passing relatively freely underneath the blocking object. With a further increase in wind speed to 13 m/s, the plume lay even closer to the ground and the object did not appear to directly obstruct the plume flow.

The results from the present experiments could be compared with simulation results from the two-dimensional model of Kou [118], previously described at the end of Section 2.3. The simulations that were closest to the scenarios studied in the

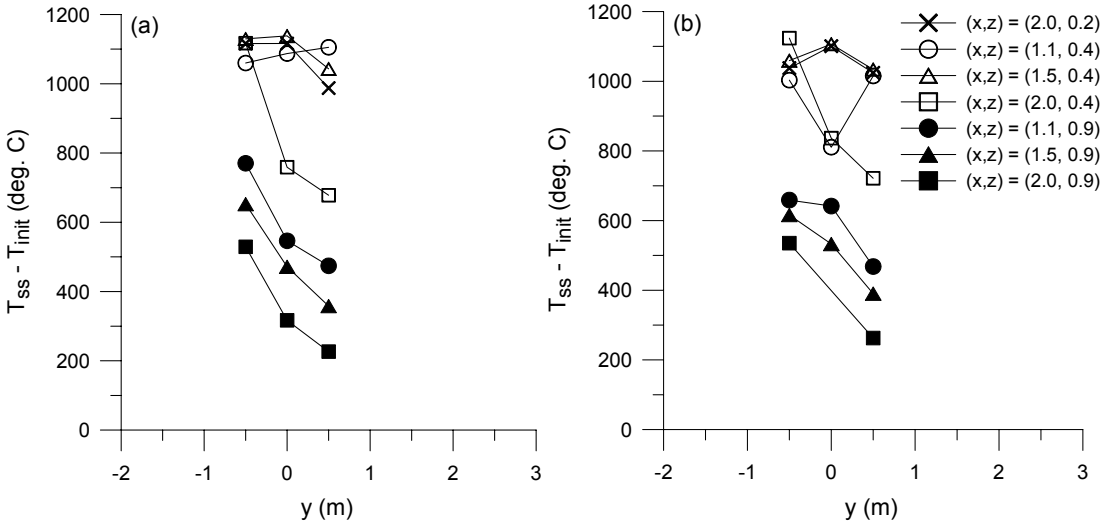

Figure 5.58: Temperature profile across width of plume upwind of blocking object, 13 m/s wind (x and z coordinates in metres), (a) test 25, (b) test 30

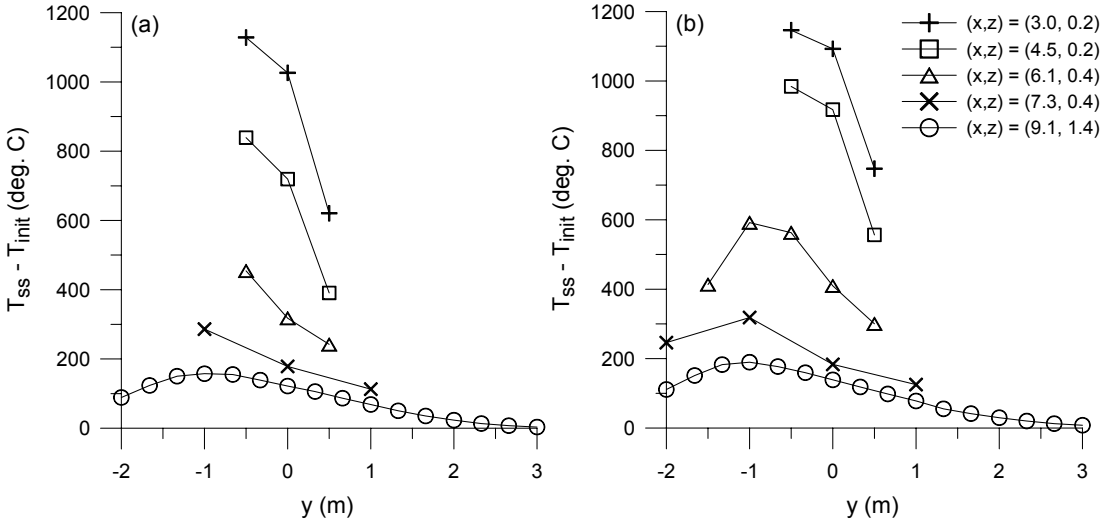

Figure 5.59: Temperature profile across width of plume underneath and downwind of blocking object, 13 m/s wind (x and z coordinates in metres), (a) test 25, (b) test 30

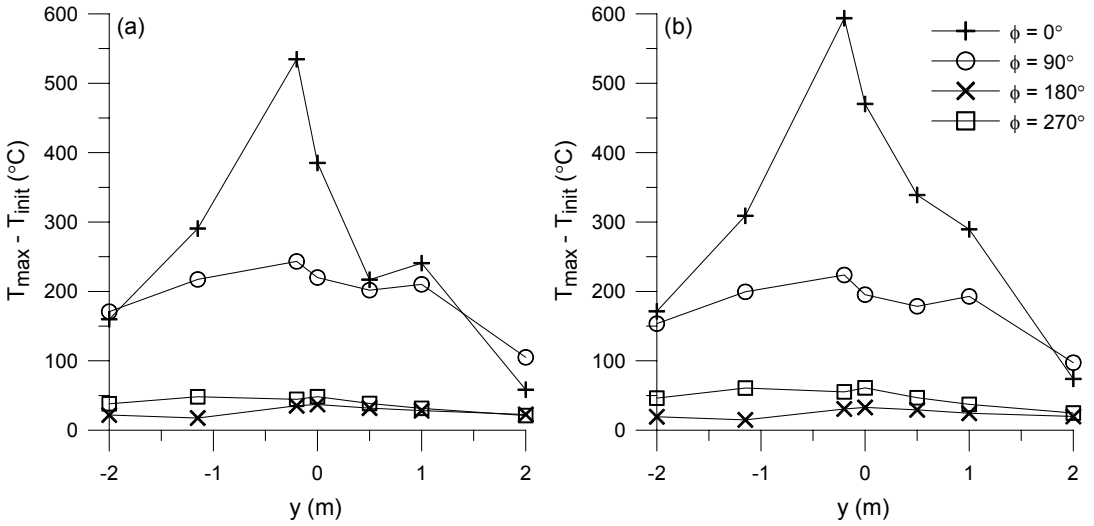

Figure 5.60: Temperature profile along inside surface of blocking object in longitudinal direction, 13 m/s wind, (a) test 25, (b) test 30

present experiments involved a cylinder height to cylinder diameter ratio of 0.5 and wind speeds of 6.1 m/s and 9.1 m/s. In the simulation with the 6.1 m/s wind, the fire was predicted to oscillate between flowing along the windward and top surfaces of the blocking object and wrapping completely around it [118]. In the present experiments (Sections 5.3.1 and 5.3.2), the plume mainly travelled underneath and along the leeward side of the object at both the 5 m/s and 7 m/s wind speeds, likely because the object was situated further away from the fuel pan and at a slightly lower elevation. (In the present study, the cylinder height-to-diameter ratio was 0.4 and the windward edge of the blocking object was 1 m downwind of, rather than aligned with, the leeward edge of the fuel pan.) The simulation results for the 9.1 m/s wind condition were in closer agreement to the experimental observations, with the fire plume flowing horizontally along the ground underneath the object before lifting off the ground well downwind of the cylinder. Differences between the simulation and experimental results were likely due to differences in the boundary conditions of the model and experiment, as well as assumptions included in the model. For instance, the ratio of the fuel pan diameter to the blocking object diameter was 0.7 in the experiments, but 1.2 in the simulations. Also, no raised floor surround was included in the simulations – the presence of this floor surround likely increased the amount of flame drag and affected the direction of plume travel past the object. Further, although the wind profile was uniform in the simulations, it was not entirely uniform across the test facility in the experimental situation [21, 165]. Finally, the model was two-dimensional and did not include

any combustion chemistry or radiation effects, thus limiting the applicability of the model predictions to real fire scenarios [118].

Data from the present experiments have been recently used in a validation study involving a computational fire physics model developed by Sandia National Laboratories [200]. Although detailed discussion of this study is outside the scope of the present thesis, relevant findings from the report [200] are summarized here. Consistent with the above discussion, it was found that comparison of the simulation results with the experimental results was dependent on the ability of the model to simulate the experimental geometry as closely as possible, including any invasive instrumentation that would affect the flow and temperature fields in the fire plume. Model assumptions and model input parameters also influenced agreement of the simulation and experimental results [200]. Additionally, the comparison was impacted by the ability to control, measure and interpret the experimental parameters; thus for model validation purposes, cooperation between experimentalists and modellers during the experimental design and post-test analysis stages is required to produce meaningful comparison of simulation and experimental results [8, 26, 115].

5.3.5 Effect of Blocking Object on Wind-Blown Fire

In this section, the effect of the blocking object on the fire is elucidated by comparing the video images and temperature contour plots presented in the above sections with the corresponding images and plots presented in the previous chapter. The comparison focusses on the 5 m/s and 10 m/s wind conditions, the lowest and highest wind speeds under which tests were conducted with and without the blocking object.

Figure 5.61 shows time-averaged video images of the fire with and without the object at the 5 m/s wind speed. (These were presented previously in Figures 4.20 and 5.22.) An approximate angle of tilt based on the upwind edge of the luminous flame envelope could be identified in each image and subsequently compared. As indicated in Figure 5.61, the luminous flame was tilted by 71° in the test with the blocking object and by 78° in the test without the blocking object. The difference of approximately 10% in the tilt angle indicates the effect of the object on the overall direction of the plume flow. Further details can be seen in the plot of temperature contours along the longitudinal midplane y=0 m for the test with the object, shown in Figure 5.62a. In the region upwind of x=2 m, the 100°C and 200°C contours

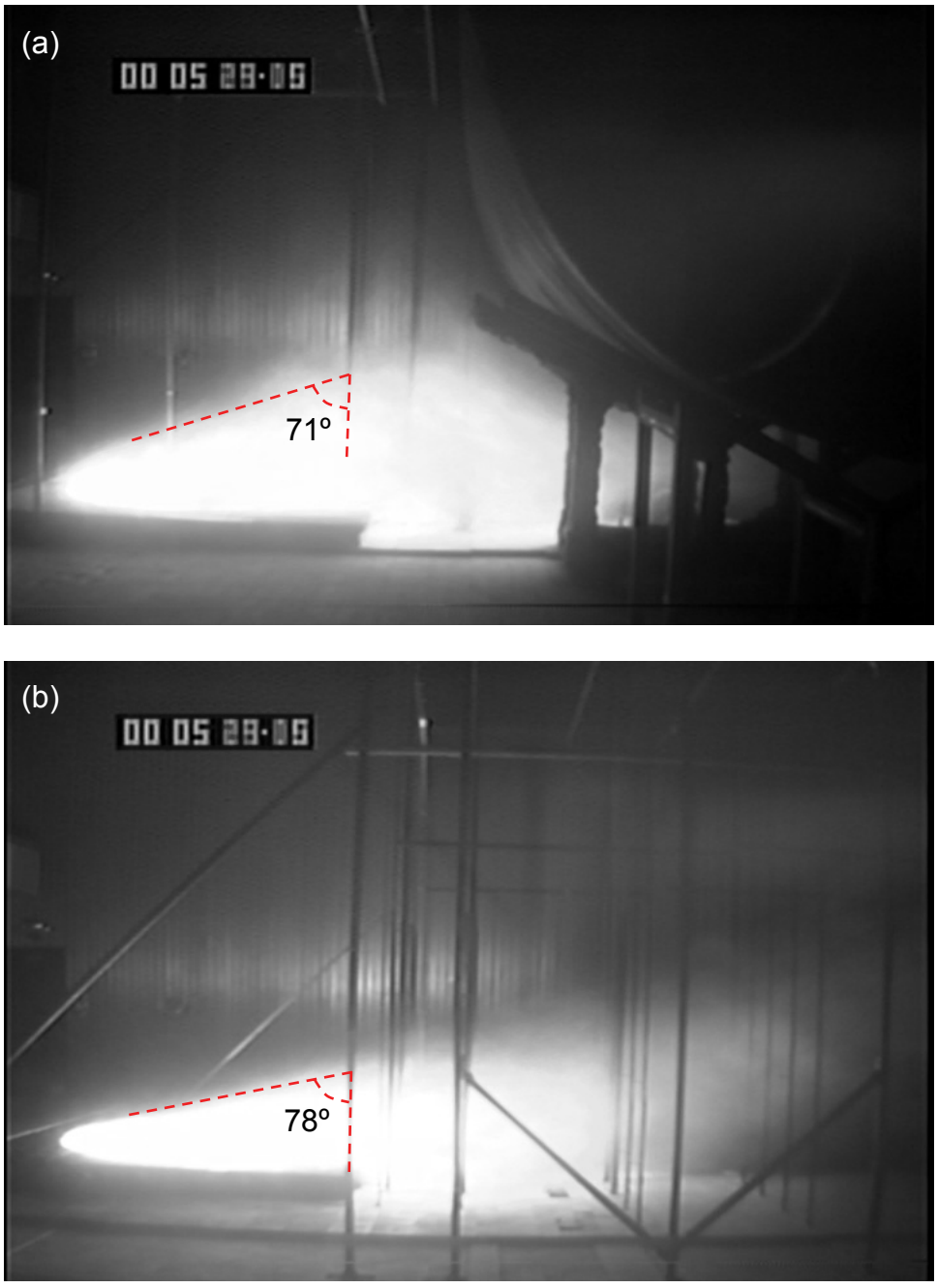

Figure 5.61: Time-averaged video images for fire in 5 m/s wind, (a) with blocking object, (b) without blocking object

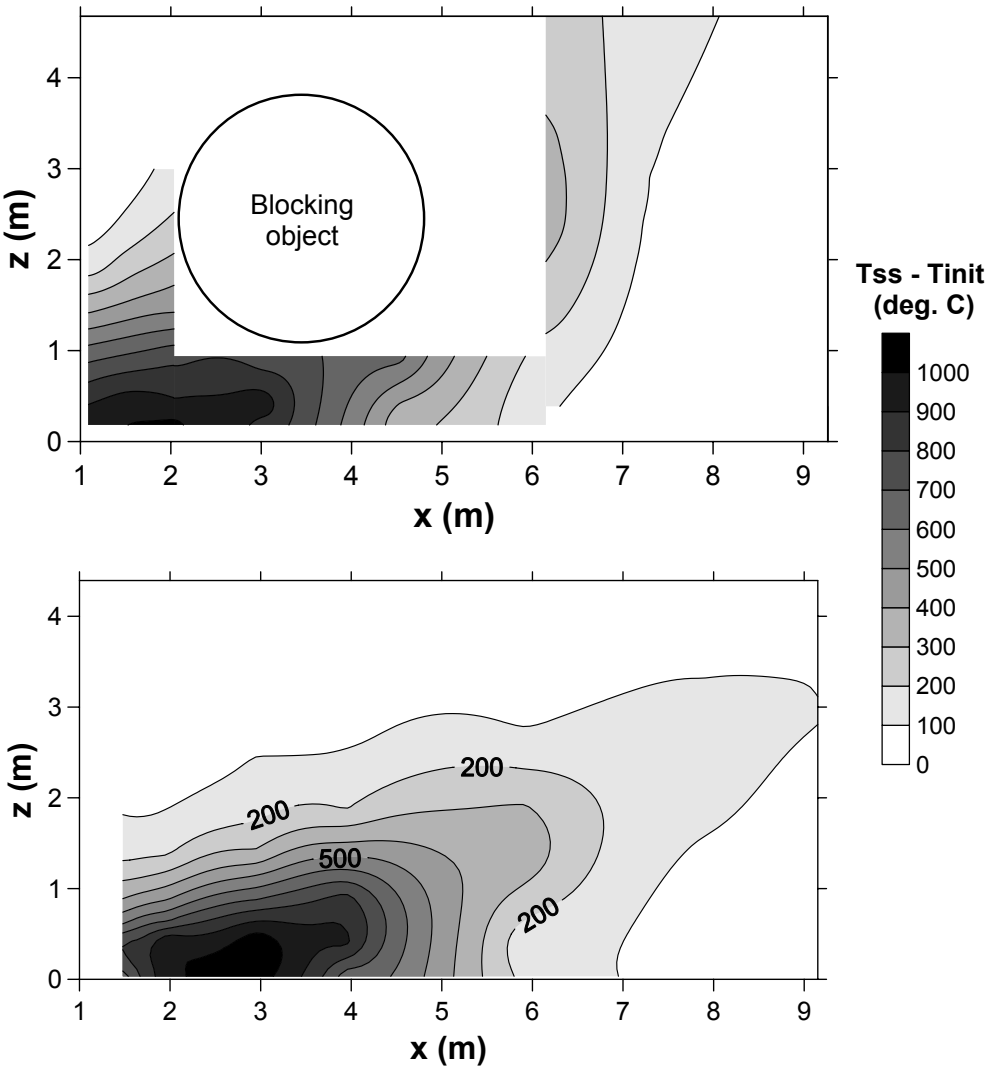

Figure 5.62: Temperature contour plots along y=0 m for fire in 5 m/s wind, (a) with blocking object, (b) without blocking object (test 32)

appeared to wrap around the upper windward portion of the object, indicating that the flow along the upwind edge of the plume was redirected by the windward side of the object. Further downwind, the approximately vertical 100°C and 200°C contours in the region x > 6 m were consistent with the plume flow rising steeply up the leeward side of the object after passing underneath it. This flow redirection reflects a change in momentum of the plume gases caused by impingement of the fire on the blocking object and contrasts with the case without the object (Figure 5.62b), in which the direction of plume travel was governed by a more direct balance between wind momentum and buoyancy effects.

The presence of the object also appeared to influence the temperature of the plume gases, particularly in the region underneath the blocking object. For example, looking along x=3 m in Figure 5.62a for the case with the blocking object, temperatures were between 800°C and 1000°C at heights of z ≤ 0.8 m. Meanwhile, at x=4 m, temperatures ranged from 600°C to 700°C at heights between z=0.5 m and 0.9 m. In contrast, in Figure 5.62b, temperatures along x=3 m were above 1000°C at heights of z ≤ 0.5 m, while at x=4 m, temperatures ranged from 800°C to 900°C at heights between z=0.5 m and 0.9 m. The above differences suggest that the core of the plume was cooler in the test involving the blocking object, consistent with previous studies that indicated significant cooling effects by thermally massive objects on surrounding flames [103, 120].

At the 10 m/s wind speed, differences in plume shape and direction were again evident when comparing the tests with and without the object. In Figure 5.63a, which shows the time-averaged video image of the fire with the object, the upwind edge of the luminous flame immediately above the fuel pan was tilted by approximately 75°, but as the fire approached the object, the tilt angle increased to approximately 105°. The latter angle also characterized the 300°C to 700°C temperature contours upwind of the object (x ≤ 2 m) in Figure 5.64a. In contrast, when the blocking object was not present (Figure 5.63b), the upwind edge of the luminous flame was tilted by 82° above the fuel pan and remained approximately parallel to the ground (tilt of 90°) downwind of the fuel pan. The above differences indicate that the presence of the object caused the plume to lie sufficiently close to the ground that tilt angles greater than 90° were formed. It should be noted, however, that tilt angles greater than 90° can only occur if the surrounding floor is not entirely level with the rim of the fuel pan, as in the present experimental setup in which a step decrease of 0.17 m height was present at the downwind edge of the raised floor surround.

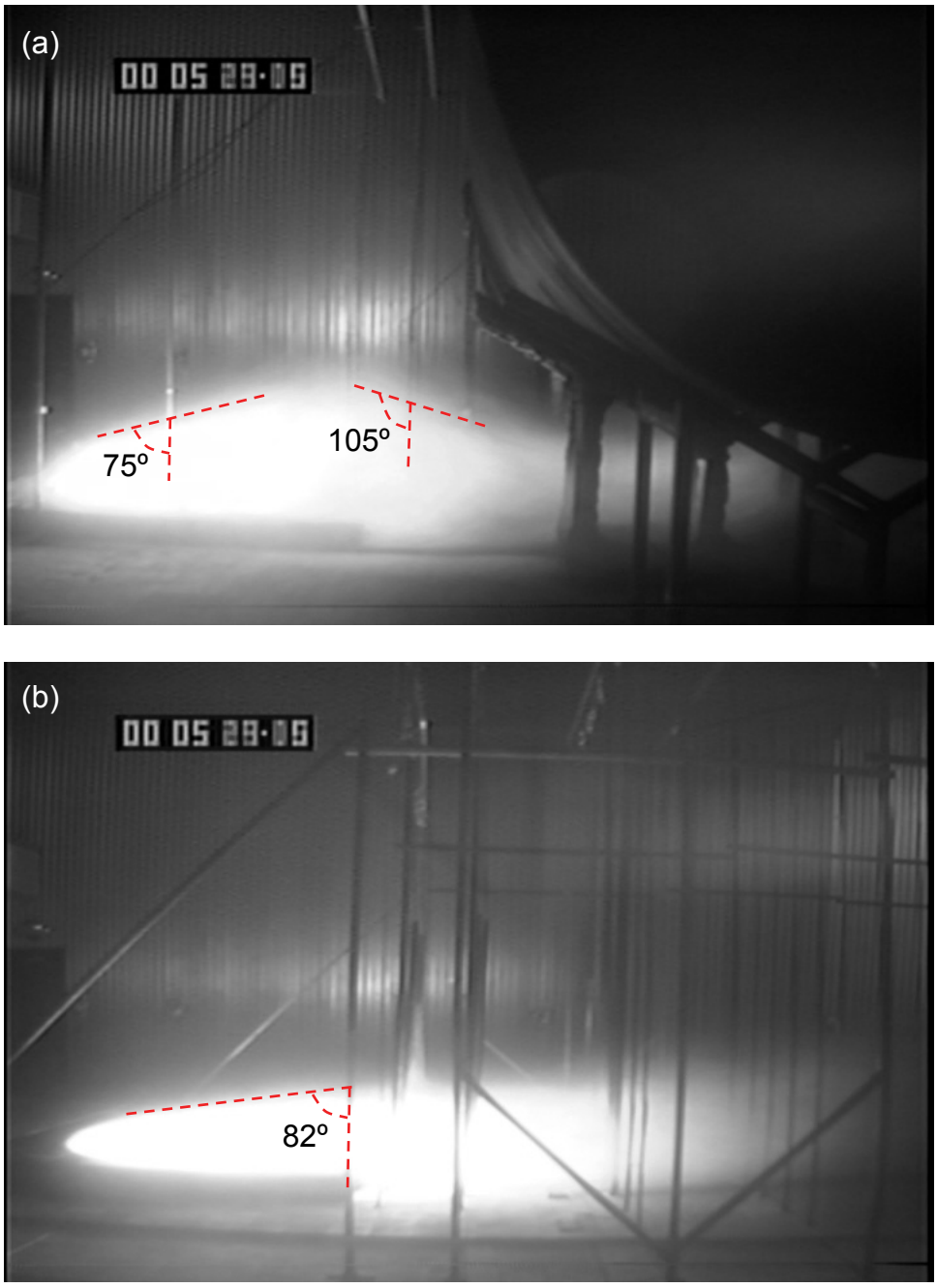

Figure 5.63: Time-averaged video images for fire in 10 m/s wind, (a) with blocking object, (b) without blocking object

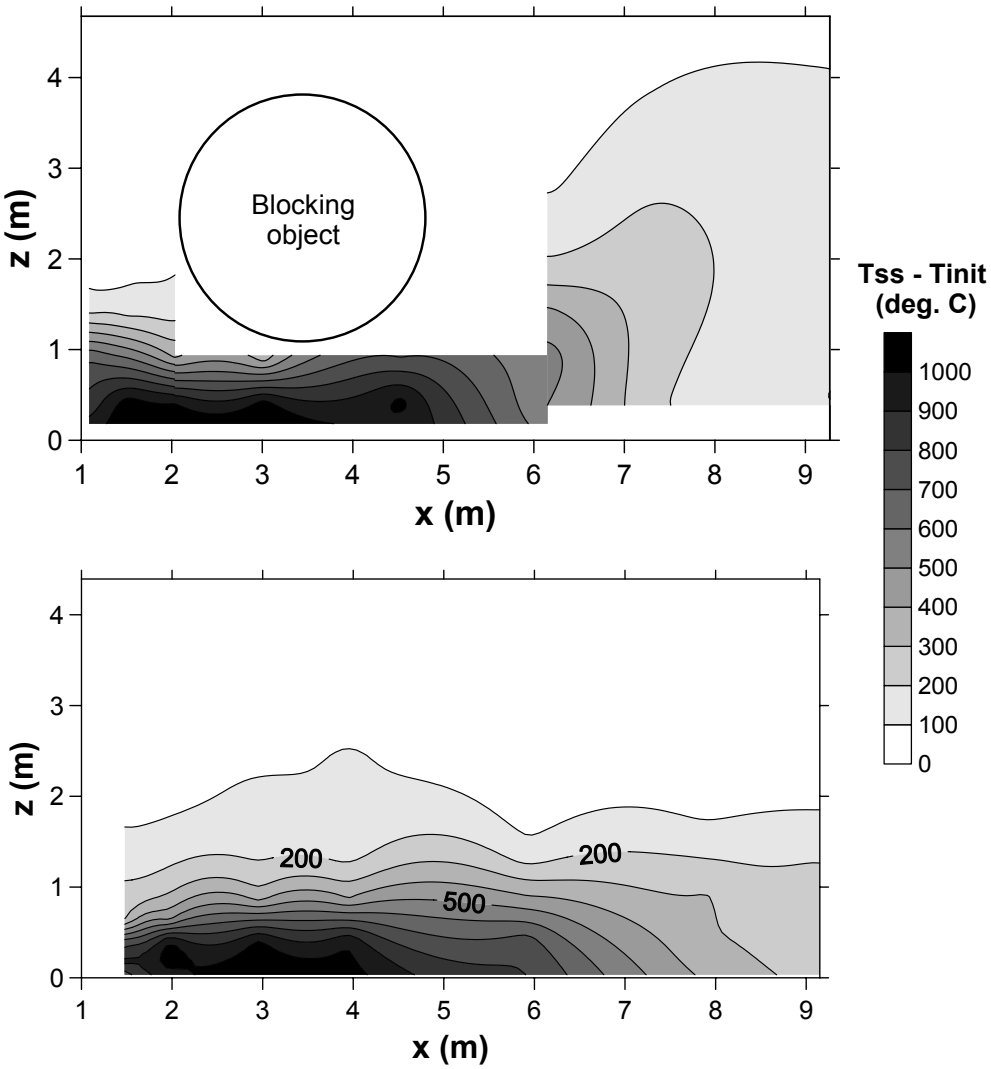

Figure 5.64: Temperature contour plots along y=0 m for fire in 10 m/s wind, (a) with blocking object, (b) without blocking object (test 29)

Further downwind, even more substantial differences in plume direction were observed between the tests with and without the object. As evident in Figure 5.64a, the plume lifted off the ground downwind of the blocking object (at approximately x=6 m), but in Figure 5.64b, it remained attached to the ground along the entire length of the test section. The presence of a low-pressure wake region downwind of the object, together with buoyancy effects, significantly affected the direction of the plume flow. This contrasted with the test without the object, in which the momentum of the wind dominated all other effects.

Temperatures in the central core of the plume near the fuel pan did not appear to be greatly affected by the presence of the object in the 10 m/s wind condition. The region in which temperatures were greater than 900°C spanned similar extents in both plots of Figure 5.64, up to approximately x=4.8 m and z=0.5 m. Since the fire plume did not impinge directly on the object, no significant cooling effect on the plume gases by the thermally massive object would be expected. On the other hand, with the plume lifting off the ground downwind of the object but remaining attached to the ground in the test without the object, the accompanying changes in air entrainment levels would affect temperatures in the core of the plume downwind of x=5 m. For instance, temperatures ranged up to 300°C at a downwind distance of x=7 m in Figure 5.64a, but ranged up to 600°C at the same downwind distance in Figure 5.64b. The longer region of plume attachment to the ground in the test without the object would have reduced the amount of cooler ambient air that could be entrained into the plume, resulting in higher temperatures in the plume core.

The temperature results discussed in the above sections provide an indication of the levels of thermal hazard posed by the fire to the blocking object and its surroundings. Additional characterization of the hazard levels was achieved via measurement of heat flux along the blocking object and in the vicinity of the fire. The heat flux results are discussed next.

5.4 Results and Discussion: Heat Flux

As described in Section 5.1.3, a large quantity of instrumentation was included in the experimental setup to measure heat flux to the ground, to the blocking object and to small cylindrical calorimeters distributed around the test enclosure. For the purposes of this thesis, only selected heat flux data will be presented. These data are chosen to provide insight into interactions between fires and thermally massive

objects, as well as into heat flux measurement methods. The present section will first detail results from heat flux gauges along the blocking object, followed by results from gauges situated downwind of the culvert along the ground. Finally, to examine sensors of significantly different sizes, results from two calorimeters and their neighbouring DFTs will be considered.

5.4.1 Heat Flux to Blocking Object

As indicated in Figure 5.9, one DFT and five HFGs were used to estimate heat flux to the central region of the blocking object. Figure 5.65 shows typical time traces of calculated values of total heat flux incident on these gauges under the 5 m/s and 13 m/s wind speeds, with the corresponding measured temperature data plotted in Figure 5.66. (For reference, the heat flux and temperature time traces corresponding to all tests are provided in Appendix G.) At the 5 m/s wind speed (Figure 5.65a), the heat flux to each gauge reached quasi-steady levels during the steady burning period of the fire (239 s to 411 s, Table 5.6), similar to the heat flux data in the previous chapter (Figure 4.40). However, it may be noted that during the first 100 s of the test, the heat flux to the DFT increased much more quickly than the heat flux to the HFG located at ϕ=315°, even though the HFG sensor plate heated up more quickly than the thicker DFT sensor plate (Figure 5.66a). This discrepancy was likely caused by greater thermal losses from the HFG sensor plate, as identified in Chapter 3,[10] and indicates potentially large dynamic measurement errors in the HFG [143].

At the 13 m/s wind speed, the heat flux to each gauge also reached quasi-steady levels (Figure 5.65b), but unlike the time trace at the 5 m/s wind speed, the heat flux to the DFT initially increased as the fire was ignited, then decreased until approximately t=200 s. At this highest wind speed, the plume did not impinge on the bottom of the blocking object (Section 5.3.4), so convective cooling of the DFT was expected. With the temperature of the DFT sensor plate increasing throughout the test due to radiative heating of the gauge (Figure 5.66b), greater convective cooling of the plate would occur and, providing the radiative heat flux remained approximately constant, the total heat flux would decrease, as seen in Figure 5.65b. In contrast, when the plume impinged on the bottom of the blocking object at the 5 m/s wind speed, radiation would have been much more significant

[10]Since the HFGs in the culvert were not wrapped with any insulation, such losses would have been greater than those associated with the previous chapters.

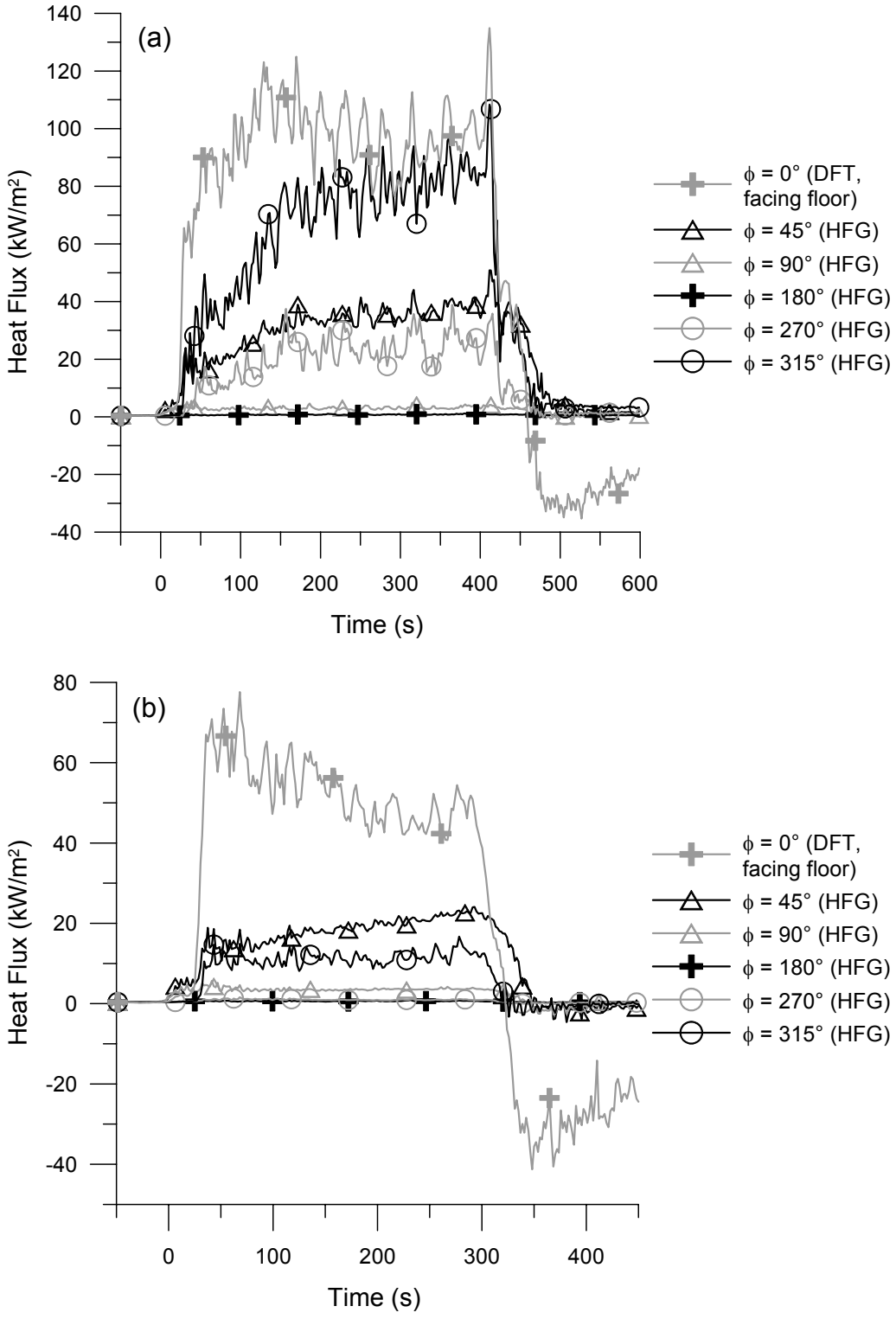

Figure 5.65: Typical plot of incident total heat flux to the blocking object, y≈0 m, (a) 5 m/s wind (test 32), (b) 13 m/s wind (test 30)

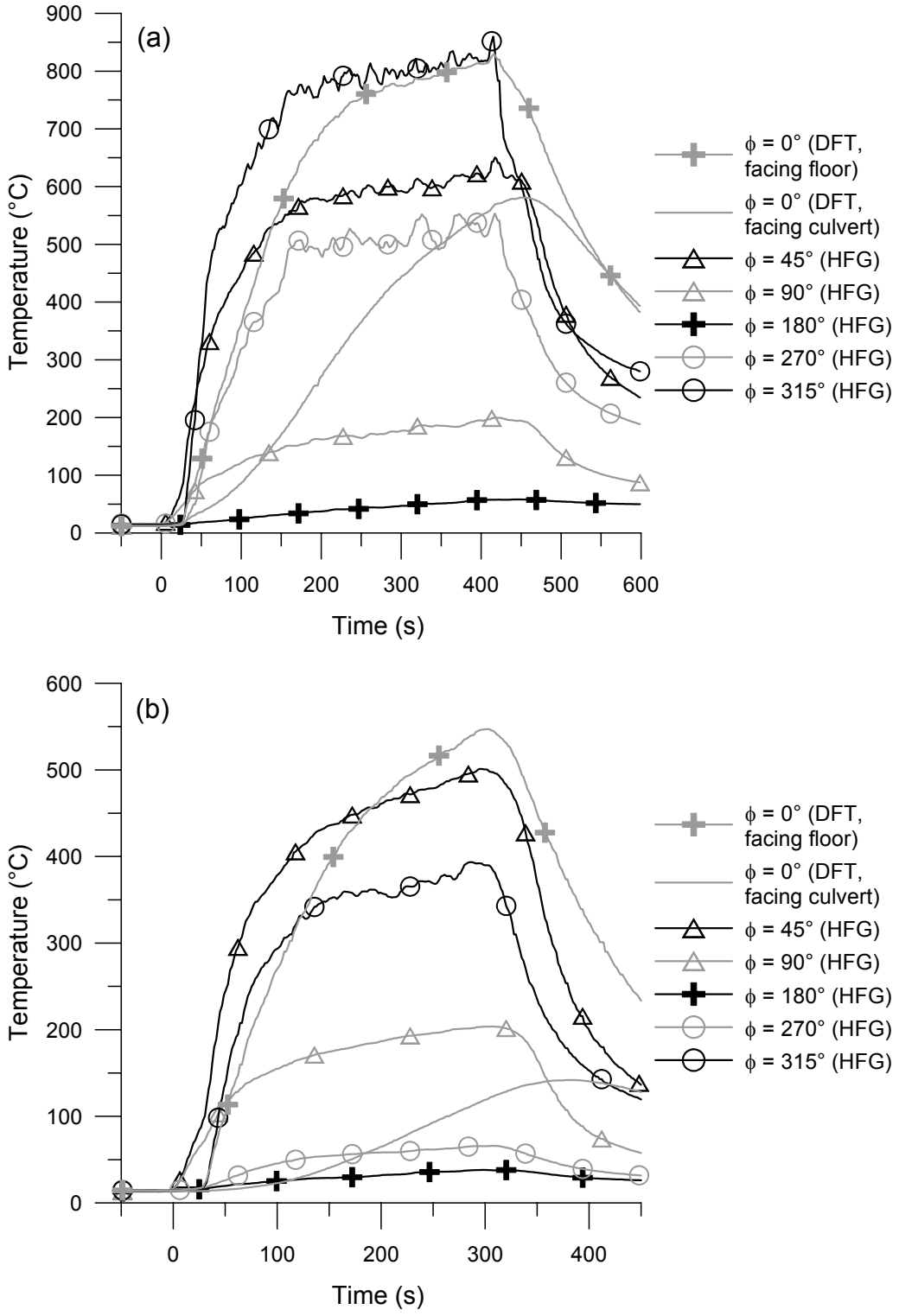

Figure 5.66: Temperatures corresponding to heat flux data shown in Figure 5.65, (a) 5 m/s wind (test 32), (b) 13 m/s wind (test 30)

than convection, resulting in the total heat flux increasing quickly to quasi-steady levels (Figure 5.65a).

In all tests, time-averaged values taken across the steady burning period were evaluated and compared. The average values were calculated using the same procedure as that employed in the previous chapter (Section 4.5), by subtracting the initial value of heat flux (averaged over three minutes immediately prior to startup of the first fan) from the value averaged over the steady burning period. Table 5.7 lists the average values of incident total heat flux to the blocking object, together with the corresponding standard deviations to provide a sense of the variation experienced within a test. The corresponding increases in temperature (again above the initial value) are shown in Table 5.8.

Table 5.7 shows that in all tests, the highest heat flux to the blocking object was measured by the DFT at the bottom (ϕ=0°). This indicates that the heat flux gauge at the bottom of the object was exposed to significant levels of radiation from the hot central core of the plume, consistent with the plume temperature contour plots shown in the previous section (e.g. Figures 5.35 and 5.36). (As indicated previously, convective cooling of this gauge would have also occurred at the higher wind speeds.) Heat flux levels measured by the HFGs decreased as distance from the bottom of the blocking object along the circumference of the cylinder increased, as indicated by the moderate to high levels of heat flux measured at $\phi = 45°$ and 315°, and lower levels of heat flux measured at $\phi = 90°$, 180° and 270°. In the tests with the 5 m/s wind, moderate levels of heat flux were also observed at the position $\phi = 270°$, as a result of the plume rising up against the leeward side of the object. The gauges at $\phi = 45°$ and 90° were exposed to lower overall levels of heat flux than the gauge at $\phi = 0°$ due to the presence of cooler gases near the upwind edge of the plume, increased radiative contribution by the ambient surroundings, and decreased radiation from the hot central core of the fire to gauges that were at a higher elevation above the ground. Meanwhile, the gauges at $\phi = 180°$ and 270° faced away from the hot central core of the fire and were thus exposed to low levels of radiation from the fire. Heat flux to these gauges would have been dominated by convection from gases flowing past the top and leeward side of the object, while heat flux to the gauge at $\phi = 315°$ would have been affected by a combination of convection and radiation from the hot plume flowing underneath the object.

In addition to any effects of differences in radiative and convective fraction to the heat flux at the different gauge locations, the measured heat flux values

Table 5.7: Increase in Incident Total Heat Flux to the Blocking Object (kW/m^2)

ϕ	0°	45°	90°	180°	270°	315°
Gauge	DFT	HFG	HFG	HFG	HFG	HFG
5 m/s Wind:						
Test 27	74 ± 11	33 ± 3	2.6 ± 0.4	0.4 ± 0.1	14 ± 3	55 ± 8
Test 32	96 ± 10	36 ± 3	2.8 ± 0.6	0.5 ± 0.1	24 ± 5	81 ± 8
7 m/s Wind:						
Test 28	44 ± 7	21 ± 1	2.6 ± 0.1	0.3 ± 0.1	1.4 ± 0.3	21 ± 3
Test 31	56 ± 6	19 ± 1	2.5 ± 0.1	0.3 ± 0.1	3.3 ± 0.6	42 ± 5
10 m/s Wind:						
Test 26	26 ± 5	18 ± 1	3.2 ± 0.1	0.3 ± 0.1	0.5 ± 0.1	6.9 ± 1.1
Test 29	50 ± 4	21 ± 1	2.9 ± 0.1	0.2 ± 0.1	0.6 ± 0.1	21 ± 2
13 m/s Wind:						
Test 25	27 ± 6	20 ± 1	3.4 ± 0.2	0.3 ± 0.1	0.3 ± 0.1	4.6 ± 1.0
Test 30	47 ± 4	20 ± 2	3.2 ± 0.2	0.3 ± 0.1	0.6 ± 0.1	11 ± 2

Table 5.8: Temperature Increases Corresponding to Table 5.7 (°C)

ϕ	0°	45°	90°	180°	270°	315°
Gauge	DFT	HFG	HFG	HFG	HFG	HFG
5 m/s Wind:						
Test 27	683 ± 30	563 ± 16	159 ± 10	28 ± 5	398 ± 13	686 ± 21
Test 32	774 ± 19	592 ± 11	169 ± 9	36 ± 5	500 ± 19	790 ± 15
7 m/s Wind:						
Test 28	523 ± 32	482 ± 10	166 ± 7	22 ± 3	103 ± 7	483 ± 16
Test 31	546 ± 38	447 ± 15	156 ± 5	24 ± 3	184 ± 5	617 ± 26
10 m/s Wind:						
Test 26	386 ± 21	446 ± 9	187 ± 5	27 ± 2	50 ± 2	287 ± 10
Test 29	576 ± 16	474 ± 9	178 ± 5	19 ± 2	46 ± 1	468 ± 9
13 m/s Wind:						
Test 25	397 ± 24	469 ± 11	197 ± 6	24 ± 2	30 ± 2	231 ± 11
Test 30	474 ± 38	458 ± 17	179 ± 8	20 ± 3	45 ± 3	353 ± 12

listed in Table 5.7 were expected to be affected by different measurement biases associated with using the DFT (ϕ=0°) and HFG (all other positions). Based on the discussion in Chapter 3, the DFT was expected to measure higher levels of heat flux than the HFG, even under the same radiative and convective conditions. In the tests without the blocking object (Chapter 4), the HFG measured heat flux levels that were approximately 20% lower than those measured by the DFT when both gauges were immersed in the radiative, optically thick flames of the fire (Table 4.14, y=0 m). The HFG data in Table 5.7 would thus be expected to be at least 20% lower than if DFTs had been used in their place. Given that the HFGs in the culvert did not have any insulation surrounding the gauge housing (as in Chapters 3 and 4), the heat flux estimates from these gauges would have been influenced by greater convective losses from the gauge housing than in the experiments of the previous chapters. This would intensify any measurement bias caused by conduction losses from the HFG sensor plate to the HFG housing and further lower the heat flux levels measured by the HFG.

Comparison of heat flux values from the two tests conducted at each wind speed (Table 5.7) showed that in general, similar heat flux levels were measured in each pair of tests at $\phi = 45°$, 90°, 180° and 270°, while heat flux levels at $\phi = 0°$ and 315° differed considerably between repeated tests. The latter two locations were affected by changes in the thermal field of the fire plume – as discussed in Section 5.2, differences in the initial temperature of the blocking object between repeated tests contributed to large differences in the thermal field of the fire plume underneath and downwind of the blocking object. Despite the poor test-to-test repeatability of the values measured at $\phi = 0°$ and 315°, a general trend of decreasing heat flux with increasing wind speed was evident at these two locations and at $\phi = 270°$. This was because as wind speed increased, significant changes in plume shape and direction occurred in the region downwind of the blocking object, with the plume rising upward along the leeward side of the object in the 5 m/s wind condition but lying flat along the ground in the 13 m/s wind condition.

The heat flux levels in Table 5.7 could be compared to those reported in the literature for large objects in fires [7, 102, 115]. Time-averaged values of incident total heat flux to a 1.4 m diameter by 6.4 m long cylinder engulfed in a 9.1 m by 18.3 m fire under low wind conditions ranged from 76 kW/m^2 to 107 kW/m^2, with the highest values corresponding to the bottom and downwind sides of the cylinder where thicker flame coverage existed [102]. In the experiment associated with Figure 2.5, which involved a 18.9 m diameter, wind-blown fire with a 3.7 m

diameter downwind blocking object, time-averaged values of incident heat flux to the object ranged from 10 kW/m^2 to 400 kW/m^2 [7]. The highest values (over 300 kW/m^2) were measured along the leeward side of the object under wind speeds of 9-10 m/s and were thought to result from increased fuel-air mixing in the wake region behind the object [7]. High levels of heat flux (over 200 kW/m^2) were also measured along the windward side of the object due to direct flame impingement on the cylinder surface [7]. For a 7.9 m diameter fire with a 1.2 m diameter downwind blocking object (Figure 2.6), incident heat flux levels ranging from approximately 70 kW/m^2 to 210 kW/m^2 were measured along the circumference of the object when the fire was affected by 6.1 m/s winds [115]. The highest values were measured along the leeward side of the cylinder and were thought to occur as a result of increased fuel-air mixing in the wake region of the object [115].

In the present experiments, heat flux values ranged from less than 0.5 kW/m^2 at the top of the cylinder (under all wind speeds) to a maximum of 96 kW/m^2 at the bottom of the cylinder (in the 5 m/s wind condition). As seen in Section 5.3.1, the fire impinged on the bottom of the blocking object under the 5 m/s wind, so maximum values of heat flux could be expected to occur in this region of the object at that wind speed. However, the maximum measured value of 96 kW/m^2 was somewhat lower than the published maximum values mentioned above, due to several possible reasons. First, the gauge at $\phi = 0^\circ$ was located at y=0.14 m, but the fire was skewed toward the -y side of the facility, as shown in Section 5.3. Thus this gauge was offset from the centreline of the plume and did not measure the true local maximum heat flux from the fire to the object. Second, the large blocking object was unable to attain thermal equilibrium with the fire during the 7-10 minute duration tests, as indicated by the blocking object temperatures which did not reach quasi-steady levels (Figure 5.20). The presence of a cooler, thermally massive object in the fire plume may have lowered the temperature of the plume gases near the object and reduced the heat flux incident on the object surface [106, 120, 201]. Third, the fire in the present experiments was much smaller than those in the experiments mentioned above, so the plume gases surrounding the heat flux gauges may not have been optically thick, resulting in radiative contributions from the cooler outer surroundings and lower overall heat flux measurements. Finally, no significant increase in fuel-air mixing was observed in the wake region behind the object, so measurement of a maximum value of heat flux on the downwind side of the object was not expected, unlike in the two high-wind experiments described above. These combined reasons may explain the lower maximum levels of heat flux

measured in the present experiment, compared to the maximum values published in the literature [7, 102, 115].

5.4.2 Heat Flux to Ground Downwind of Blocking Object

Five heat flux gauges – a DFT, HFG, Gardon gauge and two different thermopiles – were used to estimate heat flux to the ground at distances between 5.3 m and 6.0 m downwind of the fuel pan centre (Figure 5.8 and Table 5.1). Typical time traces of incident total heat flux to the DFT, HFG and Gardon gauge are shown in Figure 5.67. (For reference, the time traces from all tests are provided in Appendix H.) The corresponding time traces from the thermopiles were similar to that of the Gardon gauge and are not included in the plot for clarity. Similar to the heat flux gauges in the culvert (Section 5.4.1), quasi-steady levels of heat flux were measured during the steady burning period of the fire (196 s to 372 s, Table 5.6), so the heat flux data could be averaged across the steady burning period for subsequent comparison. Time-averaged values of the increase in incident total heat flux (calculated in the same manner as the values in Table 5.7) are provided in Table 5.9.

Typical time traces of the measured temperature data from the DFT and HFG are plotted in Figure 5.68, along with data from an exposed thermocouple located between the DFT and HFG at an elevation of z=0.08 m. Unlike the heat flux data, the sensor plate temperatures did not always reach quasi-steady levels during a test. Comparison of the sensor plate temperatures measured at the end of the steady burning period with those averaged across this period did not reveal any significant differences in terms of overall trends; therefore, to maintain consistency with the previous section, the time-averaged increases in temperature are shown in Table 5.10.

The data in Tables 5.9 and 5.10 indicate a general increase in heat flux and sensor plate temperature with increasing wind speed, consistent with an increase in tilt of the fire plume. The poor test-to-test repeatability discussed previously in Section 5.2 was clearly evident when comparing results between tests conducted at the same wind speed. Differences between each pair of repeat tests were consistent with changes in the plume temperature field as described in Sections 5.2 and 5.3. For instance, at the 10 m/s wind speed, the plume temperatures at a given distance downwind of the blocking object were hotter in the second test than in the first test (compare Figures 5.43b and 5.43c with Figures 5.44b and 5.44c), so higher

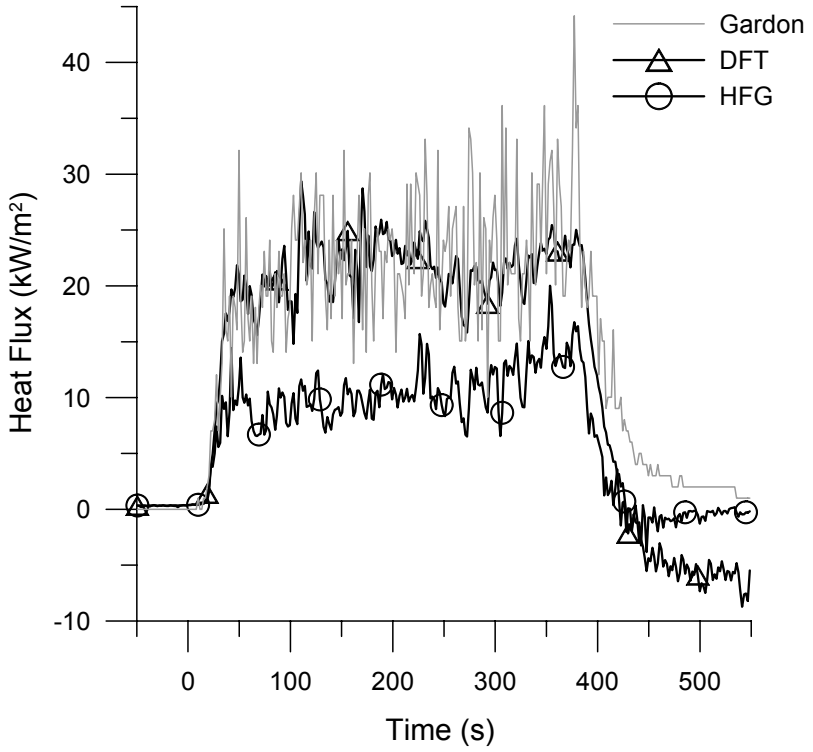

Figure 5.67: Typical plot of incident total heat flux to the ground, 7 m/s wind (test 28), x=5.3 m to 5.6 m, y=-0.5 m to -0.3 m

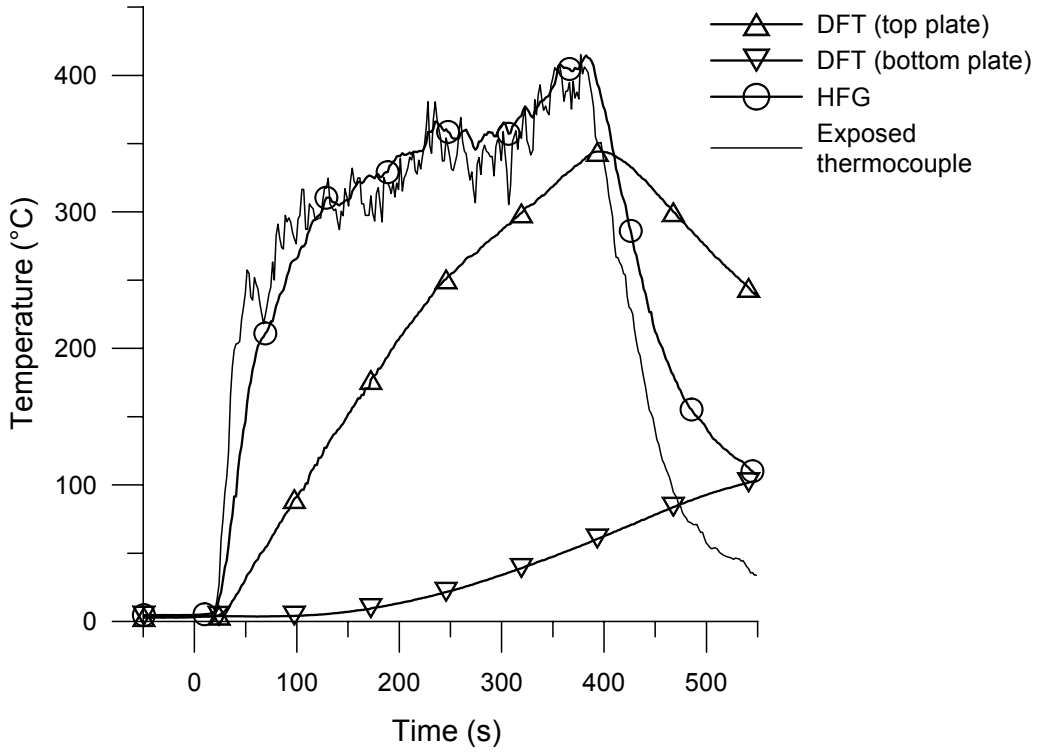

Figure 5.68: Temperatures corresponding to heat flux data shown in Figure 5.67

Table 5.9: Increase in Incident Total Heat Flux to the Ground (kW/m^2)

Gauge	DFT	HFG	Gardon	RdF thermopile	Medtherm thermopile
x location	5.35 m	5.34 m	5.58 m	5.81 m	6.04 m
y location	-0.30 m	-0.41 m	-0.48 m	-0.48 m	-0.48 m
z location	0.02 m	0.02 m	0.00 m	0.01 m	0.03 m
5 m/s Wind:					
Test 27	11 ± 1	5.1 ± 0.8	16 ± 3	7.9 ± 2.1	6.5 ± 2.0
Test 32	12 ± 1	5.5 ± 0.8	18 ± 2	9.0 ± 1.9	7.8 ± 2.0
7 m/s Wind:					
Test 28	21 ± 2	11 ± 2	23 ± 6	15 ± 5	14 ± 5
Test 31	31 ± 4	18 ± 3	30 ± 8	20 ± 5	19 ± 5
10 m/s Wind:					
Test 26	36 ± 6	27 ± 5	45 ± 13	28 ± 10	24 ± 8
Test 29	78 ± 6	52 ± 6	63 ± 15	42 ± 12	41 ± 14
13 m/s Wind:					
Test 25	47 ± 9	35 ± 7	52 ± 16	42 ± 14	41 ± 13
Test 30	87 ± 8	66 ± 7	80 ± 21	52 ± 16	46 ± 15

Table 5.10: Temperature Increases Corresponding to Table 5.9 (°C)

Gauge	DFT	HFG	Thermocouple
x location	5.35 m	5.34 m	5.37 m
y location	-0.30 m	-0.41 m	-0.37 m
z location	0.02 m	0.02 m	0.08 m
5 m/s Wind:			
Test 27	170 ± 27	236 ± 12	164 ± 17
Test 32	186 ± 22	243 ± 8	159 ± 10
7 m/s Wind:			
Test 28	270 ± 37	359 ± 19	350 ± 25
Test 31	379 ± 29	443 ± 12	410 ± 24
10 m/s Wind:			
Test 26	437 ± 32	527 ± 14	529 ± 40
Test 29	663 ± 40	681 ± 13	712 ± 34
13 m/s Wind:			
Test 25	506 ± 36	582 ± 23	624 ± 43
Test 30	652 ± 51	729 ± 18	774 ± 33

values of heat flux to the ground would be expected in the second test. Due to the poor test-to-test repeatability, it was difficult to compare results between gauges and wind speeds, but some overall patterns could be identified.

The results from the two thermopiles in Table 5.9 showed reasonably consistent agreement, with measured heat flux values agreeing to within 22%. The Medtherm values were lower than the RdF values in all tests, partly due to the presence of a 90° view restrictor covering the Medtherm sensor surface, which would prevent it from seeing much of the hot plume upwind of the gauge and also minimize any convection to the gauge [198]. The Medtherm gauge was also located further downwind from the fuel pan and thus exposed to less heat from the fire (Table 5.1). Other causes of differences between the results from the two gauges included differences in the design of the thermopiles (the Medtherm gauge was based on the Schmidt-Boelter design, while the RdF gauge was based on a manufacturer-developed microfoil design), as well as differences in calibration method and gauge sensitivity. The RdF and Medtherm data were both lower than the Gardon data in all tests, again partly due to differences in gauge location, calibration method and gauge sensitivity. Measurement biases associated with gauge type were expected to influence the results as per the discussion in Chapter 3. However, it should be noted that the Schmidt-Boelter gauge used in the cone calorimeter experiments was not the same as either of the thermopiles used in the present experiments.

Agreement was found to be generally poor when comparing the results from all five gauges (Table 5.9). The Gardon gauge and DFT consistently measured higher levels of heat flux than the HFG and thermopiles, with the DFT value being highest in tests 29 to 31 and the Gardon value being highest in all other tests. Agreement between the Gardon and DFT results was influenced by differences in the location of the gauges relative to the fire plume – although the DFT was closer to the fuel pan in the x direction and exposed to hotter gases in the fire, it was also situated further from the plume centreline in the y direction. (In most tests, the plume was skewed by approximately 0.5 m in the -y direction at the location of the heat flux gauges (Section 5.3).) Consequently, any increase in heat flux that would be measured by the DFT due to its smaller distance from the fuel pan would be offset by a decrease in heat flux caused by its greater distance from the plume centreline. The combination of these two effects, plus any measurement biases similar to those discussed in Chapter 3, would be important in determining whether the DFT or Gardon value was higher during a test. Meanwhile, the HFG, which was situated upwind of the Gardon gauge and beside the DFT (Figure 5.8), measured lower levels of heat flux than both the DFT and Gardon gauge. This could potentially be attributed to significant conduction losses through the HFG housing, which was not insulated from the brick floor in which it was recessed, as in the experiments of the previous chapters (Section 5.1.3). Additional factors influencing the heat flux data from all five gauges included soot deposition on the gauge surfaces, which was most noticeable at the two lowest wind speeds and would have affected the surface emissivity and level of absorbed heat flux, as well as differences in the surface temperature of the gauges, which would have affected the levels of soot deposition on, and convective heat transfer to, the gauges.

Effects of convective heat transfer to the DFT and HFG could be examined by considering the temperature data in Table 5.10. This table shows that the temperatures measured by the HFG were higher than those of the DFT in all tests, partly due to the HFG being situated closer to the centreline of the skewed plume than the DFT and partly due to the thicker sensor plate of the DFT taking longer to heat up (Figure 5.68). At the 5 m/s wind speed, the temperatures of both the HFG and DFT were higher than the corresponding temperatures measured by the exposed thermocouple, but as the wind speed increased, they became lower than the temperatures of the exposed thermocouple (Table 5.10). This suggests that at the high wind speeds, the HFG and DFT were convectively heated, since the gases above the gauges were hotter than the gauge surfaces, while at the low wind speeds, they

were convectively cooled. However, further investigation is required to confirm such effects because potentially large radiation errors in the temperature data may have been caused by the presence of the large blocking object and nearby calorimeters, as well as by soot deposition on the sensor surfaces. These radiation effects would have been more significant when the flow above the gauges was not optically thick (as at the lower wind speeds) and, as mentioned in Section 4.5, would have affected the temperature data from the DFT, HFG and exposed thermocouple differently due to the different geometries of the different sensors, potentially influencing the apparent trends indicated by Table 5.10. Regardless, differences in surface temperature between the DFT, HFG and water-cooled Gardon gauge and thermopiles would have contributed to some of the differences in the heat flux results presented in Table 5.9, as previously indicated in Chapter 3.

5.4.3 Heat Flux to Cylindrical Calorimeters

As described in Section 5.1.3, calorimeters were included in the experimental layout to simulate cargo packages in the aircraft accident scenario. These calorimeters were based on the same heat flux measurement technique as the DFT, but contained greater thermal mass due to their much larger size. In this section, data from two calorimeters will be compared to corresponding data from neighbouring DFTs to examine differences between heat flux sensors of vastly different sizes and shapes.

The calorimeters to be considered were situated at locations 'A' and 'D' in Figure 5.12 and Table 5.2. Nearby DFTs were situated at locations 'A' and 'B' for the first calorimeter, and locations 'D' and 'E' for the second calorimeter (Table 5.3). These calorimeters were chosen based on the plume temperature profiles shown in Section 5.3, as they appeared to be situated well inside the fire plume and exposed to significant heat flux during all tests.

The heat flux results from ϕ=90° on the calorimeters were compared to the results from the DFTs. This angular position was considered to be the most appropriate for comparison to the DFTs because it faced in the same direction as the upwind sensor plate of the DFT and was thus exposed to a similar environment as the DFT. Typical time traces of incident total heat flux to the calorimeter at location 'D' and its neighbouring DFTs are plotted in Figure 5.69, with the corresponding traces of net absorbed heat flux plotted in Figure 5.70 and the temperature time traces plotted in Figure 5.71. (For reference, the heat flux and temperature time traces corresponding to all tests are provided in Appendix I.)

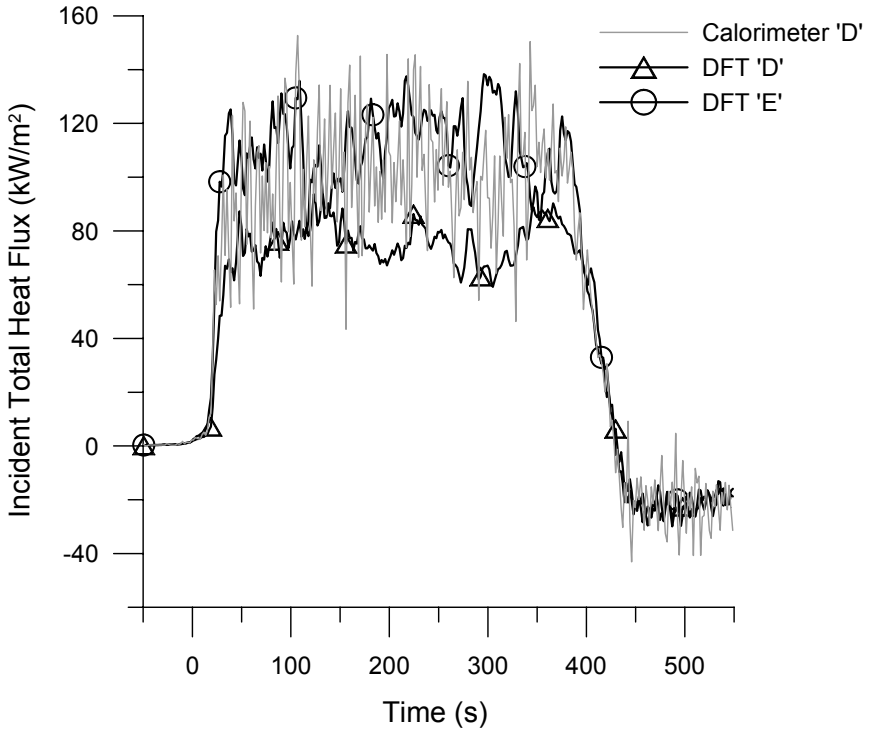

Figure 5.69: Typical plot of incident total heat flux to calorimeter and DFTs, 7 m/s wind (test 28)

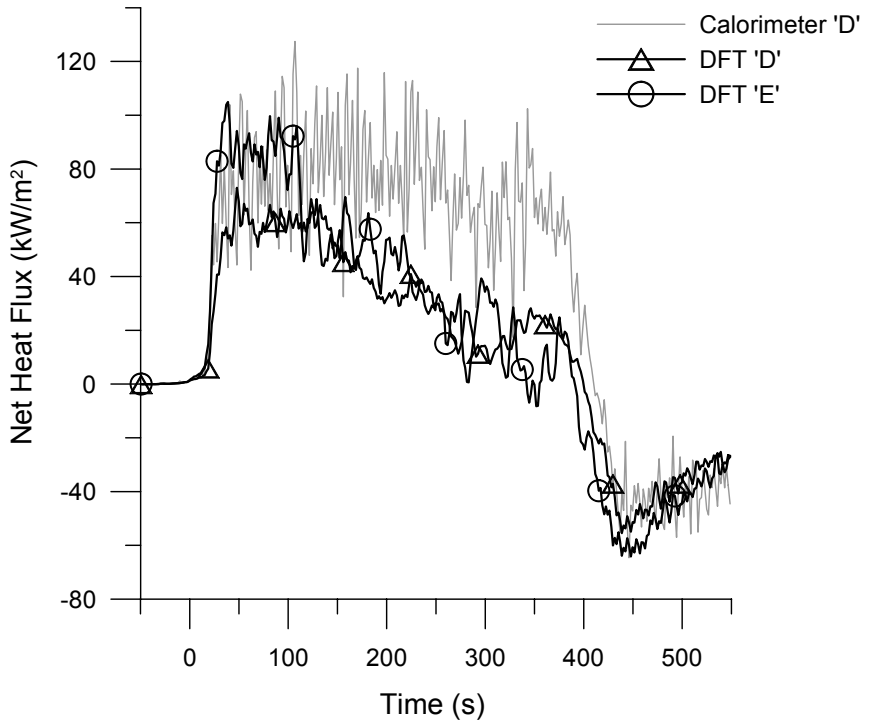

Figure 5.70: Typical plot of net heat flux absorbed by calorimeter and DFTs, 7 m/s wind (test 28)

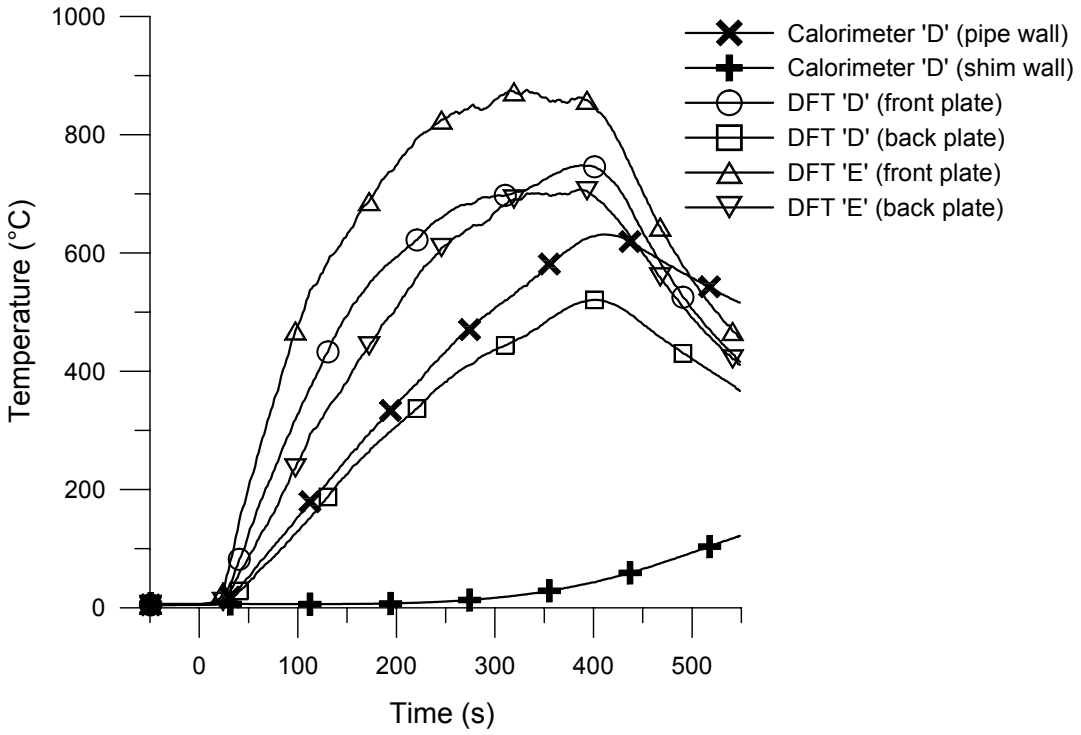

Figure 5.71: Temperatures corresponding to heat flux data shown in Figures 5.69 and 5.70

Figure 5.70 shows that the net heat flux absorbed by the DFTs decreased steadily throughout the test, while the net heat flux to the calorimeter remained relatively constant. Since the DFTs had much less thermal mass than the calorimeter, they approached equilibrium with the local fire environment much more quickly, resulting in low values of net heat flux towards the end of the test. On the other hand, the calorimeter remained cool throughout the test (the temperature of the shim wall remained less than 100°C while the fire was burning (Figure 5.71)), so it could absorb heat at approximately the same rate at the beginning and end of the test.

In contrast to the net heat flux, the levels of incident total heat flux remained reasonably steady throughout the test for both the DFTs and the calorimeter. In Figure 5.69, quasi-steady levels of incident total heat flux were evident during the steady burning period of the fire (196 s to 372 s, Table 5.6), allowing time-averaged values across the steady burning period to be evaluated and compared (Table 5.11). The time trace of heat flux to the calorimeter appeared to exhibit more noise than the time traces from the DFTs, partly due to differences in the type of thermocouple installed in each sensor. The DFTs contained ungrounded-junction, metal-sheathed

Table 5.11: Increase in Incident Total Heat Flux to Calorimeters and Neighbouring DFTs (kW/m^2)

Gauge	Calorimeter 'A'	DFT 'A'	DFT 'B'	Calorimeter 'D'	DFT 'D'	DFT 'E'
x location	1.99 m	1.98 m	1.91 m	3.40 m	3.07 m	3.08 m
y location	0.00 m	-0.54 m	0.54 m	-0.44 m	-0.67 m	0.16 m
z location	0.59 m	0.44 m	0.44 m	0.16 m	0.07 m	0.07 m
5 m/s Wind:						
Test 27	125 ± 17	154 ± 5	115 ± 9	102 ± 15	90 ± 6	99 ± 9
Test 32	133 ± 15	163 ± 7	112 ± 8	90 ± 11	69 ± 3	97 ± 8
7 m/s Wind:						
Test 28	120 ± 17	161 ± 8	97 ± 12	103 ± 20	75 ± 8	115 ± 14
Test 31	133 ± 17	172 ± 5	86 ± 6	117 ± 18	83 ± 8	118 ± 15
10 m/s Wind:						
Test 26	116 ± 19	189 ± 5	93 ± 12	169 ± 27	151 ± 11	94 ± 17
Test 29	141 ± 19	185 ± 4	111 ± 6	150 ± 23	107 ± 8	175 ± 8
13 m/s Wind:						
Test 25	129 ± 24	207 ± 9	118 ± 9	208 ± 39	170 ± 13	134 ± 14
Test 30	154 ± 42	217 ± 5	118 ± 9	219 ± 62	184 ± 9	178 ± 8

thermocouples [139], which are associated with lower noise levels in the measured temperature and calculated heat flux data than the intrinsic thermocouples installed in the calorimeter [174]. Use of more than three future temperatures to process the calorimeter temperature data would smooth the corresponding heat flux results by damping out some of the noise [103, 144, 160]; however, given that time-averaged values were to be compared, increasing the number of future temperatures was not deemed necessary and three future temperatures were maintained to permit consistency between the analyses of the calorimeter and DFT results.

Figure 5.71 shows that quasi-steady levels of temperature were not always attained by the calorimeter or DFTs during the steady burning period of each test. Temperatures measured at the end of the steady burning period were up to 10% and 30% higher than temperatures averaged across this period for the DFT and calorimeter, respectively. The continually increasing temperature levels did not prevent attainment of quasi-steady heat flux levels in Figure 5.69 because heat flux depends on rates of temperature change (cf. Equation 3.9 on page 65), which may be steady even though the magnitudes of temperature continue to increase. To provide a better indication of the hazard posed by the fire to each calorimeter, Table 5.12 lists temperatures measured by the calorimeters and DFTs at the end of the steady burning period, with an initial value subtracted to yield an increase in temperature from the beginning of the test.

In all tests, the measured heat flux from the calorimeter situated at location 'A' was between those of its neighbouring DFTs, with the DFT at location 'A' measuring higher levels of heat flux than the DFT at location 'B' (Table 5.11). These results were in agreement with the plume temperature profiles discussed in Section 5.3, which showed that the fire was skewed in the -y direction, with maximum temperatures occurring at y=-0.5 m along (x,z)=(2.0 m, 0.4 m) (Figures 5.28, 5.38, 5.48 and 5.58). Given that heat flux would be expected to decrease as distance from the plume centreline in the y direction increased (Section 4.5), the heat flux data suggested that no significant differences resulted from using the calorimeter versus the DFT to measure total heat flux.

At location 'D', differences between the heat flux measured by the calorimeter and those measured by its neighbouring DFTs varied depending on the test. In all tests at the 5 m/s and 7 m/s wind speeds, the calorimeter measured levels of heat flux that were either similar to or lower than the levels measured by the DFT at location 'E', while the DFT at location 'D' measured lower levels of heat flux than

Table 5.12: Temperature Increases Measured at End of Steady Burning Period in Calorimeters and Neighbouring DFTs(°C)

Gauge	Calorimeter 'A'	DFT 'A'	DFT 'B'	Calorimeter 'D'	DFT 'D'	DFT 'E'
x location	1.99 m	1.98 m	1.91 m	3.40 m	3.07 m	3.08 m
y location	0.00 m	-0.54 m	0.54 m	-0.44 m	-0.67 m	0.16 m
z location	0.59 m	0.44 m	0.44 m	0.16 m	0.07 m	0.07 m
5 m/s Wind:						
Test 27	764	1009	885	631	786	804
Test 32	783	1026	884	559	704	808
7 m/s Wind:						
Test 28	707	1027	816	597	737	849
Test 31	713	1025	772	674	757	862
10 m/s Wind:						
Test 26	666	1066	793	830	958	796
Test 29	793	1059	859	778	838	1033
13 m/s Wind:						
Test 25	710	1107	864	899	1003	907
Test 30	696	1097	854	851	1020	1012

both the DFT at location 'E' and the calorimeter (Table 5.11). This was consistent with the temperature profiles measured along (x,z)=(3.0 m, 0.2 m) in Figures 5.29 and 5.39, which showed maximum temperatures occurring at y=0 m and decreasing on either side of the longitudinal midplane, indicating that this region of the fire plume was not significantly skewed in the -y direction. The DFT temperature data in Table 5.12 were also in agreement with the plume temperature profiles, since the DFT at location 'E' registered higher temperatures than the DFT at location 'D'.

At the 10 m/s and 13 m/s wind speeds, the calorimeter typically measured higher levels of heat flux than both DFTs, and the DFT at location 'D' typically measured higher levels of heat flux than the DFT at location 'E' (Table 5.11). An exception existed in the results for test 29 at the 10 m/s wind speed, which reflected the same trends as those observed at the 5 m/s and 7 m/s wind speeds. It may be noted from Section 5.3 that the plume was skewed more significantly in test 26 at the 10 m/s wind speed and in both tests (tests 25 and 30) at the 13 m/s wind speed than in test 29. Indeed, the temperature profiles measured along (x,z)=(3.0 m, 0.2 m) in Figures 5.49 and 5.59 showed maximum temperatures occurring at y=-0.5 m in tests 26, 25 and 30, but at y=0 m in test 29. Since these maximum temperatures indicated the approximate location of the plume centreline, the calorimeter (at y=-0.44 m) would be closest to the plume centreline and exposed to the highest levels of heat flux in tests 26, 25 and 30. At the same time, the lowest levels of heat flux would be seen by the DFT at location 'E' (y=0.16 m), with results from the DFT at location 'D' (y=-0.67 m) falling in between, as seen in Table 5.11. On the other hand, in test 29, the DFT at location 'E' would be closest to the plume centreline, followed by the calorimeter and then the DFT at location 'D'. Heat flux levels would therefore be expected to decrease in this order, as evident in Table 5.11. The heat flux results for this calorimeter and its neighbouring DFTs thus appeared to be consistent with the changes in plume skew described in Section 5.3.

The temperature data in Table 5.12 indicated that lower temperatures were typically measured in the calorimeters than in their associated DFTs. This was likely due to the greater thermal mass of the calorimeter, which took longer to heat up than the DFTs (Figure 5.71). Also, the temperatures were measured along the unexposed surface of the sensor plate or calorimeter wall and since the calorimeter wall was thicker than the DFT sensor plate (10 mm versus 3.2 mm), lower temperatures were expected to be obtained in the calorimeter. However, this difference would have been much more significant during early times in the test, when the calorimeter was cold, than at the end of the steady burning period, after the calorimeter

had been heated by the fire. The calorimeter surface temperatures calculated by IHCP1D at the end of the steady burning period were found to be approximately 2% higher than the corresponding temperatures listed in Table 5.12, indicating that only a small temperature gradient existed through the thickness of the calorimeter wall at this time. On the other hand, large temperature gradients were expected to occur both longitudinally and circumferentially along the calorimeter wall, particularly if the calorimeter was not uniformly engulfed in the fire. For instance, the calorimeter at location 'D' was expected to experience a circumferential temperature gradient because the bottom of the calorimeter was in contact with the fire bricks on the floor of the test enclosure and thus would have been cooler than the rest of the calorimeter surface. Such gradients would have affected the temperature and heat flux data from the calorimeters more significantly than those from the DFTs, which were smaller and more likely to have been uniformly engulfed in the fire. Detailed examination of the effects of these lateral gradients is recommended.

Wind speed appeared to affect heat flux levels to the calorimeter at location 'D' more greatly than at location 'A'. In Table 5.11, the heat flux to the calorimeter at location 'D' generally increased with increasing wind speed, due to the plume tilting further over (Section 5.3). However, the same trend was not evident among the data for the calorimeter at location 'A'. This calorimeter was close enough to the fuel pan that the upwind side of the cylinder was likely not exposed to significant changes in the local fire environment, even as the plume tilted further over. The temperatures in Table 5.12 varied across a range of 127°C over all tests for the calorimeter at location 'A', as opposed to a range of 340°C for the calorimeter at location 'D'. This suggests that the calorimeter at location 'A' was situated in a similar region of the fire plume in each test, while the calorimeter at location 'D' became more greatly enveloped in the hot central region of the plume as the fire tilted further over.

In general, differences between the DFT and calorimeter results appeared to be dominated by differences in the location of each sensor relative to the hottest regions of the fire plume in each test. This is consistent with the results from Chapter 4 and suggests that the 2 m diameter fire was not sufficiently large to maintain a uniform environment around each calorimeter and its neighbouring DFTs. As seen in Section 5.3, large temperature gradients existed in the y direction and could account for the differences in measured heat flux levels between the calorimeters and DFTs. Thus, in these tests, there were no evident effects of sensor size on the

measured heat flux levels, even though such effects have been previously observed in experiments where the fire was significantly larger than the sensors [6, 24, 103].

5.5 Summary

In this chapter, video, temperature and heat flux results were presented for a 2 m diameter Jet A fire in 5 m/s to 13 m/s crosswinds, with a 2.7 m diameter, 10.8 m long, cylindrical blocking object located 3.4 m downwind of the fuel pan centre. Both the presence of the object and the wind speed were shown to affect the shape and direction of the plume. At the 5 m/s wind speed, the blocking object interfered significantly with the plume, which impinged on the lower portion of the culvert before spreading upward along the leeward side. At the 7 m/s wind speed, the plume tilted further over and continued to impinge on the bottom of the blocking object, but did not spread up the leeward side. As the wind speed increased to 10 m/s, the plume lay close to the ground, passing freely underneath the blocking object, while at a wind speed of 13 m/s, the plume lay even closer to the ground, with the object situated well above the plume flow. In comparison to the experiments of the previous chapter, the plume flow was observed to be redirected by the object. At a 10 m/s wind speed, the plume lifted off the ground at a distance closer to the fuel pan than when the blocking object was not in place, suggesting that the direction of plume travel downwind of the object was affected by the low-pressure wake region behind the object. The thermally massive object also appeared to have a cooling effect on the plume gases when the fire impinged directly on it. Further, the initial temperature of the blocking object appeared to affect the thermal development of the fire and repeatability of the tests, while a 0.20 m offset in the position of the object appeared to cause the plume to become skewed in the -y direction by 4° to 8°.

Heat flux results were consistent with the above observations of plume shape and direction under the different wind speeds. Differences between results from adjacent gauges were attributed mainly to differences in the location of each sensor relative to the fire plume, as well as to differences in gauge type. Results appeared consistent with the trends observed in Chapters 3 and 4. No significant effect of sensor size was evident in the heat flux data from the calorimeters and their neighbouring DFTs.

Chapter 6

Closure

This thesis presents the first systematic characterization of the thermal environment in a turbulent fire under controlled crosswind conditions, with and without a large downwind blocking object. The scenarios were intended to simulate transportation accidents in which the fire represented a burning pool of aviation fuel and the blocking object simulated an aircraft fuselage. Jet A fires of 2 m diameter were established in crosswinds of 3 m/s to 13 m/s. A 2.7 m diameter, 10.8 m long, cylindrical blocking object was also placed 3.4 m downwind of the fuel pan centre. Video images, thermocouples and heat flux gauges were used to characterize the thermal field and overall geometry of the fire plume, as well as describe the effects of wind speed and the blocking object on fire plume development.

Interpretation of heat flux data from the fire experiments was enhanced by a set of laboratory-scale experiments that were conducted to examine the steady-state responses of different heat flux gauges to various controlled radiative and mixed radiative-convective heating conditions. Data from a Schmidt-Boelter gauge, Gardon gauge, Directional Flame Thermometer and Hemispherical Heat Flux Gauge were compared to help identify sources of uncertainty for each gauge when used in wind-blown fire environments.

6.1 Conclusions

The conclusions of this study are as follows:

1. Time-averaged temperature contour plots were successfully used to enhance visual analysis of the fire geometry. Estimates of plume tilt, flame length and

flame drag were obtained from temperature contour plots of the fire without the blocking object and were found to be consistent with results obtained from corresponding video images of the fire. Therefore, a temperature-based method of estimating flame geometry provides improvement over visually-based methods in cases where significant smoke blockage of the luminous flame envelope occurs.

2. For the fires without the blocking object, the wind speed significantly affected the shape and direction of the fire plume. As the wind speed increased from 3 m/s to 10 m/s, the extent of flame drag and plume tilt increased, indicating the increasing importance of the wind momentum relative to buoyancy effects in the fire. The flame length (referenced to the centre of the fuel pan) also increased, with a significant jump in length observed between wind speeds of 7 m/s and 10 m/s. This large increase has not previously been reported in the literature and indicates the additional importance of the large decrease in overall air entrainment into the fire caused by interactions between the fire plume and the floor under extremely high levels of plume tilt and flame drag.

3. Experimental boundary conditions (e.g. the configuration of the surrounding floor) and the method used to define and measure each geometrical flame parameter (e.g. referencing to the centre of the fuel pan or the centre of the flame base) influenced agreement between the measured flame geometry data and values predicted using published semi-empirical correlations. The use of a single angle to describe flame tilt may not be appropriate in fires influenced by significant plume curvature. These factors should be considered when using published correlations to estimate flame geometry.

4. The presence of the blocking object significantly affected overall fire plume development. At a wind speed of 5 m/s, the plume was redirected to flow around the object and the thermally massive object appeared to have a cooling effect on the surrounding hot plume gases. At a higher wind speed of 10 m/s, the direction of the fire plume was influenced by the presence of a low-pressure wake region behind the object. Greater amounts of cooler ambient air were entrained into the plume downwind of the object, resulting in lower plume temperatures compared to the corresponding test without the blocking object.

5. Of the four types of heat flux gauge used in this study (DFT, HFG, Gardon gauge and Schmidt-Boelter gauge), the DFT was the most suitable for mea-

suring total incident heat flux in mixed radiative-convective environments. Although the DFT was in some cases affected by natural convection losses from the sensor surface and/or lateral conduction along the surface of the sensor plate, these losses can be either minimized or modelled and accounted for. In contrast, the HFG was affected by significant heat losses from the sensor plate to the gauge housing and was therefore not as suitable for measuring heat flux as the DFT. Meanwhile, the Gardon and Schmidt-Boelter gauges were affected by discrepancies between the radiation-based calibration environments and the mixed radiative-convective measurement environments because of additional measurement uncertainty introduced by different gauge sensitivities to the radiative and convective portions of the total heat transfer. Differences in sensor surface temperature between the water-cooled Gardon and Schmidt-Boelter gauges and the non-water-cooled DFT also caused significant differences in the measured total heat flux due to convective heating, rather than cooling, of the water-cooled gauges. Consequently, use of Gardon and Schmidt-Boelter gauges in environments involving significant convection should be avoided, particularly if the sensors have not been calibrated specifically for those environments or if the measurement results are to be used to estimate heat flux to a surrounding surface that is not cooled to the same temperature as the gauge surface. The results obtained will allow improvement of future heat flux measurement and analysis in mixed radiative-convective conditions such as wind-blown fires.

6.2 Recommendations

The following recommendations for future research are made based on the results of this study.

1. The effect of the floor configuration surrounding the fuel pan should be examined. A set of experiments corresponding to the ones presented in this work, but with a floor entirely level with the rim of the fuel pan, should be conducted to determine any effects on the geometric characteristics of the fire plume of the 0.17 m step decrease in elevation at the edges of the raised floor surround.

2. For fires with a downwind blocking object, more detailed measurements should be made to fully characterize the obstructed, wind-blown fire plume. In particular, more measurements are needed at the base of the fire to verify the potential for decreased air entrainment into the fire through the presence of an oxygen-starved region. Also, more measurements are needed to investigate whether the fire plume is always demarcated by the presence of counter-rotating vortices downwind of the blocking object.

3. Analysis of the data from the present experiments should be extended to examine transient characteristics of the fire behaviour. Detailed analysis of transient effects will help elucidate the physics of air entrainment and mixing in the fire plume. Air entrainment in wind-blown fires should be additionally investigated by conducting flow visualization studies and collecting more detailed measurements of temperature and extensive measurements of velocity at the base of the fire. This will provide insight into how flame geometry and fire behaviour are affected by changes in air entrainment levels.

4. To assist with the above, additional experiments of the type presented here should be conducted with higher sampling rates and longer test durations to enhance the present dataset. Different fire sizes, fuel types and wind speeds may also be considered. With controlled wind conditions such as those characterizing the present experiments, a critical source of scatter in the experimental data may be systematically eliminated, allowing future improvement of correlations for predicting flame geometry and of numerical models for predicting fire behaviour.

5. The transient behaviour of the DFT and HFG should be further investigated in order to enhance current understanding of gauge operation and quantification of gauge measurement uncertainty in mixed radiative-convective environments. Detailed knowledge of the transient response of each gauge will help improve interpretation of heat flux measurements in highly turbulent environments such as wind-blown fires.

6. The data corresponding to all eight measurement stations distributed around the circumference of each calorimeter should be analyzed to determine effects of lateral conduction on the heat flux measurements. The calorimeter should also be tested together with the DFT in a much larger fire to allow comparison

of measurements made in a more uniform fire environment. This will help reveal any effects of sensor size on measured heat flux levels.

References

[1] Planas-Cuchi, E., Montiel, H., and Casal, J. A survey of the origin, type and consequences of fire accidents in process plants and in the transportation of hazardous materials. *Process Safety and Environmental Protection: Transactions of the Institution of Chemical Engineers, Part B*, 75:3–8, 1997.

[2] Oggero, A., Darbra, R.M., Muñoz, M., Planas, E., and Casal, J. A survey of accidents occurring during the transport of hazardous substances by road and rail. *Journal of Hazardous Materials*, 133:1–7, 2006.

[3] Hovingh, J., Thomas, G.R., Carlson, R.W., and Sheaffer, M.K. Fire and furnace testing of transportation packages for radioactive materials: Facilities and measurements. In *Transportation, Storage, and Disposal of Radioactive Materials - 1999*, volume 390, pages 91–100. American Society of Mechanical Engineers, Pressure Vessels and Piping Division, 1999.

[4] Burgess, M.H. and Fry, C.J. Fire testing for package approval. *RAMTRANS (International Journal of Radioactive Materials Transport)*, 1:7–16, 1990.

[5] Suo-Anttila, J. and Gritzo, L. The effects of wind on fire environments containing large cylinders. *Combustion Science and Technology*, 181:68–77, 2009.

[6] Keltner, N.R., Nicolette, V.F., Brown, N.N., and Bainbridge, B.L. Test unit effects on heat transfer in large fires. *Journal of Hazardous Materials*, 25:33–47, 1990.

[7] Suo-Anttila, J.M. and Gritzo, L.A. Thermal measurements from a series of tests with a large cylindrical calorimeter on the leeward edge of a JP-8 pool fire in cross-flow. Technical Report SAND2001-1986, Sandia National Laboratories, Albuquerque, NM, 2001.

[8] Lam, C.S. *Thermal Characterization of a Pool Fire in Crosswind with a Large Adjacent Cylindrical Object: Experimental Design.* M.A.Sc. thesis, University of Waterloo, Waterloo, Ontario, Canada, 2003.

[9] Mudan, K.S. Thermal radiation hazards from hydrocarbon pool fires. *Progress in Energy and Combustion Science*, 10:59–80, 1984.

[10] Considine, M. Thermal radiation hazard ranges from large hydrocarbon pool fires. Safety and Reliability Directorate SRD R297, United Kingdom Atomic Energy Authority, Culcheth, Warrington, 1984.

[11] Moorhouse, J. and Pritchard, M.J. Thermal radiation hazards from large pool fires and fireballs - a literature review. In *The Assessment of Major Hazards*, pages 397–428. The Institution of Chemical Engineers Symposium Series No. 71, 1982.

[12] Modak, A.T. Thermal radiation from pool fires. Technical Report 22361-5, Factory Mutual Research Corporation, Norwood, MA, 1976.

[13] de Ris, J. Fire radiation - a review. In *17th Symposium (International) on Combustion*, pages 1003–1016, The Combustion Institute, Pittsburgh, PA, 1979.

[14] Shokri, M. and Beyler, C.L. Radiation from large pool fires. *Journal of Fire Protection Engineering*, 1:141–149, 1989.

[15] Pitts, W.M., Murthy, A.V., de Ris, J.L., Filtz, J.R., Nygård, K., Smith, D., and Wetterlund, I. Round robin study of total heat flux gauge calibration at fire laboratories. *Fire Safety Journal*, 41:459–475, 2006.

[16] Bryant, R., Womeldorf, C., Johnsson, E., and Ohlemiller, T. Radiative heat flux measurement uncertainty. *Fire and Materials*, 27:209–222, 2003.

[17] Gardon, R. An instrument for the direct measurement of intense thermal radiation. *The Review of Scientific Instruments*, 24:366–370, 1953.

[18] Ingason, H. and Wickström, U. Measuring incident radiant heat flux using the plate thermometer. *Fire Safety Journal*, 42:161–166, 2007.

[19] Lam, C.S. and Weckman, E.J. Steady-state heat flux measurements in radiative and mixed radiative-convective environments. *Fire and Materials*, 2009. Published online February 19, 2009 at Wiley InterScience, www.interscience.wiley.com.

[20] Randsalu, E.J. *Measurement of Fuel Regression Rate in a Jet-A Fuelled Fire in Crosswind*. M.A.Sc. thesis, University of Waterloo, Waterloo, Ontario, Canada, 2005.

[21] Best, Christopher. M.A.Sc. thesis, University of Waterloo, Waterloo, Ontario, Canada. In preparation.

[22] Drysdale, D. *An Introduction to Fire Dynamics*. John Wiley and Sons, New York, 2nd edition, 1998.

[23] Beyler, C.L. *The SFPE Handbook of Fire Protection Engineering*, Fire Hazard Calculations for Large, Open Hydrocarbon Fires, pages 3–268 – 3–314. National Fire Protection Association, Quincy, MA, 3rd edition, 2002.

[24] Keltner, N.R., Acton, R.U., and Gill, W. Evaluating the hazards of large petrochemical fires. In *Fire Hazard and Fire Risk Assessment*, Hirschler, M.M., editor, pages 37–43, American Society for Testing and Materials, Philadelphia, PA, 1992. ASTM Special Technical Publication 1150.

[25] Raj, P.K. LNG fires: A review of experimental results, models and hazard prediction challenges. *Journal of Hazardous Materials*, 140:444–464, 2007.

[26] Gritzo, L.A., Senseny, P.E., Xin, Y., and Thomas, J.R. The international FORUM of fire research directors: A position paper on verification and validation of numerical fire models. *Fire Safety Journal*, 40:485–490, 2005.

[27] Weckman, E.J. *The Structure of the Flowfield Near the Base of a Medium-Scale Pool Fire*. Ph.D. thesis, University of Waterloo, Waterloo, Ontario, Canada, 1987.

[28] Hogben, C.D.A. *Determination of the Radiative Properties of an Acetone Pool Fire*. M.A.Sc. thesis, University of Waterloo, Waterloo, Ontario, Canada, 1998.

[29] Zhou, X.C. and Gore, J.P. A study of entrainment and flow patterns in pool fires using particle imaging velocimetry. Technical Report NIST-GCR-97-706, National Institute of Standards and Technology, Gaithersburg, MD, 1996.

[30] Emmons, H.W. Some observations on pool burning. In *International Symposium on the Use of Models in Fire Research*, pages 50–67, National Academy of Sciences, Washington, D.C., 1961. NAS/NRC Publication 786.

[31] Rasbash, D.J., Rogowski, Z.W., and Stark, G.W.V. Properties of fires of liquids. *Fuel*, 35:94–107, 1956.

[32] Souil, J.M., Vantelon, J.P., Joulain, P., and Grosshandler, W.L. Experimental and theoretical study of thermal radiation from freely burning kerosene pool fires. *Progress in Astronautics and Aeronautics*, 105(Part 1: Flames and Configuration):388–401, 1986.

[33] Hamins, A., Fischer, S.J., Kashiwagi, T., Klassen, M.E., and Gore, J.P. Heat feedback to the fuel surface in pool fires. *Combustion Science and Technology*, 97:37–62, 1994.

[34] Koseki, H. and Yumoto, T. Air entrainment and thermal radiation from heptane pool fires. *Fire Technology*, 24:33–47, 1988.

[35] Burgess, D.S., Strasser, A., and Grumer, J. Diffusive burning of liquid fuels in open trays. *Fire Research Abstracts and Reviews*, 3:177–192, 1961.

[36] Chatris, J.M., Quintela, J., Folch, J., Planas, E., Arnaldos, J., and Casal, J. Experimental study of burning rate in hydrocarbon pool fires. *Combustion and Flame*, 126:1373–1383, 2001.

[37] Alger, R.S., Corlett, R.C., Gordon, A.S., and Williams, F.A. Some aspects of structures of turbulent pool fires. *Fire Technology*, 15:142–156, 1979.

[38] Gritzo, L.A., Gill, W., and Nicolette, V.F. Estimates of the extent and character of the oxygen-starved interior in large pool fires. In *Very Large-Scale Fires*, Keltner, N.R., Alvares, N.J., and Grayson, S.J., editors, pages 84–98. American Society for Testing and Materials, 1998. ASTM Special Technical Publication 1336.

[39] McCaffrey, B.J. Purely buoyant diffusion flames: Some experimental results. Technical Report NBSIR 79-1910, National Bureau of Standards, Washington, D.C., 1979.

[40] Zukoski, E.E., Cetegen, B.M., and Kubota, T. Visible structure of buoyant diffusion flames. In *20th Symposium (International) on Combustion*, pages 361–366, The Combustion Institute, Pittsburgh, PA, 1984.

[41] Hall, A.R. Pool burning. *Oxidation and Combustion Reviews*, 6:169–225, 1973.

[42] Shinotake, A., Koda, S., and Akita, K. An experimental study of radiative properties of pool fires of an intermediate scale. *Combustion Science and Technology*, 43:85–97, 1985.

[43] Gritzo, L.A., Nicolette, V.F., Tieszen, S.R., Moya, J.L., and Holen, J. Heat transfer to the fuel surface in large pool fires. In *Transport Phenomena in Combustion (Volume 1)*, Chan, S.H., editor, pages 701–712, Taylor and Francis, Washington, D.C., 1996.

[44] Adiga, K.C., Ramaker, D.E., Tatem, P.A., and Williams, F.W. Modeling thermal radiation in open liquid pool fires. In *Second International Symposium on Fire Safety Science*, pages 241–250. International Association for Fire Safety Science, 13-17 June 1988.

[45] Brosmer, M.A. and Tien, C.L. Radiative energy blockage in large pool fires. *Combustion Science and Technology*, 51:21–37, 1987.

[46] Hottel, H.C. Review: Certain laws governing diffusive burning of liquids. *Fire Research Abstracts and Reviews*, 1:41–44, 1959.

[47] Babrauskas, V. Estimating large pool fire burning rates. *Fire Technology*, 19:251–261, 1983.

[48] Blinov, V.I. and Khudyakov, G.N. Diffusion burning of liquids. Technical report, Izdatel'stvo Akademii Nauk SSSR, Moscow, 1961. T-1490a-c, English Translation: U.S. Army Engineer Research and Development Laboratories, Information Resources Branch, Translation Analysis Section, Fort Belvoir, VA.

[49] Blinov, V.I. and Khudyakov, G.N. On certain regularities of diffusion burning of liquids. *Doklady Akademii Nauk SSSR*, 113:1094–1098, 1957. English Translation: Doklady Physical Chemistry, 113:241-244, 1957.

[50] Nakakuki, A. Heat transfer in small scale pool fires. *Combustion and Flame*, 96:311–324, 1994.

[51] Lam, C.S., Randsalu, E.J., Weckman, E.J., Brown, A.L., Gill, W., and Gritzo, L.A. Fuel regression rates of hydrocarbon pool fires in crosswinds. In *Interflam*

2004 Conference Proceedings, pages 117–128, Interscience Communications, Edinburgh, Scotland, 5-7 July 2004.

[52] Koseki, H., Iwata, Y., Natsume, Y., Takahashi, T., and Hirano, T. Tomakomai large scale crude oil fire experiments. *Fire Technology*, 36:24–38, 2000.

[53] Mulholland, G.W., Henzel, V., and Babrauskas, V. The effect of scale on smoke emission. In *Second International Symposium on Fire Safety Science*, pages 347–357. International Association for Fire Safety Science, 13-17 June 1988.

[54] Koseki, H. and Mulholland, G.W. The effect of diameter on the burning of crude oil pool fires. *Fire Technology*, 27:54–65, 1991.

[55] Muñoz, M., Arnaldos, J., Casal, J., and Planas, E. Analysis of the geometric and radiative characteristics of hydrocarbon pool fires. *Combustion and Flame*, 139:263–277, 2004.

[56] Yumoto, T. Heat transfer from flame to fuel surface in large pool fires. *Combustion and Flame*, 17:108–110, 1971.

[57] Magnus, G. Tests on combustion velocity of liquid fuels and temperature distribution in flames and beneath surface of the burning liquid. In *International Symposium on the Use of Models in Fire Research*, pages 76–92, National Academy of Sciences, Washington, D.C., 1961. NAS/NRC Publication 786.

[58] Yamaguchi, T. and Wakasa, K. Oil pool fire experiment. In *First International Symposium on Fire Safety Science*, pages 911–918. International Association for Fire Safety Science, 7-11 October 1985.

[59] Hägglund, B. and Persson, L. The heat radiation from petroleum fires. FOA Rapport C 20126-D6(A3), Försvarets Forskningsanstalt, Stockholm, 1976.

[60] Crocker, W.P. and Napier, D.H. Thermal radiation hazards of liquid pool fires and tank fires. In *Hazards in the Process Industries: Hazards IX*, pages 159–184. The Institution of Chemical Engineers Symposium Series No. 97, 1986.

[61] Atallah, S. and Raj, P.P.K. Radiation from LNG fires. In *LNG Safety Program, Interim Report on Phase II Work*. American Gas Association, Batelle Columbus Laboratories, 1974. Project IS-3-1.

[62] Atallah, S. and Allan, D.S. Safe separation distances from liquid fuel fires. *Fire Technology*, 7:47–56, 1971.

[63] Parker, R.O. Calculating thermal radiation hazards in large fires. *Fire Technology*, 10:147–152, 1974.

[64] Raj, P.K. Exposure of a liquefied gas container to an external fire. *Journal of Hazardous Materials*, 122:37–49, 2005.

[65] Howell, J.R. A catalog of radiation heat transfer configuration factors. 2nd edition. http://www.me.utexas.edu/∼howell/index.html. Accessed October 2007.

[66] Hamilton, D.C. and Morgan, W.R. Radiant-interchange configuration factors. Technical Note 2836, National Advisory Committee for Aeronautics (NACA), Washington, 1952.

[67] Mudan, K.S. Geometric view factors for thermal radiation hazard assessment. *Fire Safety Journal*, 12:89–96, 1987.

[68] Rein, Jr., R.G., Sliepcevich, C.M., and Welker, J.R. Radiation view factors for tilted cylinders. *Journal of Fire and Flammability*, 1:140–153, 1970.

[69] Stannard, Jr., J.H. Thermal radiation hazards associated with marine LNG spills. *Fire Technology*, 13:35–41, 1977.

[70] Davis, B.C. and Bagster, D.F. Computational aspects of radiation view factors of pool and jet fires. In *Safety and Loss Prevention in the Chemical and Oil Processing Industries*, pages 209–218. The Institution of Chemical Engineers Symposium Series No. 120, 1990.

[71] Guelzim, A., Souil, J.M., and Vantelon, J.P. Suitable configuration factors for radiation calculation concerning tilted flames. *Journal of Heat Transfer*, 115:489–492, 1993.

[72] Smith, R.K. Radiation effects on large fire plumes. In *11th Symposium (International) on Combustion*, pages 507–515, The Combustion Institute, Pittsburgh, PA, 1967.

[73] Koski, J.A. Measurement of temperature distributions in large pool fires with the use of directional flame thermometers. In *Transportation, Storage, and*

Disposal of Radioactive Materials - 2000, volume 408, pages 111–115. American Society of Mechanical Engineers, Pressure Vessels and Piping Division, 2000.

[74] Planas-Cuchi, E. and Casal, J. Flame temperature distribution in a pool-fire. *Journal of Hazardous Materials*, 62:231–241, 1998.

[75] Devia, F. and Fossa, M. Fire modelling and cooling of storage tanks in case of radiation from large pool fires. In *Proceedings of the 16th IASTED International Conference: Modelling and Simulation*, pages 446–451. International Association of Science and Technology for Development, 18-20 May 2005.

[76] Muñoz, M., Planas, E., Ferrero, F., and Casal, J. Predicting the emissive power of hydrocarbon pool fires. *Journal of Hazardous Materials*, 144:725–729, 2007.

[77] Burgess, D. and Hertzberg, M. Radiation from pool flames. In *Heat Transfer in Flames*, Afgan, N.H. and Beer, J.M., editors, pages 413–430, Scripta Book Company, Washington, D.C., 1974.

[78] Koseki, H. Combustion properties of large liquid pool fires. *Fire Technology*, 25:241–255, 1989.

[79] Yang, J.C., Hamins, A., and Kashiwagi, T. Estimate of the effect of scale on radiative heat loss fraction and combustion efficiency. *Combustion Science and Technology*, 96:183–188, 1994.

[80] Welker, J.R. and Sliepcevich, C.M. Bending of wind-blown flames from liquid pools. *Fire Technology*, 2:127–135, 1966.

[81] Thomas, P.H., Pickard, R.W., and Wraight, H.G.H. On the size and orientation of buoyant diffusion flames and the effect of wind. Fire Research Note 516, Fire Research Station, Joint Fire Research Organization, Boreham Wood, UK, 1963.

[82] Moorhouse, J. Scaling criteria for pool fires derived from large scale experiments. In *The Assessment of Major Hazards*, pages 165–179. The Institution of Chemical Engineers Symposium Series No. 71, 1982.

[83] de Faveri, D.M., Vidili, A., Pastorino, R., and Ferraiolo, G. Wind effects on diffusion flames of fires of high source momentum. *Journal of Hazardous Materials*, 22:85–100, 1989.

[84] Nedelka, D., Moorhouse, J., and Tucker, R.F. The Montoir 35m diameter LNG pool fire experiments. In *Ninth International Conference on Liquefied Natural Gas*, Institute of Gas Technology, International Gas Union, and International Institute of Refrigeration, Nice, France, 17-20 October 1989. Session III, Paper 3.

[85] Welker, J.R., Pipkin, O.A., and Sliepcevich, C.M. The effect of wind on flames. *Fire Technology*, 1:122–129, 1965.

[86] Pritchard, M.J. and Binding, T.M. FIRE2: A new approach for predicting thermal radiation levels from hydrocarbon pool fires. In *Major Hazards Onshore and Offshore*, pages 491–505. The Institution of Chemical Engineers Symposium Series No. 130, 1992.

[87] Gritzo, L.A., Moya, J.L., and Murray, D. Fire characterization and object thermal response for a large flat plate adjacent to a large JP-4 fuel fire. Technical Report SAND97-0047, Sandia National Laboratories, Albuquerque, NM, 1997.

[88] Thomas, P.H. Fire spread in wooden cribs: Part III, the effect of wind. Fire Research Note 600, Fire Research Station, Joint Fire Research Organization, Boreham Wood, UK, 1965.

[89] Thomas, P.H. The size of flames from natural fires. In *9th Symposium (International) on Combustion*, pages 844–859, The Combustion Institute, Pittsburgh, PA, 1963.

[90] Duffy, A.R., Gideon, D.N., and Putnam, A.A. Dispersion and radiation experiments. In *LNG Safety Program, Interim Report on Phase II Work*. American Gas Association, Batelle Columbus Laboratories, 1974. Project IS-3-1.

[91] Welker, J.R. Radiant heating from LNG fires. In *LNG Safety Program, Interim Report on Phase II Work*. American Gas Association, Batelle Columbus Laboratories, 1974. Project IS-3-1.

[92] Ferrero, F., Muñoz, M., and Arnaldos, J. Effects of thin-layer boilover on flame geometry and dynamics in large hydrocarbon pool fires. *Fuel Processing Technology*, 88:227–235, 2007.

[93] Chatris, J.M., Planas, E., Arnaldos, J., and Casal, J. Effects of thin-layer boilover on hydrocarbon pool fires. *Combustion Science and Technology*, 171:141–161, 2001.

[94] Pipkin, O.A. and Sliepcevich, C.M. Effect of wind on buoyant diffusion flames. *Industrial and Engineering Chemistry Fundamentals*, 3:147–154, 1964.

[95] Lois, E. and Swithenbank, J. Fire hazards in oil tank arrays in a wind. In *17th Symposium (International) on Combustion*, pages 1087–1098, The Combustion Institute, Pittsburgh, PA, 1979.

[96] Apte, V.B., Green, A.R., and Kent, J.H. Pool fire plume flow in a large-scale wind tunnel. In *Third International Symposium on Fire Safety Science*, pages 425–434. International Association for Fire Safety Science, 8-12 July 1991.

[97] Capener, E.L. and Alger, R.S. Characterization and suppression of aircraft and fuel fires. In *Western States Section Meeting of the Combustion Institute*, Monterey, CA, 30-31 October 1972. Paper WSCI 72-26.

[98] Welker, J.R. and Sliepcevich, C.M. Burning rates and heat transfer from wind-blown flames. *Fire Technology*, 2:211–218, 1966.

[99] Lautkaski, R. Validation of flame drag correlations with data from large pool fires. *Journal of Loss Prevention in the Process Industries*, 5:175–180, 1992.

[100] Koski, J.A., Bobbe, J.G., Arviso, M., Wix, S.D., Beene, Jr., D.E., Byrd, R., and Graupmann, J. Experimental determination of the shipboard fire environment for simulated radioactive material packages. Technical Report SAND97-0506, Sandia National Laboratories, Albuquerque, NM, 1997.

[101] Planas-Cuchi, E., Casal, J., Lancia, A., and Bordignon, L. Protection of equipment engulfed in a pool fire. *Journal of Loss Prevention in the Process Industries*, 9:231–240, 1996.

[102] Bainbridge, B.L. and Keltner, N.R. Heat transfer to large objects in large pool fires. *Journal of Hazardous Materials*, 20:21–40, 1988.

[103] Gregory, J.J., Keltner, N.R., and Mata, Jr., R. Thermal measurements in large pool fires. *Journal of Heat Transfer*, 111:446–454, 1989.

[104] Schneider, M.E., Keltner, N.R., and Kent, L.A. Thermal measurements in the nuclear winter fire test. Technical Report SAND88-2839, Sandia National Laboratories, Albuquerque, NM, 1989.

[105] Kramer, M.A., Greiner, M., Koski, J.A., Lopez, C., and Suo-Anttila, A. Measurements of heat transfer to a massive cylindrical calorimeter engulfed in a circular pool fire. *Journal of Heat Transfer*, 125:110–117, 2003.

[106] Kramer, M.A., Greiner, M., and Koski, J.A. Radiation heat transfer to the leeward side of a massive object suspended over a pool fire. In *Proceedings of the ASME Heat Transfer Division - 2001*, volume 369-4, pages 145–148. American Society of Mechanical Engineers, 2001. Paper IMECE2001/HTD-24250.

[107] Schneider, M.E. and Kent, L.A. Measurements of gas velocities and temperatures in a large open pool fire. *Fire Technology*, 25:51–80, 1989.

[108] Nakos, J.T. and Keltner, N.R. The radiative-convective partitioning of heat transfer to structures in large pool fires. In *Heat Transfer Phenomena in Radiation, Combustion, and Fires*, volume 106, pages 381–387. American Society of Mechanical Engineers, Heat Transfer Division, 1989.

[109] Keltner, N.R., Gill, W., and Kent, L.A. Simulating fuel spill fires under the wing of an aircraft. In *Fourth International Symposium on Fire Safety Science*, pages 1017–1028. International Association for Fire Safety Science, 13-17 July 1994.

[110] Lautkaski, R. Evaluation of BLEVE risks of tank wagons carrying flammable liquids. *Journal of Loss Prevention in the Process Industries*, 22:117–123, 2009.

[111] Birk, A.M. and VanderSteen, J.D.J. On the transition from non-BLEVE to BLEVE failure for a 1.8 m^3 propane tank. *Journal of Pressure Vessel Technology*, 128:648–655, 2006.

[112] Birk, A.M., Poirier, D., and Davison, C. On the response of 500 gal propane tanks to a 25% engulfing fire. *Journal of Loss Prevention in the Process Industries*, 19:527–541, 2006.

[113] Moodie, K., Cowley, L.T., Denny, R.B., Small, L.M., and Williams, I. Fire engulfment tests on a 5 tonne LPG tank. *Journal of Hazardous Materials*, 20:55–71, 1988.

[114] Venart, J.E.S. Boiling liquid expanding vapor explosions (BLEVE): Possible failure mechanisms. In *Very Large-Scale Fires*, Keltner, N.R., Alvares, N.J., and Grayson, S.J., editors, pages 112–132. American Society for Testing and Materials, 1998. ASTM Special Technical Publication 1336.

[115] Blanchat, T.K., Sundberg, D., and Brown, A. Well-characterized open pool experiment data and analysis for model validation and development. Technical Report SAND2006-7508, Sandia National Laboratories, Albuquerque, NM, 2006.

[116] Greiner, M. and Suo-Anttila, A. Validation of the Isis-3D computer code for simulating large pool fires under a variety of wind conditions. *Journal of Pressure Vessel Technology*, 126:360–368, 2004.

[117] Greiner, M. and Suo-Anttila, A. Radiation heat transfer and reaction chemistry models for risk assessment compatible fire simulations. *Journal of Fire Protection Engineering*, 16:79–103, 2006.

[118] Kou, H.S. *Turbulent Buoyant Flow and Pressure Variations Around a Circular Cylinder in a Cross Uniform Flow Near the Ground*. Ph.D. thesis, University of Notre Dame, Notre Dame, IN, 1984.

[119] Tunc, M. and Venart, J.E.S. Incident radiation from an engulfing pool fire to a horizontal cylinder - part I. *Fire Safety Journal*, 8:81–87, 1984/85.

[120] Nicolette, V.F. and Larson, D.W. The influence of large, cold objects on engulfing fire environments. In *Heat and Mass Transfer in Fires*, volume 141, pages 63–70. American Society of Mechanical Engineers, Heat Transfer Division, 1990.

[121] Incropera, F.P. and DeWitt, D.P. *Fundamentals of Heat and Mass Transfer*. John Wiley & Sons, New York, 4th edition, 1996.

[122] Keltner, N.R. Heat flux measurements: Theory and applications. In *Thermal Measurements in Electronics Cooling*, Azar, K., editor, pages 273–320, CRC Press, Boca Raton, FL, 1997.

[123] Childs, P.R.N., Greenwood, J.R., and Long, C.A. Heat flux measurement techniques. *Proceedings of the Institution of Mechanical Engineers, Part C*, 213:655–677, 1999.

[124] Gritzo, L.A., Gill, W., and Keltner, N. Thermal measurements to characterize large fires. In *Proceedings of the 41st International Instrumentation Symposium*, pages 337–346, Instrument Society of America, Aurora, CO, 7-11 May 1995.

[125] Diller, T.E. Advances in heat flux measurements. In *Advances in Heat Transfer*, volume 23, pages 279–368, Academic Press, Inc., Boston, MA, 1993.

[126] Arai, N., Matsunami, A., and Churchill, S.W. A review of measurements of heat flux density applicable to the field of combustion. *Experimental Thermal and Fluid Science*, 12:452–460, 1996.

[127] Gardon, R. A transducer for the measurement of heat-flow rate. *Journal of Heat Transfer*, 82:396–398, 1960.

[128] Borell, G.J. and Diller, T.E. A convection calibration method for local heat flux gages. *Journal of Heat Transfer*, 109:83–89, 1987.

[129] Kuo, C.H. and Kulkarni, A.K. Analysis of heat flux measurement by circular foil gages in a mixed convection/radiation environment. *Journal of Heat Transfer*, 113:1037–1040, 1991.

[130] Young, M.F. Effect of free-stream velocity vector and aspect ratio on the output of a free-standing circular disk heat flux gage. *Journal of Heat Transfer*, 106:229–233, 1984.

[131] Keltner, N. Thermal measurements in fire safety testing - are we playing with fire? In *Fire Calorimetry*, Hirschler, M.M. and Lyon, R.E., editors, Federal Aviation Administration Technical Center, Atlantic City, NJ, 1995. DOT/FAA/CT-95/46.

[132] Brookley, C.E. and Liller, C.A. Convective heat flux gage measurements in air at flows up to 7.1 liters/sec and temperatures up to 540°C. In *Proceedings of the 40th International Instrumentation Symposium*, pages 303–316, Instrument Society of America, Baltimore, MD, 1-5 May 1994. Paper 94-1039.

[133] Keltner, N.R. and Wildin, M.W. Transient response of circular foil heat-flux gauges to radiative fluxes. *The Review of Scientific Instruments*, 46:1161–1166, 1975.

[134] Sobolik, K.B., Keltner, N.R., and Beck, J.V. Measurement errors for thermocouples attached to thin plates: Application to heat flux measurement devices. In *Heat Transfer Measurements, Analysis, and Flow Visualization*, volume 112, pages 15–22. American Society of Mechanical Engineers, Heat Transfer Division, 1989.

[135] Malone, E.W. Design and calibration of thin-foil heat flux sensors. *ISA Transactions*, 7:175–180, 1968.

[136] Kidd, C.T. and Nelson, C.G. How the Schmidt-Boelter gage really works. In *Proceedings of the 41st International Instrumentation Symposium*, pages 347–368, Instrument Society of America, Aurora, CO, 7-11 May 1995.

[137] Nakos, J.T. Uncertainty analysis of steady state incident heat flux measurements in hydrocarbon fuel fires. Technical Report SAND2005-7144, Sandia National Laboratories, Albuquerque, NM, 2005.

[138] Fry, C.J. Pool fire testing at AEE Winfrith. In *Proceedings of the 9th International Symposium on the Packaging and Transportation of Radioactive Materials*, pages 1587–1594, Washington, DC, 11-16 June 1989.

[139] Keltner, N.R. Directional flame thermometers - a tool for measuring thermal exposure in furnaces and improving control. In *Interflam 2007 Conference Proceedings*, Interscience Communications, London, UK, 3-5 September 2007. CD version only.

[140] Wickström, U. The plate thermometer - a simple instrument for reaching harmonized fire resistance tests. *Fire Technology*, 30:195–208, 1994.

[141] Keltner, N.R. and Beck, J.V. Surface temperature measurement errors. *Journal of Heat Transfer*, 105:312–318, 1983.

[142] Keltner, N.R. and Moya, J.L. Defining the thermal environment in fire tests. *Fire and Materials*, 14:133–138, 1989.

[143] Blanchat, T.K., Humphries, L.L., and Gill, W. Sandia heat flux gauge thermal response and uncertainty models. Technical Report SAND2000-1111, Sandia National Laboratories, Albuquerque, NM, 2000.

[144] Beck, J.V. *User's Manual for IHCP1D.* Beck Engineering Consultants Company, Okemos, MI, 7th edition, 1999.

[145] Blackwell, B.F., Douglass, R.W., and Wolf, H. A user's manual for the Sandia One-Dimensional Direct and Inverse Thermal (SODDIT) code. Technical Report SAND85-2478, Sandia National Laboratories, Albuquerque, NM, 1987.

[146] Torvi, D.A. *Heat Transfer in Thin Fibrous Materials Under High Heat Flux Conditions.* Ph.D. thesis, University of Alberta, Edmonton, Alberta, Canada, 1997.

[147] Cavanagh, J.M., Torvi, D.A., Gabriel, K.S., and Ruff, G.A. Test method for evaluating fabric flammability and predicted skin burn injury in microgravity. *Microgravity Science and Technology*, 18:14–26, 2006.

[148] Hornbaker, D.R. and Rall, D.L. Thermal perturbations caused by heat-flux transducers and their effect on the accuracy of heating-rate measurements. *ISA Transactions*, 3:123–130, 1964.

[149] Holmberg, D.G. and Womeldorf, C.A. Performance and modeling of heat flux sensors in different environments. In *Proceedings of the ASME Heat Transfer Division - 1999*, volume 364-4, pages 71–77. American Society of Mechanical Engineers, 1999.

[150] Bachmann, R.C., Chambers, J.T., and Giedt, W.H. Investigation of surface heat-flux measurements with calorimeters. *ISA Transactions*, 4:143–151, 1965.

[151] Robertson, A.F. and Ohlemiller, T.J. Low heat-flux measurements: Some precautions. *Fire Safety Journal*, 25:109–124, 1995.

[152] User's guide for the cone calorimeter. Technical report, Fire Testing Technology Ltd., West Sussex, UK, 2001. Issue 1.7a.

[153] Jones, L. Personal communication, Medtherm Corporation, Huntsville, AL, 2007.

[154] Reese, J. Personal communication, Vatell Corporation, Christiansburg, VA, 2008.

[155] Blanchat, T.K., Humphries, L.L., and Gill, W. Sandia heat flux gauge thermal response and uncertainty models. In *Thermal Measurements: The Foundation of Fire Standards*, Gritzo, L.A. and Alvares, N.J., editors, pages 81–110, American Society for Testing and Materials, West Conshohocken, PA, 2002. ASTM Special Technical Publication 1427.

[156] Lam, C.S. and Weckman, E.J. Heat flux measurements in radiative and mixed radiative-convective environments. In *2006 Spring Technical Meeting*, pages N2.1–N2.6, Combustion Institute/Canadian Section, Waterloo, Ontario, 2006.

[157] Keltner, N.R. Personal communication, Fire Instrumentation Research and Engineering Services, Albuquerque, NM, 2003–2006.

[158] Beck, J.V., Blackwell, B., and St. Clair, Jr., C.R. *Inverse Heat Conduction: Ill-Posed Problems*. Wiley-Interscience, New York, 1985.

[159] Kramer, M.A., Greiner, M., Koski, J.A., and Lopez, C. Uncertainty of heat transfer measurements in an engulfing pool fire. In *Thermal Measurements: The Foundation of Fire Standards*, Gritzo, L.A. and Alvares, N.J., editors, pages 111–127, American Society for Testing and Materials, West Conshohocken, PA, 2002. ASTM Special Technical Publication 1427.

[160] Figueroa, V.G., Nakos, J.T., and Murphy, J.E. Uncertainty analysis of heat flux measurements estimated using a one-dimensional inverse heat conduction program. Technical Report SAND2005-0339, Sandia National Laboratories, Albuquerque, NM, 2005.

[161] Nakos, J.T., Gill, W., and Keltner, N.R. An analysis of flame temperature measurements using sheathed thermocouples in JP-4 pool fires. In *Proceedings of the ASME/JSME Thermal Engineering Joint Conference*, pages 283–289. American Society of Mechanical Engineers, 1991.

[162] Gill, W. Personal communication, Sandia National Laboratories, Albuquerque, NM, 2002–2003.

[163] Keltner, N.R. Personal communication, Fire Instrumentation Research and Engineering Services, Albuquerque, NM, June 2009.

[164] Goldstein, R.J., Sparrow, E.M., and Jones, D.C. Natural convection mass transfer adjacent to horizontal plates. *International Journal of Heat and Mass Transfer*, 16:1025–1035, 1973.

[165] Weisinger, J. *Characterization of the University of Waterloo Live Fire Research Facility Wind Generation System*. M.A.Sc. thesis, University of Waterloo, Waterloo, Ontario, Canada, 2004.

[166] Chevron Global Aviation. Material safety data sheet: Aviation turbine fuel. MSDS 513, revision 19 (April 18, 2003). http://www.chevronglobalaviation.com/docs/aviation_turbine_fuel.doc. Accessed June 2008.

[167] ExxonMobil Aviation. World jet fuel specifications. 2005 edition. http://www.exxonmobil.com/AviationGlobal/Files/WorldJetFuelSpecifications2005.pdf. Accessed June 2008.

[168] Gill, W. and Nakos, J.T. Personal communication, Sandia National Laboratories, Albuquerque, NM, September 2006.

[169] Holman, J.P. *Experimental Methods for Engineers*. McGraw-Hill, Boston, 7th edition, 2001.

[170] Nakos, J.T. Uncertainty analysis of thermocouple measurements used in normal and abnormal thermal environment experiments at Sandia's radiant heat facility and Lurance Canyon burn site. Technical Report SAND2004-1023, Sandia National Laboratories, Albuquerque, NM, 2004.

[171] Dieck, R.H. Measurement uncertainty models. *ISA Transactions*, 36:29–35, 1997.

[172] Coleman, H.W. and Steele, W.G. Engineering application of experimental uncertainty analysis. *AIAA Journal*, 33:1888–1896, 1995.

[173] Coleman, H.W. and Steele, Jr., W.G. *Experimentation and Uncertainty Analysis for Engineers*. John Wiley & Sons, New York, 1989.

[174] OMEGA Engineering, Inc. *The Temperature Handbook*. Stamford, CT, 21st century, 2nd edition, 2000.

[175] National Instruments Corporation. FieldPoint operating instructions, FP-TC-120 and cFP-TC-120 8-channel thermocouple input modules. http://www.ni.com/pdf/manuals/373344a.pdf. October 2002 edition, Accessed May 2005.

[176] Kinzie, P.A. *Thermocouple Temperature Measurement*. John Wiley & Sons, New York, 1973.

[177] Brohez, S., Delvosalle, C., and Marlair, G. A two-thermocouples probe for radiation corrections of measured temperatures in compartment fires. *Fire Safety Journal*, 39:399–411, 2004.

[178] Jones, J.C. Suggestions towards improved reliability of thermocouple temperature measurement in combustion tests. In *Thermal Measurements: The Foundation of Fire Standards*, Gritzo, L.A. and Alvares, N.J., editors, pages 16–31, American Society for Testing and Materials, West Conshohocken, PA, 2002. ASTM Special Technical Publication 1427.

[179] Luo, M. Effects of radiation on temperature measurement in a fire environment. *Journal of Fire Sciences*, 15:443–461, 1997.

[180] Pitts, W.M., Braun, E., Peacock, R.D., Mitler, H.E., Johnsson, E.L., Reneke, P.A., and Blevins, L.G. Temperature uncertainties for bare-bead and aspirated thermocouple measurements in fire environments. In *Thermal Measurements: The Foundation of Fire Standards*, Gritzo, L.A. and Alvares, N.J., editors, pages 3–15, American Society for Testing and Materials, West Conshohocken, PA, 2002. ASTM Special Technical Publication 1427.

[181] Francis, J. and Yau, T.M. On radiant network models of thermocouple error in pre and post flashover compartment fires. *Fire Technology*, 40:277–294, 2004.

[182] Newman, J.S. and Croce, P.A. A simple aspirated thermocouple for use in fires. *Journal of Fire and Flammability*, 10:326–336, 1979.

[183] Blevins, L.G. and Pitts, W.M. Modeling of bare and aspirated thermocouples in compartment fires. *Fire Safety Journal*, 33:239–259, 1999.

[184] Young, C.N. *Thermocouple Compensation*. M.A.Sc. thesis, University of Waterloo, Waterloo, Ontario, Canada, 1998.

[185] Walker, J.D. and Stocks, B.J. Thermocouple errors in forest fire research. *Fire Technology*, 4:59–62, 1968.

[186] Heitor, M.V. and Moreira, A.L.N. Thermocouples and sample probes for combustion studies. *Progress in Energy and Combustion Science*, 19:259–278, 1993.

[187] Bradley, D. and Matthews, K.J. Measurement of high gas temperatures with fine wire thermocouples. *Journal of Mechanical Engineering Science*, 10:299–305, 1968.

[188] Golden Software, Inc., Golden, CO. *Surfer 8*, 2002.

[189] Delfiner, P. and Delhomme, J.P. Optimum interpolation by Kriging. In *Display and Analysis of Spatial Data*, Davis, J.C. and McCullagh, M.J., editors, pages 96–114, John Wiley & Sons, London, 1975.

[190] Isaaks, E.H. and Srivastava, R.M. *An Introduction to Applied Geostatistics*. Oxford University Press, New York, 1989.

[191] McGuirk, J.J. and Rodi, W. The calculation of three-dimensional turbulent free jets. In *Turbulent Shear Flows I*, Durst, F., Launder, B.E., Schmidt, F.W., and Whitelaw, J.H., editors, pages 71–83, Springer-Verlag, Berlin, 1979.

[192] Sfeir, A.A. The velocity and temperature fields of rectangular jets. *International Journal of Heat and Mass Transfer*, 19:1289–1297, 1976.

[193] Tieszen, S.R., Nicolette, V.F., Gritzo, L.A., Holen, J.K., Murray, D., and Moya, J.L. Vortical structures in pool fires: Observation, speculation, and simulation. Technical Report SAND96-2607, Sandia National Laboratories, Albuquerque, NM, 1996.

[194] Kamotani, Y. and Greber, I. Experiments on a turbulent jet in a cross flow. *AIAA Journal*, 10:1425–1429, 1972.

[195] Mizner, G.A. and Eyre, J.A. Radiation from liquefied gas fires on water. *Combustion Science and Technology*, 35:33–57, 1983.

[196] Moffat, R.J. Experimental methods in heat transfer. In *Experimental Heat Transfer, Fluid Mechanics, and Thermodynamics 1988: Proceedings of the First World Conference*, pages 13–31, Elsevier Science, New York, 1988.

[197] RdF Corporation. Simplified heat flow measurement. http://www.rdfcorp.com/anotes/pa-hfs/pa-hfs_01.shtml. Accessed October 2008.

[198] Keltner, N.R. Personal communication, Fire Instrumentation Research and Engineering Services, Albuquerque, NM, July 2009. Regarding unpublished work by D.J. LeBlanc, Worcester Polytechnic Institute, Worcester, MA, 1997.

[199] Lopez, C., Koski, J.A., and Razani, A. Estimates of error introduced when one-dimensional inverse heat transfer techniques are applied to multi-dimensional problems. In *Proceedings of the 2000 National Heat Transfer Conference*, volume 2, pages 671–676. American Society of Mechanical Engineers, Heat Transfer Division, 2000. Paper NHTC2000-12037.

[200] Brown, A.L., Gill, W., Evans, G., and Jarboe, D. Validation predictions of a 13 m/s cross-wind fire for Fuego and the University of Waterloo dataset. Technical Report SAND2008-0919, Sandia National Laboratories, Albuquerque, NM, 2008.

[201] Gritzo, L.A. and Nicolette, V.F. Coupling of large fire phenomenon with object geometry and object thermal response. *Journal of Fire Sciences*, 15:427–442, 1997.

Appendix A

Transient Heat Flux Data from Cone Calorimeter Experiments

This Appendix contains typical time traces of data obtained by the Schmidt-Boelter gauge, Gardon gauge, DFT and HFG in the radiative, convective and mixed radiative-convective conditions of the cone calorimeter experiments described in Chapter 3. The plots permit comparison of the radiation-dominated condition produced by the cone calorimeter at 600°C to the convection-dominated condition produced by convective flow #2, and the mixed radiative-convective condition produced by convective flow #2 and the cone calorimeter at 600°C.

Figures A.1 to A.3 show the Schmidt-Boelter and Gardon gauge time traces in the radiative, convective and mixed radiative-convective conditions, respectively. With data collection for these gauges commencing after the heat sources were applied, the plots indicate that the heat sources and gauge responses were at steady state in all tests.

Figure A.4 contains a time trace of heat flux and temperature from the DFT in the convective condition. Both total and net heat flux are shown. The net heat flux levels were lower in magnitude than the total heat flux levels because the net heat flux does not account for reradiation from the sensor surface (Equation 3.7, page 59). The plot shows that the heat flux levels initially increased when the convective flow was first applied, then decreased as the DFT sensor plate warmed up, reducing the convective heat transfer to the gauge.

Figure A.5 shows the DFT time trace corresponding to a test in which the first 1200 s involved only radiation being imposed on the gauge. This was followed by

application of a convective airflow during the remaining 1200 s to produce a mixed radiative-convective environment. When the convective airflow was first added (t=1200 s), the heat flux to the DFT immediately decreased, indicating cooling of the sensor surface by the airflow. The heat flux subsequently increased as the sensor plate temperature decreased with time and the cooling effect of the airflow was diminished.

Figures A.6 and A.7 contain time traces of total heat flux and temperature from the HFG for tests similar to those shown for the DFT. The plots indicate that the HFG experienced trends in temperature and heat flux similar to those described for the DFT, although lower levels of total heat flux were generally measured due to greater conduction losses from the HFG sensor plate to the HFG housing.

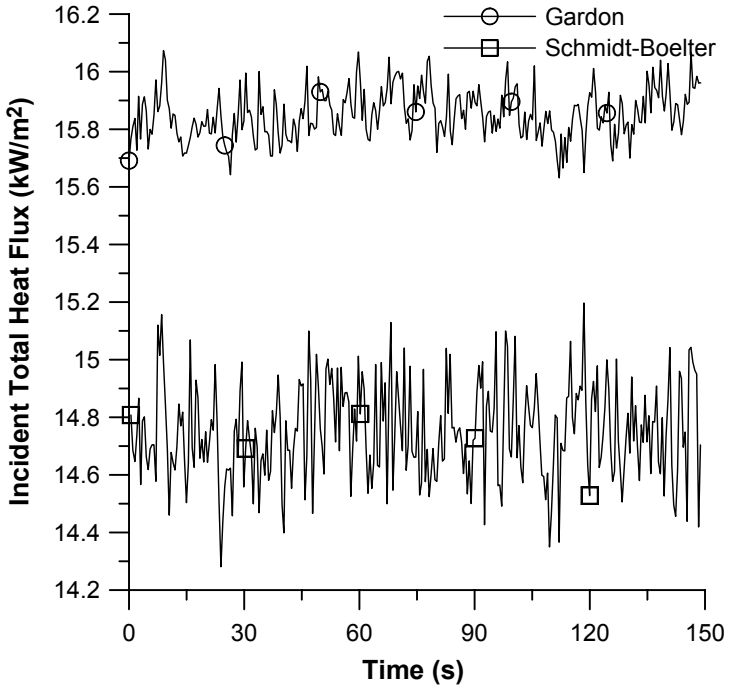

Figure A.1: Time trace of incident total heat flux from Schmidt-Boelter and Gardon gauges in test condition with cone calorimeter at 600°C and no airflow

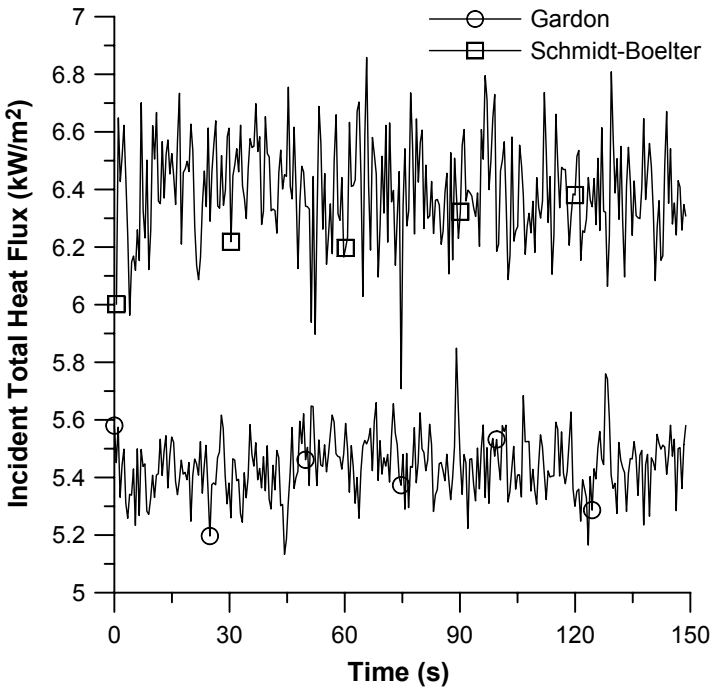

Figure A.2: Time trace of incident total heat flux from Schmidt-Boelter and Gardon gauges in test condition with convective flow #2 and no cone calorimeter

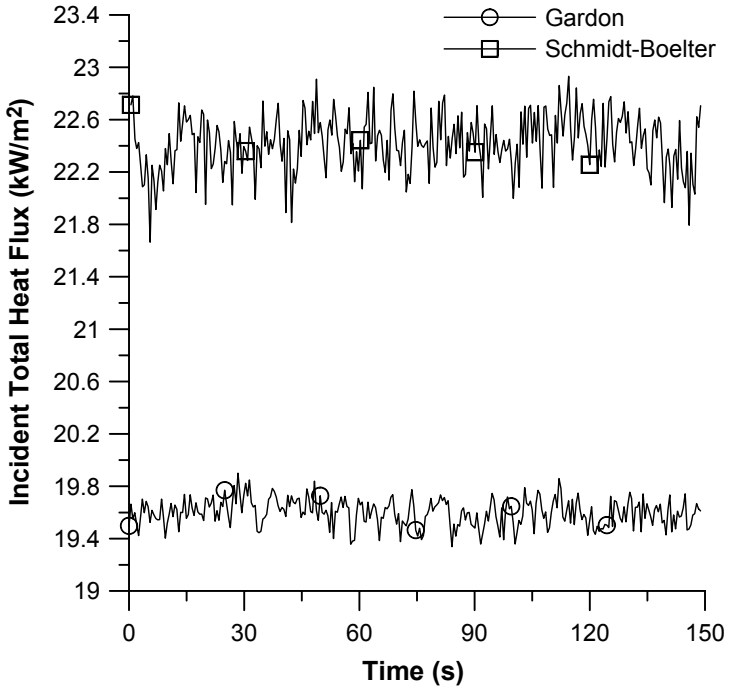

Figure A.3: Time trace of incident total heat flux from Schmidt-Boelter and Gardon gauges in test condition with cone calorimeter at 600°C and convective flow #2

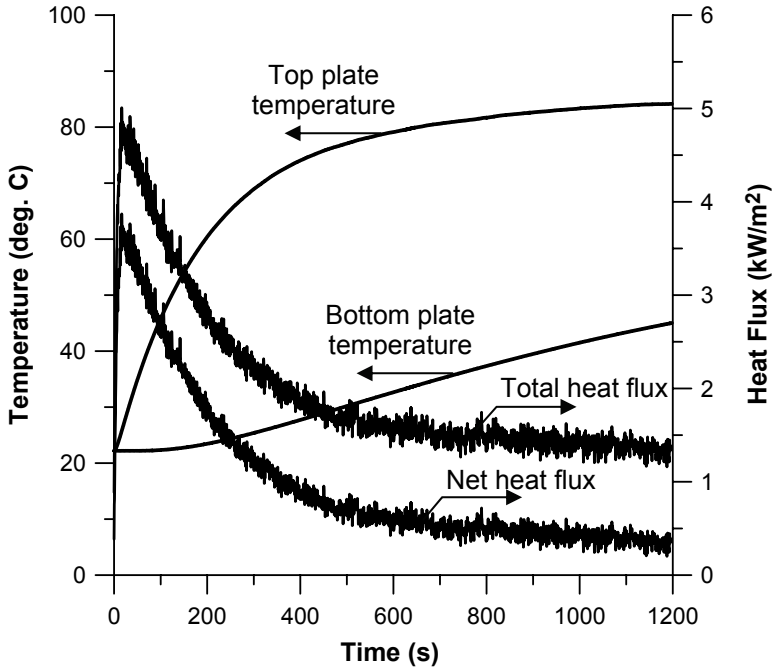

Figure A.4: Time trace of DFT temperature and heat flux for test condition with convective flow #2 and no cone calorimeter

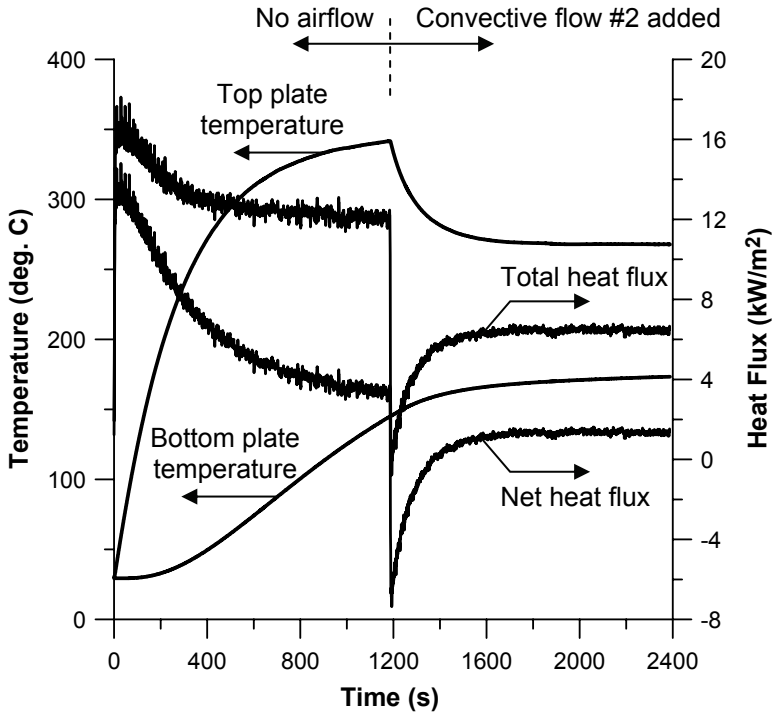

Figure A.5: Time trace of DFT temperature and heat flux for test condition with cone calorimeter at 600°C and convective flow #2

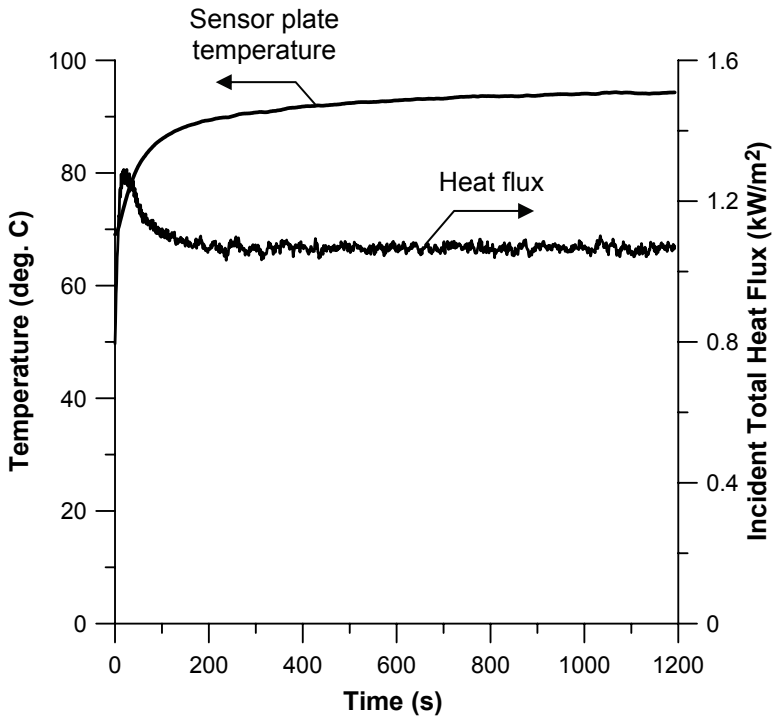

Figure A.6: Time trace of HFG temperature and incident total heat flux for test condition with convective flow #2 and no cone calorimeter

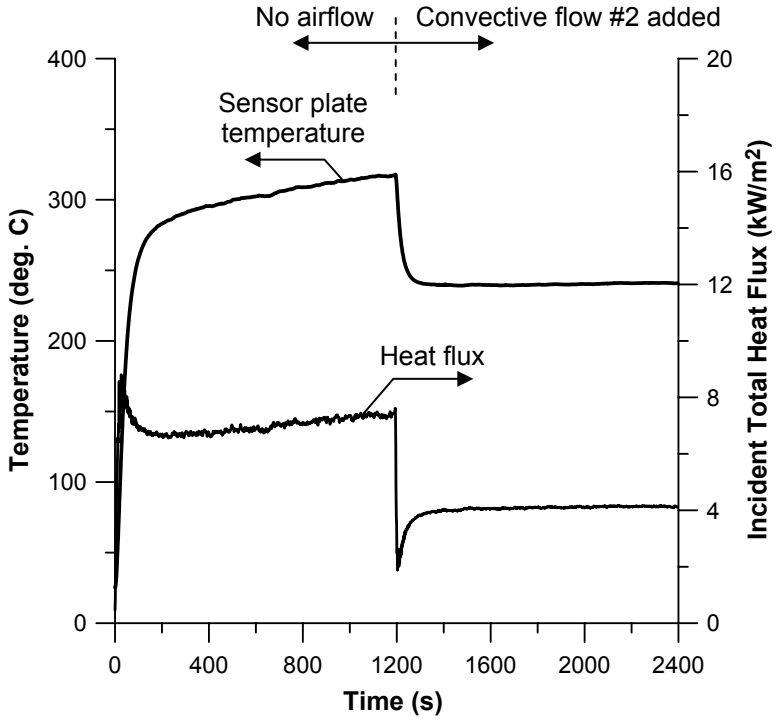

Figure A.7: Time trace of HFG temperature and incident total heat flux for test condition with cone calorimeter at 600°C and convective flow #2

Appendix B

Plume Temperature Data from Tests With No Blocking Object

This Appendix lists the following data for thermocouples used to measure plume temperature in the fire tests without the blocking object: the x, y and z coordinates in metres, the initial temperature measured prior to startup of the first fan, the time-averaged increase in temperature measured during the steady burning period of each test, and the standard deviation corresponding to this temperature increase. All temperatures are in degrees Celsius. The values of time-averaged temperature increase were used to generate the contour plots in Section 4.4. Although the standard deviations were not specifically discussed, they are included here for reference. Values printed in bold indicate results from thermocouples that failed partway through the test, as mentioned at the beginning of Section 4.4.

				Test 44 (3 m/s)			Test 38 (5 m/s)			Test 43 (7 m/s)			Test 42 (10 m/s)		
Channel	x (m)	y (m)	z (m)	Tss - Tinit (deg. C)	Tinit (deg. C)	Standard deviation	Tss - Tinit (deg. C)	Tinit (deg. C)	Standard deviation	Tss - Tinit (deg. C)	Tinit (deg. C)	Standard deviation	Tss - Tinit (deg. C)	Tinit (deg. C)	Standard deviation
B11 TC1	1.48	-1.50	0.03	149.8	0.3	6.8	109.2	10.0	6.7	140.8	3.2	9.6	147.5	5.0	10.0
B12 TC2	1.48	-1.50	0.14	196.9	0.0	8.4	150.1	9.9	8.7	184.8	2.9	16.3	204.0	4.6	21.4
B13 TC3	1.48	-1.50	0.39	360.0	-0.2	25.9	258.3	8.9	29.9	267.6	2.7	23.7	245.9	3.8	22.4
B14 TC4	1.48	-1.50	0.64	403.9	-0.4	37.6	243.4	8.2	28.9	192.0	2.6	14.4	168.3	3.6	9.6
B15 TC5	1.48	-1.50	0.89	287.3	-0.5	29.0	141.9	8.1	14.1	128.2	2.7	5.1	123.7	3.7	3.4
B16 TC6	1.48	-1.50	1.39	94.7	-0.3	2.9	56.3	8.0	2.0	57.4	2.8	1.4	55.3	3.7	1.6
B17 TC8	1.48	-1.00	0.03	379.4	3.7	6.9	356.7	16.4	10.7	438.3	4.9	10.9	444.0	7.6	15.5
B18 TC9	1.48	-1.00	0.14	610.0	3.6	33.1	743.0	18.0	46.2	971.5	4.9	21.9	1027.8	7.0	9.8
B21 TC10	1.48	-1.00	0.39	834.0	1.0	32.0	852.2	10.8	31.9	861.4	3.9	37.7	852.5	5.2	45.9
B22 TC11	1.48	-1.00	0.64	622.6	0.8	28.1	630.2	9.7	29.2	526.4	3.7	29.3	427.9	4.8	28.2
B23 TC12	1.48	-1.00	0.89	427.0	0.7	21.0	398.9	9.8	16.9	232.4	3.7	13.1	204.3	4.8	7.8
B24 TC13	1.48	-1.00	1.39	122.9	0.7	5.2	93.3	9.2	3.8	75.9	3.7	1.9	78.3	4.6	3.5
B47 TC15	1.48	-0.50	0.03	633.3	4.9	8.0	608.3	22.0	9.6	622.5	5.8	7.8	636.5	8.9	6.2
B48 TC16	1.48	-0.50	0.14	981.9	3.8	22.8	856.3	21.2	36.3	1008.2	5.2	30.3	1062.8	7.6	18.7
B51 TC17	1.48	-0.50	0.39	925.4	1.0	36.8	810.9	11.3	46.2	682.5	4.0	36.0	658.5	5.5	28.0
B52 TC18	1.48	-0.50	0.64	813.7	0.8	23.5	561.0	10.1	23.0	352.6	3.8	18.4	286.6	5.1	11.7
B53 TC19	1.48	-0.50	0.89	570.6	0.9	15.2	324.8	10.0	12.5	274.9	3.9	6.0	251.0	5.1	6.0
B54 TC20	1.48	-0.50	1.39	**150.3**	0.8	5.6	123.3	9.4	3.0	83.7	3.8	2.3	72.7	4.9	2.4
A21 TC22	1.48	0.00	0.03	717.7	4.0	17.0	642.3	21.8	11.4	708.0	5.7	15.0	713.1	8.5	12.1
A22 TC23	1.48	0.00	0.14	827.2	2.4	22.0	752.4	17.7	10.3	901.6	4.5	13.6	946.2	6.7	10.2
A23 TC24	1.48	0.00	0.39	877.9	0.8	40.2	810.4	11.3	38.2	756.1	3.8	24.8	748.2	5.3	32.0
A24 TC25	1.48	0.00	0.64	687.7	0.7	31.8	563.6	10.5	23.9	371.8	3.7	18.1	298.6	5.1	13.1
A25 TC26	1.48	0.00	0.89	523.5	0.8	11.6	396.7	10.7	12.8	275.6	3.8	6.9	249.6	5.2	6.4
A26 TC27	1.48	0.00	1.39	204.9	0.9	7.4	164.3	10.1	2.6	145.6	3.9	3.2	**129.0**	5.0	5.9
A51 TC29	1.48	0.50	0.03	611.6	3.5	16.9	587.1	22.0	8.5	584.2	5.9	8.8	583.0	8.5	9.6
A52 TC30	1.48	0.50	0.14	919.5	3.2	31.6	868.6	20.0	18.3	947.4	5.2	13.7	959.1	7.7	10.3
A53 TC31	1.48	0.50	0.39	900.1	0.7	40.5	838.2	11.9	28.0	764.4	3.8	38.6	725.1	5.4	29.0
A54 TC32	1.48	0.50	0.64	675.7	0.7	32.8	543.2	10.9	22.6	337.8	3.8	21.8	237.7	5.1	11.3
A55 TC33	1.48	0.50	0.89	475.6	0.7	17.0	**327.6**	10.7	13.6	187.8	3.8	3.6	176.1	4.9	11.7
A56 TC34	1.48	0.50	1.39	140.6	0.7	6.0	**125.2**	9.9	5.4	70.1	3.8	2.2	61.7	4.9	2.2
A57 TC36	1.48	1.00	0.03	486.2	2.9	26.1	670.8	19.8	20.3	671.3	5.8	15.0	714.0	8.9	17.7
A58 TC37	1.48	1.00	0.14	460.0	2.6	36.9	797.6	18.4	53.1	959.7	5.2	35.9	1046.0	8.2	15.8
A61 TC38	1.48	1.00	0.39	771.4	0.8	42.8	704.7	12.1	27.8	552.9	3.8	14.5	504.9	5.3	18.2
A62 TC39	1.48	1.00	0.64	592.8	0.6	28.5	447.1	11.3	24.1	237.8	3.7	6.8	202.5	5.1	7.1
A63 TC40	1.48	1.00	0.89	398.5	0.6	16.7	258.8	10.7	7.3	216.6	3.7	2.9	191.0	4.9	5.1
A64 TC41	1.48	1.00	1.39	136.6	0.6	2.8	106.0	9.9	1.9	75.9	3.7	1.2	67.1	4.8	1.6

				Test 44 (3 m/s)			Test 38 (5 m/s)			Test 43 (7 m/s)			Test 42 (10 m/s)		
Channel	x (m)	y (m)	z (m)	Tss - Tinit (deg. C)	Tinit (deg. C)	Standard deviation	Tss - Tinit (deg. C)	Tinit (deg. C)	Standard deviation	Tss - Tinit (deg. C)	Tinit (deg. C)	Standard deviation	Tss - Tinit (deg. C)	Tinit (deg. C)	Standard deviation
A65 TC43	1.48	1.50	0.03	109.6	1.0	4.5	134.1	12.1	5.5	88.3	4.0	3.5	87.8	5.8	5.6
A66 TC44	1.48	1.50	0.14	121.8	1.2	4.7	108.2	11.6	4.5	115.6	4.0	6.0	127.5	5.4	10.4
A67 TC45	1.48	1.50	0.39	150.3	0.9	8.7	153.8	10.9	13.8	117.3	4.0	10.6	105.2	5.1	10.6
A68 TC46	1.48	1.50	0.64	165.8	1.1	5.2	171.2	11.3	6.2	121.5	4.2	2.1	121.0	5.5	3.3
A71 TC47	1.48	1.50	0.89	120.5	0.7	3.6	119.4	10.4	2.6	103.7	3.9	1.7	101.0	5.0	2.0
A72 TC48	1.48	1.50	1.39	56.4	0.5	1.5	59.5	9.5	1.5	42.1	3.7	0.8	30.9	4.7	0.9
B25 TC50	1.97	-1.50	0.03	148.6	1.1	5.8	138.3	10.9	6.4	161.8	4.2	9.9	179.5	5.7	11.7
B26 TC51	1.97	-1.50	0.14	201.2	1.3	7.9	141.8	10.9	8.4	198.5	4.2	16.3	222.0	5.6	22.5
B27 TC52	1.97	-1.50	0.39	399.7	1.3	28.4	306.6	10.5	38.5	386.6	4.2	33.3	359.6	5.3	34.1
B28 TC53	1.97	-1.50	0.64	432.0	1.3	39.7	293.9	10.2	34.1	218.7	4.3	20.7	173.2	5.4	11.9
B31 TC54	1.97	-1.50	0.89	399.3	1.0	34.4	260.5	9.7	25.7	178.5	4.1	9.6	160.6	5.1	4.7
B32 TC55	1.97	-1.50	1.39	175.3	0.9	8.4	119.8	9.3	3.4	137.5	3.9	2.6	137.8	4.8	2.9
B33 TC57	1.97	-1.00	0.03	318.6	2.1	14.0	426.6	13.1	22.2	618.8	4.5	20.0	752.6	6.4	20.4
B34 TC58	1.97	-1.00	0.14	512.0	1.9	31.7	688.5	12.8	57.0	1004.5	4.3	30.7	1091.2	6.0	13.0
B35 TC59	1.97	-1.00	0.39	784.5	1.0	50.4	860.7	10.8	41.5	883.6	3.9	41.8	863.7	5.5	51.0
B36 TC60	1.97	-1.00	0.64	662.6	1.1	25.2	671.6	10.6	31.9	596.4	4.0	24.7	479.7	5.4	25.7
B37 TC61	1.97	-1.00	0.89	491.9	1.0	15.8	487.8	10.5	20.9	268.4	4.0	22.4	217.8	5.3	10.9
B38 TC62	1.97	-1.00	1.39	203.9	1.2	6.4	146.7	9.8	6.7	137.7	4.1	3.3	132.8	5.2	4.4
B41 TC64	1.97	-0.50	0.03	672.5	2.9	17.5	715.1	16.3	16.9	726.9	4.9	16.9	805.9	6.8	26.0
B42 TC65	1.97	-0.50	0.14	989.7	2.2	44.1	1011.6	14.4	29.1	1055.8	4.4	33.5	1113.6	5.9	20.8
B43 TC66	1.97	-0.50	0.39	1047.6	1.0	28.9	901.6	11.1	43.0	782.9	3.8	44.3	764.9	5.5	43.1
B44 TC67	1.97	-0.50	0.64	**807.4**	0.9	33.2	648.5	10.7	32.7	433.2	3.8	24.7	**339.5**	5.3	10.6
B45 TC68	1.97	-0.50	0.89	633.5	0.7	33.8	512.1	10.6	17.6	213.0	3.7	9.3	**231.3**	5.2	8.2
B46 TC69	1.97	-0.50	1.39	264.8	0.6	16.4	162.2	9.6	5.7	80.4	3.7	1.8	**107.7**	5.1	3.8
A27 TC71	1.97	0.00	0.03	989.5	2.4	35.1	974.5	17.3	29.0	897.9	4.9	55.6	895.3	6.9	29.6
A28 TC72	1.97	0.00	0.14	977.9	2.4	31.3	941.2	16.4	17.2	1002.4	4.8	13.6	1060.8	6.6	10.9
A31 TC73	1.97	0.00	0.39	1094.3	1.2	21.2	1010.6	12.1	30.8	1005.2	4.0	42.0	1006.9	5.6	45.5
A32 TC74	1.97	0.00	0.64	876.6	0.8	59.4	691.1	10.8	45.5	561.6	3.8	30.9	486.7	5.2	24.6
A33 TC75	1.97	0.00	0.89	618.4	0.8	25.1	486.6	10.7	18.7	351.9	3.8	16.3	319.9	5.1	13.6
A34 TC76	1.97	0.00	1.39	280.0	0.8	9.2	187.9	9.7	5.0	174.4	3.8	4.9	161.7	4.9	4.3
A35 TC78	1.97	0.50	0.03	715.6	2.1	25.9	902.6	16.2	26.0	851.9	4.9	21.3	868.6	6.5	17.2
A36 TC79	1.97	0.50	0.14	887.7	1.9	42.7	1052.2	15.5	21.5	1046.0	4.6	15.6	1077.5	6.2	15.6
A37 TC80	1.97	0.50	0.39	1010.8	1.1	42.1	950.5	12.3	39.0	917.4	4.1	51.5	904.9	5.6	43.2
A38 TC81	1.97	0.50	0.64	799.9	1.1	50.1	650.5	11.5	34.9	486.3	4.2	23.0	355.7	5.5	16.9
A41 TC82	1.97	0.50	0.89	612.4	0.9	21.4	488.3	11.1	14.2	295.7	3.8	7.9	240.5	5.1	12.2
A42 TC83	1.97	0.50	1.39	288.6	0.8	6.1	192.1	10.1	5.1	146.3	3.7	2.6	120.5	4.9	3.3

				Test 44 (3 m/s)			Test 38 (5 m/s)			Test 43 (7 m/s)			Test 42 (10 m/s)		
Channel	x (m)	y (m)	z (m)	Tss - Tinit (deg. C)	Tinit (deg. C)	Standard deviation	Tss - Tinit (deg. C)	Tinit (deg. C)	Standard deviation	Tss - Tinit (deg. C)	Tinit (deg. C)	Standard deviation	Tss - Tinit (deg. C)	Tinit (deg. C)	Standard deviation
A43 TC85	1.97	1.00	0.03	290.0	1.7	12.9	456.6	14.0	25.1	782.7	4.6	23.6	989.5	6.6	17.3
A44 TC86	1.97	1.00	0.14	503.4	1.3	34.0	754.5	13.2	55.4	937.8	4.2	38.2	1041.7	5.9	18.1
A45 TC87	1.97	1.00	0.39	753.3	0.8	46.6	746.7	11.9	38.8	599.9	3.8	17.7	542.1	5.3	24.1
A46 TC88	1.97	1.00	0.64	659.2	0.8	34.2	549.4	11.2	28.6	324.4	3.8	14.3	268.2	5.1	9.0
A47 TC89	1.97	1.00	0.89	453.5	0.8	19.5	347.9	11.0	16.6	202.4	3.9	3.8	173.8	5.0	5.8
A48 TC90	1.97	1.00	1.39	197.6	0.9	5.4	157.5	10.0	3.0	128.5	3.9	2.5	119.8	4.9	3.1
A73 TC92	1.97	1.50	0.03	164.9	1.1	4.9	166.2	11.6	6.3	148.6	4.1	4.1	163.2	5.6	9.6
A74 TC93	1.97	1.50	0.14	164.9	1.1	6.3	159.5	11.3	6.7	163.8	4.0	8.2	188.0	5.3	15.4
A75 TC94	1.97	1.50	0.39	207.2	0.9	10.6	226.2	11.0	17.0	229.3	3.9	15.2	216.7	5.1	19.7
A76 TC95	1.97	1.50	0.64	247.2	0.9	11.1	216.8	11.0	11.0	169.1	4.0	3.2	158.3	5.2	5.8
A77 TC96	1.97	1.50	0.89	230.3	0.8	11.4	176.5	10.6	5.9	159.3	4.0	2.9	152.4	5.1	5.0
A78 TC97	1.97	1.50	1.39	116.0	0.9	2.4	122.8	9.9	2.4	102.2	4.0	2.1	94.5	5.0	3.0
B61 TC99	2.96	-2.00	0.03	40.7	1.2	1.3	42.7	10.1	1.6	38.0	4.3	1.6	33.0	5.3	1.3
B62 TC100	2.96	-2.00	0.39	39.9	0.7	1.8	23.4	9.5	1.1	33.5	3.9	2.7	28.9	4.9	2.8
B63 TC101	2.96	-2.00	0.89	113.5	0.7	14.0	64.7	9.3	4.8	60.7	3.9	3.0	55.7	4.8	1.8
B64 TC102	2.96	-2.00	1.39	82.2	0.8	10.3	44.4	9.0	2.5	45.1	3.7	1.1	49.8	4.7	1.1
B65 TC103	2.96	-2.00	1.89	44.0	0.9	1.9	31.8	9.0	1.0	36.7	3.7	0.9	41.4	4.7	1.0
B66 TC104	2.96	-2.00	2.39	27.1	1.3	0.8	27.3	9.1	0.9	24.7	3.8	0.6	27.0	4.7	0.8
B67 TC105	2.96	-2.00	2.89	19.7	1.6	0.8	25.3	9.2	0.7	17.9	3.8	0.5	19.9	4.8	0.6
B68 TC106	2.96	-2.00	3.39	28.6	1.7	4.1	14.2	9.2	0.4	11.1	3.9	0.4	12.0	4.9	0.5
B71 TC108	2.96	-1.50	0.03	96.1	1.5	3.4	65.3	10.9	2.5	85.4	4.5	4.7	91.0	5.8	5.6
B72 TC109	2.96	-1.50	0.39	285.4	1.0	17.4	278.9	10.1	29.6	385.0	4.1	34.5	398.3	5.2	32.1
B73 TC110	2.96	-1.50	0.89	396.8	0.9	24.3	377.3	9.6	25.4	253.5	3.9	23.0	181.0	5.0	13.6
B74 TC111	2.96	-1.50	1.39	175.9	0.8	23.5	136.5	9.3	16.9	57.4	3.8	1.7	60.2	4.8	1.4
B75 TC112	2.96	-1.50	1.89	136.8	1.1	5.5	95.2	9.4	3.8	87.6	3.8	2.0	90.6	4.8	1.9
B76 TC113	2.96	-1.50	2.39	65.9	1.3	1.5	45.4	9.2	1.2	44.6	3.8	1.0	42.3	4.8	1.2
B77 TC114	2.96	-1.50	2.89	22.5	1.5	1.0	20.7	9.1	0.6	19.3	3.8	0.6	21.6	4.7	0.8
B78 TC115	2.96	-1.50	3.39	36.3	1.6	4.3	22.3	9.2	0.7	19.9	3.9	0.6	21.9	4.8	0.7
C11 TC117	2.96	-1.00	0.03	210.0	2.0	8.7	207.4	12.1	12.7	325.8	4.8	15.3	488.5	6.1	19.4
C12 TC118	2.96	-1.00	0.39	583.6	1.2	27.8	673.7	10.9	43.4	756.3	4.0	40.4	784.5	5.4	36.5
C13 TC119	2.96	-1.00	0.89	589.9	1.0	33.9	544.7	10.3	22.0	385.3	3.9	18.8	292.7	5.1	16.1
C14 TC120	2.96	-1.00	1.39	339.3	1.0	15.3	205.4	9.6	13.9	146.1	3.9	4.9	134.9	5.0	3.9
C15 TC121	2.96	-1.00	1.89	160.7	1.1	11.9	93.6	9.2	3.4	94.6	3.8	1.8	93.2	4.8	2.7
C16 TC122	2.96	-1.00	2.39	84.9	1.5	2.1	46.9	9.3	1.3	43.5	3.9	1.0	40.7	4.9	1.0
C17 TC123	2.96	-1.00	2.89	52.8	1.7	1.5	45.5	9.4	1.3	34.6	4.0	0.9	32.0	4.9	0.9
C18 TC124	2.96	-1.00	3.39	38.8	1.8	4.1	35.4	9.4	1.2	22.2	4.1	0.8	19.7	5.0	0.8

				Test 44 (3 m/s)			Test 38 (5 m/s)			Test 43 (7 m/s)			Test 42 (10 m/s)		
Channel	x (m)	y (m)	z (m)	Tss - Tinit (deg. C)	Tinit (deg. C)	Standard deviation	Tss - Tinit (deg. C)	Tinit (deg. C)	Standard deviation	Tss - Tinit (deg. C)	Tinit (deg. C)	Standard deviation	Tss - Tinit (deg. C)	Tinit (deg. C)	Standard deviation
C21 TC126	2.96	-0.50	0.03	507.1	2.2	21.4	639.5	18.3	25.9	722.1	5.0	23.4	839.3	6.6	18.6
C22 TC127	2.96	-0.50	0.39	976.4	1.2	44.6	945.0	11.4	47.2	788.9	3.8	45.5	817.2	5.3	39.2
C23 TC128	2.96	-0.50	0.89	831.2	0.9	62.0	592.6	10.3	33.1	309.5	3.7	13.1	261.9	5.0	7.5
C24 TC129	2.96	-0.50	1.39	466.9	0.8	21.2	296.6	9.7	17.3	158.6	3.7	3.6	153.6	4.8	2.5
C25 TC130	2.96	-0.50	1.89	218.4	1.0	13.3	125.3	9.2	5.5	113.4	3.7	2.8	114.6	4.7	2.3
C26 TC131	2.96	-0.50	2.39	113.9	1.1	4.3	96.9	9.1	1.9	74.9	3.7	1.5	72.5	4.7	1.8
C27 TC132	2.96	-0.50	2.89	77.4	1.4	1.0	93.5	9.4	2.0	53.3	3.8	1.2	48.0	4.8	1.1
C28 TC133	2.96	-0.50	3.39	60.9	1.6	3.0	47.0	9.1	1.4	43.9	3.8	1.1	42.9	4.8	2.0
C51 TC135	2.96	0.00	0.03	876.6	1.9	53.4	1034.6	14.8	30.8	1015.0	4.7	56.7	1070.2	6.5	40.3
C52 TC136	2.96	0.00	0.39	1119.2	1.2	25.2	1086.0	11.8	17.3	1023.2	4.0	34.7	1025.2	5.4	39.4
C53 TC137	2.96	0.00	0.89	862.4	0.8	57.5	686.7	10.8	40.1	425.2	3.8	14.9	347.5	5.0	8.5
C54 TC138	2.96	0.00	1.39	363.1	0.7	36.3	317.0	10.0	15.5	**169.8**	3.9	7.3	173.3	4.9	5.9
C55 TC139	2.96	0.00	1.89	**174.3**	0.9	12.5	165.1	9.4	7.8	140.7	3.9	1.4	146.7	5.0	2.8
C56 TC140	2.96	0.00	2.39	120.4	1.3	8.0	108.3	9.2	4.9	**74.1**	3.8	3.4	**79.9**	4.8	3.1
C57 TC141	2.96	0.00	2.89	**44.6**	1.5	2.9	**54.7**	9.2	3.0	**44.4**	3.9	2.6	**45.8**	4.8	2.3
C58 TC142	2.96	0.00	3.39	53.9	1.7	2.6	66.3	9.1	2.7	42.7	3.9	0.8	40.7	4.8	1.9
D21 TC144	2.96	0.50	0.03	477.3	1.8	33.2	699.7	14.4	30.9	1071.2	4.5	15.7	1050.5	6.2	16.4
D27 TC145	2.96	0.50	0.39	947.3	1.0	69.4	985.2	12.3	38.8	957.2	4.0	48.5	962.1	5.5	31.9
D23 TC146	2.96	0.50	0.89	747.5	0.8	50.8	585.2	11.1	29.6	406.9	3.7	14.9	291.9	5.1	9.3
D24 TC147	2.96	0.50	1.39	425.6	0.7	22.2	282.3	10.1	13.6	146.9	3.7	3.9	137.2	4.8	3.2
D25 TC148	2.96	0.50	1.89	155.1	0.9	13.1	108.0	9.7	2.9	80.9	3.6	2.8	**89.0**	4.8	3.5
D26 TC149	2.96	0.50	2.39	120.9	1.3	3.2	94.7	9.5	2.0	86.4	3.8	2.3	**71.0**	4.8	1.1
D22 TC150	2.96	0.50	2.89	102.3	1.3	2.0	86.9	9.1	1.8	68.9	3.6	1.3	**67.9**	4.5	3.4
D28 TC151	2.96	0.50	3.39	30.3	1.7	3.6	38.3	9.1	1.4	16.2	3.9	1.0	**14.9**	4.8	0.5
D41 TC153	2.96	1.00	0.03	166.9	1.6	10.2	282.1	12.9	13.4	350.2	4.3	16.9	609.3	5.9	44.4
D42 TC154	2.96	1.00	0.39	534.2	0.8	29.9	660.2	11.2	45.7	603.4	3.8	27.5	533.0	5.0	34.4
D43 TC155	2.96	1.00	0.89	515.5	0.6	33.2	467.7	10.6	28.9	218.1	3.8	12.4	179.7	4.9	7.6
D44 TC156	2.96	1.00	1.39	307.6	0.7	20.9	206.3	9.7	9.0	159.5	3.7	7.3	156.7	4.7	4.0
D45 TC157	2.96	1.00	1.89	145.1	1.0	10.3	118.5	9.5	3.9	100.6	3.7	5.2	97.7	4.7	3.1
D46 TC158	2.96	1.00	2.39	91.5	1.1	8.1	78.3	9.3	6.5	60.6	3.7	6.0	58.0	4.7	4.2
D47 TC159	2.96	1.00	2.89	56.4	1.3	6.0	49.6	9.2	2.9	38.8	3.8	3.4	40.3	4.7	2.6
D48 TC160	2.96	1.00	3.39	44.7	1.4	5.3	35.5	9.1	1.7	21.8	3.8	0.7	21.4	4.8	0.7
D51 TC162	2.96	1.50	0.03	103.4	1.4	5.0	87.9	11.1	4.6	89.8	4.2	4.0	99.5	5.3	9.2
D52 TC163	2.96	1.50	0.39	195.8	0.8	9.2	227.1	10.7	15.6	266.9	3.8	12.8	270.6	5.0	23.5
D53 TC164	2.96	1.50	0.89	285.4	0.7	19.7	223.8	10.3	16.0	151.0	3.8	3.6	136.1	4.9	5.4
D54 TC165	2.96	1.50	1.39	150.9	0.7	7.7	96.7	9.7	3.6	86.3	3.7	1.8	76.4	4.7	2.5

				Test 44 (3 m/s)			Test 38 (5 m/s)			Test 43 (7 m/s)			Test 42 (10 m/s)		
Channel	x (m)	y (m)	z (m)	Tss - Tinit (deg. C)	Tinit (deg. C)	Standard deviation	Tss - Tinit (deg. C)	Tinit (deg. C)	Standard deviation	Tss - Tinit (deg. C)	Tinit (deg. C)	Standard deviation	Tss - Tinit (deg. C)	Tinit (deg. C)	Standard deviation
D55 TC166	2.96	1.50	1.89	105.5	0.9	2.3	95.7	9.5	2.6	86.4	3.7	1.9	84.0	4.7	2.4
D56 TC167	2.96	1.50	2.39	78.6	1.2	1.4	71.1	9.4	1.7	54.6	3.8	1.3	51.3	4.7	1.7
D57 TC168	2.96	1.50	2.89	37.1	1.3	1.0	45.5	9.2	1.1	29.1	3.7	0.7	26.2	4.7	0.8
D58 TC169	2.96	1.50	3.39	47.1	1.7	5.9	33.6	9.2	0.8	26.8	3.8	0.6	25.6	4.7	0.8
D81 TC171	2.96	2.00	0.03	55.4	0.6	1.5	31.0	9.7	1.6	27.6	3.7	0.9	22.1	4.7	1.3
D82 TC172	2.96	2.00	0.39	85.2	0.2	3.2	66.6	9.2	2.5	55.8	3.4	1.5	52.8	4.4	1.8
D83 TC173	2.96	2.00	0.89	77.5	0.2	2.6	76.5	9.2	2.6	69.5	3.3	1.7	67.9	4.3	2.1
D84 TC174	2.96	2.00	1.39	62.0	0.2	2.0	54.1	8.8	1.6	56.5	3.2	1.3	58.9	4.2	2.3
D85 TC175	2.96	2.00	1.89	47.1	0.3	1.0	48.7	8.6	1.3	36.4	3.2	1.0	36.1	4.1	1.1
D86 TC176	2.96	2.00	2.39	41.0	0.6	0.8	46.6	8.6	1.1	38.2	3.2	1.0	39.6	4.1	1.2
D87 TC177	2.96	2.00	2.89	35.3	0.7	2.3	44.6	8.5	1.1	33.8	3.2	0.9	34.7	4.1	1.1
D88 TC178	2.96	2.00	3.39	41.8	0.9	5.9	32.8	8.4	0.8	22.2	3.2	0.6	22.3	4.1	0.7
E61 TC180	3.94	-2.00	0.03	30.6	1.2	1.3	28.5	9.8	1.3	23.6	4.3	1.1	22.3	5.1	1.2
E62 TC181	3.94	-2.00	0.39	36.1	0.7	1.9	23.9	9.4	0.9	31.0	3.9	2.3	28.8	4.8	2.9
E63 TC182	3.94	-2.00	0.89	117.5	0.7	15.5	66.9	9.1	12.7	46.7	3.8	7.1	41.6	4.8	3.3
E64 TC183	3.94	-2.00	1.39	103.4	0.8	13.9	59.8	9.0	10.2	33.2	3.7	1.9	35.1	4.6	0.8
E65 TC184	3.94	-2.00	1.89	86.1	1.1	7.1	50.6	9.0	3.4	42.9	3.7	1.1	45.5	4.7	1.1
E66 TC185	3.94	-2.00	2.39	56.4	1.4	3.0	27.1	9.1	0.9	44.0	3.8	1.1	45.3	4.7	1.1
E67 TC186	3.94	-2.00	2.89	47.0	1.4	2.2	27.0	9.1	1.0	32.0	3.8	0.9	32.6	4.7	1.0
E68 TC187	3.94	-2.00	3.39	39.1	1.7	3.7	14.2	9.3	0.5	14.9	3.8	0.4	15.3	4.8	0.5
E71 TC189	3.94	-1.50	0.03	45.7	1.3	2.8	35.1	10.2	1.9	49.6	4.3	2.8	64.9	5.3	4.8
E72 TC190	3.94	-1.50	0.39	174.8	1.0	9.1	164.2	9.8	20.9	259.4	4.0	31.1	311.6	5.0	34.1
E73 TC191	3.94	-1.50	0.89	274.0	0.9	11.9	303.5	9.5	18.3	206.3	3.9	21.4	137.9	4.9	10.7
E74 TC192	3.94	-1.50	1.39	236.8	0.9	17.0	188.8	9.3	12.8	80.7	3.8	5.1	65.3	4.9	1.7
E75 TC193	3.94	-1.50	1.89	152.1	1.1	19.3	81.3	9.2	7.5	59.4	3.8	1.0	62.5	4.8	1.1
E76 TC194	3.94	-1.50	2.39	89.6	1.3	8.3	50.6	9.1	2.5	57.6	3.8	1.0	60.1	4.7	1.3
E77 TC195	3.94	-1.50	2.89	34.8	1.4	2.4	19.6	9.0	0.7	23.2	3.8	0.6	23.5	4.7	0.7
E78 TC196	3.94	-1.50	3.39	45.3	1.6	4.6	19.7	9.1	0.7	20.9	3.8	0.7	21.6	4.8	0.8
E81 TC198	3.94	-1.00	0.03	109.5	1.7	6.8	80.9	10.9	5.9	154.5	4.5	12.3	255.2	5.7	17.8
E82 TC199	3.94	-1.00	0.39	378.0	1.3	15.8	478.1	10.3	27.9	549.1	4.0	24.0	617.7	5.3	21.8
E83 TC200	3.94	-1.00	0.89	579.3	1.0	47.8	501.3	9.9	32.6	338.5	4.0	17.5	243.6	5.0	14.8
E84 TC201	3.94	-1.00	1.39	502.2	1.0	38.8	286.6	9.5	24.5	137.4	3.9	8.0	113.4	4.9	3.1
E85 TC202	3.94	-1.00	1.89	321.6	1.2	31.2	145.2	9.4	10.6	104.1	3.8	2.6	104.1	4.9	2.5
E86 TC203	3.94	-1.00	2.39	131.1	1.3	18.9	59.0	9.1	4.4	50.1	3.8	1.3	49.7	4.8	1.5
E87 TC204	3.94	-1.00	2.89	71.9	1.3	6.7	42.8	9.1	1.3	44.6	3.8	1.3	46.1	4.7	1.5
E88 TC205	3.94	-1.00	3.39	57.1	1.4	5.3	30.3	9.0	1.1	33.9	3.8	1.0	34.9	4.7	1.2

				Test 44 (3 m/s)			Test 38 (5 m/s)			Test 43 (7 m/s)			Test 42 (10 m/s)		
Channel	x (m)	y (m)	z (m)	Tss - Tinit (deg. C)	Tinit (deg. C)	Standard deviation	Tss - Tinit (deg. C)	Tinit (deg. C)	Standard deviation	Tss - Tinit (deg. C)	Tinit (deg. C)	Standard deviation	Tss - Tinit (deg. C)	Tinit (deg. C)	Standard deviation
C71 TC207	3.94	-0.50	0.03	217.6	1.8	12.8	358.3	12.0	18.3	465.9	4.6	25.3	652.3	6.1	26.8
C72 TC208	3.94	-0.50	0.39	572.6	1.3	28.9	762.7	11.0	43.2	686.9	3.9	47.4	742.2	5.3	34.1
C73 TC209	3.94	-0.50	0.89	896.8	1.0	52.9	745.6	10.1	47.2	395.3	3.9	26.3	304.7	5.0	13.1
C74 TC210	3.94	-0.50	1.39	732.8	0.9	71.8	438.4	9.8	27.1	151.3	3.8	5.5	132.2	4.9	3.4
C75 TC211	3.94	-0.50	1.89	420.6	1.1	40.1	174.7	9.5	16.1	105.7	3.8	2.5	97.3	4.8	2.9
C76 TC212	3.94	-0.50	2.39	194.4	1.3	26.5	77.9	9.3	5.4	64.8	3.8	2.0	59.6	4.9	1.9
C77 TC213	3.94	-0.50	2.89	103.7	1.4	8.2	64.7	9.2	2.1	65.4	3.8	1.6	62.3	4.8	1.8
C78 TC214	3.94	-0.50	3.39	57.4	1.5	5.5	32.3	9.1	1.2	38.2	3.8	1.0	40.5	4.7	1.3
C61 TC216	3.94	0.00	0.03	375.0	1.4	24.6	641.6	13.1	22.1	928.1	4.3	58.8	1026.2	6.0	34.1
C62 TC217	3.94	0.00	0.39	563.0	0.8	40.3	921.8	11.7	39.6	991.3	3.7	43.2	988.9	5.2	32.6
C63 TC218	3.94	0.00	0.89	853.5	0.6	50.3	833.9	10.4	63.5	550.7	3.7	26.7	384.7	4.8	17.7
C64 TC219	3.94	0.00	1.39	707.0	0.7	72.6	467.4	9.7	40.5	185.5	3.6	8.4	150.5	4.7	5.1
C65 TC220	3.94	0.00	1.89	411.5	0.9	46.7	192.1	9.3	15.4	118.8	3.6	2.5	116.2	4.6	3.3
C66 TC221	3.94	0.00	2.39	218.1	1.2	21.6	120.6	9.2	5.9	112.8	3.7	2.8	117.7	4.7	3.9
C67 TC222	3.94	0.00	2.89	87.6	1.3	11.8	57.5	8.9	2.1	57.7	3.7	1.8	57.9	4.6	2.6
C68 TC223	3.94	0.00	3.39	70.4	1.6	5.1	55.6	9.1	2.1	51.6	3.8	2.4	60.0	4.8	3.7
D11 TC225	3.94	0.50	0.03	166.7	1.8	11.1	376.9	13.3	17.1	628.7	4.7	26.6	1012.2	6.2	28.9
D12 TC226	3.94	0.50	0.39	592.2	1.1	44.5	768.2	11.9	39.7	945.1	4.0	45.0	965.1	5.4	38.8
D17 TC227	3.94	0.50	0.89	764.7	1.1	69.7	624.3	11.2	53.0	526.5	4.3	30.2	351.3	5.3	18.0
D14 TC228	3.94	0.50	1.39	550.5	0.8	53.8	365.3	10.0	28.4	160.0	3.9	7.4	150.8	4.8	6.8
D15 TC229	3.94	0.50	1.89	320.3	1.1	29.6	152.5	9.7	11.9	119.9	3.9	3.3	125.3	4.9	3.6
D16 TC230	3.94	0.50	2.39	171.4	1.4	18.6	99.5	9.5	3.8	86.4	4.0	2.6	91.6	4.9	3.0
D13 TC231	3.94	0.50	2.89	81.6	1.4	4.1	73.6	9.2	2.0	59.2	3.8	1.9	65.1	4.7	3.7
D18 TC232	3.94	0.50	3.39	53.8	1.9	4.1	39.0	9.6	1.2	30.7	4.2	0.7	35.1	5.1	1.7
D31 TC234	3.94	1.00	0.03	90.1	1.4	7.0	147.0	11.6	7.6	200.1	4.3	11.9	228.7	5.4	23.3
D32 TC235	3.94	1.00	0.39	315.5	1.0	18.2	446.5	11.0	23.6	535.7	4.0	25.3	526.5	5.2	33.4
D33 TC236	3.94	1.00	0.89	487.1	0.8	35.4	457.2	10.5	33.9	245.7	3.9	20.9	157.6	5.0	7.1
D34 TC237	3.94	1.00	1.39	359.7	0.9	36.9	238.0	9.9	22.4	132.9	3.8	3.8	133.7	4.8	3.6
D35 TC238	3.94	1.00	1.89	201.1	1.1	24.5	96.2	9.5	8.0	82.9	3.8	2.2	83.2	4.8	2.6
D36 TC239	3.94	1.00	2.39	102.9	1.3	9.4	76.6	9.3	2.5	75.9	3.8	2.0	80.5	4.8	2.2
D37 TC240	3.94	1.00	2.89	48.0	1.4	2.9	48.0	9.2	1.4	36.5	3.8	1.3	37.7	4.7	1.2
D38 TC241	3.94	1.00	3.39	70.4	1.6	5.0	47.4	9.2	1.2	36.8	3.8	0.8	35.6	4.8	0.9
D61 TC243	3.94	1.50	0.03	56.3	1.4	2.8	52.2	10.6	2.4	77.9	4.4	3.4	95.9	5.3	7.4
D62 TC244	3.94	1.50	0.39	149.8	0.9	10.6	157.1	10.2	10.9	193.5	3.9	11.3	193.9	5.0	20.3
D63 TC245	3.94	1.50	0.89	229.0	0.7	17.8	196.5	10.0	19.1	120.1	3.9	5.6	110.3	4.9	4.5
D64 TC246	3.94	1.50	1.39	190.1	0.9	15.9	111.7	9.7	13.7	85.8	3.9	2.6	80.2	4.9	2.7

				Test 44 (3 m/s)			Test 38 (5 m/s)			Test 43 (7 m/s)			Test 42 (10 m/s)		
Channel	x (m)	y (m)	z (m)	Tss - Tinit (deg. C)	Tinit (deg. C)	Standard deviation	Tss - Tinit (deg. C)	Tinit (deg. C)	Standard deviation	Tss - Tinit (deg. C)	Tinit (deg. C)	Standard deviation	Tss - Tinit (deg. C)	Tinit (deg. C)	Standard deviation
D65 TC247	3.94	1.50	1.89	112.3	1.0	8.0	68.1	9.4	3.2	74.0	3.8	1.8	73.2	4.8	2.4
D66 TC248	3.94	1.50	2.39	53.2	1.3	6.3	42.8	9.2	1.5	46.8	3.8	1.3	48.5	4.8	1.6
D67 TC249	3.94	1.50	2.89	52.8	1.3	2.8	45.9	9.1	1.3	42.9	3.8	1.2	43.4	4.8	1.3
D68 TC250	3.94	1.50	3.39	57.3	1.4	6.2	35.5	9.1	1.0	32.7	3.8	0.9	35.2	4.8	1.1
D71 TC252	3.94	2.00	0.03	48.1	1.2	1.7	45.6	10.1	1.7	32.5	4.3	1.2	27.7	5.1	1.3
D72 TC253	3.94	2.00	0.39	62.0	0.8	2.9	50.1	9.8	2.2	44.0	3.9	2.1	39.0	5.0	2.2
D73 TC254	3.94	2.00	0.89	81.9	0.7	7.0	68.8	9.7	3.2	62.0	3.9	2.0	60.1	4.8	2.4
D74 TC255	3.94	2.00	1.39	63.5	0.8	7.3	38.7	9.4	1.9	42.0	3.8	1.2	45.2	4.8	1.6
D75 TC256	3.94	2.00	1.89	71.4	1.0	2.9	57.5	9.3	1.9	55.4	3.8	1.5	54.3	4.8	2.1
D76 TC257	3.94	2.00	2.39	69.8	1.3	2.0	63.8	9.4	1.9	57.2	3.8	1.5	56.1	4.8	2.1
D77 TC258	3.94	2.00	2.89	48.4	1.3	3.6	41.7	9.1	1.3	39.9	3.8	1.2	41.5	4.7	1.4
D78 TC259	3.94	2.00	3.39	50.2	1.5	4.4	27.6	9.0	0.9	20.9	3.8	0.6	21.6	4.8	0.8
E11 TC261	5.92	-3.00	0.39	8.1	0.5	0.4	5.4	8.9	0.3	3.6	3.8	0.3	3.8	4.5	0.3
E12 TC262	5.92	-3.00	0.89	9.3	0.4	0.4	8.3	8.7	0.4	5.6	3.6	0.3	5.8	4.4	0.4
E13 TC263	5.92	-3.00	1.39	7.6	0.8	0.6	5.8	8.9	0.4	5.6	3.8	0.4	6.6	4.6	0.4
E14 TC264	5.92	-3.00	1.89	16.7	0.9	2.0	6.8	8.9	0.5	10.6	3.8	0.5	12.6	4.6	0.5
E15 TC265	5.92	-3.00	2.39	25.3	1.2	2.9	6.5	8.9	0.4	13.8	3.8	0.4	15.7	4.7	0.6
E16 TC266	5.92	-3.00	2.89	33.8	1.5	2.7	5.8	9.0	0.4	12.6	3.9	0.4	14.3	4.8	0.5
E17 TC267	5.92	-3.00	3.39	37.9	1.7	2.9	7.1	9.2	0.4	13.9	4.0	0.4	15.7	4.9	0.6
E18 TC269	5.92	-3.00	4.39	41.2	2.0	3.7	6.2	9.6	0.6	8.7	4.5	0.4	9.8	5.2	0.5
E21 TC271	5.92	-2.00	0.39	13.0	0.8	1.0	7.1	9.2	0.5	13.3	3.9	1.9	19.3	4.8	3.7
E22 TC272	5.92	-2.00	0.89	50.4	0.8	8.4	65.8	9.1	11.1	57.3	3.8	10.7	49.5	4.7	8.0
E23 TC273	5.92	-2.00	1.39	97.8	1.0	16.0	93.5	9.1	10.6	44.9	3.8	6.4	32.8	4.7	2.1
E24 TC274	5.92	-2.00	1.89	125.1	1.1	17.5	78.3	9.1	8.9	30.9	3.8	1.3	33.3	4.7	1.1
E25 TC275	5.92	-2.00	2.39	111.3	1.1	21.4	40.1	8.9	6.4	27.0	3.7	0.9	30.6	4.7	1.0
E26 TC276	5.92	-2.00	2.89	79.9	1.3	19.4	19.1	9.0	2.9	18.7	3.7	0.7	21.5	4.7	0.7
E27 TC277	5.92	-2.00	3.39	74.8	1.6	12.3	19.4	9.2	2.2	26.4	3.9	1.1	29.2	4.9	1.0
E28 TC279	5.92	-2.00	4.39	63.4	1.8	9.6	10.6	9.4	0.7	17.6	4.0	0.8	19.6	4.9	0.8
E35 TC281	5.92	-1.00	0.39	69.2	1.2	3.9	146.0	9.7	10.9	283.5	4.0	14.6	397.2	5.0	21.3
E36 TC282	5.92	-1.00	0.89	188.2	1.1	14.5	337.0	9.5	25.7	252.8	3.9	20.9	238.6	5.0	16.3
E37 TC283	5.92	-1.00	1.39	305.7	1.2	21.4	331.1	9.4	27.3	140.0	4.0	14.8	90.6	5.0	6.1
E38 TC284	5.92	-1.00	1.89	333.6	1.4	17.3	243.8	9.4	23.2	62.4	4.1	5.7	50.4	5.0	2.1
E31 TC285	5.92	-1.00	2.39	288.1	1.2	22.8	140.8	9.1	18.4	46.0	3.8	1.8	48.4	4.7	1.8
E32 TC286	5.92	-1.00	2.89	205.2	1.2	21.6	59.5	9.0	13.1	27.4	3.6	0.9	28.2	4.6	1.1
E33 TC287	5.92	-1.00	3.39	147.2	1.2	16.7	38.7	9.0	6.1	33.5	3.6	1.3	36.3	4.6	1.3
E34 TC289	5.92	-1.00	4.39	88.6	1.3	11.9	15.5	8.9	0.8	22.2	3.6	1.1	23.4	4.6	1.1

				Test 44 (3 m/s)			Test 38 (5 m/s)			Test 43 (7 m/s)			Test 42 (10 m/s)		
Channel	x (m)	y (m)	z (m)	Tss - Tinit (deg. C)	Tinit (deg. C)	Standard deviation	Tss - Tinit (deg. C)	Tinit (deg. C)	Standard deviation	Tss - Tinit (deg. C)	Tinit (deg. C)	Standard deviation	Tss - Tinit (deg. C)	Tinit (deg. C)	Standard deviation
E41 TC291	5.92	0.00	0.39	75.5	1.1	4.7	125.5	10.3	13.0	449.3	4.1	23.0	751.9	5.1	32.2
E42 TC292	5.92	0.00	0.89	98.2	1.1	5.5	265.3	10.1	17.8	493.9	4.0	24.8	406.2	4.9	29.1
E43 TC293	5.92	0.00	1.39	127.7	1.0	13.2	366.6	9.6	22.3	279.3	3.8	29.5	124.5	4.8	12.7
E44 TC294	5.92	0.00	1.89	198.5	1.1	15.7	307.6	9.4	36.2	99.5	3.8	10.3	62.8	4.8	3.1
E45 TC295	5.92	0.00	2.39	249.4	1.3	21.1	180.7	9.3	27.0	50.2	3.8	3.2	50.0	4.8	2.2
E46 TC296	5.92	0.00	2.89	212.7	1.4	18.1	77.9	9.2	13.7	36.1	3.8	1.4	36.9	4.9	1.7
E47 TC297	5.92	0.00	3.39	154.9	1.5	18.3	44.6	9.2	6.7	33.9	3.8	1.2	34.9	4.9	1.2
E48 TC299	5.92	0.00	4.39	94.6	1.7	13.1	19.4	9.2	1.9	25.9	4.0	1.1	26.4	4.9	0.9
E51 TC301	5.92	1.00	0.39	52.5	1.0	4.5	105.6	9.9	11.1	225.6	3.9	17.3	294.1	4.8	29.3
E52 TC302	5.92	1.00	0.89	173.9	0.7	14.0	239.6	9.7	25.2	271.4	3.7	36.7	151.4	4.7	23.7
E53 TC303	5.92	1.00	1.39	252.2	0.9	21.5	229.7	9.5	27.2	150.5	3.7	23.1	76.5	4.7	6.5
E54 TC304	5.92	1.00	1.89	246.9	1.0	26.6	149.5	9.2	23.3	58.0	3.6	5.7	57.1	4.6	2.1
E55 TC305	5.92	1.00	2.39	185.5	1.0	23.6	76.8	9.1	13.4	39.3	3.6	1.5	44.7	4.6	1.5
E56 TC306	5.92	1.00	2.89	130.8	1.2	19.1	40.5	9.1	8.1	28.2	3.6	1.1	30.7	4.7	1.2
E57 TC307	5.92	1.00	3.39	99.7	1.4	16.3	32.7	9.0	2.8	31.9	3.7	1.1	33.4	4.8	1.1
E58 TC309	5.92	1.00	4.39	75.9	1.6	9.3	19.3	9.1	0.8	21.7	3.9	0.8	22.3	4.9	1.0
F11 TC311	5.92	2.00	0.39	16.2	0.5	0.9	13.6	9.2	0.7	23.6	3.7	1.6	28.9	4.5	3.2
F12 TC312	5.92	2.00	0.89	38.4	0.4	5.5	31.0	9.1	3.0	33.3	3.5	2.3	36.6	4.4	2.5
F13 TC313	5.92	2.00	1.39	65.3	0.5	7.0	43.2	9.0	7.4	37.3	3.4	1.6	41.9	4.4	1.7
F14 TC314	5.92	2.00	1.89	64.8	0.5	14.4	32.0	8.7	7.1	28.1	3.4	1.2	31.6	4.3	1.3
F15 TC315	5.92	2.00	2.39	47.1	0.8	13.2	20.7	8.8	2.8	24.9	3.4	0.9	27.8	4.4	1.4
F16 TC316	5.92	2.00	2.89	48.9	1.0	10.4	16.4	8.7	1.1	23.3	3.5	0.8	25.5	4.5	1.2
F17 TC317	5.92	2.00	3.39	60.2	1.2	9.1	20.9	8.8	0.8	29.4	3.6	1.0	31.3	4.6	1.1
F18 TC319	5.92	2.00	4.39	52.7	1.5	4.4	13.8	9.0	0.9	18.6	3.9	0.8	20.7	4.8	1.0
F21 TC321	5.92	3.00	0.39	8.3	0.7	0.4	5.8	9.3	0.4	5.2	4.0	0.3	5.3	4.8	0.4
F22 TC322	5.92	3.00	0.89	10.2	0.6	0.4	8.3	9.2	0.5	7.4	3.9	0.4	7.6	4.7	0.5
F23 TC323	5.92	3.00	1.39	7.6	0.7	0.4	5.5	9.1	0.4	6.5	3.8	0.4	7.3	4.7	0.5
F24 TC324	5.92	3.00	1.89	18.2	0.9	1.1	12.7	9.0	0.6	19.2	3.8	0.7	21.5	4.7	0.9
F25 TC325	5.92	3.00	2.39	25.4	0.9	2.8	13.4	8.9	0.7	18.1	3.7	0.8	20.8	4.7	0.8
F26 TC326	5.92	3.00	2.89	34.5	1.1	2.2	14.1	8.9	0.5	19.1	3.7	0.6	21.1	4.7	0.9
F27 TC327	5.92	3.00	3.39	42.2	1.4	3.3	16.2	9.0	0.6	17.4	3.7	0.6	18.6	4.8	0.8
F28 TC329	5.92	3.00	4.39	41.3	1.5	3.0	13.2	9.0	0.8	14.1	3.9	0.6	15.3	4.9	0.7
G21 TC331	7.89	-3.00	0.39	5.1	0.8	0.3	4.1	9.0	0.2	2.6	4.0	0.3	2.7	4.7	0.3
G22 TC332	7.89	-3.00	0.89	5.7	0.8	0.6	4.4	9.0	0.2	3.3	3.9	0.3	3.5	4.7	0.3
G23 TC333	7.89	-3.00	1.39	9.1	0.8	1.7	3.5	8.9	0.6	3.5	3.8	0.4	4.2	4.6	0.4
G24 TC334	7.89	-3.00	1.89	22.5	0.9	3.6	6.9	8.8	1.6	7.2	3.7	0.5	8.9	4.6	0.5

				Test 44 (3 m/s)			Test 38 (5 m/s)			Test 43 (7 m/s)			Test 42 (10 m/s)		
Channel	x (m)	y (m)	z (m)	Tss - Tinit (deg. C)	Tinit (deg. C)	Standard deviation	Tss - Tinit (deg. C)	Tinit (deg. C)	Standard deviation	Tss - Tinit (deg. C)	Tinit (deg. C)	Standard deviation	Tss - Tinit (deg. C)	Tinit (deg. C)	Standard deviation
G25 TC335	7.89	-3.00	2.39	35.8	1.1	6.2	8.5	8.9	1.8	8.5	3.7	0.4	10.3	4.7	0.5
G26 TC336	7.89	-3.00	2.89	42.5	1.2	7.6	7.9	8.9	2.4	10.6	3.8	0.4	13.1	4.7	0.5
G27 TC337	7.89	-3.00	3.39	46.5	1.4	8.8	6.8	9.0	2.0	10.6	3.8	0.4	13.0	4.7	0.5
G28 TC339	7.89	-3.00	4.39	43.2	1.4	10.0	6.3	9.3	0.6	10.2	4.0	0.4	11.8	4.8	0.6
G31 TC341	7.89	-2.00	0.39	6.0	0.7	0.4	3.0	9.0	0.3	7.2	3.9	1.4	14.0	4.7	3.1
G32 TC342	7.89	-2.00	0.89	13.0	0.9	1.7	25.8	9.0	5.4	45.9	3.8	9.6	46.6	4.7	8.6
G33 TC343	7.89	-2.00	1.39	41.6	1.0	6.2	71.9	9.0	9.9	57.9	3.8	9.4	30.8	4.8	5.2
G34 TC344	7.89	-2.00	1.89	84.6	1.1	13.1	86.2	9.0	13.1	34.9	3.8	6.0	17.2	4.7	1.3
G35 TC345	7.89	-2.00	2.39	111.8	1.1	13.6	76.2	9.0	15.2	19.3	3.8	2.4	19.0	4.7	0.7
G36 TC346	7.89	-2.00	2.89	120.5	1.2	12.9	53.9	9.0	12.7	13.4	3.7	0.5	15.9	4.8	0.6
G37 TC347	7.89	-2.00	3.39	110.4	1.5	10.8	30.5	9.3	7.7	13.1	3.9	0.4	14.8	4.9	0.6
G38 TC349	7.89	-2.00	4.39	87.3	1.6	11.0	12.0	9.3	3.0	12.1	4.0	0.5	13.5	4.9	0.7
G61 TC351	7.89	-1.00	0.39	15.1	1.1	0.7	23.3	9.4	3.0	142.2	4.1	11.8	264.5	5.0	22.4
G62 TC352	7.89	-1.00	0.89	24.3	1.1	3.7	137.5	9.3	12.4	207.4	4.0	17.0	237.9	4.9	18.9
G63 TC353	7.89	-1.00	1.39	63.1	1.1	9.0	201.9	9.3	14.4	156.9	3.9	16.1	121.8	4.9	12.8
G64 TC354	7.89	-1.00	1.89	109.0	1.1	10.0	193.9	9.2	11.1	85.6	3.9	11.9	45.0	4.9	5.4
G65 TC355	7.89	-1.00	2.39	117.3	1.1	12.8	167.5	9.1	11.8	37.2	3.8	7.5	24.2	4.9	1.2
G66 TC356	7.89	-1.00	2.89	116.7	1.4	12.5	131.9	9.4	12.1	18.7	3.9	2.4	19.5	5.0	0.8
G67 TC357	7.89	-1.00	3.39	114.0	1.5	8.5	84.0	9.3	11.4	14.0	3.9	0.9	15.1	5.0	0.7
G68 TC359	7.89	-1.00	4.39	104.7	1.6	8.4	26.4	9.4	8.4	15.9	4.1	0.7	18.8	5.0	0.7
G71 TC361	7.89	0.00	0.39	28.4	1.1	1.4	29.5	9.7	1.7	114.8	4.1	10.4	313.2	5.0	17.5
G72 TC362	7.89	0.00	0.89	26.3	1.0	1.2	47.7	9.6	6.4	213.7	3.9	7.9	307.3	4.8	15.3
G73 TC363	7.89	0.00	1.39	23.2	1.0	1.7	83.0	9.4	11.1	229.0	3.8	13.8	179.9	4.8	19.7
G74 TC364	7.89	0.00	1.89	29.6	1.0	3.1	130.3	9.3	10.5	162.4	3.8	16.1	66.8	4.8	8.6
G75 TC365	7.89	0.00	2.39	40.7	1.1	5.0	150.9	9.3	11.2	74.6	3.8	11.4	27.4	4.8	1.9
G76 TC366	7.89	0.00	2.89	61.9	1.3	5.8	136.7	9.2	16.3	28.6	3.8	6.0	22.1	4.9	1.1
G77 TC367	7.89	0.00	3.39	80.4	1.5	6.3	93.3	9.2	15.8	18.2	3.9	1.8	19.6	4.9	0.9
G78 TC369	7.89	0.00	4.39	100.0	1.7	6.8	31.6	9.3	7.4	14.6	4.1	0.6	15.9	5.0	0.7
F41 TC371	7.89	1.00	0.39	14.0	0.9	1.0	23.5	9.6	2.5	96.9	4.1	8.5	160.5	4.9	18.9
F42 TC372	7.89	1.00	0.89	31.8	0.8	5.8	101.7	9.5	12.8	194.0	3.9	25.4	161.5	4.8	31.2
F43 TC373	7.89	1.00	1.39	79.7	0.9	9.6	146.2	9.5	15.5	155.9	3.8	21.8	79.1	4.8	18.6
F44 TC374	7.89	1.00	1.89	109.8	1.0	10.2	149.0	9.3	13.7	77.3	3.8	16.8	28.7	4.8	2.8
F45 TC375	7.89	1.00	2.39	116.2	1.1	10.3	129.7	9.2	17.2	30.7	3.8	4.8	25.9	4.8	1.1
F46 TC376	7.89	1.00	2.89	119.2	1.3	10.1	93.9	9.2	16.0	19.3	3.8	0.8	22.7	4.9	1.0
F47 TC377	7.89	1.00	3.39	117.4	1.4	9.8	55.5	9.2	15.8	17.1	3.8	0.6	19.6	4.9	0.8
F48 TC379	7.89	1.00	4.39	97.4	1.6	11.2	22.7	9.3	7.5	16.1	4.1	0.7	18.2	5.0	0.9

				Test 44 (3 m/s)			Test 38 (5 m/s)			Test 43 (7 m/s)			Test 42 (10 m/s)		
Channel	x (m)	y (m)	z (m)	Tss - Tinit (deg. C)	Tinit (deg. C)	Standard deviation	Tss - Tinit (deg. C)	Tinit (deg. C)	Standard deviation	Tss - Tinit (deg. C)	Tinit (deg. C)	Standard deviation	Tss - Tinit (deg. C)	Tinit (deg. C)	Standard deviation
F31 TC381	7.89	2.00	0.39	6.5	0.7	0.3	4.0	9.3	0.3	9.2	4.0	0.9	13.4	4.7	2.1
F32 TC382	7.89	2.00	0.89	11.8	0.7	1.3	13.6	9.3	1.9	18.3	3.8	1.9	18.9	4.8	2.4
F33 TC383	7.89	2.00	1.39	25.1	0.8	4.2	30.5	9.2	7.6	16.6	3.8	2.2	16.4	4.8	1.0
F34 TC384	7.89	2.00	1.89	51.8	0.9	11.3	46.5	9.1	11.4	19.4	3.8	2.9	20.8	4.8	1.0
F35 TC385	7.89	2.00	2.39	63.4	1.0	11.5	35.1	9.0	8.9	16.1	3.8	0.8	18.0	4.8	0.9
F36 TC386	7.89	2.00	2.89	70.2	1.2	10.7	23.9	9.1	7.1	14.5	3.8	0.7	16.0	4.8	0.7
F37 TC387	7.89	2.00	3.39	71.6	1.3	13.0	14.6	9.0	4.5	13.4	3.8	0.5	15.2	4.8	0.7
F38 TC389	7.89	2.00	4.39	59.7	1.5	8.9	10.9	9.2	1.7	14.1	4.0	0.6	16.3	5.0	0.8
F81 TC391	7.89	3.00	0.39	6.8	1.7	0.3	4.5	10.0	0.3	3.7	5.0	0.3	3.8	5.8	0.3
F82 TC392	7.89	3.00	0.89	6.7	1.7	0.2	5.3	9.9	0.3	4.7	4.9	0.3	4.9	5.7	0.4
F83 TC393	7.89	3.00	1.39	5.2	1.7	0.6	3.6	9.8	0.3	4.4	4.7	0.3	5.2	5.7	0.4
F84 TC394	7.89	3.00	1.89	12.1	1.9	1.6	4.1	9.8	0.4	7.4	4.7	0.4	9.0	5.7	0.5
F85 TC395	7.89	3.00	2.39	22.6	2.0	3.2	5.5	9.8	1.3	9.9	4.7	0.5	12.0	5.7	0.6
F86 TC396	7.89	3.00	2.89	29.0	2.2	3.1	6.5	9.7	1.4	10.3	4.7	0.4	12.3	5.7	0.7
F87 TC397	7.89	3.00	3.39	32.4	2.3	4.4	6.4	9.7	0.9	10.8	4.7	0.5	12.1	5.7	0.6
F88 TC399	7.89	3.00	4.39	30.3	2.4	6.4	8.1	9.8	0.7	11.5	4.8	0.6	13.2	5.8	0.7
G11 TC401	9.15	-3.00	0.39	3.8	0.4	0.2	2.8	8.4	0.2	2.5	3.6	0.4	2.6	4.3	0.3
G12 TC402	9.15	-3.00	0.89	5.4	0.3	0.9	3.2	8.3	0.2	2.5	3.4	0.3	2.4	4.1	0.3
G13 TC403	9.15	-3.00	1.39	9.8	0.2	2.2	2.6	8.2	0.4	2.4	3.2	0.4	3.0	4.0	0.4
G14 TC404	9.15	-3.00	1.89	19.7	0.2	3.1	5.9	8.1	2.0	3.5	3.1	0.4	4.6	4.0	0.4
G15 TC405	9.15	-3.00	2.39	28.7	0.4	5.5	8.6	8.2	3.0	4.6	3.1	0.3	6.0	4.0	0.4
G16 TC406	9.15	-3.00	2.89	34.4	0.7	5.8	10.7	8.3	4.6	5.8	3.3	0.3	7.3	4.2	0.4
G17 TC407	9.15	-3.00	3.39	40.6	0.9	8.6	10.1	8.5	4.5	5.8	3.4	0.3	7.1	4.2	0.4
G18 TC409	9.15	-3.00	4.39	44.2	1.1	9.2	8.4	8.8	2.4	7.2	3.7	0.4	8.4	4.4	0.6
G41 TC411	9.15	-2.00	0.39	6.4	0.6	0.3	2.7	8.7	0.2	4.3	3.8	0.7	10.0	4.6	2.5
G42 TC412	9.15	-2.00	0.89	8.8	0.7	1.3	8.4	8.7	2.7	30.7	3.7	8.1	33.5	4.5	8.1
G43 TC413	9.15	-2.00	1.39	21.7	0.7	5.2	45.7	8.7	10.5	46.2	3.7	10.3	32.9	4.5	7.1
G44 TC414	9.15	-2.00	1.89	48.8	0.8	8.1	71.1	8.7	14.0	41.7	3.6	9.0	17.6	4.5	3.6
G45 TC415	9.15	-2.00	2.39	75.4	1.0	9.6	81.7	8.7	13.2	20.4	3.6	5.1	10.8	4.6	0.8
G46 TC416	9.15	-2.00	2.89	89.2	1.1	10.1	74.1	9.0	14.4	11.7	3.7	1.6	12.2	4.7	0.5
G47 TC417	9.15	-2.00	3.39	90.1	1.2	8.8	58.1	8.9	12.0	9.6	3.7	0.5	11.2	4.7	0.6
G48 TC419	9.15	-2.00	4.39	80.9	1.3	8.7	25.1	9.1	8.5	9.1	3.8	0.4	10.7	4.8	0.6
G51 TC421	9.15	-1.00	0.39	8.9	1.0	0.6	7.5	9.3	1.5	75.0	4.2	9.5	196.8	5.0	17.9
G52 TC422	9.15	-1.00	0.89	9.2	1.0	1.1	54.4	9.2	7.9	169.1	4.0	13.8	219.7	4.9	18.9
G53 TC423	9.15	-1.00	1.39	20.7	1.0	4.0	119.3	9.2	13.2	151.1	3.9	12.5	155.6	4.9	16.2
G54 TC424	9.15	-1.00	1.89	43.9	1.0	7.7	144.2	9.2	12.7	111.3	3.8	12.6	71.6	4.9	11.1

				Test 44 (3 m/s)			Test 38 (5 m/s)			Test 43 (7 m/s)			Test 42 (10 m/s)		
Channel	x (m)	y (m)	z (m)	Tss - Tinit (deg. C)	Tinit (deg. C)	Standard deviation	Tss - Tinit (deg. C)	Tinit (deg. C)	Standard deviation	Tss - Tinit (deg. C)	Tinit (deg. C)	Standard deviation	Tss - Tinit (deg. C)	Tinit (deg. C)	Standard deviation
G55 TC425	9.15	-1.00	2.39	68.7	1.1	9.5	137.4	9.2	11.3	61.1	3.8	11.3	22.8	4.9	4.3
G56 TC426	9.15	-1.00	2.89	74.6	1.2	8.7	122.2	9.2	9.8	29.1	3.8	9.3	12.6	4.9	0.8
G57 TC427	9.15	-1.00	3.39	71.9	1.4	8.0	98.4	9.2	9.8	14.3	3.8	3.9	11.7	5.0	0.6
G58 TC429	9.15	-1.00	4.39	75.0	1.5	6.7	50.7	9.5	9.7	10.7	4.1	0.6	11.8	5.0	0.6
G81 TC431	9.15	0.00	0.39	15.2	1.0	1.2	14.7	9.4	1.0	63.9	4.1	8.4	204.1	4.9	22.2
G82 TC432	9.15	0.00	0.89	14.0	0.9	0.7	20.2	9.4	3.4	120.5	3.9	9.1	**248.5**	4.9	10.9
G83 TC433	9.15	0.00	1.39	13.7	1.0	1.0	29.4	9.4	5.0	163.1	3.9	7.6	183.1	4.9	14.8
G84 TC434	9.15	0.00	1.89	15.1	1.0	1.6	48.4	9.3	6.9	151.5	3.8	11.3	92.5	4.9	13.8
G85 TC435	9.15	0.00	2.39	20.0	1.1	2.7	82.3	9.2	8.0	102.9	3.8	14.8	29.5	4.9	5.9
G86 TC436	9.15	0.00	2.89	26.3	1.3	3.5	103.0	9.4	8.4	53.6	3.8	9.5	16.7	4.9	0.9
G87 TC437	9.15	0.00	3.39	35.9	1.3	3.5	94.9	9.1	11.5	20.0	3.8	5.6	11.3	4.9	0.6
G88 TC439	9.15	0.00	4.39	61.5	1.3	4.6	52.1	9.1	9.7	11.4	4.1	0.9	12.2	4.9	0.7
F51 TC441	9.15	1.00	0.39	8.3	1.0	0.4	10.2	9.6	1.1	49.4	4.2	6.6	99.4	5.0	11.8
F52 TC442	9.15	1.00	0.89	14.6	1.0	1.6	48.6	9.7	8.7	133.2	4.1	15.6	122.8	5.1	22.8
F53 TC443	9.15	1.00	1.39	30.5	1.1	6.4	94.7	9.6	10.6	132.3	4.0	17.6	84.1	5.0	21.1
F54 TC444	9.15	1.00	1.89	59.1	1.0	7.3	112.4	9.4	11.3	97.1	3.9	16.6	24.4	4.9	7.4
F55 TC445	9.15	1.00	2.39	72.5	1.3	8.2	114.5	9.3	10.2	51.8	3.9	12.3	13.7	5.0	0.8
F56 TC446	9.15	1.00	2.89	76.4	1.4	8.1	102.5	9.2	15.0	21.8	3.9	5.1	12.0	5.0	0.6
F57 TC447	9.15	1.00	3.39	75.1	1.4	7.1	77.4	9.2	16.1	10.3	3.9	1.5	10.9	5.0	0.6
F58 TC449	9.15	1.00	4.39	76.1	1.5	7.6	37.0	9.4	11.9	9.4	4.2	0.6	9.7	5.1	0.7
F61 TC451	9.15	2.00	0.39	5.7	2.2	0.4	2.1	10.4	0.2	5.2	5.4	0.7	8.2	6.2	1.3
F62 TC452	9.15	2.00	0.89	6.2	2.2	0.4	6.3	10.4	1.6	9.7	5.3	1.5	10.0	6.3	1.9
F63 TC453	9.15	2.00	1.39	11.4	2.3	2.5	22.5	10.4	7.1	12.4	5.3	3.2	8.4	6.3	0.9
F64 TC454	9.15	2.00	1.89	33.6	2.3	6.6	41.8	10.3	11.6	16.6	5.2	6.9	10.7	6.3	0.7
F65 TC455	9.15	2.00	2.39	45.9	2.5	9.3	41.8	10.2	9.9	15.1	5.2	4.3	11.0	6.3	0.6
F66 TC456	9.15	2.00	2.89	54.5	2.6	10.1	36.1	10.2	8.9	10.9	5.2	0.8	12.1	6.3	0.6
F67 TC457	9.15	2.00	3.39	59.6	2.7	9.5	25.7	10.3	8.1	8.9	5.2	1.2	9.9	6.4	0.6
F68 TC459	9.15	2.00	4.39	53.9	2.8	7.7	19.2	10.3	6.6	10.3	5.4	0.5	11.4	6.4	0.7
F71 TC461	9.15	3.00	0.39	3.6	0.5	0.2	2.4	9.0	0.2	2.2	3.8	0.3	2.5	4.6	0.3
F72 TC462	9.15	3.00	0.89	3.7	0.4	0.2	2.7	8.9	0.2	2.4	3.6	0.2	2.4	4.6	0.3
F73 TC463	9.15	3.00	1.39	4.9	0.6	0.5	3.1	8.9	0.3	2.8	3.6	0.3	3.3	4.6	0.3
F74 TC464	9.15	3.00	1.89	10.0	0.8	1.8	3.5	9.0	0.4	4.1	3.7	0.3	5.1	4.7	0.4
F75 TC465	9.15	3.00	2.39	19.4	1.0	3.4	5.6	9.0	1.5	5.5	3.8	0.4	6.9	4.8	0.5
F76 TC466	9.15	3.00	2.89	25.5	1.2	4.8	6.3	9.1	2.5	5.9	3.9	0.4	7.3	5.0	0.5
F77 TC467	9.15	3.00	3.39	26.6	1.3	5.5	6.6	9.2	2.3	6.7	4.0	0.4	7.5	5.1	0.5
F78 TC469	9.15	3.00	4.39	23.5	1.4	5.8	6.8	9.4	1.3	6.9	4.2	0.5	7.5	5.2	0.6

Appendix C

Transient Heat Flux Data from Tests With No Blocking Object

This Appendix contains time traces of data obtained from the DFT, HFG and Gardon gauge located near the longitudinal midplane y=0 m in the experiments of Chapter 4. Time traces of incident total heat flux to all three gauges in the 3 m/s, 5 m/s, 7 m/s and 10 m/s wind conditions are shown, together with time traces of the net heat flux absorbed by the DFT. Corresponding time traces of temperature from the HFG and DFT are also provided, along with time traces from a thermocouple placed immediately above the gauges (Section 4.1.4). The data corresponding to the 7 m/s wind condition were previously shown in Figures 4.40 and 4.41, and are included here for completeness. In general, trends similar to those described for Figures 4.40 and 4.41 at the beginning of Section 4.5 can be seen at all wind speeds.

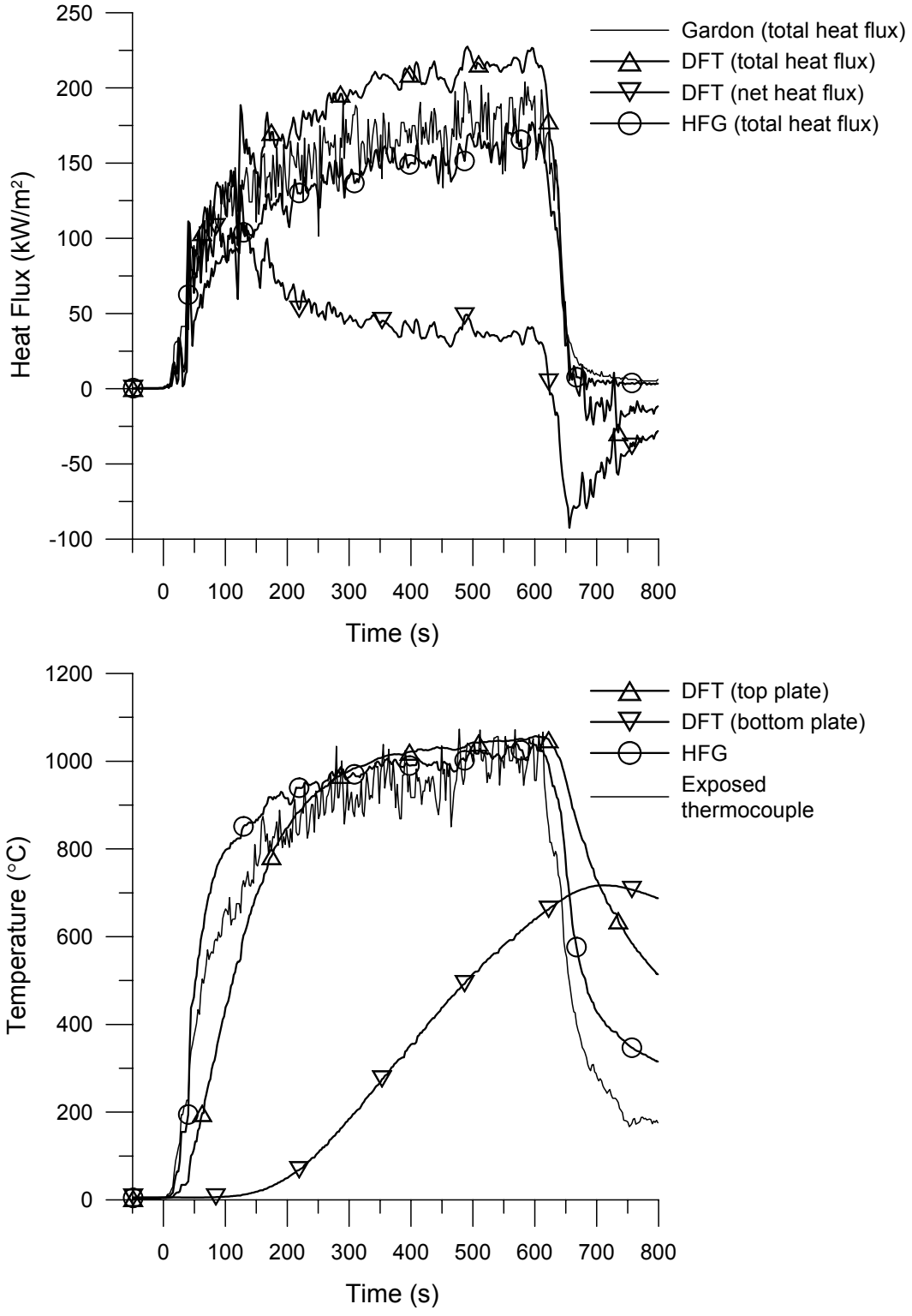

Figure C.1: Time trace of heat flux to the ground and corresponding temperatures, 3 m/s wind (x=2.64 m, y≈0 m)

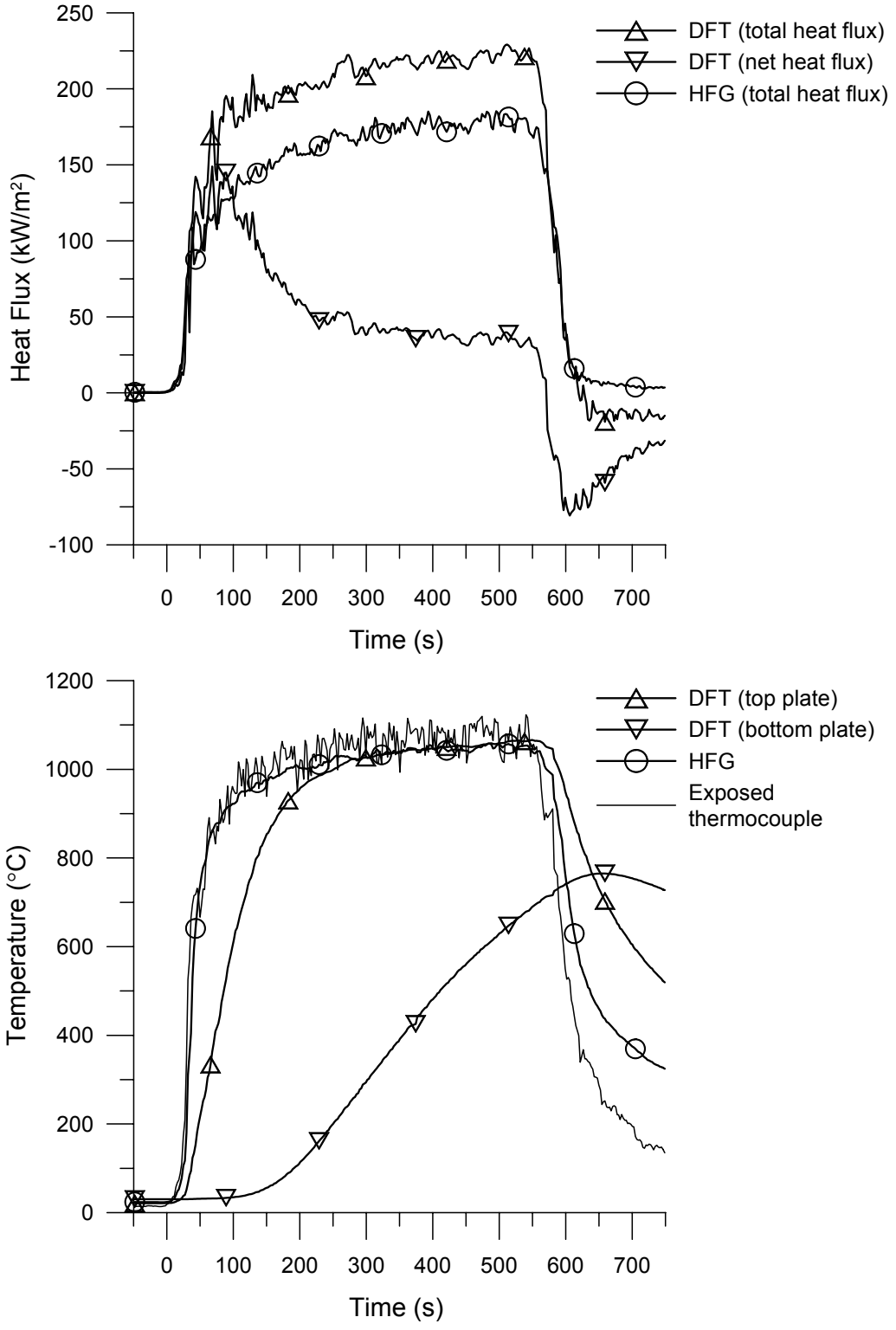

Figure C.2: Time trace of heat flux to the ground and corresponding temperatures, 5 m/s wind (x=2.64 m, y≈0 m; Gardon data unavailable)

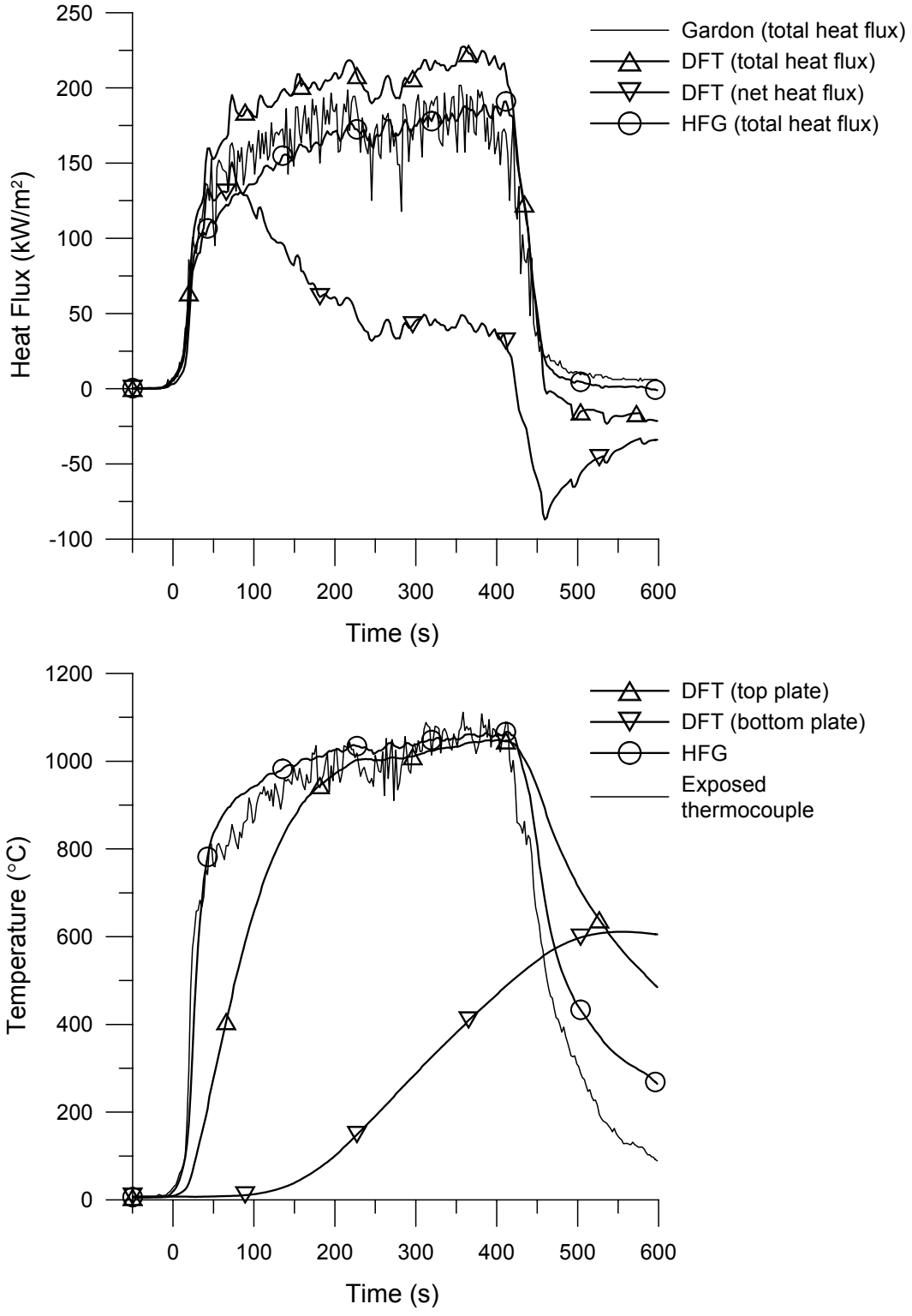

Figure C.3: Time trace of heat flux to the ground and corresponding temperatures, 7 m/s wind (x=2.64 m, y≈0 m)

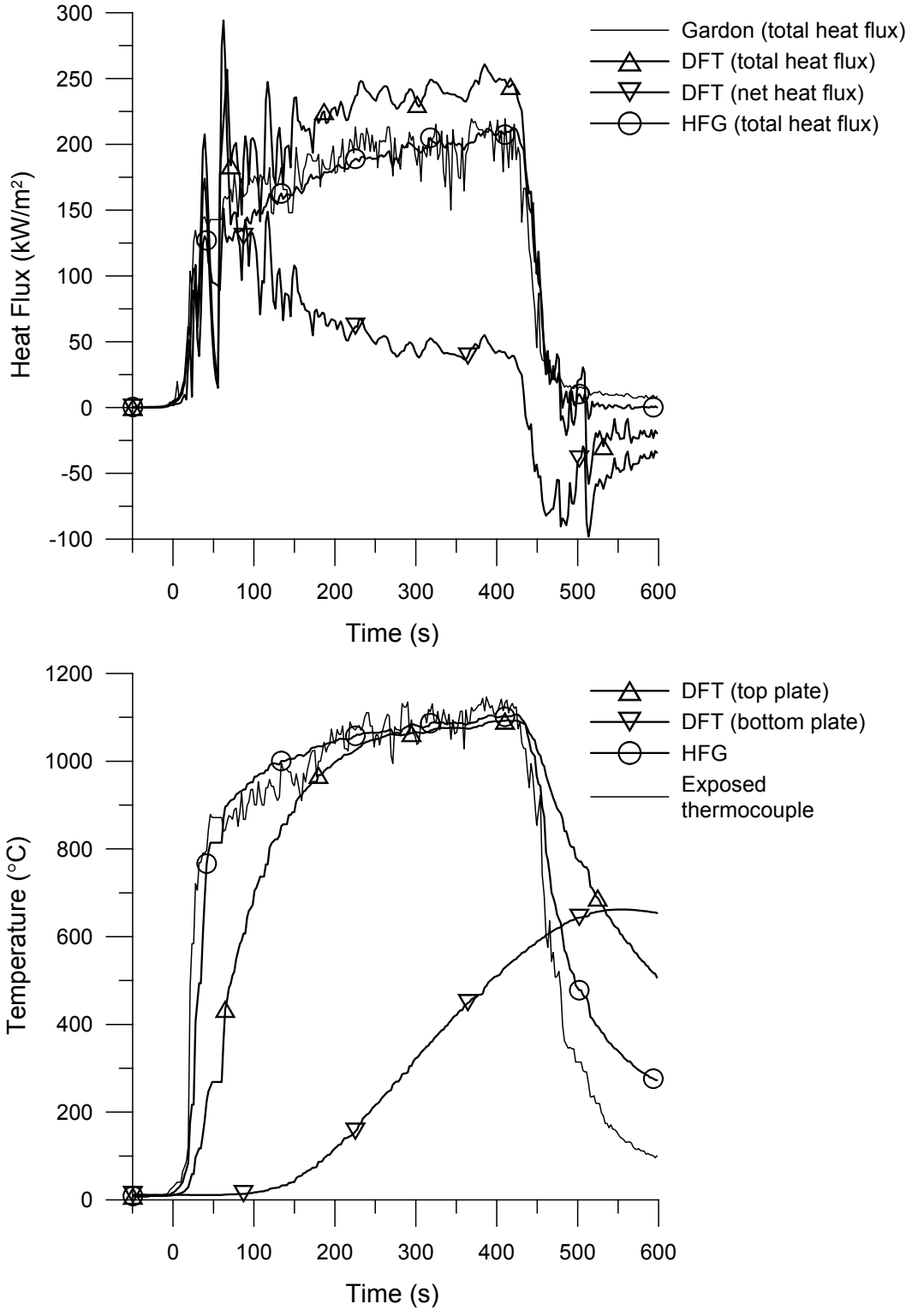

Figure C.4: Time trace of heat flux to the ground and corresponding temperatures, 10 m/s wind (x=2.64 m, y≈0 m)

Appendix D

Plume Temperature Data from Tests With Blocking Object

This Appendix lists the following data for thermocouples used to measure plume temperature in the fire tests with the blocking object: the x, y and z coordinates in metres, the initial temperature measured prior to startup of the first fan, the time-averaged increase in temperature measured during the steady burning period of each test, and the standard deviation corresponding to this temperature increase. All temperatures are in degrees Celsius. The values of time-averaged temperature increase were used to generate the line and contour plots of fire plume temperature in Section 5.3. Although the temperature standard deviations were not specifically discussed, they are included here for reference. Additional thermocouples beyond the ones listed here were installed on the thermocouple rakes at y=±0.5 m and ±1 m (Figures 5.4 and 5.5), but were not presented in Section 5.3 because they did not provide any additional information about the fire. To facilitate the discussion of results and prevent the temperature line plots from becoming too crowded, the data from these additional thermocouples were not included in the present work.

In the following chart, values printed in bold indicate results from thermocouples that failed partway through the test, as mentioned at the beginning of Section 5.3. A few thermocouples failed right at the beginning of the test, resulting in missing data points. No thermocouple rakes were present at (x,y)=(6.1 m, -1.0 m), (6.1 m, -1.5 m) or (7.3 m, -2.0 m) during tests 25 to 28, so no data were available at those locations during these tests.

				Test 27 (5 m/s)			Test 32 (5 m/s)			Test 28 (7 m/s)			Test 31 (7 m/s)		
Channel	x (m)	y (m)	z (m)	Tss - Tinit (deg. C)	Tinit (deg. C)	Standard deviation	Tss - Tinit (deg. C)	Tinit (deg. C)	Standard deviation	Tss - Tinit (deg. C)	Tinit (deg. C)	Standard deviation	Tss - Tinit (deg. C)	Tinit (deg. C)	Standard deviation
Vertical rakes in longitudinal midplane:															
2TC Fire1	1.09	0.00	0.40	876.9	13.4	25.2	901.8	10.9	34.2	948.4	3.9	11.1	781.4	15.4	15.6
0TC Fire2	1.09	0.00	0.92	731.9	13.8	32.2	674.2	11.4	36.1	**453.6**	3.7	19.6	651.6	14.9	27.7
1TC Fire3	1.09	0.00	1.43	**211.3**	13.4	27.8	390.0	11.3	25.2	**154.5**	3.5	10.9	227.1	14.8	10.1
2TC Fire4	1.09	0.00	1.95	**58.8**	13.2	7.4	134.6	11.2	18.7	**127.7**	3.5	19.2	31.4	14.7	1.1
0TC Fire5	1.09	0.00	2.46	--	--	--	42.4	10.4	3.3	**82.4**	2.7	14.1	26.4	13.9	0.9
1TC Fire6	1.09	0.00	2.99	--	--	--	25.4	10.3	1.4	**28.4**	2.6	3.4	17.8	13.8	0.3
7TC Fire13	1.52	0.00	0.40	933.8	14.8	27.3	960.3	11.8	27.5	1019.9	4.5	18.5	1011.8	15.3	12.1
0TC Fire14	1.52	0.00	0.91	669.0	13.9	37.8	723.6	11.4	47.3	613.3	3.9	33.9	635.6	14.7	36.4
3TC Fire15	1.52	0.00	1.43	372.8	13.4	29.7	451.3	11.1	39.1	207.1	3.3	16.4	244.0	14.6	15.8
1TC Fire16	1.52	0.00	1.95	**155.1**	13.1	11.9	250.6	11.1	22.6	**126.8**	3.3	8.0	119.4	14.7	9.3
6TC Fire17	1.52	0.00	2.47	72.3	12.5	19.0	115.1	10.5	18.6	**56.6**	2.8	9.3	28.3	13.9	2.7
7TC Fire18	1.52	0.00	2.99	**28.0**	12.4	5.2	55.9	10.7	8.3	**38.0**	2.8	13.1	15.9	14.1	1.5
4TC Fire25	2.04	0.00	0.18	1008.8	15.4	34.1	1026.9	11.3	25.3	1048.5	4.0	22.5	1052.0	15.2	17.8
5TC Fire26	2.04	0.00	0.40	914.7	14.8	45.7	918.3	11.3	53.2	887.1	3.9	54.2	908.7	15.8	52.5
6TC Fire27	2.04	0.00	0.93	686.1	14.0	47.3	770.9	11.8	54.8	568.3	4.0	39.5	595.5	14.9	51.9
6TC Fire28	2.04	0.00	1.43	412.0	13.6	41.3	493.8	11.3	42.2	254.6	3.5	12.7	238.0	15.0	13.8
0TC Fire61	3.02	0.00	0.20	890.4	17.0	63.2	860.4	11.3	56.1	941.7	3.8	54.0	997.5	16.4	35.0
1TC Fire62	3.02	0.00	0.39	957.2	14.9	59.1	974.3	11.3	56.1	950.5	3.6	67.7	1000.1	15.5	45.5
2TC Fire63	3.02	0.00	0.90	648.6	13.6	50.8	750.2	11.3	56.4	475.0	3.5	29.3	492.7	15.3	31.7
2TC Fire33	4.53	0.00	0.20	366.5	15.5	23.1	331.6	11.5	18.9	534.1	3.8	26.2	626.1	15.6	38.2
3TC Fire34	4.53	0.00	0.41	438.2	14.8	23.9	396.8	11.3	26.8	622.5	3.7	35.3	744.2	15.4	51.4
4TC Fire35	4.53	0.00	0.94	632.9	13.6	38.0	631.9	11.4	43.1	655.0	3.7	47.3	839.8	15.0	68.5
0TC Dwnd33	6.15	0.00	3.83	241.4	13.1	43.3	282.5	12.3	34.9	101.2	4.2	15.7	134.2	15.1	20.4
1TC Dwnd34	6.15	0.00	3.37	286.9	13.2	43.1	318.7	12.5	35.4	137.5	4.1	16.9	206.4	15.1	22.4
2TC Dwnd35	6.15	0.00	2.86	316.3	13.3	44.4	340.6	12.5	36.1	182.9	4.0	24.7	288.9	15.1	25.6
3TC Dwnd36	6.15	0.00	2.38	330.0	13.4	43.7	344.1	12.6	35.6	263.0	3.9	34.4	399.6	15.1	26.7
4TC Dwnd37	6.15	0.00	1.89	290.5	13.6	38.3	292.1	12.4	28.7	369.0	3.8	27.4	474.5	15.1	31.6
5TC Dwnd38	6.15	0.00	1.39	225.4	13.7	29.2	237.3	12.2	24.2	362.6	3.8	22.6	438.1	15.2	24.3
6TC Dwnd39	6.15	0.00	0.91	144.0	14.3	14.6	152.7	13.3	8.5	303.6	4.0	17.5	321.1	15.5	23.6
7TC Dwnd40	6.15	0.00	0.39	104.6	14.4	9.2	109.9	16.2	4.6	244.8	4.1	16.8	221.9	15.6	20.9
0TC Dwnd41	7.33	0.00	3.90	136.1	13.2	21.3	134.7	12.4	20.3	153.6	4.1	14.9	201.2	15.2	17.9
1TC Dwnd42	7.33	0.00	3.42	123.5	13.2	19.7	115.6	12.6	17.4	184.5	4.0	14.9	228.8	15.2	18.2
2TC Dwnd43	7.33	0.00	2.91	109.3	13.3	18.8	94.8	12.6	15.0	197.4	3.9	20.4	226.8	15.1	23.8
3TC Dwnd44	7.33	0.00	2.39	95.9	13.4	19.2	80.3	12.8	10.8	193.1	3.9	19.5	207.6	15.2	28.4
4TC Dwnd45	7.33	0.00	1.90	80.8	13.6	17.6	67.5	13.0	10.1	168.8	3.9	19.0	178.4	15.2	25.6
5TC Dwnd46	7.33	0.00	1.41	58.6	13.7	14.9	50.6	13.9	9.6	128.4	4.0	17.9	130.0	15.3	20.9

				Test 27 (5 m/s)			Test 32 (5 m/s)			Test 28 (7 m/s)			Test 31 (7 m/s)		
Channel	x (m)	y (m)	z (m)	Tss - Tinit (deg. C)	Tinit (deg. C)	Standard deviation	Tss - Tinit (deg. C)	Tinit (deg. C)	Standard deviation	Tss - Tinit (deg. C)	Tinit (deg. C)	Standard deviation	Tss - Tinit (deg. C)	Tinit (deg. C)	Standard deviation
6TC Dwnd47	7.33	0.00	0.90	42.1	13.8	9.5	41.0	15.4	5.7	98.1	4.1	16.5	99.9	15.4	16.7
7TC Dwnd48	7.33	0.00	0.39	30.4	13.8	4.4	27.7	19.2	2.7	77.9	4.4	12.3	78.0	15.5	12.3
0TC Plu9	9.27	0.00	4.68	51.9	12.9	5.9	42.1	12.2	4.6	87.0	3.8	7.5	97.8	15.1	8.2
1TC Plu10	9.27	0.00	4.08	38.6	13.0	5.7	31.6	12.3	3.9	85.1	3.7	9.4	86.3	15.0	12.0
2TC Plu11	9.27	0.00	3.48	31.5	13.1	4.5	26.1	12.5	4.3	72.0	3.7	6.5	69.3	15.0	11.6
3TC Plu12	9.27	0.00	2.88	24.6	13.1	4.7	17.7	15.8	4.3	61.1	3.6	7.3	61.1	15.0	11.3
4TC Plu13	9.27	0.00	2.28	20.4	13.3	5.0	13.3	16.7	2.8	53.4	3.7	8.3	51.0	15.1	8.3
5TC Plu14	9.27	0.00	1.68	17.4	13.3	2.0	12.1	17.9	1.5	48.7	3.8	5.0	44.6	15.2	5.4
6TC Plu15	9.27	0.00	1.09	14.9	13.4	1.3	12.4	15.8	1.0	42.8	3.9	2.5	41.1	15.1	3.1
7TC Plu16	9.27	0.00	0.49	12.2	13.4	1.6	6.7	19.0	1.1	37.5	4.0	4.0	38.7	15.2	4.0
Vertical rakes on +y side of test enclosure:															
3TC Fire7	1.09	0.50	0.42	**880.5**	13.6	27.1	820.8	11.2	35.3	756.8	7.4	27.6	821.6	14.8	35.7
4TC Fire8	1.09	0.50	0.94	**462.6**	13.6	30.1	529.0	11.6	25.3	**385.1**	4.9	51.1	476.8	14.7	22.3
1TC Fire19	1.53	0.50	0.41	933.8	14.0	38.5	922.5	11.1	37.2	917.7	3.7	60.1	843.3	14.9	46.1
2TC Fire20	1.53	0.50	0.92	613.8	13.7	40.7	551.5	11.3	44.0	475.4	3.7	27.9	412.5	14.7	30.5
7TC Fire29	1.86	0.50	0.18	943.4	14.7	47.2	964.9	11.6	48.8	928.7	4.2	72.3	879.9	15.5	59.9
0TC Fire30	1.86	0.50	0.32	857.5	13.9	63.6	868.8	11.1	65.2	733.4	3.6	76.3	669.9	14.8	54.2
1TC Fire31	1.86	0.50	0.91	619.5	13.4	55.3	591.6	11.2	59.2	435.1	3.5	33.9	390.1	14.6	32.6
3TC Fire64	3.02	0.50	0.20	534.1	16.1	32.9	506.6	11.3	31.9	709.8	3.7	101.8	596.1	15.9	66.9
4TC Fire65	3.02	0.50	0.39	674.6	14.9	65.2	641.7	11.4	59.2	649.9	3.6	88.5	562.7	15.3	64.0
5TC Fire36	4.53	0.50	0.20	246.3	14.7	30.0	223.5	11.7	20.7	422.5	4.0	47.2	412.7	15.5	63.2
6TC Fire37	4.53	0.50	0.41	313.9	14.4	18.5	293.6	11.8	13.3	485.9	4.0	48.4	472.6	15.4	66.9
7TC Fire38	4.53	0.50	0.92	489.7	13.7	32.0	513.6	12.0	34.7	388.2	4.0	42.7	428.5	15.2	60.3
3TC Dwnd28	6.15	0.50	2.31	277.2	13.2	23.5	299.8	12.9	16.8	208.5	3.7	23.5	308.0	15.1	33.8
5TC Dwnd30	6.15	0.50	1.32	244.2	13.5	20.9	252.0	12.6	18.7	282.7	3.6	30.9	351.1	15.0	56.6
7TC Dwnd32	6.15	0.50	0.33	102.7	14.1	10.1	107.0	12.0	7.0	235.1	3.9	29.3	181.0	15.3	28.6
3TC Dwnd12	7.33	1.00	2.35	73.0	13.1	14.1	70.2	13.1	12.8	131.4	3.7	24.9	122.1	14.9	31.0
5TC Dwnd14	7.33	1.00	1.35	54.8	13.4	11.0	50.4	14.5	7.2	126.8	3.8	22.3	104.2	15.0	17.9
7TC Dwnd16	7.33	1.00	0.36	21.0	13.5	4.8	21.1	15.3	3.4	94.1	4.0	12.4	79.3	15.2	12.7
Vertical rakes on -y side of test enclosure:															
0TC Fire39	1.09	-0.50	0.42	876.7	14.0	12.5	944.3	11.1	26.6	889.9	3.8	11.0	953.9	15.2	23.7
1TC Fire40	1.09	-0.50	0.93	810.4	13.9	13.5	689.4	11.2	46.1	838.4	3.8	12.0	646.5	14.5	28.1
6TC Fire45	1.52	-0.50	0.41	914.4	15.1	13.1	988.0	11.4	29.0	946.9	4.2	10.6	982.8	15.7	19.9
7TC Fire46	1.52	-0.50	0.92	819.4	14.2	33.3	812.7	11.6	58.1	842.6	4.0	34.0	677.3	15.2	34.5
4TC Fire51	1.86	-0.50	0.19	960.6	16.7	35.4	937.6	11.0	36.9	998.6	4.1	24.8	972.0	16.4	21.0
5TC Fire52	1.86	-0.50	0.41	1050.8	14.3	30.2	1010.8	11.2	24.3	1059.9	3.9	19.4	1014.3	15.4	12.9
6TC Fire53	1.86	-0.50	0.92	683.6	14.1	56.0	1006.2	11.3	59.5	670.2	3.9	37.4	904.2	15.2	22.1

Channel	x (m)	y (m)	z (m)	Test 27 (5 m/s) Tss - Tinit (deg. C)	Test 27 (5 m/s) Tinit (deg. C)	Test 27 (5 m/s) Standard deviation	Test 32 (5 m/s) Tss - Tinit (deg. C)	Test 32 (5 m/s) Tinit (deg. C)	Test 32 (5 m/s) Standard deviation	Test 28 (7 m/s) Tss - Tinit (deg. C)	Test 28 (7 m/s) Tinit (deg. C)	Test 28 (7 m/s) Standard deviation	Test 31 (7 m/s) Tss - Tinit (deg. C)	Test 31 (7 m/s) Tinit (deg. C)	Test 31 (7 m/s) Standard deviation
5TC Fire55	3.00	-0.50	0.21	777.8	16.5	52.3	692.3	11.3	41.6	873.6	3.8	72.3	914.9	16.3	46.2
6TC Fire56	3.00	-0.50	0.40	1021.1	14.8	50.7	1005.2	11.4	47.3	1046.6	3.8	45.4	1069.6	15.7	21.3
0TC Fire58	4.53	-0.50	0.20	369.6	15.9	32.7	330.5	11.7	17.3	508.7	3.9	36.7	604.4	16.2	37.5
1TC Fire59	4.53	-0.50	0.41	454.2	14.8	34.7	397.7	11.4	23.3	632.8	3.7	46.8	732.4	15.7	52.1
2TC Fire60	4.53	-0.50	0.93	757.5	13.6	69.6	814.0	11.2	68.5	732.6	3.6	55.2	814.5	15.1	66.3
3TC Dwnd4	6.15	-0.50	2.33	350.3	13.3	43.0	377.6	12.6	39.0	291.3	3.9	24.9	412.2	15.0	34.6
5TC Dwnd6	6.15	-0.50	1.33	178.9	13.7	24.6	194.9	12.2	21.1	414.7	3.8	25.3	480.7	15.1	22.5
7TC Dwnd8	6.15	-0.50	0.35	88.1	14.5	8.9	96.9	13.2	6.6	255.8	4.0	19.7	255.5	15.5	24.7
0TC Dwnd49	6.10	-1.00	2.40	--	--	--	291.9	12.8	51.4	--	--	--	322.7	15.1	51.6
6TC Dwnd50	6.10	-1.00	1.42	--	--	--	148.6	12.0	21.2	--	--	--	427.0	15.0	41.2
7TC Dwnd51	6.10	-1.00	0.40	--	--	--	98.3	14.4	9.7	--	--	--	263.6	15.2	19.6
3TC Dwnd52	6.10	-1.50	2.40	--	--	--	200.9	12.2	25.1	--	--	--	200.8	14.9	43.1
4TC Dwnd53	6.10	-1.50	1.39	--	--	--	136.4	12.2	14.6	--	--	--	263.1	15.0	35.4
5TC Dwnd54	6.10	-1.50	0.39	--	--	--	91.0	12.4	6.8	--	--	--	168.2	15.0	19.0
3TC Dwnd20	7.33	-1.00	2.37	84.1	13.4	12.9	83.4	12.6	8.5	187.8	3.7	22.3	193.1	15.0	15.7
5TC Dwnd22	7.33	-1.00	1.37	59.7	13.7	6.2	60.0	15.6	4.2	145.7	3.8	18.2	136.8	15.1	19.9
7TC Dwnd24	7.33	-1.00	0.38	36.3	14.1	4.6	35.4	17.4	3.8	84.5	4.1	13.5	87.5	15.3	15.8
1TC Dwnd55	7.32	-2.00	2.40	--	--	--	50.7	12.3	5.4	--	--	--	53.1	14.9	12.6
6TC Dwnd56	7.32	-2.00	1.42	--	--	--	28.8	12.9	2.7	--	--	--	67.8	15.1	10.1
7TC Dwnd57	7.32	-2.00	0.40	--	--	--	19.2	13.0	2.1	--	--	--	66.1	15.1	5.9
Horizontal rake:															
0PR TC -2m	9.06	-2.00	4.92 for 5-7 m/s wind; 1.42 for 10-13 m/s wind	83.9	13.6	9.4	82.5	12.7	9.6	55.4	4.5	16.3	71.7	15.8	12.6
1PR TC -1_66m	9.06	-1.66		80.6	13.6	9.6	79.8	12.6	7.9	66.0	4.5	15.0	83.2	15.7	11.5
2PR TC -1_33m	9.06	-1.33		77.2	13.6	10.0	73.0	12.7	7.6	76.8	4.5	12.0	92.4	15.8	9.4
3PR TC -1m	9.06	-1.00		73.3	13.6	8.9	67.8	12.7	7.1	81.0	4.4	10.5	99.4	15.7	8.5
4PR TC -0_66m	9.06	-0.66		70.6	13.7	9.8	62.1	12.7	8.1	87.7	4.5	7.6	107.0	15.8	9.0
5PR TC -0_33m	9.06	-0.33		67.5	13.8	10.2	58.8	12.9	7.9	89.0	4.7	7.2	107.0	15.9	10.8
6PR TC 0m	9.06	0.00		66.7	14.0	9.7	58.1	13.2	6.9	88.2	4.9	8.2	106.8	16.1	10.5
7PR TC 0_33m	9.06	0.33		65.1	14.2	7.7	57.8	13.4	6.3	83.5	5.3	8.1	99.7	16.4	10.6
0PR TC 0_66m	9.06	0.66		64.5	12.9	7.8	61.8	12.1	6.5	76.9	4.0	8.8	90.0	15.1	11.3
1PR TC 1m	9.06	1.00		62.2	12.9	9.1	63.1	12.1	7.0	69.5	3.9	8.4	79.4	15.1	9.5
2PR TC 1_33m	9.06	1.33		53.4	12.8	8.9	58.8	11.9	8.1	53.6	3.8	7.9	61.2	15.0	9.7
3PR TC 1_66m	9.06	1.66		45.6	12.8	7.5	52.4	11.9	8.8	42.3	3.8	7.6	49.7	15.0	9.2
4PR TC 2m	9.06	2.00		32.8	12.8	7.7	39.0	12.0	10.0	28.4	3.8	7.4	35.7	14.9	9.5
5PR TC 2_33m	9.06	2.33		23.2	12.8	5.2	26.7	12.1	6.8	17.8	3.8	4.5	22.8	15.1	5.9
6PR TC 2_66m	9.06	2.66		18.2	12.9	4.7	19.4	11.9	5.0	10.8	3.8	3.1	14.6	15.0	4.7
7PR TC 3m	9.06	3.00		15.1	12.9	3.3	16.1	12.1	2.3	6.6	4.0	2.4	9.4	15.2	3.6

				Test 26 (10 m/s)			Test 29 (10 m/s)			Test 25 (13 m/s)			Test 30 (13 m/s)		
Channel	x (m)	y (m)	z (m)	Tss - Tinit (deg. C)	Tinit (deg. C)	Standard deviation	Tss - Tinit (deg. C)	Tinit (deg. C)	Standard deviation	Tss - Tinit (deg. C)	Tinit (deg. C)	Standard deviation	Tss - Tinit (deg. C)	Tinit (deg. C)	Standard deviation
Vertical rakes in longitudinal midplane:															
2TC Fire1	1.09	0.00	0.40	1036.5	9.3	13.2	834.1	7.7	26.2	1087.1	4.8	19.5	810.7	12.9	8.9
0TC Fire2	1.09	0.00	0.92	695.1	9.9	31.4	673.3	7.8	31.4	546.5	5.0	46.3	641.6	12.4	24.8
1TC Fire3	1.09	0.00	1.43	**101.7**	9.7	6.7	173.7	7.7	13.9	157.1	5.0	8.9	162.5	12.2	3.4
2TC Fire4	1.09	0.00	1.95	**42.1**	9.6	3.5	**30.5**	7.6	0.9	142.8	5.0	12.9	31.5	12.1	0.8
0TC Fire5	1.09	0.00	2.46	**26.3**	9.0	6.7	**26.1**	7.0	1.0	83.2	4.2	15.5	26.9	11.4	1.4
1TC Fire6	1.09	0.00	2.99	**18.6**	8.7	2.2	**15.3**	6.7	0.5	126.0	4.2	14.0	17.4	11.3	0.8
7TC Fire13	1.52	0.00	0.40	1072.2	10.3	17.6	1054.4	8.6	13.5	1138.1	5.6	16.3	1106.7	13.1	11.8
0TC Fire14	1.52	0.00	0.91	549.2	9.8	30.8	593.7	7.9	36.8	471.5	5.1	37.5	532.7	12.3	36.4
3TC Fire15	1.52	0.00	1.43	153.2	9.6	8.1	161.4	7.4	13.9	123.8	4.8	6.5	164.7	12.0	4.5
1TC Fire16	1.52	0.00	1.95	72.1	9.5	4.1	95.2	7.5	6.4	115.9	4.8	9.4	92.8	12.1	4.0
6TC Fire17	1.52	0.00	2.47	46.9	9.0	6.1	**23.3**	6.9	0.5	59.2	4.4	15.5	24.8	11.2	0.8
7TC Fire18	1.52	0.00	2.99	50.1	8.8	4.6	**11.3**	7.0	0.5	50.2	4.4	21.4	**12.5**	11.4	0.6
4TC Fire25	2.04	0.00	0.18	1061.1	9.9	20.2	1076.8	10.8	17.8	1116.2	4.9	19.5	1100.8	13.8	19.7
5TC Fire26	2.04	0.00	0.40	755.5	10.1	44.4	1001.6	9.1	40.2	759.0	5.0	48.8	836.8	14.7	47.0
6TC Fire27	2.04	0.00	0.93	373.6	9.9	27.3	**378.8**	8.9	14.8	316.8	5.2	42.1	--	--	--
6TC Fire28	2.04	0.00	1.43	63.9	9.8	3.9	**151.2**	8.3	4.9	47.2	4.9	1.7	208.9	12.8	13.2
0TC Fire61	3.02	0.00	0.20	903.5	10.7	79.3	1092.5	11.0	18.5	1026.3	5.0	50.7	1092.6	15.6	22.2
1TC Fire62	3.02	0.00	0.39	753.0	10.0	75.9	1060.1	8.2	38.5	826.4	5.0	72.0	961.4	13.8	53.6
2TC Fire63	3.02	0.00	0.90	171.7	9.8	14.1	356.4	8.2	12.3	78.9	5.0	5.7	280.0	13.3	12.4
2TC Fire33	4.53	0.00	0.20	629.7	10.7	54.2	963.4	10.2	45.3	719.3	5.2	48.9	917.4	13.8	45.4
3TC Fire34	4.53	0.00	0.41	661.1	10.3	63.3	1032.1	8.4	45.3	705.7	5.0	48.0	928.1	13.4	50.0
4TC Fire35	4.53	0.00	0.94	377.4	9.6	32.6	686.6	9.8	59.3	255.4	5.0	34.3	398.7	12.8	43.8
0TC Dwnd33	6.15	0.00	3.83	44.6	9.6	7.4	54.0	11.2	8.3	28.7	5.4	4.8	36.9	12.9	4.4
1TC Dwnd34	6.15	0.00	3.37	58.6	9.7	9.3	70.6	10.9	7.7	34.6	5.5	4.4	47.8	13.0	4.9
2TC Dwnd35	6.15	0.00	2.86	65.8	9.7	13.2	90.2	10.0	9.6	38.9	5.5	4.4	54.5	13.0	5.1
3TC Dwnd36	6.15	0.00	2.38	80.7	9.7	13.8	121.0	9.9	13.2	47.6	5.5	4.5	69.6	13.1	5.0
4TC Dwnd37	6.15	0.00	1.89	127.8	9.8	24.2	229.6	10.0	32.1	66.4	5.4	6.0	95.1	13.2	7.5
5TC Dwnd38	6.15	0.00	1.39	215.7	9.9	30.5	429.5	10.9	39.2	120.7	5.4	23.0	207.3	13.2	27.3
6TC Dwnd39	6.15	0.00	0.91	294.8	10.3	32.1	543.1	10.3	27.5	301.5	6.2	26.2	413.4	13.7	22.0
7TC Dwnd40	6.15	0.00	0.39	252.9	10.4	27.1	500.1	8.9	38.6	317.8	7.5	30.6	409.8	13.8	17.5
0TC Dwnd41	7.33	0.00	3.90	56.4	9.6	13.1	97.7	9.1	15.1	33.4	5.4	6.3	45.2	13.0	6.7
1TC Dwnd42	7.33	0.00	3.42	73.9	9.6	12.3	130.1	9.7	16.1	46.6	5.5	8.4	62.0	13.1	8.1
2TC Dwnd43	7.33	0.00	2.91	96.8	9.7	16.4	172.2	9.5	20.7	57.8	5.5	9.1	79.4	13.0	11.1
3TC Dwnd44	7.33	0.00	2.39	130.2	9.8	16.7	225.5	10.3	22.2	78.4	5.5	10.9	114.2	13.2	15.3
4TC Dwnd45	7.33	0.00	1.90	151.7	9.8	18.2	261.3	10.6	22.9	113.2	6.6	14.5	171.7	13.3	17.8
5TC Dwnd46	7.33	0.00	1.41	144.0	9.9	21.1	254.4	9.3	35.7	158.4	7.4	18.8	206.7	13.3	13.4

				Test 26 (10 m/s)			Test 29 (10 m/s)			Test 25 (13 m/s)			Test 30 (13 m/s)		
Channel	x (m)	y (m)	z (m)	Tss - Tinit (deg. C)	Tinit (deg. C)	Standard deviation	Tss - Tinit (deg. C)	Tinit (deg. C)	Standard deviation	Tss - Tinit (deg. C)	Tinit (deg. C)	Standard deviation	Tss - Tinit (deg. C)	Tinit (deg. C)	Standard deviation
6TC Dwnd47	7.33	0.00	0.90	133.9	10.1	24.8	238.0	8.8	45.9	178.5	8.8	24.9	207.6	13.6	18.3
7TC Dwnd48	7.33	0.00	0.39	109.5	10.2	23.3	211.8	8.9	54.1	178.5	10.4	34.1	183.3	13.6	23.0
0TC Plu9	9.27	0.00	4.68	46.8	9.5	4.9	78.3	10.1	6.2	30.4	5.2	3.9	41.6	13.1	4.8
1TC Plu10	9.27	0.00	4.08	66.8	9.5	7.4	100.5	10.9	9.2	43.7	5.3	6.2	60.6	13.0	8.4
2TC Plu11	9.27	0.00	3.48	81.4	9.6	8.7	115.0	8.6	9.6	60.3	5.9	6.1	79.8	12.9	9.0
3TC Plu12	9.27	0.00	2.88	87.0	9.6	10.8	119.2	10.1	12.8	78.0	8.4	8.8	102.4	13.1	9.4
4TC Plu13	9.27	0.00	2.28	88.1	9.7	12.3	122.1	10.4	19.6	96.7	8.7	10.6	116.1	13.3	8.8
5TC Plu14	9.27	0.00	1.68	80.0	9.9	10.3	115.5	8.3	16.2	104.0	10.8	10.8	119.9	13.7	8.7
6TC Plu15	9.27	0.00	1.09	73.3	9.9	8.3	114.8	8.3	12.2	113.8	11.8	9.3	119.6	13.5	7.4
7TC Plu16	9.27	0.00	0.49	64.8	10.0	9.8	98.6	8.3	14.1	114.1	10.8	18.7	109.7	13.7	12.4
Vertical rakes on +y side of test enclosure:															
3TC Fire7	1.09	0.50	0.42	1142.6	9.4	35.3	949.0	7.8	27.8	**1105.2**	4.8	23.1	1015.2	12.4	27.8
4TC Fire8	1.09	0.50	0.94	422.1	9.7	26.0	507.2	7.9	30.1	474.3	5.0	39.0	468.0	12.3	19.4
1TC Fire19	1.53	0.50	0.41	958.8	9.6	53.5	979.1	8.2	31.0	1043.2	4.9	47.1	1033.9	12.8	32.3
2TC Fire20	1.53	0.50	0.92	396.1	9.8	24.6	423.6	8.1	23.7	358.1	4.9	25.7	390.3	12.6	17.6
7TC Fire29	1.86	0.50	0.18	889.1	10.1	84.4	987.0	9.6	41.7	987.6	5.3	60.1	1024.3	13.6	47.3
0TC Fire30	1.86	0.50	0.32	630.1	9.7	72.5	732.9	8.2	43.5	678.1	4.9	69.4	721.4	12.8	47.2
1TC Fire31	1.86	0.50	0.91	276.7	9.5	25.1	340.6	7.8	20.9	226.5	4.8	22.2	262.7	12.3	13.1
3TC Fire64	3.02	0.50	0.20	540.6	10.7	60.9	767.9	8.7	65.3	620.7	5.0	48.3	747.4	14.6	48.5
4TC Fire65	3.02	0.50	0.39	404.6	10.3	43.3	626.7	8.8	49.2	387.5	5.0	44.0	506.1	13.7	38.7
5TC Fire36	4.53	0.50	0.20	328.6	10.3	46.9	665.5	11.5	73.3	390.7	5.3	49.1	556.5	13.6	44.4
6TC Fire37	4.53	0.50	0.41	322.6	10.1	42.6	681.8	9.2	73.0	332.9	5.3	45.2	485.0	13.4	39.5
7TC Fire38	4.53	0.50	0.92	118.8	9.8	16.2	336.7	11.1	22.6	93.5	5.4	16.1	151.2	13.2	8.9
3TC Dwnd28	6.15	0.50	2.31	66.4	9.6	9.4	114.8	12.9	10.2	47.2	5.9	3.1	64.2	13.1	4.8
5TC Dwnd30	6.15	0.50	1.32	108.7	9.7	20.3	327.8	9.0	37.4	91.9	5.6	13.5	131.2	13.1	10.5
7TC Dwnd32	6.15	0.50	0.33	181.1	10.2	24.0	394.1	8.6	50.6	242.0	5.5	31.0	300.3	13.5	22.0
3TC Dwnd12	7.33	1.00	2.35	57.6	9.5	11.9	126.5	9.6	15.2	45.8	6.0	6.4	54.3	12.9	5.2
5TC Dwnd14	7.33	1.00	1.35	77.9	9.7	14.5	142.0	8.5	23.6	75.3	8.4	10.4	88.5	13.1	9.1
7TC Dwnd16	7.33	1.00	0.36	86.0	9.9	13.9	145.3	8.6	25.3	112.9	12.5	19.2	125.1	13.3	11.5
Vertical rakes on -y side of test enclosure:															
0TC Fire39	1.09	-0.50	0.42	979.8	10.1	12.9	983.4	7.7	20.0	1059.8	4.8	17.6	1003.2	12.2	18.0
1TC Fire40	1.09	-0.50	0.93	**608.6**	9.6	40.1	655.1	7.7	30.4	770.3	4.8	76.6	658.8	12.0	35.0
6TC Fire45	1.52	-0.50	0.41	1082.7	10.2	14.5	1020.1	8.2	19.0	1129.8	5.1	16.8	1059.3	13.3	14.6
7TC Fire46	1.52	-0.50	0.92	757.1	10.2	37.9	647.7	8.1	38.2	652.4	5.3	54.0	615.9	12.7	33.2
4TC Fire51	1.86	-0.50	0.19	1070.5	10.9	11.5	1001.5	9.7	18.1	1115.9	4.7	10.2	1037.6	15.0	16.7
5TC Fire52	1.86	-0.50	0.41	1078.4	9.9	20.1	1072.0	8.5	15.1	1117.3	4.9	21.0	1123.8	13.3	13.3
6TC Fire53	1.86	-0.50	0.92	628.4	9.9	30.3	572.8	8.5	31.8	529.1	5.1	30.8	535.3	12.8	32.1

				Test 26 (10 m/s)			Test 29 (10 m/s)			Test 25 (13 m/s)			Test 30 (13 m/s)		
Channel	x (m)	y (m)	z (m)	Tss - Tinit (deg. C)	Tinit (deg. C)	Standard deviation	Tss - Tinit (deg. C)	Tinit (deg. C)	Standard deviation	Tss - Tinit (deg. C)	Tinit (deg. C)	Standard deviation	Tss - Tinit (deg. C)	Tinit (deg. C)	Standard deviation
5TC Fire55	3.00	-0.50	0.21	1075.9	11.0	41.7	1045.8	8.6	35.8	1128.4	5.0	34.9	1146.3	15.1	22.9
6TC Fire56	3.00	-0.50	0.40	1056.9	10.4	38.6	1074.7	9.4	22.9	1017.8	5.1	44.4	1056.2	14.3	38.6
0TC Fire58	4.53	-0.50	0.20	760.2	11.6	54.7	853.7	8.5	48.4	839.2	5.2	61.1	984.3	14.3	42.0
1TC Fire59	4.53	-0.50	0.41	809.6	10.9	51.3	942.4	8.5	57.8	811.4	5.1	70.9	962.1	13.9	49.1
2TC Fire60	4.53	-0.50	0.93	503.0	9.7	41.1	505.9	8.7	51.4	232.5	5.0	26.5	346.8	13.3	27.8
3TC Dwnd4	6.15	-0.50	2.33	113.3	9.7	9.9	134.3	9.3	10.3	65.2	5.8	4.1	93.2	13.0	5.1
5TC Dwnd6	6.15	-0.50	1.33	318.0	9.8	35.1	358.1	9.0	44.7	129.1	5.3	20.1	219.6	13.1	28.0
7TC Dwnd8	6.15	-0.50	0.35	366.8	10.6	41.2	542.2	8.8	40.3	454.4	5.6	41.2	562.9	13.6	32.3
0TC Dwnd49	6.10	-1.00	2.40	--	--	--	104.1	9.2	16.3	--	--	--	83.3	12.9	8.6
6TC Dwnd50	6.10	-1.00	1.42	--	--	--	187.9	8.2	40.6	--	--	--	138.0	12.9	19.3
7TC Dwnd51	6.10	-1.00	0.40	--	--	--	403.6	8.3	61.2	--	--	--	591.8	13.1	34.0
3TC Dwnd52	6.10	-1.50	2.40	--	--	--	68.1	8.8	19.9	--	--	--	73.2	12.6	9.0
4TC Dwnd53	6.10	-1.50	1.39	--	--	--	135.7	8.1	26.4	--	--	--	129.4	12.7	13.2
5TC Dwnd54	6.10	-1.50	0.39	--	--	--	198.6	8.1	44.3	--	--	--	413.5	12.7	47.2
3TC Dwnd20	7.33	-1.00	2.37	195.4	9.7	18.1	160.8	10.7	24.5	86.2	5.7	12.8	128.8	12.9	11.4
5TC Dwnd22	7.33	-1.00	1.37	247.3	9.9	26.3	254.1	9.8	23.6	185.3	5.8	23.8	265.5	13.1	19.2
7TC Dwnd24	7.33	-1.00	0.38	166.0	10.3	40.8	231.8	8.7	27.9	286.1	6.1	43.3	318.3	13.3	32.3
1TC Dwnd55	7.32	-2.00	2.40	--	--	--	48.1	9.3	22.7	--	--	--	79.6	12.7	19.9
6TC Dwnd56	7.32	-2.00	1.42	--	--	--	112.0	8.3	22.6	--	--	--	198.5	12.9	26.5
7TC Dwnd57	7.32	-2.00	0.40	--	--	--	100.4	8.3	17.9	--	--	--	246.1	12.7	23.1
Horizontal rake:															
0PR TC -2m	9.06	-2.00	4.92 for 5-7 m/s wind; 1.42 for 10-13 m/s wind	69.7	10.5	8.0	46.9	8.9	6.4	88.8	6.3	14.3	111.0	13.7	12.4
1PR TC -1_66m	9.06	-1.66		90.7	10.5	12.8	71.0	8.9	10.5	123.5	6.3	14.4	151.3	13.7	14.5
2PR TC -1_33m	9.06	-1.33		111.2	10.5	17.7	102.8	8.9	12.1	150.2	9.6	11.9	182.7	13.8	11.4
3PR TC -1m	9.06	-1.00		113.5	10.4	20.1	125.0	8.8	13.5	157.4	9.4	12.0	189.6	13.7	14.5
4PR TC -0_66m	9.06	-0.66		110.1	10.5	22.3	141.9	8.9	22.2	155.2	8.9	16.5	177.1	13.8	16.4
5PR TC -0_33m	9.06	-0.33		98.9	10.6	17.3	145.3	9.1	24.5	138.9	10.4	15.7	159.4	14.1	15.9
6PR TC 0m	9.06	0.00		91.3	10.7	14.6	140.3	9.3	21.6	121.7	11.1	13.9	138.8	14.4	12.3
7PR TC 0_33m	9.06	0.33		82.0	11.0	10.2	126.5	9.6	16.4	105.9	11.5	12.3	118.3	14.7	9.0
0PR TC 0_66m	9.06	0.66		68.8	9.7	9.0	106.1	8.2	14.0	86.6	10.5	9.4	98.1	13.5	5.9
1PR TC 1m	9.06	1.00		53.6	9.6	6.8	81.8	8.1	11.2	68.5	10.4	7.7	77.9	13.5	5.6
2PR TC 1_33m	9.06	1.33		40.8	9.6	5.5	56.7	8.1	8.4	50.4	9.7	5.6	55.3	13.3	5.4
3PR TC 1_66m	9.06	1.66		28.5	9.5	4.6	37.4	8.0	6.1	35.4	10.1	4.5	41.5	13.3	4.5
4PR TC 2m	9.06	2.00		19.0	9.5	4.3	24.4	8.0	4.4	23.3	9.1	3.7	29.8	13.2	3.9
5PR TC 2_33m	9.06	2.33		12.2	9.6	2.4	16.1	8.0	2.5	13.5	9.9	2.5	20.1	13.4	2.8
6PR TC 2_66m	9.06	2.66		7.8	9.6	1.1	9.9	8.0	1.7	7.4	9.2	1.9	12.6	13.2	2.4
7PR TC 3m	9.06	3.00		6.2	9.6	0.7	7.2	8.2	1.0	3.4	9.5	1.2	8.1	13.4	1.8

Appendix E

Transient Temperature Data from Blocking Object

This Appendix contains time traces of temperatures measured around the circumference of the blocking object in the centreline plane y=0 m. The temperatures were measured using thermocouples mounted to the inside surface of the blocking object (Section 5.1.3). The data corresponding to the 7 m/s wind condition (test 31) were previously shown in Figure 5.20 and are included here for completeness. The curves in each plot have similar overall shapes, with temperature increasing throughout the test until the fuel started to burn out.

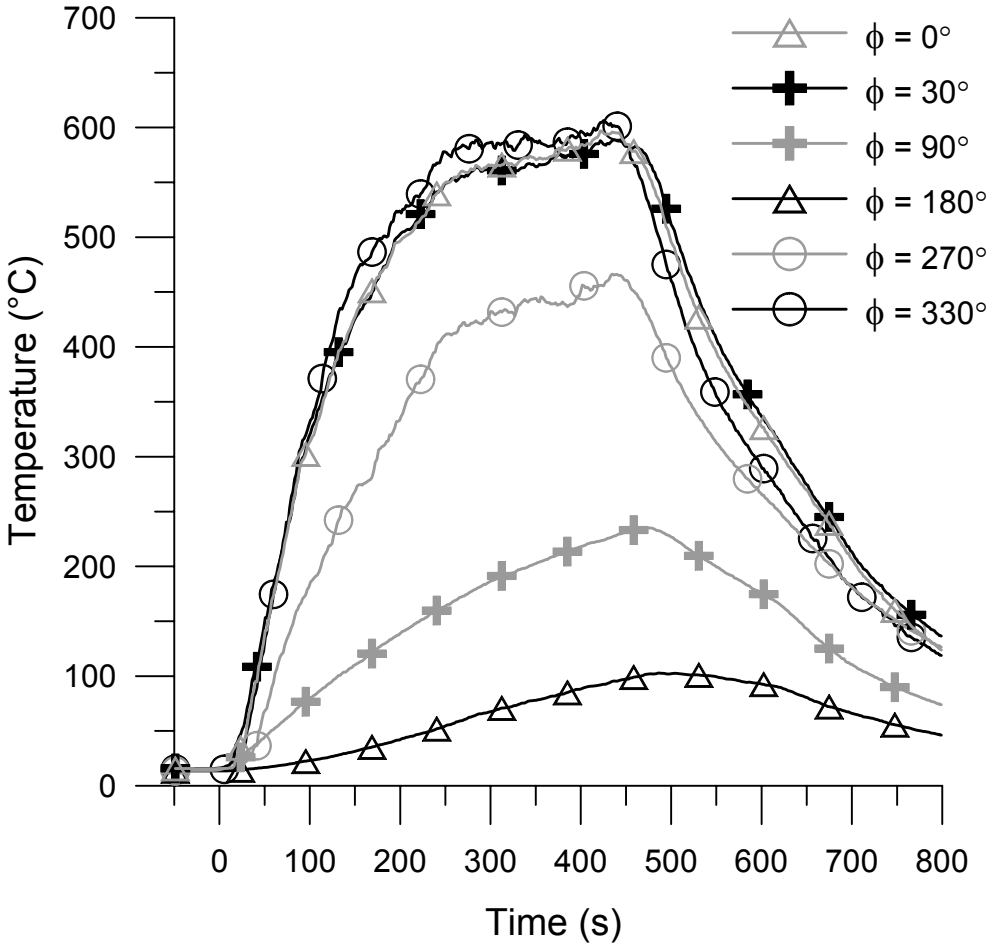

Figure E.1: Time trace of temperatures measured along inside surface of blocking object, 5 m/s wind (test 27), y=0 m

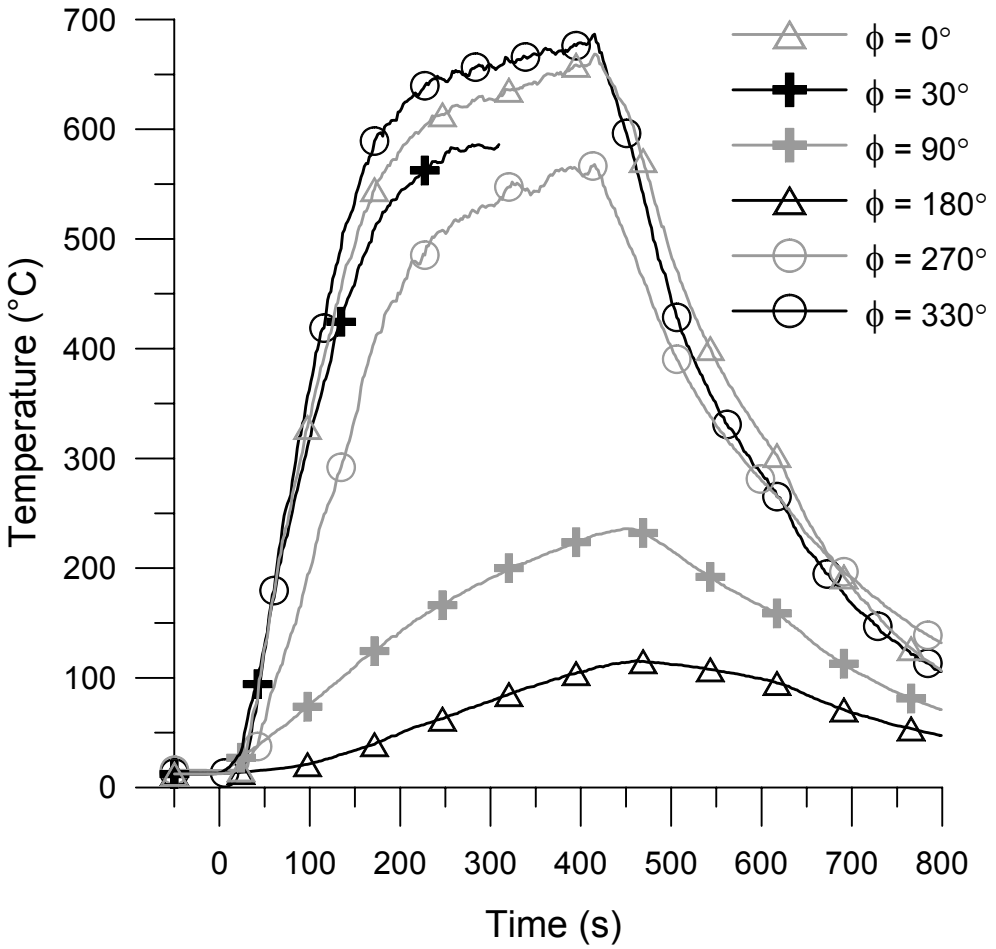

Figure E.2: Time trace of temperatures measured along inside surface of blocking object, 5 m/s wind (test 32), y=0 m (time trace at ϕ=30° cut short due to thermocouple failure)

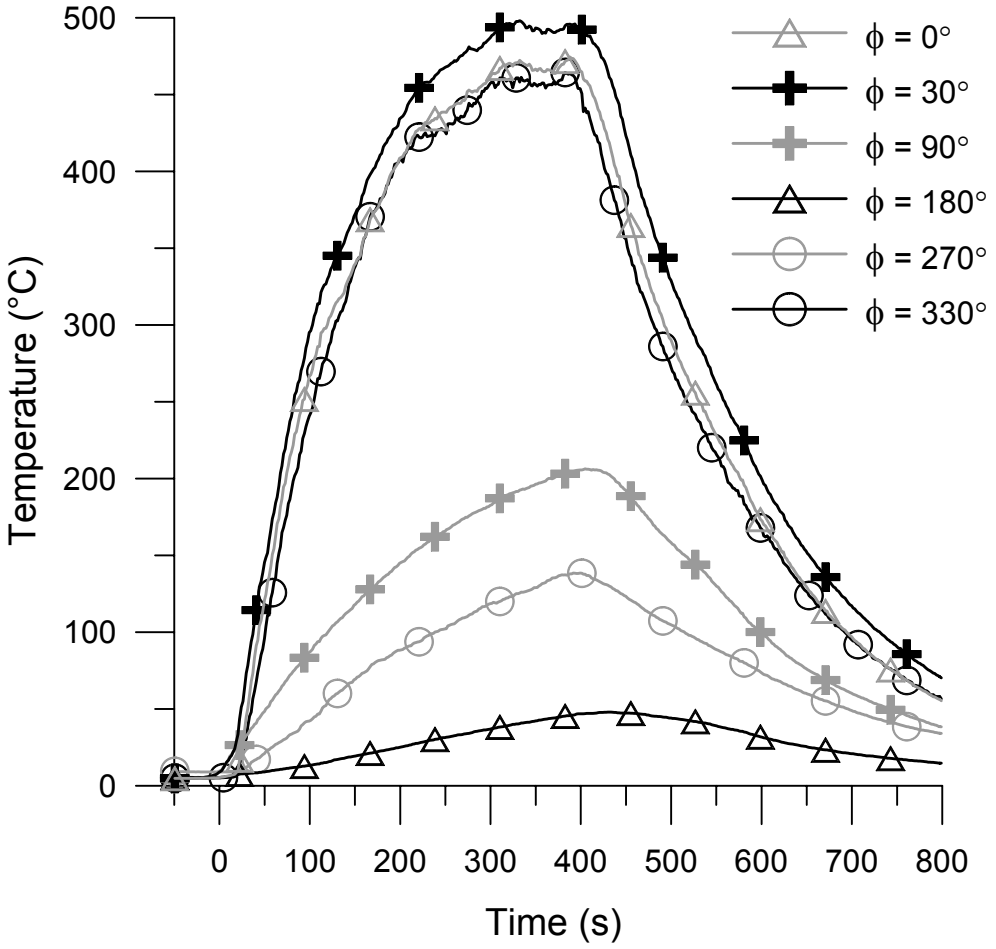

Figure E.3: Time trace of temperatures measured along inside surface of blocking object, 7 m/s wind (test 28), y=0 m

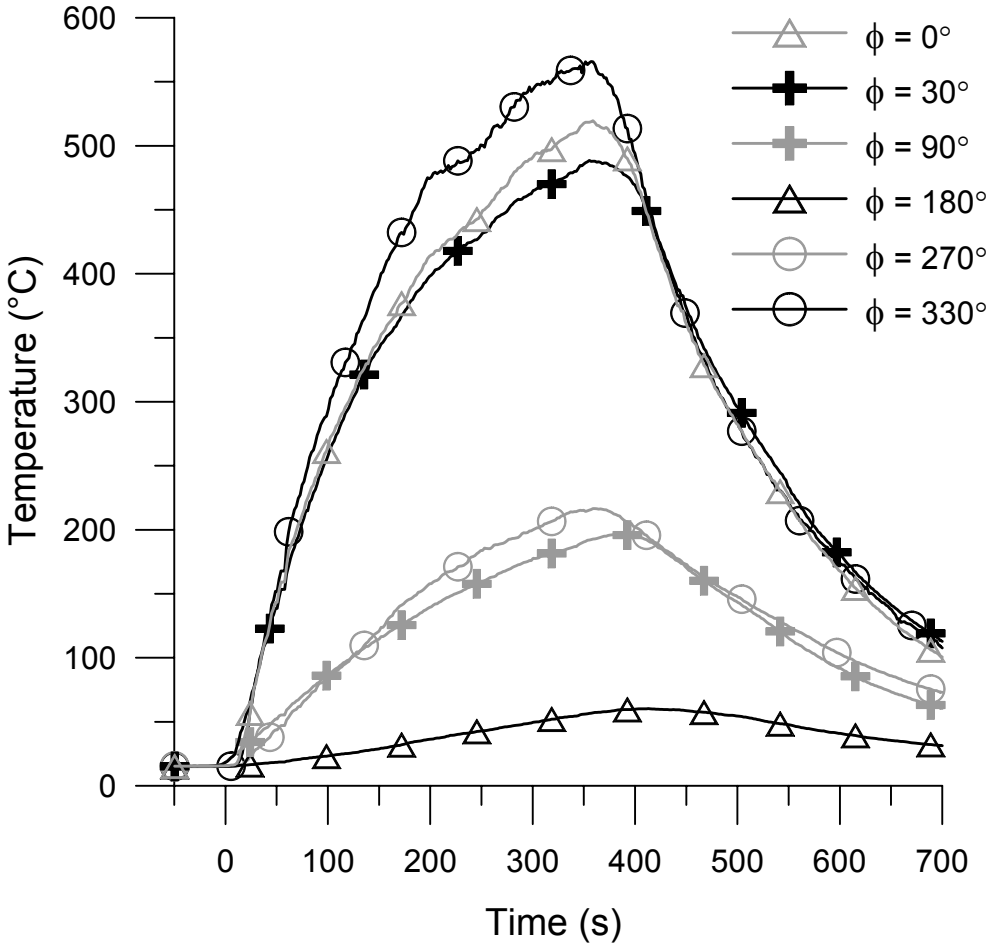

Figure E.4: Time trace of temperatures measured along inside surface of blocking object, 7 m/s wind (test 31), y=0 m

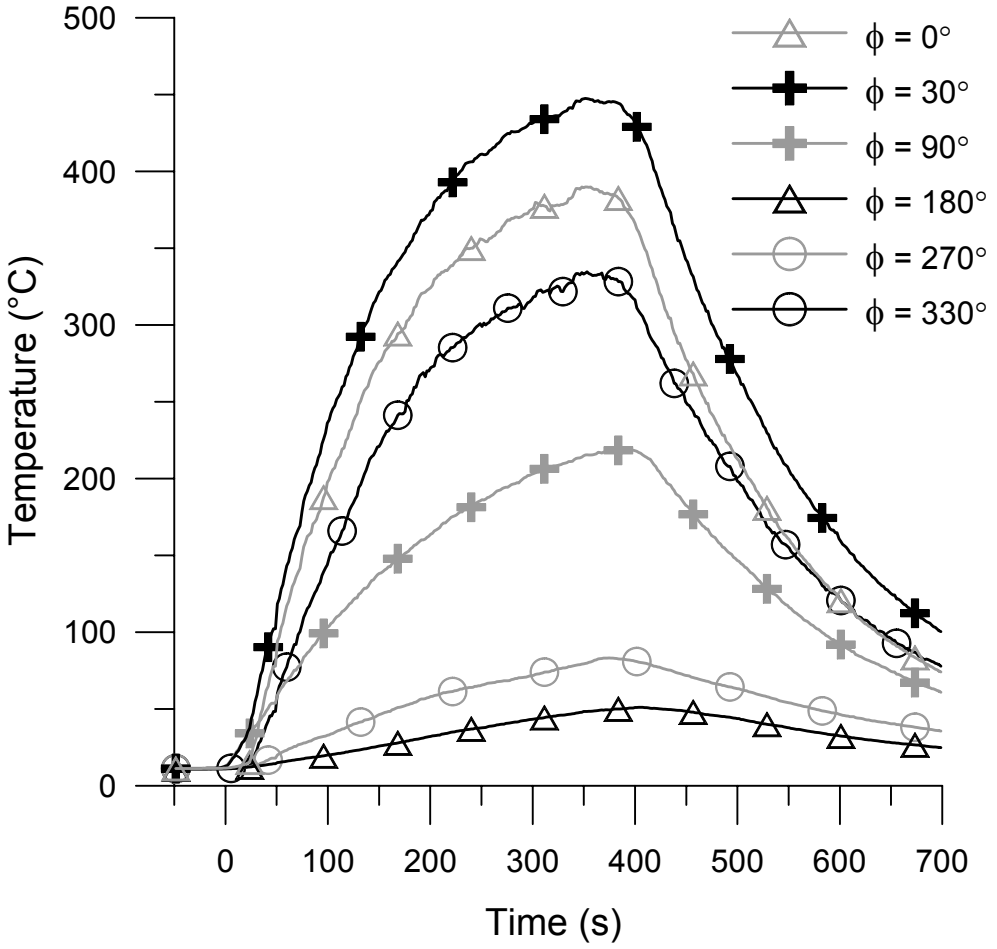

Figure E.5: Time trace of temperatures measured along inside surface of blocking object, 10 m/s wind (test 26), y=0 m

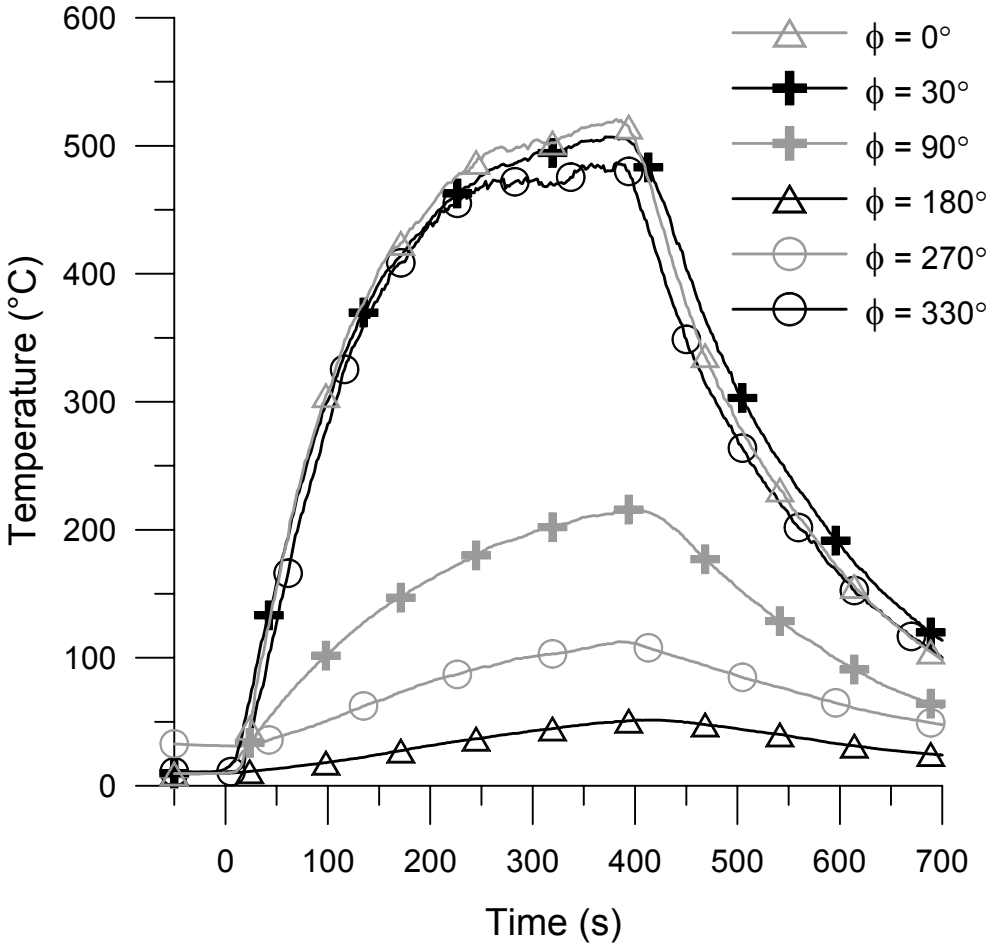

Figure E.6: Time trace of temperatures measured along inside surface of blocking object, 10 m/s wind (test 29), y=0 m

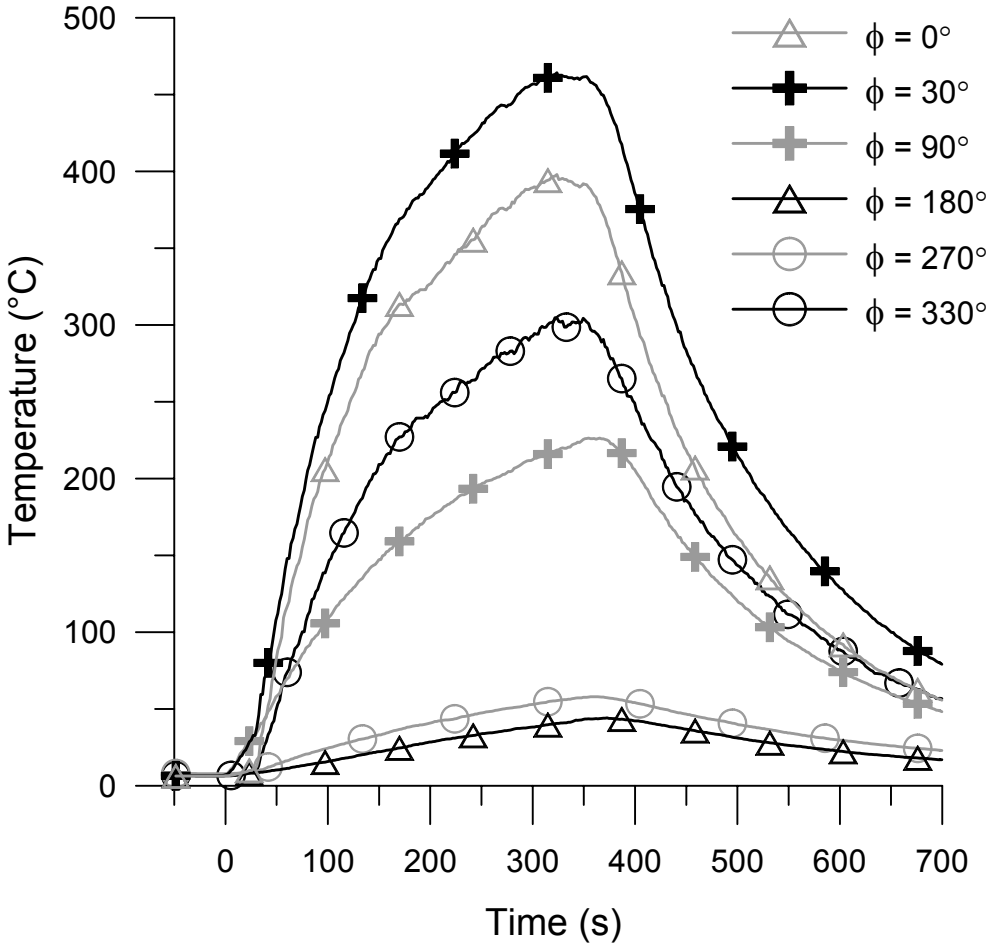

Figure E.7: Time trace of temperatures measured along inside surface of blocking object, 13 m/s wind (test 25), y=0 m

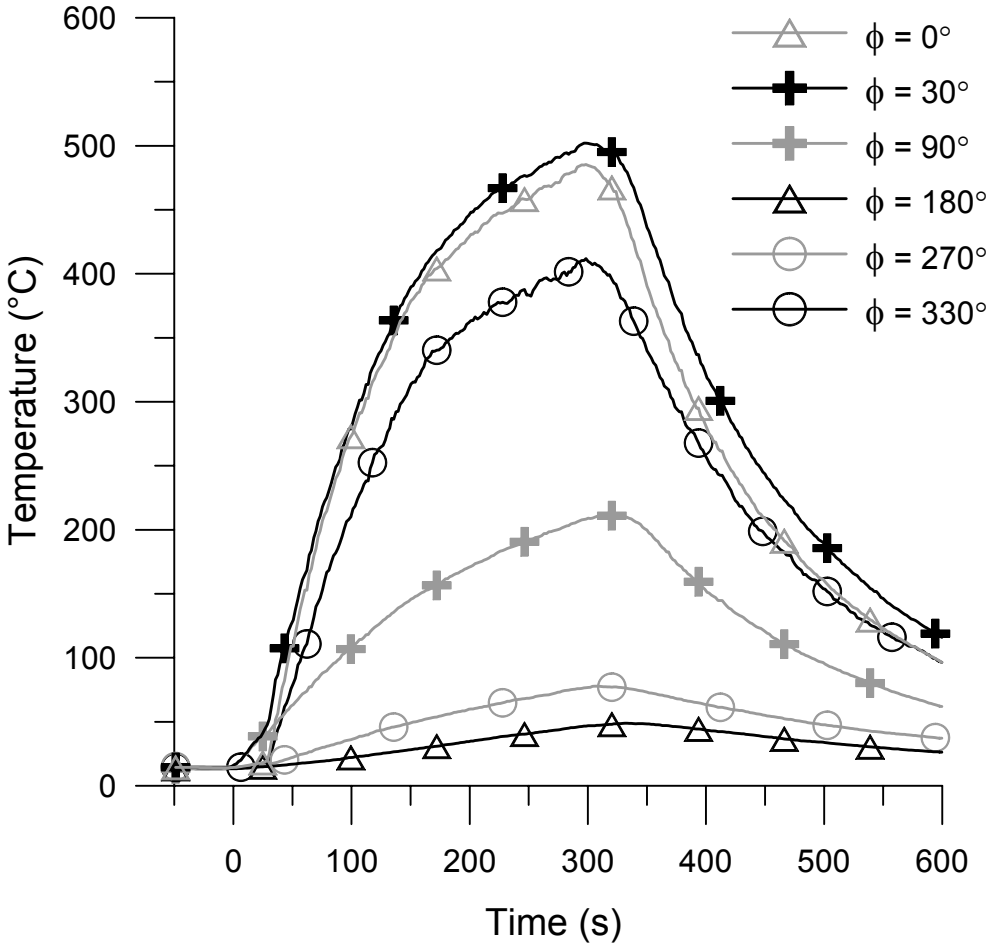

Figure E.8: Time trace of temperatures measured along inside surface of blocking object, 13 m/s wind (test 30), y=0 m

Appendix F

Blocking Object Temperature Profile Data

This Appendix lists the following data for thermocouples used to measure temperature along the inside surface of the blocking object: the y coordinate in metres, the ϕ coordinate in degrees, the initial temperature measured immediately prior to startup of the first fan, and the maximum increase in temperature measured during each test, determined using the method discussed at the beginning of Section 5.3. All temperatures are in degrees Celsius. The values of maximum temperature increase were used to generate the blocking object temperature profiles in Section 5.3. The missing data point in test 32 was due to failure of the thermocouple partway through the test. Additional thermocouples beyond the ones listed here were installed in the blocking object, but were not presented in Section 5.3 because they did not provide additional information about the fire. To facilitate the discussion of results and prevent the plots of object temperature from becoming too crowded, the data from these additional thermocouples were not included in the present work.

		Test 27 (5 m/s)		Test 32 (5 m/s)		Test 28 (7 m/s)		Test 31 (7 m/s)	
		Tmax-Tinit	Tinit	Tmax-Tinit	Tinit	Tmax-Tinit	Tinit	Tmax-Tinit	Tinit
	ϕ (deg.)	(deg. C)	(deg. C)	(deg. C)	(deg. C)	(deg. C)	(deg. C)	(deg. C)	(deg. C)
y = 0 m	0	579.3	16.3	653.4	12.5	467.8	5.7	503.3	16.4
	30	572.4	16.5	--	12.3	489.8	5.9	471.6	16.3
	60	420.4	15.0	427.8	12.3	376.1	5.8	340.9	15.5
	90	213.6	14.0	218.5	12.4	199.1	5.5	177.6	15.2
	120	95.7	13.6	109.5	12.5	66.1	4.9	59.8	15.4
	150	79.1	13.6	93.7	12.9	43.4	6.3	42.2	15.7
	180	81.9	13.7	96.4	13.7	36.1	9.8	41.0	16.1
	210	135.4	13.9	154.4	15.1	50.1	11.9	61.1	16.6
	240	242.4	13.8	308.3	15.8	61.5	11.8	90.0	16.5
	270	451.9	13.7	545.8	16.8	126.8	11.7	200.2	16.4
	300	560.5	14.0	649.5	15.8	289.2	8.3	396.0	16.0
	330	586.5	15.4	663.9	13.9	456.4	6.0	549.4	16.2

		Test 27 (5 m/s)		Test 32 (5 m/s)		Test 28 (7 m/s)		Test 31 (7 m/s)	
		Tmax-Tinit	Tinit	Tmax-Tinit	Tinit	Tmax-Tinit	Tinit	Tmax-Tinit	Tinit
	y (m)	(deg. C)	(deg. C)	(deg. C)	(deg. C)	(deg. C)	(deg. C)	(deg. C)	(deg. C)
ϕ = 0	-2	339.5	14.4	211.5	12.3	122.3	5.2	131.9	15.4
	-1.15	621.0	15.3	546.8	12.2	299.0	5.4	323.0	15.5
	-0.2	678.4	17.6	744.9	12.8	587.9	5.5	607.8	17.0
	0	579.3	16.3	653.4	12.5	467.8	5.7	503.3	16.4
	0.5	474.3	15.3	476.3	12.9	345.7	5.5	329.2	16.5
	1	348.8	15.4	328.4	12.7	298.3	5.8	258.3	16.1
	2	86.5	13.5	83.8	12.3	74.1	4.8	64.1	14.9
ϕ = 90	-2	141.1	13.5	129.6	12.1	128.1	4.8	128.0	15.1
	-1.15	185.4	13.9	179.1	12.1	166.6	5.1	162.5	15.1
	-0.2	242.2	13.8	256.8	12.2	210.3	5.1	201.9	15.2
	0	213.6	14.0	218.5	12.4	199.1	5.5	177.6	15.2
	0.5	203.4	13.7	196.9	12.3	186.2	5.7	162.8	15.1
	1	179.2	14.0	172.8	12.6	182.6	5.7	164.2	15.2
	2	103.3	13.1	101.0	11.9	101.4	4.6	90.5	14.7
ϕ = 180	-2	45.8	13.5	44.4	13.1	15.8	10.8	21.9	15.6
	-1.15	44.3	13.9	44.2	13.2	12.1	10.5	18.0	15.6
	-0.2	71.9	13.7	82.6	13.7	31.0	10.5	34.9	16.0
	0	81.9	13.7	96.4	13.7	36.1	9.8	41.0	16.1
	0.5	69.1	13.9	79.8	13.9	34.4	10.2	35.1	16.2
	1	51.2	13.4	57.6	13.2	27.7	9.3	27.9	15.6
	2	40.7	13.2	43.8	13.3	19.9	10.1	21.9	15.5
ϕ = 270	-2	163.6	13.7	141.6	15.5	49.4	10.0	73.6	16.3
	-1.15	421.9	14.5	442.4	16.7	92.7	10.7	139.4	16.8
	-0.2	470.4	13.6	579.1	16.6	119.1	11.5	192.2	16.4
	0	451.9	13.7	545.8	16.8	126.8	11.7	200.2	16.4
	0.5	251.2	13.7	303.3	16.8	89.9	11.1	140.0	16.5
	1	141.1	13.8	154.8	17.3	60.0	11.9	88.5	16.7
	2	56.1	13.3	55.9	17.2	25.2	11.6	37.3	16.4

		Test 26 (10 m/s)		Test 29 (10 m/s)		Test 25 (13 m/s)		Test 30 (13 m/s)	
		Tmax-Tinit	Tinit	Tmax-Tinit	Tinit	Tmax-Tinit	Tinit	Tmax-Tinit	Tinit
	ϕ (deg.)	(deg. C)	(deg. C)	(deg. C)	(deg. C)	(deg. C)	(deg. C)	(deg. C)	(deg. C)
y = 0 m	0	373.1	11.8	508.8	11.2	385.2	6.2	470.2	15.2
	30	433.5	12.0	493.9	11.9	455.8	6.0	486.8	15.2
	60	391.3	11.3	377.2	10.9	429.3	6.0	383.8	13.7
	90	207.5	10.8	204.8	10.1	220.0	6.1	195.3	13.0
	120	66.4	10.3	64.2	10.0	63.8	5.9	55.8	13.0
	150	41.5	10.5	40.3	12.1	38.4	6.1	35.1	13.4
	180	39.0	10.7	34.1	16.2	37.0	6.5	32.8	13.9
	210	46.7	11.1	33.1	27.6	38.9	7.4	36.9	15.1
	240	49.5	11.2	20.9	44.4	35.9	8.1	36.6	15.6
	270	72.1	11.0	70.2	42.2	48.3	9.3	61.1	15.6
	300	165.5	10.9	243.2	28.2	124.5	8.6	172.9	15.0
	330	319.0	11.3	472.0	13.7	294.6	7.4	396.7	15.2

		Test 26 (10 m/s)		Test 29 (10 m/s)		Test 25 (13 m/s)		Test 30 (13 m/s)	
		Tmax-Tinit	Tinit	Tmax-Tinit	Tinit	Tmax-Tinit	Tinit	Tmax-Tinit	Tinit
	y (m)	(deg. C)	(deg. C)	(deg. C)	(deg. C)	(deg. C)	(deg. C)	(deg. C)	(deg. C)
ϕ = 0	-2	181.5	10.7	136.5	10.5	159.8	5.8	171.3	13.3
	-1.15	325.3	11.3	291.5	10.8	290.6	5.8	308.9	13.5
	-0.2	540.2	12.3	588.9	11.6	534.5	6.4	593.7	16.1
	0	373.1	11.8	508.8	11.2	385.2	6.2	470.2	15.2
	0.5	204.3	11.2	386.6	11.6	217.0	6.4	339.0	15.4
	1	217.5	11.6	340.4	11.4	240.7	6.5	289.4	15.0
	2	52.9	10.0	85.7	10.7	58.3	5.8	73.9	12.9
ϕ = 90	-2	162.9	10.4	145.4	9.0	170.9	5.7	153.5	12.7
	-1.15	202.2	10.7	190.4	9.3	217.3	5.8	199.4	12.8
	-0.2	229.9	10.5	223.5	9.8	243.2	5.8	223.7	13.0
	0	207.5	10.8	204.8	10.1	220.0	6.1	195.3	13.0
	0.5	191.1	10.7	190.0	10.5	201.8	5.9	178.6	12.9
	1	194.3	10.8	196.3	10.3	210.2	6.3	192.8	13.0
	2	102.6	9.9	103.4	9.2	105.0	5.5	97.3	12.4
ϕ = 180	-2	25.6	10.6	14.6	17.0	21.9	6.0	19.4	13.4
	-1.15	19.0	10.8	10.4	16.5	17.6	6.4	14.9	13.3
	-0.2	35.0	10.8	31.1	17.0	35.2	6.5	30.7	13.7
	0	39.0	10.7	34.1	16.2	37.0	6.5	32.8	13.9
	0.5	34.9	11.0	32.0	16.3	31.8	6.8	29.3	14.2
	1	29.3	10.4	25.5	15.4	28.1	6.0	24.4	13.5
	2	23.9	10.3	18.2	16.7	22.7	6.0	19.7	13.4
ϕ = 270	-2	59.5	11.0	23.2	40.9	38.1	7.7	46.2	15.4
	-1.15	78.2	11.4	47.4	42.0	48.1	9.2	60.8	16.1
	-0.2	66.8	11.0	63.8	41.3	44.5	9.1	55.3	15.5
	0	72.1	11.0	70.2	42.2	48.3	9.3	61.1	15.6
	0.5	54.6	10.8	54.0	40.3	38.6	9.1	46.8	15.9
	1	44.5	11.2	35.5	42.3	31.5	9.5	37.2	16.1
	2	28.5	10.8	7.6	42.4	21.1	9.4	24.7	15.9

Appendix G

Transient Heat Flux Data from Blocking Object

This Appendix shows time traces of incident total heat flux and temperature from the DFT and HFGs distributed around the circumference of the blocking object, close to the midplane y=0 m (Section 5.1.3). Although the data corresponding to the 5 m/s and 13 m/s wind conditions (tests 32 and 30) were previously shown in Figures 5.65 and 5.66, they are included here for completeness.

Several general trends can be seen from the plots. In the tests at the lower (5 m/s and 7 m/s) wind speeds, the levels of total heat flux measured by the DFT increased to quasi-steady values, but in the tests at the higher (10 m/s and 13 m/s) wind speeds, they instead decreased gradually to quasi-steady values. As mentioned at the beginning of Section 5.4.1, this was expected to be a result of differences in the levels of radiative heating by the fire versus convective cooling by the wind.

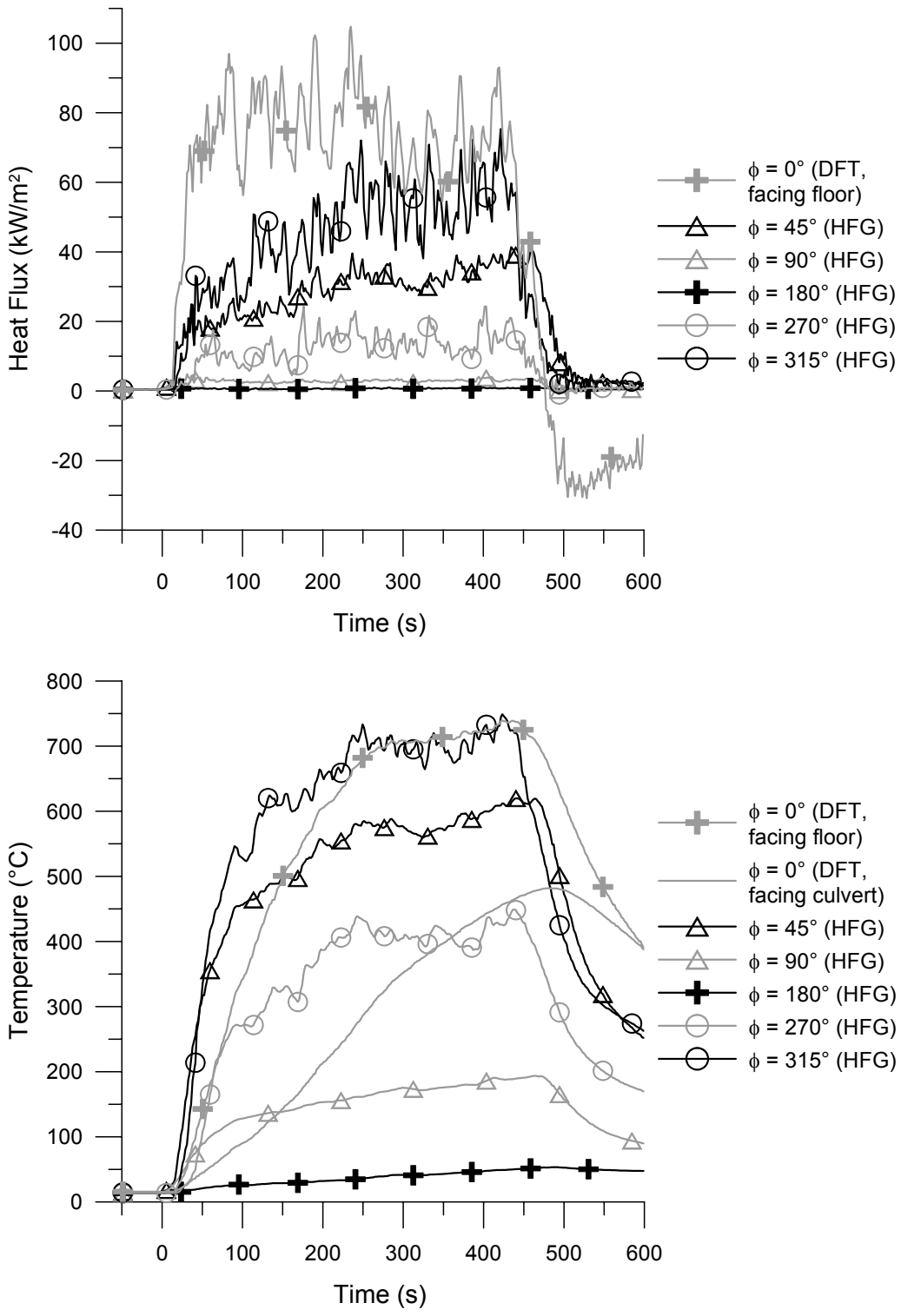

Figure G.1: Time trace of incident total heat flux to the blocking object and corresponding temperatures measured by the heat flux gauges, 5 m/s wind (test 27), y≈0 m

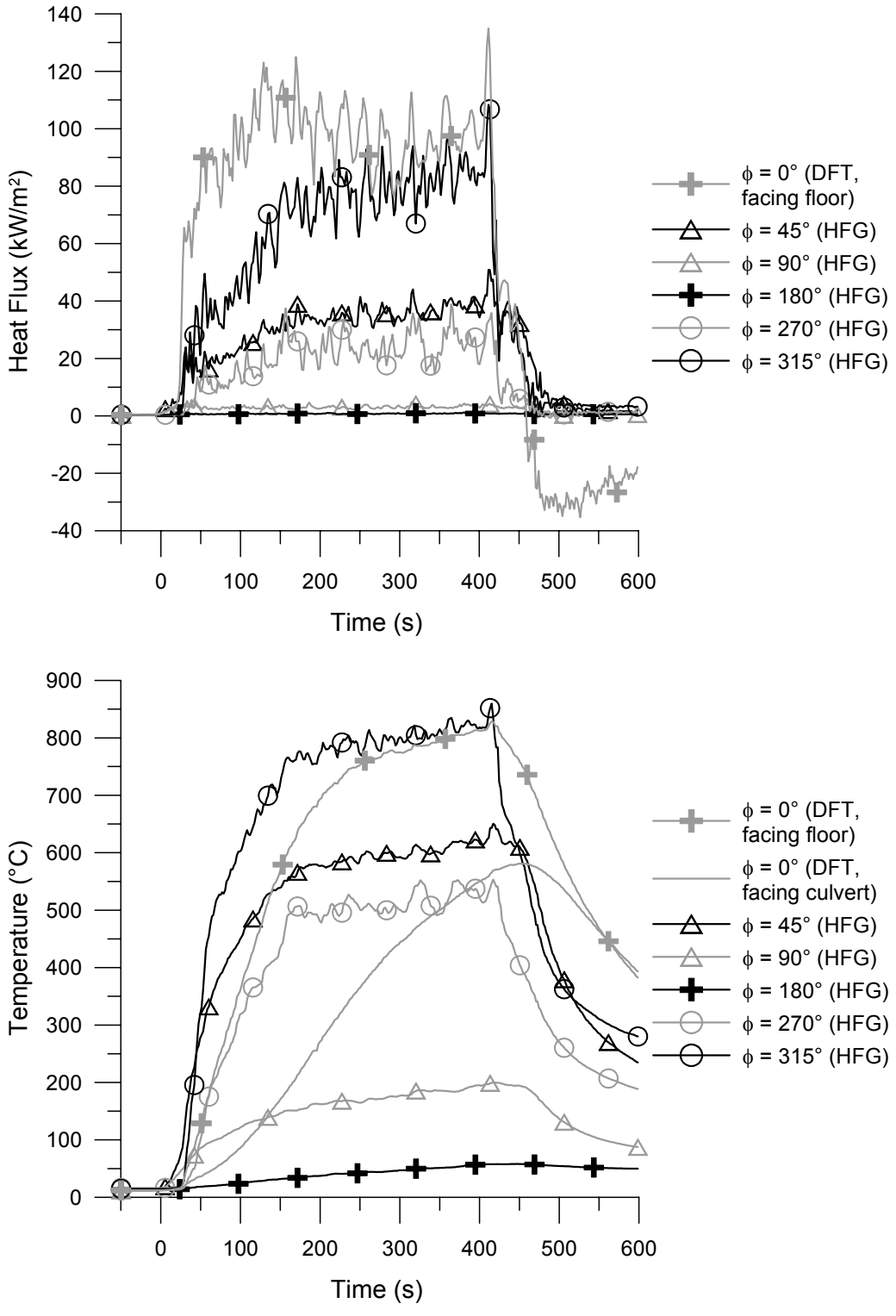

Figure G.2: Time trace of incident total heat flux to the blocking object and corresponding temperatures measured by the heat flux gauges, 5 m/s wind (test 32), y≈0 m

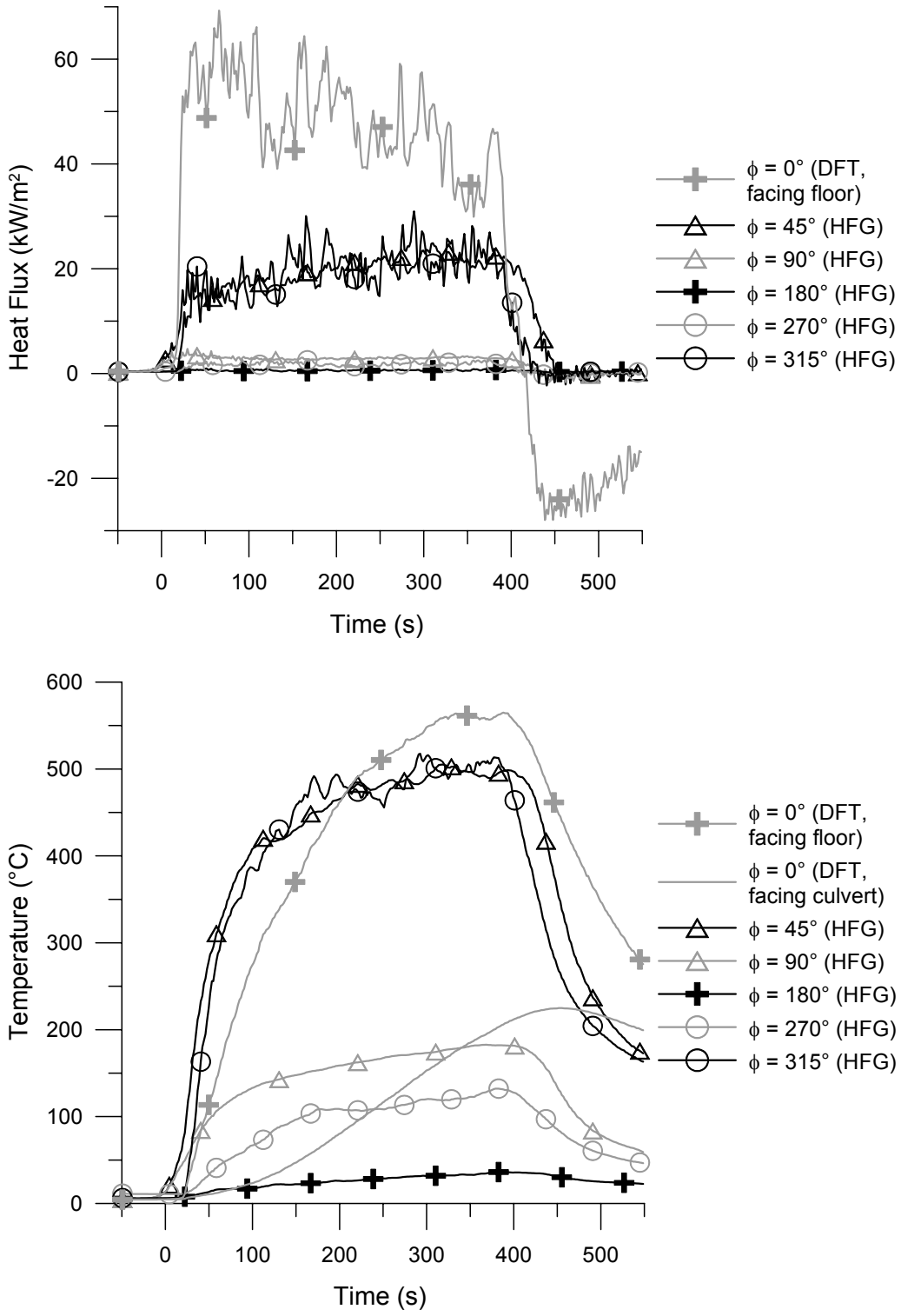

Figure G.3: Time trace of incident total heat flux to the blocking object and corresponding temperatures measured by the heat flux gauges, 7 m/s wind (test 28), y≈0 m

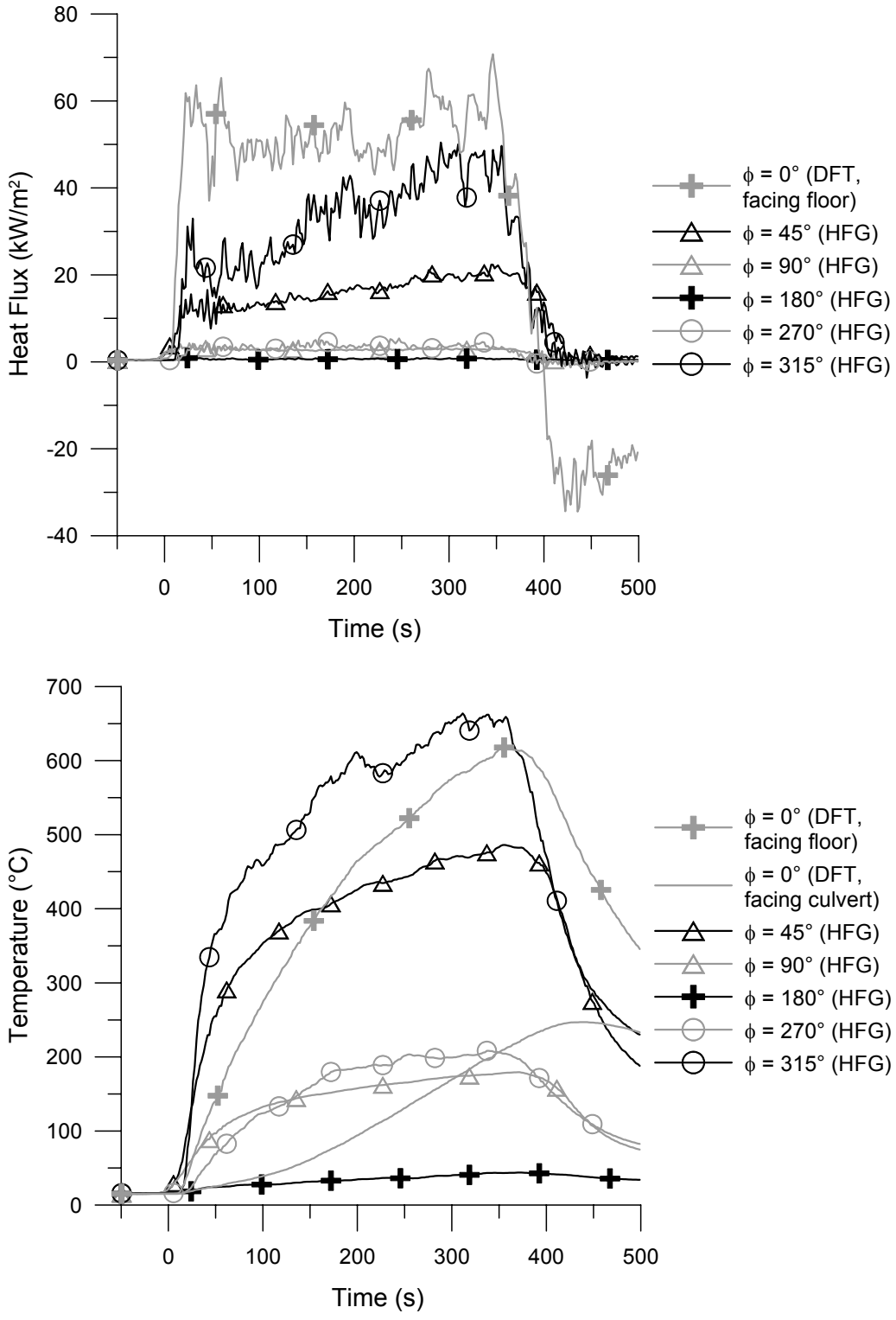

Figure G.4: Time trace of incident total heat flux to the blocking object and corresponding temperatures measured by the heat flux gauges, 7 m/s wind (test 31), y≈0 m

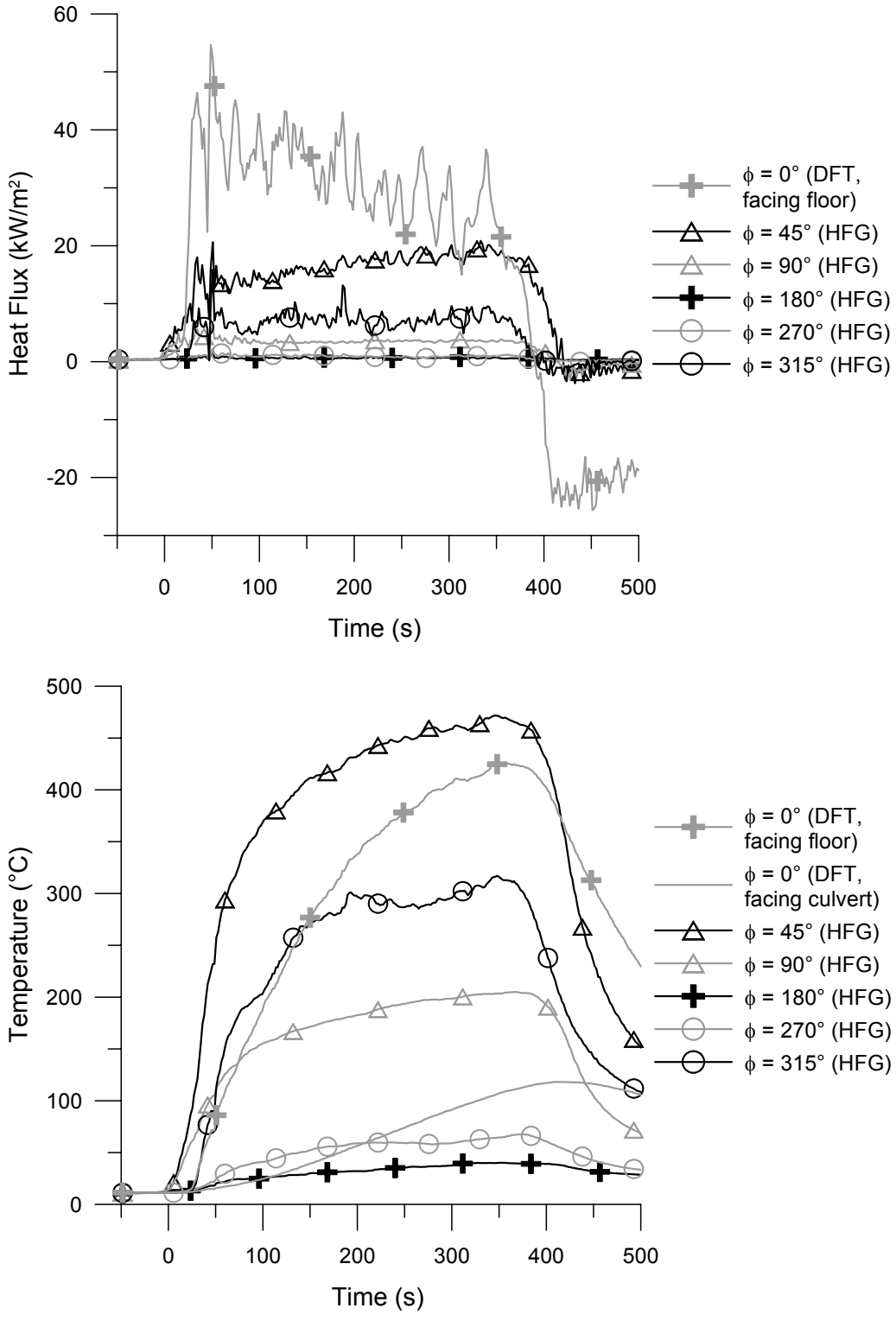

Figure G.5: Time trace of incident total heat flux to the blocking object and corresponding temperatures measured by the heat flux gauges, 10 m/s wind (test 26), y≈0 m

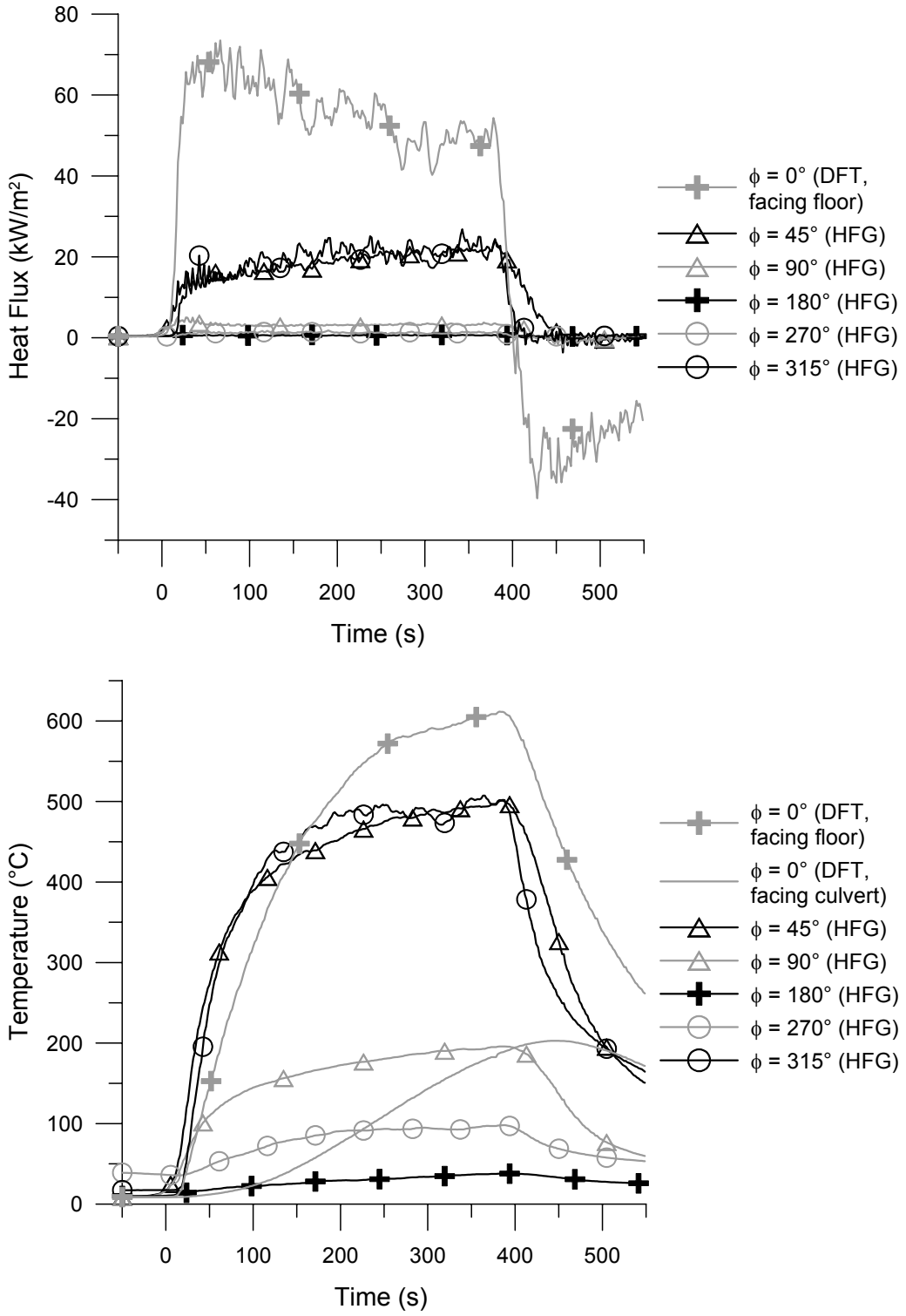

Figure G.6: Time trace of incident total heat flux to the blocking object and corresponding temperatures measured by the heat flux gauges, 10 m/s wind (test 29), y≈0 m

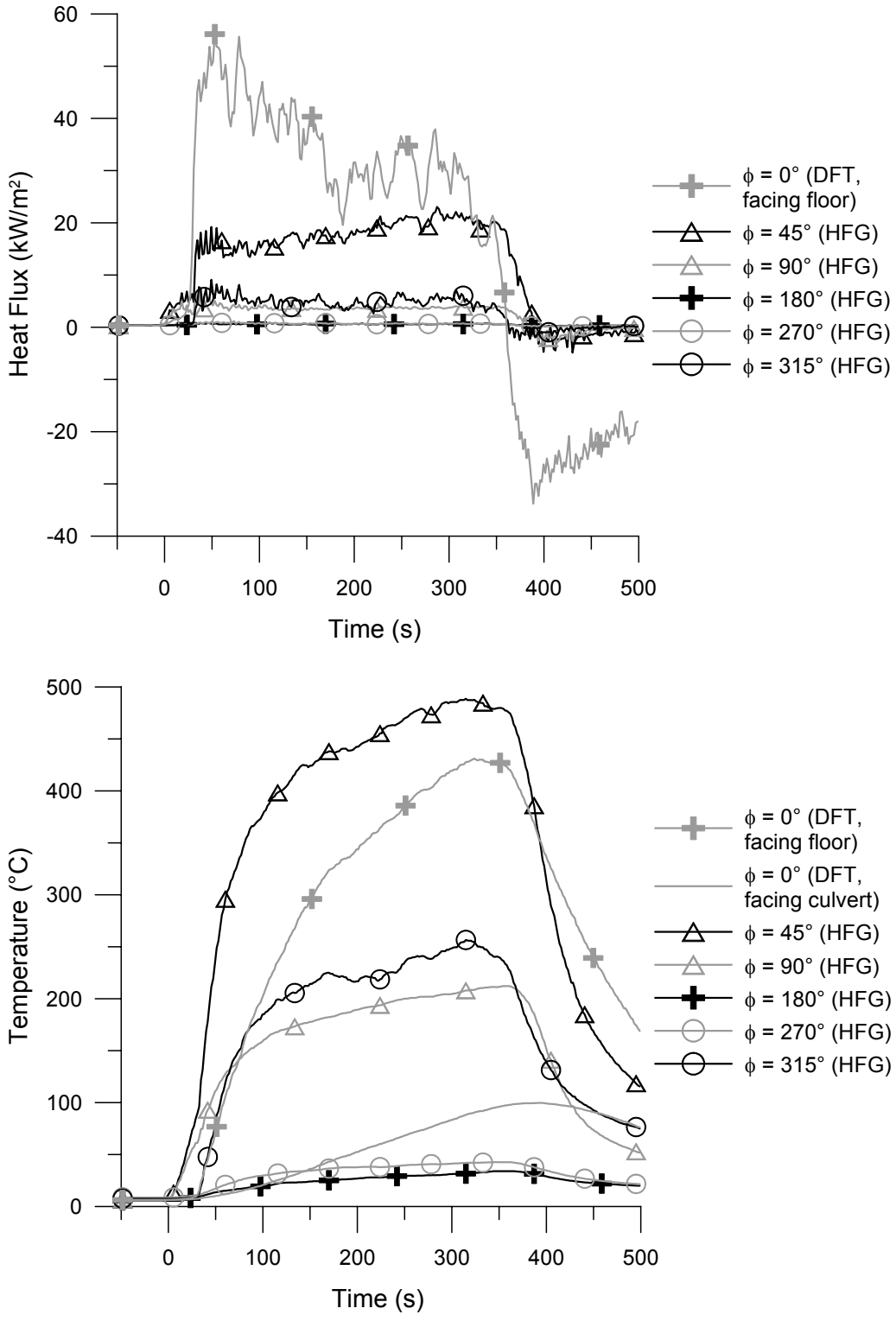

Figure G.7: Time trace of incident total heat flux to the blocking object and corresponding temperatures measured by the heat flux gauges, 13 m/s wind (test 25), y≈0 m

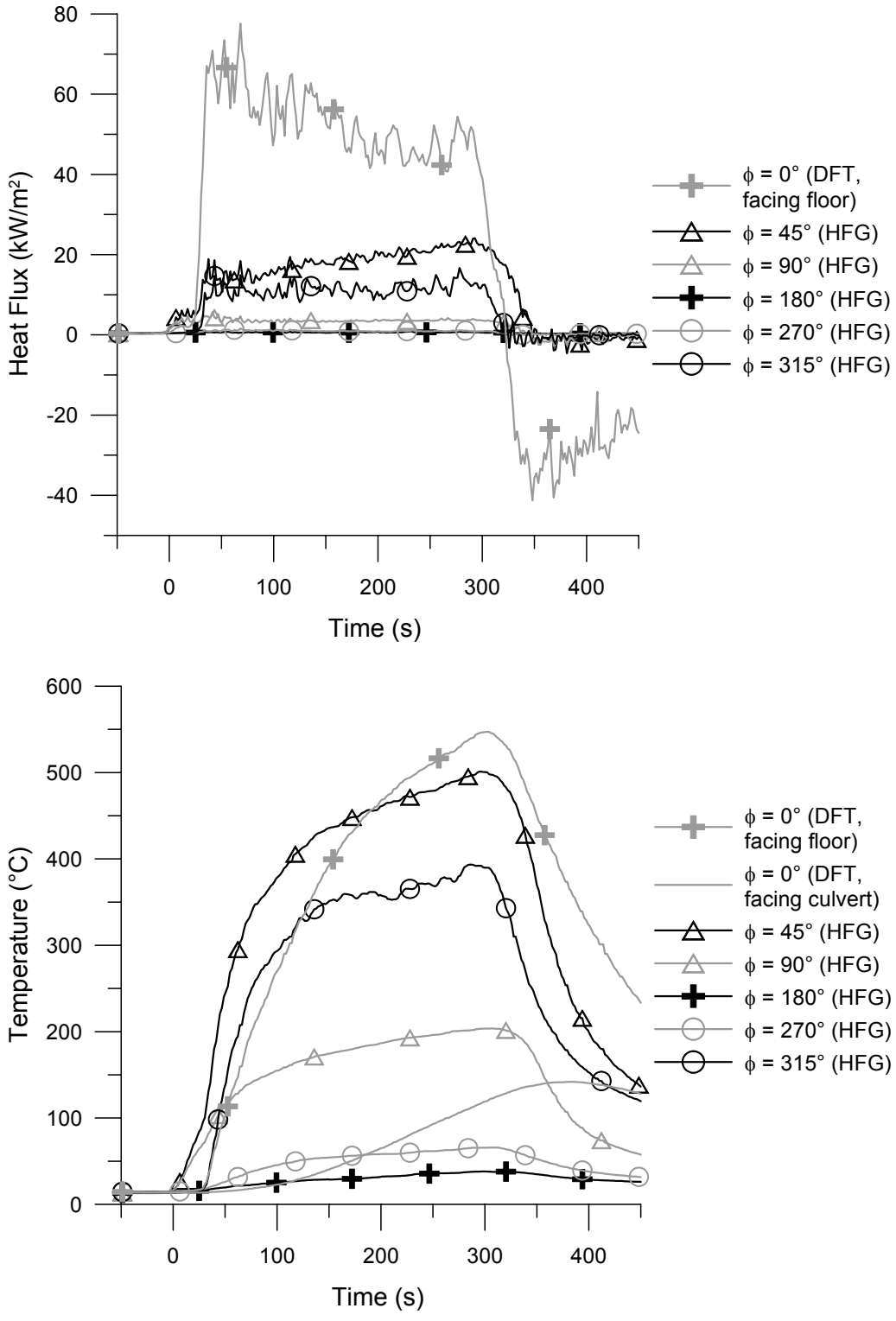

Figure G.8: Time trace of incident total heat flux to the blocking object and corresponding temperatures measured by the heat flux gauges, 13 m/s wind (test 30), y≈0 m

Appendix H

Transient Data for Heat Flux to Ground Downwind of Blocking Object

This Appendix contains time traces of data obtained from the DFT, HFG and Gardon gauge located along the floor downwind of the blocking object in the experiments of Chapter 5. Time traces of incident total heat flux are shown, together with corresponding time traces of temperature from the DFT and HFG. Also included are data measured by a thermocouple placed near the DFT and HFG (Section 5.4.2). The data corresponding to the 7 m/s wind condition (test 28) were previously shown in Figures 5.67 and 5.68, and are included here for completeness. The overall shapes of the curves in each plot are similar to those described for Figures 5.67 and 5.68.

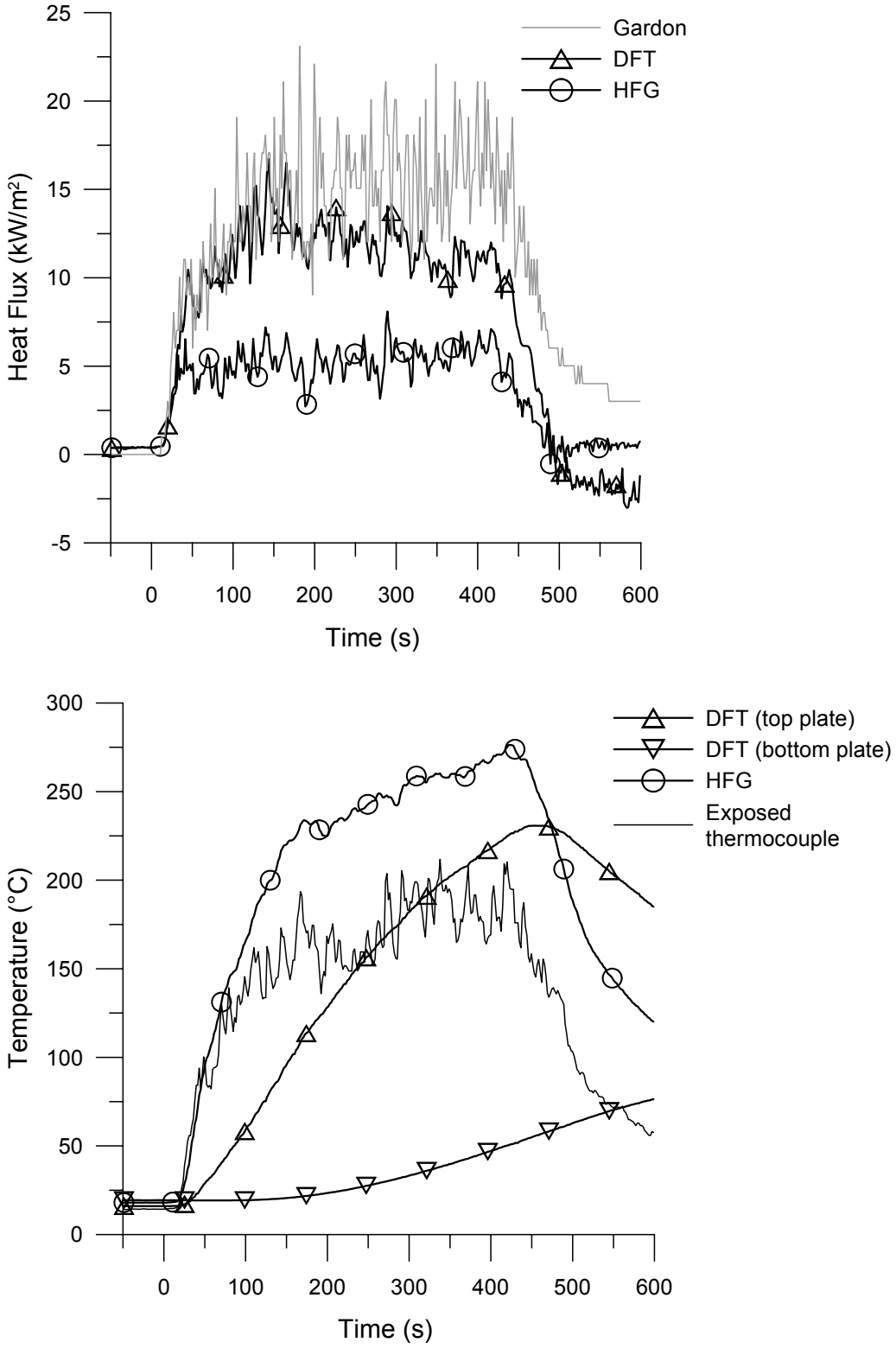

Figure H.1: Time trace of incident total heat flux to the ground and corresponding temperatures, 5 m/s wind (test 27), x=5.3 m to 5.6 m, y=-0.5 m to -0.3 m

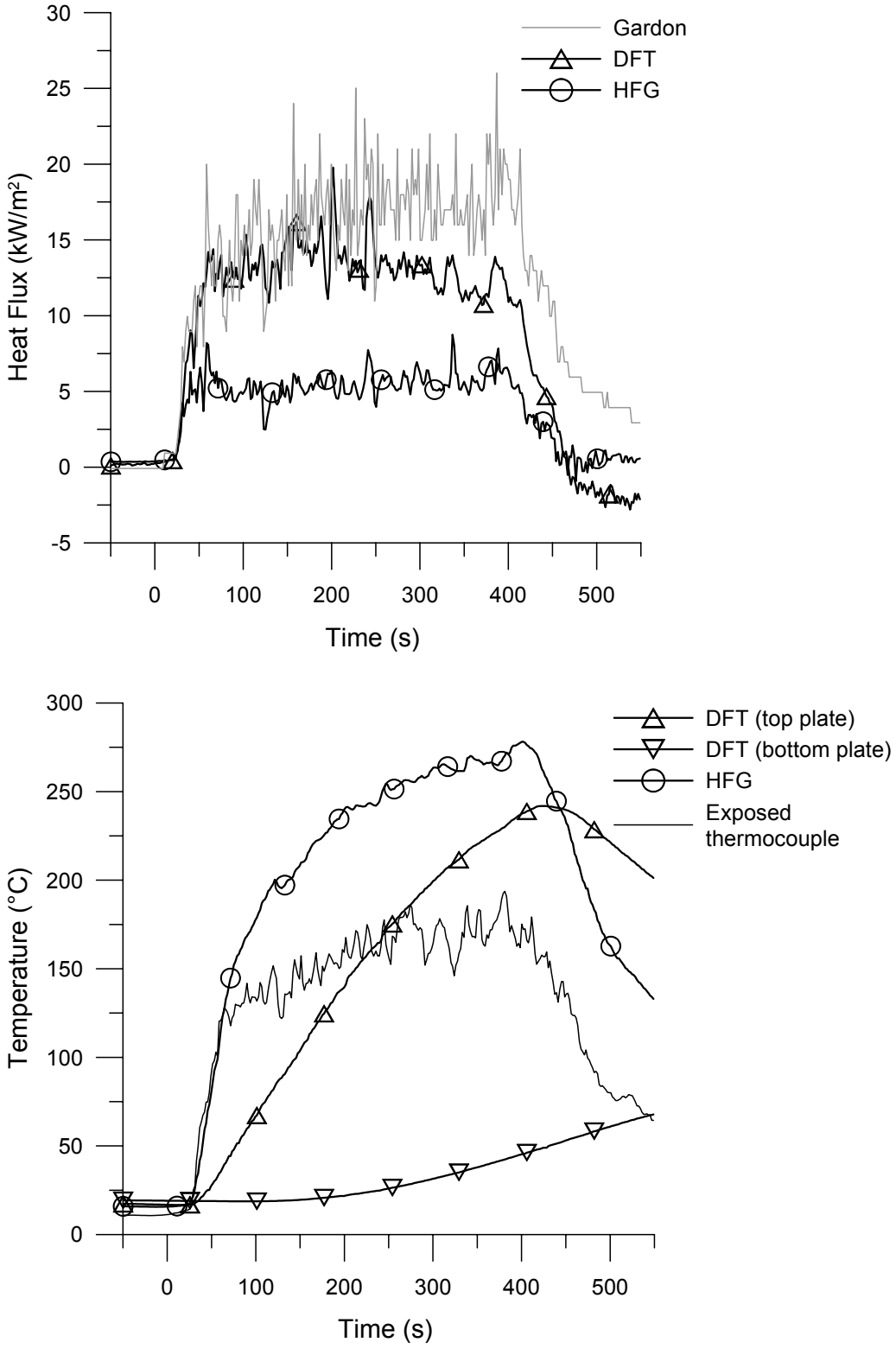

Figure H.2: Time trace of incident total heat flux to the ground and corresponding temperatures, 5 m/s wind (test 32), x=5.3 m to 5.6 m, y=-0.5 m to -0.3 m

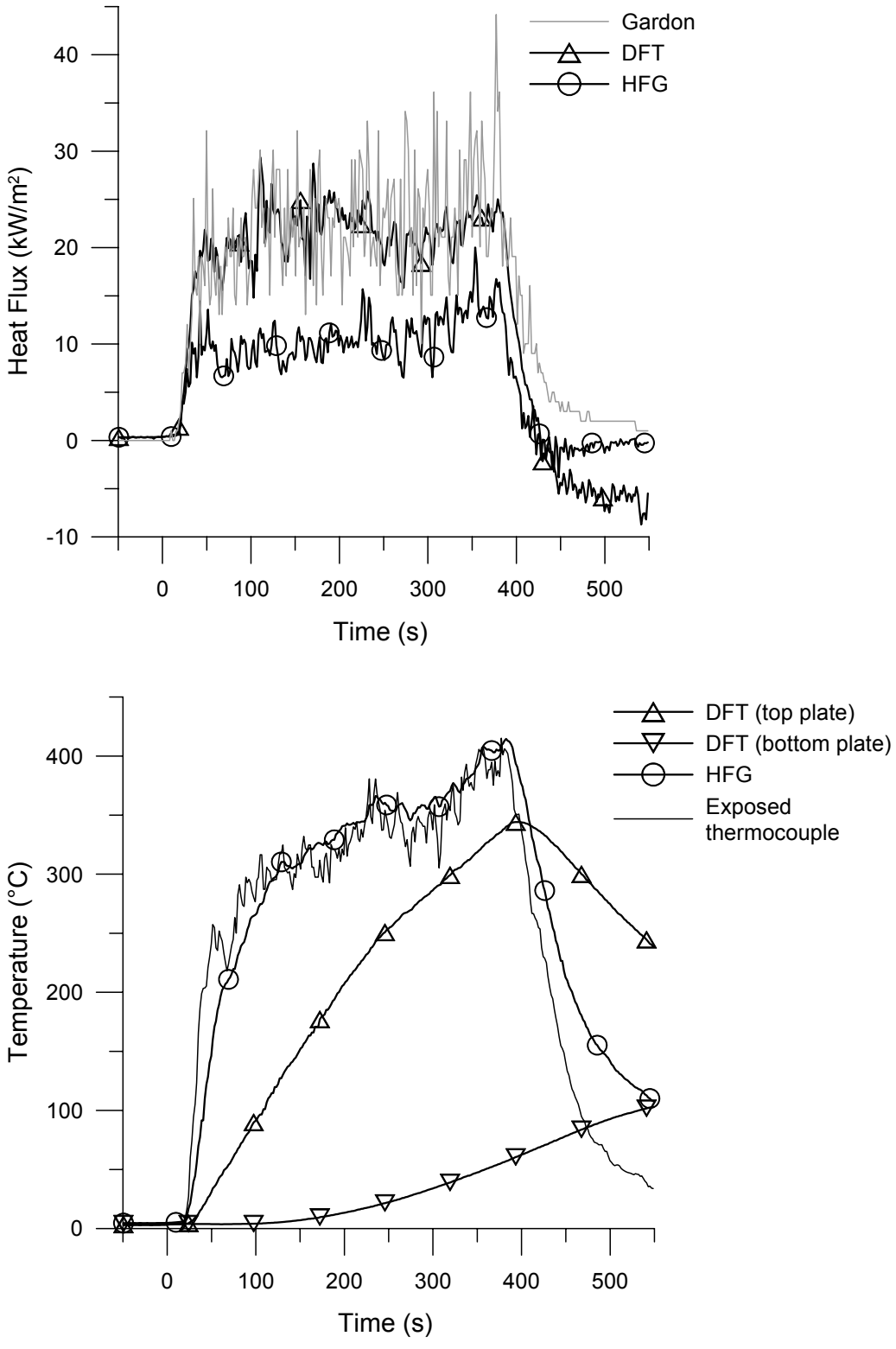

Figure H.3: Time trace of incident total heat flux to the ground and corresponding temperatures, 7 m/s wind (test 28), x=5.3 m to 5.6 m, y=-0.5 m to -0.3 m

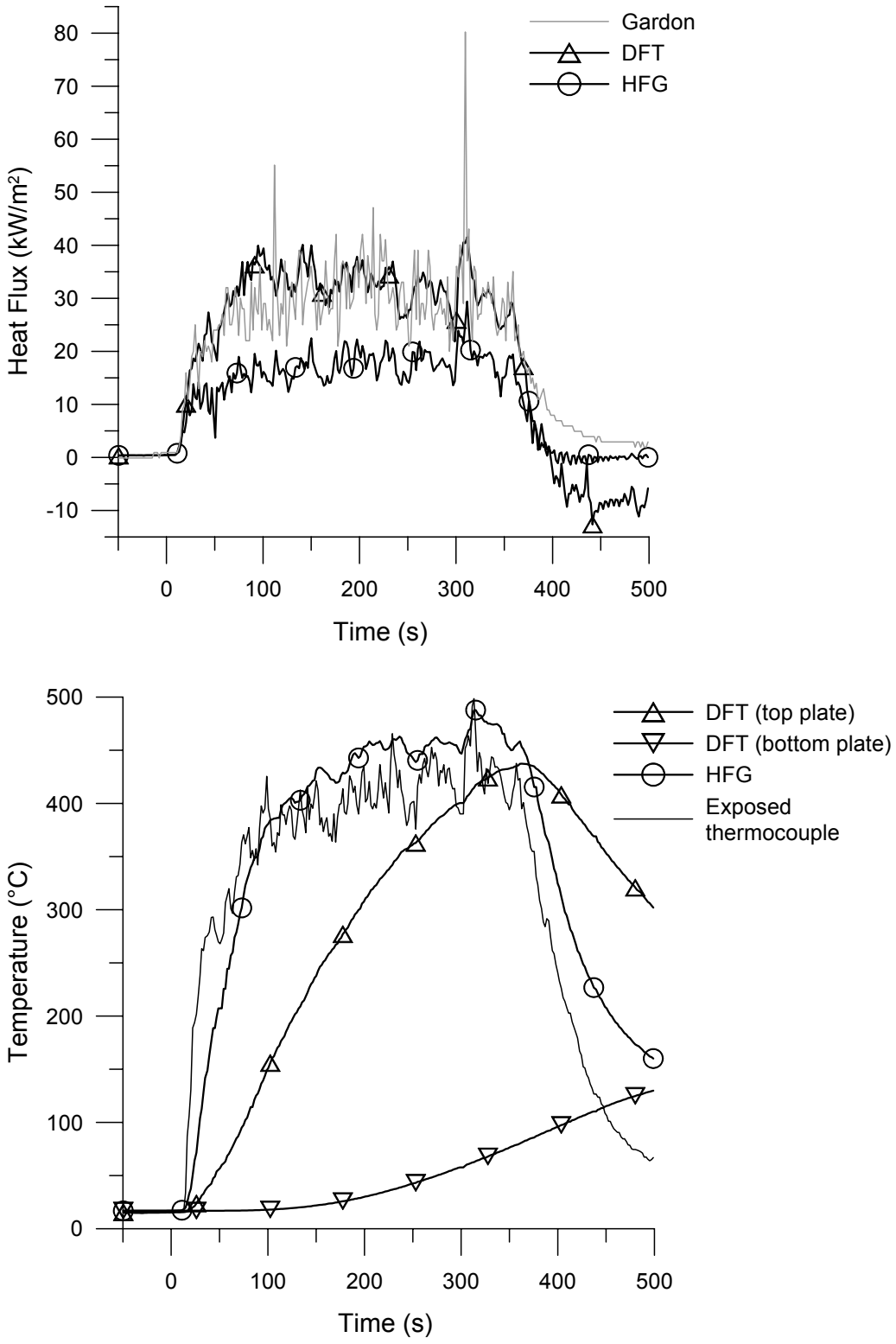

Figure H.4: Time trace of incident total heat flux to the ground and corresponding temperatures, 7 m/s wind (test 31), x=5.3 m to 5.6 m, y=-0.5 m to -0.3 m

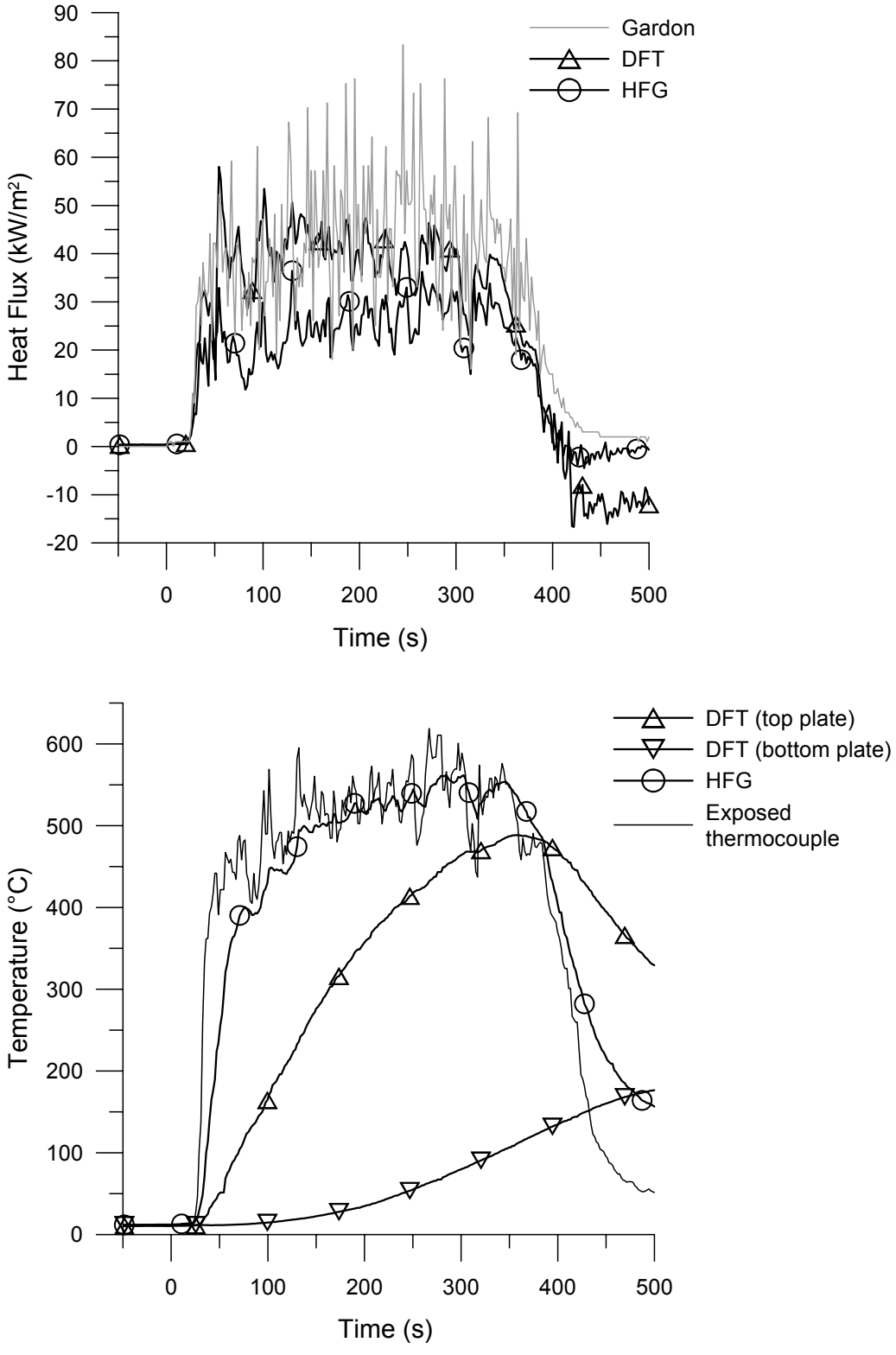

Figure H.5: Time trace of incident total heat flux to the ground and corresponding temperatures, 10 m/s wind (test 26), x=5.3 m to 5.6 m, y=-0.5 m to -0.3 m

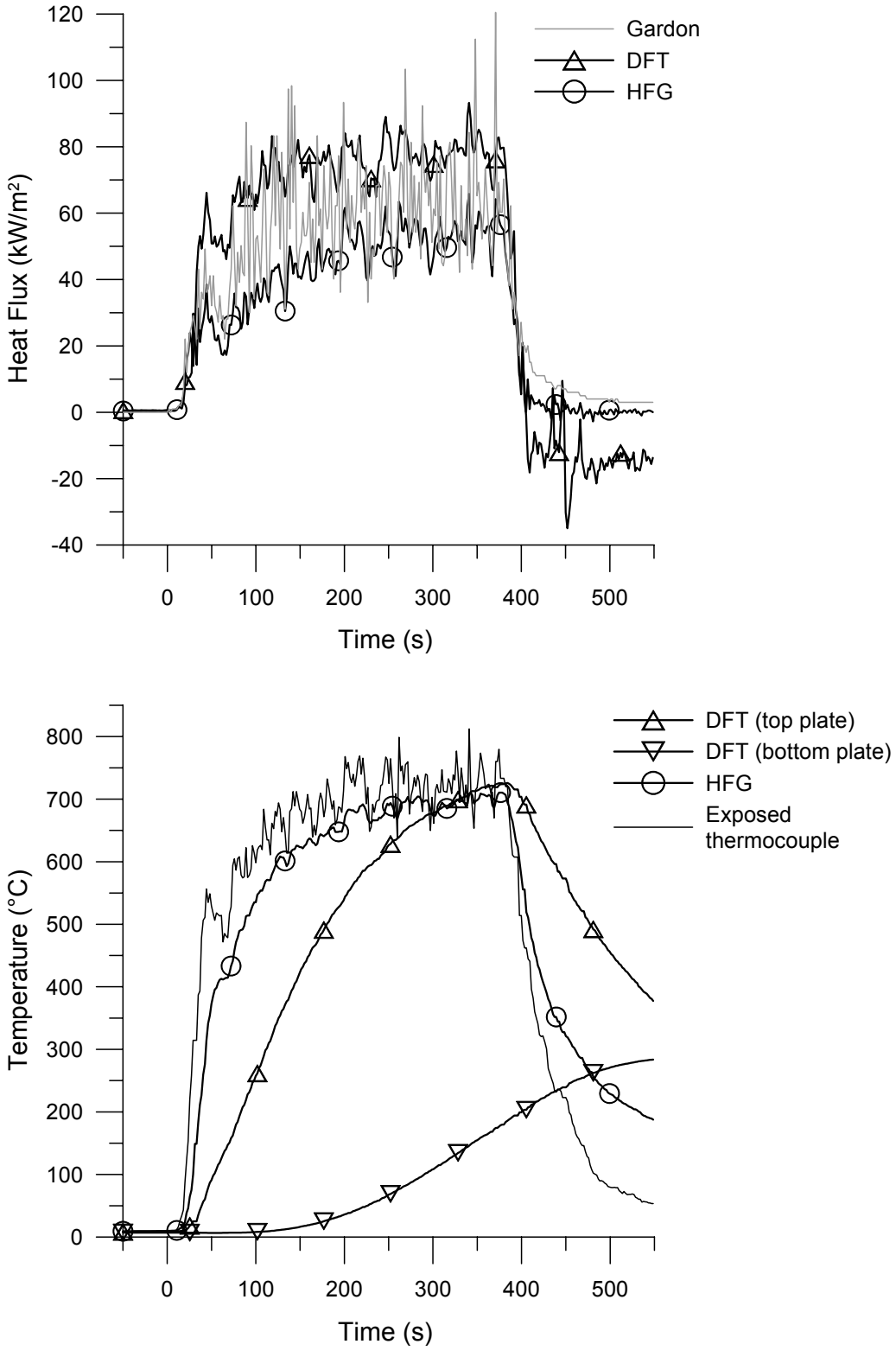

Figure H.6: Time trace of incident total heat flux to the ground and corresponding temperatures, 10 m/s wind (test 29), x=5.3 m to 5.6 m, y=-0.5 m to -0.3 m

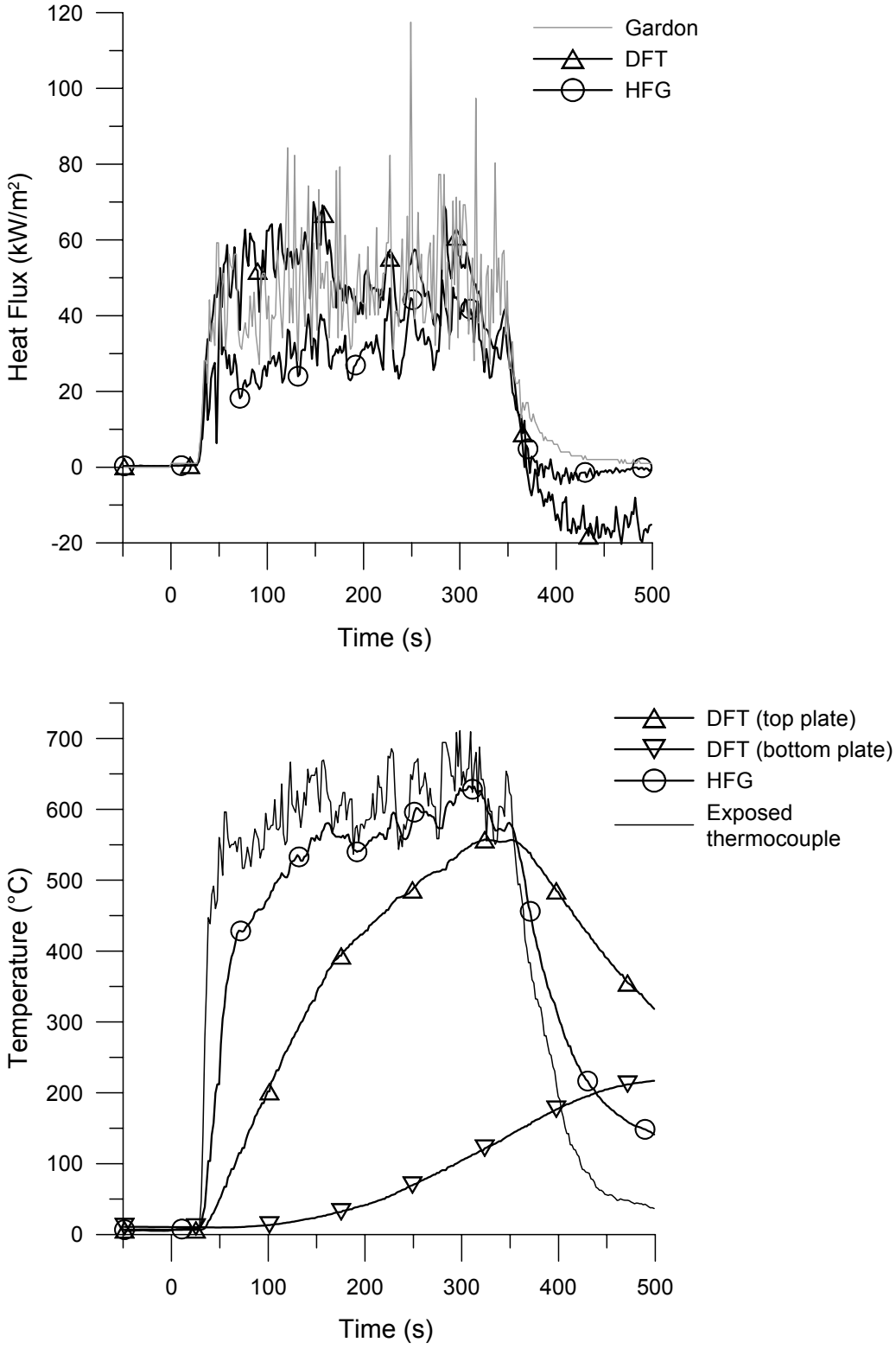

Figure H.7: Time trace of incident total heat flux to the ground and corresponding temperatures, 13 m/s wind (test 25), x=5.3 m to 5.6 m, y=-0.5 m to -0.3 m

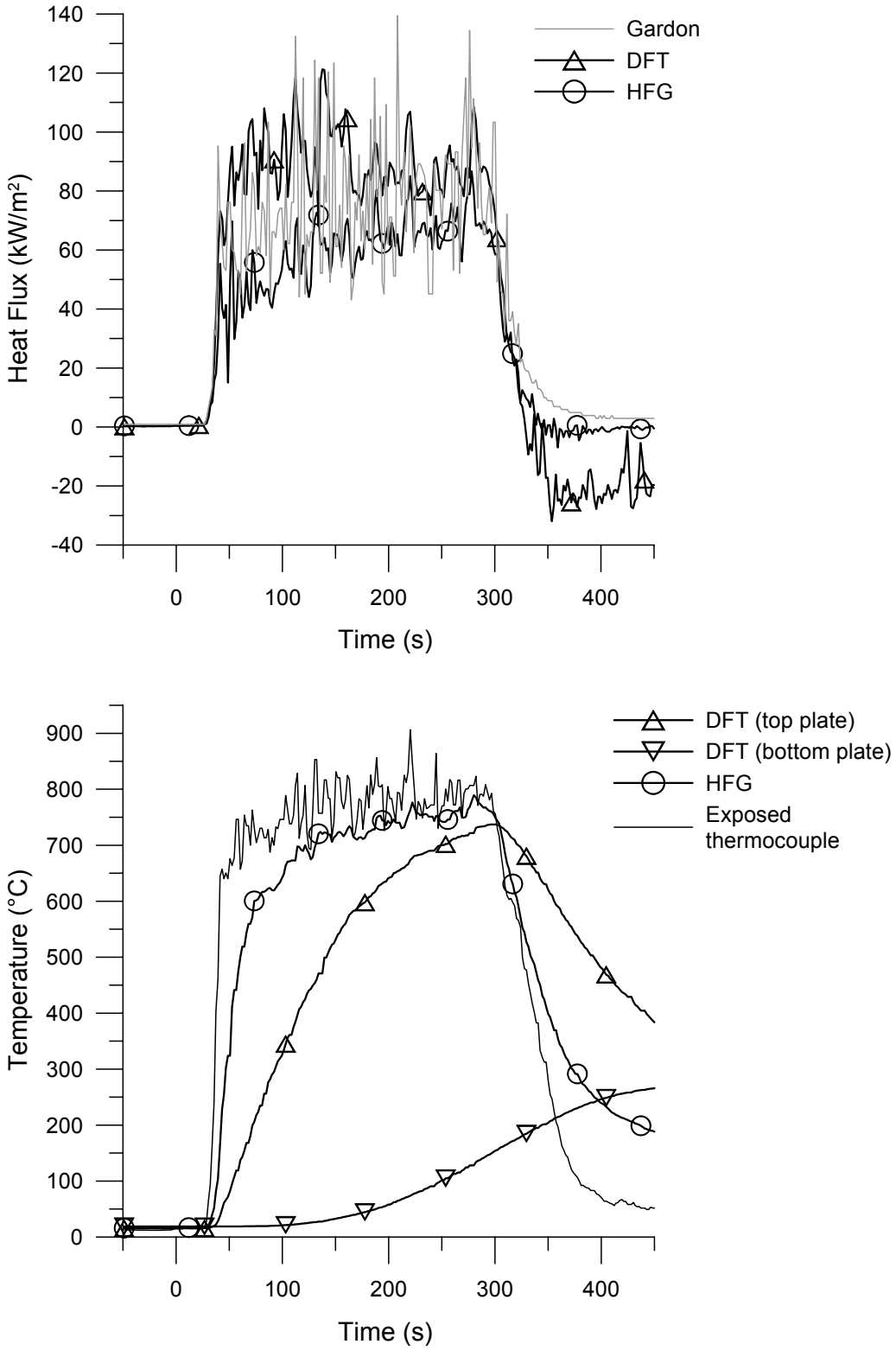

Figure H.8: Time trace of incident total heat flux to the ground and corresponding temperatures, 13 m/s wind (test 30), x=5.3 m to 5.6 m, y=-0.5 m to -0.3 m

Appendix I

Transient Heat Flux Data from Cylindrical Calorimeters

This Appendix contains time traces of data obtained from the calorimeters at locations 'A' and 'D', and from their neighbouring DFTs at locations 'A', 'B', 'C' and 'D' (Figure 5.12). Time traces of incident total heat flux and net absorbed heat flux are shown, together with time traces of temperature from each sensor. The data corresponding to calorimeter 'D' and its neighbouring DFTs in the 7 m/s wind condition (test 28) were previously shown in Figures 5.69 to 5.71, and are included here for completeness. In general, trends similar to those described for Figures 5.69 to 5.71 in Section 5.4.3 can be seen at all wind speeds.

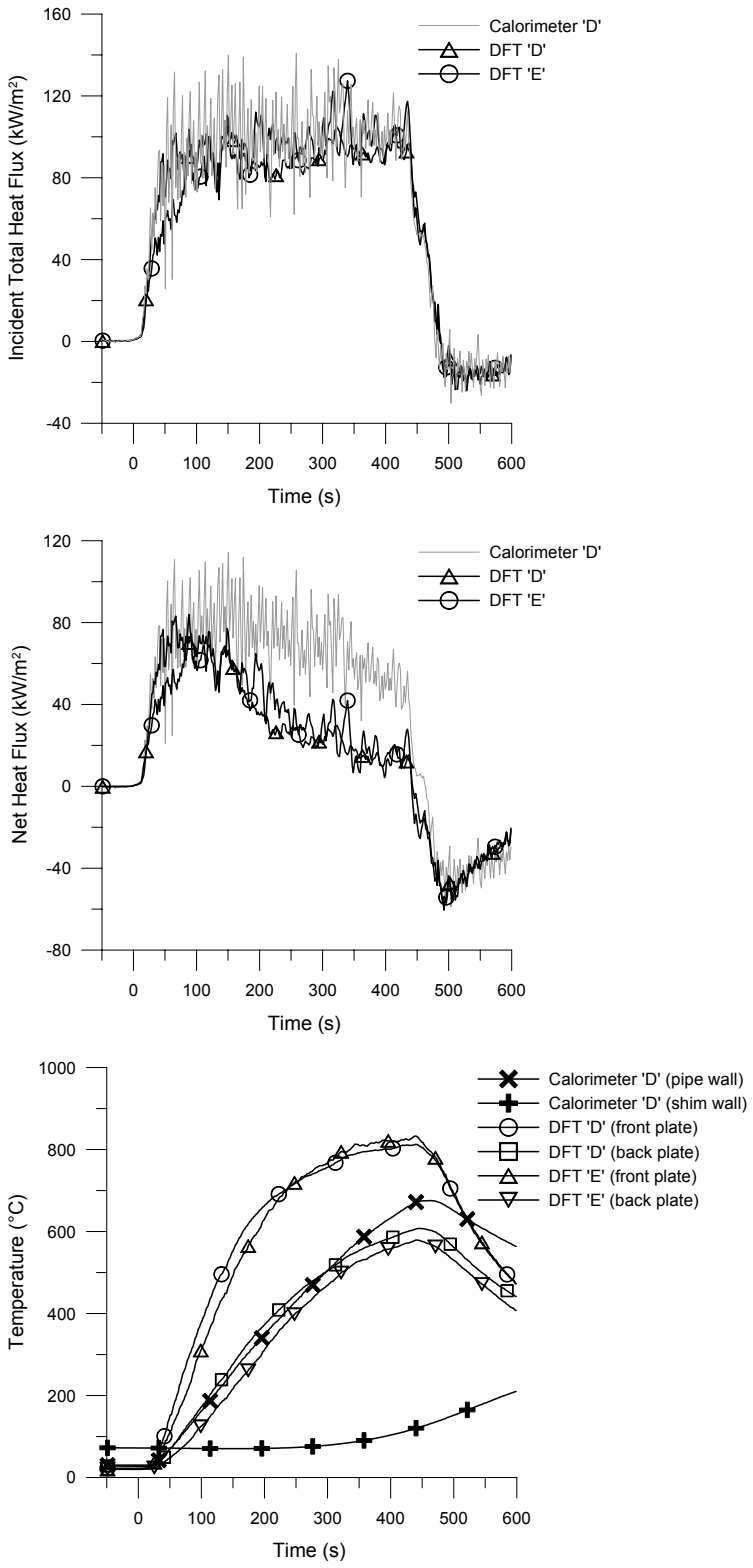

Figure I.1: Time trace of heat flux to calorimeter 'D' and neighbouring DFTs, with corresponding temperatures, 5 m/s wind (test 27)

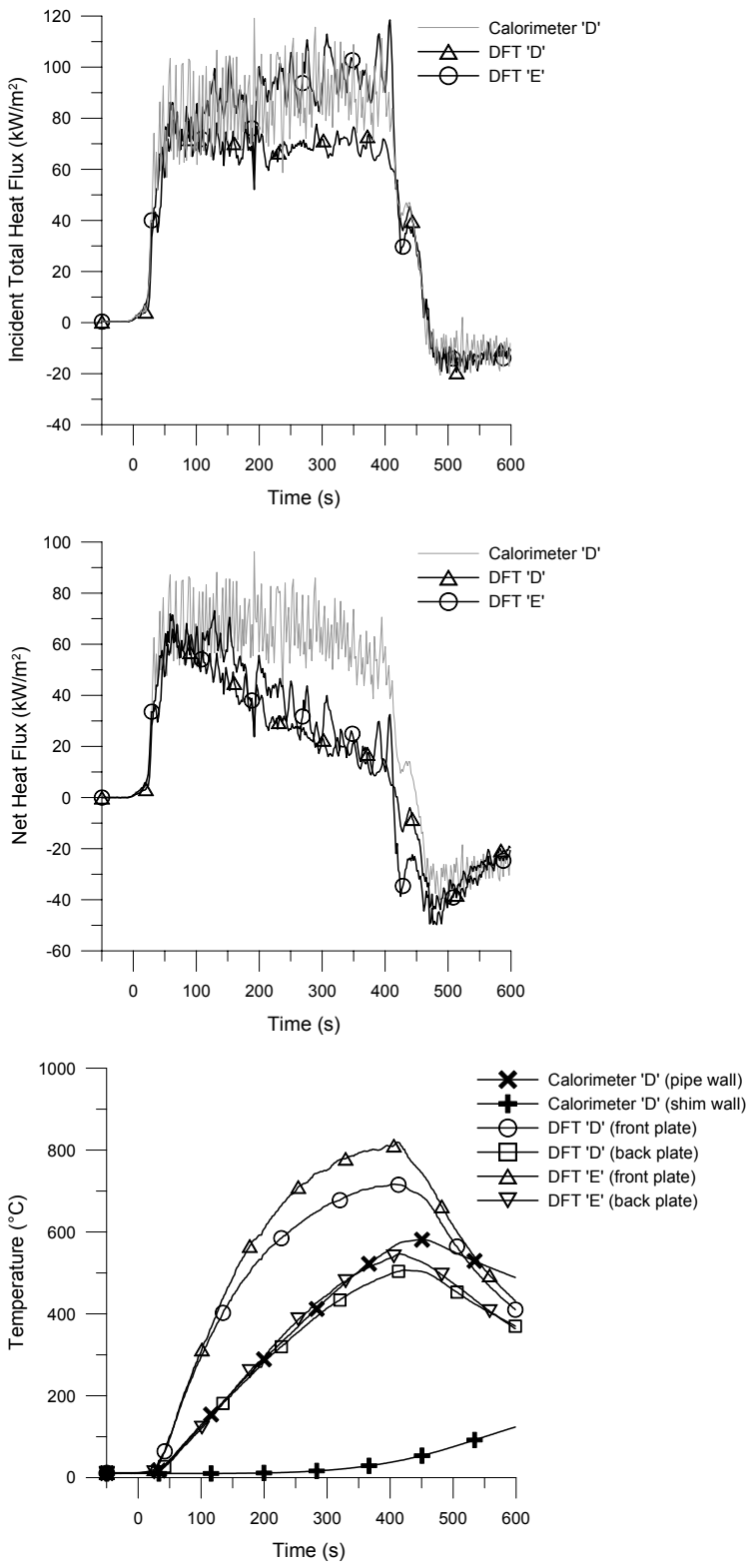

Figure I.2: Time trace of heat flux to calorimeter 'D' and neighbouring DFTs, with corresponding temperatures, 5 m/s wind (test 32)

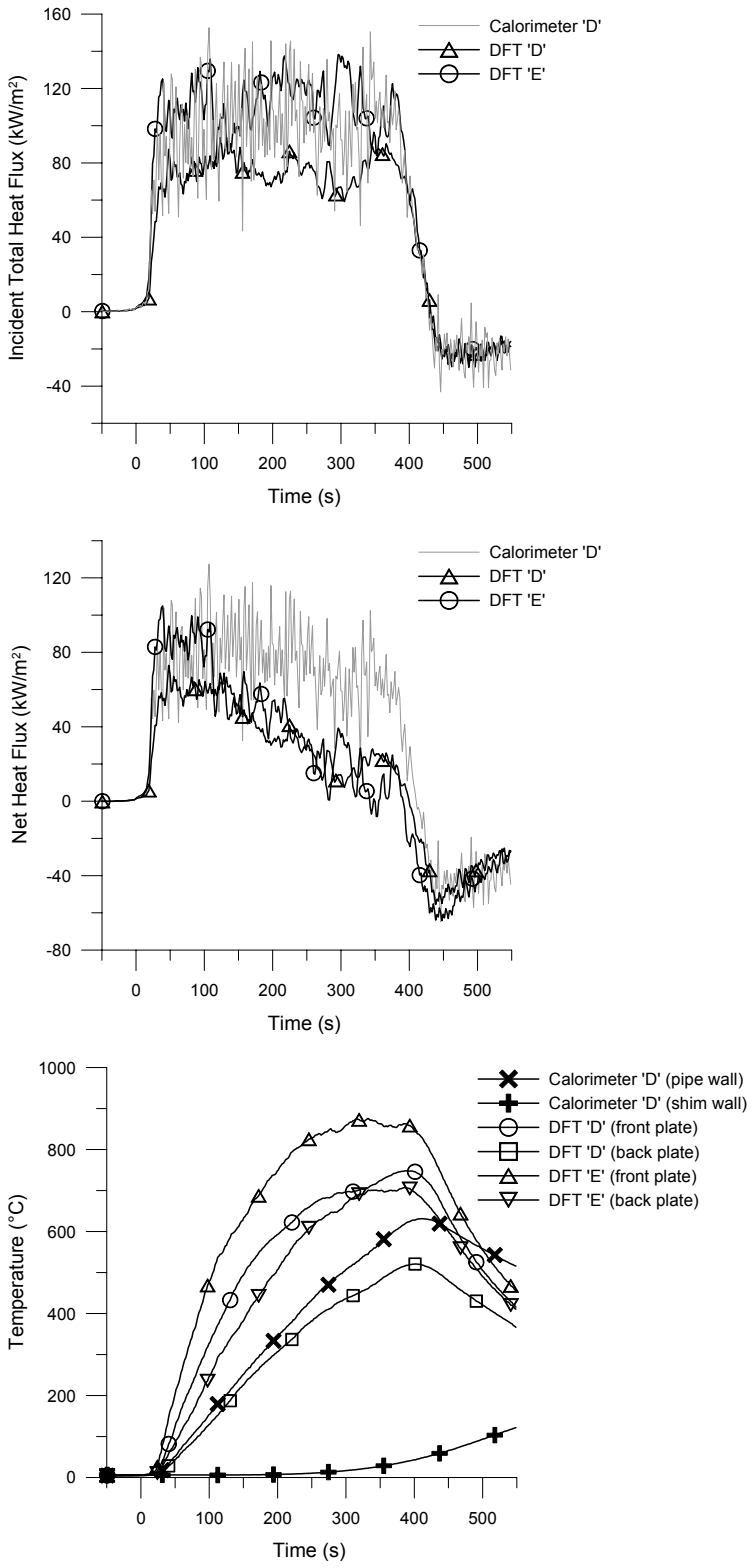

Figure I.3: Time trace of heat flux to calorimeter 'D' and neighbouring DFTs, with corresponding temperatures, 7 m/s wind (test 28)

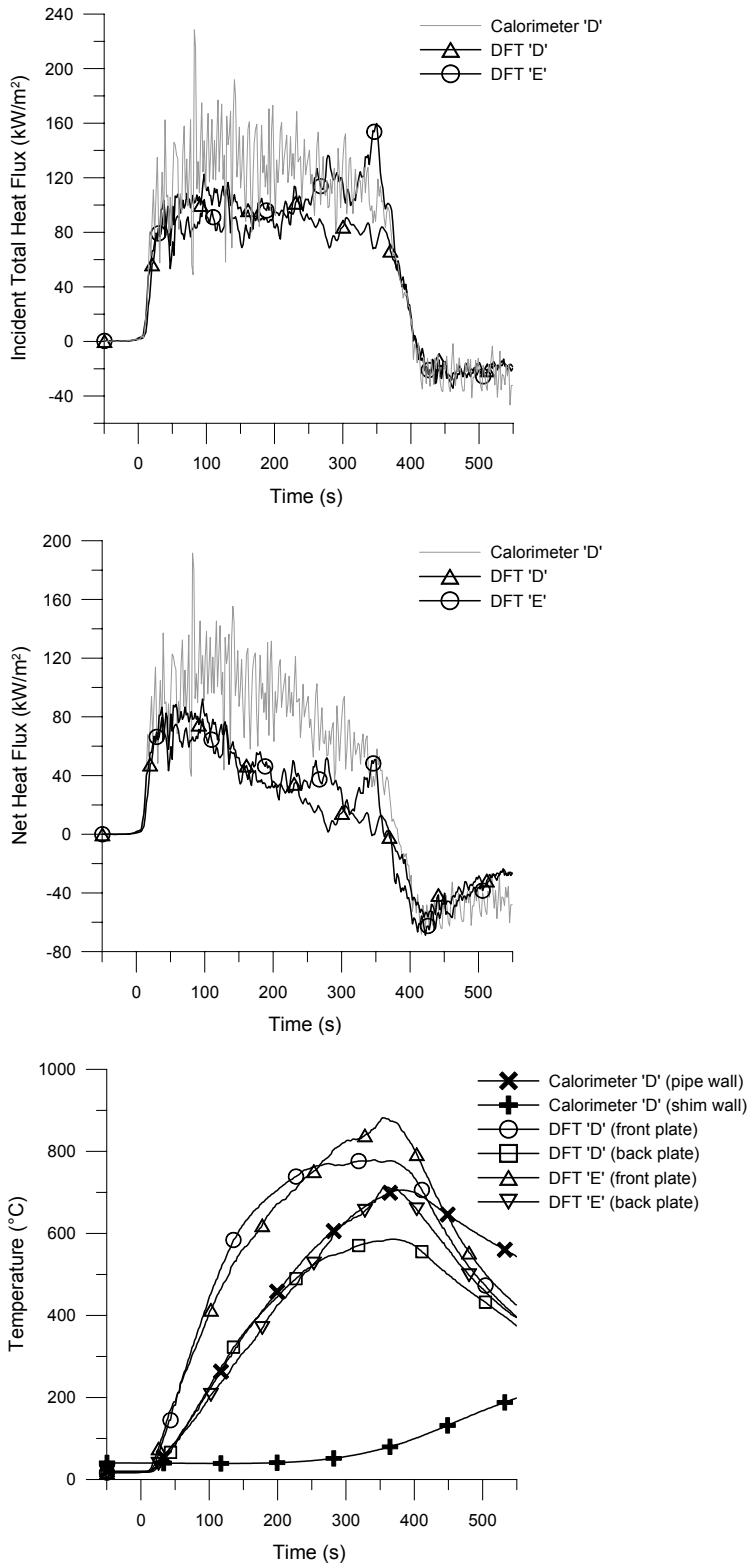

Figure I.4: Time trace of heat flux to calorimeter 'D' and neighbouring DFTs, with corresponding temperatures, 7 m/s wind (test 31)

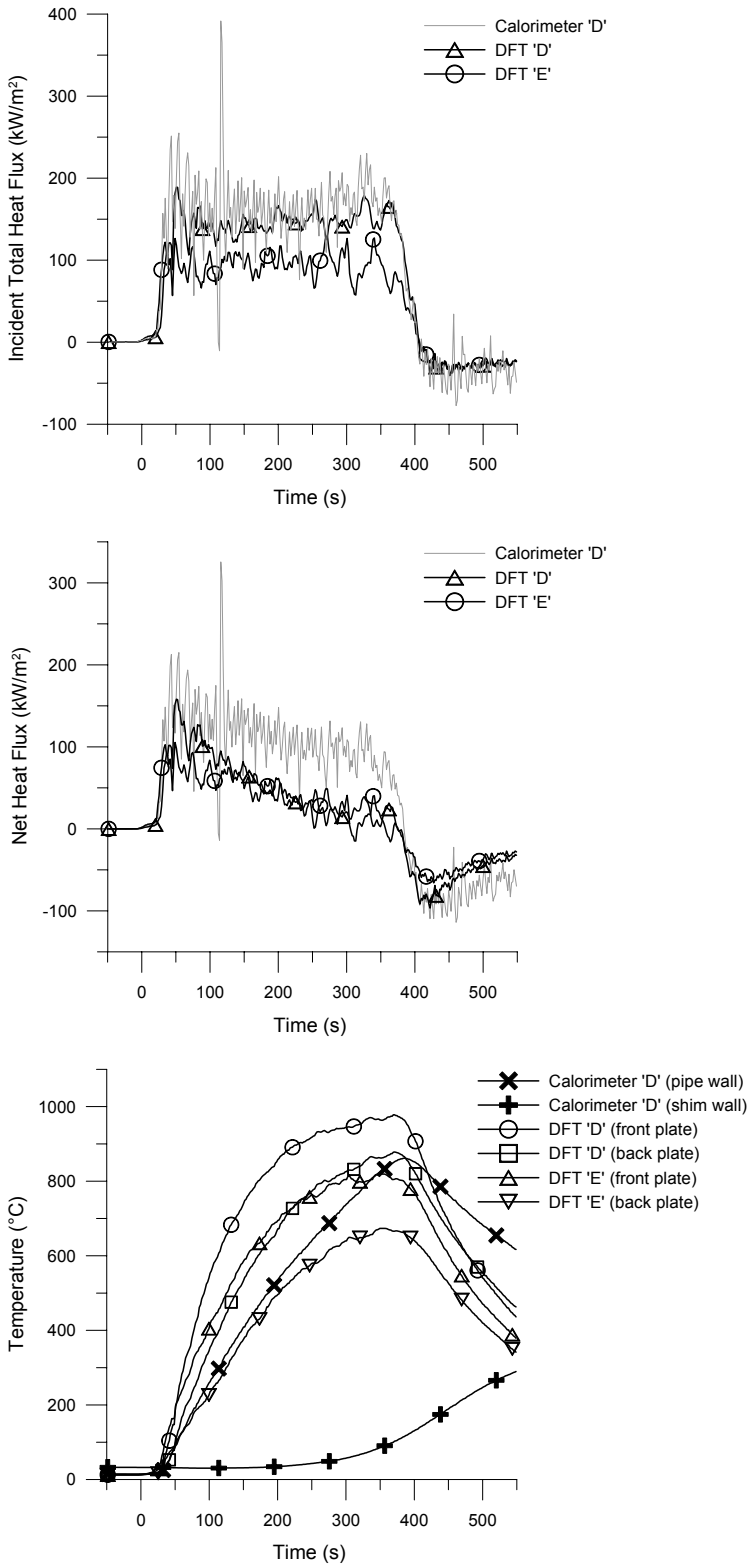

Figure I.5: Time trace of heat flux to calorimeter 'D' and neighbouring DFTs, with corresponding temperatures, 10 m/s wind (test 26)

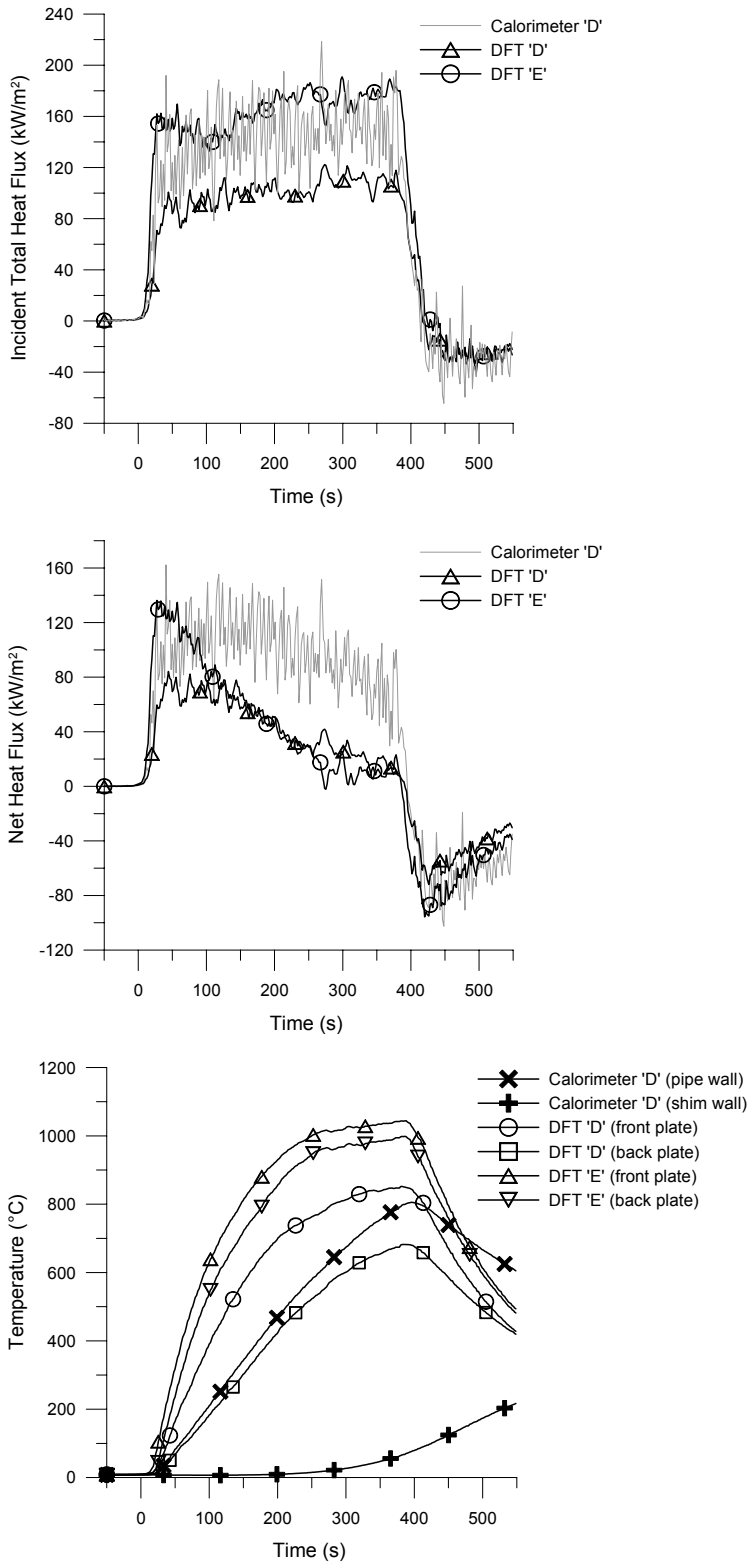

Figure I.6: Time trace of heat flux to calorimeter 'D' and neighbouring DFTs, with corresponding temperatures, 10 m/s wind (test 29)

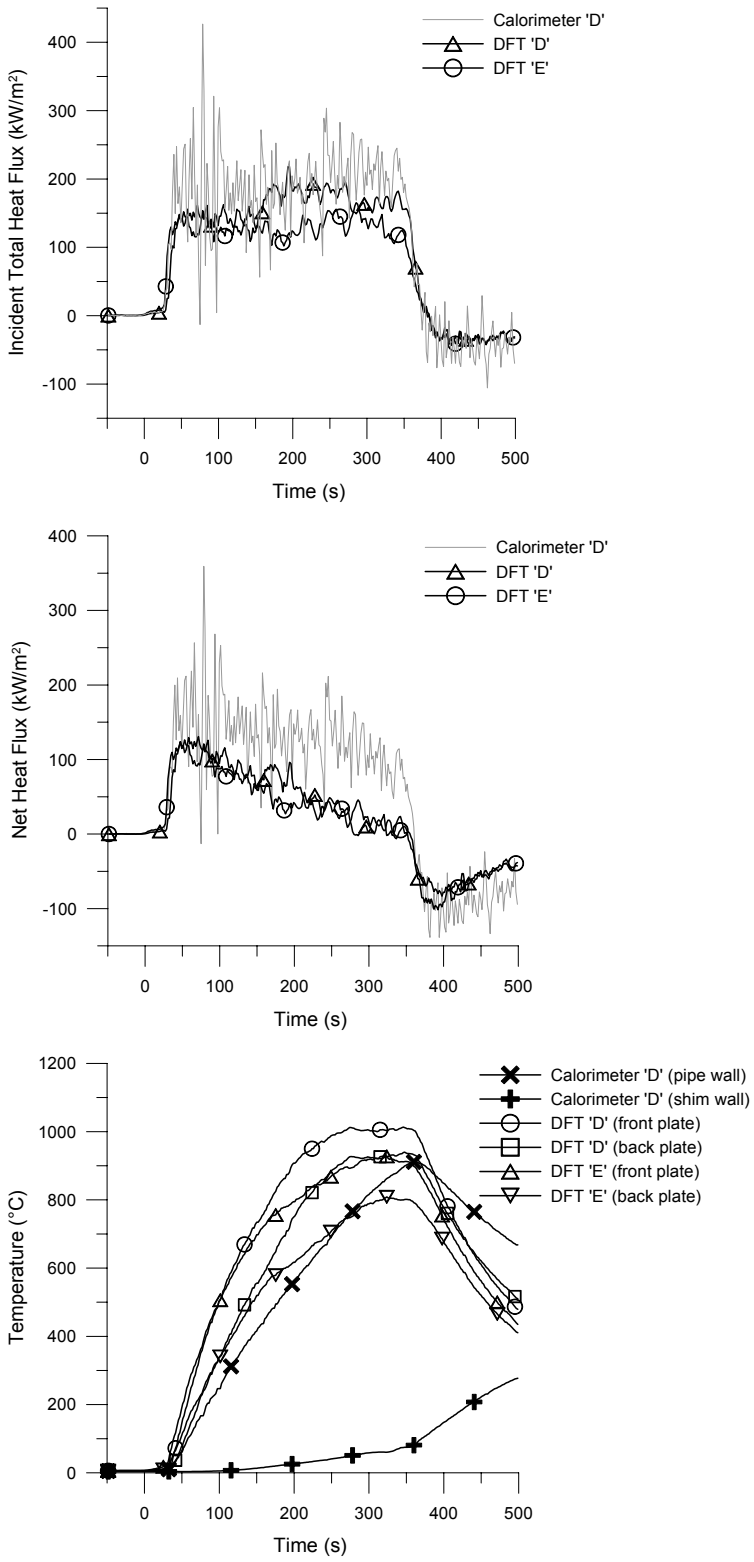

Figure I.7: Time trace of heat flux to calorimeter 'D' and neighbouring DFTs, with corresponding temperatures, 13 m/s wind (test 25)

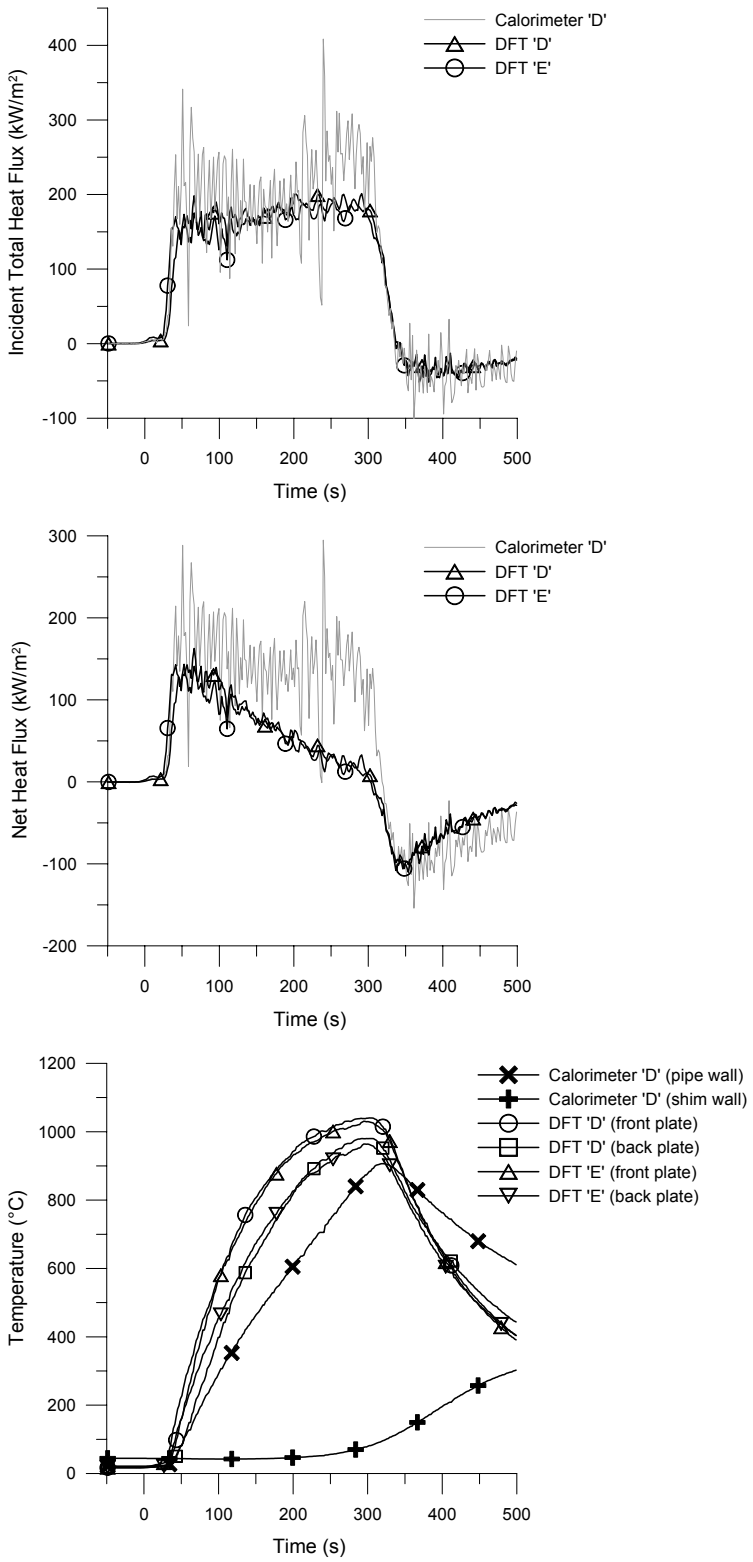

Figure I.8: Time trace of heat flux to calorimeter 'D' and neighbouring DFTs, with corresponding temperatures, 13 m/s wind (test 30)

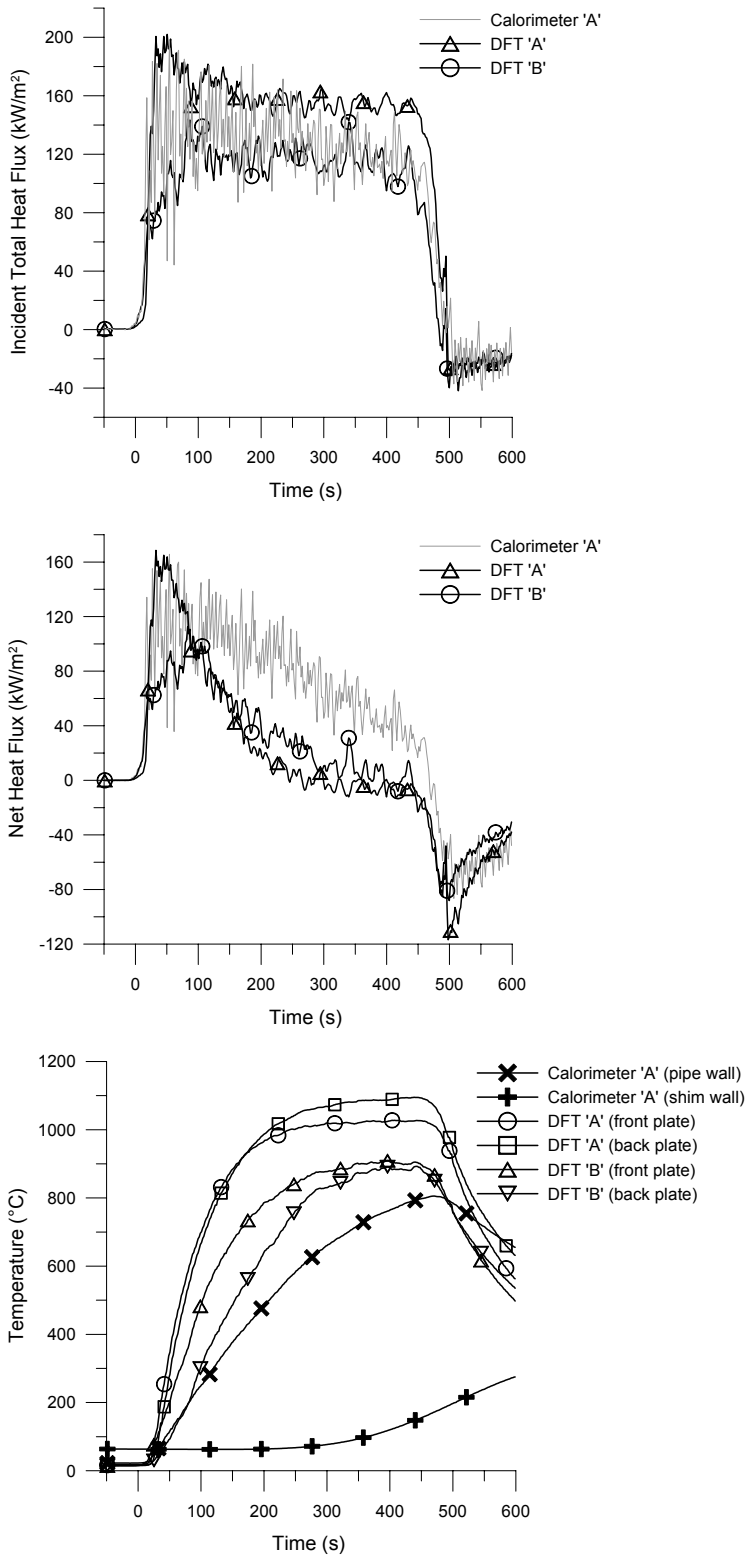

Figure I.9: Time trace of heat flux to calorimeter 'A' and neighbouring DFTs, with corresponding temperatures, 5 m/s wind (test 27)

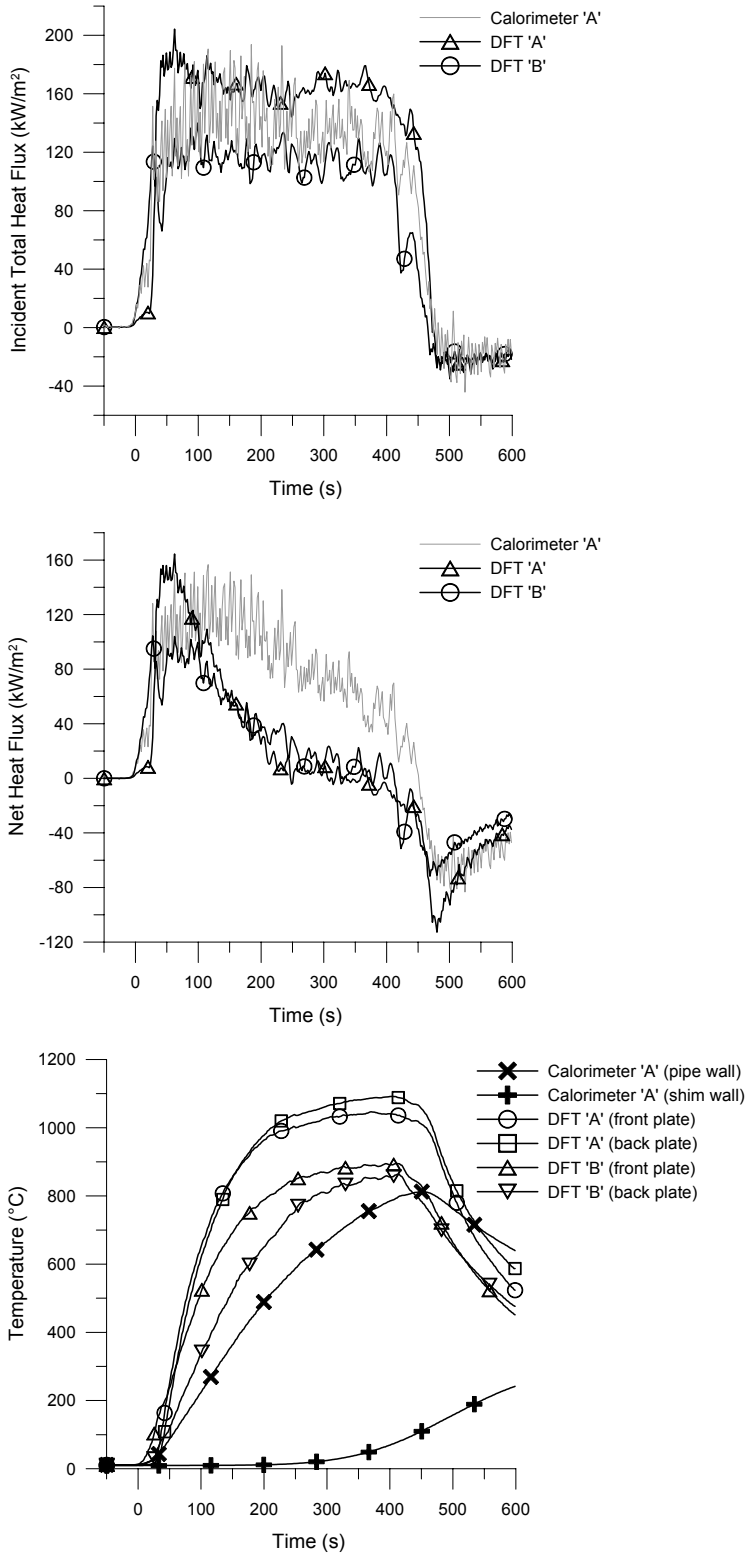

Figure I.10: Time trace of heat flux to calorimeter 'A' and neighbouring DFTs, with corresponding temperatures, 5 m/s wind (test 32)

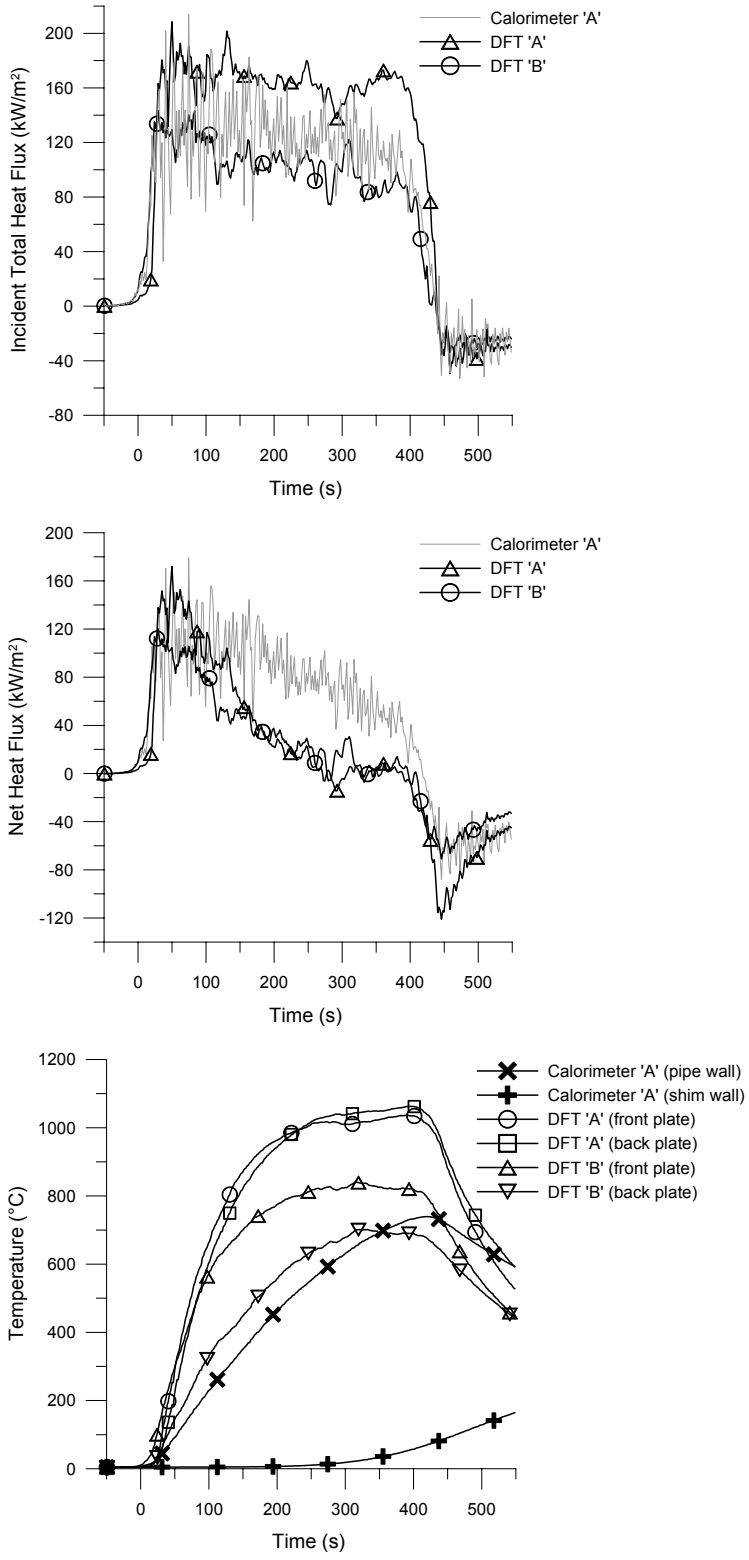

Figure I.11: Time trace of heat flux to calorimeter 'A' and neighbouring DFTs, with corresponding temperatures, 7 m/s wind (test 28)

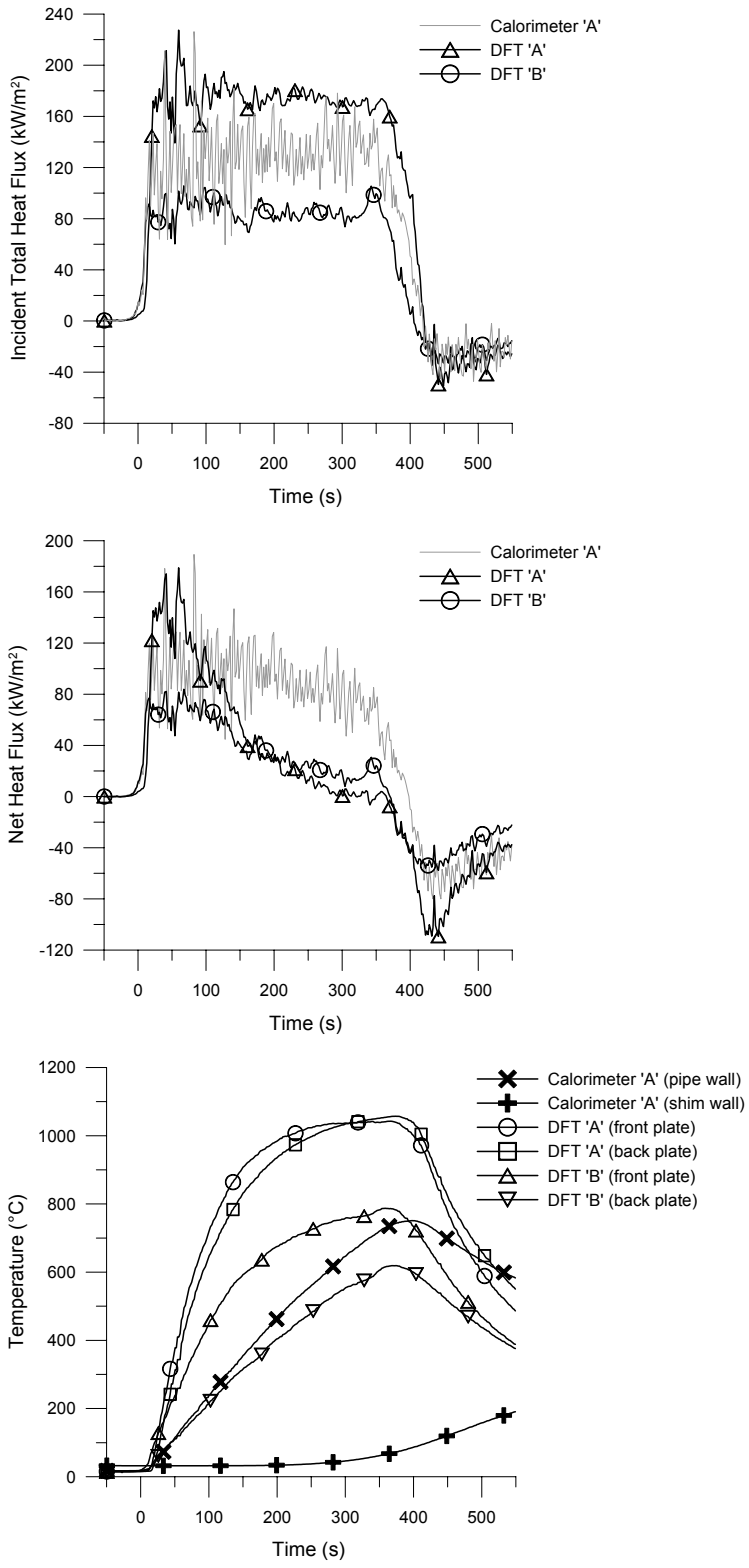

Figure I.12: Time trace of heat flux to calorimeter 'A' and neighbouring DFTs, with corresponding temperatures, 7 m/s wind (test 31)

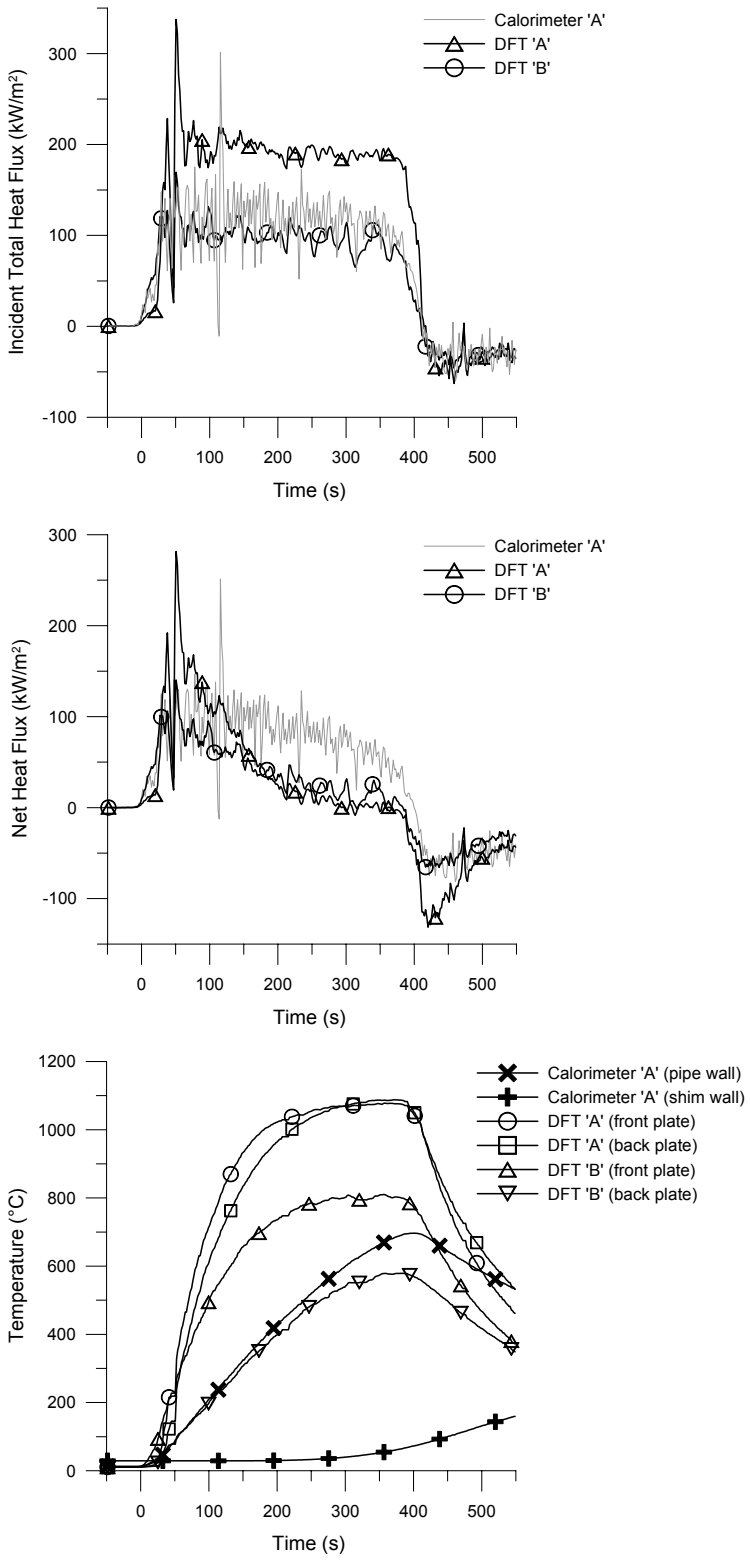

Figure I.13: Time trace of heat flux to calorimeter 'A' and neighbouring DFTs, with corresponding temperatures, 10 m/s wind (test 26)

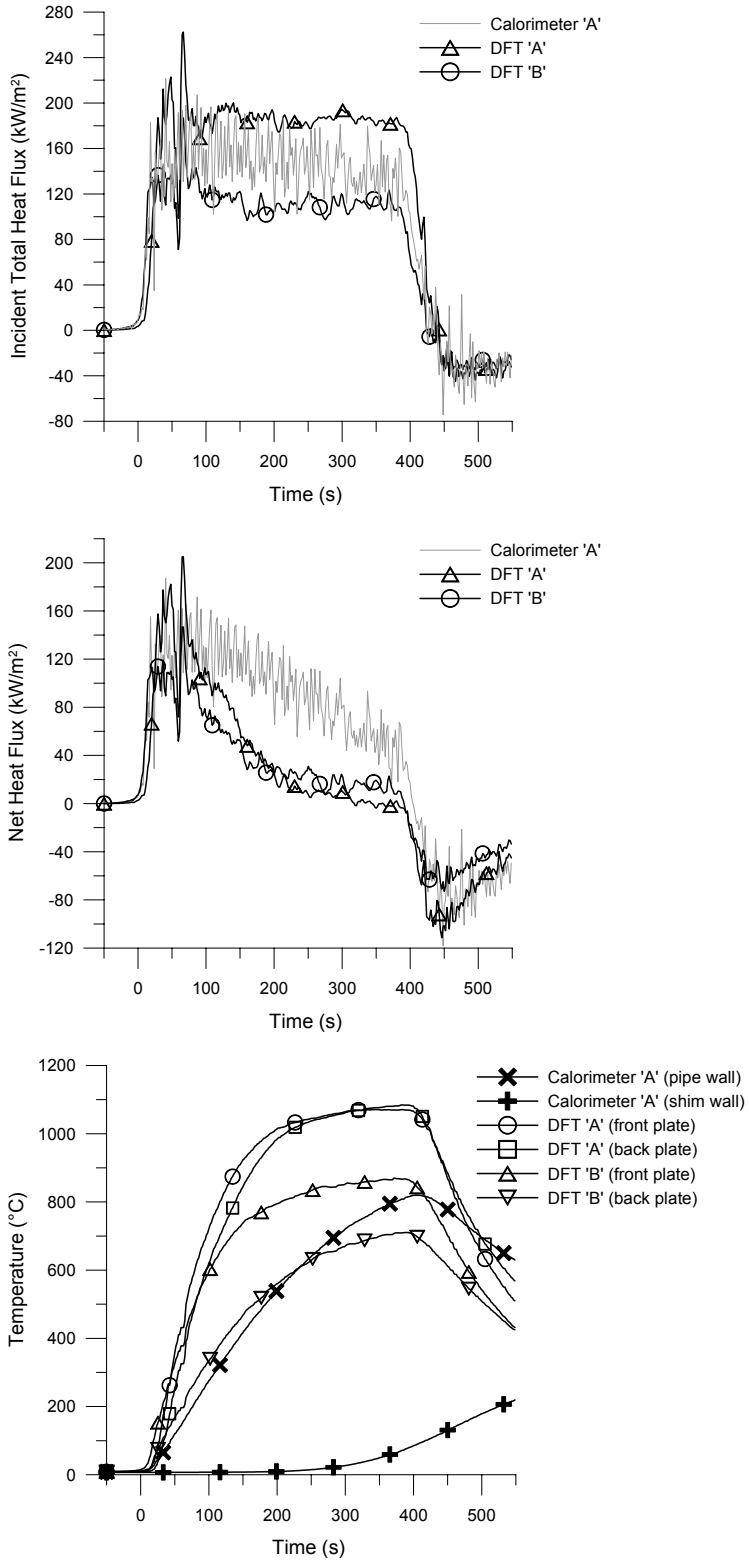

Figure I.14: Time trace of heat flux to calorimeter 'A' and neighbouring DFTs, with corresponding temperatures, 10 m/s wind (test 29)

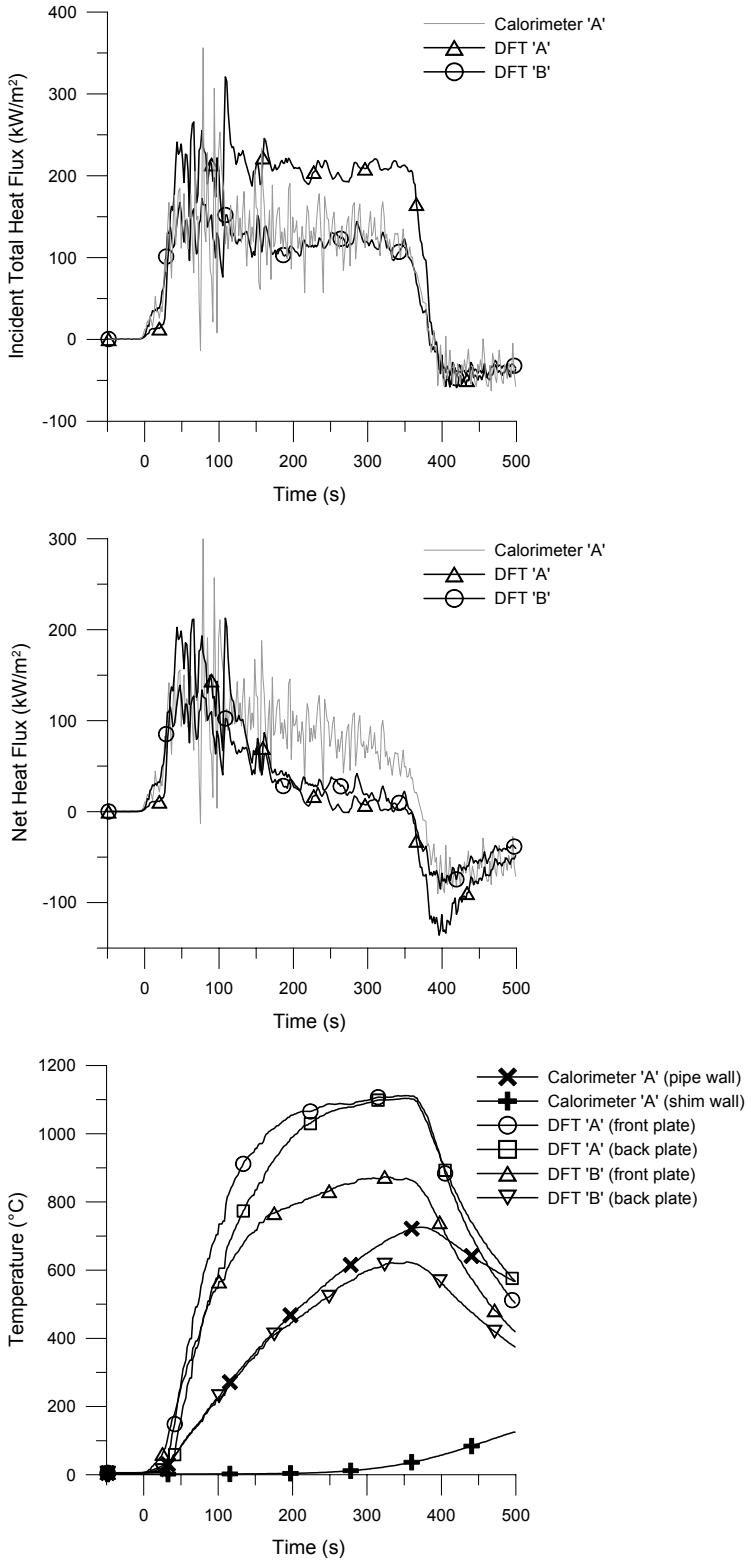

Figure I.15: Time trace of heat flux to calorimeter 'A' and neighbouring DFTs, with corresponding temperatures, 13 m/s wind (test 25)

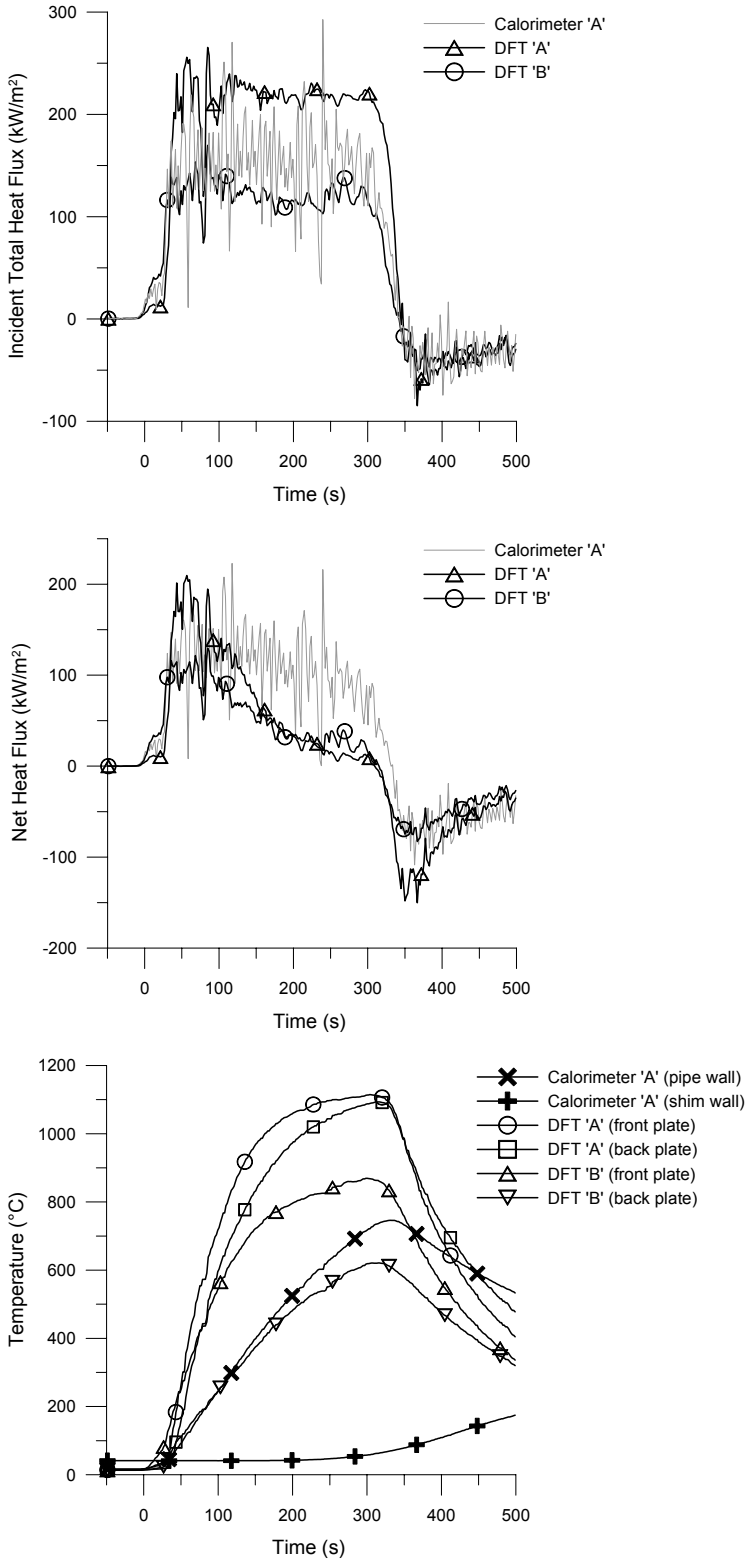

Figure I.16: Time trace of heat flux to calorimeter 'A' and neighbouring DFTs, with corresponding temperatures, 13 m/s wind (test 30)